NASA CONTRACTOR
REPORT

NASA CR-129009

S-II STAGE 1/25 SCALE MODEL BASE REGION THERMAL ENVIRONMENT TEST

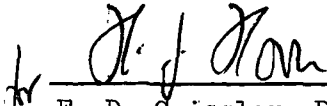## VOL. I: Test Results, Comparison with Theory and Flight Data

By J. A. Sadunas, E. P. French, and H. Sexton
Rockwell International Corporation
Space Division
Downey, California

May 1, 1973

Prepared for

NASA-GEORGE C. MARSHALL SPACE FLIGHT CENTER
Marshall Space Flight Center, Alabama   35812

1. REPORT NO. NASA CR-129009	2. GOVERNMENT ACCESSION NO.	3. RECIPIENT'S CATALOG NO.
4. TITLE AND SUBTITLE S-II Stage 1/25 Scale Model Base Region Thermal Environment Test Volume I: Test Results, Comparison with Theory and Flight Data		5. REPORT DATE May 1, 1973
		6. PERFORMING ORGANIZATION CODE
7. AUTHOR(S) J. A. Sadunas; E. P. French; H. Sexton		8. PERFORMING ORGANIZATION REPORT # SD73-SA-0061 Vol. I
9. PERFORMING ORGANIZATION NAME AND ADDRESS Rockwell International Corporation Space Division Downey, California		10. WORK UNIT NO.
		11. CONTRACT OR GRANT NO. NAS 7-200
12. SPONSORING AGENCY NAME AND ADDRESS National Aeronautics and Space Administration Washington, D. C. 20546		13. TYPE OF REPORT & PERIOD COVERED NASA Contractor Report
		14. SPONSORING AGENCY CODE

15. SUPPLEMENTARY NOTES

Volume II is NASA CR-129010

16. ABSTRACT

A 1/25 scale model S-II stage base region thermal environment test conducted at George C. Marshall Space Flight Center is presented. Analytical results are included which reflect the effect of engine operating conditions, model scale, turbo-pump exhaust gas injection on base region thermal environment. Comparisons are made between full scale flight data, model test data, and analytical results. The report is prepared in two volumes. Volume I presents the description of the test equipment, test procedures, discussion of the test results, analytical predictions and comparisons with flight data. Volume II contains the tabulation of the test data.

17. KEY WORDS Base heating, reverse flow Plume interaction, short duration model testing	18. DISTRIBUTION STATEMENT Unclassified - Unlimited E. D. Geissler, Director Aero-Astrodynamics Laboratory		
19. SECURITY CLASSIF. (of this report) Unclassified	20. SECURITY CLASSIF. (of this page) Unclassified	21. NO. OF PAGES 325	22. PRICE NTIS

MSFC - Form 3292 (May 1969)

FOREWORD

This report is submitted by the Rockwell International Corporation, Space Division to the National Aeronautics and Space Administration's George C. Marshall Space Flight Center at Huntsville, Alabama, in accordance with Task Authorization TA-68 issued persuant to NASA Contract NAS7-200.

This report presents the results of the 1/25 scale model S-II Stage base region thermal environment test conducted at MSFC under the direction of the Aero-Astrodynamics Laboratory with test engineering support provided by Space Division.

Analytical results are presented which reflect the effect of engine operating conditions, model scale, turbo-pump exhaust gas injection in the engine nozzle, and co-planar engine gimballing on the S-II base region thermal environment. Comparisons are made between full scale flight data, model test data, and the analytical results.

This report is prepared in two volumes. Volume I presents the description of the test equipment, test procedures, discussion of the test results, analytical predictions and comparisons with flight data. Volume II contains the tabulation of the test data.

The task activities were conducted with Mr. J. A. Sadunas, Task Manager, Dr. E. P. French, and Mr. H. Sexton, the responsible engineers from the Saturn Launch Vehicles Aerothermodynamics group, and Mr. D. C. Seymour as the technical coordinator for the Marshall Space Flight Center.

The authors wish to acknowledge the cooperation and valuable suggestions contributed by Messrs. D. C. Seymour and R. F. Elkin of S&E-Aero-Astrodynamics Laboratory and John Reardon of REMTECH, Inc.

CONTENTS

CONTENTS (Cont'd)

CONTENTS (Cont'd)

5.12.4 Determination of Pressures Within
        the Pitch Circle 187
5.12.5 Effect of Boundary Layer on the Base
        Region Environment 187
5.12.6 Nozzle Flow Symmetry Tests 187
5.12.7 Environment of the Inoperative
        Center Engine Nozzle 195
5.12.8 Incident Radiative Heat Flux to the
        Base Region 195

6.0 COMPARISON WITH ANALYTICAL PREDICTIONS 200

6.1 Methodology of Base Flow Analysis 200

     6.1.1 Definition of the Inviscid Flow
            Field in the J-2 Nozzle 201
     6.1.2 Nozzle Boundary Layer Calculations 203

            6.1.2.1 Thermodynamic Properties 203
            6.1.2.2 Transport Properties 204
            6.1.2.3 TPE Injection Effects 204
            6.1.2.4 Boundary Layer Calculation
                     Results 206

     6.1.3 Definition of Plume Flow Field 206

            6.1.3.1 Application of Shock Capturing
                     to the Plume Problem 210
            6.1.3.2 Typical Plume Property
                     Distributions for 1/25
                     Scale Model 212
            6.1.3.3 Property Distributions for
                     Full Scale Plumes 217

     6.1.4 Definition of the Impingement Flow
            Field 217

            6.1.4.1 Impingement Properties Based
                     on Newtonian Theory 217
            6.1.4.2 Flow Reversal After Impingement. . 217

     6.1.5 Description of the Base Flow Field 221

            6.1.5.1 Off-Axis Impingement Effects . . . 221
            6.1.5.2 An Analytical Heat Transfer
                     Parameter 223

CONTENTS (Cont'd)

CONTENTS (Cont'd)

LIST OF FIGURES

LIST OF FIGURES

LIST OF FIGURES

LIST OF FIGURES

SD73-SA-0061

LIST OF FIGURES

Page

LIST OF FIGURES

LIST OF FIGURES

Page

LIST OF TABLES

NOMENCLATURE

b	Concentration boundary layer thickness
C	Specific heat
C_P	Specific heat
C_{PQ}	Specific heat of quartz
CECO	Center engine cut-off
E	Thermoelectric potential gradient
f_{rad}	Low-to-high frequency radiation ratio
h	Convective heat transfer coefficient
h	Static enthalpy
H_o	Total enthalpy
h_{r1}	Air gap conductance due to radiation
h_{r2}	Conductance for quartz radiation to surroundings
I_o	Modified Bessel function of the first kind, zero order
I_1	Modified Bessel function of the first kind, first order
k	Conductivity
k_A	Conductivity of air
k_Q	Conductivity of quartz
M	Mach number
MPI	Main propellant ignition
Nu	Nusselt number
O/F	Oxidant to fuel ratio by weight
OECO	Outboard engine cut-off

SD73-SA-0061

NOMENCLATURE

P	Pressure
P_B	Base Pressure
P_c	Combustion Chamber Pressure
P_r	Prandtl Number
P_o	Total Pressure
PMR	Propellant mixture ratio, in combustion chamber
PMRS	PMR shift
Q	Heat flux
q	Dynamic pressure
q_{p1}	Short wave radiation; transmitted by radiometer quartz lens
q_{p2}	Long wave radiation; absorbed by radiometer quartz lens
r	Radius
Re	Reynolds Number
R_s	Total calorimeter gage sensor radius
R^*	Rocket nozzle throat radius
S	Gage slope in linear range
SPS	Second plane separation (S-IC/S-II stage interstage separation)
T	Temperature
t	Time
T_B	Calorimeter body temperature
T_F	Calorimeter foil temperature
T_G	Gas recovery temperature

SD73-SA-0061

NOMENCLATURE

T_Q	Radiometer quartz window temperature
T_R	Recovery temperature
T_S	Temperature of the surroundings (space)
T_W	Wall temperature
T_O	Total temperature
T_{AW}	Adiabatic wall temperature
TPE	Turbo-pump exhaust
U	Velocity
V	Velocity
X	Distance from J-2 engine exit plane

α	Absorptivity
β	Nozzle gimbal angle
β	Parameter in transient curve fit
$\bar{\beta}$	Average deflection of adjacent outboard engines towards each other in the pitch or yaw planes
γ	Ratio of specific heats
δ	Thickness, calorimeter sensor foil
δ	Velocity boundary layer thickness
δ_A	Thickness of air gap
δ_Q	Thickness of quartz window
θ	Stage azimuth angle
θ	Plume flow angle

SD73-SA-0061

NOMENCLATURE

θ_p	Gimbal angle, pitch plane
θ_y	Gimbal angle, yaw plane
μ	Viscosity
ν	Kinematic viscosity
ρ	Density
ρ_Q	Density of quartz
σ	Stefan-Boltzmann constant

SD73-SA-0061

1.0   INTRODUCTION

The purpose of this report is to document the results of the 1/25 scale S-II Stage base heating model test program conducted at Marshall Space Flight Center's (MSFC) Impulse Base Flow Facility. Comparisons are made between the test results, analytical predictions, and flight data in order to provide the basis for a more refined S-II base region thermal environment prediction methodology required to support S-II-14 Stage potential missions and design changes.

Base heating occurs when rocket engine exhaust plumes are highly expanded with the result that, for multi-engine configuration vehicles, plume interactions cause a small portion of the high temperature exhaust gases to be reversed to the base region as shown in Figure 1.0-1. Radiative heating is also present due to radiative heat transfer from the gaseous exhaust plumes.

HEAT SHIELD

REVERSED MASS FLOW

HIGH PRESSURE PLUME INTERACTION REGION
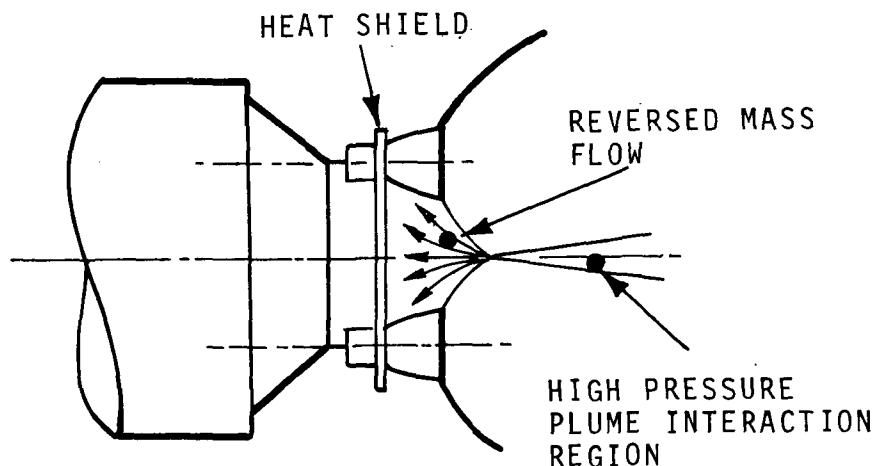
Figure 1.0-1   Exhaust Plume Interaction and
Reversed Flow Base Heating

As a result of this, it is necessary to provide extensive insulation for the engines and base region structural components in order to protect them from the severe base region thermal environment.

Analytical methods are available for predicting gaseous plume radiation with sufficient accuracy for design purposes. On the other hand, the complexity of the plume reversal heating phenomenon precludes analytical predictions of base heating with the degree of certainty required for design of the base region insulation systems.

During the design and development phase of the S-II Stage, numerous scale model, hot flow, base heating tests were run at Cornell Aeronautical Laboratories (CAL) and at the MSFC Impulse Base Flow Facility. The CAL test program, conducted during the period 1962 through 1963, included a great amount of parametric data on the effects of engine spacing, heat shield location, engine deflection, heat shield edge modification, turbo-pump gas injection into the J-2 nozzles, and the effect of S-II/S-IC interstage on S-II base region heating rates. These tests provided the necessary data for preliminary design of the major base region thermal protection systems. S-II prototype configuration base region thermal environment data were also generated in the later part of the test program. The development of the short duration test techniques, instrumentation, and the test results obtained at CAL are well documented in numerous reports; for example, References 1 through 4, also References 7, 8, and 11.

In April 1964, the S-II base model was moved from CAL to the larger altitude simulation chamber at MSFC where it was possible to extend the steady state test duration period from 3-4 milliseconds to 6-7 milliseconds. Numerous additional tests were performed at MSFC to provide heating rate data for specific gimbal patterns and off-nominal design conditions, e.g., outboard-engine-out, single-actuator-failure, and dual-actuator-failure. Effects of engine mixture ratio, structural compliance, and engine misalignment on base region heating rates were also studied.

The results of the MSFC tests were not documented at the completion of the test program.

The report is prepared in two volumes. Volume I presents the description of the test equipment, test procedures, discussion of the test results, analytical predictions, and comparisons with flight data. Volume II contains the test data tabulation and statistical analysis results. Heat shield constant heating rate contour plots are also presented for most of the test runs.

2.0 SUMMARY

The S-II Stage 1/25 Scale model tests conducted at the MSFC Impulse Base Flow Facility were successful in providing base region thermal environment data for numerous off-nominal flight conditions as well as basic parametric data on engine mixture ratio and chamber pressure variation effects on the base region thermal environment.

The short duration test technique provided data of reasonably good repeatability; the standard deviation of the mean for a typical test condition being approximately 7 percent for the heat shield heating rates, 12 percent for the thrust cone heating rates, and 5 percent for the heat shield pressures. Nozzle adaptor leakage forward of the heat shield occurred on some runs which adversely affected the quality of the thrust cone data.

Gas recovery temperature measurements, using the heated component technique, were unsuccessful. The single apparently good test case indicated gas recovery temperatures considerably below the values obtained during the CAL S-II model test program and the analytically derived values.

The results of the parametric tests were generally in agreement with CAL test data and analytical results. For example, it was determined that heat shield heating rates are proportional to chamber pressure, heat shield pressures vary as chamber pressure to the 1.3 power, while the thrust cone heating rates show a stronger dependence on chamber pressure with the values of the exponent varying from 1.5 to 2.6. The model test data showed that the effect of simultaneously varying mixture ratio and chamber pressure on the base region environment was the same as the effect of varying chamber pressure with the mixture ratio held constant.

The altitude effect test data showed a large degree of scatter, with no discernable effect within the test range of 240 to 300 thousand feet.

Tests of the S-IC/S-II interstage effects showed that the heat shield peak heating rates were unaffected by the interstage. Some increase occurred at the heat shield minimum vent area location with the interstage on. The interstage-on thrust cone heating rates and pressures, on the other hand, increased by an order of magnitude from the corresponding interstage-off values.

The nominal base region environment test results are in good agreement with those obtained in the CAL test program. The peak test average heating rate of 5.65 Btu/ft^2-sec was measured on the heat shield centerline outside the minimum vent area location. The corresponding

thrust cone value of 0.11 Btu/ft^2-sec occurred at a point midway between the outboard engines on the thrust cone closeout, Station 196, with the interstage off. With the interstage on, the peak thrust cone heating rate shifts to Station 140 and increases to 1.55 Btu/ft^2-sec. The peak interstage heating rate of 7.9 Btu/ft^2-sec was measured at Station 0. Subsequent tests showed that all the engine deflections associated with the off-nominal flight conditions cause a reduction of the interstage heating rates from the nominal value.

The engine nozzle nominal external heating rates were determined to be lower than the heat shield heating rates. The center engine is subjected to the highest heating with the peak value of 3.5 Btu/ft^2-sec which is more than double the corresponding outboard engine value.

The model test data showed that the base region heating rates are very sensitive to engine deflections. For example, the outboard-engine-out gimbal deflections almost double the heat shield nominal peak heating rate.

The outboard-engine-out engine deflections cause the peak thrust cone heating rate to increase by a factor of three. The external heating rates to the inoperative outboard engine were found to be lower than the nominal values with and without deflection of the inoperative engine.

The single-actuator-failure-inboard condition gimbal pattern 3C (Figure 5.8.1) produced the highest heating rates of the test program (excluding nozzles); the peak test average value was 29.8 Btu/ft^2-sec and occurred on the flexible curtain. Also, this condition causes the center engine nozzle external heating rates to increase by an order of magnitude.

The single-actuator-failure-outboard condition produces increased heating rates to the heat shield and thrust cone regions. However, they are less severe than those resulting from other off-nominal flight conditions.

The maximum rigid-heat shield heating rate of 22 Btu/ft^2-sec occurred with the dual actuator failure inboard engine deflection Case 4A-a (Figure 5.10-1) which also produced heating rates to the flexible curtain almost equal to the peak values measured with the single actuator failure inboard deflections. The dual actuator failure inboard condition produces extremely high heating rates to the center engine nozzle. A peak value of 350 Btu/ft^2-sec was measured with the 7.5° engine deflection pattern.

The small engine deflections of the nominal trim and structural compliance gimbal patterns tested were found to have significant effect on the base region thermal environment. For example, engine deflection Case 9 increased the peak heat shield heating rate by 60 percent and the peak thrust cone value by 50 percent from the corresponding nominal values.

The analytical results of the exhaust gas reverse flow phenomenon show that considerable differences exist between the model and full scale nozzle boundary layer temperature and velocity profiles. TPE injection is shown to have a very important effect in reducing heat shield recovery temperatures and heating rates and it explains in part the reason for the discrepancy between full scale flight and model heating rates.

The analytical results of the engine operating parameter study were generally in agreement with the scale model test results showing that the reversed flow pressures and heating rates are approximately proportional to chamber pressure. Unlike the scale model test, the analytical results showed that simultaneous variation of mixture ratio and chamber pressure (which corresponds to S-II flight condition) has a stronger effect on the base region heating rates and pressures than the variation of chamber pressure alone with mixture ratio held constant. The effect of co-planar gimballing was shown to increase significantly the stagnation pressure of the reverse flow, but have little effect on the reversed flow stagnation temperature. Consequently, the analytically derived increase of heating due to gimballing is not as strong as indicated by the model data.

The analytically predicted gas recovery temperature values were in excellent agreement with the model test results of the CAL test program, while the flight gas recovery temperature, including TPE injection effects, is overpredicted by about 900 F.

Comparison of the scale model heat shield test results with full scale flight data shows that, whereas the heating rate distribution trends are in agreement, the model convective heating rates are 2.4 times the flight values. The difference is due to TPE injection into the nozzle, which was not simulated in this test program, and to scaling effects. Reasonably good correlation could be obtained between flight and model heat shield heating rates by using the analytically predicted reverse flow bulk properties for the model and full scale conditions together with the 0.2 power turbulent flow scaling factor to account for scaling.

The flight thrust cone heating rate distribution with the interstage off was different from the model distribution, with the flight heating rates being higher at most locations than the corresponding model values. However, the peak heating rates measured during flight and the model tests were approximately the same. These results are opposite to those obtained for the heat shield. Furthermore, with the interstage on, the flight thrust cone heating rates were slightly lower than the model test values. These observed differences between the model test and flight thrust cone heating rates are attributed to the external flow field which exists only during flight. This flow field influences the reverse flow expansion process and hence the thrust cone environment.

The flight heat shield pressures were determined to be double the corresponding model values, while flight thrust cone interstage-on pressures were 10% higher than the model values.

SD73-SA-0061

Model data was not available to determine the effect of center engine cut-off (CECO) during flight on the base region environment. The analytical results predict an increase of gas recovery temperature and a decrease of base pressures which is in agreement with flight data. The heating rate parameter, formulated in the analytical section, fails to predict the increase of base region heating rates which occurs after CECO. However, the analytical results indicate that a significant increase of reverse mass flow occurs at this time. Therefore, formulation of an alternate heating rate parameter, based on the reverse mass flow, would show an increase in heating after CECO.

The effect of PMR shift on base region flight heating rates, recovery temperature, and heat shield pressures was found to be in reasonably good agreement with the PMR shift effect indicated by model test results and analytical considerations.

The data derived from these base region tests were used to define the design thermal environment of the S-II Stage which, to date, has flown twelve successful Apollo/Saturn missions. More recently, these test results were used in the redesign of S-II-13 Stage (Skylab) heat shield flexible curtain.

3.0 TEST EQUIPMENT

The tests were conducted at the MSFC's Impulse Base Flow Facility. A detailed description of this facility is given in Reference 5 from which the following facility description is abstracted.

3.1 HIGH ALTITUDE FACILITY

The Impulse Base Flow Facility (IBFF) consists of a vacuum tank, a vacuum pumping system, a model with supply tubes, a gas-handling system, a control system, and the required instrumentation. The physical layout is shown in Figure 3.1-1. The vacuum tank is set into a pit so that the model is inserted into the tank on its centerline at a convenient height, about 49 inches from the floor. Figure 3.1-2 shows the model port area in detail.

The altitude simulation chamber consists of a mild steel tank, 18 feet in diameter and 26 feet long. Two blind flanges 180° apart and on the centerline are available for special-purpose instrumentation access into the tank. A manhole is also provided for personnel access into the tank. The chamber may be evacuated to a 5×10^{-4} torr or pressurized to 100 psig. Pertinent dimensions of the chamber are given in Figure 3.1-2.

Evacuation of the chamber is in three phases:

a. Equalization of the 5,600 cubic foot chamber with a 42,000 cubic foot vacuum field to 15 mm Hg

b. Evacuation from 15 mm Hg to 50 μHg by means of a mechanical vacuum pump and a blower booster

c. Evacuation by an oil diffusion pump from 50 μHg to 0.5 μHg.

Chamber evacuation time is plotted for each phase in Figure 3.1-3.

A typical gas-handling flow schematic is shown in Figure 3.1-4. Normally, all gas is stored in standard compressed-gas cylinders. However, if large quantities of gas are required, larger storage containers are available. The model charge tube is pressurized through flow path "A" by bleeding gas from the storage cylinder. This technique applies as long as the charge tube pressure is below the cylinder pressure. Should the required charge tube pressure exceed the cylinder pressure, flow path "B" is used. Nonlubricated, air-operated compressors are used to pump up to pressures of 5,000 psi. Fuel and oxidizer gases are completely separated and use independent flow paths.

SD73-SA-0061

Figure 3.1-1 General Layout of MSFC's Impulse Base Flow Facility

1. 4" 500 PSI AIR LINE
2. INSTRUMENTATION RACK
3. CONTROL PANEL
4. MODEL
5. DIFFUSION PUMP
6. OXYGEN SUPPLY SYSTEM
7. HYDROGEN SUPPLY SYSTEM
8. OFFICE
9. VACUUM PUMP
10. MODEL ASSEMBLY AREA

MANHOLE

VACUUM TANK (6,000 CU FT)

BLIND FLANGE

GAS CYLINDER STORAGE

VACUUM FIELD 42,000 CU FT

SD73-SA-0061
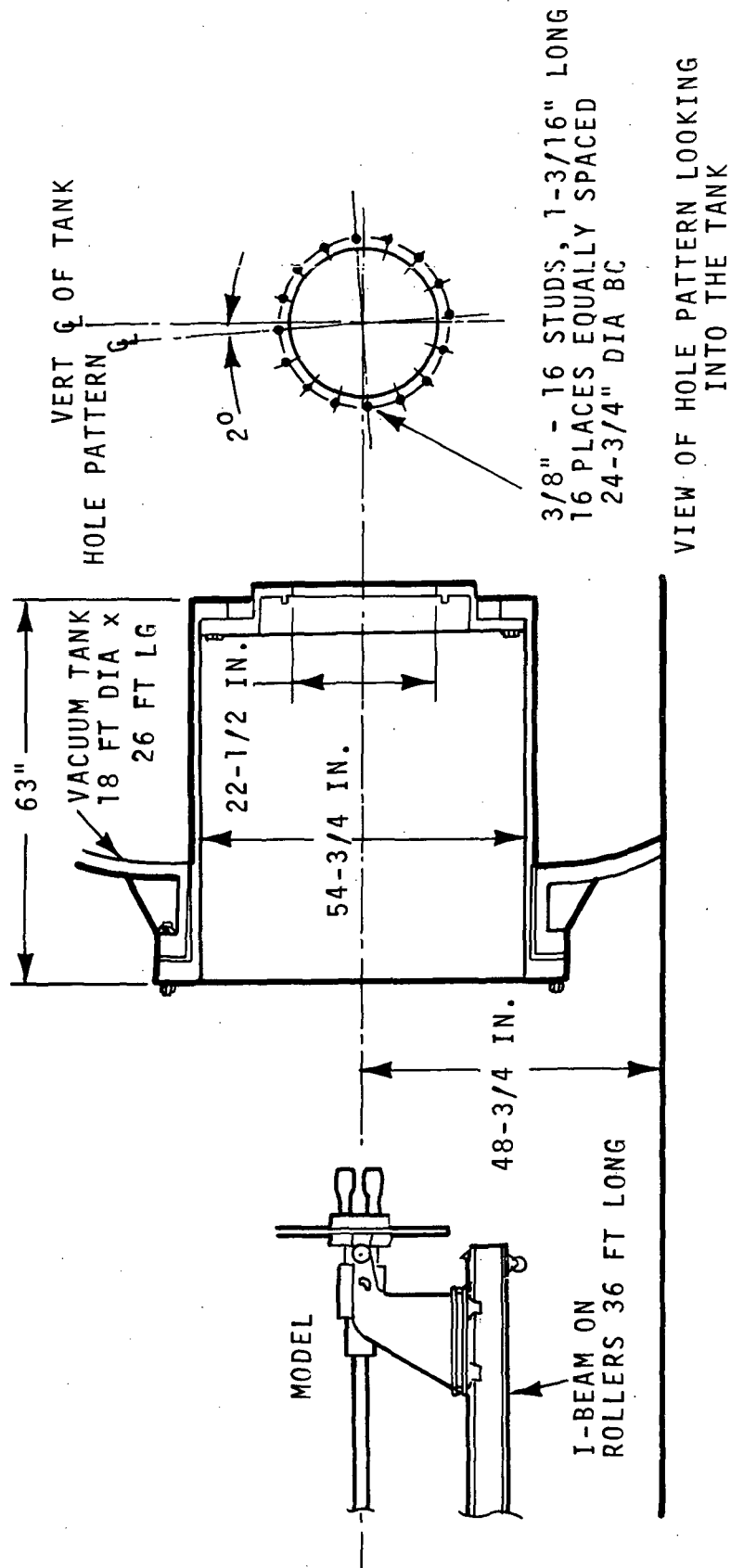
Figure 3.1-2 Model Port Area for the Altitude Chamber

SD73-SA-0061

PRESSURE (mm hg)
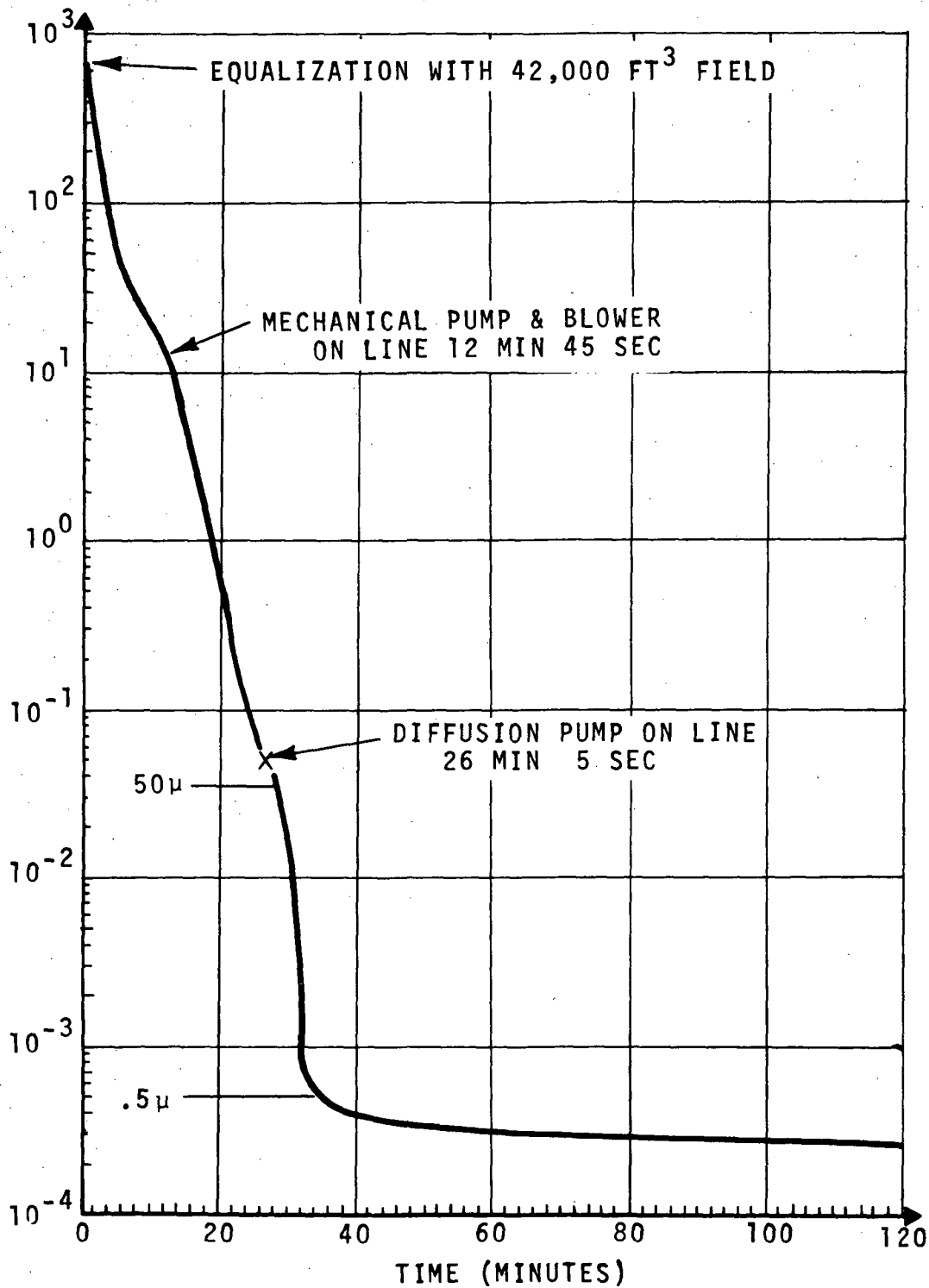
Figure 3.1-3 Vacuum Tank Pump Curve

REGULATOR

A

B

COMPRESSOR

CONTROL PANEL

TYPICAL MODEL
CHARGE TUBE

STANDARD COMPRESSED
GAS CYLINDER
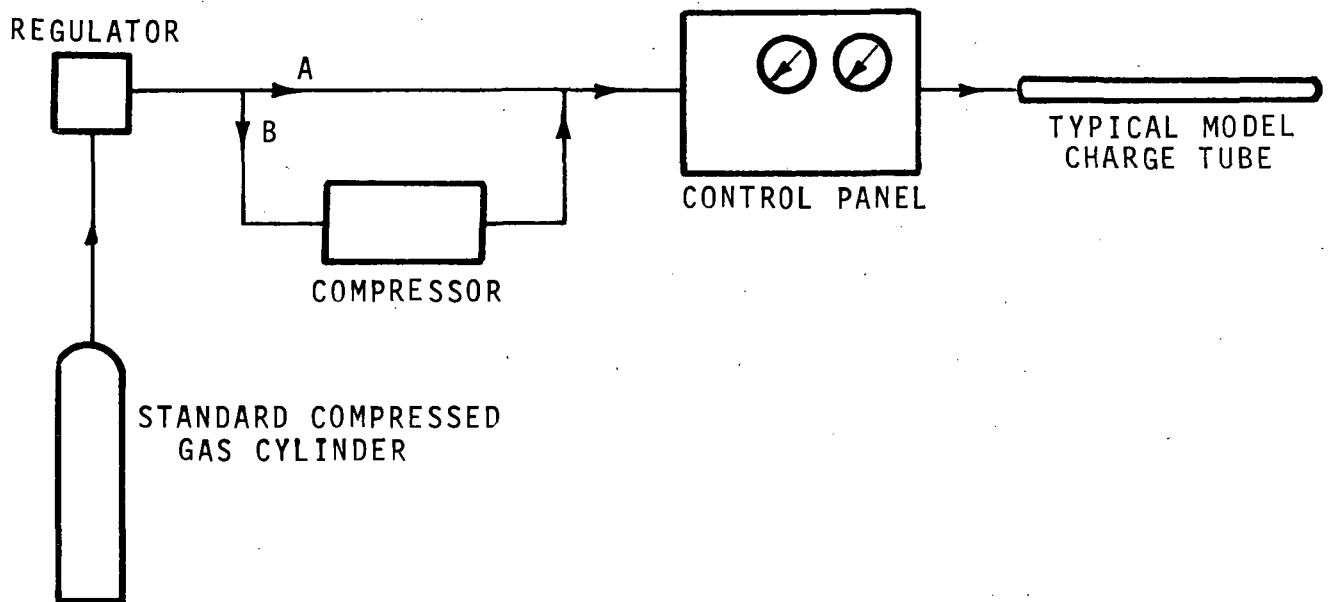
Figure 3.1-4 Typical Gas Handling System

SD73-SA-0061

3.2 COMBUSTOR

The model combustion system is identical to that described in Reference 6, the report of the three J-2 engine model test conducted at MSFC's IBFF, from which the following description is abstracted.

A schematic of the combustion system and its associated wave diagram is shown in Figure 3.2-1. The gaseous oxygen and hydrogen charge tubes are connected to metering venturis and sealed at the downstream end with mylar diaphragms. The charge tubes are pressurized to a level sufficient to maintain sonic flow at the venturi throats and to provide the design propellant mass flow to the combustion chamber.

When the diaphragms are cut, flow commences out of the charge tubes through the venturis into the combustion chamber which is common to all five engine nozzles. The nozzles in turn had diaphragms installed at the nozzle throats which prevented the burned gases from flowing out of the nozzles until the desired combustion pressure was reached. The combustion chamber is initially evacuated so that compression heating in the starting process causes the mixture to autoignite. The evacuation is achieved by means of pinholes in the nozzle throat diaphragms during the evacuation of the altitude chamber. The time that the charge tube acts as a constant pressure reservoir is given approximately by

$$t = 2L/a$$

where L is the length of the tube and a is the velocity of sound of the gas in the tube.

In order to produce constant pressure at the venturi inlets for approximately 11 milliseconds, a 6-foot long oxygen charge tube and a 25-foot long hydrogen charge tube is required.

The venturis used to meter the propellants were sized using the methodology given in Reference 7 such that sonic flow would be maintained during steady-state operation of the model.

A typical combustion chamber pressure history is presented in Figure 3.2-2 where it is seen that the combustion chamber pressure rise of 630 psia is achieved in approximately 3-4 milliseconds. When the design chamber pressure is reached, the nozzle diaphragms burst causing a blast wave to propogate to the end of the altitude chamber, reflect from the end wall and return to the base region. The time taken for the blast wave to return to the model base region is approximately 12 milliseconds which provided approximately 7-8 milliseconds of steady flow for the collection of data.

NOZZLE DIAPHRAGMS

VENTURIS

HYDROGEN CHARGE TUBE

5-1/25 SCALE
J-2 NOZZLES

OXYGEN SUPPLY TUBE

INJECTOR

COMBUSTION
CHAMBER

① $u-a$

GAS
CHARGE TUBE

②

VENTURI
DIAPHRAGM

FLOW METERING VENTURI

TIME

$u+a$
PARTICLE
PATH

②

t = TESTING TIME
= TIME OF CONSTANT
PRESSURE SUPPLY
TO VENTURI INLETS

①

$u-a$

$u = 0$
$P_1 = P_{supply}$

CHARGE TUBE EXPANSION WAVE DIAGRAM.
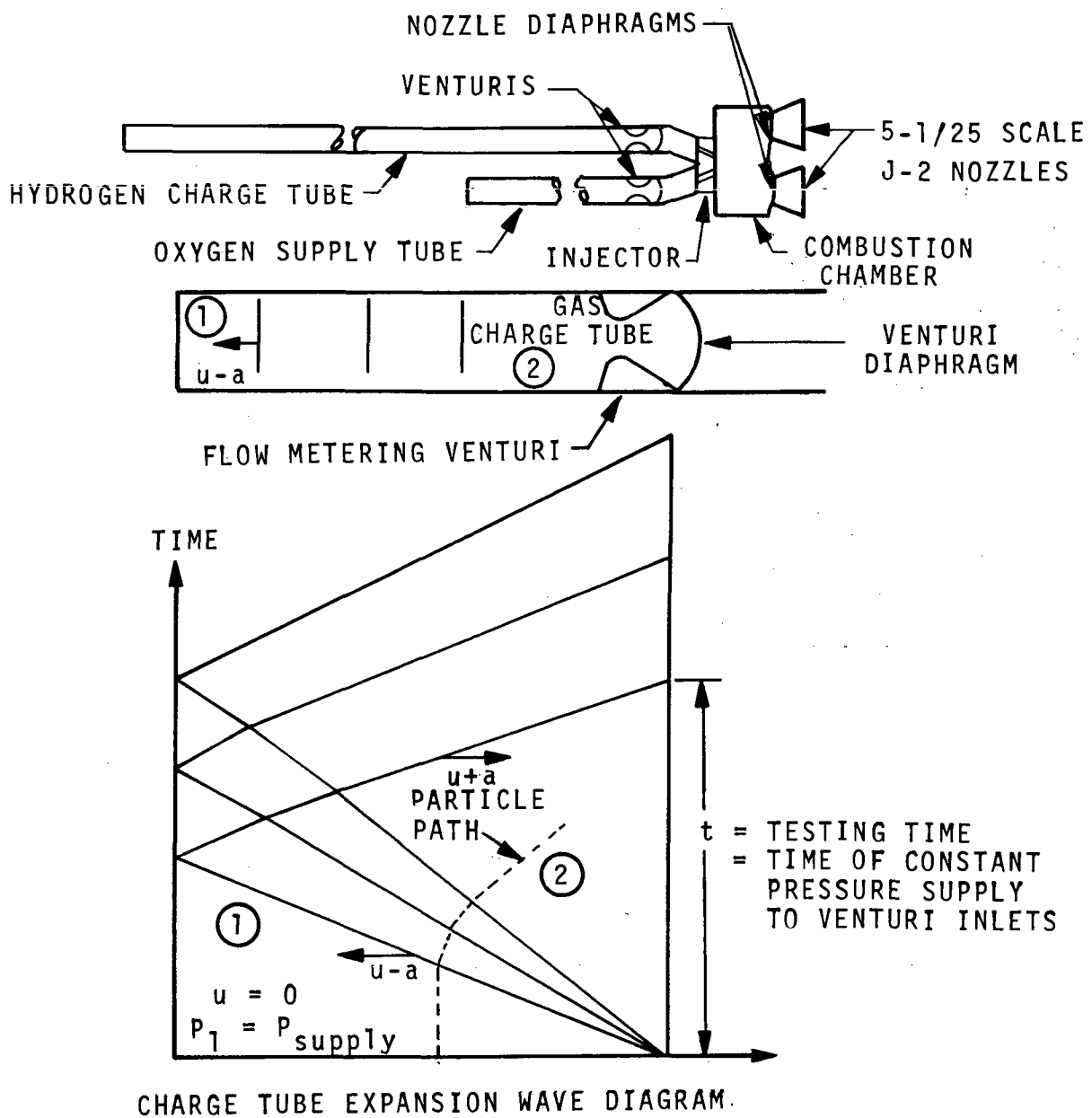
Figure 3.2-1   Model Combustion System Schematic

PRESSURE
BUILDUP
(3-4 MSEC)

STEADY COMBUSTION
(6-7 MSEC)

2 MSEC

NOZZLE
DIAPHRAGMS
RUPTURE

632 PSIA

12 MSEC

BLAST WAVE RETURN TO
MODEL FROM ALTITUDE
CHAMBER WALLS
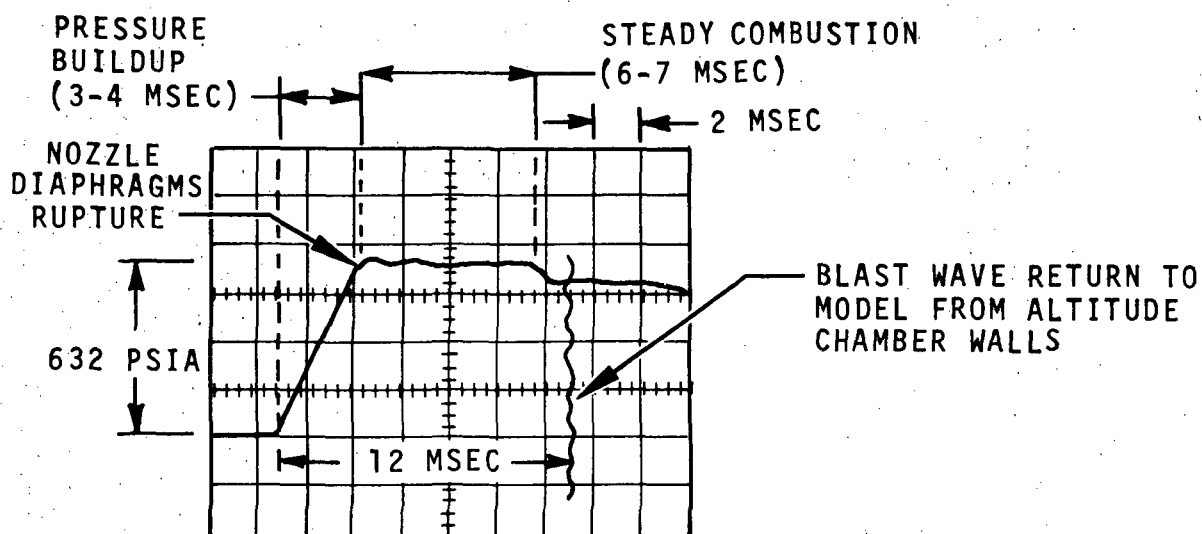
Figure 3.2-2   Typical Oscilloscope Trace of
Combustion Chamber Pressure

In addition to the charge tube expansion wave and the altitude chamber blast wave time limits on the usable run times, a third time limitation was encountered; namely, nozzle throat erosion which prevented the extension of the usable run time.

3.3 MODEL

The model used in this test program was originally built for the CAL S-II model test program described in References 1 and 8.

The test model was a 1/25-scale model of the Saturn S-II prototype vehicle consisting of five J-2 engines, rigid heat shield, flexible curtains, the LOX tank bulkhead, the thrust cone structure, and S-IC/S-II interstage. In addition, the major components located on the thrust cone and engines were also simulated. These included engine LH_2 lines, electrical power containers, propellant controls container, engine electrical control assemblies, and other components shown in Figures 3.3-3 and 3.4-3.

A schematic of the model showing the principal dimensions, taken from Reference 8, is shown in Figure 3.3-1. Most of the tests were run with the scaled 256" trapezoidal edge heat shield shown in Figure 3.3-2. Another view of the model without the heat shield is shown in Figure 3.3-3. Note the J-2 nozzle wall TPE injection ports clearly visible in Figure 3.3-3 which were used to study TPE injection effects during the CAL test program and boundary bleed effects in the present program.

Pertinent J-2 engine dimensions and nozzle contour coordinates are presented in Table 3.3-1.

The outboard engines of the model could be gimballed by means of interchangeable gimbal blocks such that the engine deflection patterns could be rotated relative to the base and heat shield instrumentation which remained fixed.

3.4 INSTRUMENTATION

The instrumentation used in this test program was identical to that of Reference 6 from which the following is abstracted.

Pressure instrumentation was employed for the propellant charge tubes, venturi meters, combustion chamber, exhaust nozzle exits, and the base plate. Heat transfer instrumentation was located in the model nozzles and on the base plate.

A Heise (0-2500 psi) precision laboratory gage, bourdon tube type, graduated in 5 psi increments was used to monitor the initial charge tube pressures. This gage was temperature compensated from (-) 25 to (+) 125 F.

SCALED 256" TRAPEZOIDAL
HEAT SHIELD CONFIGURATION

#2

#1

#5

#3

INTERSTAGE

8.40

3.20

STA. -16
STA. 0

HEAT SHIELD

STA. 44

4.00 4.64

J-2
NOZZLE

GIMBAL
POINT

TURBO-PUMP
EXHAUST
PLENUM RINGS

.48 2.24

STA. 100
STA. 112

ENGINE
MOUNTING
RING

2.23

STA. 156

STA. 196

THRUST CONE

LOX TANK BULKHEAD
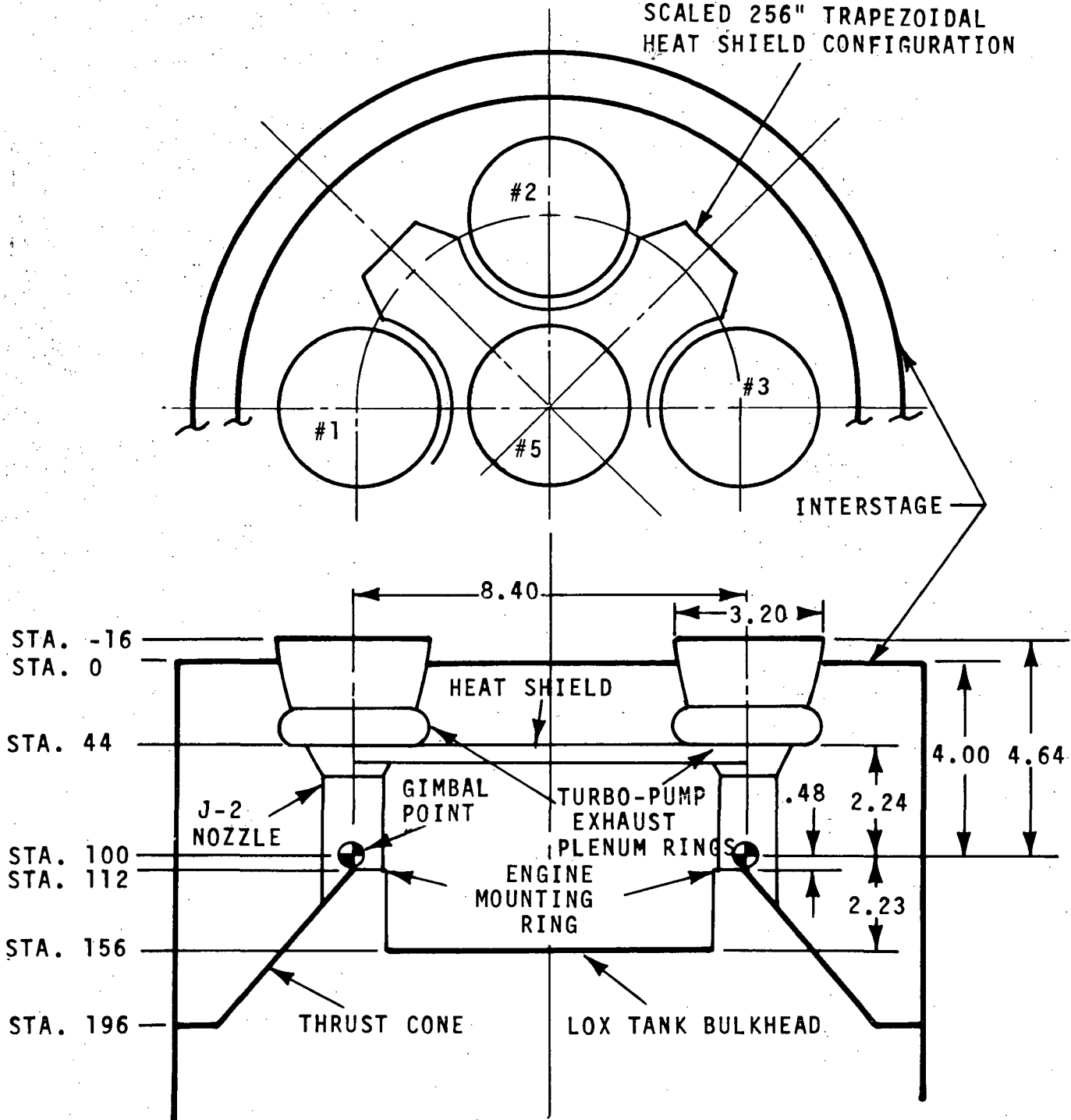
NOTE: #2 AND #5 ENGINES
OMITTED FOR CLARITY

Figure 3.3-1   S-II Prototype Model Schematic

SD73-SA-0061

Figure 3.3-2 Test Model With Heat Shield And Ring Gages

SD73-SA-0061
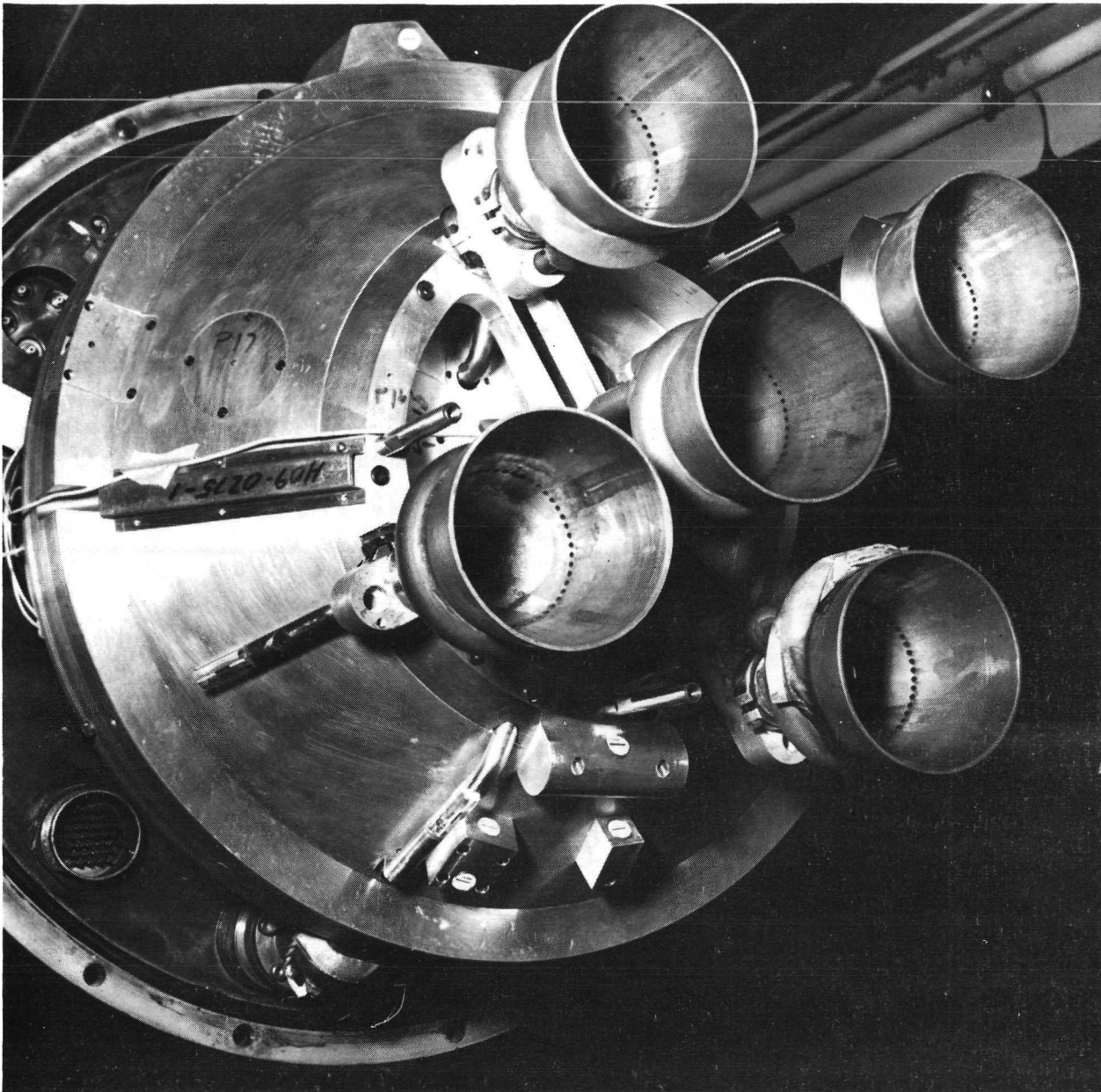
Figure 3.3-3 Test Model With Heat Shield Removed
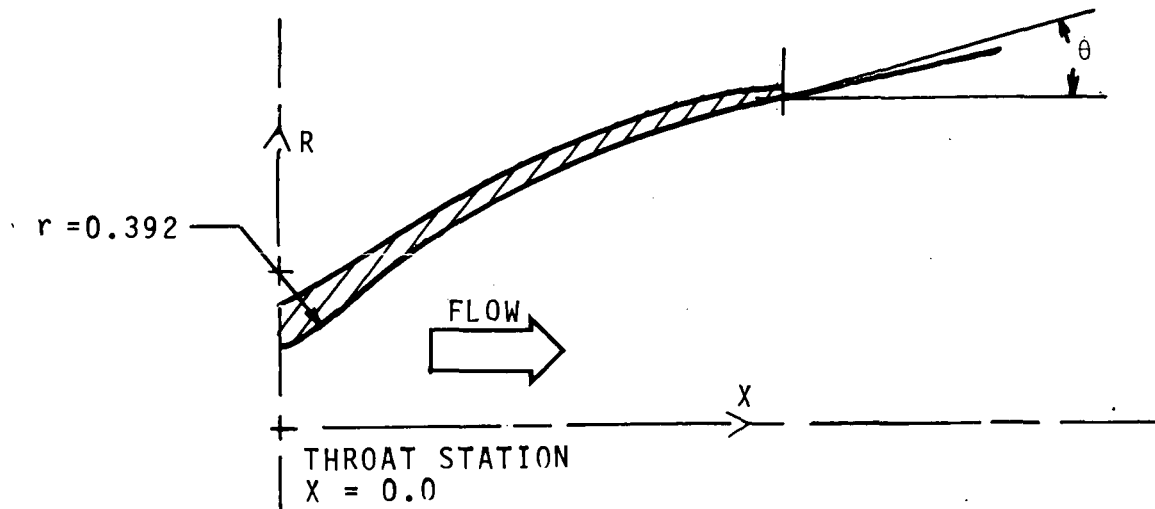
FULL SCALE ENGINE PARAMETERS

AREA PATIO = 27.5
NOZZLE LIP ANGLE = 3°
NOZZLE THROAT RADIUS (r *) = 7.347 INCHES
NOZZLE EXIT RADIUS, INTERNAL = 38.528 INCHES
NOZZLE EXIT RADIUS, EXTERNAL = 40.000 INCHES

NOZZLE WALL COORDINATES

X/r*	(R/r*) INTERNAL	(θ) INTERNAL	(R/r*) EXTERNAL
0 OR LESS	-	-	2.52
0.18100	1.04430	27.50000	2.52
1.00000	1.46430	26.78600	2.52
2.00000	1.95890	25.83200	2.52
3.00000	2.43180	24.77500	2.68
4.00000	2.88120	23.59500	3.19
5.00000	3.30460	22.27000	4.19
6.00000	3.69920	20.76900	3.85
7.00000	4.06190	19.05400	4.21
8.00000	4.38850	17.07600	4.54
9.00000	4.67440	14.76600	4.82
10.00000	4.91340	12.03700	5.06
11.00000	5.09800	8.76200	5.25
12.00000	5.21790	4.77100	5.38
12.38400	5.24400	3.00000	5.444

Table 3.3-1   J-2 Engine Nozzle Wall Coordinates

The venturi pressures were measured using Kistler, Series 601, piezo-electric crystal transducers and the combustion chamber pressure (P_c) was measured by a Kistler, Series 720 transducer. Due to the severe thermal environment (approximately 6,000 F) under which the P_c transducer was required to operate, thermal isolation of the Kistler transducer diaphragm was made by coating the end of the transducer with a layer of Silastic (Dow Chemical) No. 731 RTV approximately 1/16-inch thick by 5/16-inch diameter. It was determined during this test program that the Kistler transducer in the combustion chamber should be removed, cleaned, and recoated with new RTV and recalibrated after a maximum of 16 test runs. The transducer indicated excessive pressure after the RTV deteriorated.

The exhaust nozzle and base plate pressures were measured by Hidyne variable reluctance pressure transducers which determined the difference between local applied pressure and a reference (altitude chamber) pressure. The differential pressure transducers utilized were selected from the following:

Hidyne Part Number	Pressure Range (psid)
HR-1/10D	0-0.1
HR-3D	0-3.0
HR-15D	0-15.0

The electrical output of the pressure transducers was directed to a cathode follower whose output was amplified, exhibited on a Tetronix, Type 502A, Dual Beam Oscilloscope, and photographed by a Polaroid camera.

Heat transfer rates were determined by gages manufactured by Astro Space Labs in accordance with MSFC drawings 80M41618 and 80M41550. Gage part number 80M41550 (Type "A") was used in the exhaust nozzles while gage part number 80 M41618 (Standard) was used on the base plate. A cross section of a typical heat transfer gage is shown by Figure 3.4-1. These thin film gages operated on the principle of sensing a transient surface temperature. The sensing element was a platinum strip which had been fused onto the Pyrex slug. Since the heat capacity of the platinum strip was negligible, the film temperature was equal to the instantaneous surface temperature of the Pyrex substrate, and it could be related to the heat transfer rate as discussed in Reference 10. These gages sensed both radiative and convective heating.

Gas recovery temperature was measured by means of the heated cylindrical component technique previously used in the CAL S-II model test program and described in Reference 8. The heat shield heat flux gage Q_7 was replaced with the heated component during the gas recovery temperature measurement runs.

PLATINUM FILM RESISTOR
(0.1 micron nominal thickness;
deposit and bake on pyrex
slug @ 1250°F)

<u>NOTES</u>

1. Paint over end of platinum film resistor to copper wire.

2. Solder copper wire to silver strip.

3. Resistance @ room temperature is 100 ohms ± 25 ohms.

PYREX SLUG

0.063 Thick x 0.375 Dia.

0.025

SILVER STRIP
(2 Places)

POTTING COMPOUND

WIRE
(Copper, 30 or 32 Gage, Stranded
with teflon insulation)

Figure 3.4-1 Cross Sectional View of Heat Transfer Gage

SD73-SA-0061

Heat shield instrumentation is shown in Figure 3.4-2 and the thrust cone region instrumentation is shown in Figure 3.4-3. The coordinates of these transducers are given in Tables 3.4-1 and 3.4-2.

In addition, special instrumentation was installed on some of the runs on the engine nozzles and the region between the heat shield and the thrust cone.

The location of the special ring gages (Q70, 80, 90, and 100) used to measure heating rates forward of the heat shield in the vicinity of engine #1 is shown Figure 3.4-4 and can also be seen in Figure 3.3-2. This gage arrangement was subsequently replaced by gages Q110 and Q120, Figure 3.4-5, because the flow was blocked and the flow pattern was being altered by the original ring gage arrangement.

Engine nozzle wall external surface heating rates were measured by means of the strip gages shown in Figures 3.4-6 and 3.4-7. The nozzle gage angular orientation coordinate system used to describe the gage locations is given in Figure 3.4-8.

The location of the nonflowing nozzle gages N_1 through N_5 is shown in Figure 3.4-9 and the flowing nozzle lip gages N_1, N_2 in Figure 3.4-10. The coordinates of the various nozzle gages for the different runs are given in Table 3.4-3.
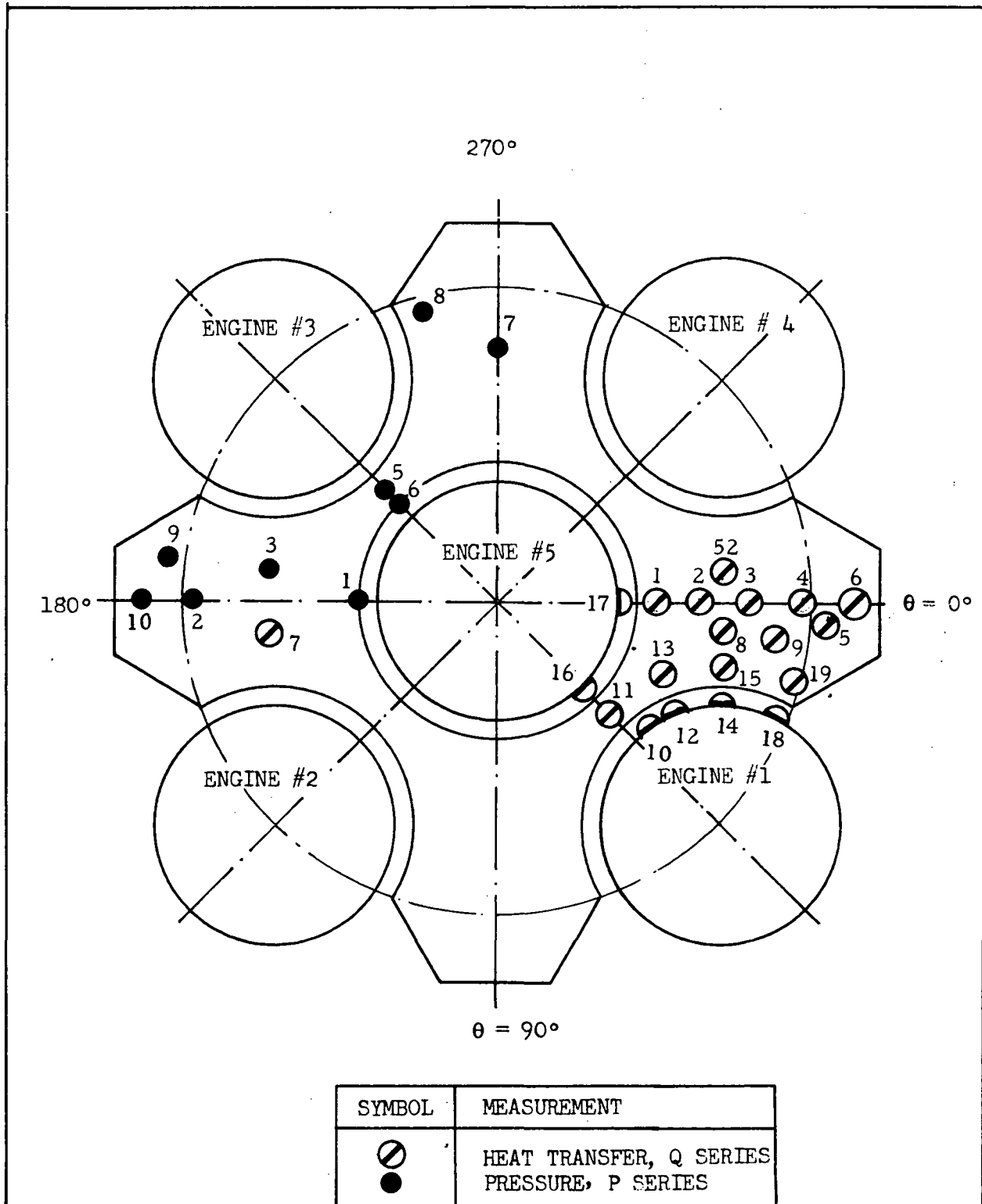
Figure 3.4-2 Heat Shield Instrumentation

270°

180°

18 17 16 15

20 21 22 23 24 25 0°

#3 #4

#2 #1

41 53

43

46

4

38 49 30 54

33 31

49 32 29 26 27 28

34 55 44

40

36 35

39

37

θ = 90°

SYMBOL	MEASUREMENT
⊘	HEAT TRANSFER, Q SERIES
●	PRESSURE , P SERIES
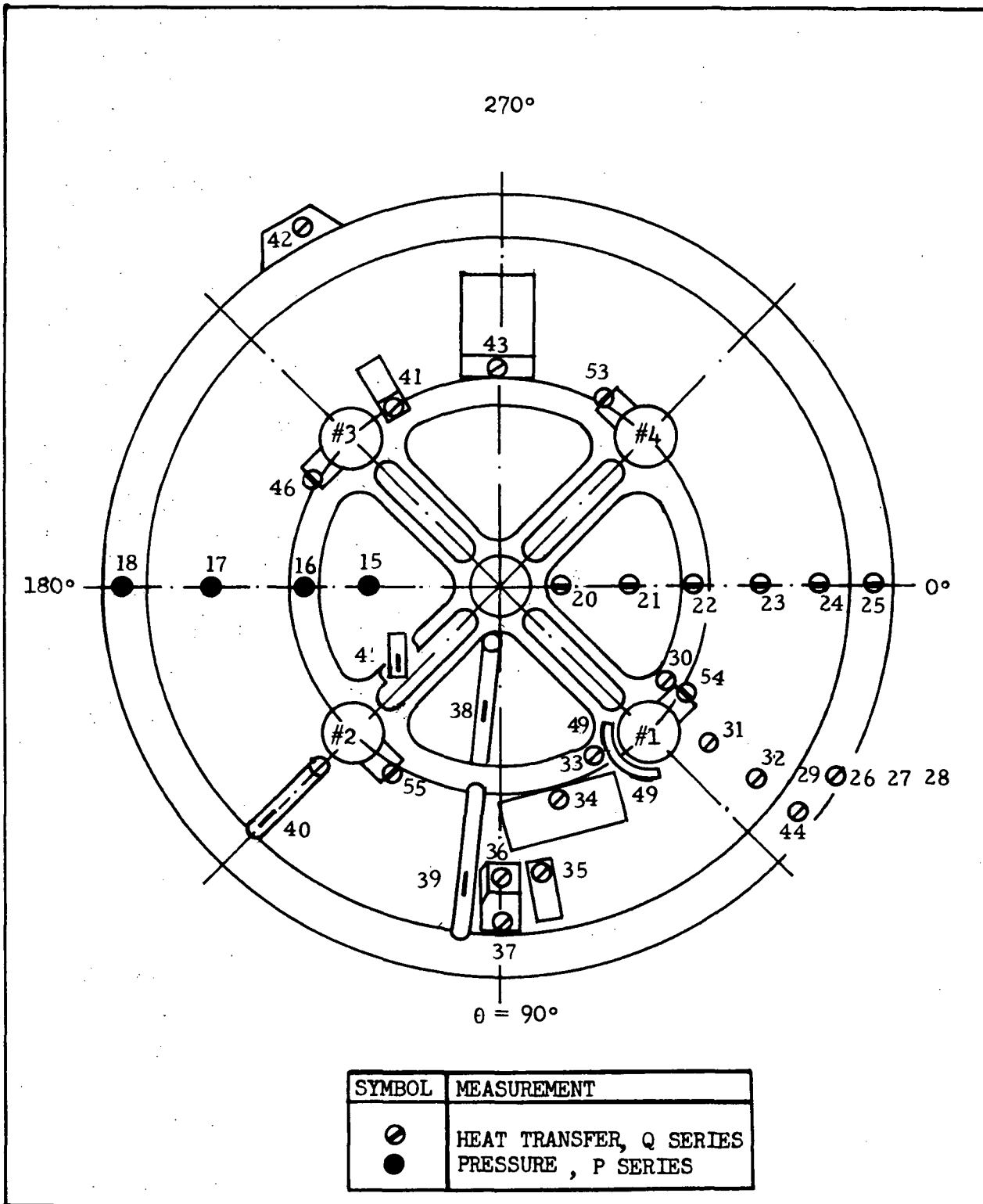
Figure 3.4-3 Thrust Cone Instrumentation

TABLE 3.4-1

HEAT SHIELD INSTRUMENTATION LOCATIONS

Gage	Radius	θ	Vehicle Station	Location
P_1	1.80	180°	-	Eng. #5 Heat Shield Cone
P_2	3.95	180°	44	Heat Shield
P_3	3.00	187.5°	44	Heat Shield
P_4		NONE		
P_5	2.09	225°	44	Heat Shield
P_6	1.80	225°	-	Eng. #5 Heat Shield Cone
P_7	3.32	270°	44	Heat Shield
P_8	3.95	255°	44	Heat Shield
P_9	4.32	187.5°	44	Heat Shield
P_{10}	4.69	180°	44	Heat Shield
P_{11}	3.32	180°	44	Heat Shield
Q_1	2.10	0°	44	Heat Shield
Q_2	2.62	0°	44	Heat Shield
Q_3	3.31	0°	44	Heat Shield
Q_4	4.00	0°	44	Heat Shield
Q_5	4.35	4°	44	Heat Shield
Q_6	4.70	0°	44	Heat Shield
Q_7	3.00	172.5°	44	Heat Shield
Q_8	3.00	7.5°	44	Heat Shield
Q_9	3.65	7.5°	44	Heat Shield
Q_{10}	2.61	40°	-	Engine #1 Curtain

SD73-SA-0061

TABLE 3.4-1 (Cont'd)

Gage	Radius	θ	Vehicle Station	Location
Q_{11}	2.03	45°	44	Heat Shield
Q_{12}	-	-	-	Engine #1 Curtain
Q_{13}	2.38	25°	44	Heat Shield
Q_{14}	-	-	-	Engine #1 Curtain
Q_{15}	3.08	16°	44	Heat Shield
Q_{16}	1.68	45°	-	Engine #5 Curtain
Q_{17}	1.68	0°	-	Engine #5 Curtain
Q_{18}	-	-	-	Engine #1 Curtain
Q_{19}	4.00	15°	44	Heat Shield
Q_{52}	3.00	325.5°	44	Heat Shield

NOTE: Gages Q_{10}, Q_{12}, Q_{14}, and Q_{18} are mounted on the #1 engine flexible curtain attachment flange, and gages Q_{16} and Q_{17} are mounted on the #5 engine heat shield cone as shown in Figures 3.3-2 and 3.4-2.

TABLE 3.4-2

THRUST STRUCTURE INSTRUMENTATION LOCATIONS

Gage	Radius	θ	Vehicle Station	Location
P_{15}	2.60	180°	160	LOX Tank Bulkhead
P_{16}	3.92	180°	112	Engine Mounting Ring
P_{17}	5.76	180°	160	Thrust Cone
P_{18}	7.60	180°	196	Aft Interstage Panel
Q_{20}	1.20	0°	146.25	LOX Tank Bulkhead
Q_{21}	2.60	0°	146.25	LOX Tank Bulkhead
Q_{22}	3.92	0°	112	Engine Mounting Ring
Q_{23}	5.20	0°	140	Thrust Cone
Q_{24}	6.40	0°	180	Thrust Cone
Q_{25}	7.60	0°	196	Aft Interstage Panel
Q_{26}	7.92	Variable	193	Aft Interstage
Q_{27}	7.92	Variable	44	Aft Interstage
Q_{28}	7.92	Variable	3	After Interstage
Q_{29}	7.80	Variable	0	After Interstage-Aft Face
Q_{30}	3.92	29.5°	112	Engine Mounting Ring
Q_{31}	5.20	37°	140	Thrust Cone
Q_{32}	6.40	37°	180	Thrust Cone
Q_{33}	3.92	60.5°	112	Engine Mounting Ring
Q_{34}	4.44	76°	105	Electrical Power Container
Q_{35}	5.80	81°	155	Distribution Panel
Q_{36}	5.90	90°	175	Propellant Mgmnt Cont.

SD73-SA-0061

TABLE 3.4-2 (Cont'd)

Gage	Radius	θ	Vehicle Station	Location
Q_{37}	6.80	90°	175	Propellant Mgmnt Cont.
Q_{38}	2.60	97°	123	Center Engine LH_2 Line
Q_{39}	6.00	97°	146	Center Engine LH_2 Line
Q_{40}	6.60	135°	162	Outboard Engine LH_2 Line
Q_{41}	4.20	240°	117	ARMA
Q_{42}	8.28	243°	200	LOX Tank Pressure Switch
Q_{43}	4.44	270°	100	Signal Conditioner
Q_{44}	7.60	37°	196	Aft Interstage Panel
Q_{45}	2.64	1.41°	135	Outboard Engine LOX Line
Q_{46}	4.93	208°	60	Engine #3 Electrical Control Assembly
Q_{47}	—————— NONE ——————			
Q_{48}	–	–	60-70	Engine #1 Special Small Glass Rod to Simulate Propellant Lines
Q_{49}	–	–	60-70	
Q_{50}*	–	180°	–	LOX Tank Bulkhead & Thrust Cone Interchangeably at P_{15} and P_{17} Locations
Q_{51}**	–	180°	–	
Q_{53}	4.93	298°	60	Engine #4 Electrical Control Assembly
Q_{54}	4.93	28°	60	Engine #1 Electrical Control Assembly
Q_{55}	4.93	118°	60	Engine #2 Electrical Control Assembly

*   1/4 inch diameter cylinder
** 1 inch diameter cylinder

NOTE: Interstage gages Q_{26}, Q_{27}, Q_{28}, and Q_{29} were located at 0°, 29.2°, or 45° as specified in the data log.
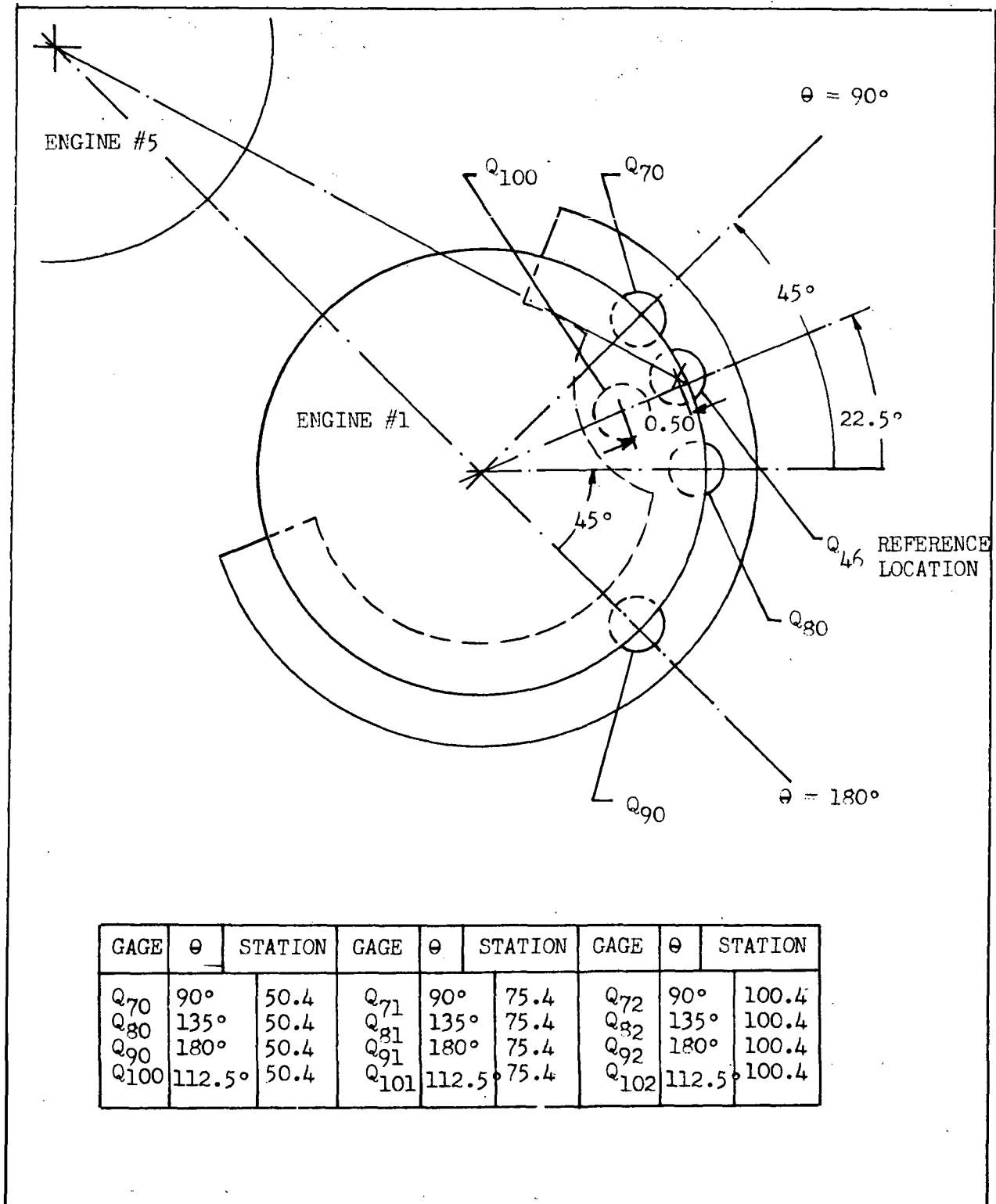
Figure 3.4-4 Ring Gage Locations

GAGE	θ	STATION	GAGE	θ	STATION	GAGE	θ	STATION
Q_{70}	90°	50.4	Q_{71}	90°	75.4	Q_{72}	90°	100.4
Q_{80}	135°	50.4	Q_{81}	135°	75.4	Q_{82}	135°	100.4
Q_{90}	180°	50.4	Q_{91}	180°	75.4	Q_{92}	180°	100.4
Q_{100}	112.5°	50.4	Q_{101}	112.5°	75.4	Q_{102}	112.5°	100.4

#4 ENGINE

NOTE: LETTER AFTER
THESE GAGES INDICATES
AS FOLLOWS:-

NONE	#4 ENGINE SIDE OF ENGINE #1
A	#2 ENGINE SIDE OF ENGINE #1
B	#1 ENGINE SIDE OF ENGINE #2
C	#3 ENGINE SIDE OF ENGINE #2

$\theta = 0°$

22.5°

4.0 R

$Q_{110,111,112}$

1.0 R

$Q_{120,121,122}$

1 R

1.5 R

#1
ENGINE

$\theta = 45°$

GAGE	STATION
$Q_{110,120}$	55
$Q_{111,121}$	75
$Q_{112,122}$	95

Figure 3.4-5 Alternate Ring Gage Locations
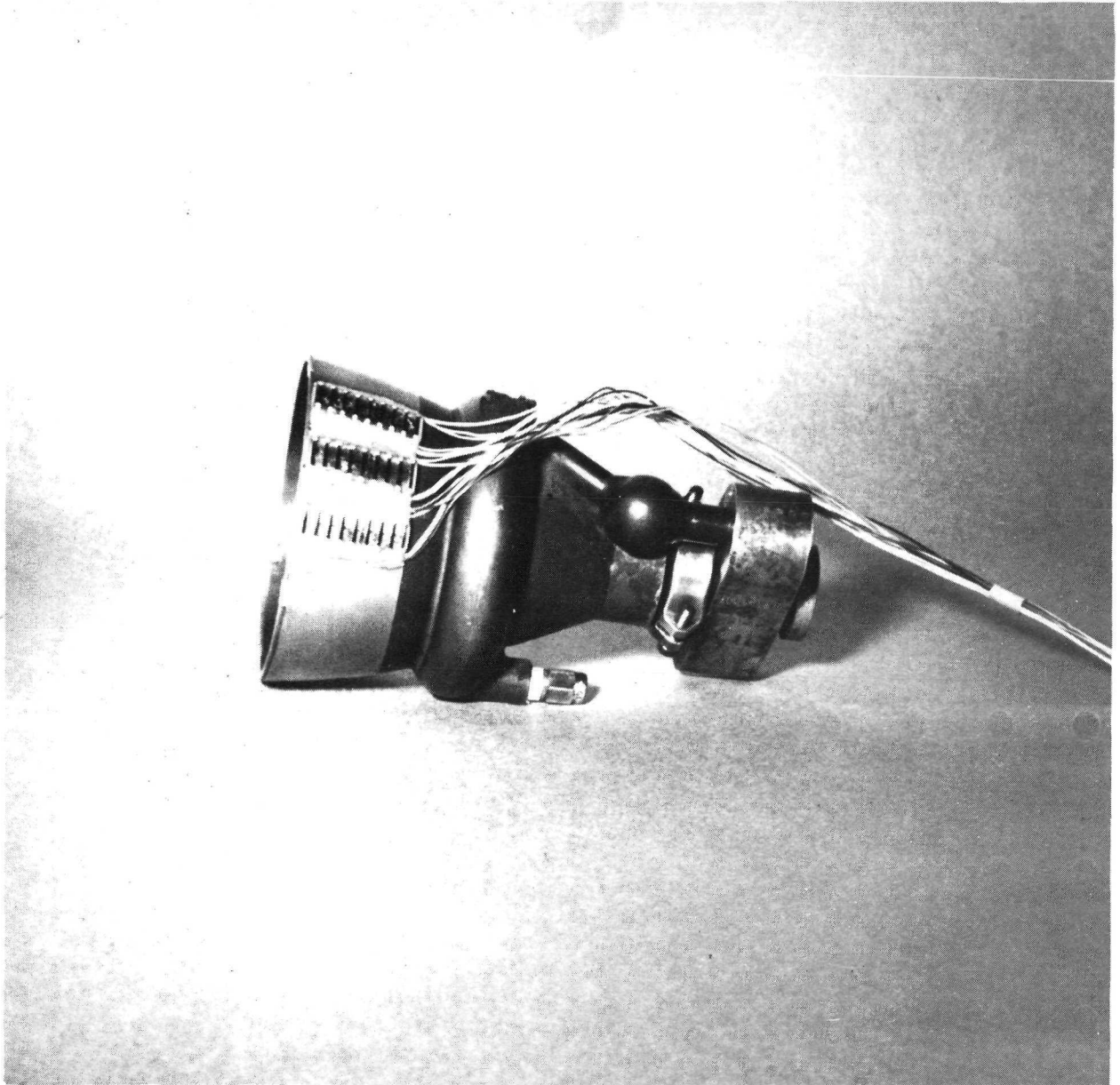
Figure 3.4-6 Engine Nozzle Strip Gages

SD73-SA-0061

AXIAL
LOCATIONS

GAGE STRIPS SPACED
CIRCUMFERENTIALLY 22-1/2°
APART, CENTER TO CENTER

9 8 7 6 5 4 3 2 1

9 8 7 6 5 4 3 2 1

9 8 7 6 5 4 3 2 1

.12"
(TYP)
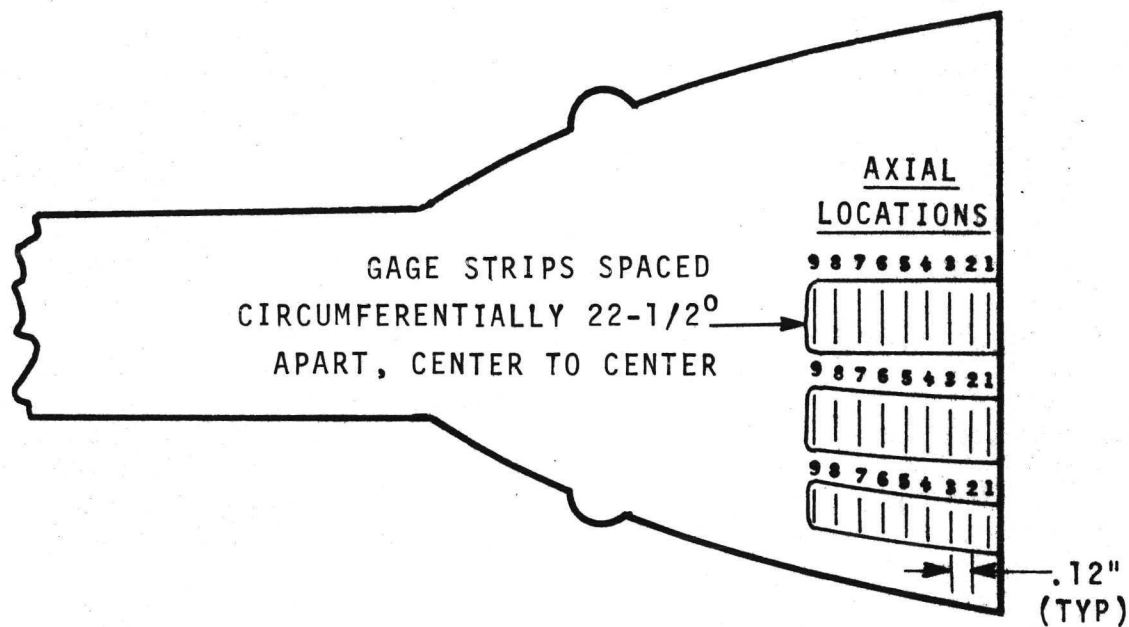
THIS GAGE ARRANGEMENT WAS USED DURING THE CAL TEST PROGRAM
AND SOME OF THE EARLIER RUNS OF THE PRESENT TESTS. FOR
SPECIFIC GAGE LOCATIONS SEE TABLE 3.4-3.

Figure 3.4-7   External Nozzle Wall Instrumentation

270°

180°   270°

#3

90°   0°

90°   180°

#4

0°   270°

#5

180°   0°

270°   0°

#2

180°   90°

0°   90°

#1

270°   180°

OUTBOARD ENG.
ANGULAR POSITION

90° ← MODEL AND #5 ENG. ANGULAR
POSITIONS
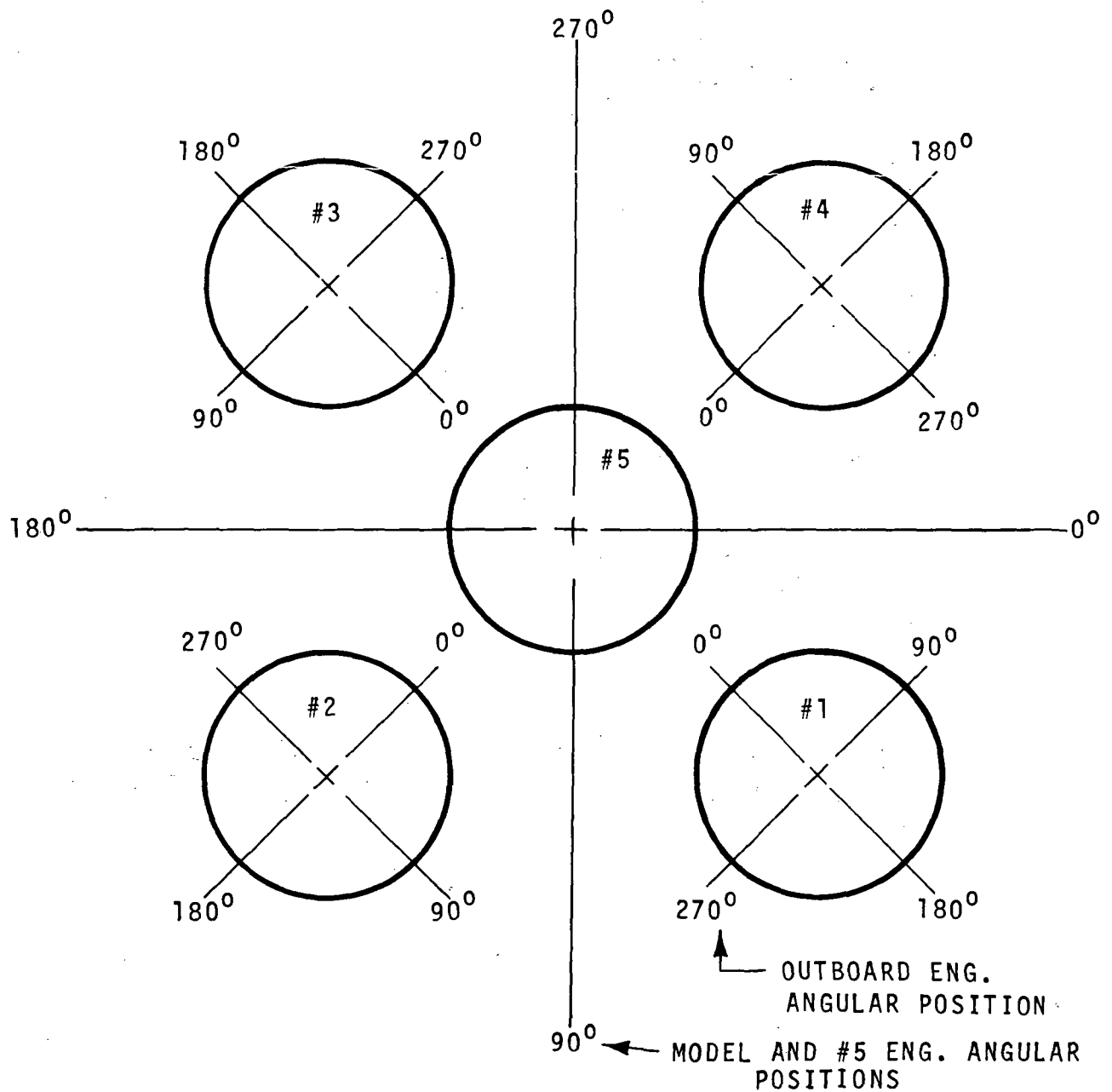
VIEW FROM THE REAR OF THE MODEL
LOOKING FORWARD

Figure 3.4-8   Nozzle Angular Orientation

INTERNAL CONTOURED
HEAT TRANSFER GAGES

EXTERNAL CONTOURED
HEAT TRANSFER GAGES

SECTION ZZ
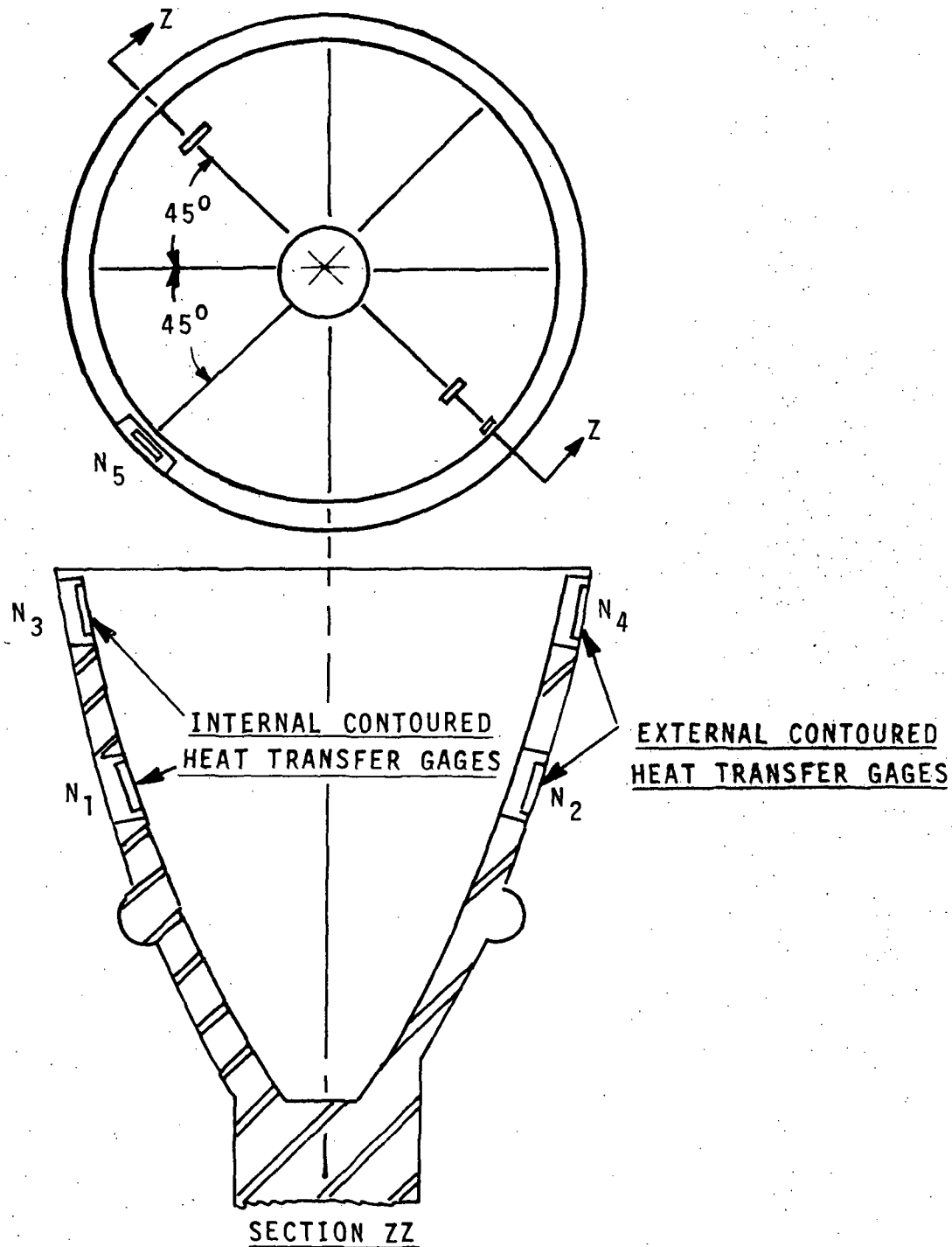
Figure 3.4-9   Non-Flowing Instrumented Nozzle

Rev July 6, 1973

SD73-SA-0061

SECTION ZZ
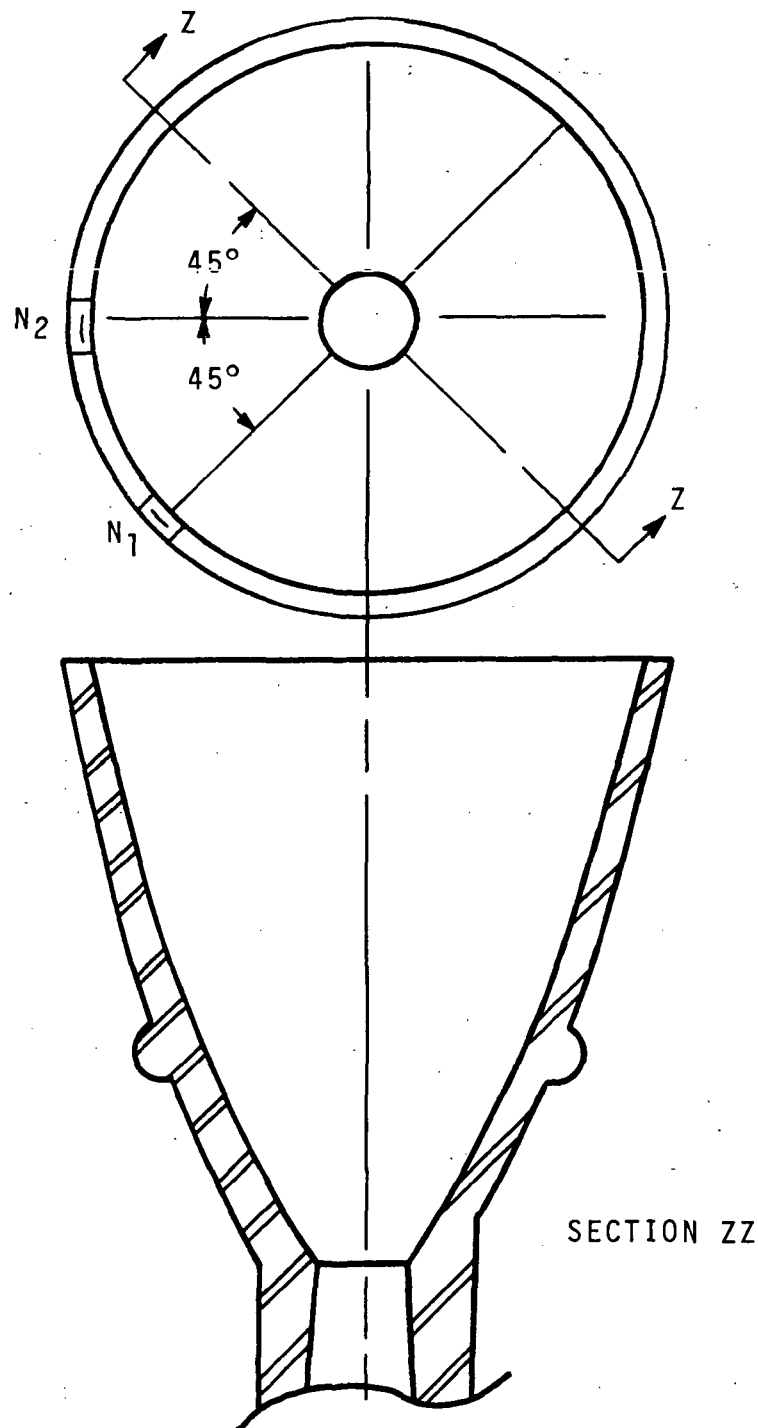
Figure 3.4-10 Instrumented Flowing Nozzle

SD73-SA-0061

Table 3.4-3 Nozzle Gauge Coordinates

X - DISTANCE FROM NOZZLE EXIT PLANE, INCHES (FULL SCALE)
θ - ANGULAR LOCATION, SEE FIGURE 3.4-8

LOG	RUNS	ENGINE NUMBER	GAGE K θ	GAGE K X	GAGE L θ	GAGE L X	GAGE M θ	GAGE M X	GAGE SUB-SCRIPT
4.2A	358-360	2 (NON FLOWING)	NOT USED		NOT USED		*	1.00	1
								--	2
								--	3
								--	4
								--	5
								16.00	6
								19.00	7
								22.00	8
12.1	343-348	5	315°	--	337.5°	--	0°	1.00	1
				4.00		--		--	2
				--		7.00		--	3
				10.00		10.00		--	4
				13.00		13.00		--	5
				16.00		16.00		16.00	6
				19.00		19.00		19.00	7
				--		22.00		22.00	8
				25.00		25.00		25.00	9
12.1A	440-442	4	292.5°	1.20	315°	1.20	337.5°	1.20	1
				4.30		4.30		4.30	2
				7.40		7.40		7.40	3
				10.60		10.60		10.60	4
12.3	355-357	5	NOT USED		NOT USED		0°	1.00	1
								16.00	6
								19.00	7
								22.00	8
13.1.1	430-434	4	315°	1.17	337.5°	1.17	0°	1.17	1
				4.29		4.29		4.29	2
				7.42		7.42		7.42	3
				10.55		10.55		10.55	4
13.1.1A	435-438	4	292.5°	1.17	315°	1.17	337.5°	1.17	1
27.1	641-643			4.29		4.29		4.29	2
				7.42		7.42		7.42	3
				10.55		10.55		10.55	4
23.1	623-624	5	292.5°	2.45	315°	2.45	337.5°	2.45	1
				5.97		5.97		5.97	2
	625-629		270°	9.09	292.5°	9.09	315°	9.09	3
				12.32		12.32		12.32	4
				15.34		15.34		15.34	5
				18.08		18.08		18.08	6

* ANGULAR LOCATION NOT RECORDED

Table 3.4-3 (Continued)

X - DISTANCE FROM NOZZLE EXIT PLANE, INCHES (FULL SCALE)
θ - ANGULAR LOCATION, SEE FIGURE 3.4-8

LOG	RUNS	ENGINE NUMBER	GAGE K		GAGE L		GAGE M		GAGE SUB-SCRIPT
			θ	X	θ	X	θ	X	
27.2.1 4.9	644-646	4	315°	1.45	337.5°	1.85	0°	1.85	1
				4.95		4.95		4.95	2
				8.10		8.10		8.10	3
				11.20		10.80		10.80	4
				14.30		13.90		14.30	5
				17.50		17.10		17.10	6
27.2.2	647-649	1	22.5°	1.45	45°	1.85	67.5°	1.85	1
				4.95		4.95		4.95	2
				8.10		8.10		8.10	3
				11.20		10.80		10.80	4
				14.30		13.90		14.30	5
				17.50		17.10		17.10	6
27.3	661-664	4	312.5°	2.45	337°	2.45	0°	2.45	1
				5.97		5.97		5.97	2
				9.09		9.09		9.09	3
				12.22		12.22		12.22	4
				15.34		15.34		15.34	5
				18.08		18.08		18.08	6
28.1	672-676	3 (NON FLOWING)	337.5°	1.45	0°	1.85	22.5°	1.85	1
				4.95		4.95		4.95	2
				8.10		8.10		8.10	3
				11.20		10.80		10.80	4
				14.30		13.90		14.30	5
				17.50		17.10		17.10	6
			GAGE G		GAGE H		GAGE J		
			θ	X	θ	X	θ	X	
4.1	300-302	5 (NON FLOWING)	337.5°	--	0°	1.00	22.5°	1.00	1
				4.00		--		--	2
				--		7.00		--	3
				10.00		10.00		--	4
				13.00		13.00		--	5
				16.00		16.00		16.00	6
				19.00		19.00		19.00	7
				22.00		22.00		22.00	8
				25.00		--		25.00	9
4.2	303-306	3 (NON FLOWING)	292.5°	--	315°	1.00	337.5°	1.00	1
				4.00		--		--	2
				--		7.00		--	3
				10.00		10.00		--	4
				13.00		13.00			5
				16.00		16.00		16.00	6
				19.00		19.00		19.00	7
				22.00		22.00		22.00	8
				25.00		--		25.00	9

SD73-SA-0061

Table 3.4-3 (Continued)

X - DISTANCE FROM NOZZLE EXIT PLANE INCHES (FULL SCALE)
θ - ANGULAR LOCATION, SEE FIGURE 3.4-8

LOG	RUNS	ENGINE NUMBER	GAGE K		GAGE L		GAGE M		GAGE SUB-SCRIPT
			θ	X	θ	X	θ	X	
23.1.1	665-669	5	312.5°	2.45	337°	2.45	0°	2.45	1
				5.97		5.97		5.97	2
				9.09		9.09		9.09	3
				12.22		12.22		12.22	4
				15.34		15.34		15.34	5
				18.08		18.08		18.08	6
23.2	627-629	5	270°	2.45	292.5°	2.45	315°	2.45	1
				5.97		5.97		5.97	2
				9.09		9.09		9.09	3
				12.12		12.22		12.22	4
				15.34		15.34		15.34	5
	650-665		315°	18.08	337.5°	18.08	0°	18.08	6
23.3	656-660	5	315°	1.45	337.5°	1.85	0°	1.85	1
				4.95		4.95		4.95	2
				8.10		8.10		8.10	3
				11.20		10.80		10.80	4
				14.30		13.90		14.30	5
				17.50		17.10	315°	17.10	6
23.4	694-699	5	315°	1.95	337.5°	1.95	0°	1.95	1
				4.70		4.70		4.30	2
				7.43		7.43		7.03	3
				11.30		11.30		10.90	4
				14.40		14.40		14.10	5
23.5 & 23.6	677-679 680-688	5	315°	1.45	337.5°	1.85	0°	1.85	1
				4.95		4.95		4.95	2
				8.10		8.10		8.10	3
				11.20		10.80		10.80	4
				14.30		13.90		14.30	5
23.7	689-693	5	315°	1.95	337.5°	1.95	0°	1.95	1
				5.45		4.70		4.30	2
				8.15		7.43		7.03	3
				11.30		11.30		10.90	4
				13.70		13.30		14.10	5
26.1	630-635	5	312.5°	2.45	337.°	2.45	0°	2.45	1
				5.97		5.97		5.97	2
				9.09		9.09		9.09	3
				12.22		12.22		12.22	4
				15.34		15.34		15.34	5
				18.08		18.08		18.08	6
26.2	636-640	4	312.5°	2.45	337°	2.45	0°	2.45	1
				5.97		5.97		5.97	2
				9.09		9.09		9.09	3
				12.22		12.22		12.22	4
				15.34		15.34		15.34	5
				18.08		18.08		18.08	6

Table 3.4-3 (Continued)

X - DISTANCE FROM NOZZLE EXIT PLANE, INCHES (FULL SCALE)
θ- ANGULAR LOCATION, SEE FIGURE 3.4-8

LOG	RUNS	ENGINE NUMBER	GAGE N		GAGE SUB- SCRIPT
			θ	X	
4.1	300-301	5 (NON FLOWING)	135° 315° 135° -- 45°	43.00 43.00 6.00 -- 0.00	1 2 3 4 5*
4.2	303-306	3 (NON FLOWING)	90° 270° 90° -- 0°	43.00 43.00 6.00 -- 0.00	1 2 3 4 5*
6.1	235-245	5	180° 225°	--	1* 2*
6.2	246-252	5	180° 225°	-- --	1* 2*

*NOZZLE LIP GAGES

4.0 TEST PROCEDURE

The test procedures of this test program were identical, except for the heat transfer data reduction technique, to those described in Reference 6 for the three engine model test program conducted at MSFC's Impulse Base Flow Facility. The descriptions of the calibration and pressure data reduction procedures are taken from Reference 6.

4.1 CALIBRATION

Prior to installation, each pressure transducer was calibrated for voltage output versus applied pressure. The voltage variation of the transducers was linear over the calibration range of pressures and over the range of pressures encountered during the tests. These calibrations, in conjunction with estimated values for applied pressures to be experienced during testing, provided the basis for adjusting the gain of the data recording system to achieve maximum "readability" of the oscilloscope traces.

The heat transfer gages were calibrated individually by Astro Space Labs. A typical calibration plot of temperature versus resistance is shown in Figure 4.1-1. At the temperatures encountered during the tests, the gage resistance change was linear when plotted against temperature. This information was used to determine the value of the shunt resistor that was inserted into the heat transfer gage instrumentation circuitry to generate the same voltage change that would be produced if the gage increased in resistance due to heating. This calibration resistor allowed the recording equipment to be set for the expected temperature increase.

4.2 DATA REDUCTION

The Hidyne pressure transducers were evacuated on both sides of the diaphragm during the evacuation of the altitude chamber. One side of all the Hidyne transducers was evacuated through a common manifold that was closed immediately before the venturi diaphragms were ruptured. With the manifold sealed to altitude chamber pressure changes during the data collection period, the pressure to which the altitude chamber and manifold was evacuated became the reference pressure to the Hidyne transducers. During data reduction, the reference or initial pressure was added to the measured pressure difference to obtain absolute applied pressure.
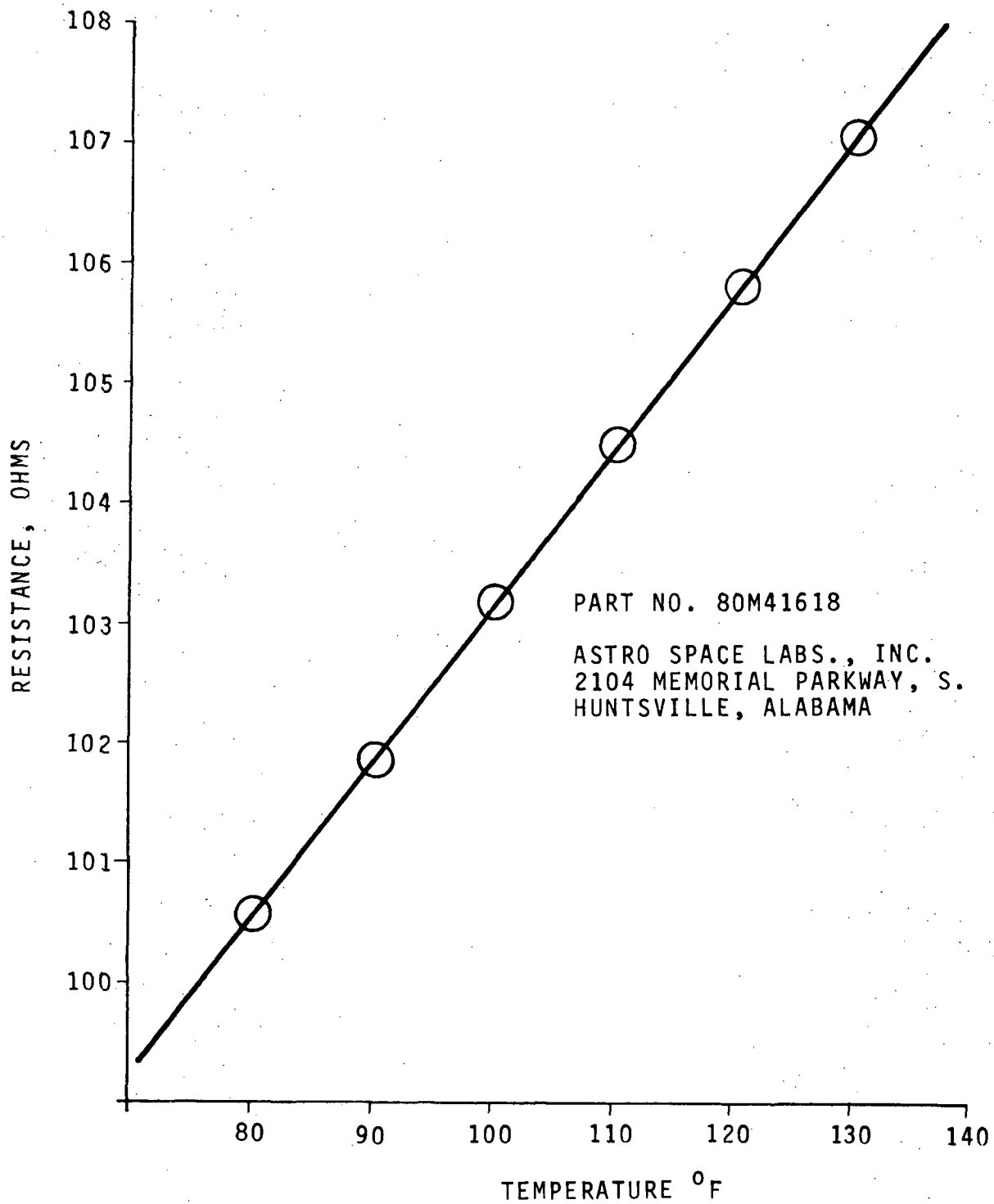
Figure 4.1-1 Sample Heat Transfer Gage Calibration Plot

The Kistler pressure transducers, used in the combustion chamber and the venturi throats, measured absolute pressure. However, for convenience in data reduction they were referenced to known pressures existing before the model was fired. The reference pressure for the transducer in the combustion chamber was the altitude chamber pressure, and the reference pressure for the venturi throat transducer was the initial charge tube pressure.

The heat transfer gages used during this test program were of a type generally referred to as thin film resistance thermometers. The gage uses a thin platinum film to measure the surface temperature of a Pyrex disc on which it is mounted. It does not provide a direct measurement of the heat transfer to the body, but the heat flux at any instant may be determined from the surface temperature history according to the theory of heat conduction for a semi-infinite slab with a uniform initial temperature. This makes it possible to measure the surface temperature history of the body and calculate the heat transfer rate.

The equation for unsteady one-dimensional heat conduction in a semi-infinite solid is

$$c\rho \, \frac{\partial T}{\partial t} = \frac{\partial}{\partial y} \left(k \, \frac{\partial T}{\partial y} \right)$$

where c, ρ, and k are specific heat, density, and thermal conductivity, respectively, of the solid on which the thin film thermometer is mounted. T is the temperature which is a function of distance from the surface, y, and time, t.

If c, ρ, and k are considered to be functions of temperature, the above equation is nonlinear and must be solved by numerical techniques.

During the CAL S-II model test program, "q-meters" were developed which eliminated the lengthy and costly numerical integrations required to solve for the heat flux from the measured temperature histories. The "q-meter," References 8 and 12, is a passive electrical analog which converts the temperature signal from the thin film heat transfer gages into a corresponding signal of heat transfer rate.

This "q-meter" heat transfer data reduction technique was used throughout the present test program.

SD73-SA-0061

5.0 EXPERIMENTAL RESULTS

The test program was oriented to obtain base region heating rate data for off-nominal flight conditions such as outboard-engine-out, actuator failures, and engine deflection effects. Very limited pressure data was obtained during this test program.

Some data was obtained to determine effects of engine oxidant to fuel (O/F) mixture ratio, chamber pressure, and altitude variations on the base region thermal environment. An unsuccessful attempt was made to measure base region gas recovery temperature by means of the heated component technique previously employed in the CAL test program.

No attempt was made to investigate the effects of turbo-pump exhaust gas (TPE) injection into the nozzle on base region thermal environment although the TPE gas manifold and injection slots were utilized to study the effects of nozzle wall boundary layer suction on base region thermal environment.

The latter part of the test program was devoted to obtaining engine nozzle wall heating rate data for operating and nonoperating engines, with and without engine deflections including engine thrust build-up effects.

The nominal model configuration for this test program consisted of the scaled 256-inch heat shield configuration, no interstage and no engine deflections with the engine operating conditions being O/F = 5.0, chamber pressure of 632 psia, and a simulated altitude of 240,000 feet.

It should be noted that the majority of the runs were made with O/F = 5.5 and chamber pressure of 715 psia which closely corresponds to the average S-II flight J-2 engine combustion chamber operating conditions of O/F = 5.75 and P_c = 725 psia experienced during flights AS-501 through AS-512.

A summary of the base heating tests conducted in this test program is presented in Table 5-1.

TABLE 5-1

SUMMARY OF S-II BASE$_1$
HEATING TESTS AT MSFC

Run Series	Log	Purpose/Conditions
CO1	INITIAL TESTS	
	CO1	Initial tests by CAL at MSFC - nominal configuration
CO2	TESTS OF FLOW METERING VENTURIS	
	CO2.1	Hot flow
	CO2.2	Cold flow } Not Listed
	CO2.3	Venturi modifications
CO3	TESTS OF O/F CAPABILITY	
	CO3.1	Nominal - O/F = 5.0
	CO3.2	O/F = 4.5
	CO3.3	O/F = 5.5
CO4	MODEL FLOW SYMMETRY	
	CO4.1	Nominal except instrumented nozzles
	CO4.2	Nominal except Case 3Ac deflection pattern and instrumented nozzles
	CO4.3	Nominal except special large diameter passage to nozzle throat on nozzles indicated
CO5	EVALUATION OF THRUST STRUCTURE HEATING	
	CO5	Attempt to shield thrust cone from all flow except that from the heat shield by using a large flow blocking disk

---

[1] Early runs at MSFC were run under two test plans which used identical log numbers for different conditions. In this list, the log numbers from the initial test plan have been revised to conform with the purposes of the later numbering system, and a series of checkout (CO) runs have been added for model operational tests.

TABLE 5-1 (Cont'd)

Run Series	Log	Purpose/Conditions

1 COMPARISON OF HUNTSVILLE TESTS TO THE CORNELL TESTS

1.1 Nominal conditions
1.2 Nominal conditions except altitude as high as possible
1.3 Nominal conditions except 210 inch heat shield configuration
1.4 Nominal conditions except 210 heat shield configuration and altitude as high as possible
1.5 Nominal conditions except P_c = 715 psia

2 EFFECT OF ENGINE MIXTURE RATIO

2.1 Nominal conditions except O/F = 5.5 and P_c = 715 psia
2.2 Nominal conditions except O/F = 4.5 and P_c = 546 psia
2.3 Nominal conditions except interstage in place, O/F = 5.5 and P_c = 715 psia
2.4 Nominal conditions except Case 3C deflection pattern O/F = 5.5 and P_c = 715 psia

3 DETERMINATION OF RECOVERY TEMPERATURE WITH CASE 3C DEFLECTION PATTERN

3.1 Nominal conditions heated component heated to 100°F
3.2 Nominal conditions heated component heated to as high a temperature as possible (not run)
3.3 Nominal conditions except O/F = 5.5, P_c = 715 psia and heated component heated to 100°F
3.4 Nominal conditions except O/F = 5.5, P_c = 715 psia and heated component at as high a temperature as possible

3A DETERMINATION OF RECOVERY TEMPERATURES WITH CASE 3Ca DEFLECTION PATTERN

3.1A Nominal conditions, heated component at 100°F
3.2A Nominal conditions, heated component at maximum temperature
3.3A Nominal conditions except O/F = 5.5, P_c = 715 psia and heated component at 100°F
3.4A Nominal conditions except O/F = 5.5, P_c = 715 psia and heated component at maximum temperature

TABLE 5-1 (Cont'd)

Run Series	Log	Purpose/Conditions
4		EFFECT OF INOPERATIVE ENGINES AND OF ACTUATOR FAILURE
	4.1	Nominal conditions except nonflowing instrumented nozzle in the No. 5 position
	4.2	Nominal conditions except Case 2 deflection and nonflowing instrumented nozzle in the No. 3 position
	4.2A	Nominal conditions except nonflowing nozzle in position No. 2 and Case 2A deflection pattern
	4.3	Nominal conditions except Case 3C deflection pattern
	4.4	Nominal conditions except Case 4A deflection pattern and the scaled 210 inch heat shield configuration
	4.5.1A 4.5.1B	Nominal conditions except O/F = 5.5, P_c = 715 psia, nonflowing nozzle in position No. 3, and Case 2 deflection pattern
	4.5.2A 4.5.2B	The same as Log 4.5.1A & 4.5.1B but with the interstage on
5		EFFECT OF SINGLE ACTUATOR FAILURES AT 3° AND 5° GIMBAL ANGLES
	5.1	Nominal conditions except Case 5 deflection pattern
	5.2	Nominal conditions except Case 6 deflection pattern
6		DETERMINATION OF ATTACHMENT FLANGE ENVIRONMENT
	6.1	Nominal conditions except Case 4A deflection pattern with instrumented flowing nozzle in the center engine position, lip gage N_2 is to be located directly across from engine No. 3
	6.2	Nominal conditions with instrumented flowing nozzle in the center engine position
7		TEST OF SIMULATED S-IV-TYPE SHIELD
	7.1	Test of simulated S-IV-type heat shield
8		DETERMINATION OF PRESSURES WITHIN THE PITCH CIRCLE
	8.1	Nominal conditions, static pressure probe even with the nozzle exit plane
	8.2	Nominal conditions, stagnation pressure probe even with the nozzle exit plane
9		EFFECT OF BOUNDARY LAYER BLEED
	9.1.1	Nominal conditions, boundary layer bleed
	9.1.2	Nominal conditions, boundary layer bleed

TABLE 5-1 (Cont'd)

Run Series	Log	Purpose/Conditions
11		EFFECT OF SINGLE ACTUATOR FAILURE OUTBOARD AT A 5° GIMBAL ANGLE
	11.1	Nominal conditions except Case 5A deflection pattern
	11.2	Nominal conditions except Case 5A deflection pattern and maximum altitude
	11.3	Nominal conditions except Case 5B deflection pattern
12		EFFECT OF DUAL 7.5° ACTUATOR FAILURES
	12.1	Nominal condition except Case 4A-a deflection pattern
	12.1A	Same as Log 12.1 except O/F = 5.5 and P_c = 715 psia
	12.2	Same as Log 12.1 except different instrumentation
	12.3	Nominal conditions except Case 4A-b deflection pattern
13		EFFECT OF DUAL 5° ACTUATOR FAILURES
	13.1.1 ⎫ 13.1.1A ⎬	Nominal conditions except Case 7 deflection pattern
14		ENVIRONMENT OF J-2 ENGINE COMPONENTS
	14.1 ⎫ 14.1A ⎬	Nominal conditions
	14.2	Nominal conditions except with interstage
	14.3	Nominal conditions except Case 3B deflection pattern
	14.4	Nominal conditions except Case 3B deflection pattern with interstage on
15		DOCUMENTATION OF THRUST STRUCTURE HEATING WITH O/F = 5.5
	15.3.1 ⎫ 15.3.2 ⎬	Nominal except with interstage, O/F = 5.5 and P_c = 715 psia
16		SINGLE ACTUATOR FAILURE EFFECTS WITH INTERSTAGE AND O/F = 5.5
	16.1	Nominal except interstage on, O/F = 5.5, P_c = 715 psia and deflection Case 3B
	16.3	Nominal except interstage on, O/F = 5.5, P_c = 715 psia and deflection Case 3C
	16.4	Nominal except interstage on, O/F = 5.5, P_c = 715 psia and deflection Case 5 (Not Recorded)
18		NOMINAL TRIM OF 0.8° IN PITCH AND YAW PLUS THRUST STRUCTURE COMPLIANCE
	18.1	Nominal except Case 8 deflection pattern

TABLE 5-1 (Cont'd)

Run Series	Log	Purpose/Conditions
19		NOMINAL TRIM OF 0.8° IN PITCH OR YAW PLUS THRUST STRUCTURE COMPLIANCE
	19.1	Nominal except Case 9 deflection pattern
	19.2	Nominal except Case 9A deflection pattern
	19.2.2A } 19.2.2B	Nominal except Case 9B deflection pattern, O/F = 5.5 and P_c = 715 psia, with interstage
	19.2.3A } 19.2.3B	Nominal except Case 9B deflection pattern, O/F = 5.5 and P_c = 715 psia
	19.3	Nominal except Case 9B deflection pattern
20		OUTBOARD ENGINE FAILURES WITH 5.5 MIXTURE RATIO
	20.1.1 } 20.1.2 } 20A.1.2	Nominal except O/F = 5.5, P_c = 715 psia, nonflowing nozzle in No. 3 position, and Case 2B deflection pattern. Runs numbered 20A.1 use Case 2B modified deflection pattern
	20.2.1 } 20.2.2	Same as Log 20.1 with interstage skirt installed
21		SINGLE ACTUATOR FAILURE INBOARD AT 3 DEGREES
	21.1	Nominal except O/F = 5.5, P_c = 715 psia, and Case 6A deflection pattern
	21.2	Same as Log 21.1 with interstage skirt installed
22		SINGLE ACTUATOR FAILURE OUTBOARD AT 3 DEGREES
	22.1	Nominal except O/F = 5.5, P_c = 715 psia and Case 6B deflection pattern
	22.2	Same as Log 22.1 with interstage skirt installed
23		CENTER NOZZLE WALL ENVIRONMENT WITH ACTUATOR FAILURES
	23.1.1	Nominal except deflection Case 8, O/F = 5.5, and P_c = 715 psia
	23.2	Nominal except deflection Case 6A, O/F = 5.5, and P_c = 715 psia
	23.3	Nominal except deflection Case 10, O/F = 5.5, and P_c = 715 psia
	23.4	Nominal except deflection Case 11, O/F = 5.5, and P_c = 715 psia
	23.5	Nominal except deflection Case 12, O/F = 5.5, and P_c = 715 psia
	23.6	Nominal except deflection Case 12, O/F = 5.5, and P_c = 465 psia
	23.7	Nominal except deflection Case 12, O/F = 5.5, and P_c = 215 psia

TABLE 5-1 (Concluded)

Run Series	Log	Purpose/Conditions
24		THRUST CONE RADIATION
	24.1.1	Nominal except flow symmetry nozzles, O/F = 5.5, and P_c = 715 psia
25		HEAT SHIELD PRESSURES WITH ENGINE DEFLECTIONS
	25.1	Nominal except deflection Case 3C with nozzles and adaptors rotated 180°, O/F = 515, and P_c = 715 psia
	25.2	Nominal except deflection Case 6A with nozzles and adaptors rotated 180°, O/F = 5.5, and P_c = 715 psia
26		NULL NOZZLE WALL HEATING RATES
	26.1	Nominal except O/F = 5.5, P_c = 715 psia, and skirt gages on the center nozzle
	26.2	Nominal except O/F = 5.5, P_c = 715 psia, and skirt gage on outboard nozzles
27		OUTBOARD NOZZLE WALL ENVIRONMENT WITH ACTUATOR FAILURES
	27.1	Nominal except deflection Case 8, O/F = 5.5, and P_c = 715 psia
	27.2.1 } 27.2.2	Nominal except deflection Case 6A, O/F = 5.5, and P_c = 715 psia
	27.3	Nominal except deflection Case 10, O/F = 5.5, and P_c = 715 psia
28		ENVIRONMENT OF AN INOPERATIVE OUTBOARD ENGINE
	28.1	Nominal except deflection Case 2B modified, O/F = 5.5, and P_c = 715 psia

The test values for all the conditions tested are recorded in the data Logs of Section 3.0, Volume II. All the test data presented in the following Sections are the test average values listed in Section 2.0 of Volume II.

The constant heating rate contours presented in the various sections of this report were obtained by means of linear interpolation between the heating rate values for the gages indicated in each plot. Additional constant heating rate contours, corresponding to the mean + 3σ values, are presented in Section 4.0 of Volume II.

5.1 EFFECT OF ALTITUDE

The effect of altitude, or ambient pressure, on base region heating rates was studies by reducing the chamber pressure to the minimum possible value which corresponds to approximately 305,000 feet altitude. Heat shield and thrust cone heating rates were measured and are recorded in Log 1.3 and 1.4. Only three thrust cone pressures were recorded; no heat shield pressure data was obtained. No discernable altitude effect is apparent from these results.

Altitude investigations carried out in Reference 1 with the 1/25 S-II scale model indicated that the critical altitude is reached between 160,000 and 200,000 feet for the S-II configuration; consequently, no variation in base region heating rates and pressures is expected for the range of altitudes investigated ($\simeq 238,000$ to 305,000 feet) in this test. Comparable results were obtained in the CAL tests of Reference 8 where the altitude was varied from 236,000 feet (33μ Hg A) to 266,500 feet (6μ Hg A).

5.2 EFFECT OF MIXTURE RATIO AND CHAMBER PRESSURE VARIATION

The effect of simultaneously varying engine mixture ratio (PMR) and engine chamber pressure (P_c) on base region thermal environment was studied and the results were recorded in Logs 2.1 through 2.4 for the nominal configuration, the interstage-on case and the single actuator failure case. The simultaneous variation of PMR and P_c corresponds to the in-flight operating condition of the S-II stage J-2 engines. The mixture ratio tests were carried out at O/F = 4.5 and 5.5 with the corresponding chamber pressure values of 546 and 715 psia.

The nominal test condition results (O/F = 5.0, P_c = 632 psia) are recorded in Log 1.1

5.2.1 Heat Shield Heating Rates

The variation of heat shield heating rates with PMR and P_c is shown in Figure 5.2.1-1. It is seen that the heat shield heating rates show a linear dependence on engine chamber pressure.
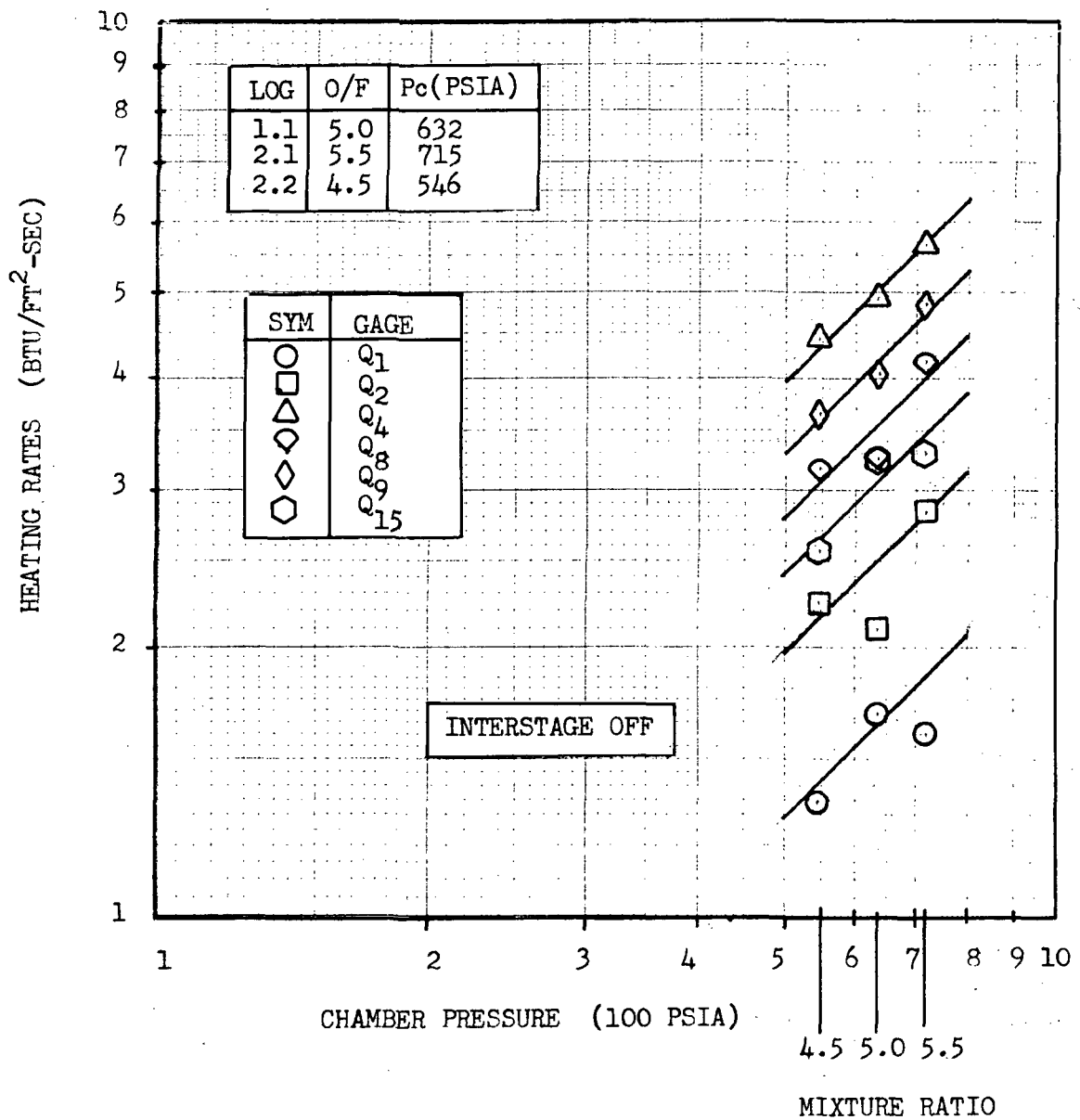
Figure 5.2.1-1 Effect Of Chamber Mixture Ratio and Pressure
On Heat Shield Heating Rates

SD73-SA-0061

A very limited investigation of increased mixture ratio and chamber pressure effects was carried out in the CAL test program as reported in Reference 8. Increasing O/F mixture ratio to 5.5 and chamber pressure to 715 psia, from the nominal values of 5.0 and 632 psia respectively, resulted in increased heat shield heating rates and decreased thrust cone heating rates. Consequently, these tests were inconclusive.

Comparison of the data of Figure 5.2.1-1 with the constant mixture ratio and varying chamber pressure data of Figure 5.3.1-1 shows that the observed variation of heating rates in Figure 5.2.1-1 is primarily due to changes in chamber pressure.

5.2.2 Thrust Cone Heating Rates

The effect of simultaneously varying chamber pressure and mixture ratio on thrust cone heating rates is presented in Figure 5.2.2-1. A large amount of thrust cone heating rate data was recorded during this test program, especially for the nominal O/F = 5.0 condition. However, problems were encountered with nozzle adaptor leakage which rendered some of the thrust cone data to be of questionable validity. The mean values, for a particular gage show a large degree of scatter between different run series reflecting the difficulty of obtaining reliable thrust cone heating rate data. Consequently, the heating rates presented in Figure 5.2.2-1 represents the arithmetic mean of the test runs listed.

From Figure 5.2.2-1 it is seen that the thrust cone heating rates are proportional to chamber pressure to the 2.6 power. Also shown for comparison in Figure 5.2.2-1 is the corresponding constant O/F ratio variable chamber pressure data trend of Section 5.3.2 (Figure 5.3.2-1) which indicates that the thrust cone heating rates vary as chamber pressure to the 1.52 power. It is doubtful that this appreciably different thrust cone heating-rate-chamber-pressure-dependence is real and due only to the mixture ratio effect.

5.2.3 Heat Shield Pressures

The effect of simultaneously varying chamber pressure and mixture ratio on the heat shield pressures is shown in Figure 5.2.3-1.

The base heat shield pressures appear to increase with chamber pressure to the 1.3 power over the chamber pressure and mixture ratio range investigated. These results follow similar trends found in the chamber pressure effect investigation reported in Reference 1 where the chamber pressure was varied and the mixture ratio held constant at 5.0. A comparison with Reference 1 data is shown in Figure 5.2.3-2 which indicates that the base pressure variation resulting from mixture ratio-chamber pressure change is primarily due to change in chamber pressure.
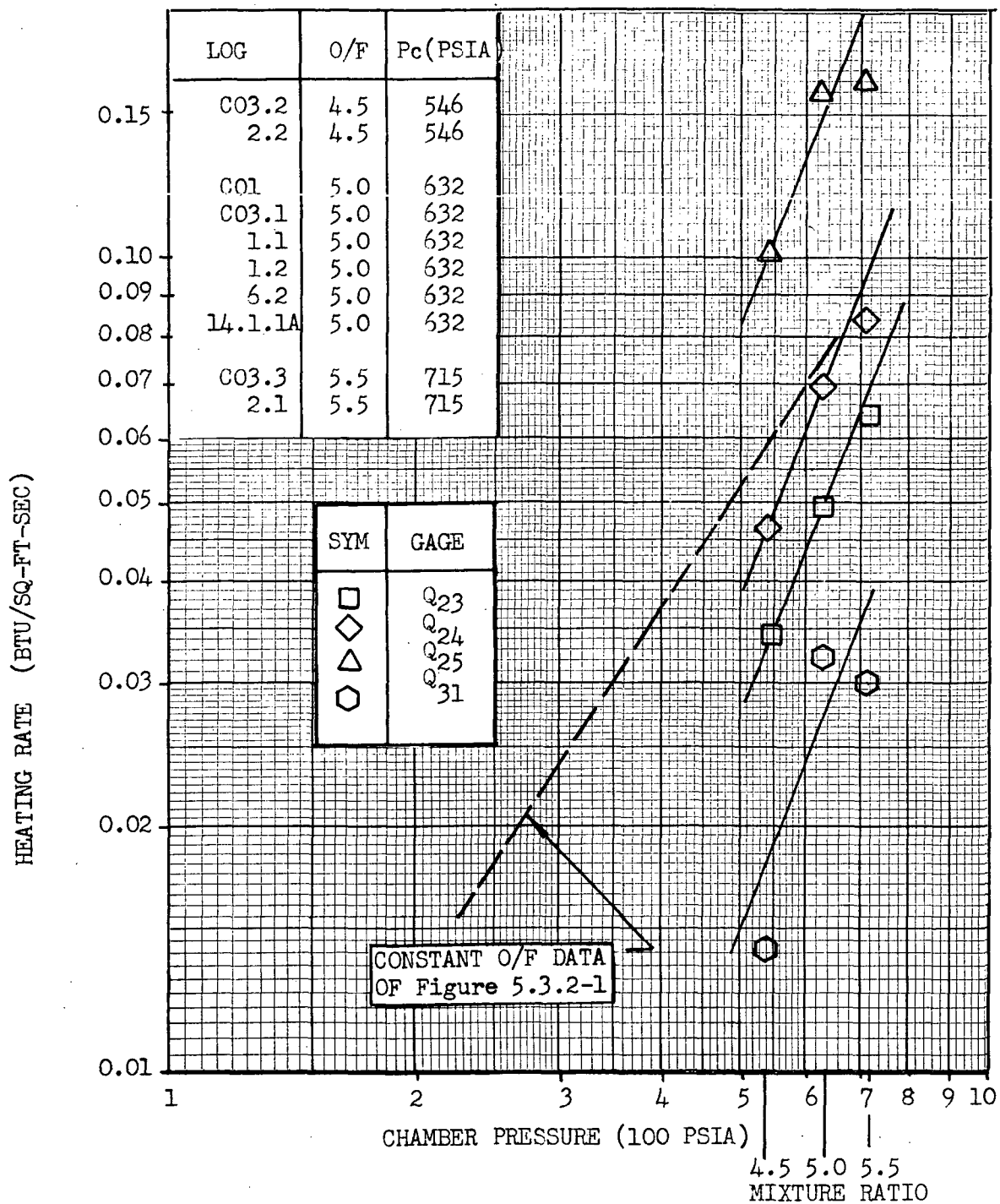
Figure 5.2.2-1 Effect of Chamber Pressure and Mixture
Ratio on Thrust Cone Heating Rates

SYM	GAGE	SYM	GAGE
◇ ▢ ◇	P_2 P_3 P_5	△ ○ ◇	P_7 P_8 P_{11}

LOG	O/F	Pc(PSIA)
2.2	4.5	546
9.1.2	5.0	632
2.1	5.5	715

BASE PRESSURE (PSIA)

CHAMBER PRESSURE (100 PSIA)

4.5   5.0   5.5
MIXTURE RATIO
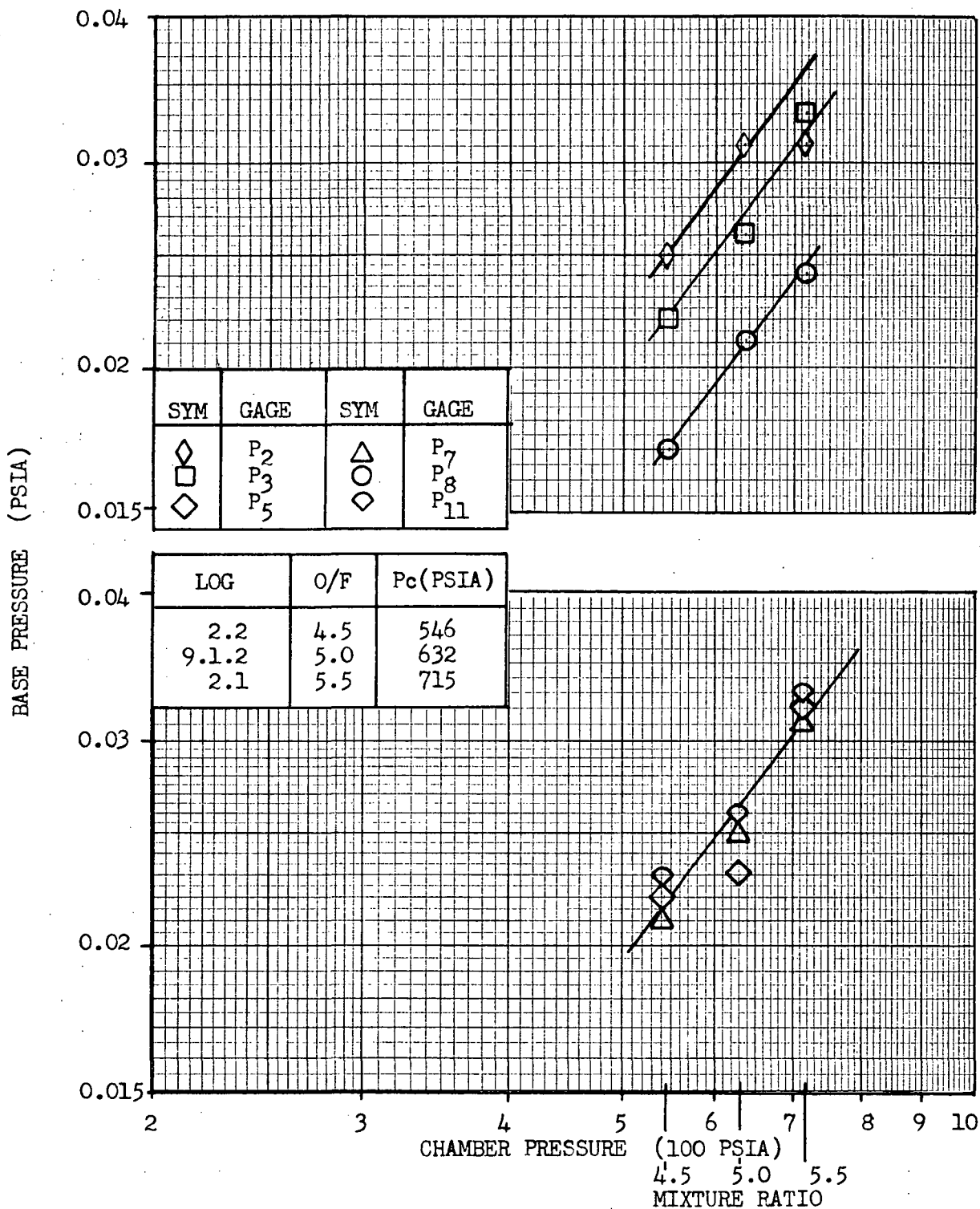
Figure 5.2.3-1   Effect of Chamber Mixture Ratio and Pressure
Variation on Heat Shield Pressures
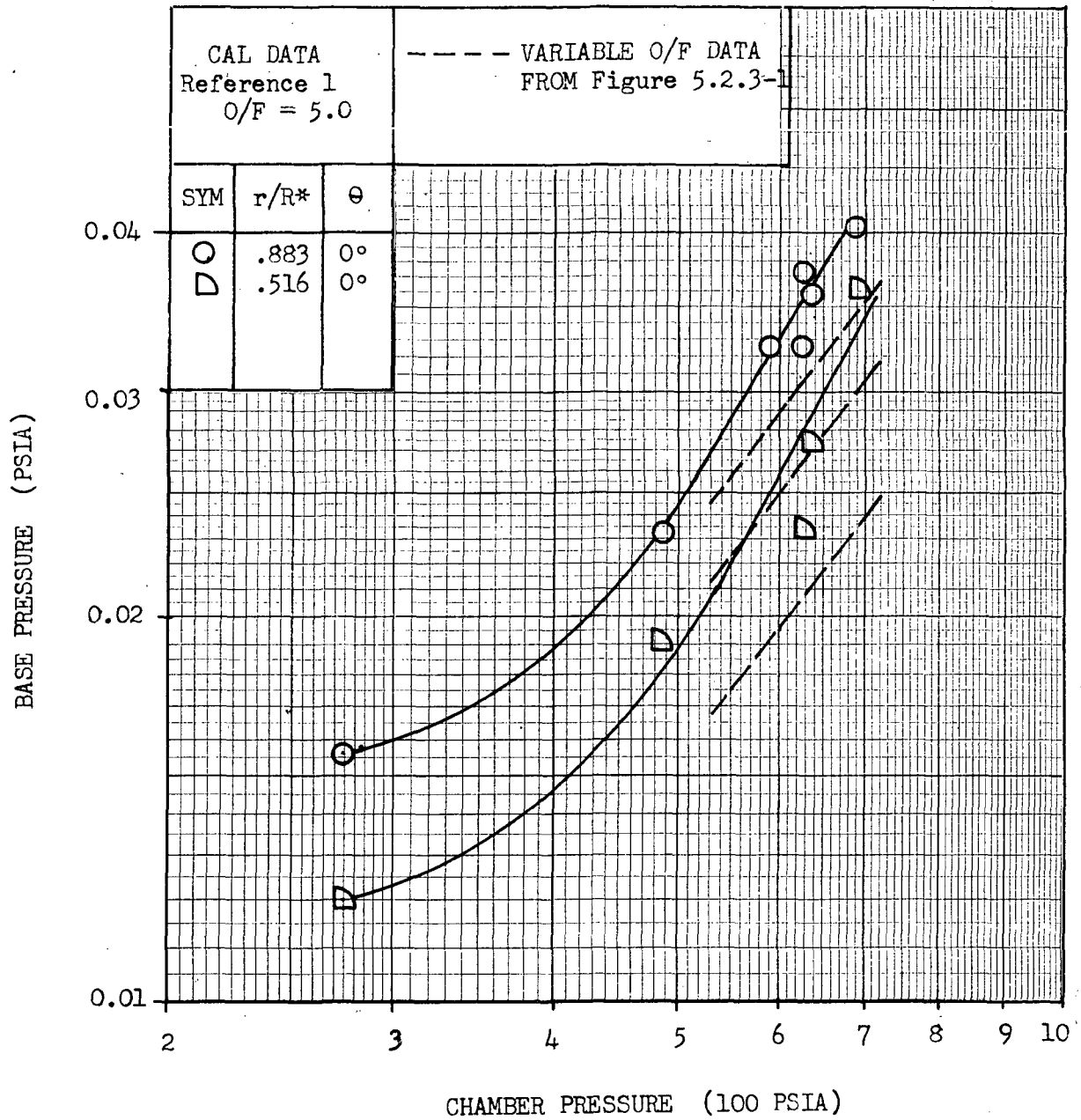
Figure 5.2.3-2   Comparison with Constant O/F Ratio Pressure Data

5.3 EFFECT OF CHAMBER PRESSURE VARIATION

Very limited data was obtained to determine the effect of chamber pressure variation on base region thermal environment. The test runs of data Log 1.5 correspond to an increased chamber pressure of 715 psia and nominal O/F mixture ratio of 5.0 with interstage off and no engine gimballing. Also, in Run Series 23, the purpose of which was to determine center engine nozzle wall environment with actuator failures, test runs were made with chamber pressures of 215, 465, and 715 psia at a constant mixture ratio of 5.5. Heat shield heating rates and one thrust cone heating rate were recorded during these test runs which provide an indication of chamber pressure effects on the base region heating rates.

No pressure measurements were recorded during the chamber pressure effect test runs.

5.3.1 Heat Shield Heating Rates

The higher chamber pressure (715 psia) heat shield heating rate data of Log 1.5 showed a reduction of the heating rates from the P_c = 632 psia values of Log 1.1 which is opposite to the results presented in References 2 and 3 as well as analytical considerations. Therefore, these data must be considered to be erroneous. The results presented in References 1, 2, and 3 indicate that the heat shield heating rates are approximately proportional to the chamber pressure with some variation existing with location on the heat shield.

Figure 5.3.1-1 presents the base heat shield heating rate variation with chamber pressure for the transient engine deflection case corresponding to dual actuator failure at 5 degrees inboard; i.e., engine deflection Case 12, Figure 5.10-1. Again the corresponding no-deflection data of Reference 1 is shown for comparison. It is seen that most of the heat shield and flexible curtain heating rate trends agree reasonably well with the no-deflection data trends established in Reference 1.

5.3.2 Thrust Cone Heating Rates

The effect of chamber pressure increase on thrust cone heating rates for the nominal test configuration is recorded in Log 1.5. The results are inconclusive since about half of the gages indicate a decrease of heating rates with increasing chamber pressures, which is opposite to the expected trend.

One thrust cone heating rate (Q25) was recorded during Run Series 23 test runs where the center engine nozzle environment was investigated with a transient dual actuator failure gimbal pattern. Test runs were made with chamber pressures of 215, 465, and 715 psia and constant mixture ratio of 5.5. The resulting thrust cone heating rate variation is presented in Figure 5.3.2-1. It is seen that the heating rates at this thrust cone location are proportional to chamber pressure to the 1.52 power as compared to the linear variation of the heat shield heating rates shown in Figure 5.3.1-1.
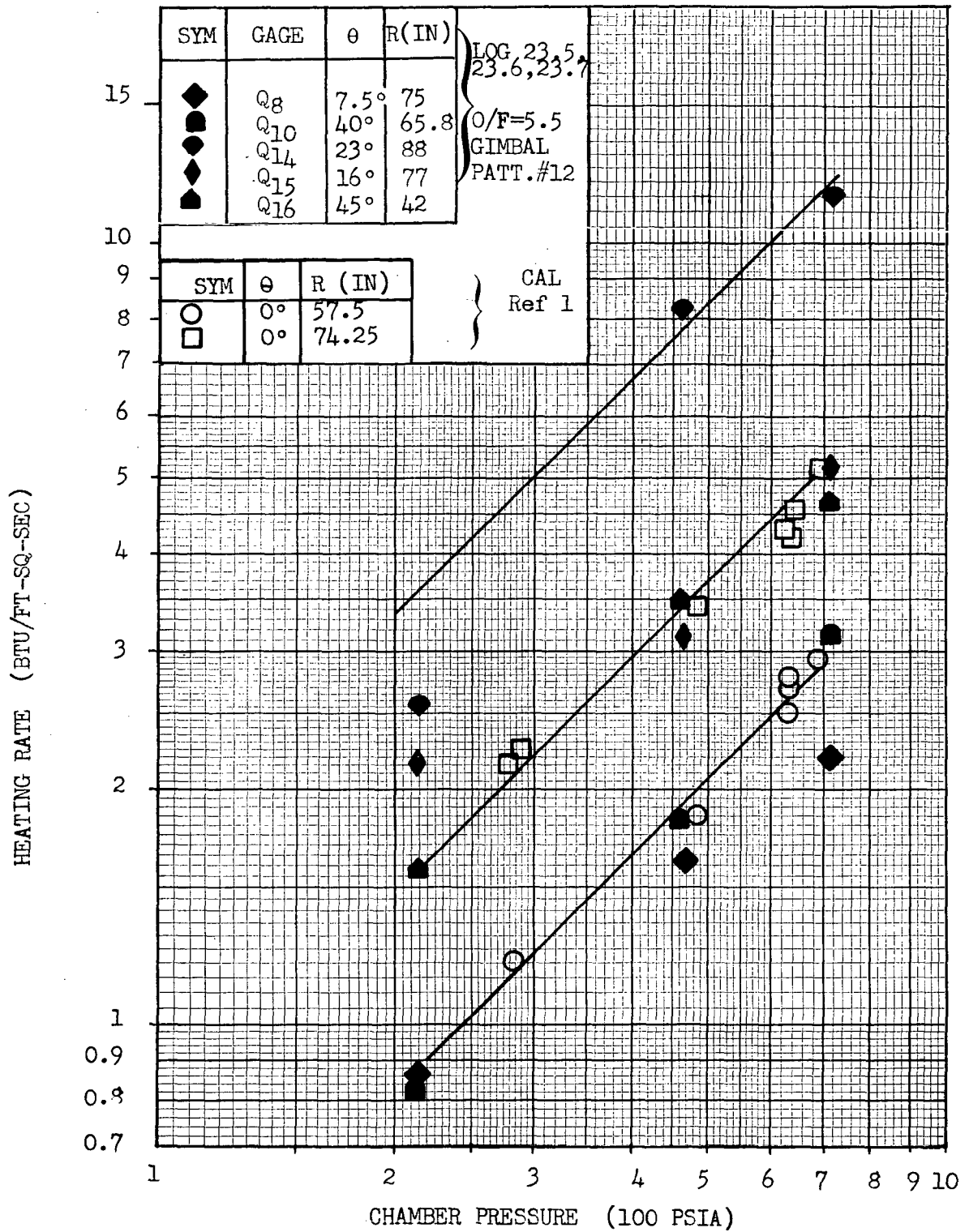
Figure 5.3.1-1   Effect of Chamber Pressure Variation On
Heat Shield Heating Rates

SD73-SA-0061
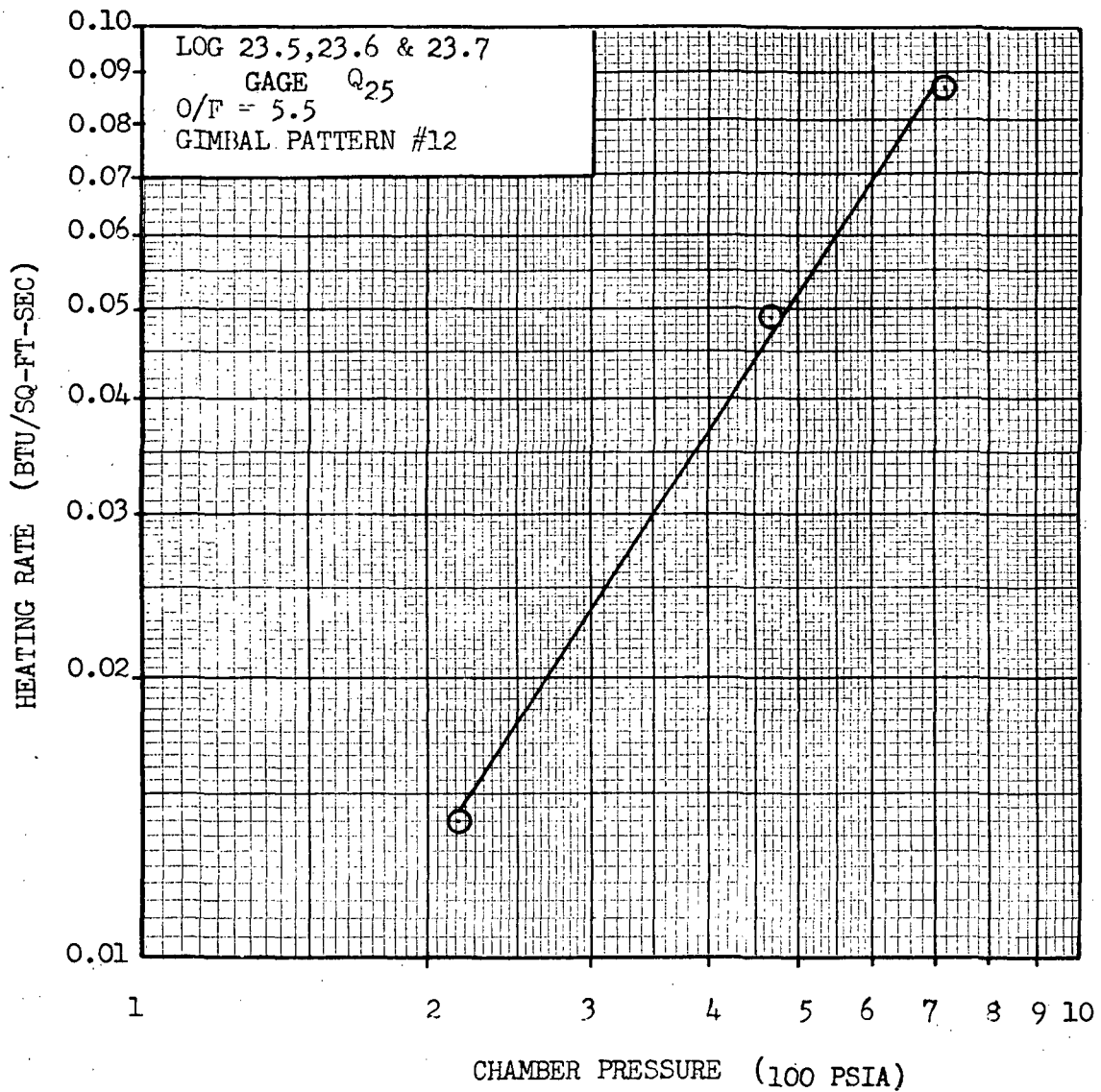
Figure 5.3.2-1   Effect of Chamber Pressure Variation on Thrust
Cone Heating Rates

5.3.3 Nozzle Heating Rates

The effect of chamber pressure on nozzle heating rates was studied in connection with the dual-actuator-failure-inboard engine deflection Case 12. The results are presented in Section 5.10, Figure 5.10.3-7, where it is seen that the nozzle heating rates are proportional to chamber pressure.

5.4 EFFECT OF INTERSTAGE

Numerous tests were run to determine the effect of the S-IC/S-II stage interstage on the S-II base region thermal environment for the nominal no-deflection configuration and the off-nominal flight conditions of outboard-engine-out and actuator failures. Interstage effects for the nominal flight conditions are discussed in the following section while the effects on off-nominal flight conditions are treated under the appropriate sections dealing with the specific failure condition.

5.4.1 Heat Shield Heating Rates

The effect of the interstage on the heat shield heating rates is shown in Figure 5.4.1-1. The corresponding results obtained in the CAL test program for the 256-inch heat shield configuration are also shown for comparison. It is seen that the peak heating rate is unchanged. The interstage effect is most pronounced at the heat shield location where the area between the nozzles is minimum. The heating rates at this location increased by 25% from the interstage-off values on the heat shield centerline and by 40% near the outboard engine.

It is seen from Figure 5.4.1-1 that similar trends were obtained in the CAL test program with the 256-inch heat shield configuration with the exception that the heating rates around the outboard engine were practically unchanged by the interstage.

5.4.2 Thrust Cone Heating Rates

The effect of the interstage on the thrust cone heating rates is presented in Figure 5.4.2-1 together with the corresponding data of Reference 8 for comparison. It is seen that the interstage effect is extremely pronounced on the thrust cone heating rates. With the interstage on, heating rates are found to increase by as much as a factor of 30 from the interstage-off values. Very good agreement was obtained with the corresponding CAL test results.

5.4.3 Thrust Cone Pressures

The effect of interstage on the thrust cone pressures is summarized in Table 5.4.3-1. With the interstage on, the pressures are from 18 to 30 times the corresponding interstage-off values. These results are consistent with the thrust cone heating rate data of Section 5.4.2; however, the corresponding pressure results obtained in the CAL test

HEAT SHIELD CENERLINE VARIATION

CAL DATA
Reference 8
O/F = 5.0

SYM	INTRST
▲	ON
◆	OFF

MSFC DATA
O/F = 5.5

SYM	INTRST	LOG
☐	ON	2.3
○	OFF	2.1

HEATING RATE (BTU/SQ-FT-SEC)

MODEL RADIUS R (INCHES)

PERIPHERAL VARIATION AROUND
OUTBOARD ENGINE AT r = 2.1 IN

PERIPHERAL ANGLE φ (DEGREES)
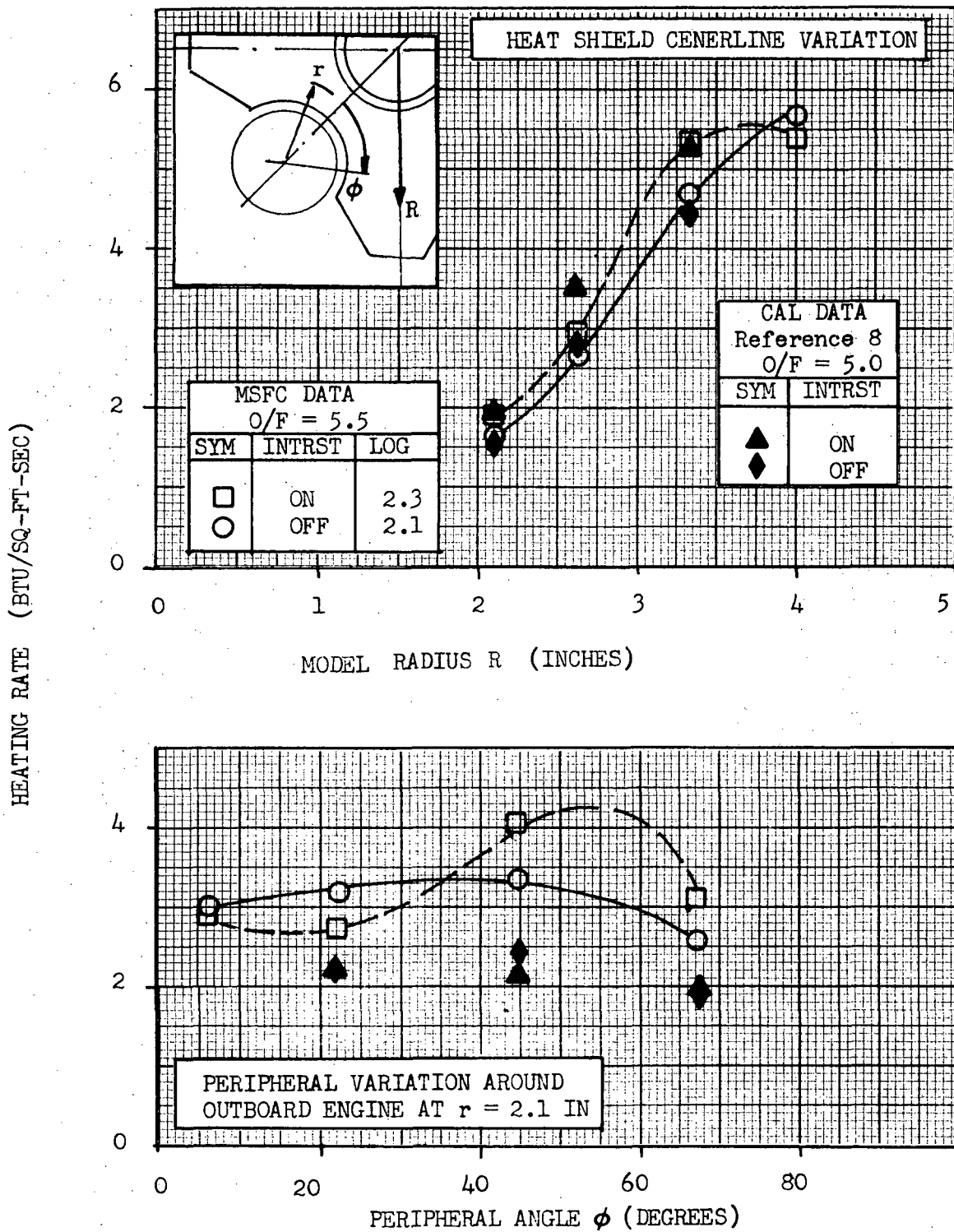
Figure 5.4.1-1 Effect of Interstage On Heat Shield Heat Rates
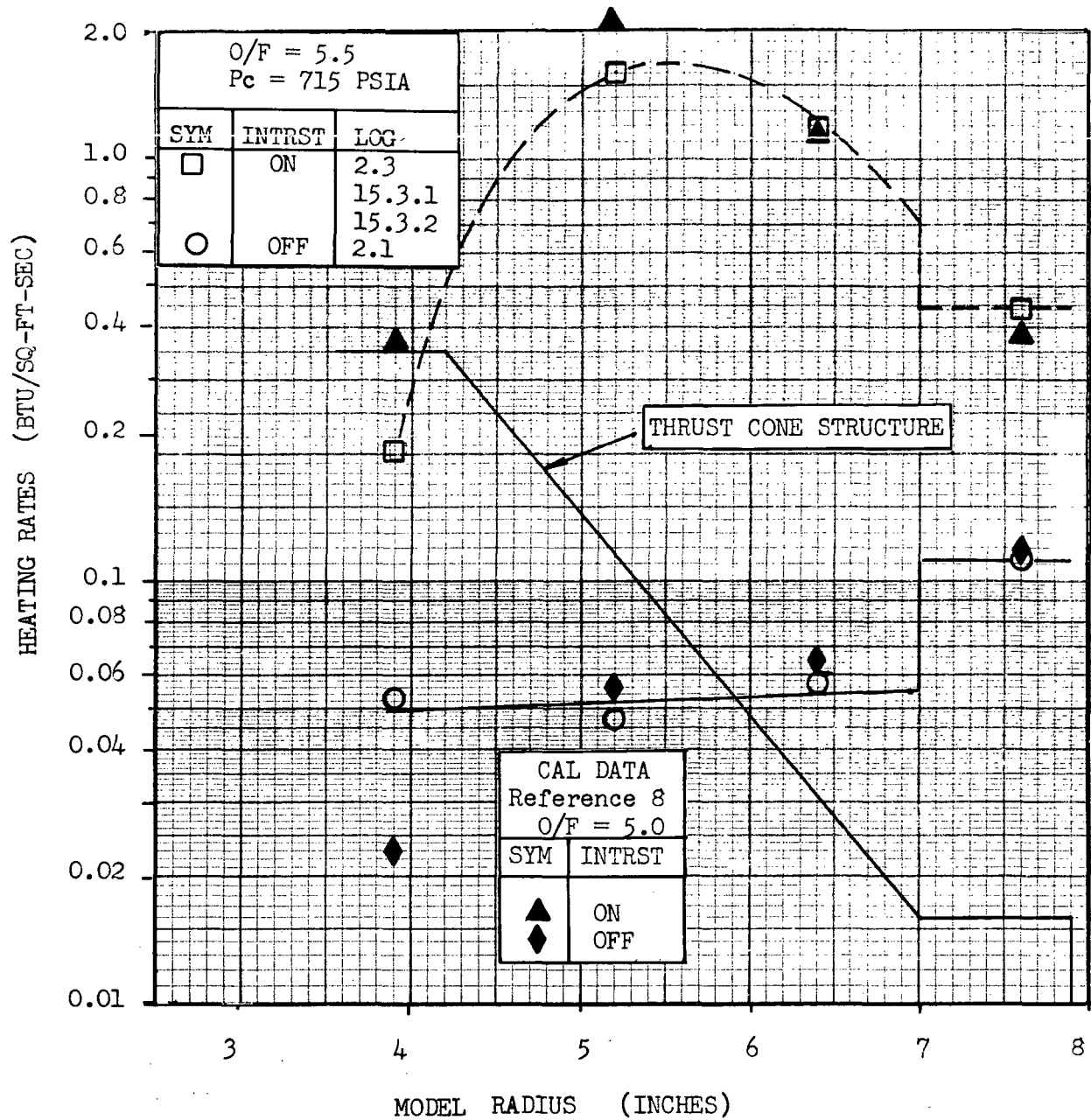
Figure 5.4.2-1 Effect of Interstage on Thrust Cone Heat Rates

program, shown in Table 5.4.3-1, indicate a pressure increase due to interstage of 8 to 15 times the interstage-off values. The discrepancy between the results of the two test programs is most probably due to the difficulties experienced in the CAL test program in obtaining steady flow conditions in the thrust cone region because of the shorter test period available for data acquisition.

TABLE 5.4.3-1

EFFECT OF INTERSTAGE ON THRUST CONE PRESSURES

	PRESENT TEST $O/F = 5.5$, $P_c = 715$ psia			CAL DATA, REFERENCE 8 $O/F = 5.0$, $P_c = 632$ psia		
	INTERSTAGE		PRESSURE	INTERSTAGE		PRESSURE
	OFF	ON	RATIO	OFF	ON	RATIO
GAGE	P_1	P_2	P_2/P_1	P_3	P_4	P_4/P_3
P_{15}	--	--		0.0010	0.0173	17.3
P_{16}	0.00160	0.0300	18.8	--	--	--
P_{17}	0.00154	0.0280	18.2	0.0025	0.0220	8.8
P_{18}	0.00100	0.0300	30.0	0.0010	0.0153	15.3

5.5 RECOVERY TEMPERATURE

An attempt was made to measure the recovery temperature of the reversed flow gas at the base heat shield by means of the heated component technique previously used in the CAL tests and reported in Reference 8.

The test runs corresponded to single actuator failure conditions, i.e., gimbal patterns 3C and 3Ca with mixture ratios of $O/F = 5.0$ and 5.5. In general, insufficient data was obtained for a particular test condition or the data showed such a degree of scatter that it was not possible to obtain even an approximate value of the recovery temperature. The test results are tabulated in data Logs 3.1, 3.1A, 3.2A, 3.3, 3.4, 3.3A, and 3.4A.

The only apparently useful data obtained from these tests was with the engine deflection pattern 3C, O/F = 5.5 recorded in Log 3.3 and 3.4.

The results are presented in Figure 5.5-1 where,by linear extrapolation of the heating rates,the recovery temperature at the heated component is seen to be approximately 1200 F. It should be noted that this recovery temperature is for the quadrant in which the resultant deflection of the outboard engines is 0°, whereas the maximum heating rates occur in the opposite heat shield quadrant.

Recovery temperature investigations were carried out in the CAL test program using the heated base heat shield technique for the no-deflection case and a range of chamber pressures from 300 to 700 psia. The results are reported in Reference 1. The S-II scale model used in the test was slightly different from the final S-II configuration model used in the present test program in that the heat shield was located at S-II Station 29 instead of Station 44. The results presented in Reference 1 show that the recovery temperature varied from 1750 F, with P_c = 300 psia, to 2500 F, with P_c = 700 psia. In Reference 8, where the heated component technique was used to measure recovery temperature, it was determined that the gas recovery temperature was approximately 2300 F with P_c = 630 psia.

Both Reference 1 and 8 report difficulties in obtaining good quality recovery temperature data. For example, using the heated base technique, unknown temperature differences existed between the heated base and the heat transfer gages. The gage calibration factors changed due to repeated cycling from low to high temperatures; and, uncertainties of the temperature effect on the film coefficient, discussed in Reference 11, affect the accurate extrapolation of the recovery temperature data to the zero-heating wall temperature, i.e., the gas recovery temperature.

In view of the very limited gas recovery temperature data obtained in the present test, it is not possible to determine whether the 1100 to 1300 F difference in gas recovery temperature between the present test results and those of References 1 and 8 is due to the engine deflections of gimbal pattern 3C or experimental error.

5.6 BASE REGION ENVIRONMENT FOR THE NOMINAL CONFIGURATION

The test results for various off-nominal flight conditions are presented and discussed in the following sections. In these discussions comparisons are made with the corresponding environments for nominal flight. Therefore, heating rate and pressure distributions are presented in this section for the configurations corresponding to nominal flight for several values of chamber mixture ratio and pressure which occur during a typical S-II flight.
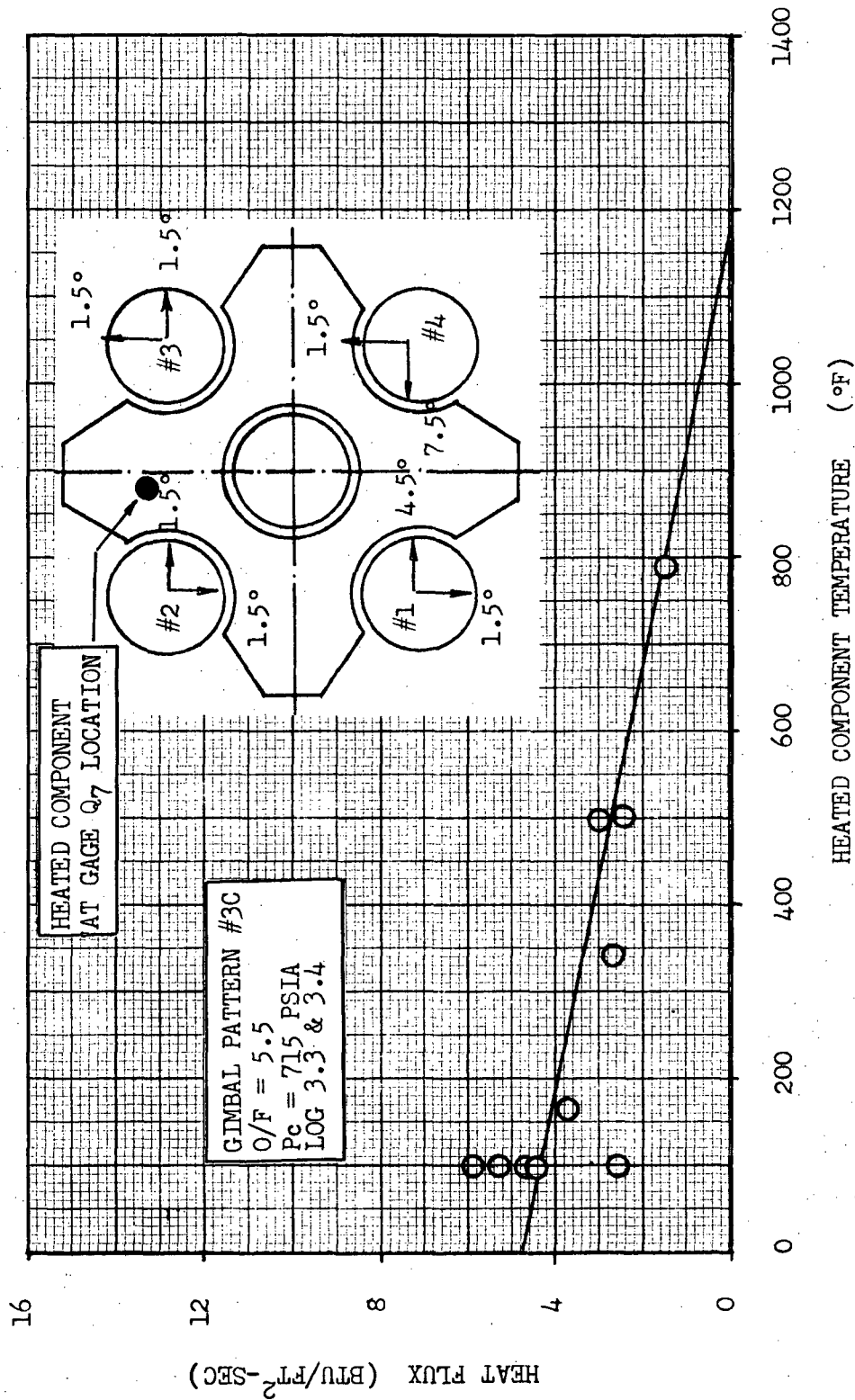
Figure 5.5-1 Gas Recovery Temperature at Gage Q_7 Location

5.6.1 Heat Shield Heating Rates

Constant heating rate distributions are presented in Figures 5.6.1-1, 5.6.1-2, and 5.6.1-3 for chamber mixture ratios of 4.5, 5.0, and 5.5 respectively. Figure 5.6.1-1 and 5.6.1-3 indicate that the model heating rates are not symmetrical about the heat shield centerline even for the no-deflection case. Similar asymmetrical variations were found in the CAL results as reported in Reference 8. As expected, the heating rate distribution remains essentially unchanged with increasing mixture ratio, with the peak measured heating rate increasing from 4.5 Btu/ft^2-sec at O/F = 4.5 to 4.9 Btu/ft^2-sec at O/F = 5.0 and 5.65 Btu/ft^2-sec at O/F = 5.5.

The effect of interstage on the heat shield heating rates is shown in Figure 5.6.1-4. Comparing with the corresponding interstage-off distribution, presented in Figure 5.6.1-3, it is seen that the peak heating rate is practically unchanged. The largest change in heating rates takes place in the region of minimum area between the nozzles, where the interstage-on heating rates increased by as much as 20% from corresponding interstage-off values.

5.6.2 Thrust Cone Heating Rates

Thrust cone surface heating rates for the interstage-off and inter-stage-on condition are presented in Figures 5.6.2-1 and 5.6.2-2 respectively. The constant heating rate contours are based on the thrust cone surface gage data only. Numerous heating rates of base region components located forward of the heat shield in the thrust cone region are recorded in Log 2.1, for the interstage-off case and Logs 15.3.1 and 15.3.2 for the interstage-on case.

Referring to Figures 5.6.2-1 and 5.6.2-2, it is seen that the effect of the interstage on the thrust cone heating rates is to increase the heating rates by an order of magnitude from the corresponding interstage-off values, i.e., by a factor of 20 to 30 in most cases. The thrust cone region least affected by the interstage is the thrust cone close-out at Station 196, where the heating rates increase by a factor of 4.

Thrust cone region heating rates in the vicinity of Engine No. 1 forward of the heat shield were measured by means of the ring gages shown in Figure 3.4-4. Heating rates for this region with and without the interstage are presented in Figure 5.6.2-3. It is seen that with inter-stage off most of the heating rates are from 2 to 4 times the thrust cone surface values directly below the ring gages. The interstage-on heating rates, on the other hand, with the exception of gage Q90 are comparable to or lower than the thrust cone surface values. Note also that the interstage-on heating rate variation with S-II Station is opposite to that for the interstage-off case, i.e., the interstage-on heating rate trend shows increasing heating rates with Station while the interstage-off case, for Station greater than 75, heating rates show a decrease with S-II Station.

(4.42)

4.0

3.5

3.0

2.5

ENGINE #4

ENGINE #1

1.0

2.0

1.5

☐(0.58)

☐(1.78)

☐(2.02)

NO DEFLECTIONS
INTERSTAGE OFF
O/F = 4.5
Pc = 546 PSIA
LOG 2.2

HEATING RATES IN BTU/FT^2-SEC
TO 72°F SURFACE
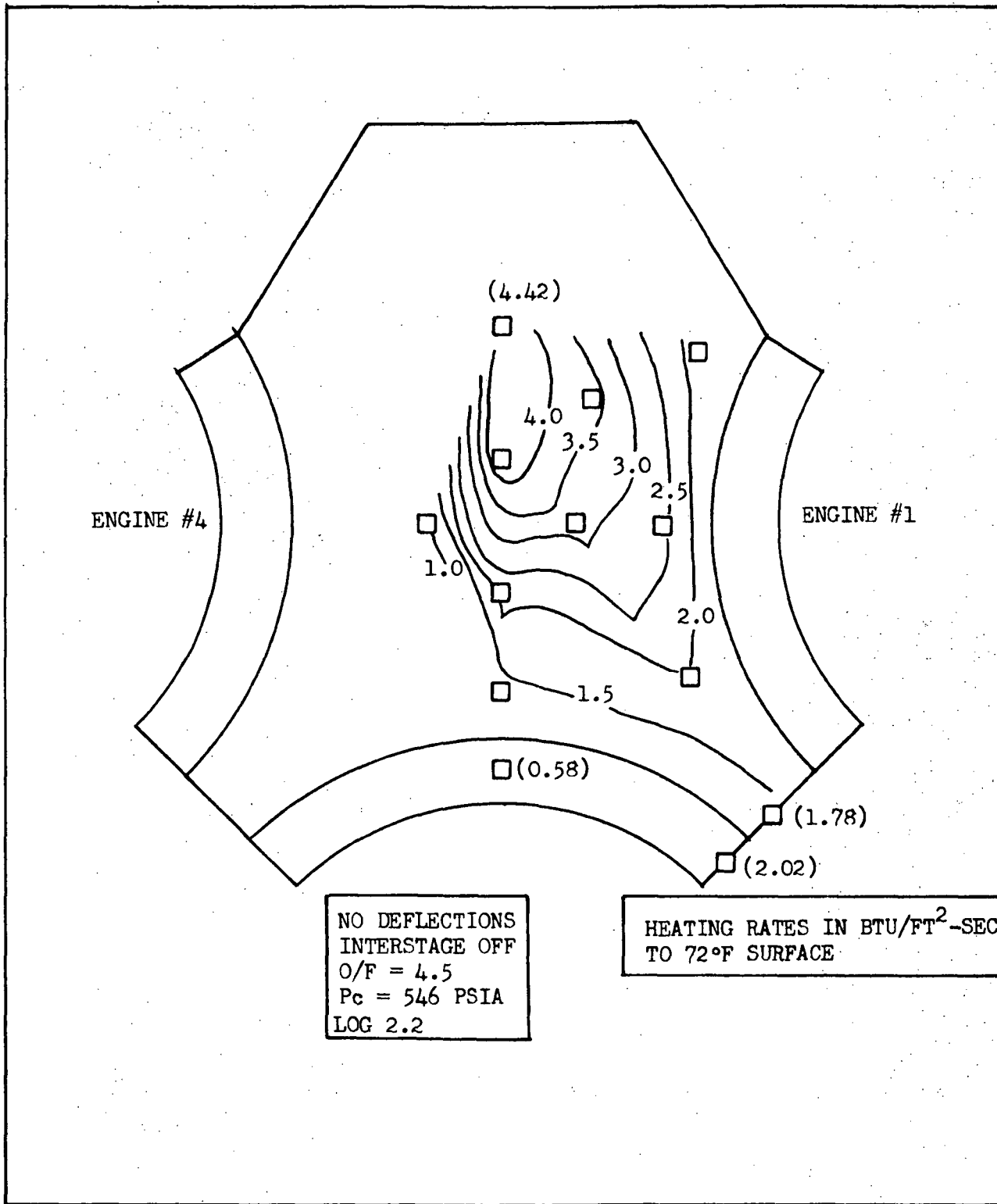
Figure 5.6.1-1   Heat Shield Heating Rates With No Deflections, O/F = 4.5
and Interstage Off

- 68 -
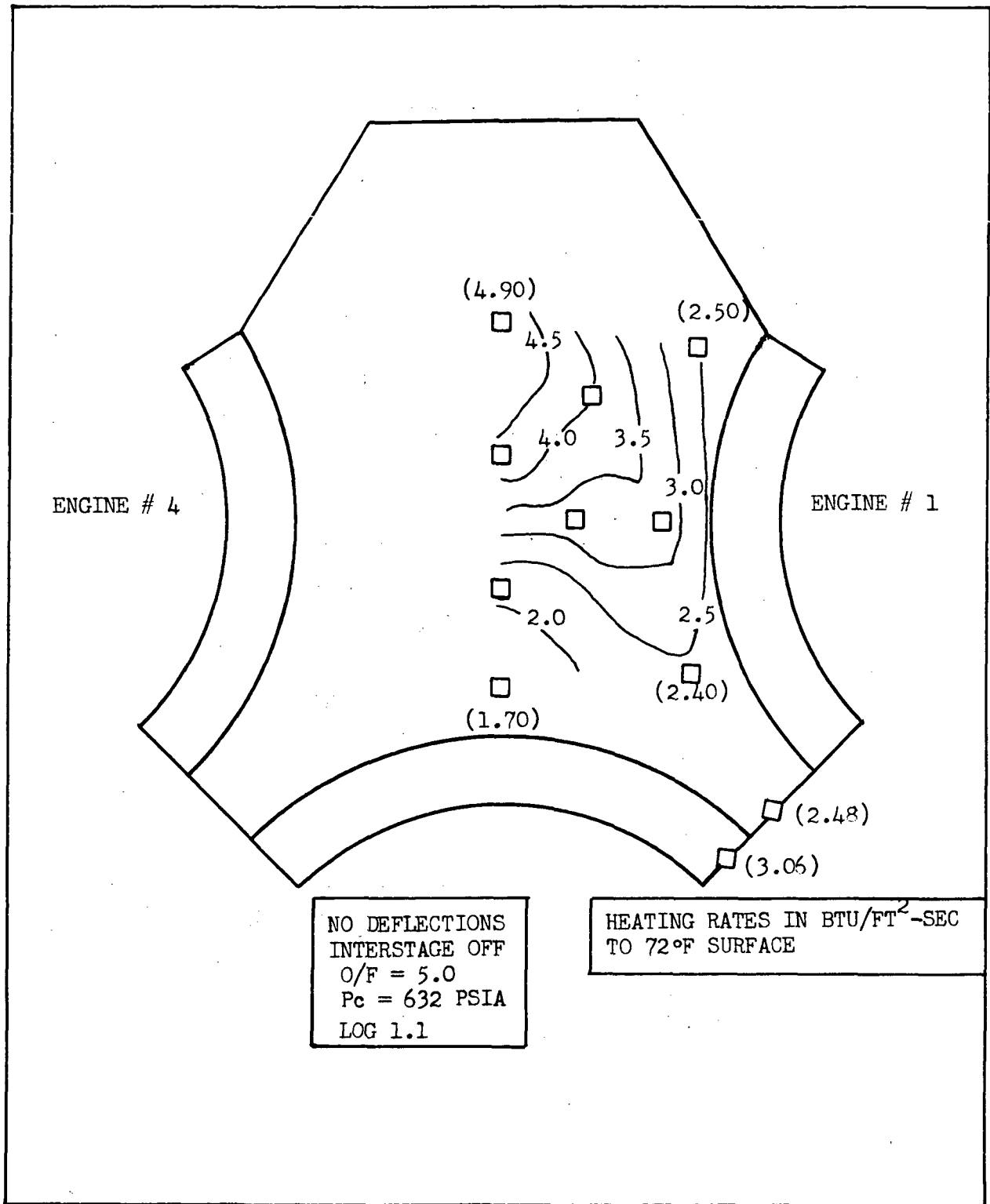
Figure 5.6.1-2 Heat Shield Heating Rates With No Deflections, O/F = 5.0
and Interstage Off

SD73-SA-0061

ENGINE # 4

ENGINE # 1

(5.65)

(2.45)

5.5

5.0

4.5

4.0

(1.98)

3.5

3.0

2.0   2.5

(1.60)

(0.79)

(3.53)

(2.94)

NO DEFLECTION
INTERSTAGE OFF
O/F = 5.5
Pc = 715 PSIA
LOG 2.1

HEATING RATES IN BTU/FT^2-SEC
TO 72°F SURFACE
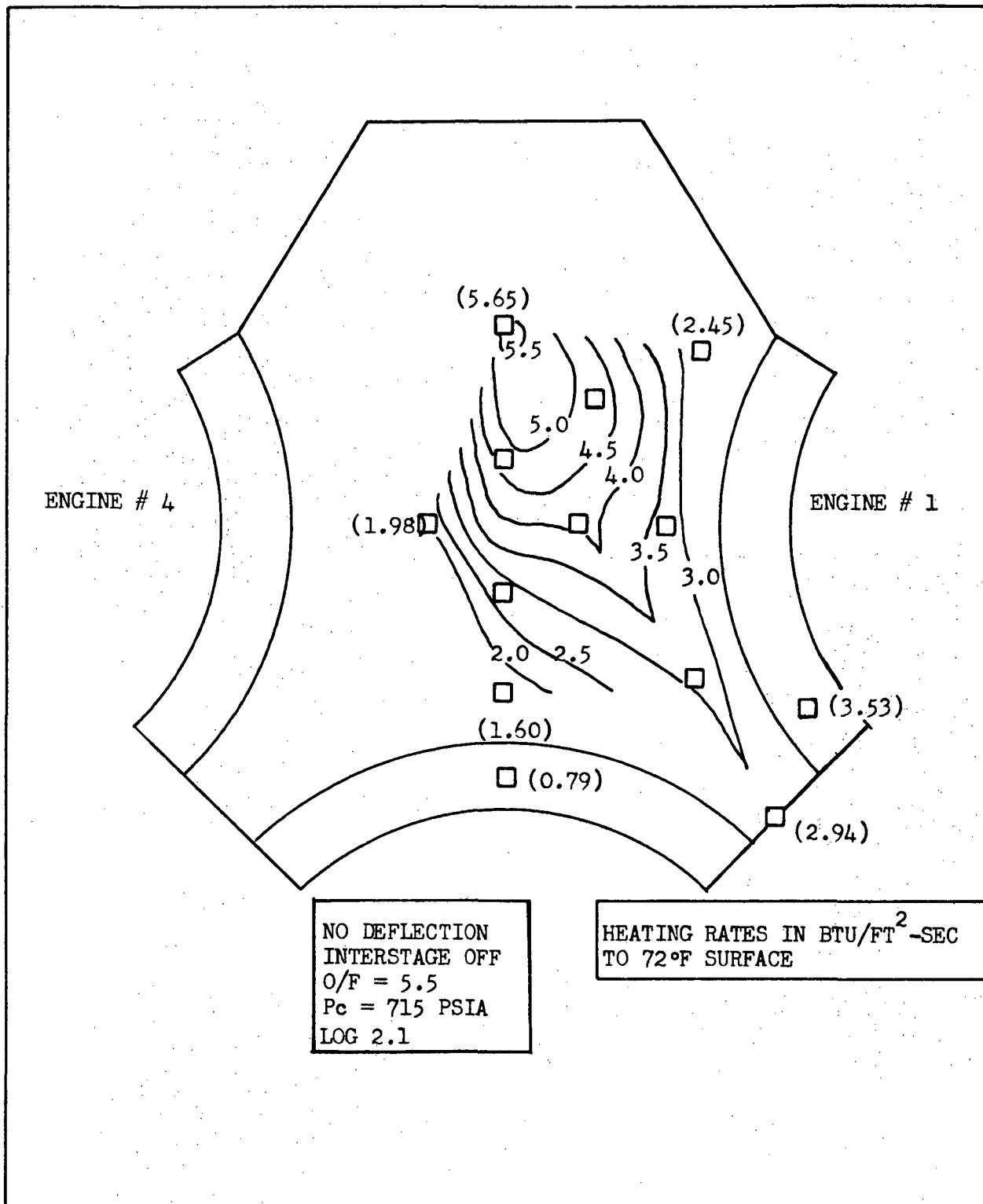
Figure 5.6.1-3 Heat Shield Heating Rates With No Deflections, O/F = 5.5
and Interstage Off

(5.36)

(3.06)

5.0

3.5

(5.34)

4.5

4.0

ENGINE # 4

ENGINE # 1

3.0

2.5

2.0

(1.82)

(2.91)

(3.46)

NO DEFLECTION
INTERSTAGE ON
O/F = 5.5
Pc = 715 PSIA
LOG 2.3

HEATING RATES IN BTU/FT^2-SEC
TO 72°F SURFACE
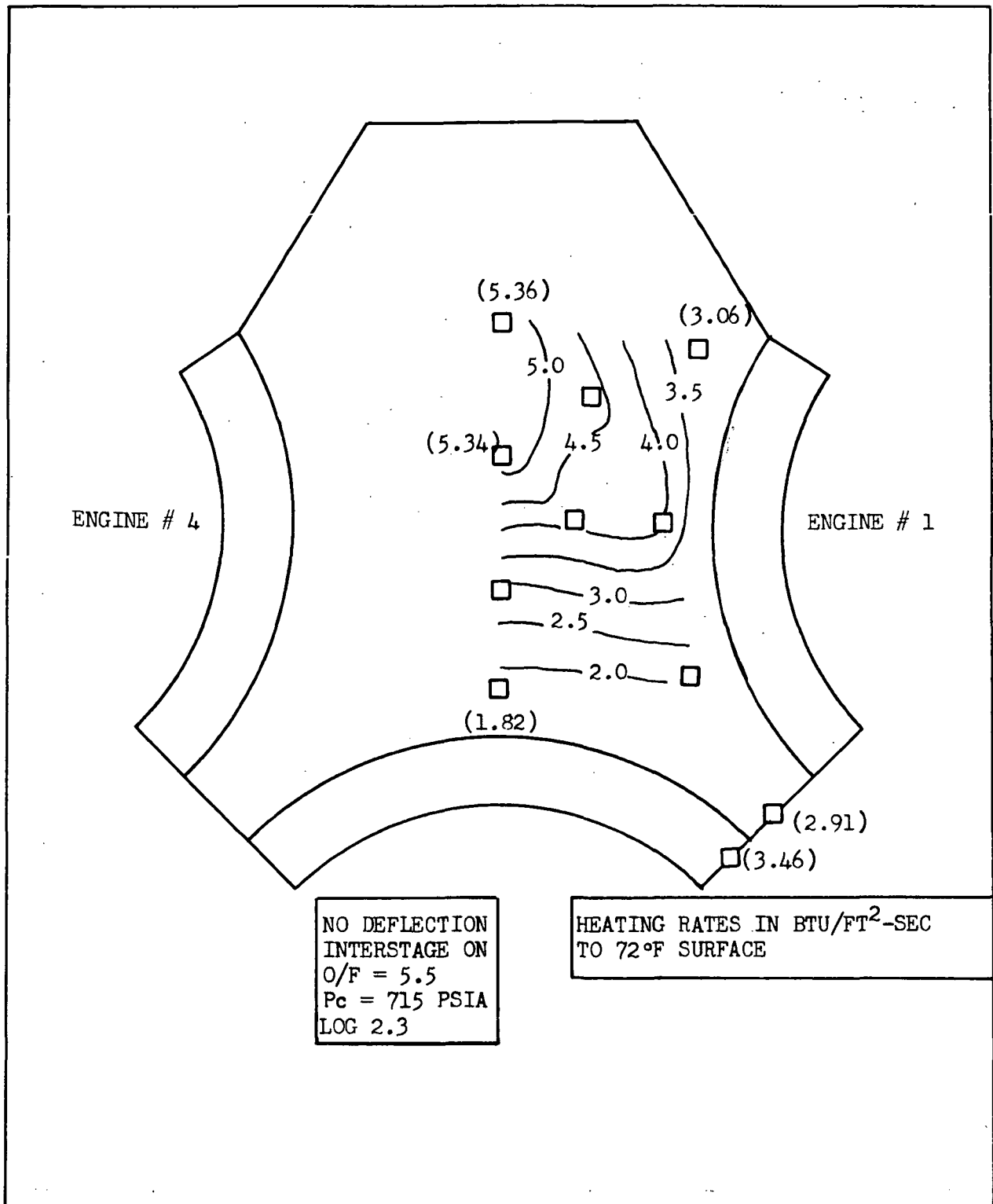
Figure 5.6.1-4   Heat Shield Heating Rates With No Deflections, O/F = 5.5
And Interstage On

SD73-SA-0061

NO DEFLECTIONS
INTERSTAGE OFF
O/F = 5.5
Pc = 715 PSIA
LOG 2.1

(0.011)

0.025

(0.05)

0.046

0.054

0.057

(0.11)

HEATING RATES IN BTU/SQ-FT-SEC
TO 72°F WALL
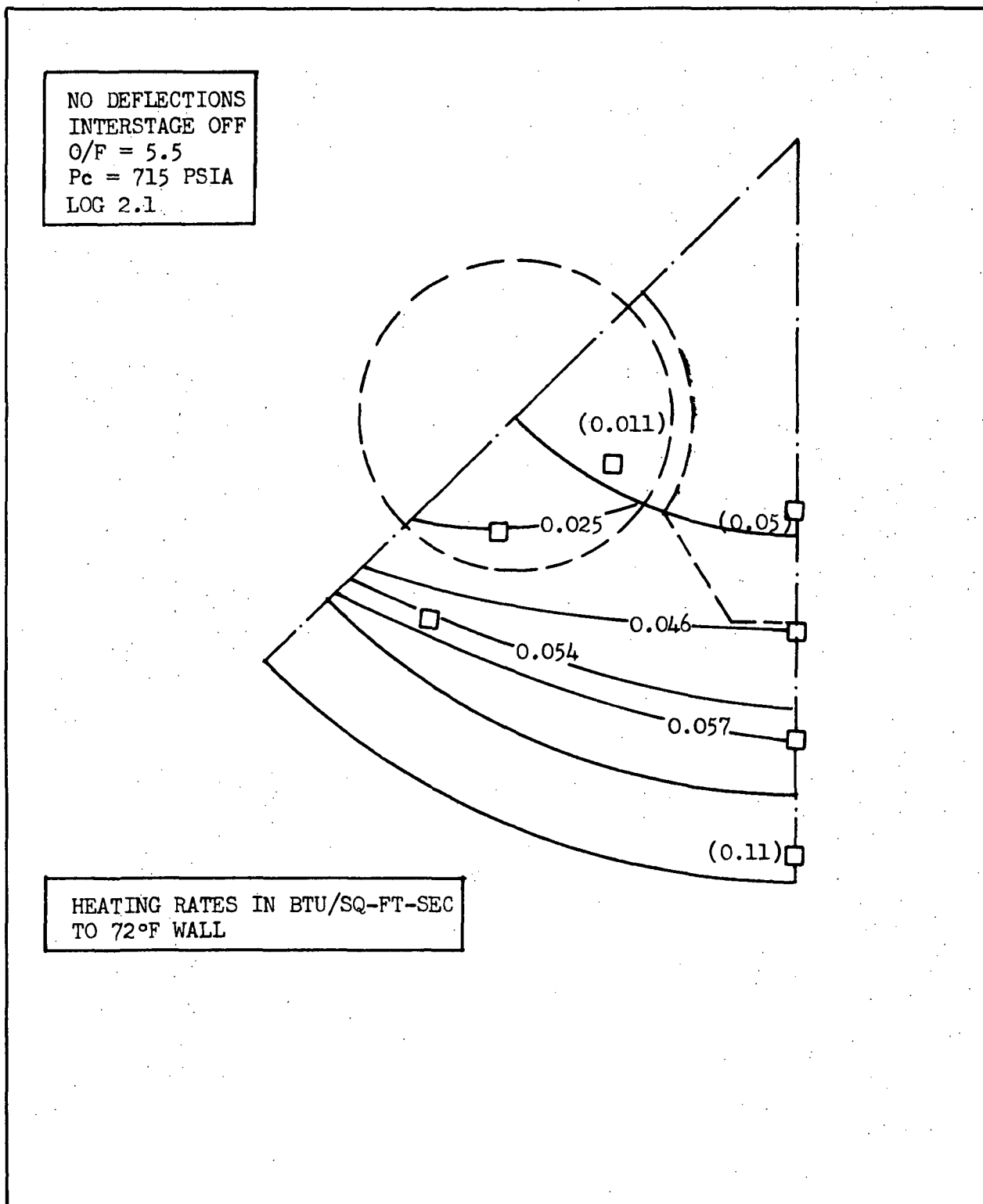
Figure 5.6.2-1   Thrust Cone Heating Rates with No Deflections, O/F = 5.5
and Interstage Off

NO DEFLECTIONS
INTERSTAGE ON
O/F = 5.5
Pc = 715 PSIA
LOG 2.3,15.3.1
& 15.3.2

0.3   0.674

0.396   0.8   1.0   (1.55)

1.2   1.4

1.154

(0.218)

(0.447)

HEATING RATES IN BTU/SQ-FT-SEC
TO 72°F WALL
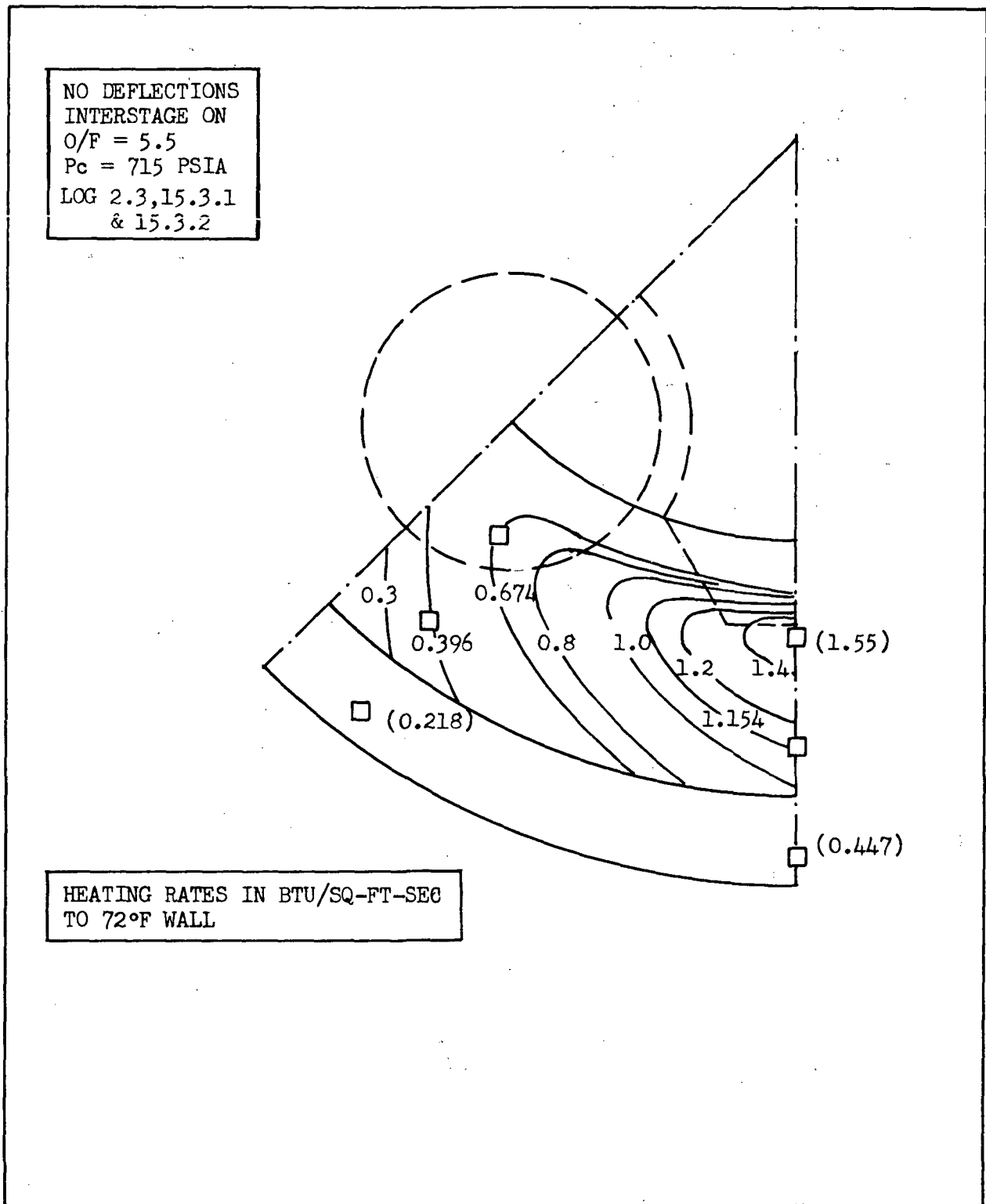
Figure 5.6.2-2 Thrust Cone Heating Rates with No Deflections, O/F = 5.5
and Interstage On
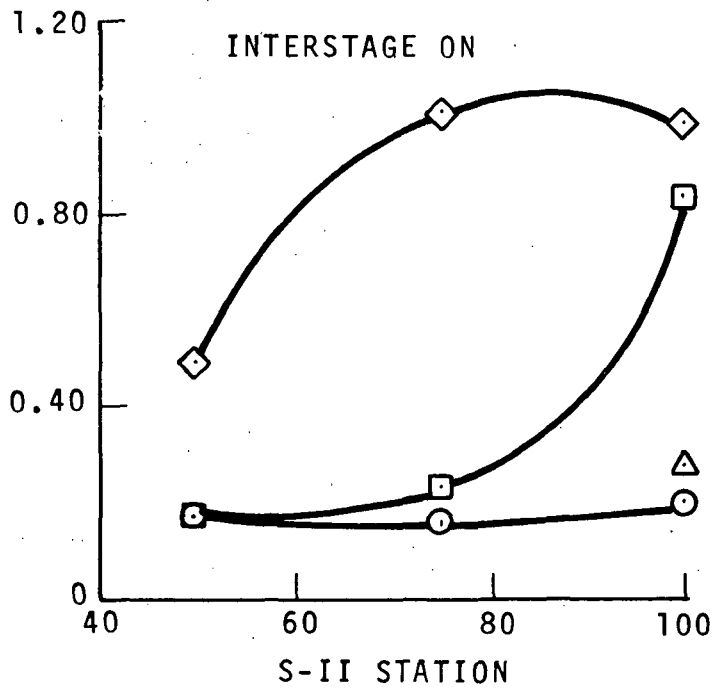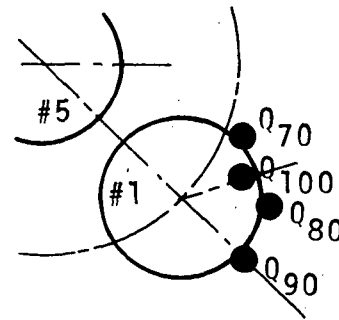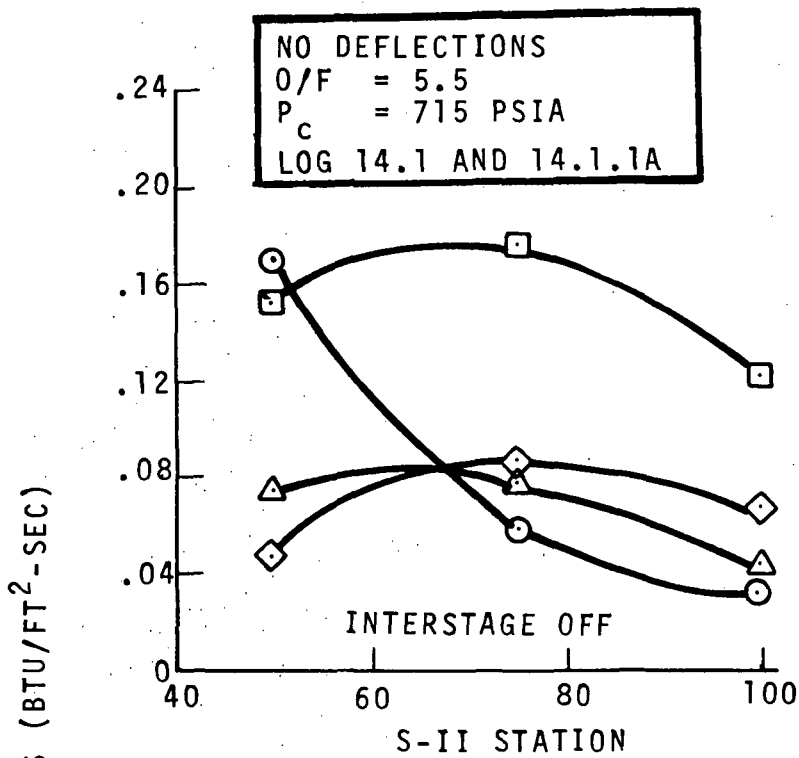
Figure 5.6.2-3   Thrust Cone Region Heating Rates with
no Deflections

SD73-SA-0061

5.6.3 Interstage Heating Rates

The interstage heating rate distribution is presented in Figure 5.6.3-1 for the no-deflection case and O/F = 5.5. Note that the peak heating rate occurs mid-way between two outboard engines at S-II Station O. The heating rates rapidly decay from this location in the axial and peripheral directions.

5.6.4 Engine Nozzle Heating Rates

The heating rates to the exterior surfaces of the center and outboard engine nozzles are presented in Figure 5.6.4-1. The heating rates are for the nominal case with no engine deflections, O/F mixture ratio of 5.5. and chamber pressure of 715 psia. It is seen that the center engine is subjected to higher heating rates than the outboard engine. The peak heating rate is 3.25 Btu/ft^2-sec and occurs at about 10 inches forward (full scale) of the nozzle exit plane. Peripherally, the location of the peak heating rate corresponds to the intersection of the outboard-engine-plume-interaction-region-plane with the center engine.

The heating rate distribution on the outboard engine is more uniform than that on the center engine with the peak heating rate being 1.5 Btu/ft^2-sec at 12 inches forward of the exit plane at the peripheral location closest to the center engine.

In Figure 5.6.4-1 some heating rates of the outboard engine nozzle measured in the CAL test program are shown for comparison. The heating rate levels are in good agreement; however, the CAL results indicate a continually increasing heating rate with distance from the nozzle exit plane whereas the present test results show that the heating rates peak out at 12 inches from the exit plane. It should be noted that the CAL data corresponds to the lower mixture ratio of 5.0 and chamber pressure of 632 psia. It is unlikely that this difference alone would cause the observed shift in the heating rate distributions.

5.6.5 Heat Shield Pressures

The heat shield pressure distribution is presented in Figure 5.6.5-1 for the interstage-off condition and O/F = 5.5. It is seen that the heat shield pressure distribution is much more uniform than the heating rate distribution presented in Figure 5.6.1-3. The ratio of maximum to minimum heat shield pressure is 1.38, while the corresponding ratio for the heating rates is 3.53.

Heat shield pressures are recorded in Log 2.2 for the O/F = 4.5 and P_c = 546 psia condition. These data show that on the average the heat shield pressures are reduced by 29% from the O/F = 5.5, P_c = 715 psia value while the chamber pressure reduction is 24%.
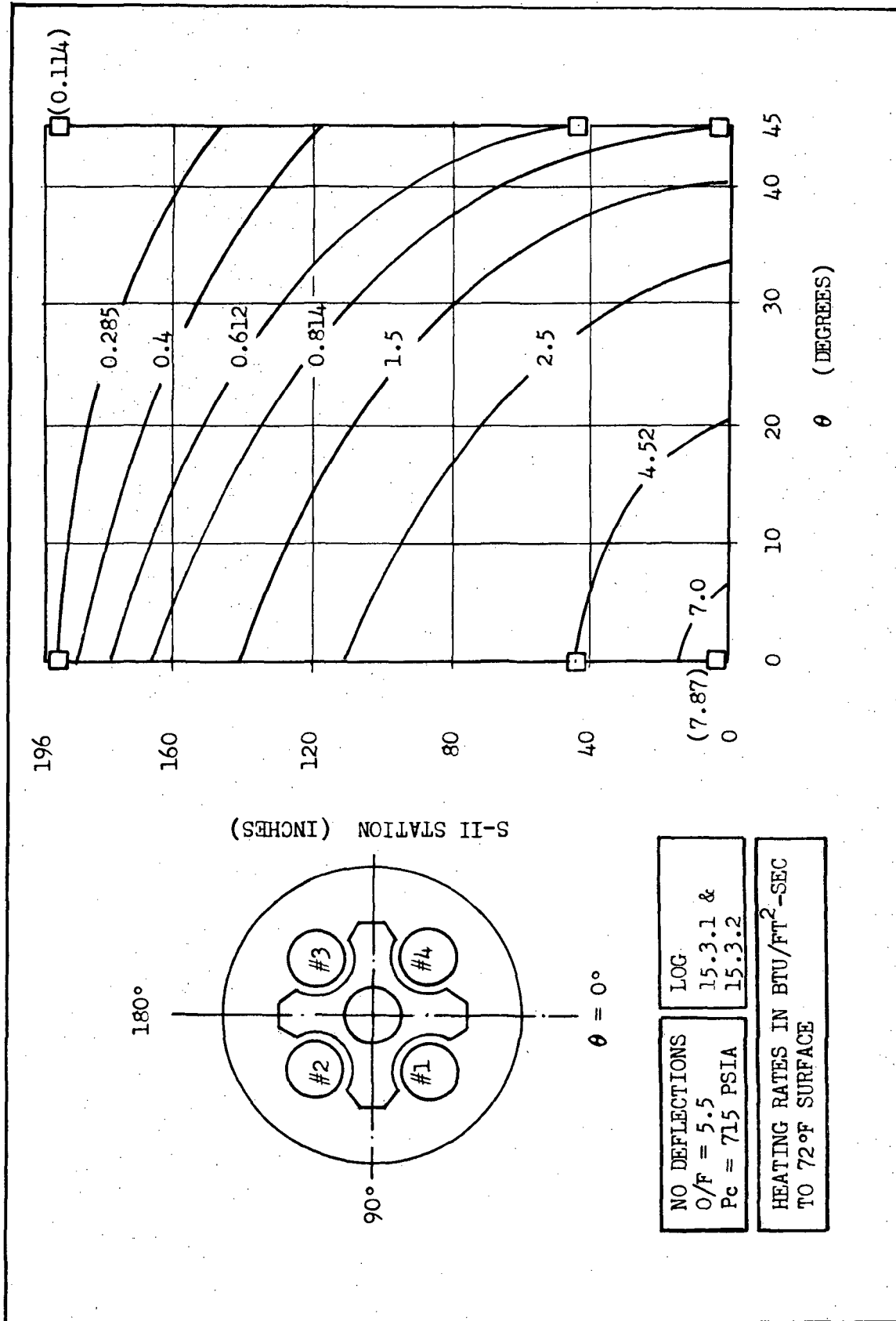
Figure 5.6.3-1   Interstage Heating Rates with No Deflections, O/F = 5.5

SYM	GAGE	LOG	
		CENTER	OUTBRD
○	K	26.1	26.2
□	L	26.1	26.2
◇	M	26.1	26.2
◆	M		REF. 1
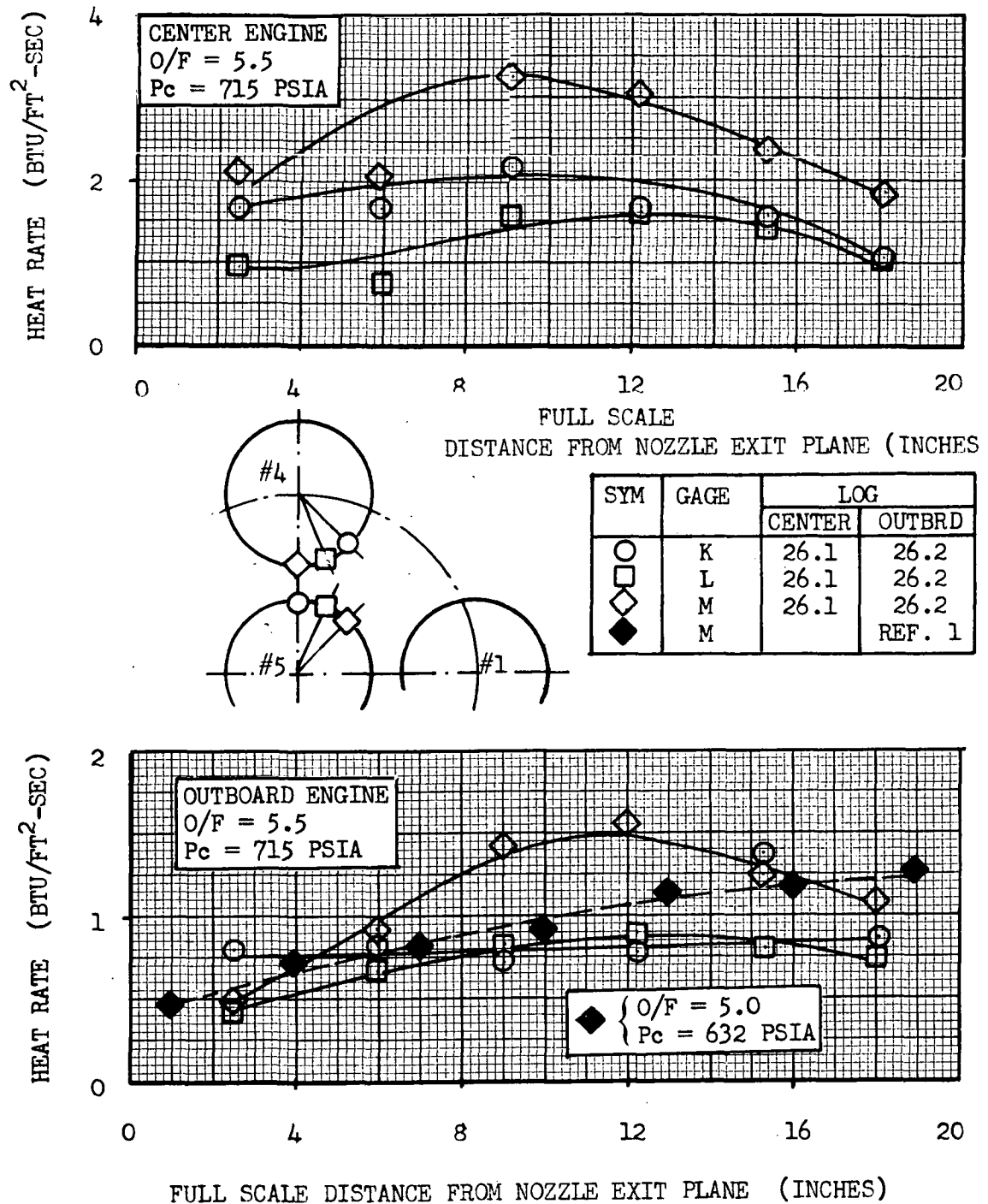
Figure 5.6.4-1   Center and Outboard Engine Nozzle Heating Rates
with No Deflections
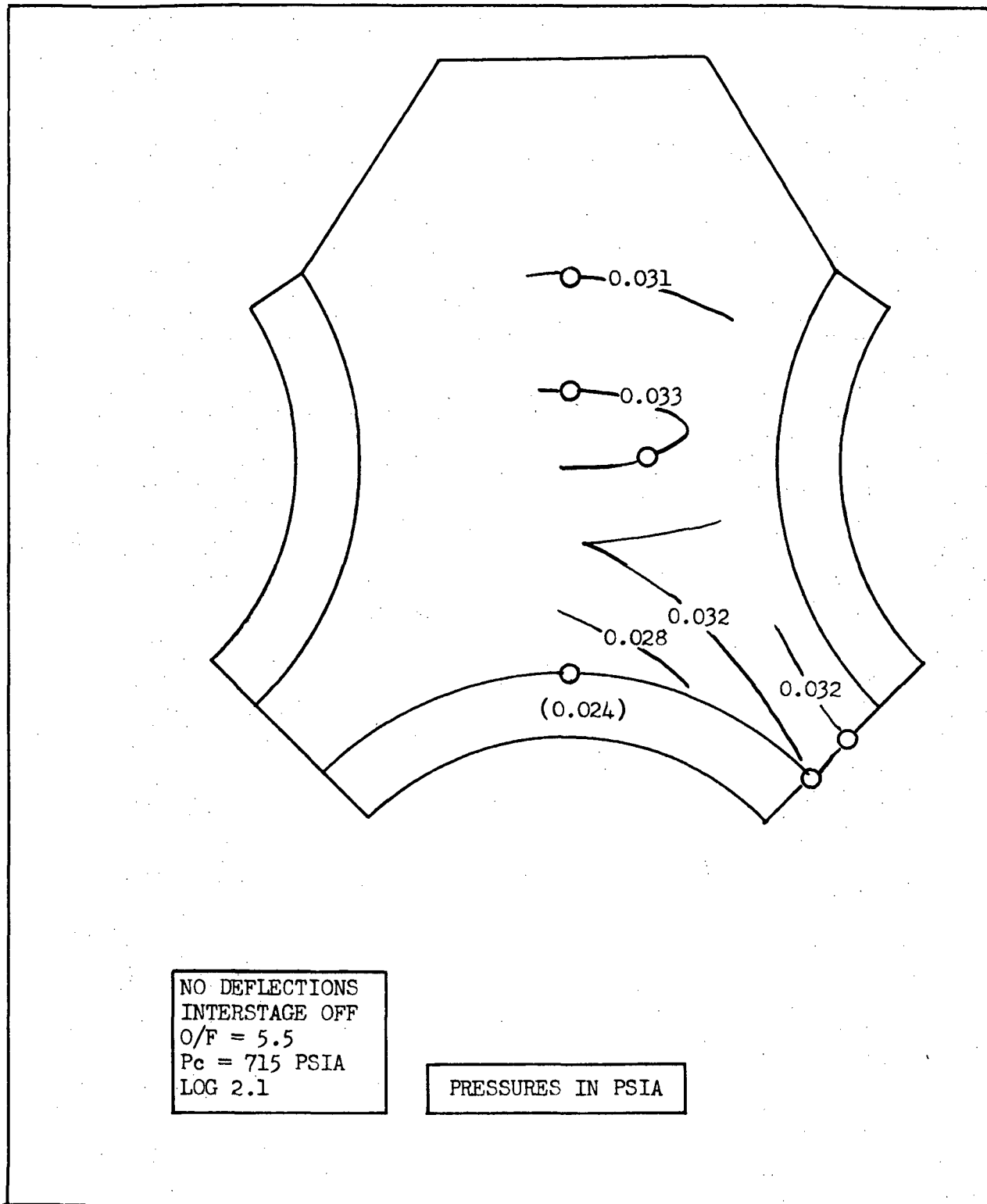
Figure 5.6.5-1 Heat Shield Pressure Distribution With No Deflections

NO DEFLECTIONS
INTERSTAGE OFF
O/F = 5.5
Pc = 715 PSIA
LOG 2.1

PRESSURES IN PSIA

5.6.6 Thrust Cone Pressures

Only four pressure transducers were located on the thrust cone. Therefore, very limited pressure data is available for this region. However, the results indicate that with the interstage off, the thrust cone pressures are fairly uniform with location and an order of magnitude lower than the heat shield pressures. With the interstage on, the thrust cone pressures approach the heat shield values. A summary of the thrust cone pressure results is presented in Table 5.6.6-1.

TABLE 5.6.6-1

Thrust Cone Pressure With No Engine Deflections

INTERSTAGE	OFF	OFF	ON	ON	ON
O/F	5.0	5.0	5.5	5.5	5.5
P_c (psia)	632	632	715	715	715
Log	1.1	1.2	2.3	15.3.1	15.3.2
TRANSDUCER	PRESSURE (PSIA)				
P15	–	–	–	.030	.028
P16	.0014	.0016	.0290	–	–
P17	.0013	.0017	.0268	.024	.024
P18	.0013	.0006	.0286	–	–

5.7 BASE REGION ENVIRONMENT WITH AN OUTBOARD ENGINE OUT

Heat shield, thrust cone, inoperative engine nozzle, and interstage heating rates were determined for several outboard-engine-out engine deflection conditions. Most of the tests were run at an O/F mixture ratio of 5.5. The gimbal patterns for which heating rate data was obtained are shown in Figure 5.7-1. The modified 2B gimbal pattern is the same as gimbal pattern 2B except that the inoperative engine was also gimballed. The effect of an outboard-engine-out failure on the heating rates of the various base region components is discussed in following sections.

5.7.1 Heat Shield Heating Rates

Heat shield heating rates corresponding to several outboard-engine-out gimbal patterns are presented in Figures 5.7.1-1 through 5.7.1-4 for the interstage-off condition. The effect of interstage is shown in Figures 5.7.1-5 and 5.7.1-6 for two gimbal patterns.

Comparison of the outboard-engine-out heating rate distributions presented in Figures 5.7.1-1 through 5.7.1-3 with the corresponding nominal heating rate distributions of Figures 5.6.1-2 (O/F = 5.0) and 5.6.1-3 (O/F = 5.5) shows that the heating rates in the vicinity of an outboard engine increase with the deflection of the opposite outboard engine towards it. Also, the peak heating rates increase with increasing engine deflection and shifts from the heat shield centerline in the direction of the outboard engine deflection. Typical heat flux variations with engine deflection angle for several gage locations are shown in Figure 5.7.1-4, which shows that the no-deflection case peak heating rate of 5.65 Btu/ft^2-sec increases to 9.32 Btu/ft^2-sec for the most severe engine-out gimbal pattern 2B and shifts from the heat shield centerline to the vicinity of the outboard engine.

The effect of interstage on the outboard-engine-out heating rates is shown in Figures 5.7.1-5 and 5.7.1-6 for gimbal pattern 2 and 2B respectively. Comparison with the corresponding interstage-off heating rates presented in Figure 5.7.1-2 and 5.7.1-3 shows that in the case of gimbal pattern 2, the peak heating rate decreases by 12 percent whereas in the case of gimbal pattern 2B, the peak heating rate increases by 11 percent. Note also that there is a slight overall drop in heating rates with the interstage-on and gimbal pattern 2, which is contrary to the observed interstage effect in the nominal heat shield data presented in Figures 5.6.1-3 and 5.6.1-4.

Figure 5.7.1-7 shows the heat shield heating rate distribution for engine-out gimbal pattern 2B modified, which is the same as gimbal pattern 2B except for the deflection of the inoperative engine. Comparison with the 2B-gimbal pattern heating rates of Figure 5.7.1-3 shows that deflection of the inoperative engine has no discernable effect on the heating rates in the opposite heat shield quadrant.
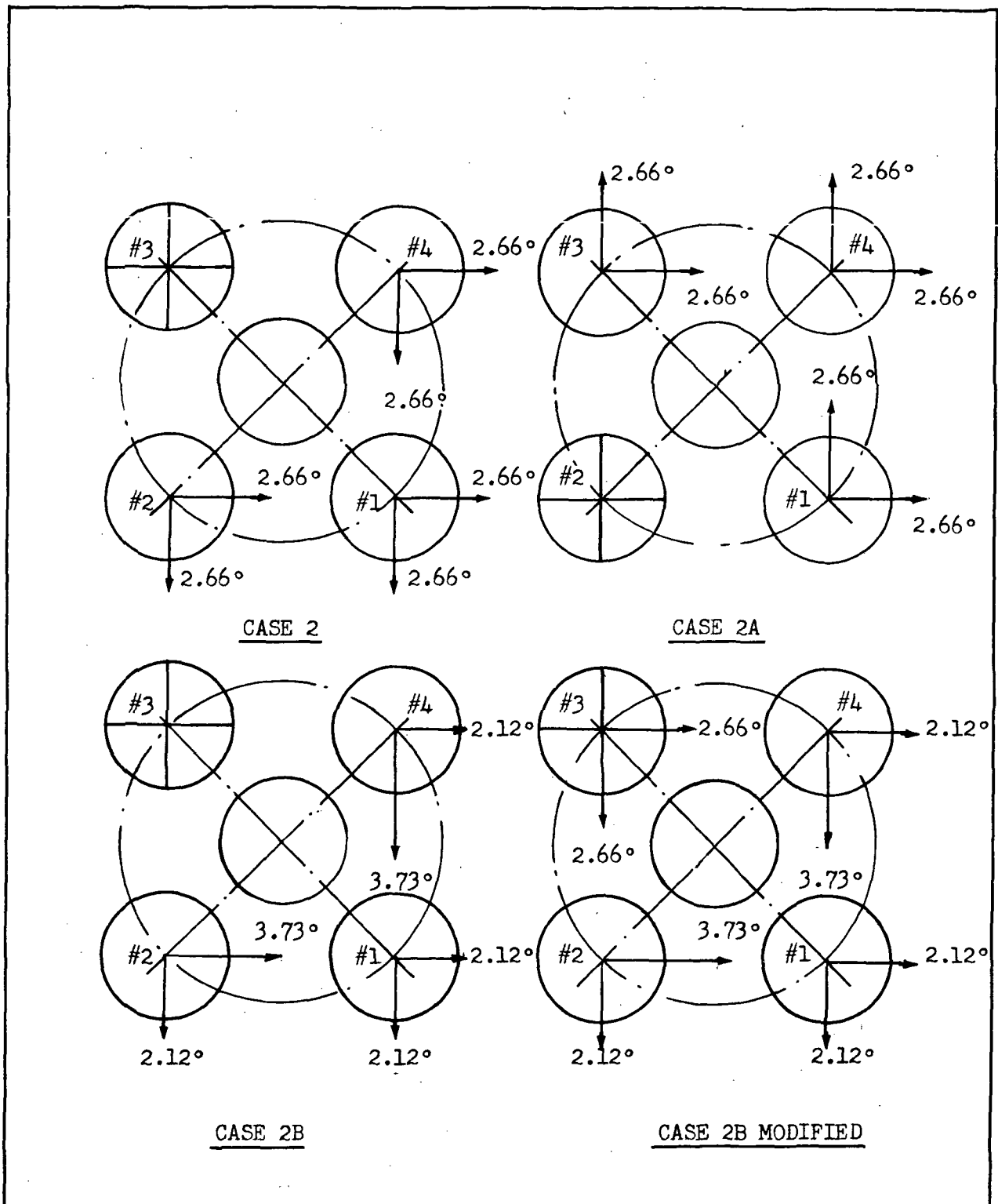
Figure 5.7-1 Outboard-Engine-Out Gimbal Patterns

SD73-SA-0061
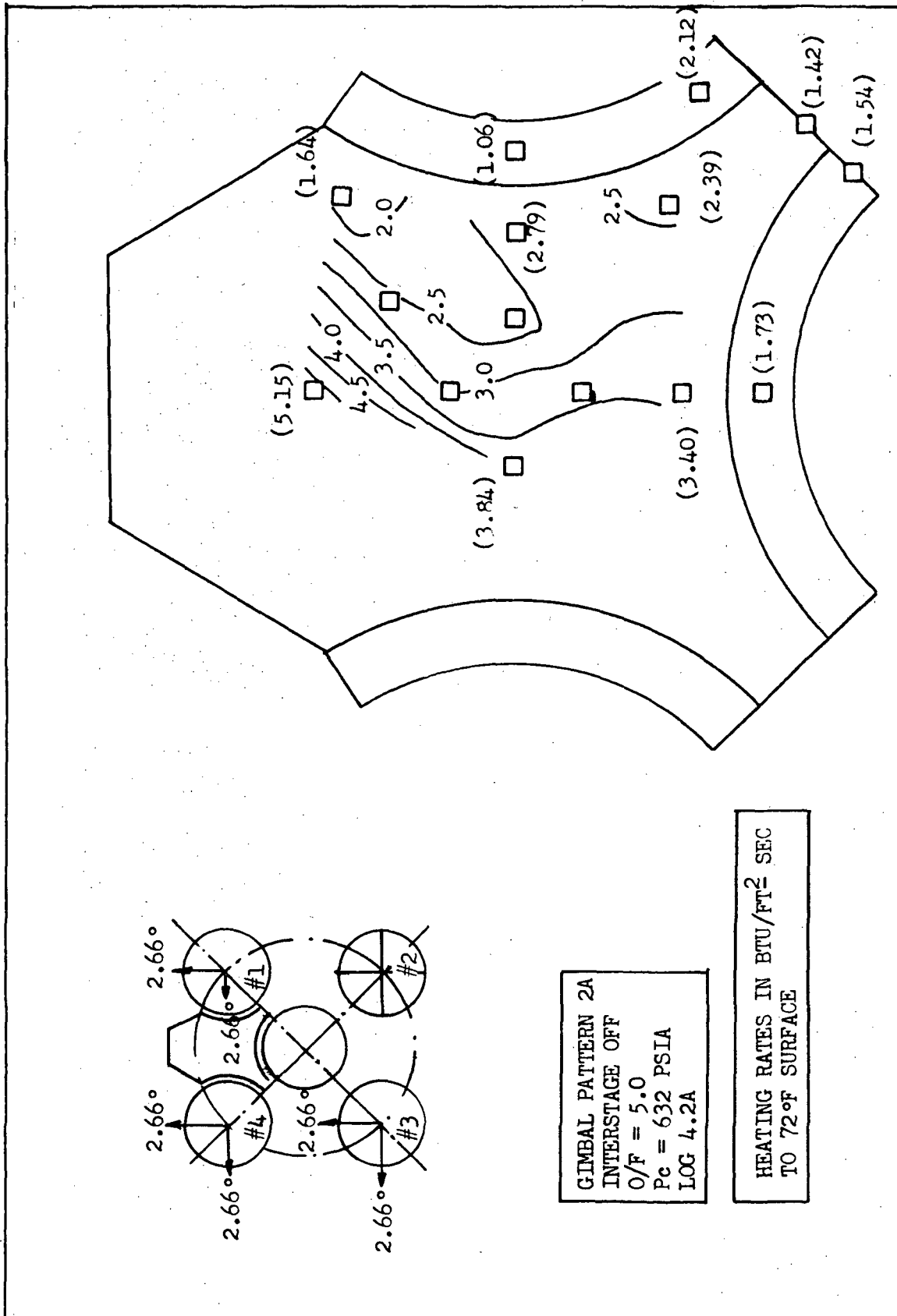
Figure 5.7.1-1 Heat Shield Heating Rates with Outboard Engine Out Gimbal Pattern 2A, Interstage Off, O/F = 5.0

GIMBAL PATTERN 2A
INTERSTAGE OFF
O/F = 5.0
Pc = 632 PSIA
LOG 4.2A

HEATING RATES IN BTU/FT^2 SEC
TO 72°F SURFACE

GIMBAL PATTERN 2
INTERSTAGE OFF
O/F = 5.5
Pc = 715 PSIA
LOG 4.5.1A &
    4.5.1B

HEATING RATES IN BTU/FT^2-SEC
TO 72°F SURFACE
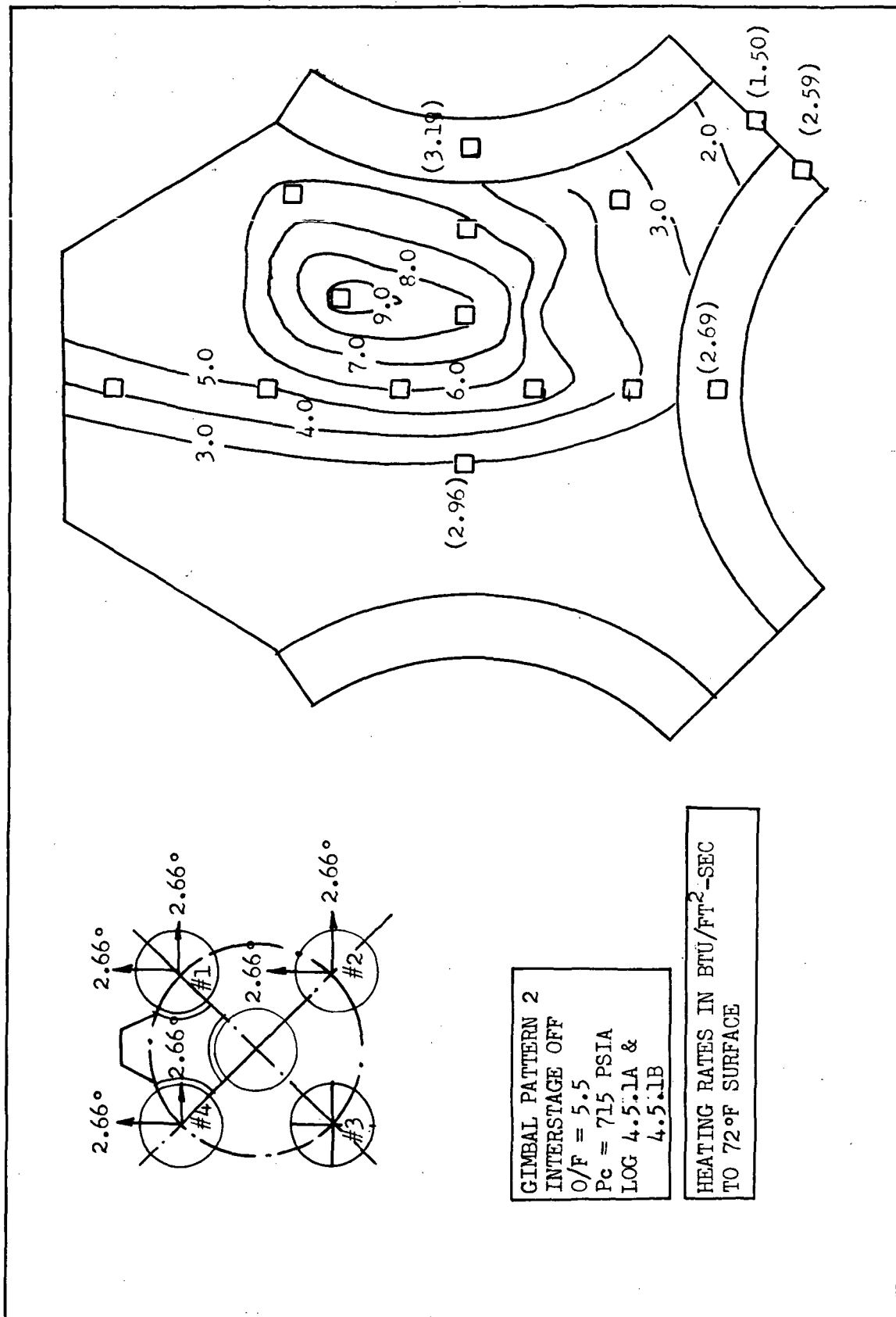
Figure 5.7.1-2 Heat Shield Heating Rates with Outboard Engine Out Gimbal Pattern 2,
Interstage Off, O/F = 5.5
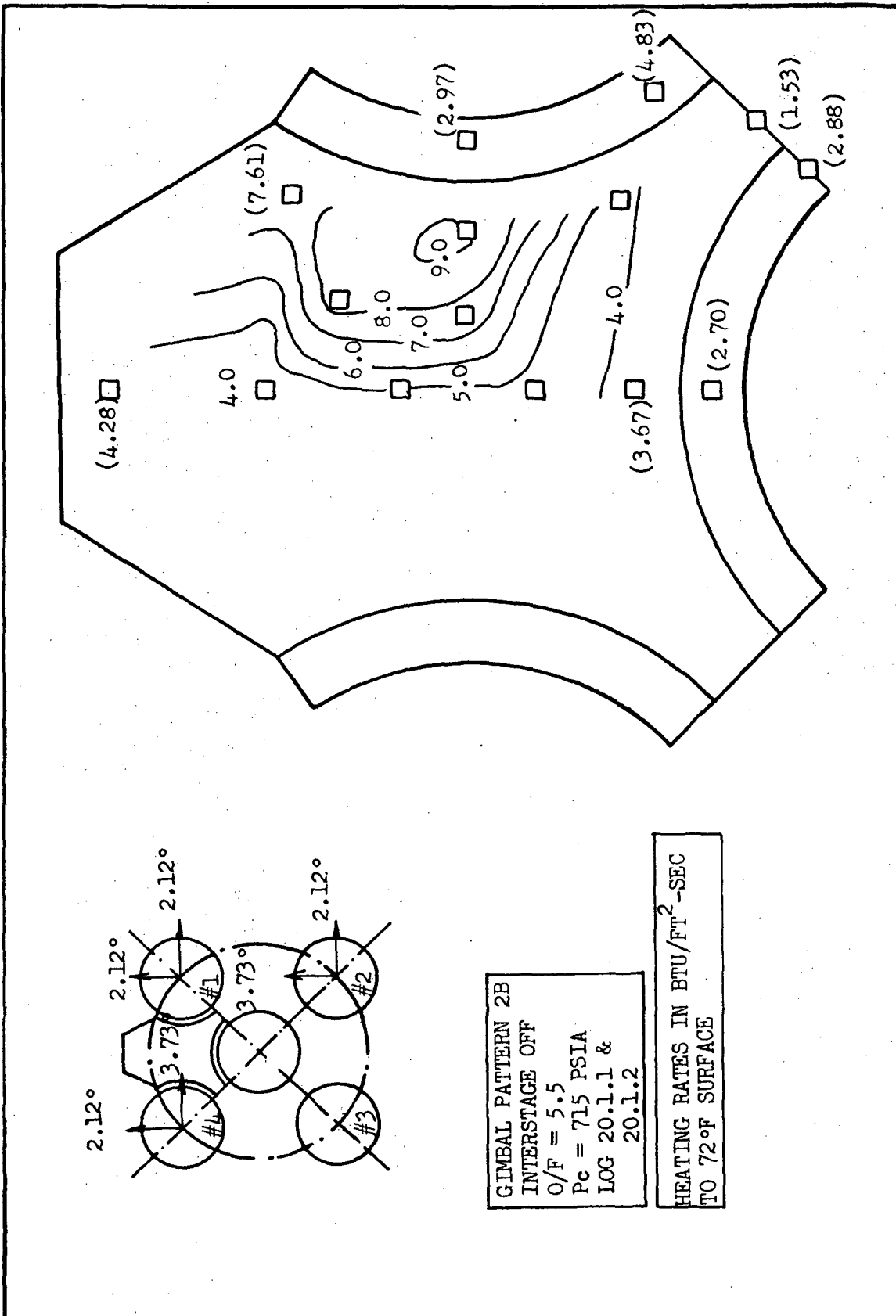
Figure 5.7.1-3 Heat Shield Heating Rates with Outboard Engine Out Gimbal Pattern 2B, Interstage Off, O/F = 5.5

GIMBAL PATTERN 2B
INTERSTAGE OFF
O/F = 5.5
Pc = 715 PSIA
LOG 20.1.1 &
        20.1.2

HEATING RATES IN BTU/FT^2-SEC
TO 72°F SURFACE

12

SYM	GAGE	R (INCH)	θ
⬡	Q₃	3.31	0°
⬠	Q₄	4.00	0°
◇	Q₈	3.00	7.5°
⬠	Q₉	3.65	7.5°
□	Q₁₃	2.38	25.0°
◇	Q₁₅	3.08	16.0°
△	Q₁₉	4.00	15.0°

8

4

0

-4   -2   0   2   4

ENGINE DEFLECTION (DEGREES)

HEATING RATE (BTU/FT²-SEC)

GIMBAL PATTERN	ENGINE DEFLECN	LOG
2	2.66°	4.5.1A,4.5.1B
2A	-2.66°	4.2A
2B	3.73°	20.1.1,20.1.2

12

8

4

0

INTERSTAGE OFF
O/F = 5.5
Pc = 715 PSIA

-4   -2   0   2   4

ENGINE DEFLECTION (DEGREES)
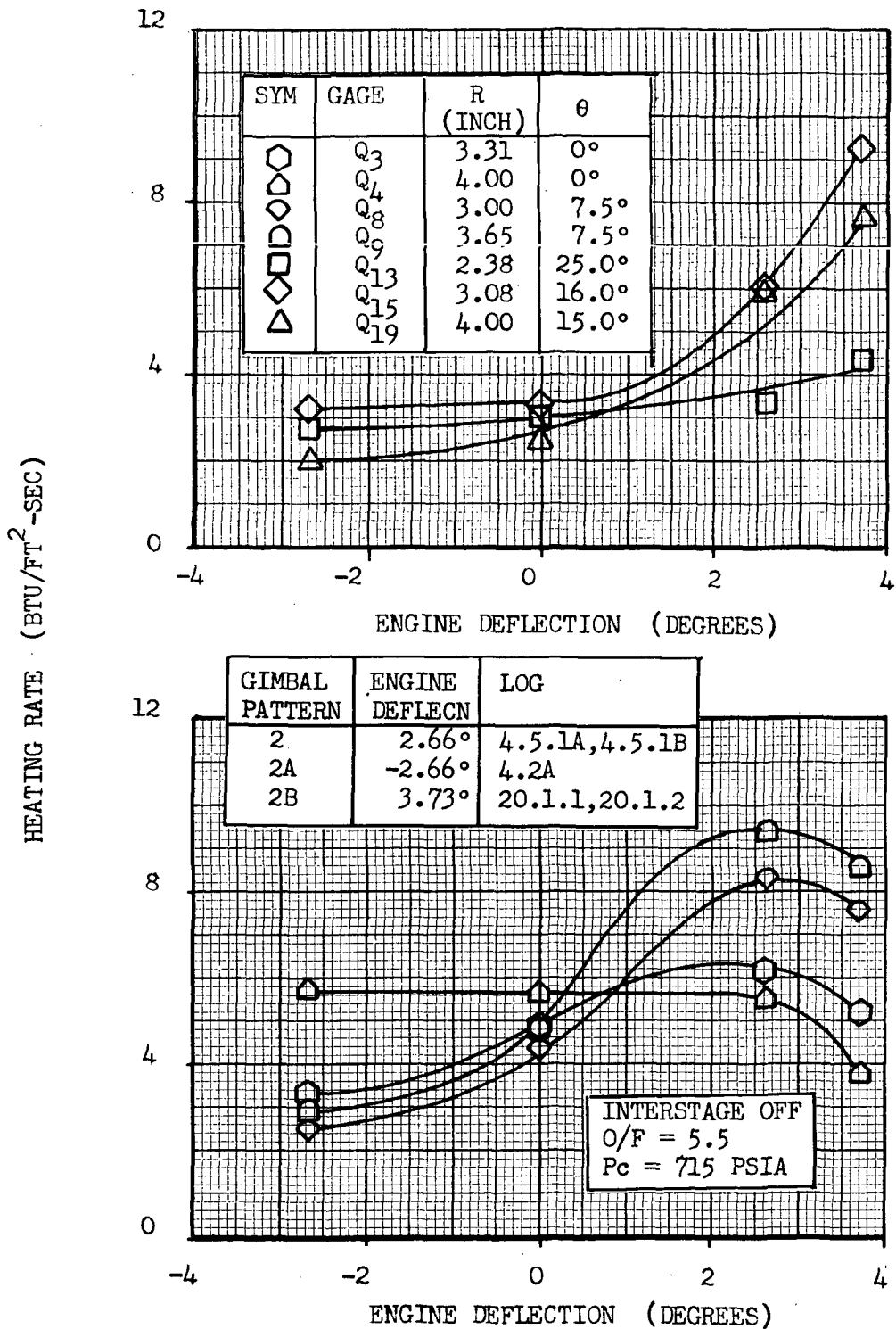
Figure 5.7.1-4 Heat Shield Heating Rate Variation with
Engine Deflection Angle, Outboard Engine Out
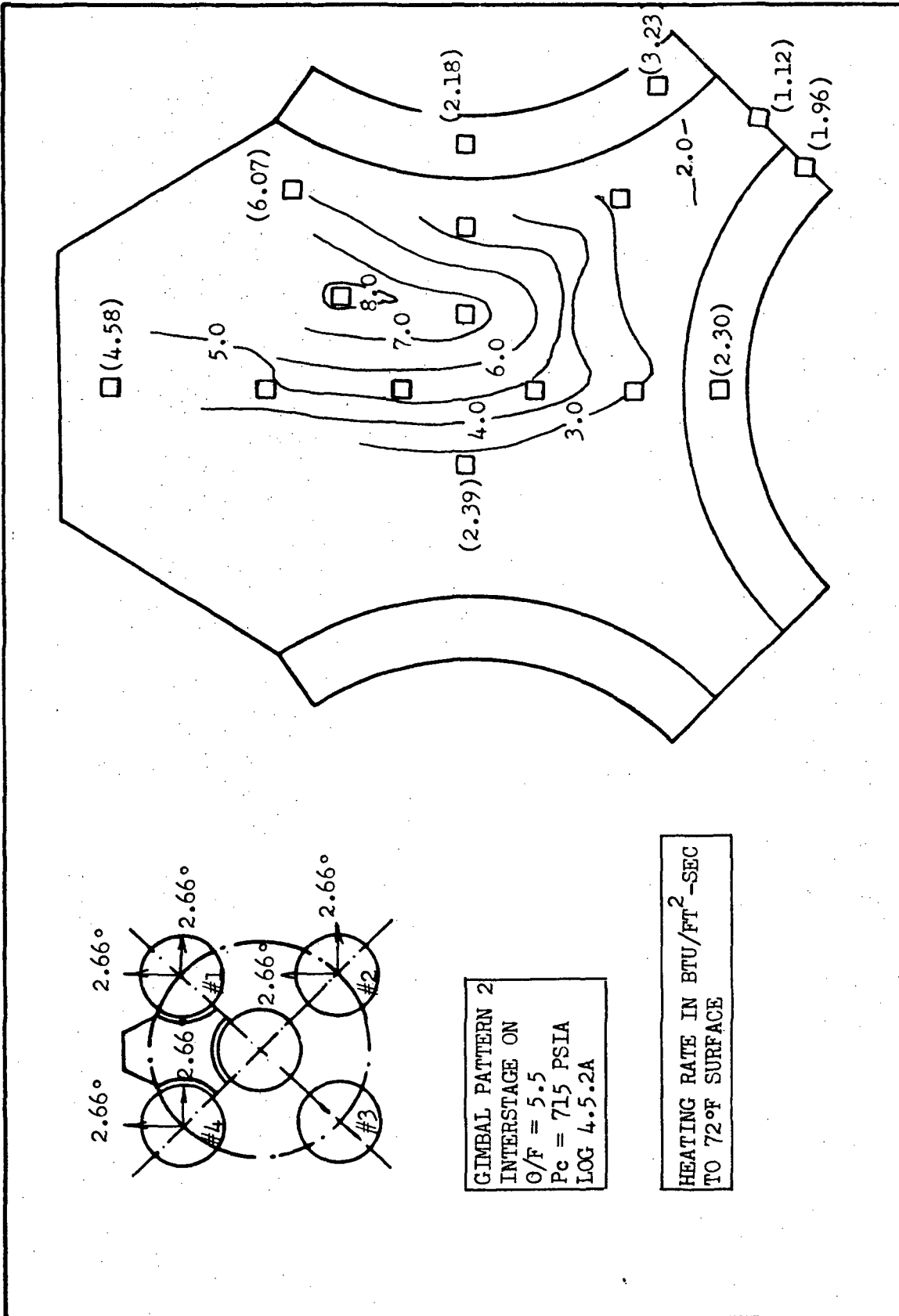
Figure 5.7.1-5 Heat Shield Heating Rates with Outboard Engine Out Gimbal Pattern 2, Interstage On, O/F = 5.5

GIMBAL PATTERN 2
INTERSTAGE ON
O/F = 5.5
Pc = 715 PSIA
LOG 4.5.2A

HEATING RATE IN BTU/FT^2-SEC
TO 72°F SURFACE
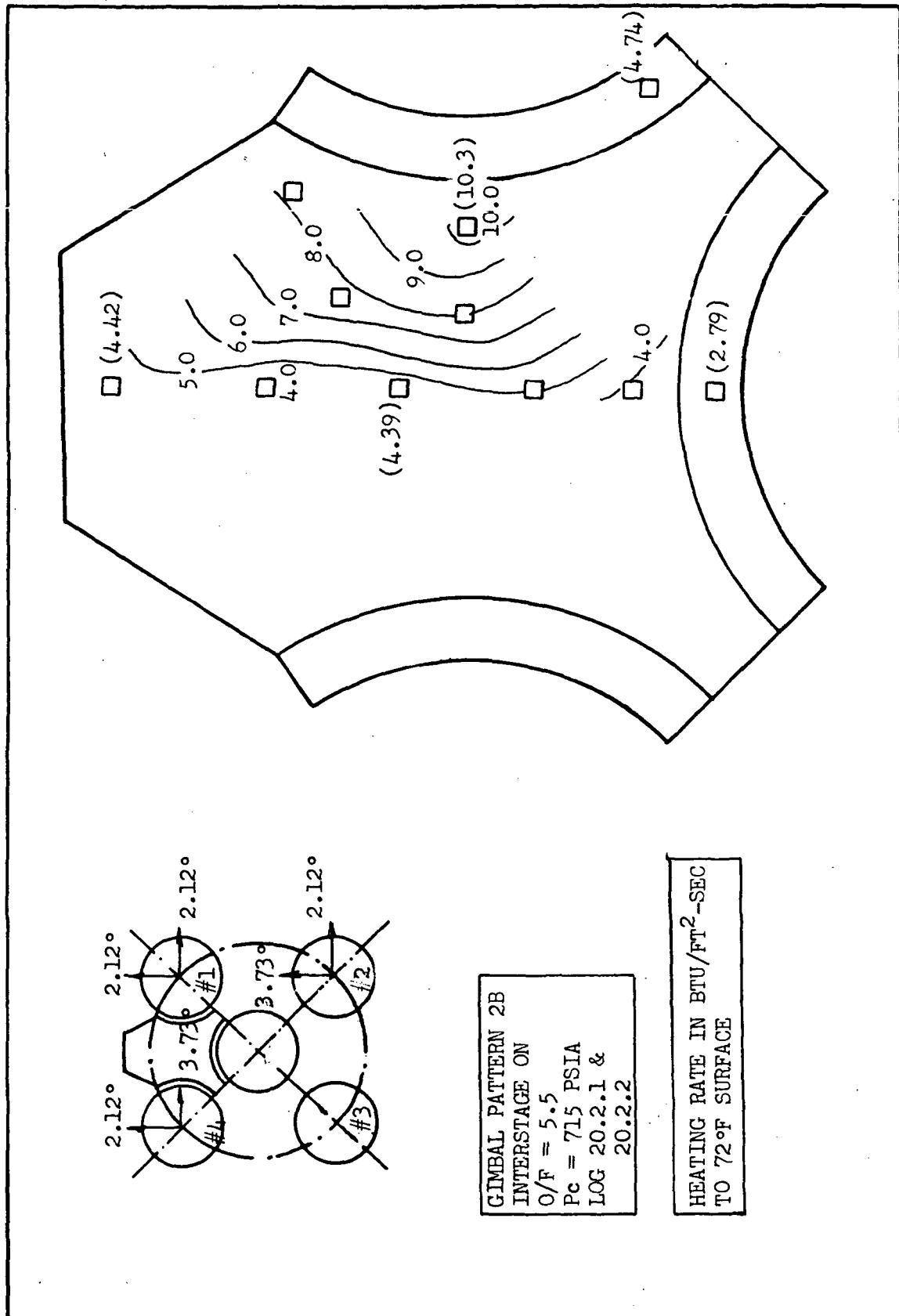
Figure 5.7.1-6 Heat Shield Heating Rates with Outboard Engine Out Gimbal Pattern 2B, Interstage On, O/F = 5.5

GIMBAL PATTERN 2B-MODIFIED
INTERSTAGE OFF
O/F = 5.5
Pc = 715 PSIA
LOG 20A.1.2

HEATING RATES IN BTU/FT^2-SEC
TO 72°F SURFACE
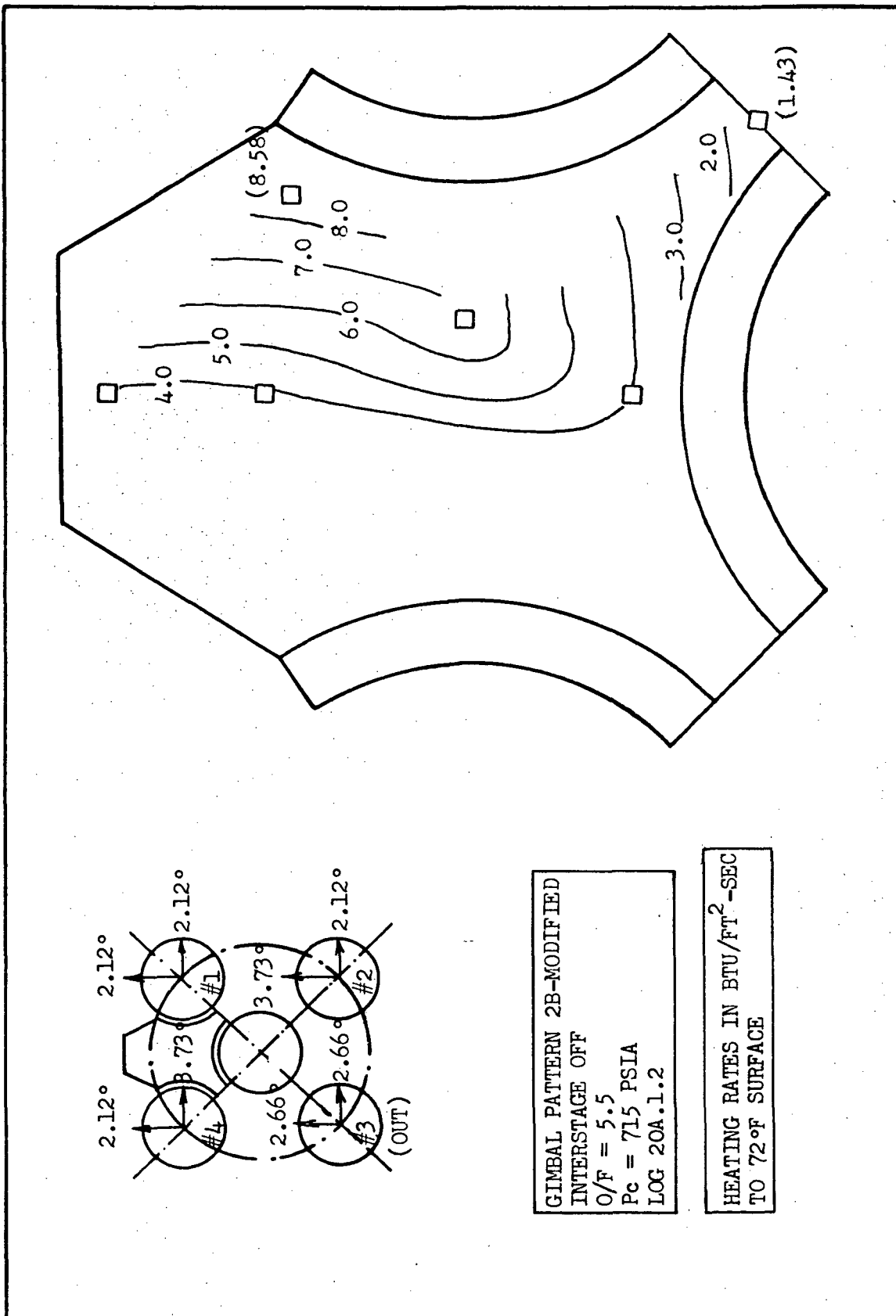
Figure 5.7.1-7 Heat Shield Heating Rates with Outboard Engine Out Gimbal Pattern 2B-Modified, Interstage Off, O/F = 5.5

5.7.2 Thrust Cone Heating Rates

Thrust cone heating rates are presented in Figures 5.7.2-1 and 5.7.2-2 for the outboard-engine-out gimbal patterns 2 and 2B respectively. The effect of engine deflection on the thrust cone heating rates with an outboard-engine-out is shown in Figures 5.7.2-3 and 5.7.2-4 for the peripheral locations of $\theta = 0°$ and $\theta = 37°$. The nominal no-deflection heating rates are also shown for comparison.

It is seen from Figure 5.7.2-3 that at $\theta = 0°$, the outboard-engine-out heating rates are lower than the nominal values on the engine mounting ring and higher than the nominal values on and in the vicinity of the thrust cone closeout at S-II Station 196. These results indicate that the heating rates at $\theta = 0°$ increase with increasing outboard deflection of the outboard engines. Gimbal pattern 2 produces the highest heating rates at $\theta = 0°$, with the thrust cone heating rates being 2.5 to 3 times the corresponding nominal values.

The effect of outboard-engine-out deflections on the thrust cone heating rates at $\theta = 37°$ is shown in Figure 5.7.2-4. It is seen that the heating rates at this location are higher than the nominal values for all gimbal patterns except gimbal pattern 2A where the adjacent engine moves away from the instrumented quadrant and the heating rates drop below the nominal value.

Thrust cone heating rates with the interstage on are presented in Figures 5.7.2-5 and 5.7.2-6 for gimbal patterns 2 and 2B respectively. Comparison with the corresponding nominal heating rates of Figure 5.6.2-2 shows that the outboard-engine-out thrust cone peak heating rate increases by 37% from the nominal value and shifts toward the thrust cone closeout at Station 196. The peak heating rates for gimbal patterns 2 and 2B are approximately the same. There is an outboard shift of the gimbal pattern 2B peak heating rate location although the engines are deflected less than in the case of gimbal pattern 2.

Additional heating rate data for the thrust cone region components are presented in the data Logs 4.5.1B, 4.5.2B, 20.2.1, and 20.2.2.

Thrust cone region heating rates in the vicinity of engines 2 and 4 were measured by means of the ring gages shown in Figure 3.4-5. Heating rates for this region with the outboard-engine-out Case 2 gimbal pattern are shown in Figure 5.7.2-7 for both the interstage-on and interstage-off conditions. The corresponding heating rates for the engine deflection Case 2B are presented in Figure 5.7.2-8. The interstage-on heating rate data indicates that very large flow gradients exist in both peripheral and axial directions in the region between the heat shield and the thrust cone.

SD73-SA-0061

(0.026)

(0.260)

(0.029)

0.054

0.083

0.102

(0.153)

GIMBAL PATTERN 2
INTERSTAGE OFF
θ/F = 5.5
Pc = 715 PSIA
LOG 4.5.1A &
    4.5.1B

2.66° 2.66°
2.66°
2.66°
2.66°
2.66°
2.66°

HEATING RATES IN BTU/FT²-SEC
TO 72°F SURFACE
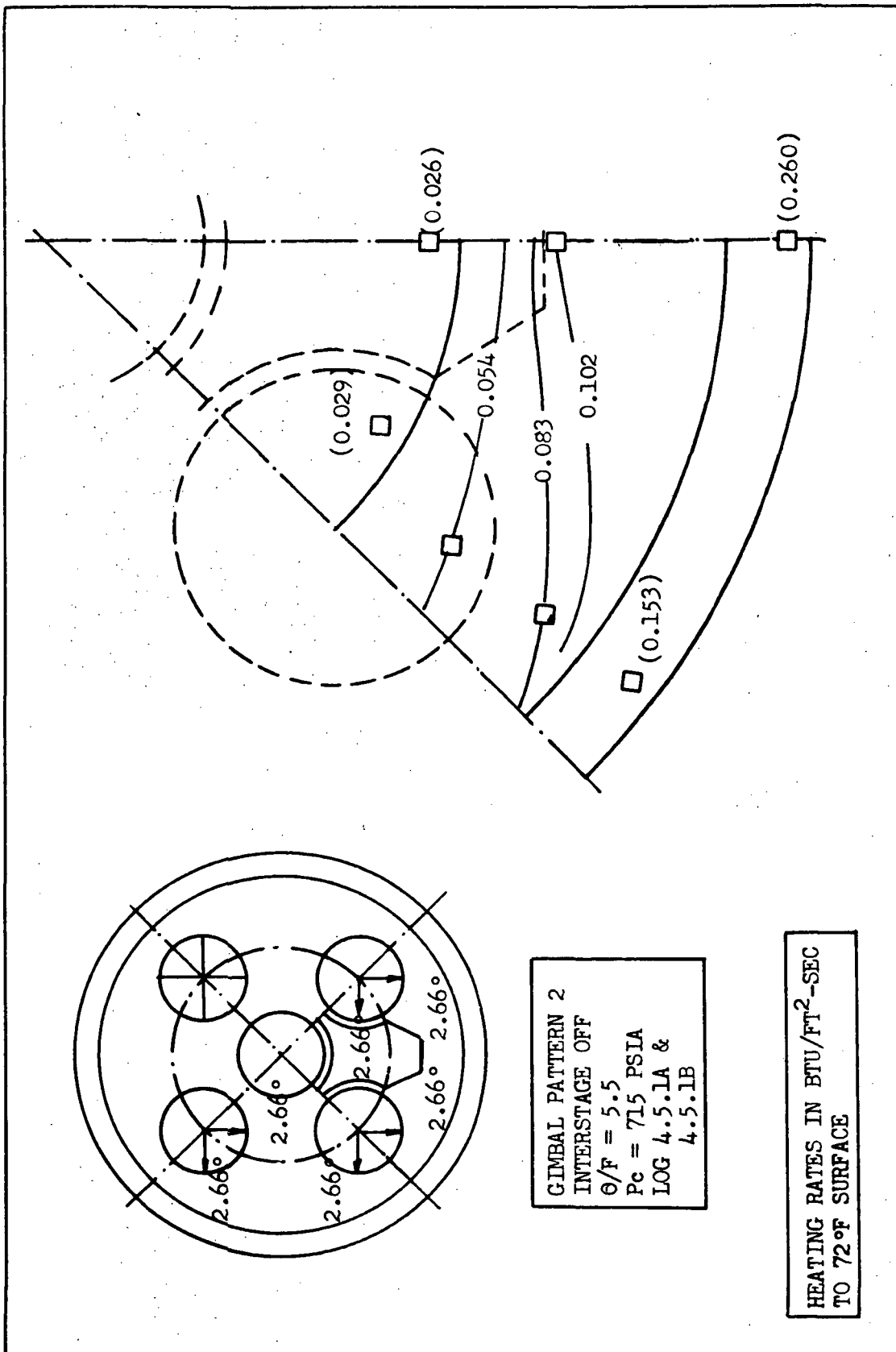
Figure 5.7.2-1 Thrust Cone Heating Rates With Outboard Engine Out Gimbal Pattern 2,
Interstage Off, O/F = 5.5

SD73-SA-0061

(0.013)

(0.238)

(0.021)

0.041

0.066

0.076

0.109

0.163

GIMBAL PATTERN 2B
INTERSTAGE OFF
O/F = 5.5
Pc = 715 PSIA
LOG 20.1.1 &
20.1.2

2.12°
3.73°
2.12°
2.12°
2.12°
3.73°
2.12°

HEATING RATES IN BTU/FT²-SEC
TO 72°F SURFACE
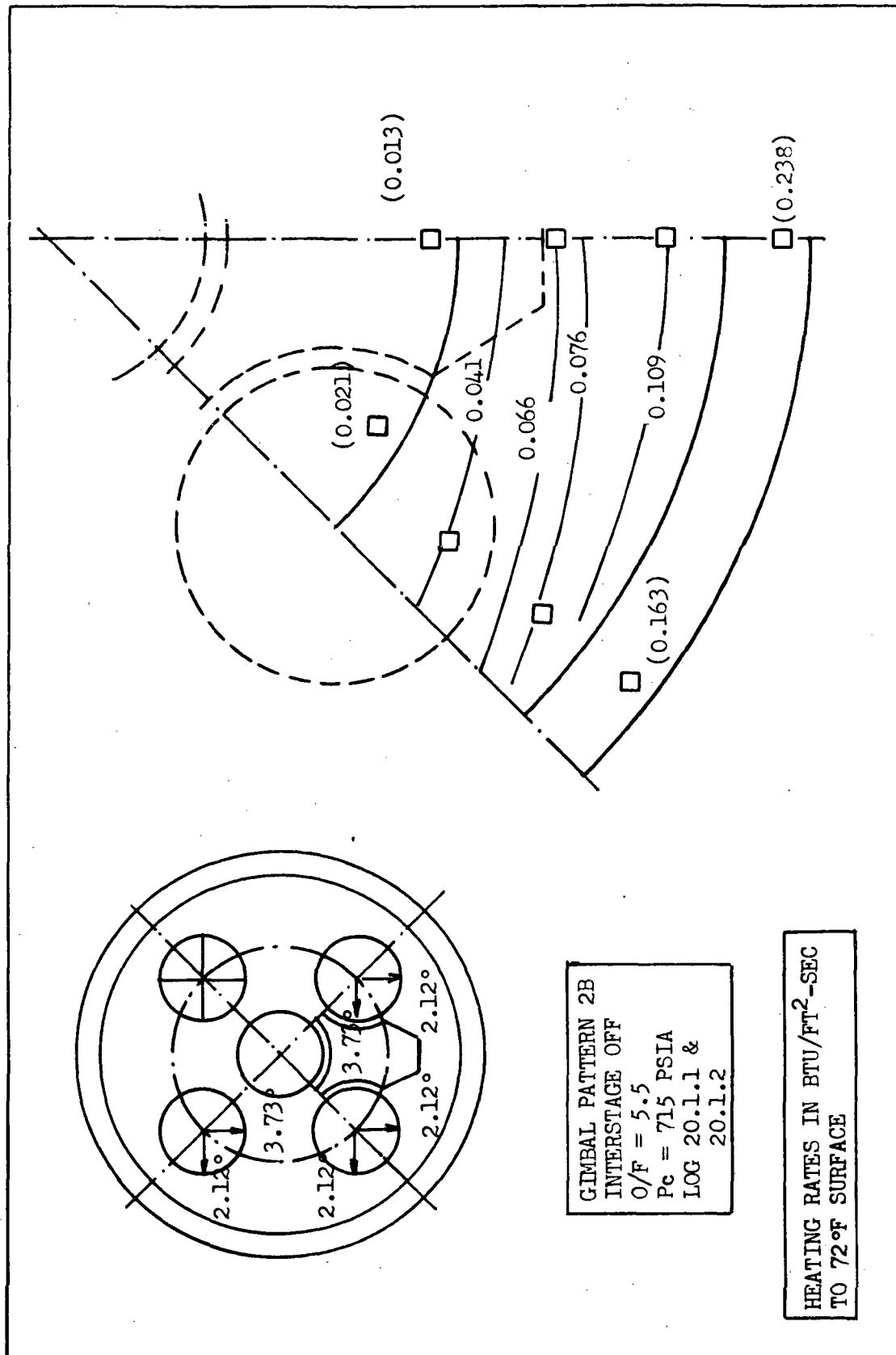
Figure 5.7.2-2 Thrust Cone Heating Rates With Outboard Engine Out Gimbal Pattern 2B, Interstage Off, O/F = 5.5

SD73-SA-0061

O/F = 5.5
Pc = 715 PSIA

THRUST CONE

SYM	GIMBAL PATTERN	LOG
△	2	4.5.1A & 4.5.1B
○	2A	4.2A
□	2B	20.1.1
◇	2B-MOD	20A.1.2
◇	NO DEFL	2.1

HETING RATES (BTU/SQ-FT-SEC)

MODEL RADIUS (INCHES)
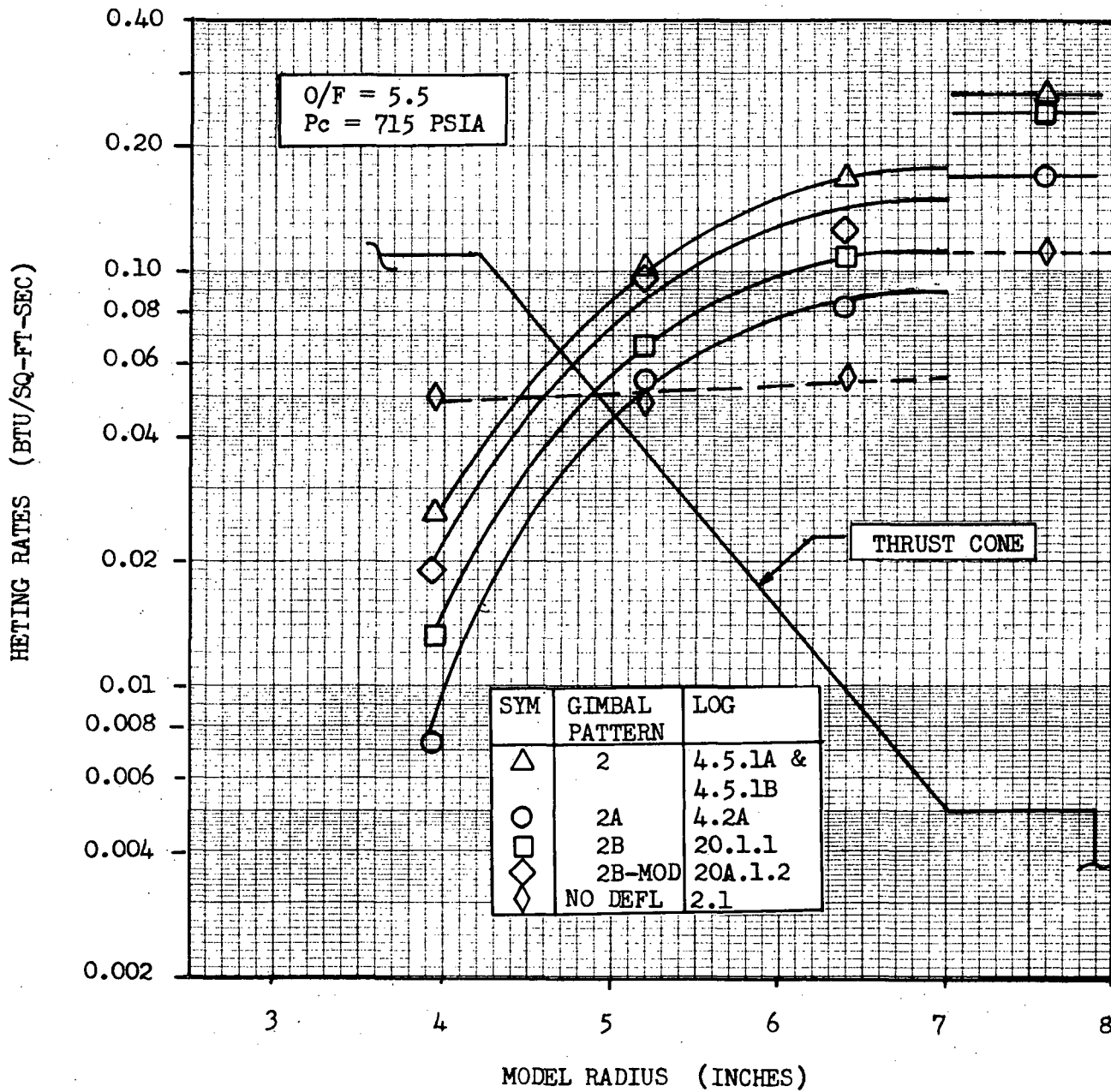
Figure 5.7.2-3   Thrust Cone Heating Rates with Outboard Engine Out
at θ = 0°
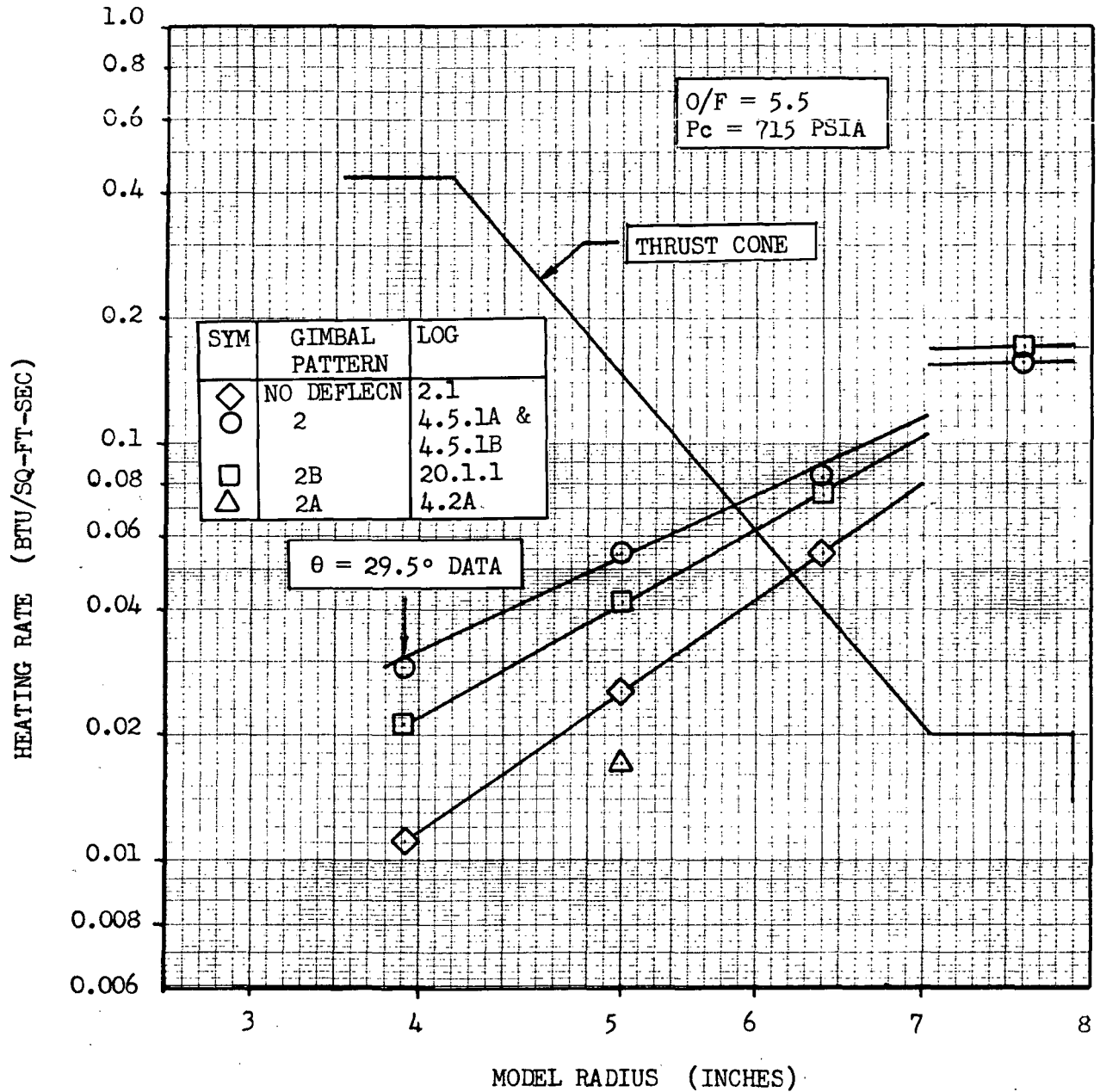
Figure 5.7.2-4 Thrust Cone Heating Rates with Outboard Engine Out
at θ = 37°

SD73-SA-0061

Space Division
North American Rockwell

GIMBAL PATTERN 2
INTERSTAGE ON
O/F = 5.5
Pc = 715 PSIA
LOG 4.5.2A &
       4.5.2B

HEATING RATES IN BTU/FT^2-SEC
TO 72°F SURFACE
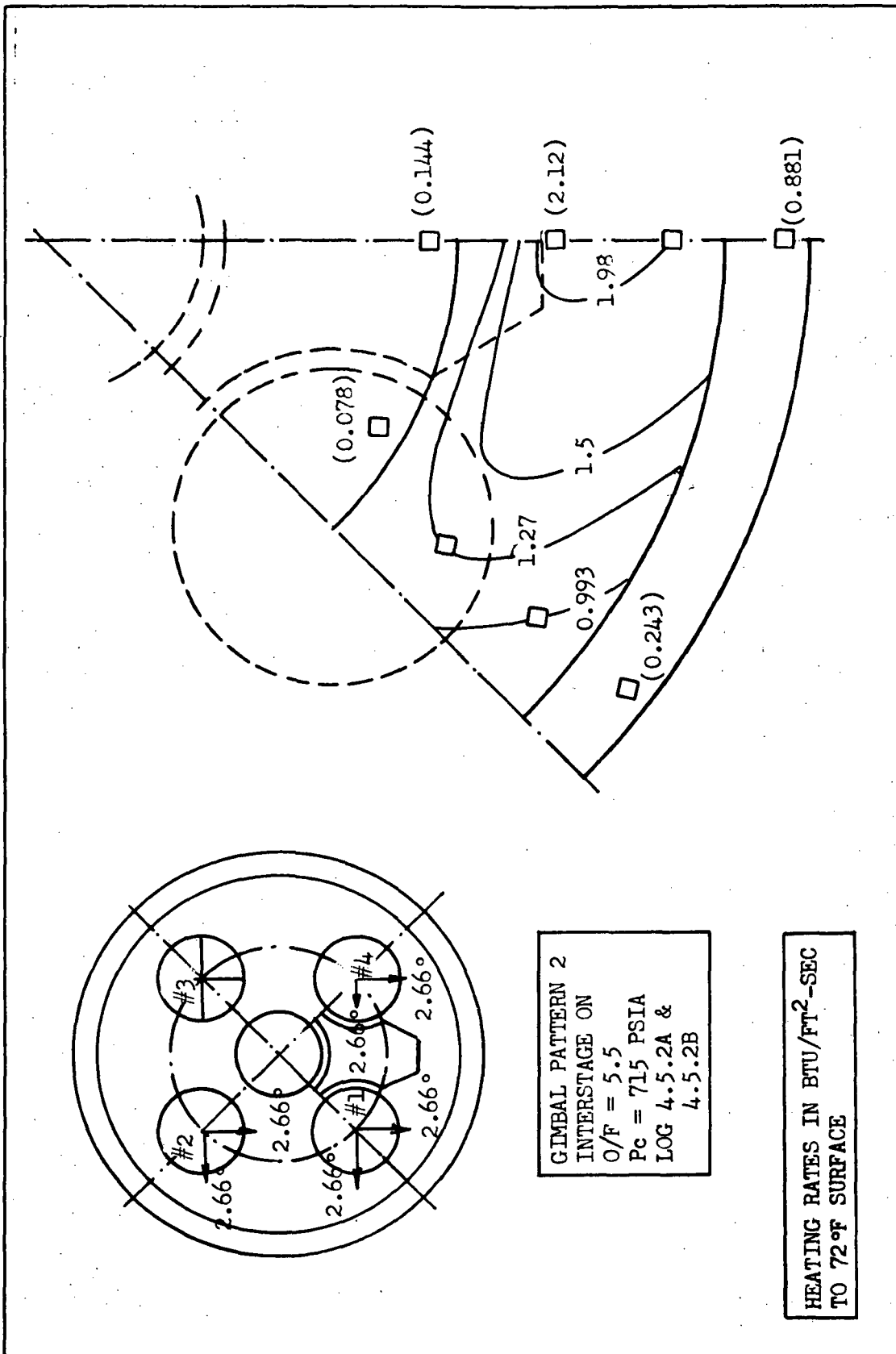
Figure 5.7.2-5   Thrust Cone Heating Rates With Outboard Engine Out Case 2,
Interstage On, O/F = 5.5

Space Division
North American Rockwell

GIMBAL PATTERN 2B
INTERSTAGE ON
O/F = 5.5
Pc = 715 PSIA
LOG 20.2.1 &
20.2.2

HEATING RATES IN BTU/FT²-SEC
TO 72°F SURFACE
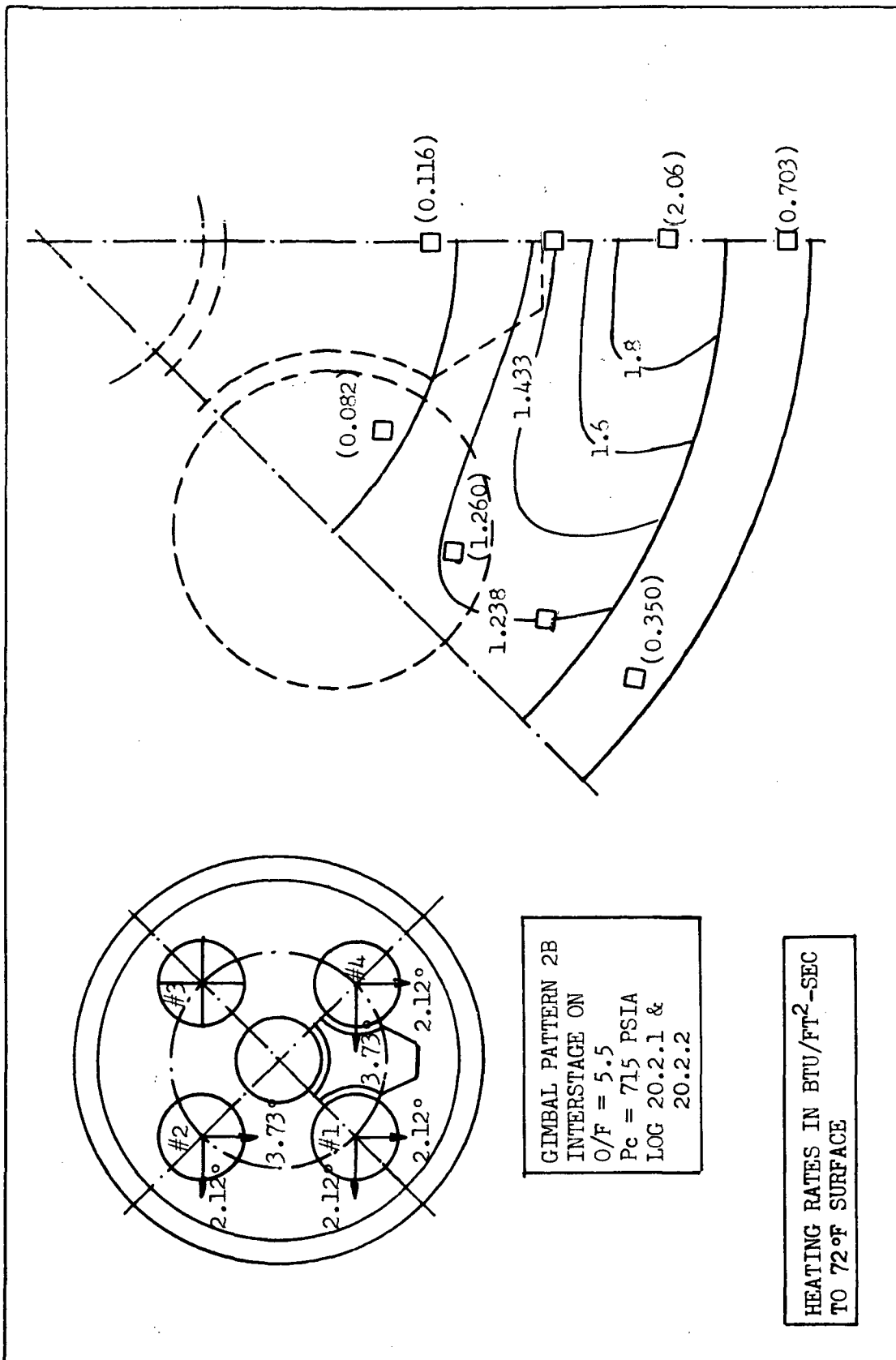
Figure 5.7.2-6 Thrust Cone Heating Rates With Outboard Engine Out Case 2B,
Interstage On, O/F = 5.5

GIMBAL PATTERN 2
INTERSTAGE OFF
GAGE ON #4 SIDE OF ENGINE #1
O/F = 5.5
Pc = 715 PSIA
LOG 4.5.1B

SYM	GAGE
O	Q110
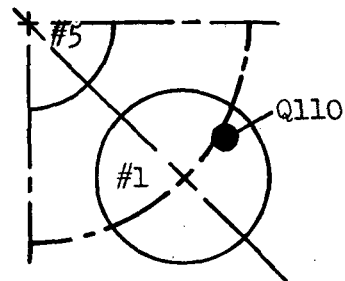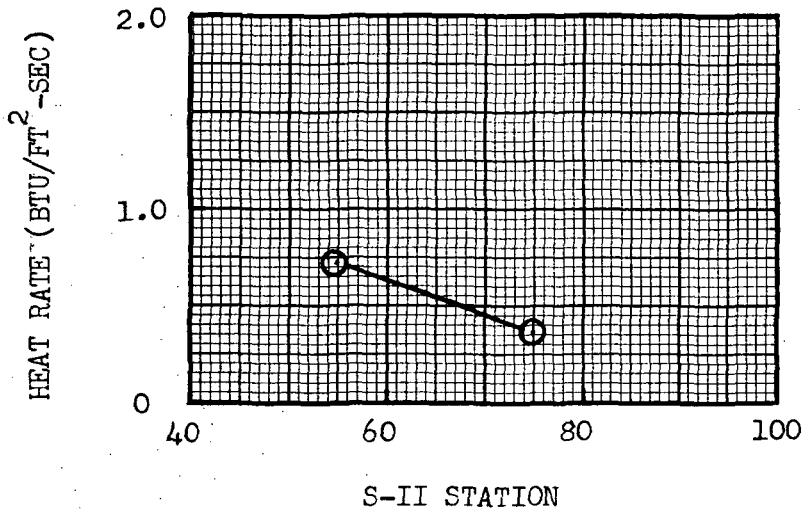
GIMBAL PATTERN 2
INTERSTAGE ON
GAGES ON #2 SIDE OF ENGINE #1
O/F = 5.5
Pc = 715 PSIA
LOG 4.5.2A & 4.5.2B

SYM	GAGE
O	Q110A
□	Q120A
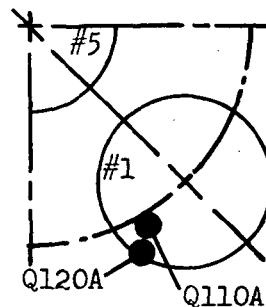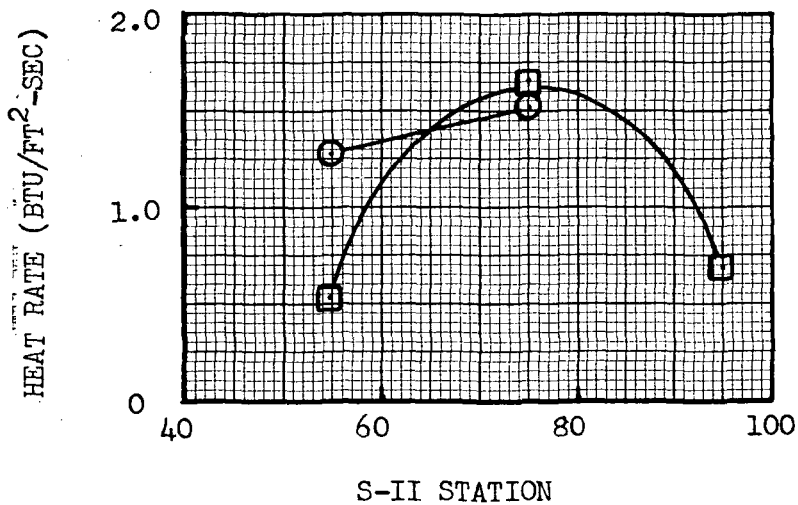
Figure 5.7.2-7 Thrust Cone Region Heating Rates with Gimbal Pattern 2

INTERSTAGE OFF
LOG 20.1.1 & 20.1.2

GIMBAL PATTERN 2B
GAGES ON #2 SIDE OF
ENGINE #1
O/F = 5.5
Pc = 715 PSIA

SYM	GAGE
O	Q110A
□	Q120A

INTERSTAGE ON
LOG 20.2.1 & 20.2.2
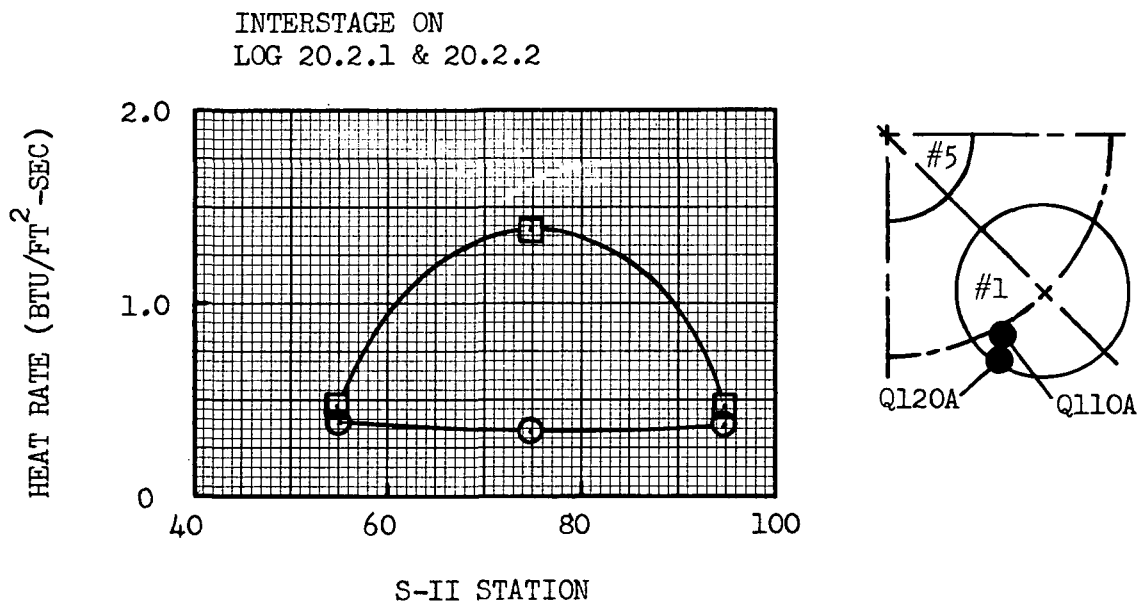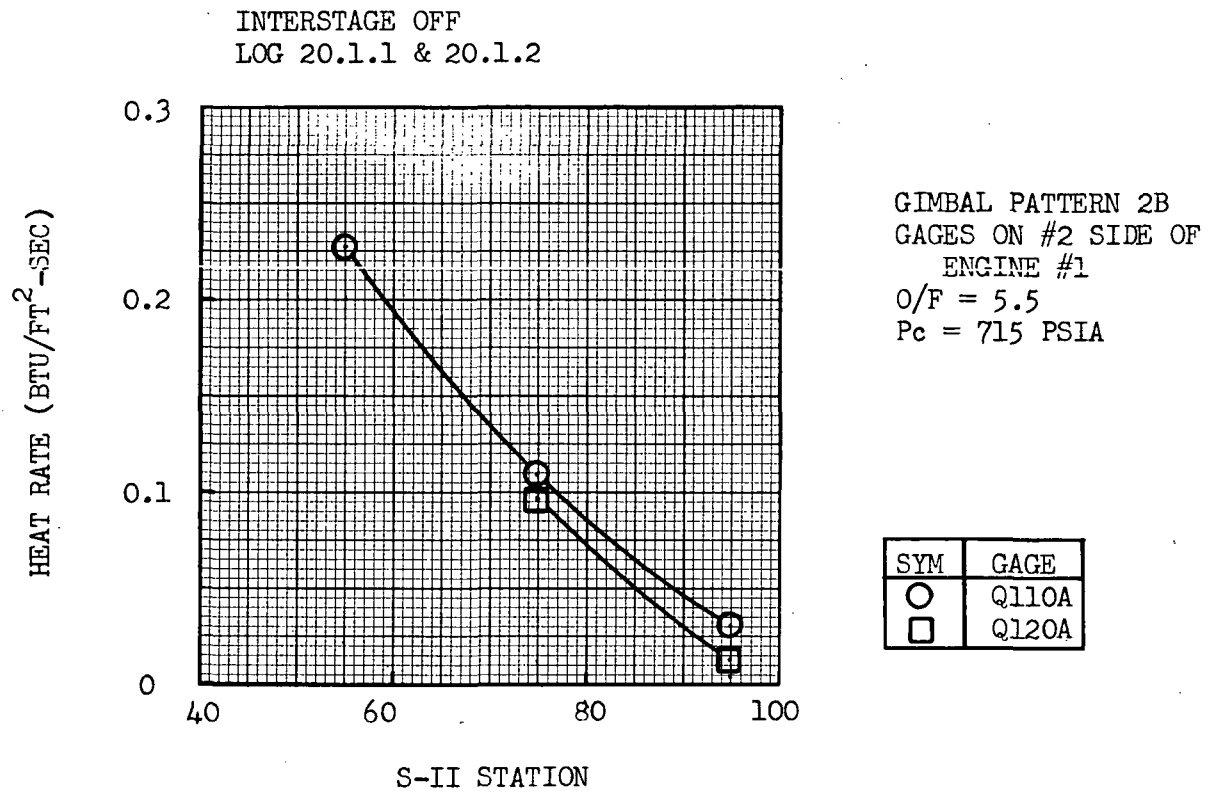
Figure 5.7.2-8 Thrust Cone Region Heating Rates with Gimbal Pattern 2B

SD73-SA-0061

5.7.3 Interstage Heating Rates

The interstage heating rates for outboard-engine-out gimbal patterns 2 and 2B are presented in Figures 5.7.3-1 and 5.7.3-2.

Only one row of heat transfer gages was used during the gimbal pattern 2 test runs and the gages were located at θ = 29.2°. A comparison of the nominal heating rates with the corresponding values for gimbal patterns 2 and 2B at θ = 29.2° is presented in Figure 5.7.3-1. It is seen that the outboard-engine-out heating rates are considerably lower than the nominal values with the peak heating rate at station 0 being reduced by 47% and 63% from the nominal value with gimbal patterns 2 and 2B respectively. Note that the engine deflection effect on the interstage heating rates decreases rapidly with S-II Station and beyond Station 120, the heating rates are practically unchanged from the nominal values.

Comparison of the gimbal pattern 2B heating rates of Figure 5.7.3-2 with the nominal heating rate distribution presented in Figure 5.6.3-1 shows that peripherally the outboard-engine-out deflection effect is most pronounced at θ = 0° where the peak heating rate is reduced by 74% from the nominal value. At θ = 45°, i.e., the peripheral location closest to the outboard engine, the heating rates increase by 40 percent at Station 58 and decrease by 30 percent at station 0 from the respective nominal values. These results are unexpected inasmuch that deflection of the engines toward the interstage produces lower than nominal interstage heating rates.

5.7.4 Inoperative Engine Nozzle Heating Rates

Heating rates to the inoperative engine nozzle were measured for several outboard-engine-out gimbal patterns. No measurements were made on the operating engines.

Figures 5.7.4-1 presents the heating rates to the inoperative outboard engine with gimbal pattern 2 engine deflections. It is seen that the inoperative nozzle heating rates are quite low. Comparison with the corresponding nominal heating rates of Figure 5.6.4-1 shows that the outboard-engine-out heating rates are practically the same as the nominal values in the region 0 to 20 inches (full scale) forward of the nozzle exit plane. The reason for the abrupt increase of nozzle heating rates beyond station 20 shown in Figure 5.7.4-1 is not clear at the present time.

Only one row of heating rate gages was recorded on the inoperative outboard engine with gimbal pattern 2A. The peripheral location of these gages was not recorded in the data Logs. The results are presented in Figure 5.7.4-2 where the heating rates are seen to be of the same magnitude as those for gimbal pattern 2.

SYM	GIMBAL PATTERN	LOG
◇	NO DEFL	15.3.1 & 15.3.2
○	2	4.5.2B
□	2B	20.2.1 & 20.2.2

O/F = 5.5
Pc = 715 PSIA

GAGE LOCATIONS
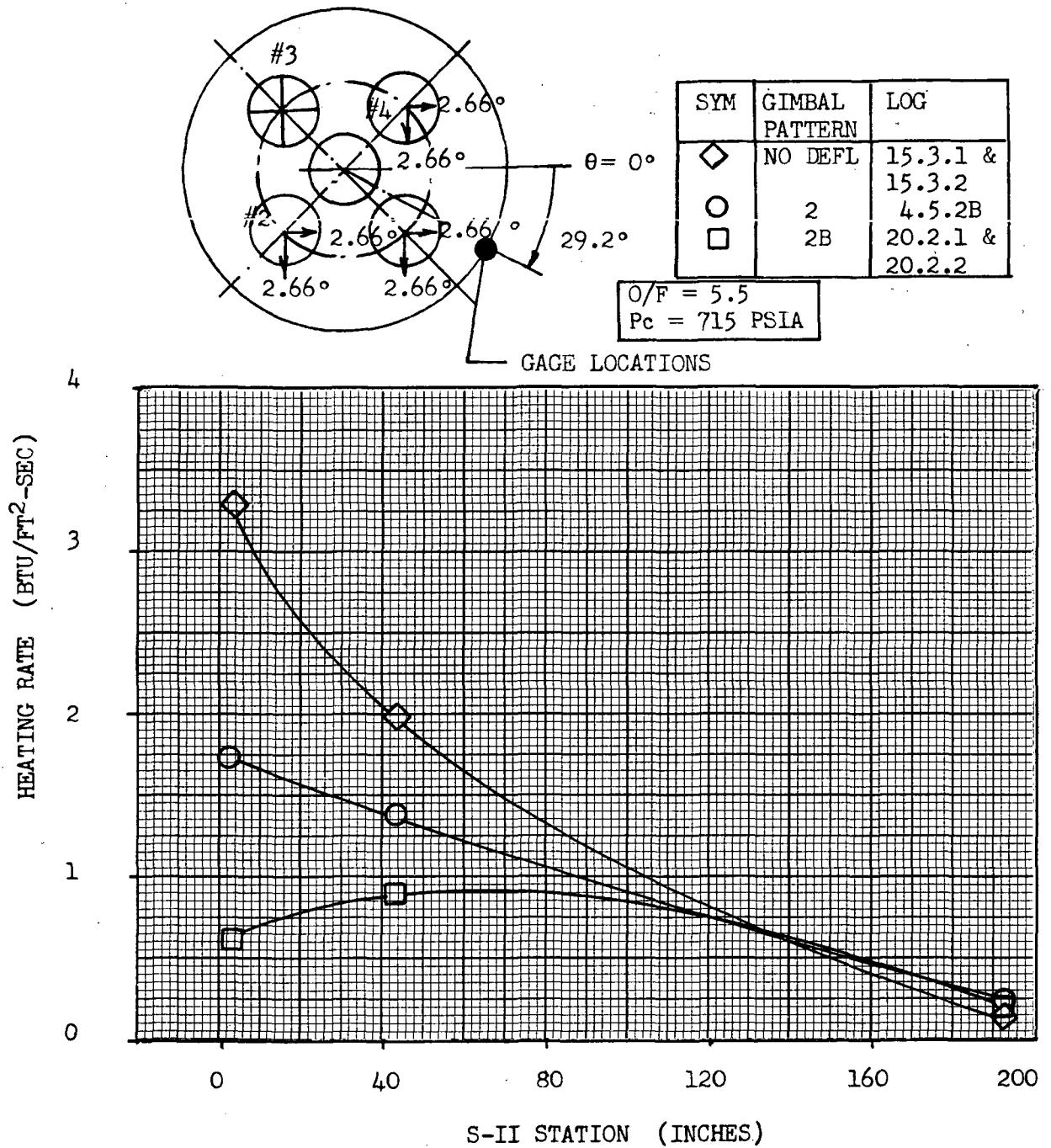
Figure 5.7.3-1 Interstage Heating Rates with Outboard Engine Out
Gimbal Patterns
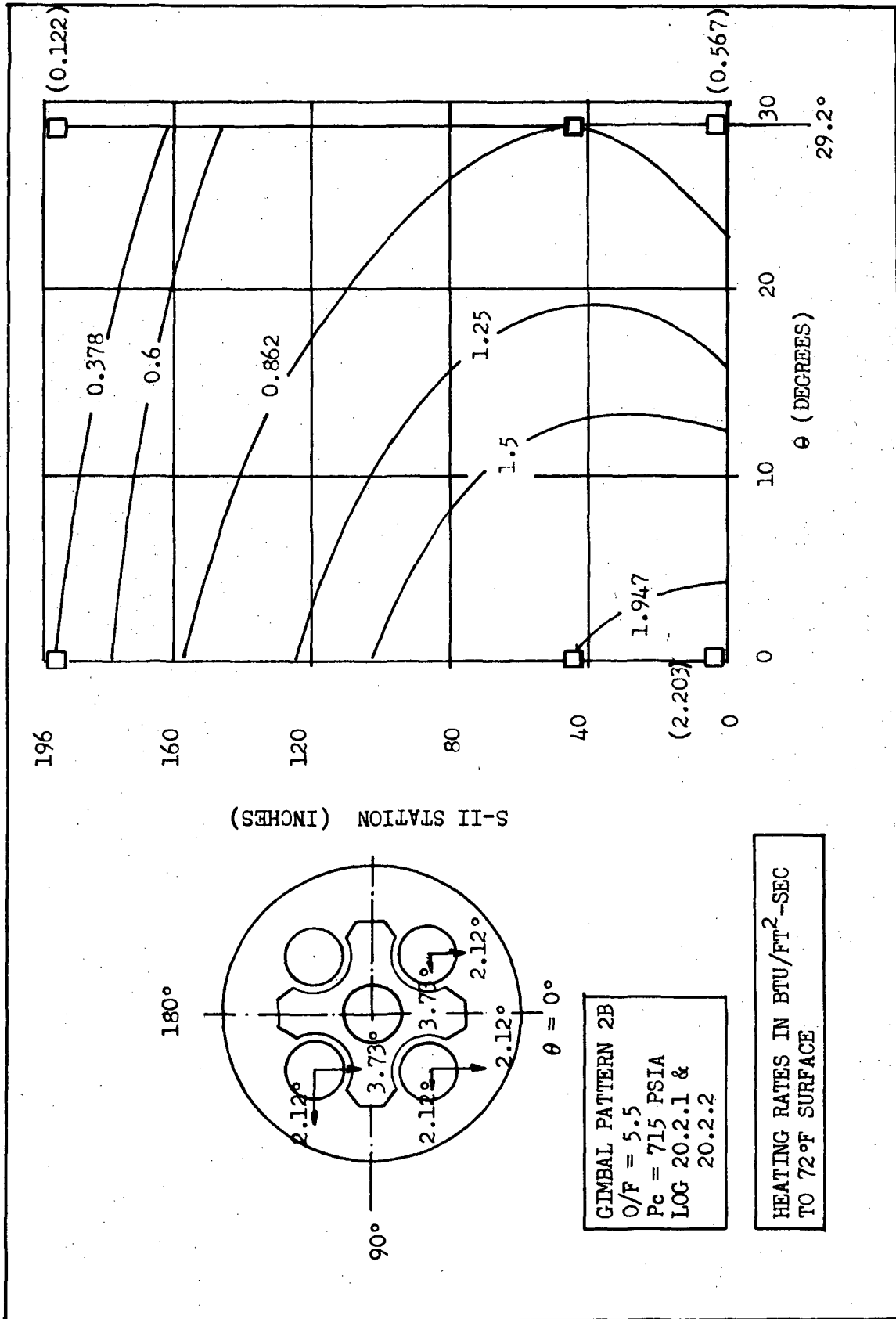
Figure 5.7.3-2 Interstage Heating Rates with Outboard Engine Out Gimbal Pattern 2
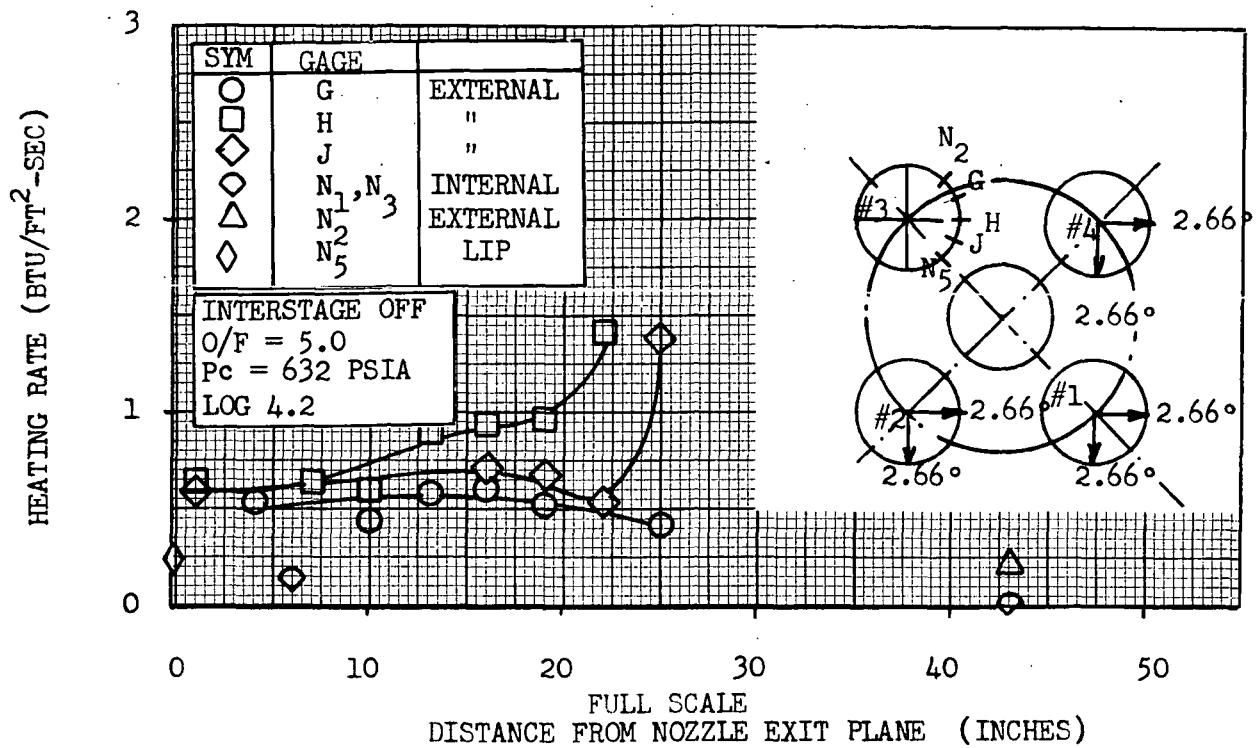
Figure 5.7.4-1   Inoperative Outboard Engine Heating Rates with
Gimbal Pattern #2
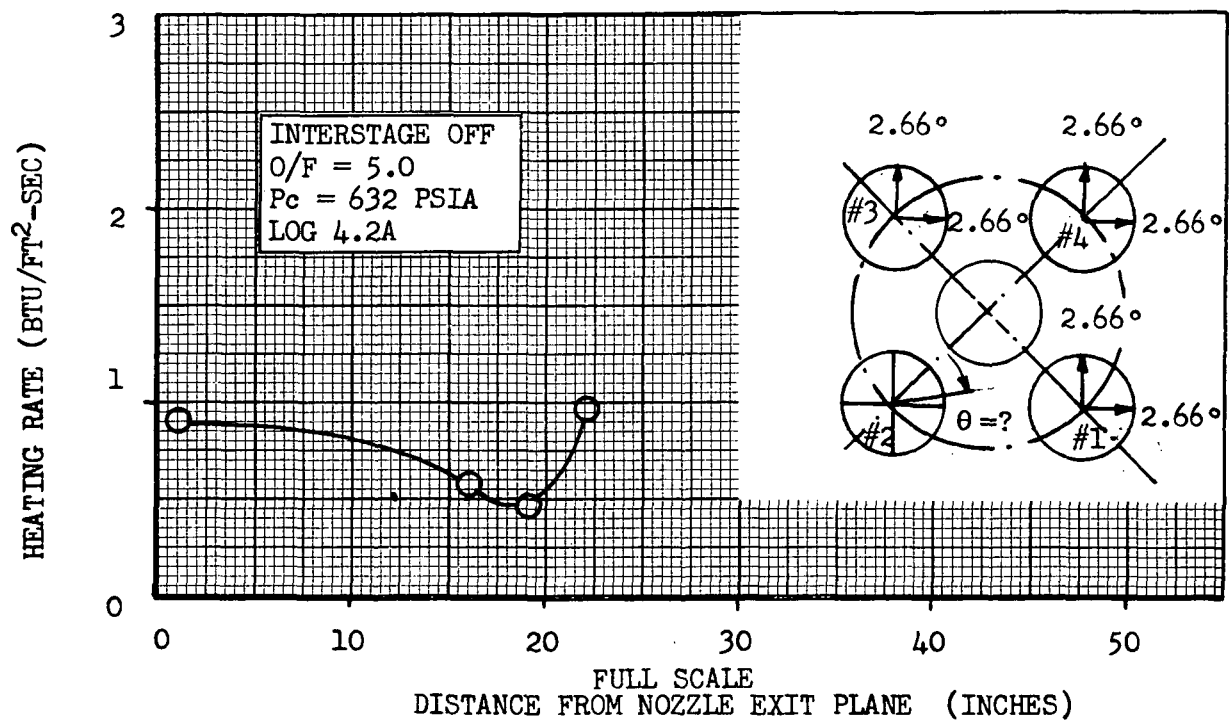
Figure 5.7.4-2   Inoperative Outboard Engine Heating Rates with
Gimbal Pattern #2A

Heating rates for the case where the inoperative engine was gimballed are presented in Figure 5.7.4-3. The heating rates are comparable to those where the inoperative engine was undeflected. Also, the heating rates are at least 50% lower than the corresponding nominal heating rates presented in Figure 5.6.4-1.
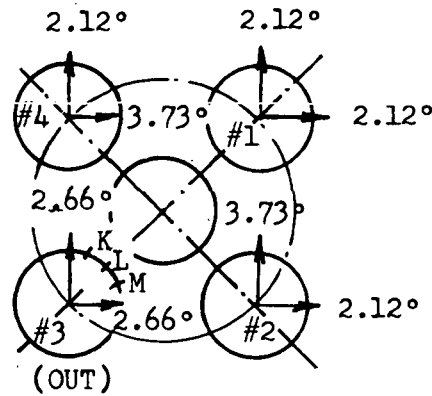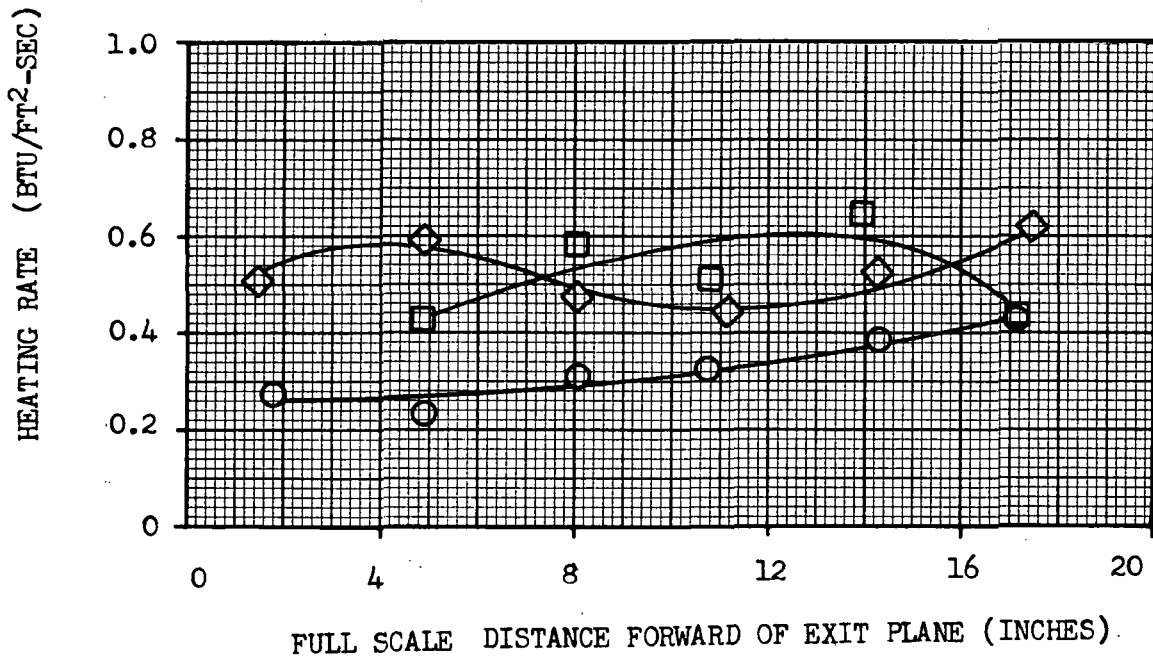
Figure 5.7.4-3 Inoperative Outboard Engine Nozzle Heating Rates
with Outboard Engine Out Gimbal Pattern 2B-Modified

5.8 BASE REGION ENVIRONMENT WITH A SINGLE ACTUATOR FAILED INBOARD

Heat shield, thrust cone, interstage and engine nozzle heating rates were determined for the single-actuator-failure-inboard gimbal patterns shown in Figure 5.8-1. Not all base region measurements were recorded for each gimbal pattern. Most of the heat shield heating rate data obtained from these tests were for the gimbal pattern 3C which produced the highest heating rates.

The majority of the test runs were carried out with O/F = 5.5; however, some data were obtained with gimbal patterns 5, 6 and 3C with O/F = 5.0. The effect of interstage was determined for the gimbal pattern 3C case only. Very little thrust cone pressure data were obtained for the single actuator failure conditions. Heat shield pressures were measured with Case 3C and 6A gimbal patterns.

It was found that the heat shield centerline heating rates were relatively unchanged by the various single actuator failure induced engine deflections. However, the heating rates in the vicinity of the outboard engine, towards which the failed actuator deflected, showed an appreciable increase from the nominal values. The maximum heating rates were determined to occur on the flexible curtain attachment flange where with gimbal pattern 3C engine deflections the peak test average heating rate was 29.8 Btu/ft^2-sec. This is the highest base region heating rate measured in the present test series, with the exception of the J-2 nozzle heating rates.

5.8.1 Heat Shield Heating Rates

Heat shield heating rate distributions for single-actuator-failure-inboard gimbal patterns 6A, 6, 5 and 3C are presented in Figures 5.8.1-1, 5.8.1-2, 5.8.1-3 and 5.8.1-4 respectively. Comparison of the heat shield nominal heating rates shown in Figure 5.6.1-3 with the gimbal Case 6A heating rates of Figure 5.8.1-1 shows that the overall heating rate level increases by a factor of 2 to 4 in the region bounded by the line connecting the center and outboard engine centerlines, while outside this region the heating rates increase from 30 to 100 percent from the corresponding nominal values. The peak heating rate increases by 75% and shifts in the direction of the failed actuator deflection.

Increased failed-actuator-deflections produce little change in the heat shield heating rates at and near the heat shield centerline, while the heating rates near the outboard engine show an appreciable increase with increasing failed-actuator-deflections as shown in Figures 5.8.1-3 and 5.8.1-4. However, the largest change in heating rate occurs on the outboard engine flexible curtain attachment flange where the test average heating rate of 29.8 Btu/ft^2-sec was measured at gage location Q_{10}.

The variation of flexible curtain attachment flange heating rates with failed-actuator-deflection angle is presented in Figure 5.8.1-5 and the corresponding variation for several heat shield gages in Figure 5.8.1-6. It is seen that a considerable variation of the heating rate-engine deflection trend exists with gage location.
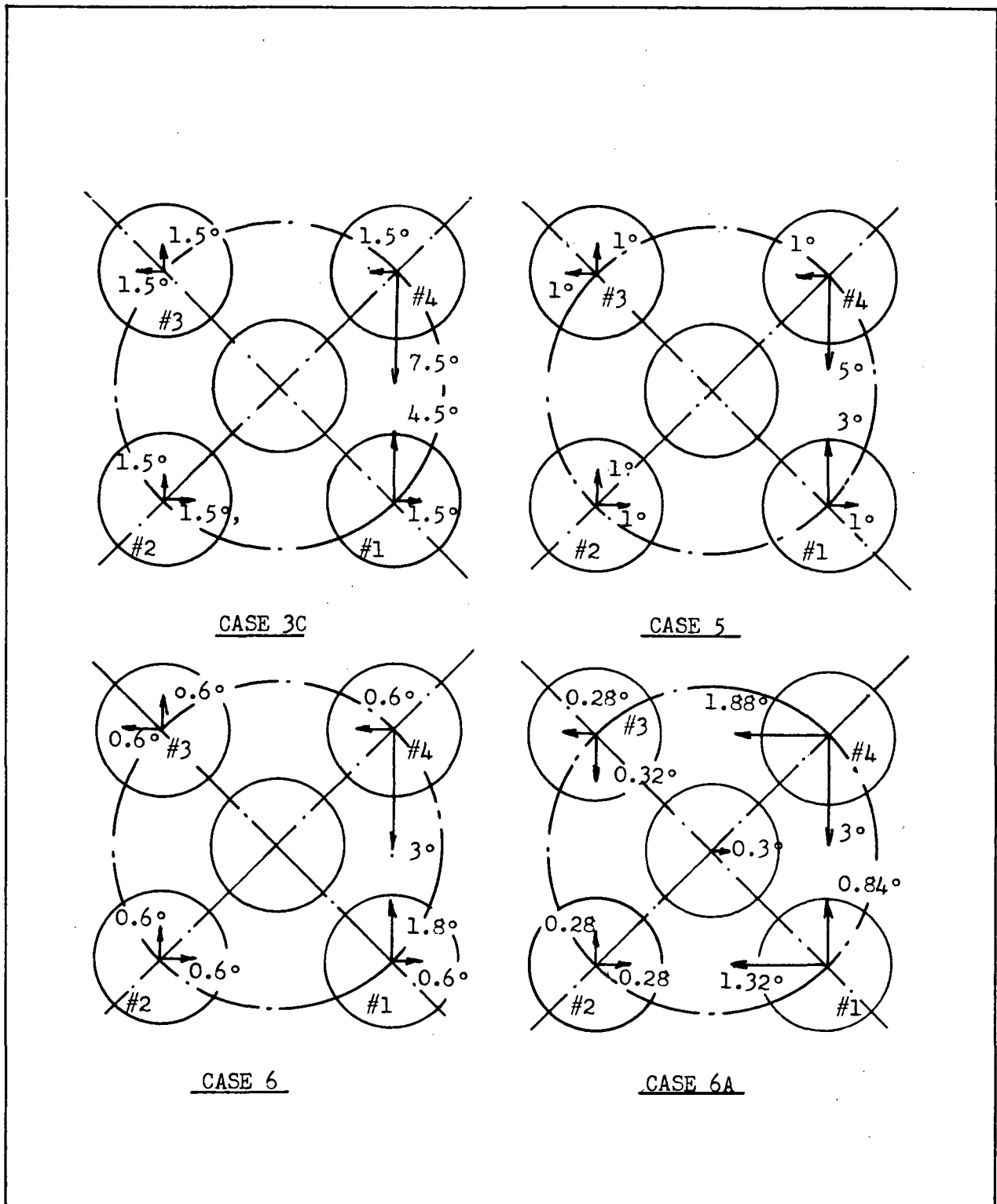
Figure 5.8-1 Single Actuator Failure Inboard Gimbal Patterns

SD73-SA-0061
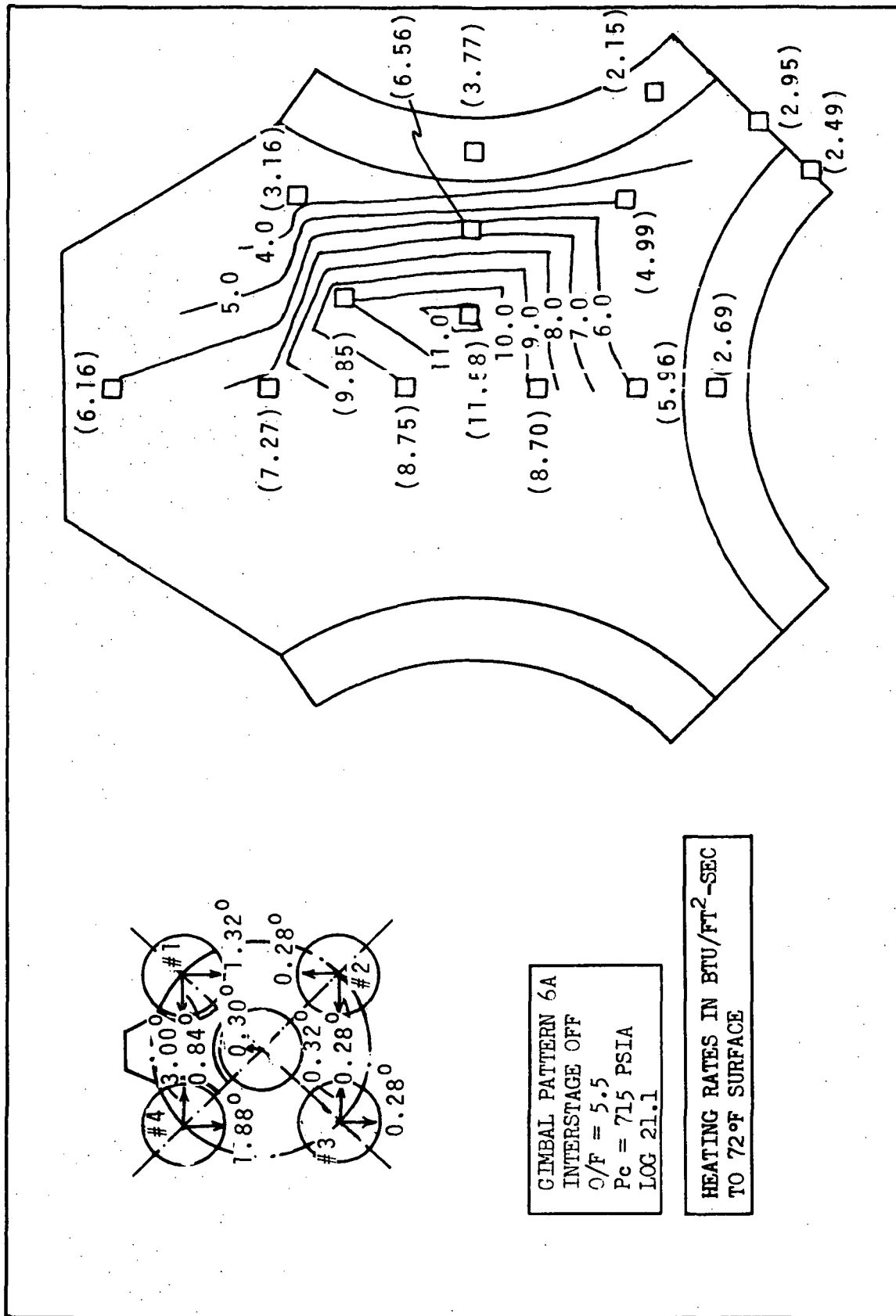
Figure 5.8.1-1 Heat Shield Heating Rates with Single Actuator Failure Inboard, Gimbal Pattern 6A, Interstage Off, O/F = 5.5

(6.56) (3.77) (2.15) (2.95) (2.49)

(3.16)

4.0

5.0

(6.16)

(7.27) (8.75) (9.85) 11.01 (11.58) 10.0 9.0 8.0 7.0 6.0 (4.99) (5.96) (2.69) (8.70)

GIMBAL PATTERN 6A
INTERSTAGE OFF
O/F = 5.5
Pc = 715 PSIA
LOG 21.1

HEATING RATES IN BTU/FT^2-SEC
TO 72°F SURFACE

#1 1.32°
0.28°
#2
3.00° 0.30°
0.84° 0.32°
0.28°
#4 #3
1.88° 0.28°
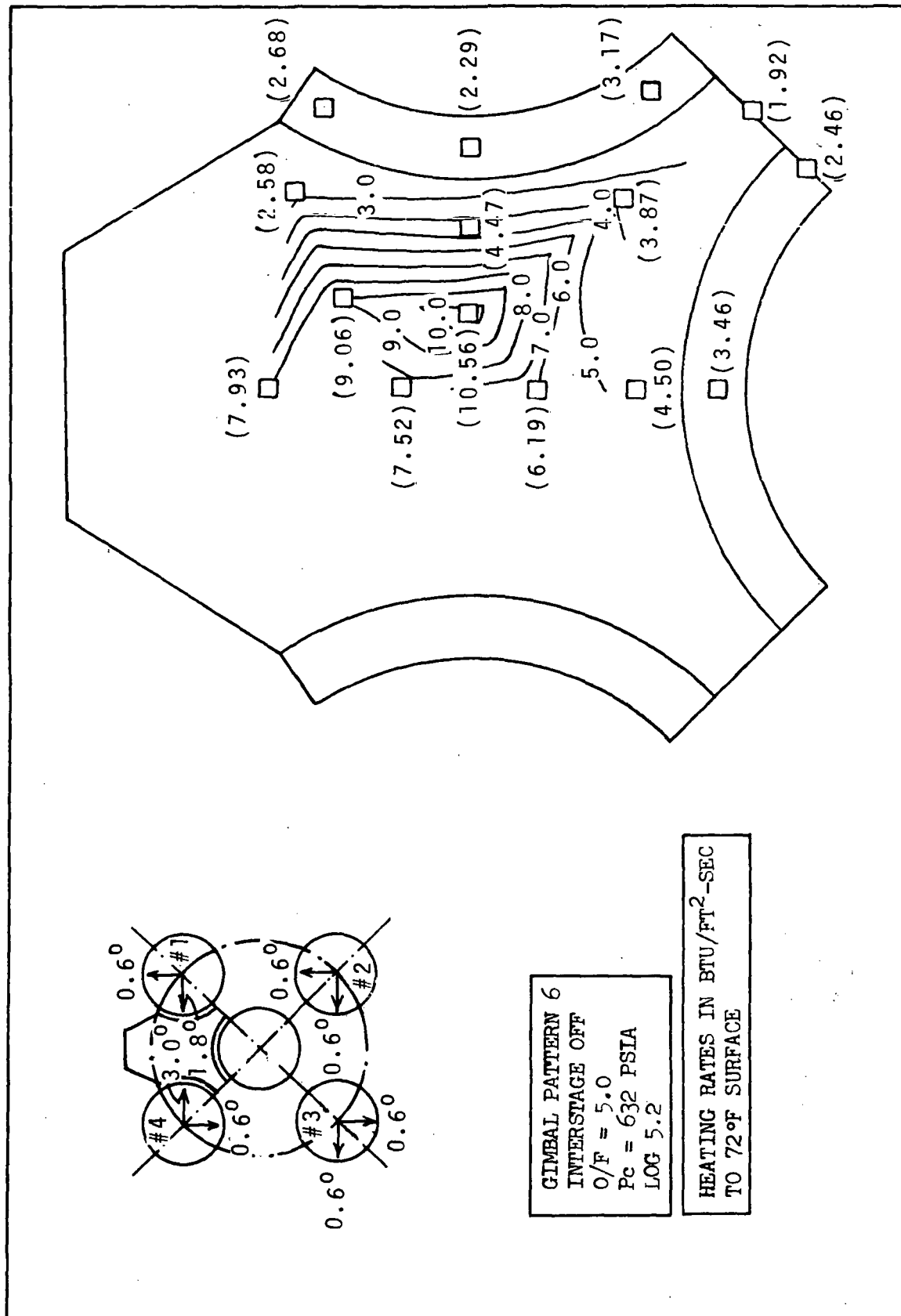
Figure 5.8.1-2 Heat Shield Heating Rates with Single Actuator Failure
Inboard, Gimbal Pattern 6, Interstage Off, O/F = 5.0

GIMBAL PATTERN 6
INTERSTAGE OFF
O/F = 5.0
Pc = 632 PSIA
LOG 5.2

HEATING RATES IN BTU/FT^2-SEC
TO 72°F SURFACE
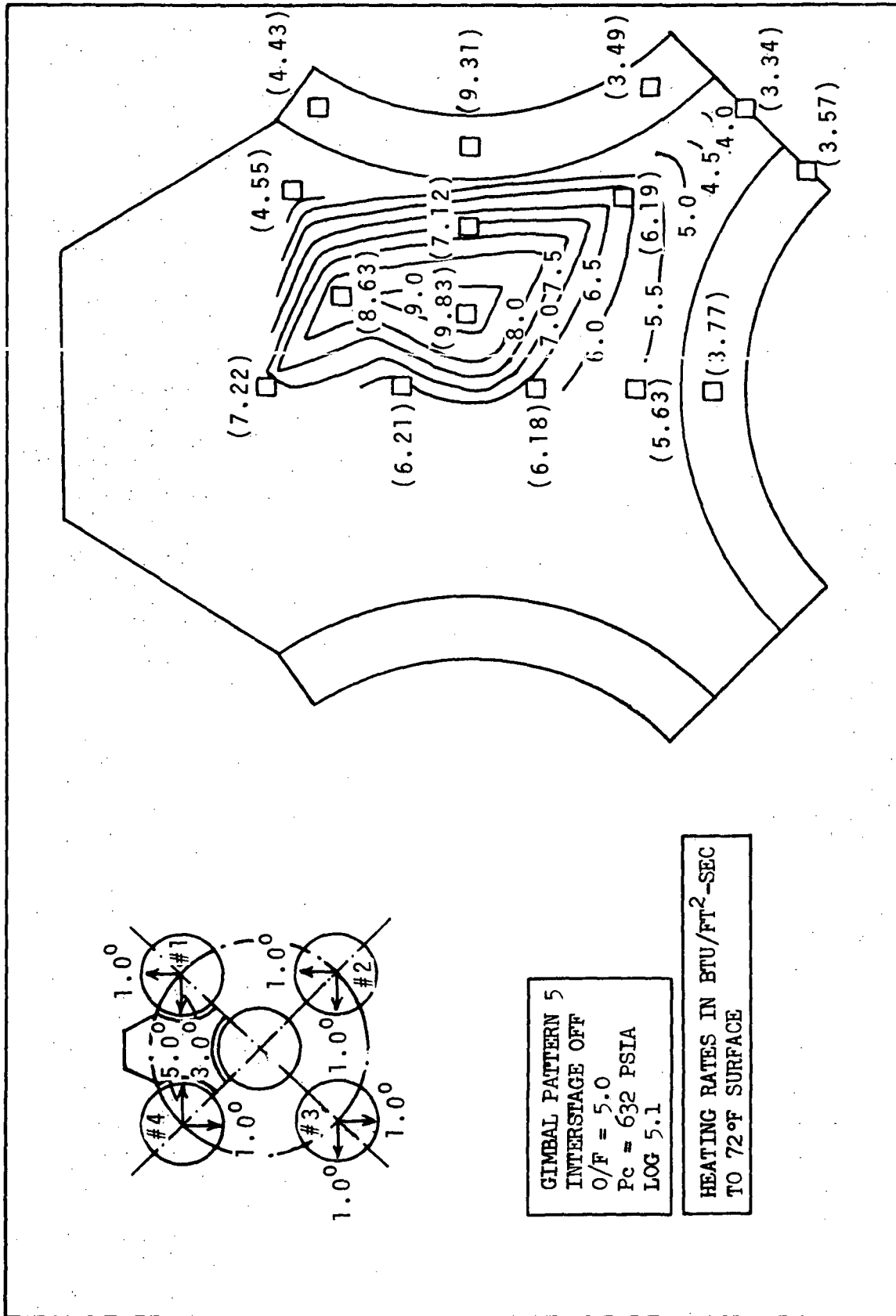
Figure 5.8.1-3 Heat Shield Heating Rates with Single Actuator Failure Inboard Gimbal Pattern 5, Interstage Off, O/F = 5.0

GIMBAL PATTERN 5
INTERSTAGE OFF
O/F = 5.0
Pc = 632 PSIA
LOG 5.1

HEATING RATES IN BTU/FT^2-SEC
TO 72°F SURFACE

SD73-SA-0061
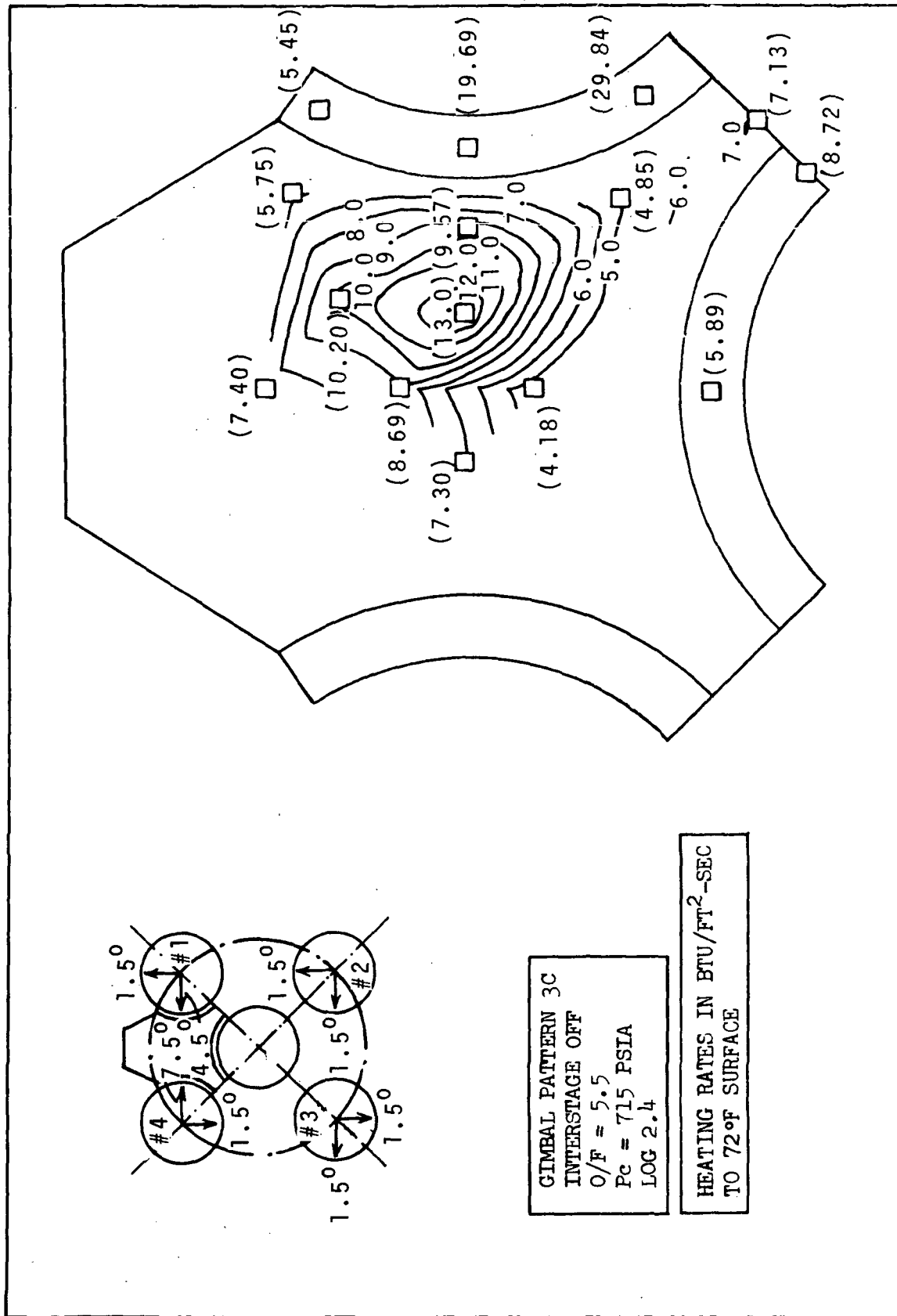
Figure 5.8.1-4 Heat Shield Heating Rates with Single Actuator Failure Inboard, Gimbal Pattern 3C, Interstage Off, O/F = 5.5

GIMBAL PATTERN 3C
INTERSTAGE OFF
O/F = 5.5
Pc = 715 PSIA
LOG 2.4

HEATING RATES IN BTU/FT^2-SEC
TO 72°F SURFACE
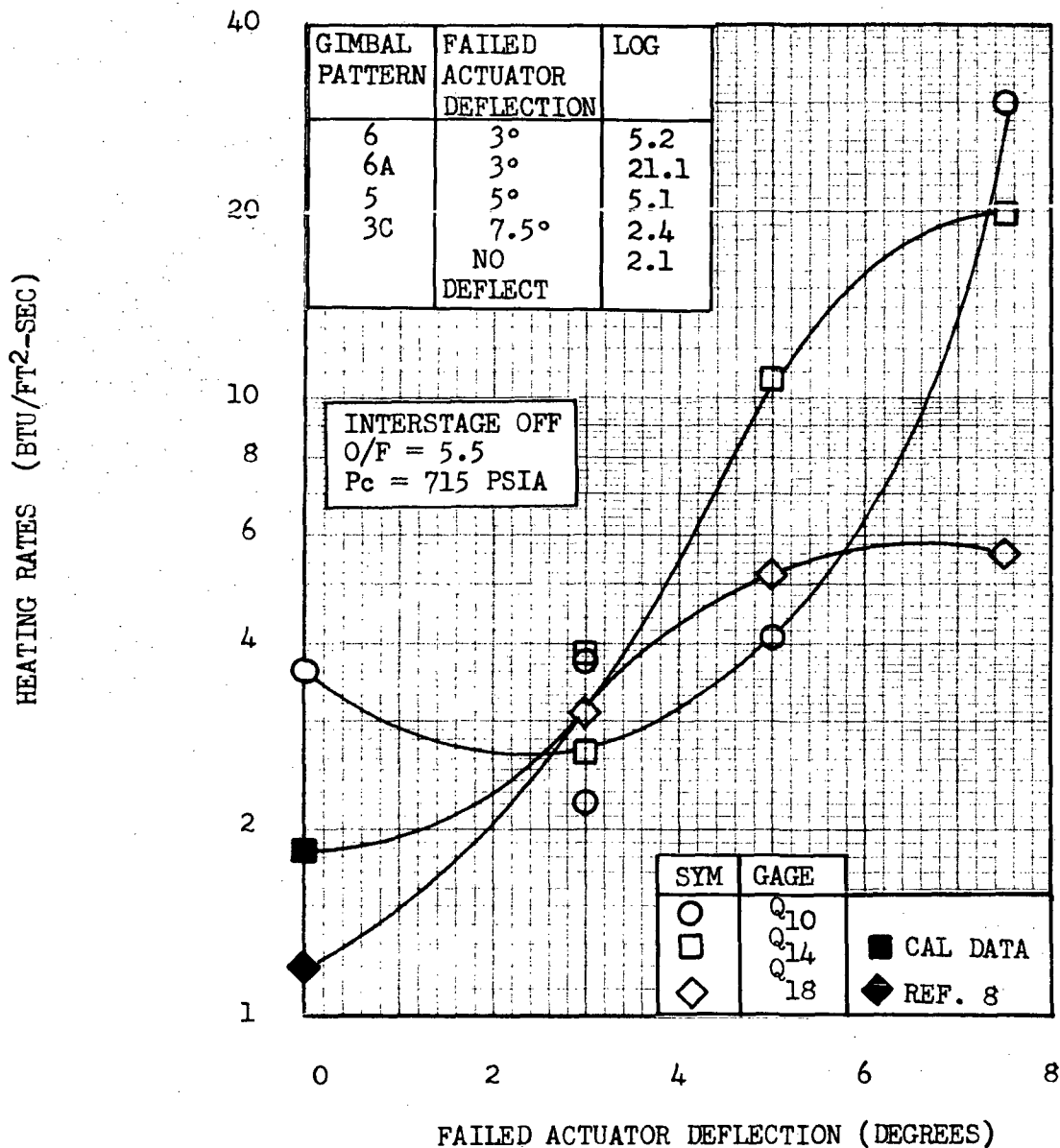
Figure 5.8.1-5 Flex Curtain Attachment Flange Heating Rates
Versus Single Actuator Failure Deflection

GIMBAL PATTERN	FAILED ACTUATOR DEFLECTION	LOG
6A	3°	21.1
6	3°	5.2
5	5°	5.1
3C	7.5°	2.4
--	0°	2.1

INTERSTAGE OFF
$O/F = 5.5$
$Pc = 715$ PSIA

HEATING RATE (BTU/FT^2-SEC)

FAILED ACTUATOR DEFLECTION (DEGREES)

SYM	GAGE
○	Q_{11}
□	Q_{13}
◇	Q_{15}
△	Q_{19}
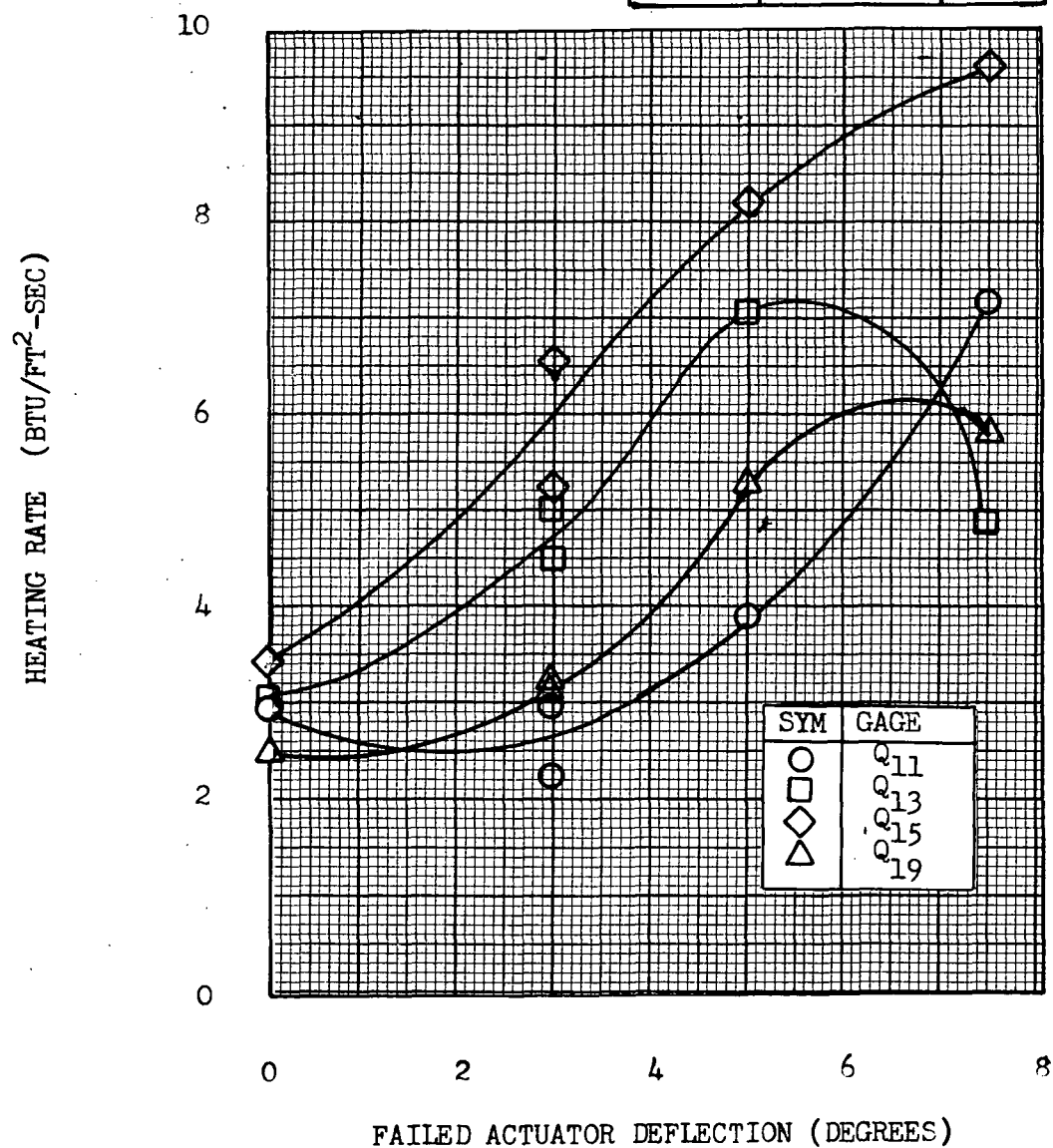
Figure 5.8.1-6 Heat Shield Heating Rate Variation With
Single Actuator Failure Deflection

The effect of mixture ratio and chamber pressure change on the heat shield heating rates with Case 3C engine deflections is obtained by comparison of the data presented in Figures 5.8.1-4 and 5.8.1-7. It is seen that by increasing the mixture ratio from 5.0 to 5.5 and the chamber pressure from 632 to 715 psia, the heating rates increase by 14.7% on the average. This agrees with the results of Sections 5.2 and 5.3 which indicated that the heating rates are proportional to chamber pressure.

The effect of interstage on the heat shield heating rates with single actuator failure gimbal pattern 6A is shown in Figure 5.8.1-8. Comparison with the corresponding interstage-off heating rates presented in Figure 5.8.1-1 shows that although the peak heating rate is unchanged, local heating rates increase by as much as 27% in the region between Engines 1 and 5. A slight reduction of the heating rates occurs at most other heat shield locations.

5.8.2 Thrust Cone Heating Rates

Thrust cone heating rates at $\theta = 0°$ are shown in Figure 5.8.2-1 for three different single-actuator-failure gimbal patterns and the corresponding nominal heating rates for comparison. It is seen that, except for gimbal pattern 6 at $Q23$ and $Q24$ gage locations, the interstage-off single-actuator-failure-inboard heating rates are lower than the corresponding nominal values.

Thrust cone heating rate distributions for gimbal pattern 3C are presented in Figures 5.8.2-2 and 5.8.2-3 for the interstage-off and the interstage-on conditions respectively. Comparison with the corresponding nominal heating rate distributions of Figures 5.6.2-1 and 5.6.2-2 shows that these single-actuator-failure-inboard heating rate distributions are very similar to the nominal distributions. The peak heating rate increased by 15% for the interstage-off and by 37% for the interstage-on condition above the nominal values.

5.8.3 Interstage Heating Rates

Interstage heating rates at $\theta = 0°$ were measured with gimbal pattern 3C only. The results are presented in Figure 5.8.3-1 together with the corresponding no-deflection heating rates for comparison. It is seen that the most severe single-actuator-failure-inboard deflection case tested produced heating rates 11% to 22% below the nominal values at $\theta = 0°$. No test data is available to determine the effect of single-actuator-failure-inboard on the interstage heating rates at $\theta = 45°$ i.e., in the vicinity of the outboard engine.

5.8.4 Nozzle Heating Rates

Nozzle heating rates were measured with the single-actuator-failure-inboard gimbal pattern 6A. The results are presented in Figures 5.8.4-1 and 5.8.4-2 for the center and the outboard Engine Number 4 respectively. Heating rates to outboard Engine Number 1 with gimbal pattern 6A deflections are shown in Figure 5.8.4-3.
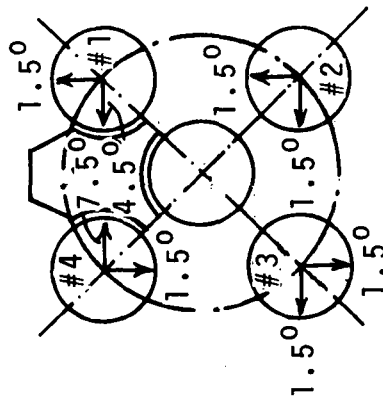
Figure 5.8.1-7 Heat Shield Heating Rates with Single Actuator Failure Inboard, Gimbal Pattern 3C, Interstage Off, O/F = 5.0

GIMBAL PATTERN 3C
INTERSTAGE OFF
O/F = 5.0
Pc = 632 PSIA
LOG 4.3

HEATING RATES IN BTU/FT²-SEC
TO 72°F SURFACE
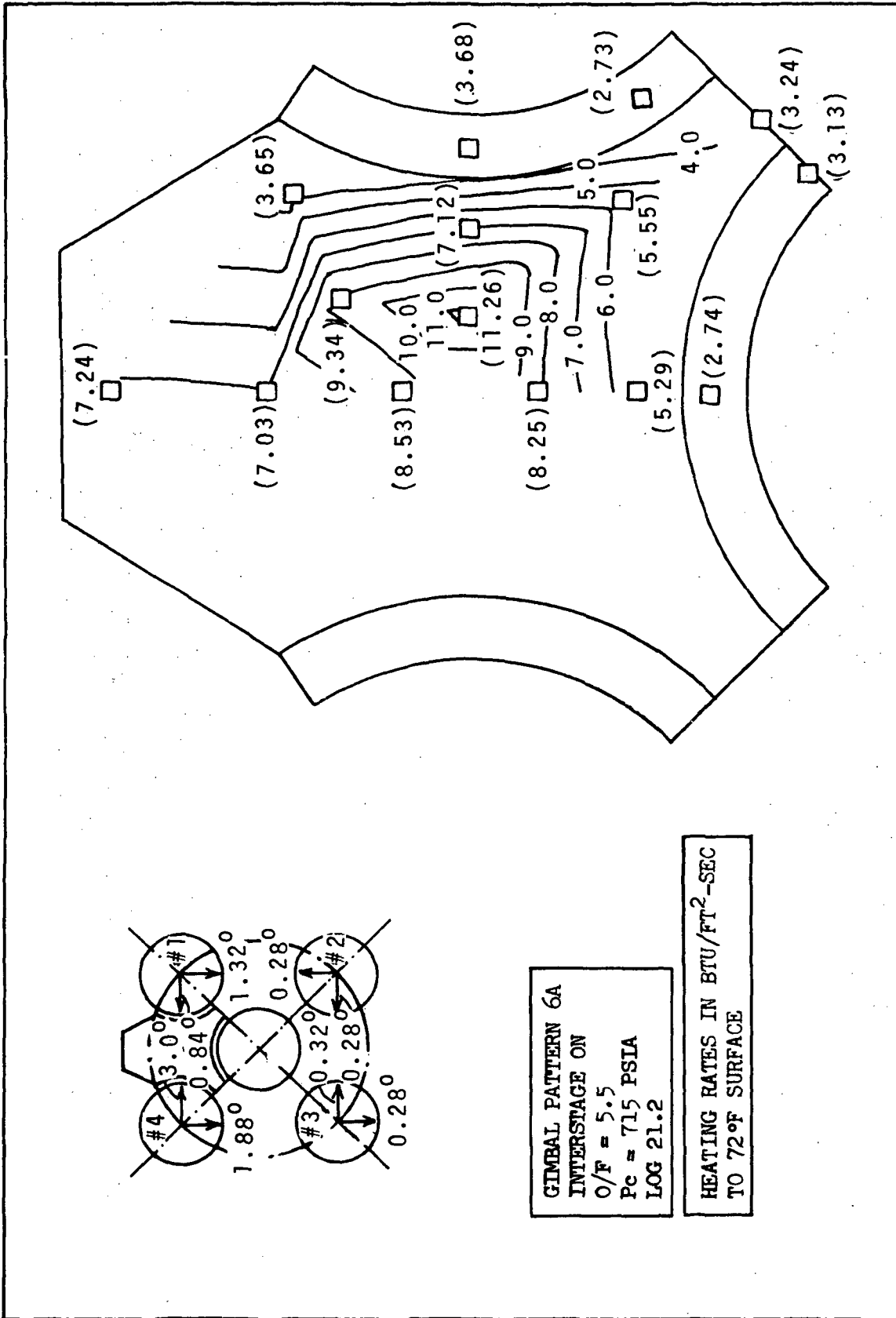
Figure 5.8.1-8   Heat Shield Heating Rates with Single Actuator Failure
Inboard, Gimbal Pattern 6A, Interstage On, O/F = 5.5

GIMBAL PATTERN 6A
INTERSTAGE ON
O/F = 5.5
Pc = 715 PSIA
LOG 21.2

HEATING RATES IN BTU/FT²-SEC
TO 72°F SURFACE
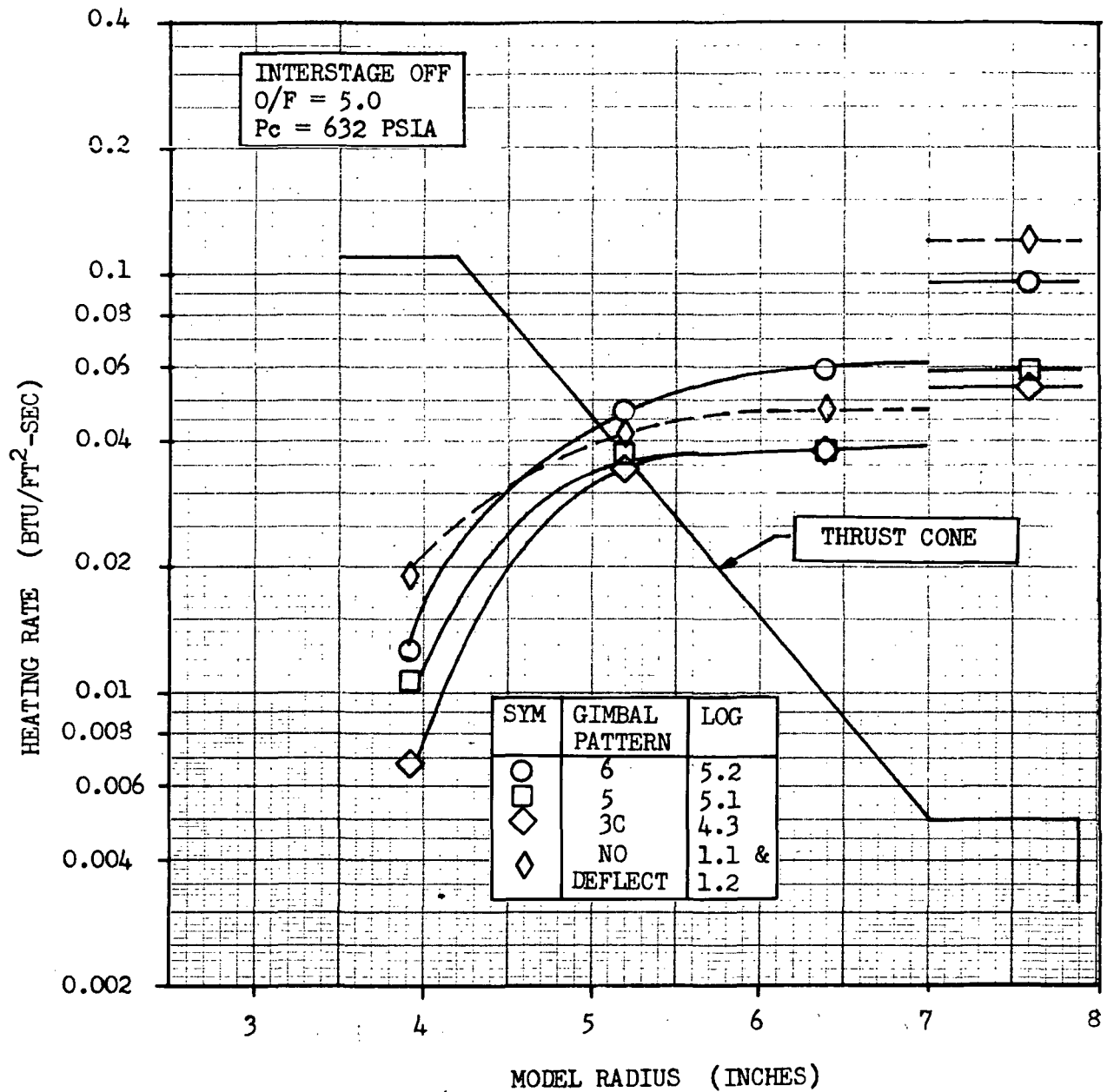
Figure 5.8.2-1 Thrust Cone Heating Rates at θ = C° With Single
Actuator Failure Inboard Engine Deflections

SD73-SA-0061
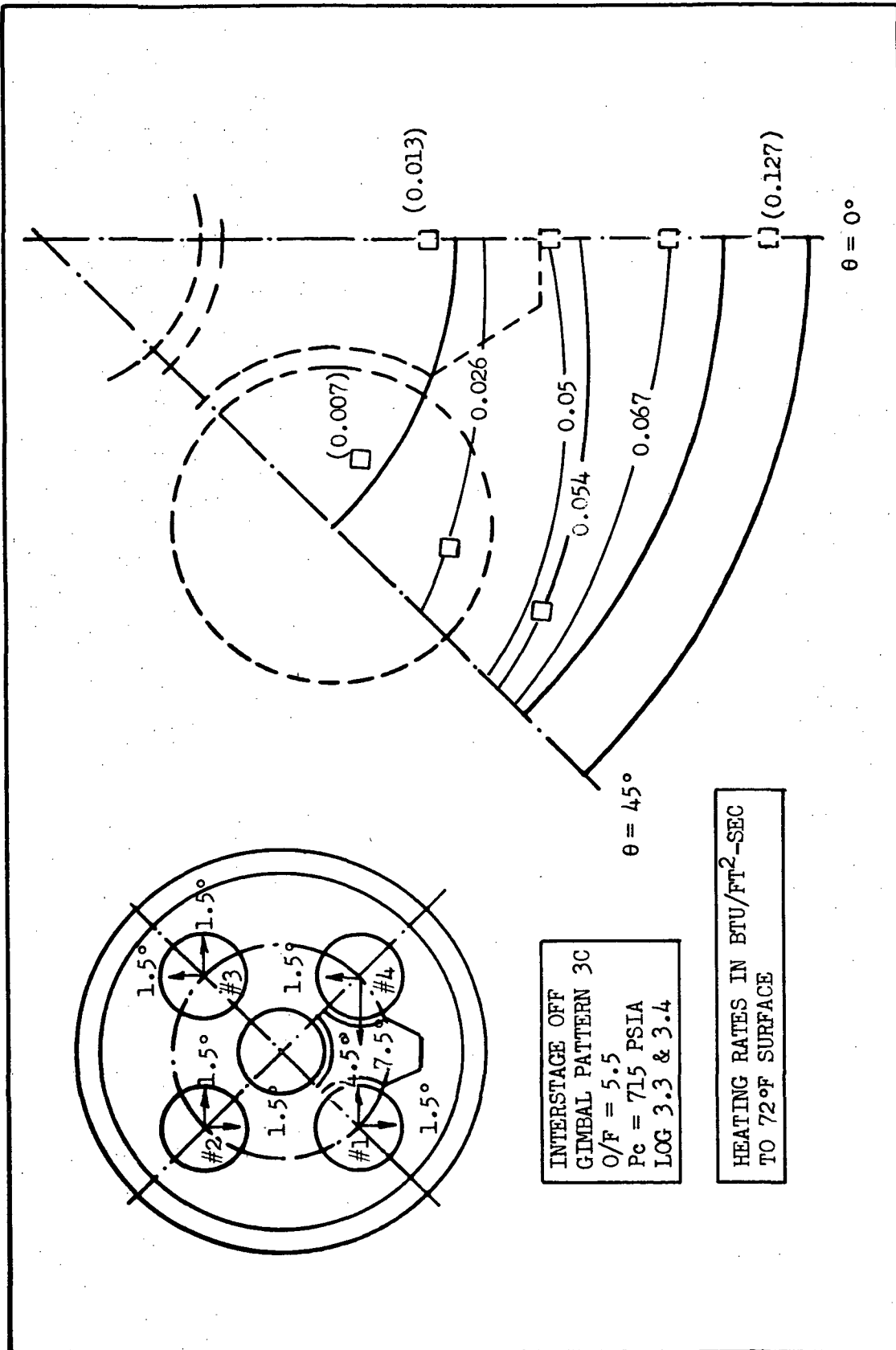
Figure 5.8.2-2 Thrust Cone Heating Rates With Single Actuator Failure Inboard Case 3C, Interstage Off, O/F = 5.5

θ = 0°

(0.013)

[] (0.127)

(0.007)

0.026

0.05

0.054

0.067

θ = 45°

INTERSTAGE OFF
GIMBAL PATTERN 3C
O/F = 5.5
Pc = 715 PSIA
LOG 3.3 & 3.4

HEATING RATES IN BTU/FT²-SEC
TO 72°F SURFACE

1.5°
#3
#4
#1
#2
1.5°
7.5°
4.5°

SD73-SA-0061
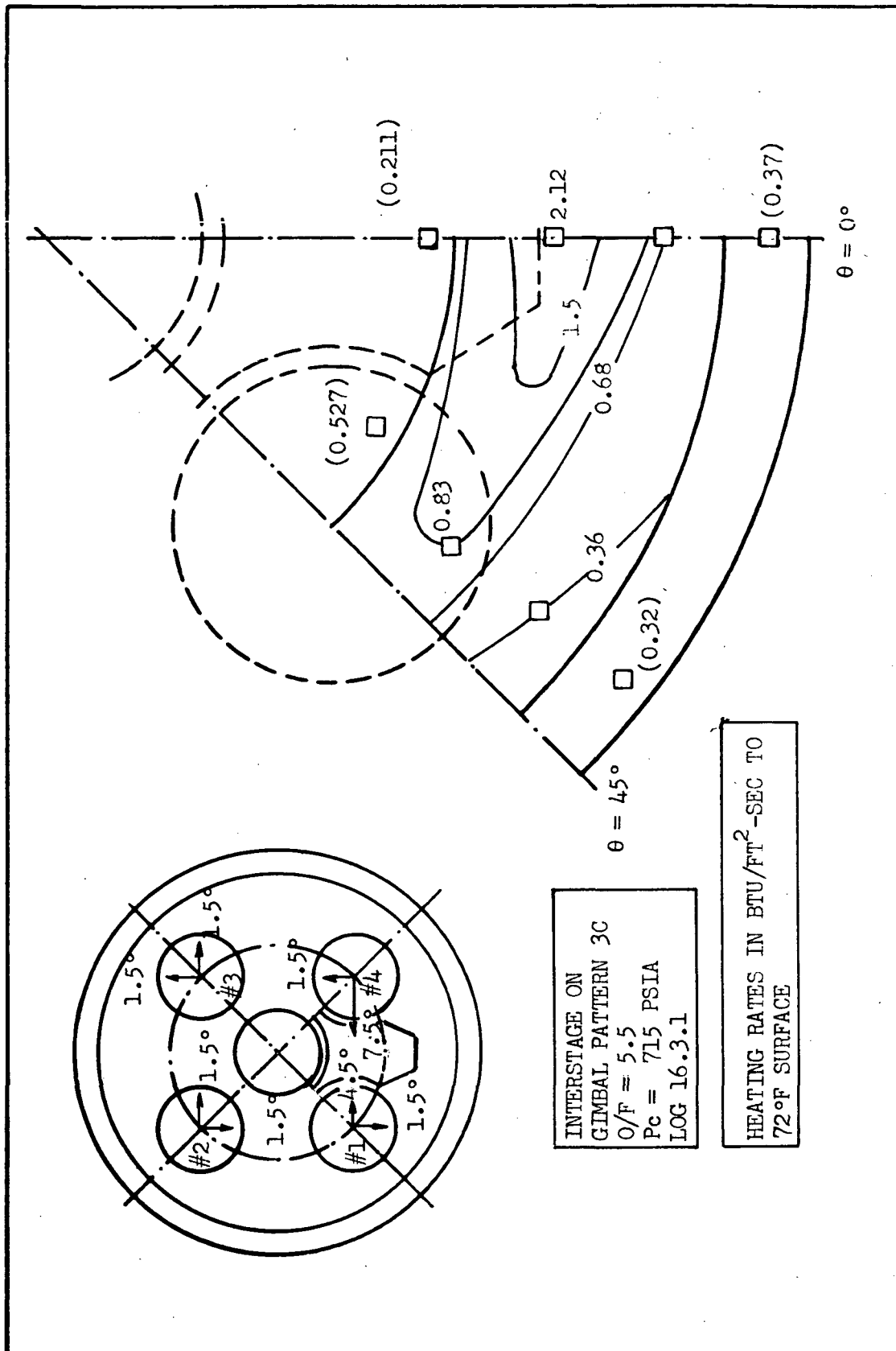
Figure 5.8.2-3 Thrust Cone Heating Rates With Single Actuator Failure Inboard Case 3C, Interstage On, O/F = 5.5
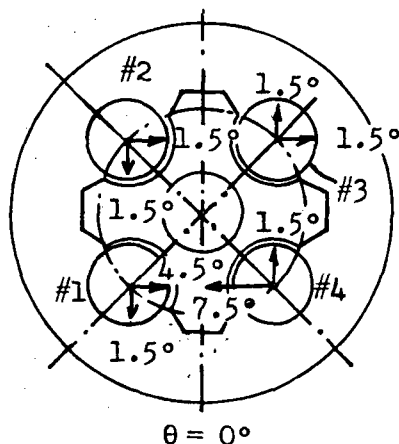
$$O/F = 5.5$$
$$Pc = 715 \text{ PSIA}$$

SYM	GIMBAL PATTERN	LOG
○	3C	16.3.1
□	NO DEFLECT	15.3.1
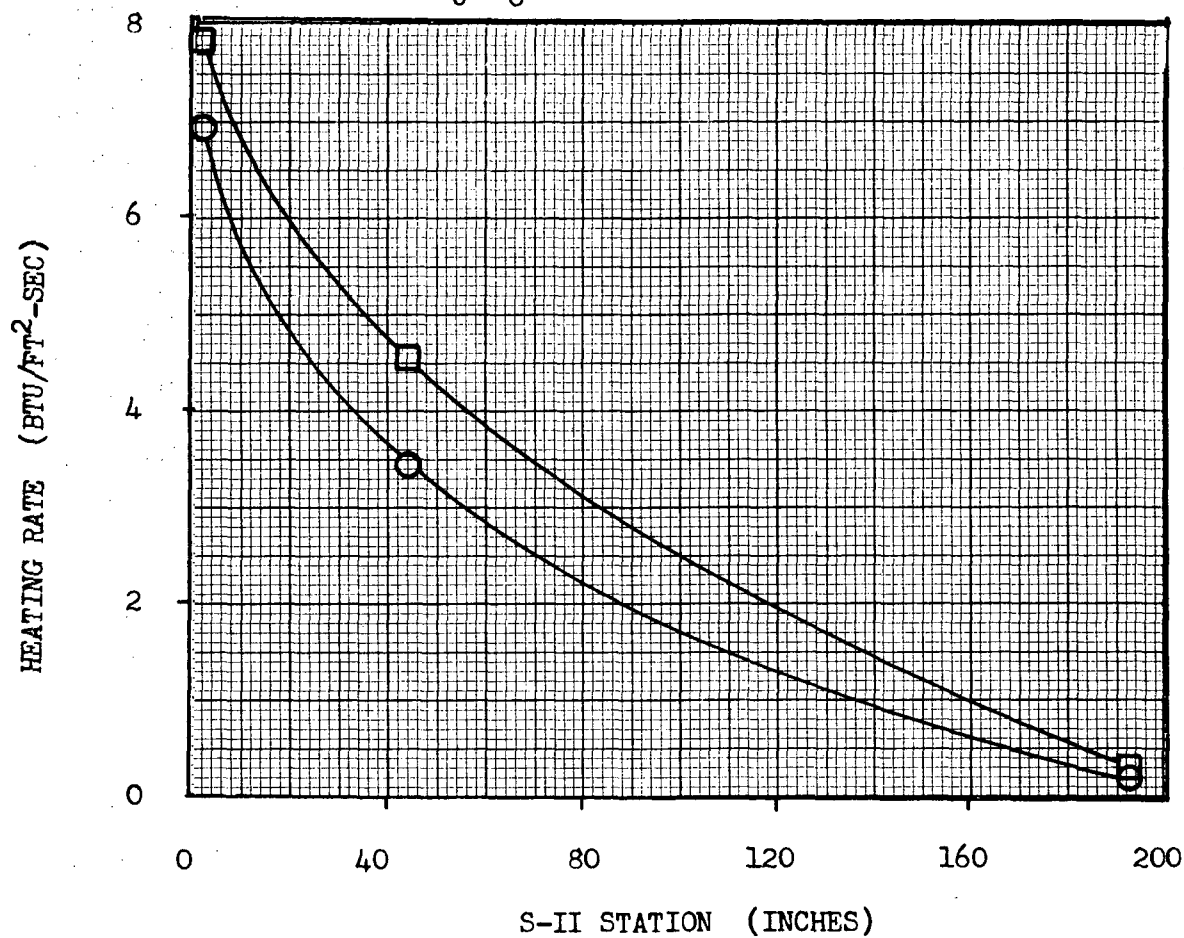
Figure 5.8.3-1　Interstage Heating Rates at θ = 0° With Single
Actuator Failure Inboard

SD73-SA-0061

SYM	GAGE
◯	K
▢	L
◇	M

```
INTERSTAGE OFF
GIMBAL PATTERN 6A
O/F = 5.5
Pc = 715 PSIA
LOG 23.2
```
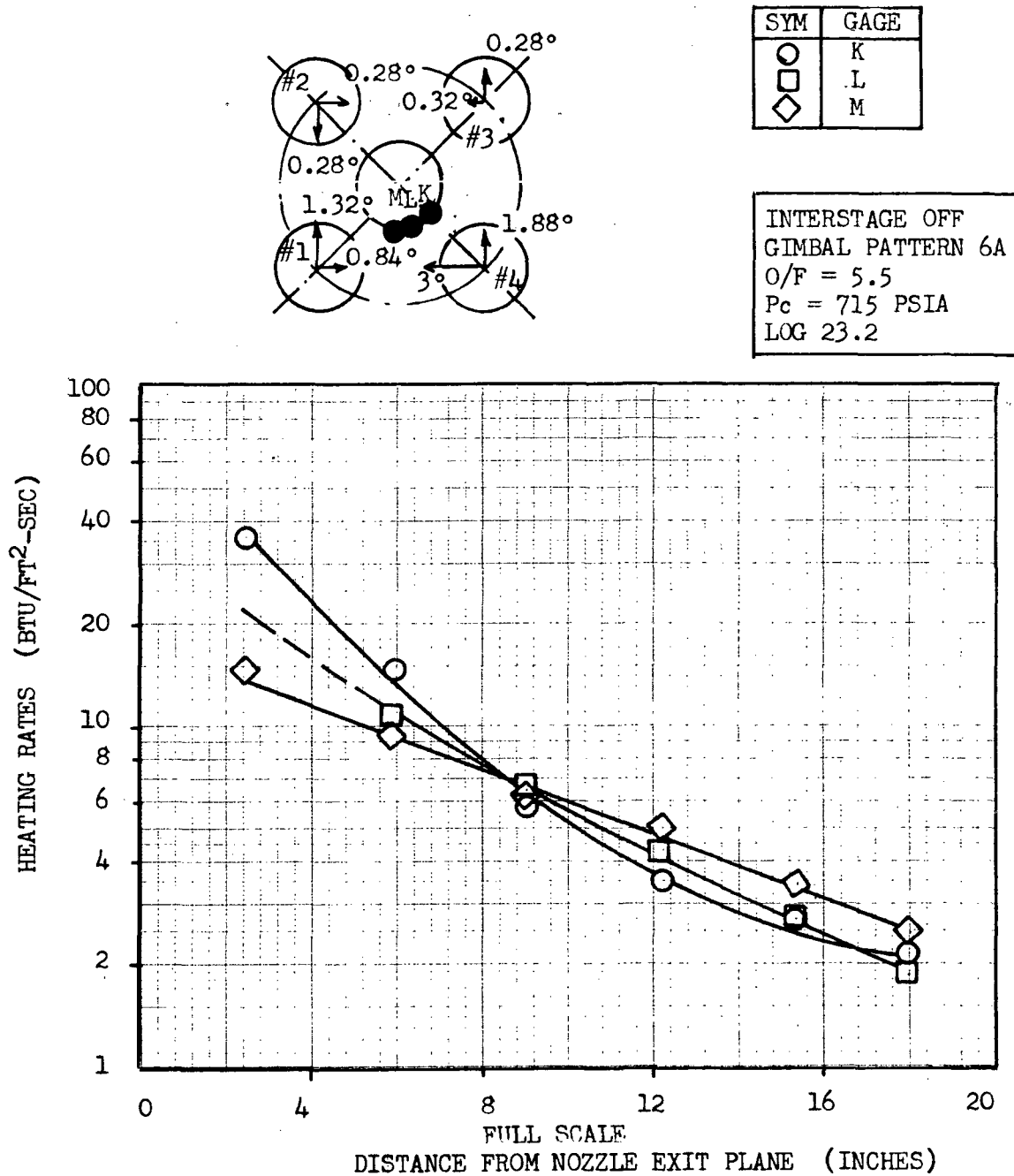
Figure 5.8.4-1 Center Engine Heating Rates With Single Actuator
Failure Inboard

SD73-SA-0061
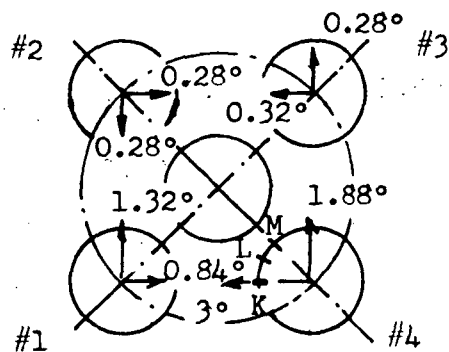
SYM	GAGE
○	K
□	L
◇	M

INTERSTAGE OFF
GIMBAL PATTERN 6A
O/F = 5.5
Pc = 715 PSIA
LOG 27.2.1
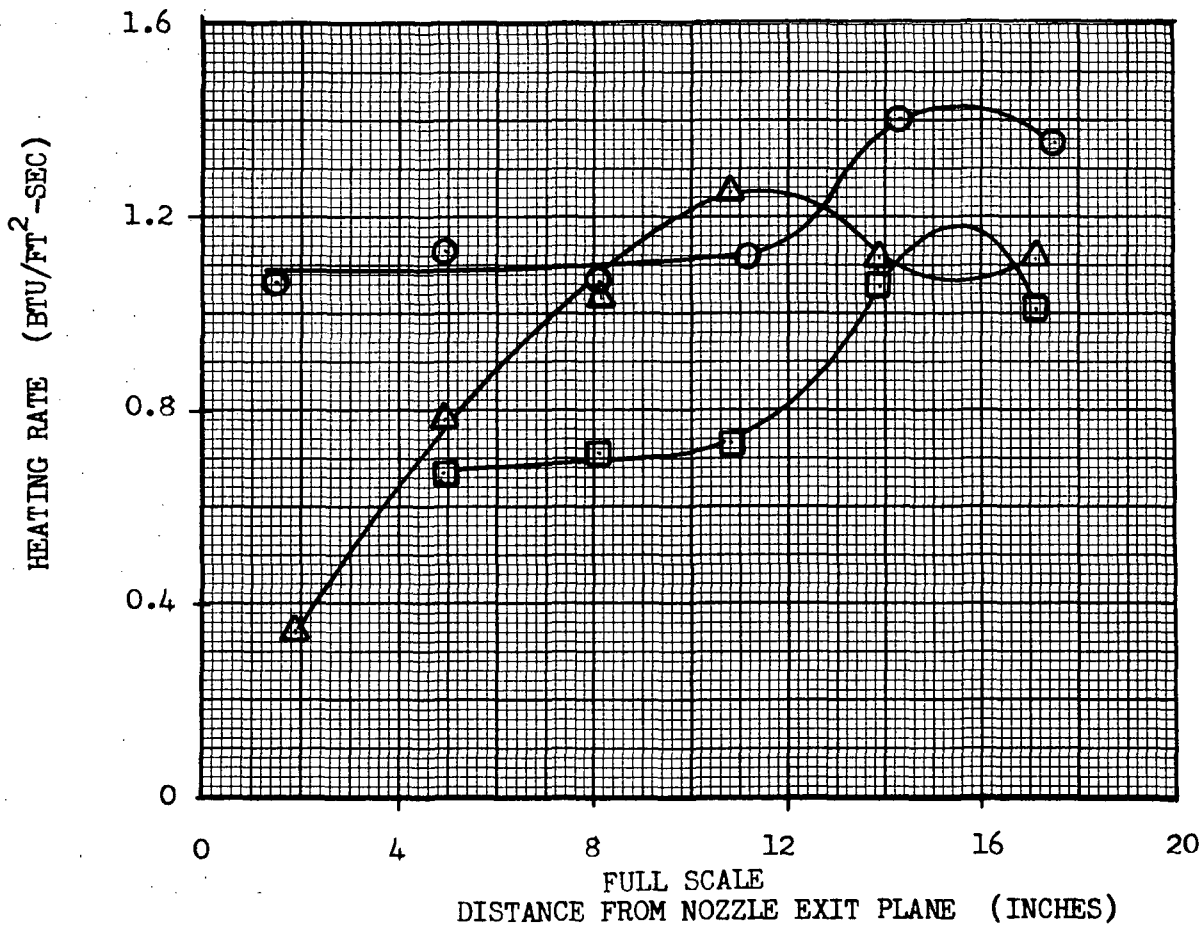
Figure 5.8.4-2   Outboard Engine #4 Heating Rates With Single
Actuator Failure Inboard
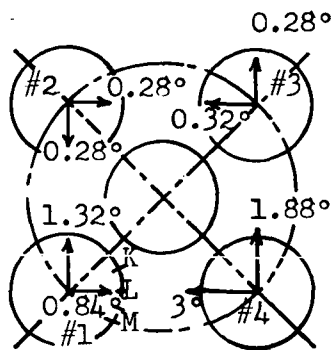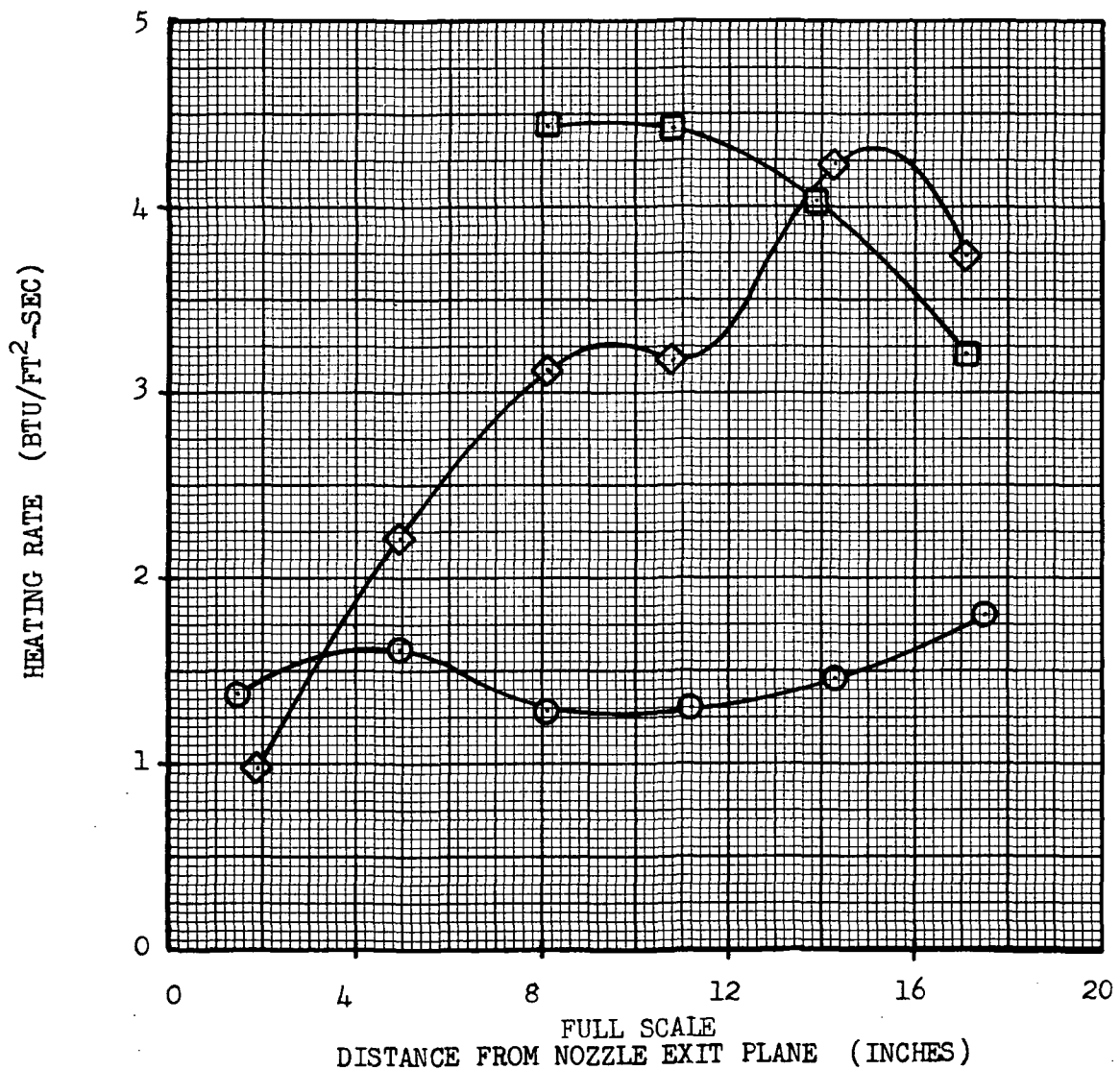
Figure 5.8.4-3 Outboard Engine #1 Heating Rates with Single
Actuator Failure Inboard

Comparison with the nominal nozzle heating rates presented in Figure
5.6.4-1 shows that the center engine heating rates increase by an
order of magnitude from the nominal values. The outboard engine #1 heating
rates are a factor of 3 higher than the nominal values while the outboard
engine #4 heating rates are practically unchanged. The peak test average
heating rate on the center engine nozzle is 35.3 Btu/ft^2-sec. It is
expected that gimbal pattern 3C would produce even higher center engine
heating rates; however nozzle heating rate data were not obtained for this
case.

5.8.5 Heat Shield Pressures

The heat shield pressure distribution corresponding to the single
actuator failure inboard Case 3C engine deflection pattern is shown in
Figure 5.8.5-1. Comparison with the corresponding nominal pressure dis-
tribution of Figure 5.6.5-1 shows that the measured Case 3C peak pressure
is almost 3 times the nominal value. Based on the pressure distribution
of Figure 5.8.5-1, it appears that the pressure near the #1 engine could
exceed the measured peak value of 0.094.

The variation of heat shield pressures with the deflection angle of
the failed actuator is shown in Figure 5.8.5-2.

5.9 BASE REGION ENVIRONMENT WITH A SINGLE ACTUATOR FAILED OUTBOARD

Heat shield, thrust cone, and interstage heating rates were
determined for the single actuator failure gimbal patterns shown in
Figure 5.9-1. No pressure data were obtained during this test series.
Most of the tests were run at O/F = 5.0 and Pc = 632 psia with the inter-
stage off condition.

It was found that the single-actuator-failure-outboard condition
could increase heat shield peak heating rates by as much as 50% above the
nominal values.

The thrust cone heating rates were substantially above the nominal
values with some local heating rates being doubled by the outboard
actuator deflections.

5.9.1 Heat Shield Heating Rates

Heat shield heating rate distributions are presented in Figures
5.9.1-1, 5.9.1-2 and 5.9.1-3 for the single-actuator-failure-outboard
gimbal patterns 5A, 5B and 3B respectively. Note that gimbal pattern 5A
has the failed actuator at 5 degrees outboard on Engine Number 3, whereas
for gimbal patterns 5B and 3B the failed actuator is on Engine Number 1.
Comparison with the nominal heating rate distribution of Figure 5.6.1-2
shows that gimbal patterns 5A and 5B produce heating rates substantially
above the nominal values. Along the heat shield centerline gimbal pattern
5A heating rates are from 1.43 to 1.56 times the corresponding nominal
values. Comparison of the gimbal pattern 5A and 5B heating rate dis-
tributions shows that the peak heat shield heating rates occur in the
quadrant between engines 2 and 3 while the failed actuator is on Engine
Number 1.

HEAT SHIELD INSTRUMENTATION
ROTATED 180°

0.065
0.063

0.07

(0.094)

0.08

0.056

0.066

0.07

0.07

#1

1.5°

1.5°

1.5°

#2

4.5°

7.5°

1.5°

1.5°

#4

1.5°

1.5°

#3

GIMBAL PATTERN 3C
INTERSTAGE OFF
O/F = 5.5
Pc = 715 PSIA
LOG 25.1

PRESSURES IN PSIA
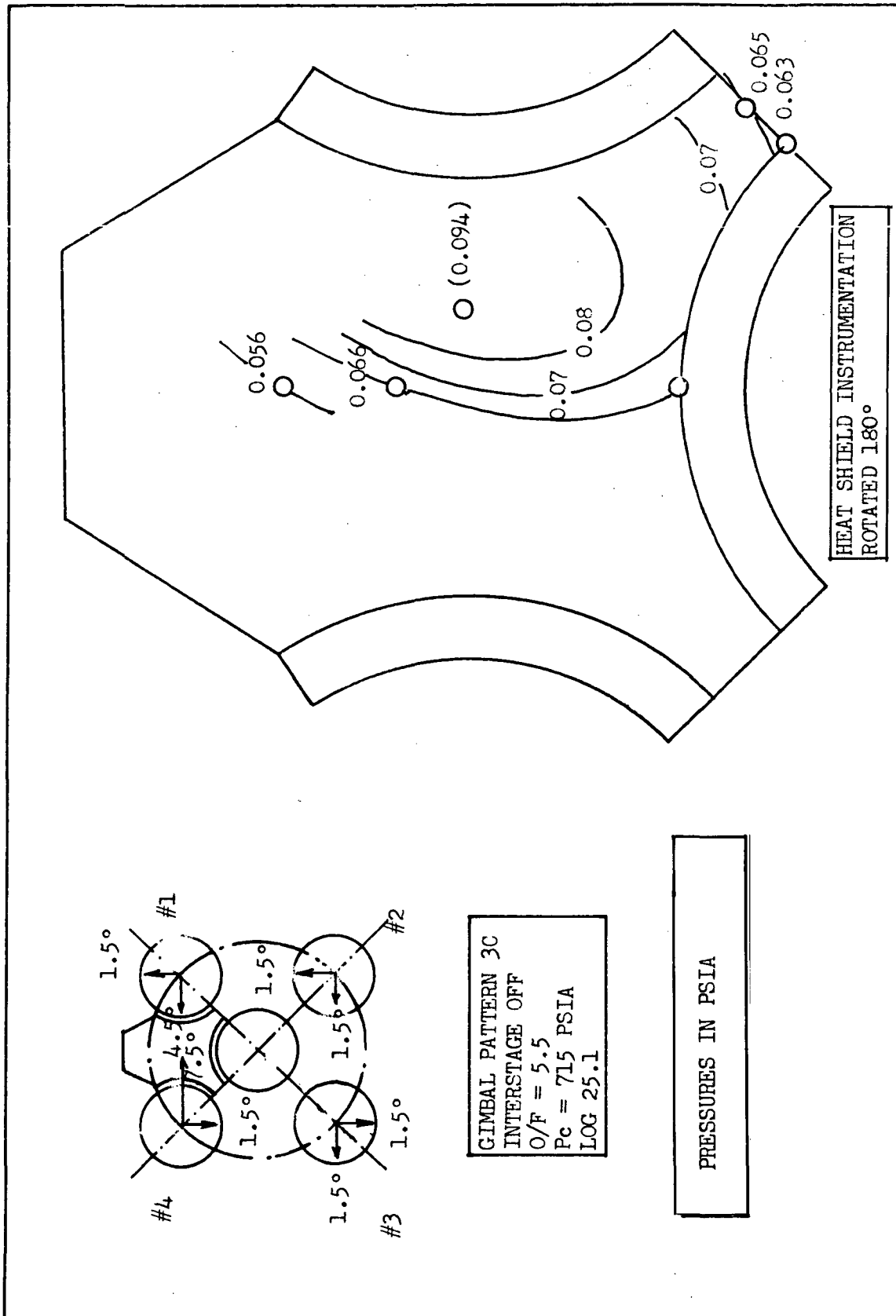
Figure 5.8.5-1 Heat Shield Pressure With Single Actuator Failure Inboard

SD73-SA-0061
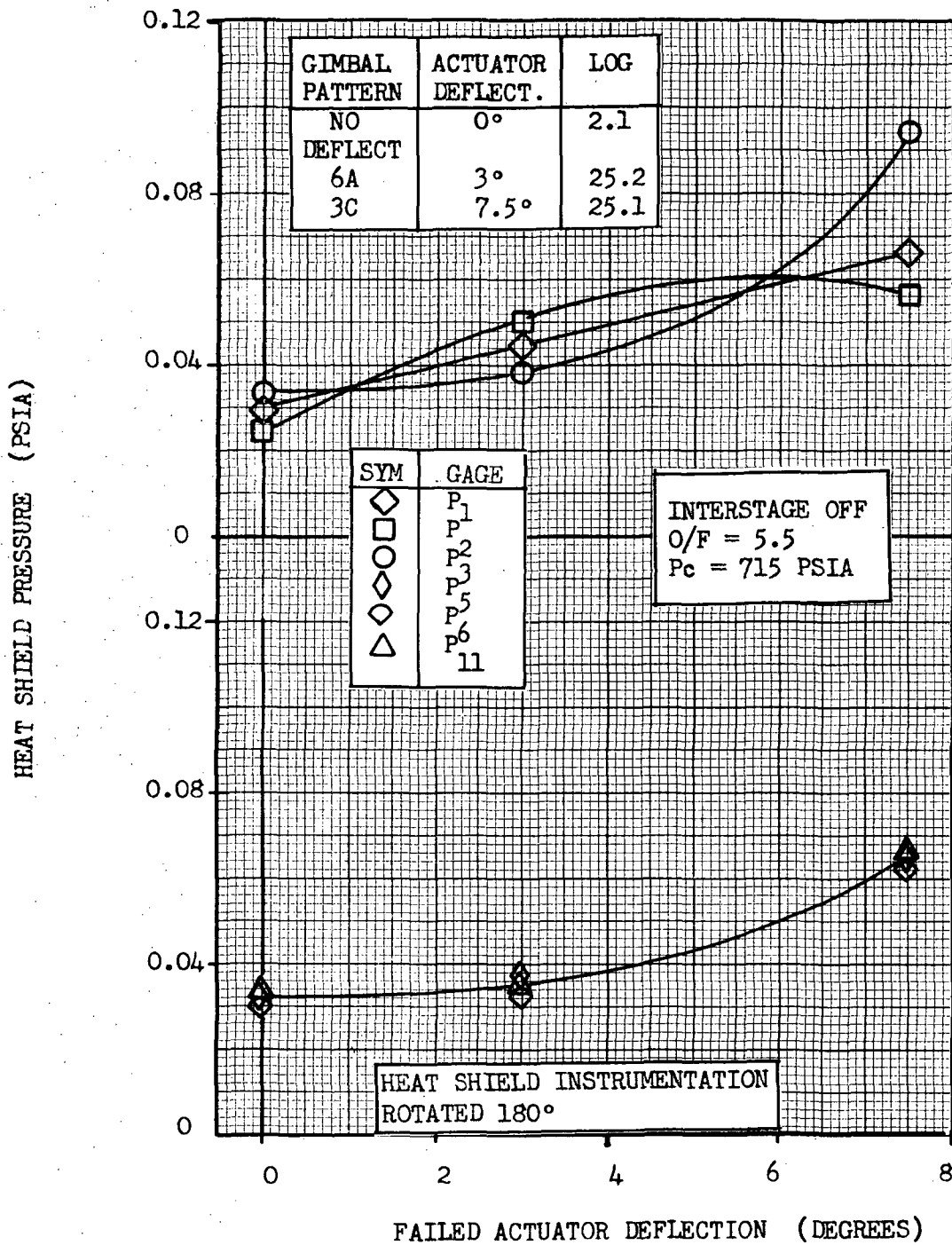
Figure 5.8.5-2   Heat Shield Pressure Variation With Single
Actuator Failure Deflection Angle
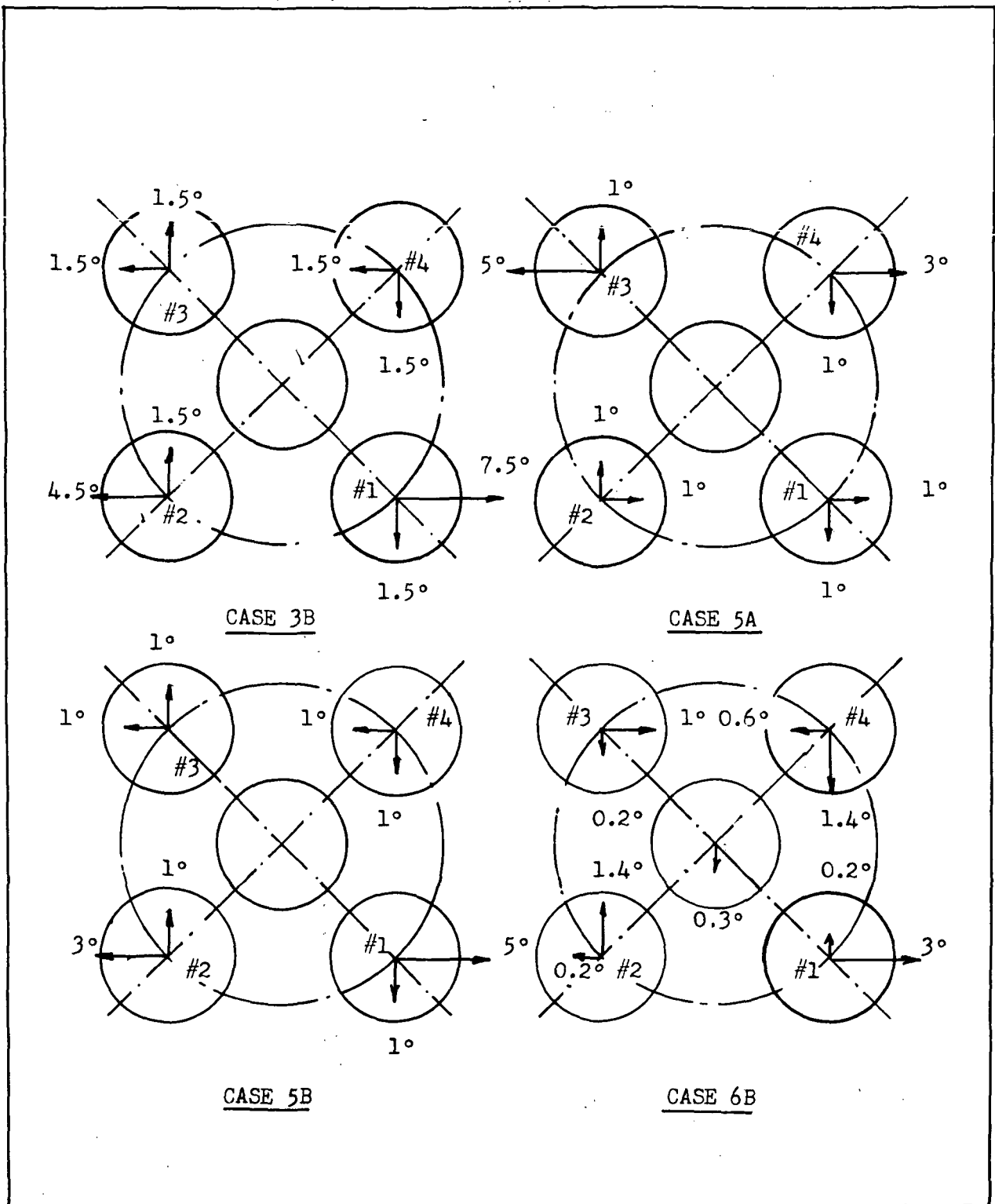
Figure 5.9-1 Single Actuator Failure Outboard Gimbal Patterns

SD73-SA-0061

GIMBAL PATTERN 5A
INTERSTAGE OFF

O/F = 5.0	
Pc = 632 PSIA	
LOG 11.1	

HEATING RATES IN BTU/FT^2-SEC
TO 72°F SURFACE
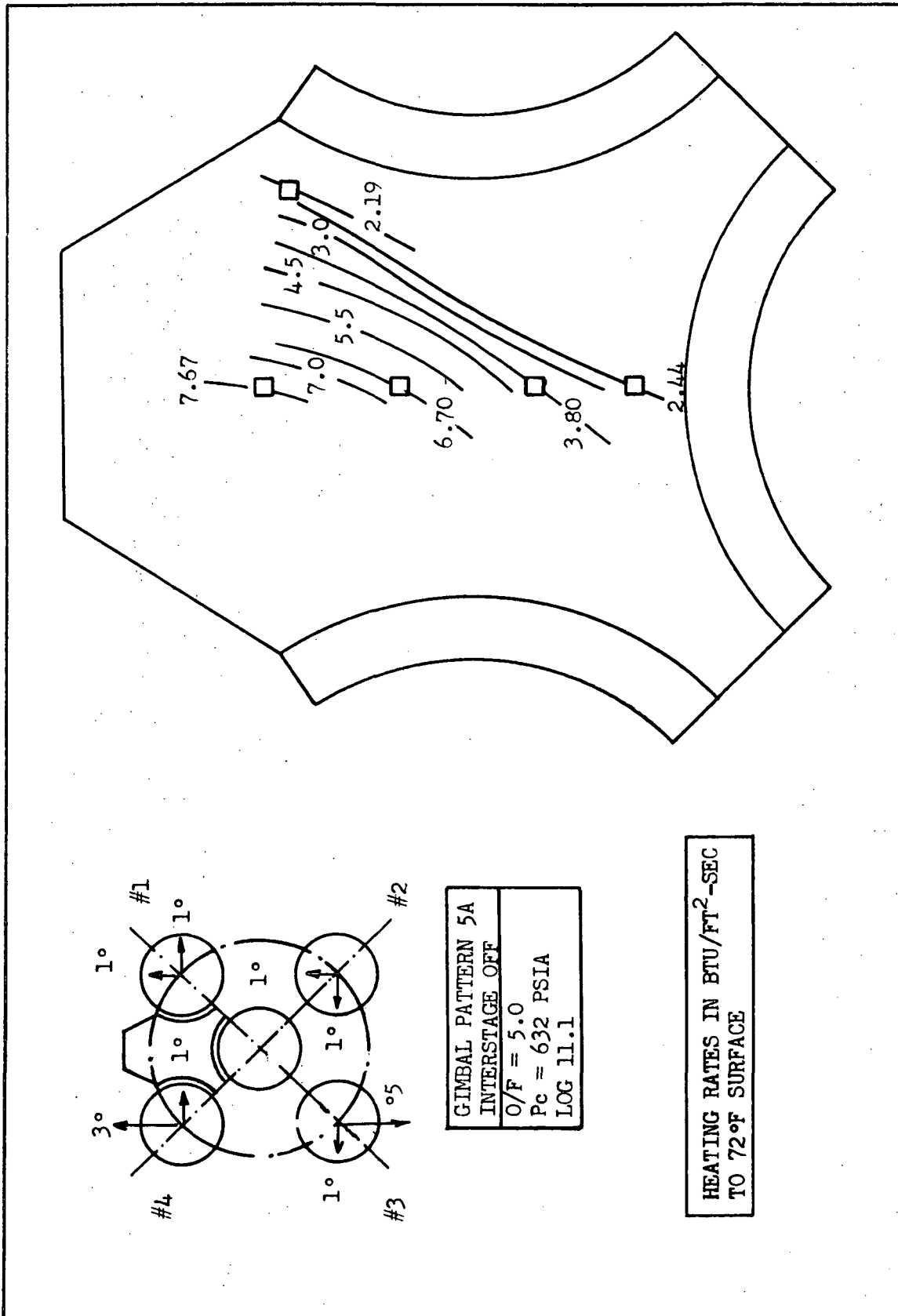
Figure 5.9.1-1 Heat Shield Heating Rates With Single Actuator Failure Outboard, Case 5A, Interstage Off
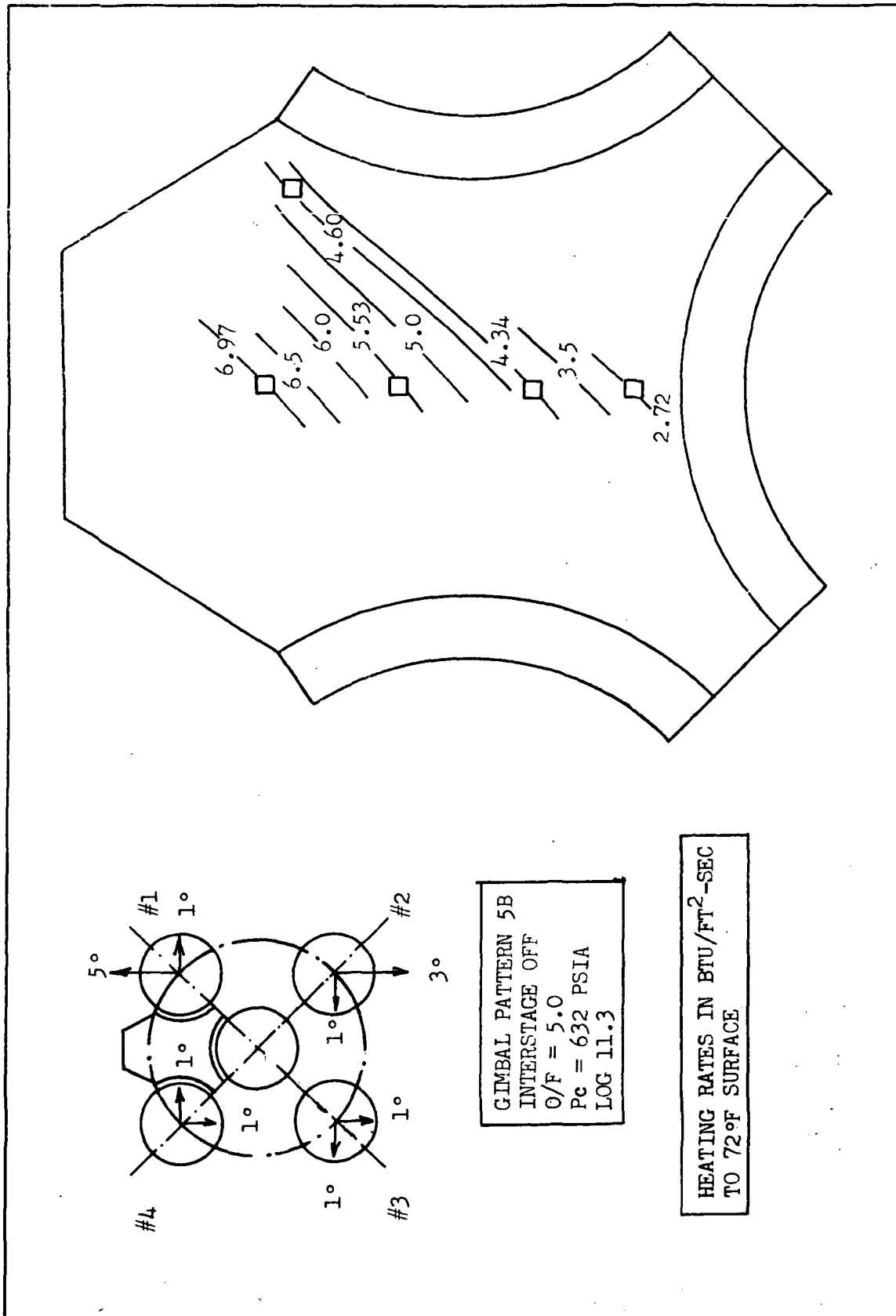
Figure 5.9.1-2 Heat Shield Heating Rates With Single Actuator Failure Outboard, Case 5B, Interstage Off

SD73-SA-0061
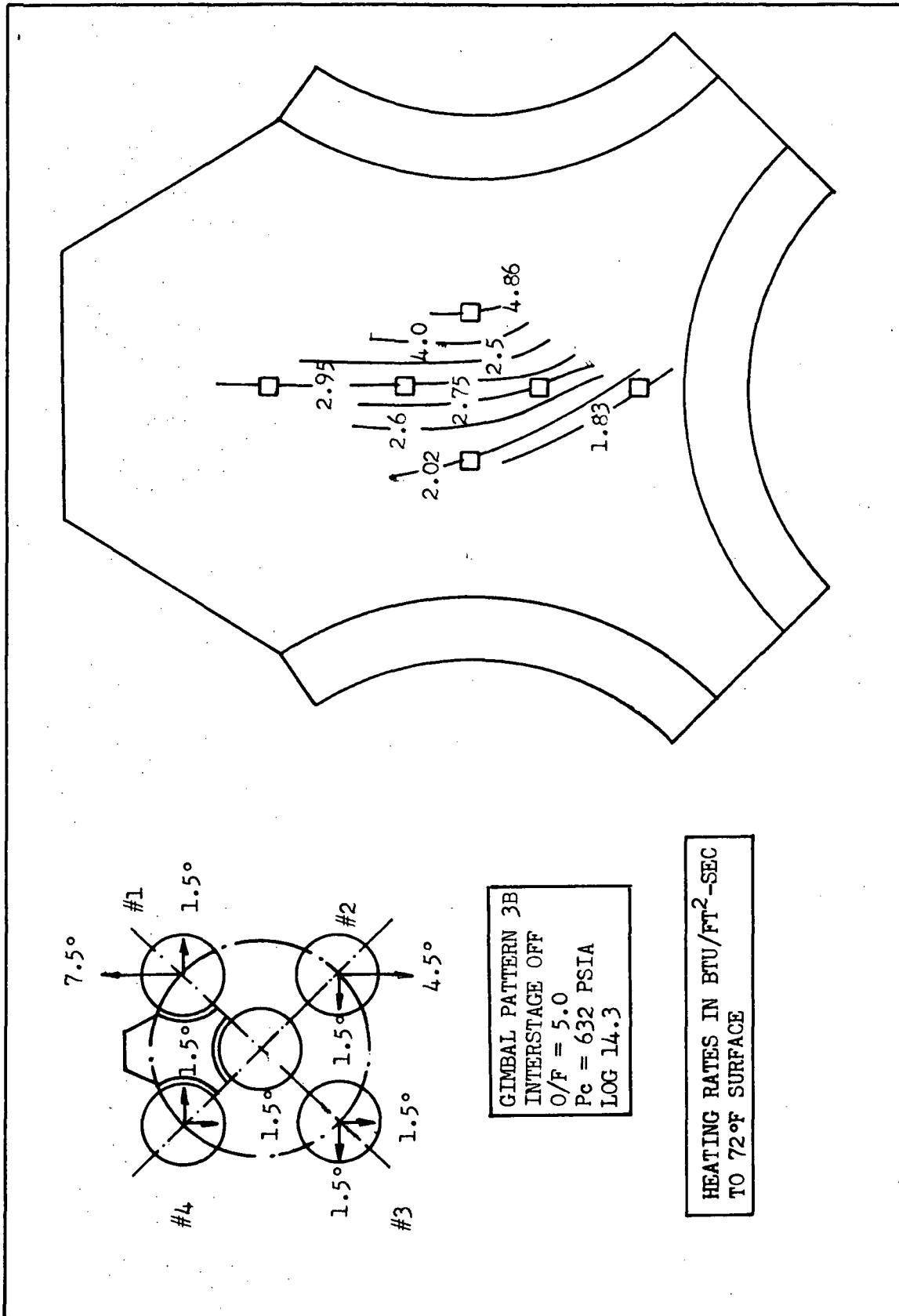
Figure 5.9.1-3 Heat Shield Heating Rates With Single Actuator Failure Outboard, Case 3B, Interstage Off

GIMBAL PATTERN 3B
INTERSTAGE OFF
O/F = 5.0
Pc = 632 PSIA
LOG 14.3

HEATING RATES IN BTU/FT^2-SEC TO 72°F SURFACE

Comparison of the gimbal pattern 3B heating rate distribution presented in Figure 5.9.1-3 with the nominal case of Figure 5.6.1-2 shows that gimbal pattern 3B produces a substantial shift of the heating rate distribution with the peak heating rate remaining approximately the same. However, it was pointed out in connection with gimbal patterns 5A and 5B that the peak heating rates may occur in the heat shield quadrant opposite to the failed actuator engine. Therefore, it is possible that gimbal pattern 3B produces heating rates above nominal values in the heat shield quadrant between engines 2 and 3. Unfortunately, heating rate data was not obtained at this location.

A comparison of the heat shield centerline heating rates for the three gimbal patterns tested is shown in Figure 5.9.1-4. The variation of the centerline heating rates with failed actuator deflection angle is presented in Figure 5.9.1-5. From Figure 5.9.1-5 it appears that a gimbal pattern with 2.5° to 3° outboard deflection would produce the highest heating rates. Consequently, gimbal pattern 6B could produce the highest heat shield heating rates; however, no data was recorded for this case. Note that in this figure, gimbal pattern 5A heating rates were plotted as one degree deflection data.

The effect of the interstage on the heat shield heating rates can be evaluated by comparison of Figure 5.9.1-3 and Figure 5.9.1-6 for the gimbal pattern 3B case. It is seen that the peak heating rate is increased by 5.5%, while other gage locations show a change from -10% to +16% from the corresponding interstage-off values.

5.9.2 Thrust Cone Heating Rates

A comparison of the thrust cone nominal and single-actuator-failure-outboard heating rates is shown in Figures 5.9.2-1 and 5.9.2-2 for $\theta = 0°$ and $\theta = 37°$ locations respectively. It is seen that, except for the engine mounting ring, the thrust cone heating rates are increased by the single-actuator-failure-outboard engine deflections. The highest heating rates occur with gimbal pattern 3B where the heating rates are approximately double the nominal values at and near the thrust cone closeout, and $\theta = 0°$.

Near the outboard engine, Figure 5.9.2-2, gimbal pattern 6B heating rates are very close to the corresponding nominal values while gimbal pattern 5A and 5B heating rates are double the nominal values on the engine mounting ring and directly below the heat shield. In all cases the heating rates near the thrust cone closeout, Station 196, are very close to the nominal values.

The effect of the interstage on the thrust cone heating rates with gimbal pattern 6B engine deflections is shown in Figure 5.9.2-3 and 5.9.2-4. Comparison of Figure 5.9.2-3 with the thrust cone nominal heating rate distribution shows that there is a 15 to 25 percent reduction of the peak heating rates accompanied by an outboard shift of the peak heating rate location.

SYM	GIMBAL PATTERN	LOG
○	5A	11.1
□	5B	11.3
◇	3B	14.3
▲	NO DEFLECT	1.1

INTERSTAGE OFF
O/F = 5.0
Pc = 632 PSIA
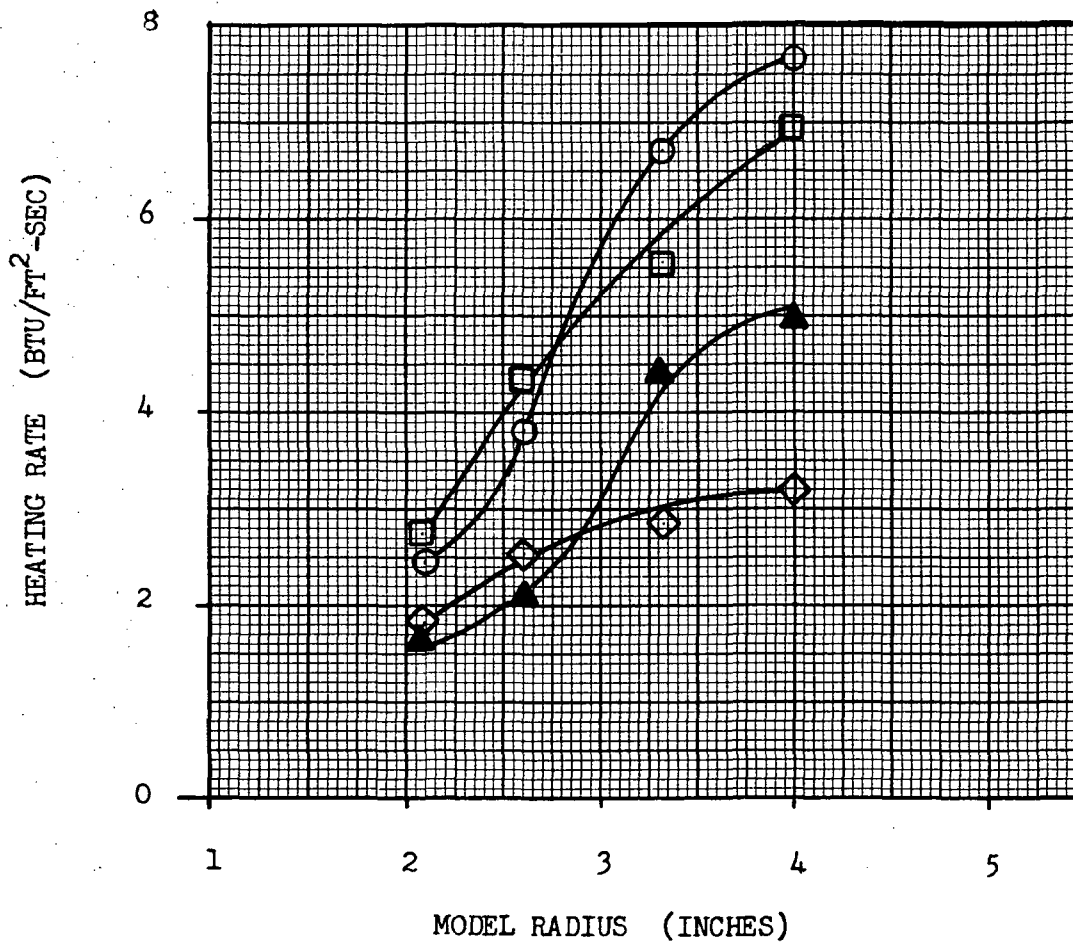
Figure 5.9.1-4   Heat Shield Heating Rates With Single
Actuator Failure Outboard Deflection at θ = 0°

SYM	GAGE
○	Q_1
□	Q_2
◇	Q_3
△	Q_4

GIMBAL PATTERN	DEFLECTION (OUTBOARD)	LOG
5A	1° *	11.1
5B	5°	11.3
3B	7.5°	14.3
NO DEFLECT	0°	1.1

* SEE GIMBAL
  PATTERN 5A

INTERSTAGE OFF
O/F = 5.0, Pc=632 PSIA
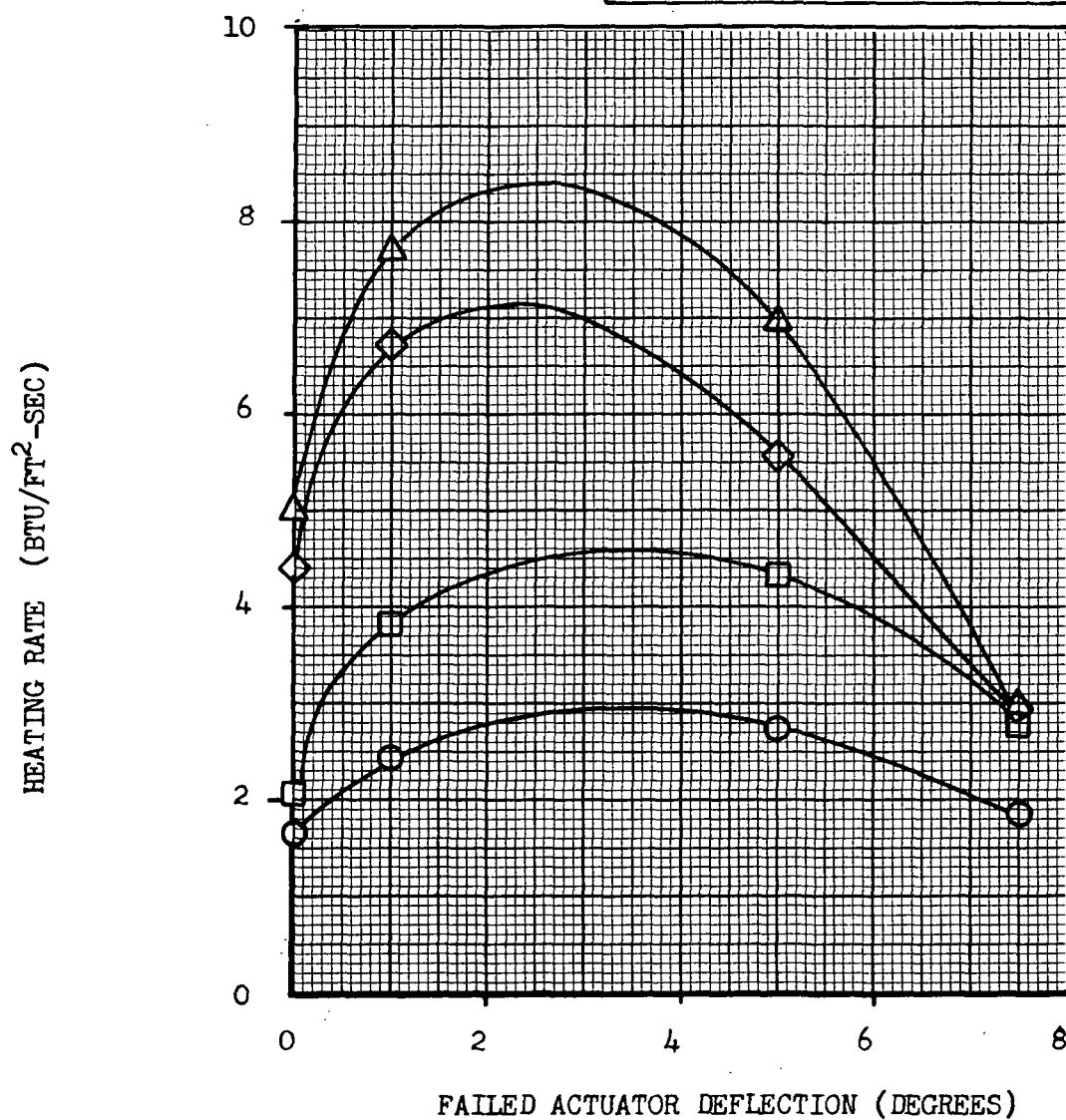
Figure 5.9.1-5   Variation Of Heat Shield Heating Rates With
                 Outboard Deflection Of Failed Actuator At θ = 0°
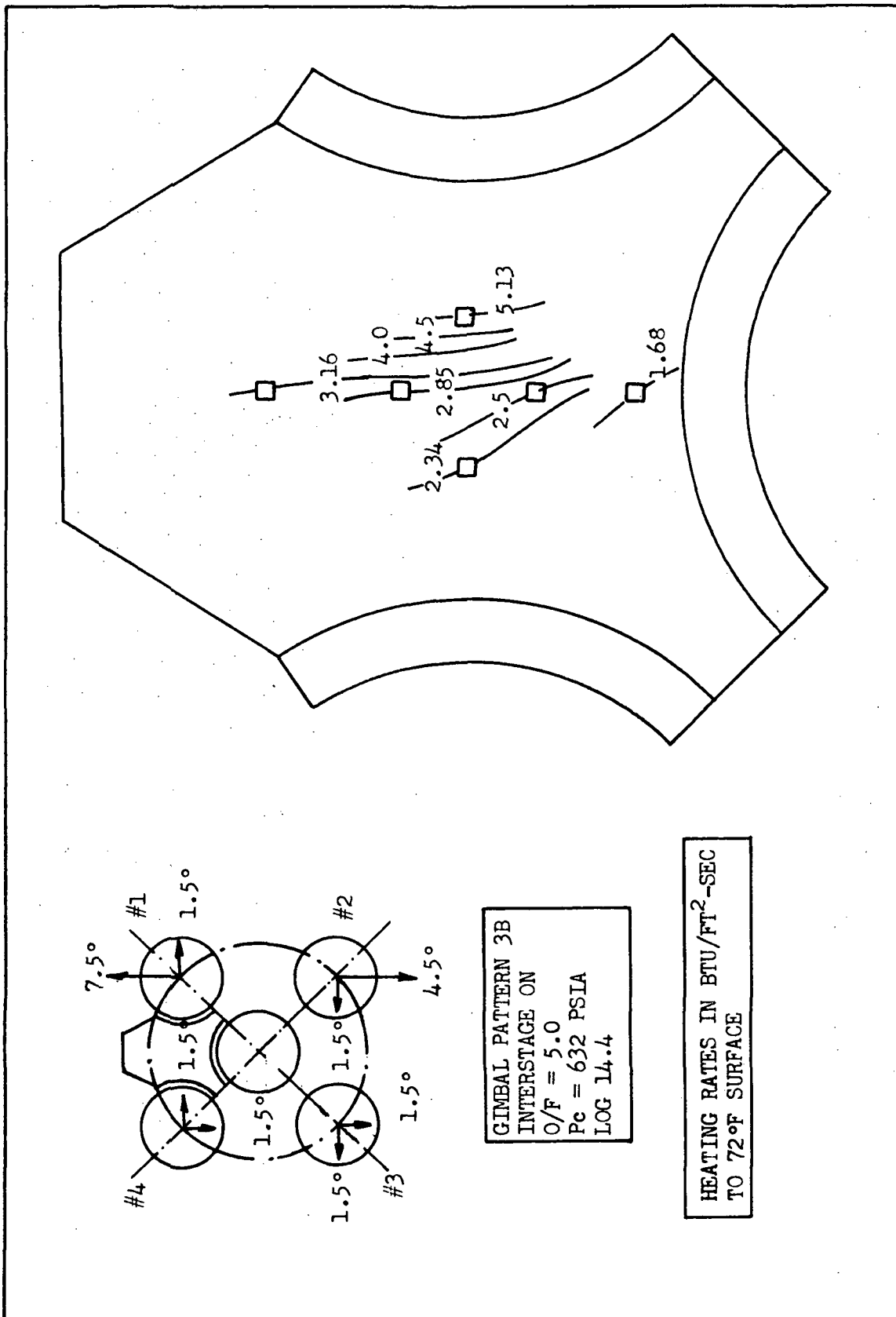
Figure 5.9.1-6 Heat Shield Heating Rates With Single Actuator Failure Outboard, Case 3B, Interstage On

GIMBAL PATTERN 3B
INTERSTAGE ON
O/F = 5.0
Pc = 632 PSIA
LOG 14.4

HEATING RATES IN BTU/FT^2-SEC
TO 72°F SURFACE

SD73-SA-0061
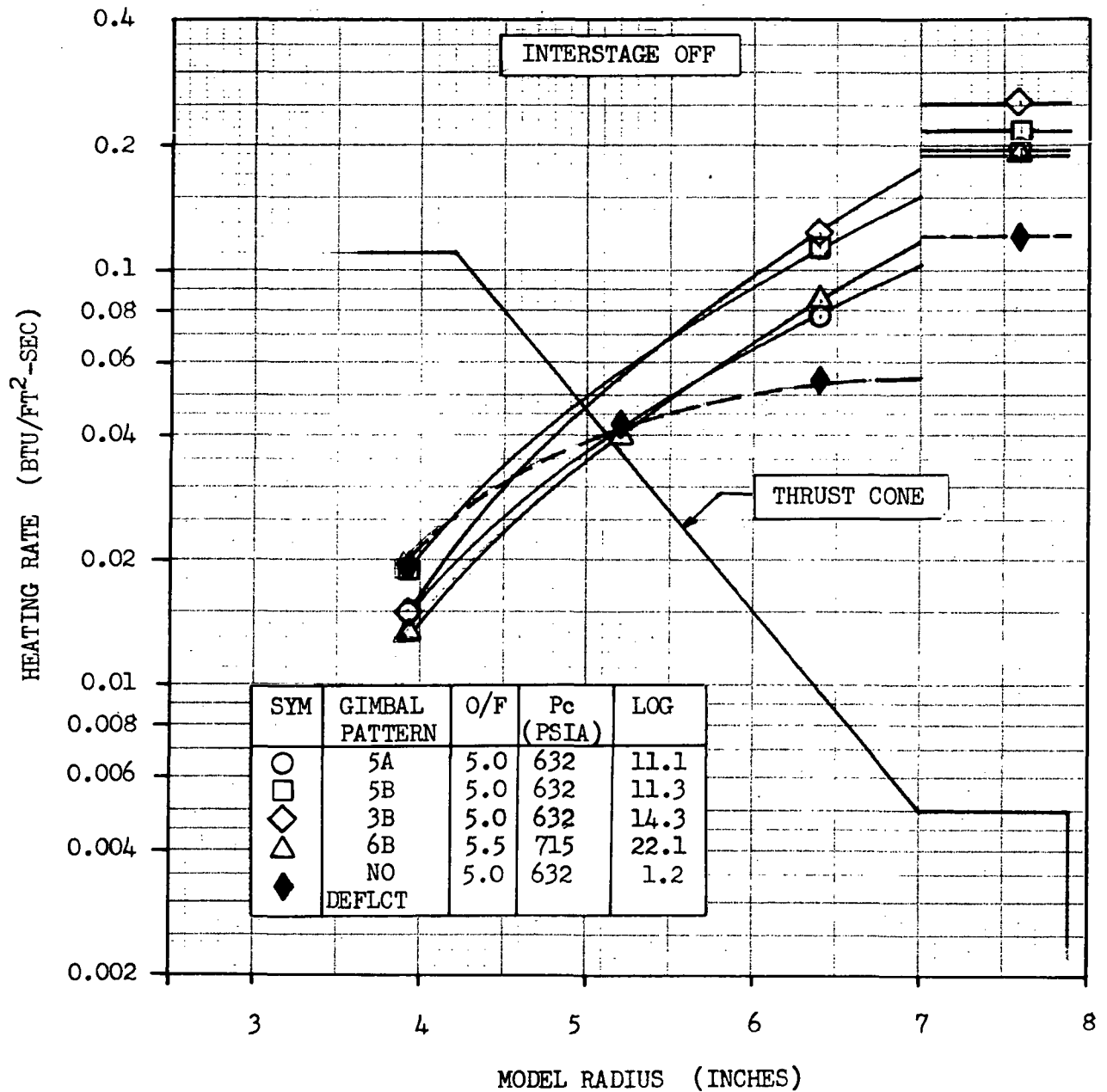
Figure 5.9.2-1   Thrust Cone Heating Rates at θ = 0° With
Single Actuator Failure Outboard

SD73-SA-0061
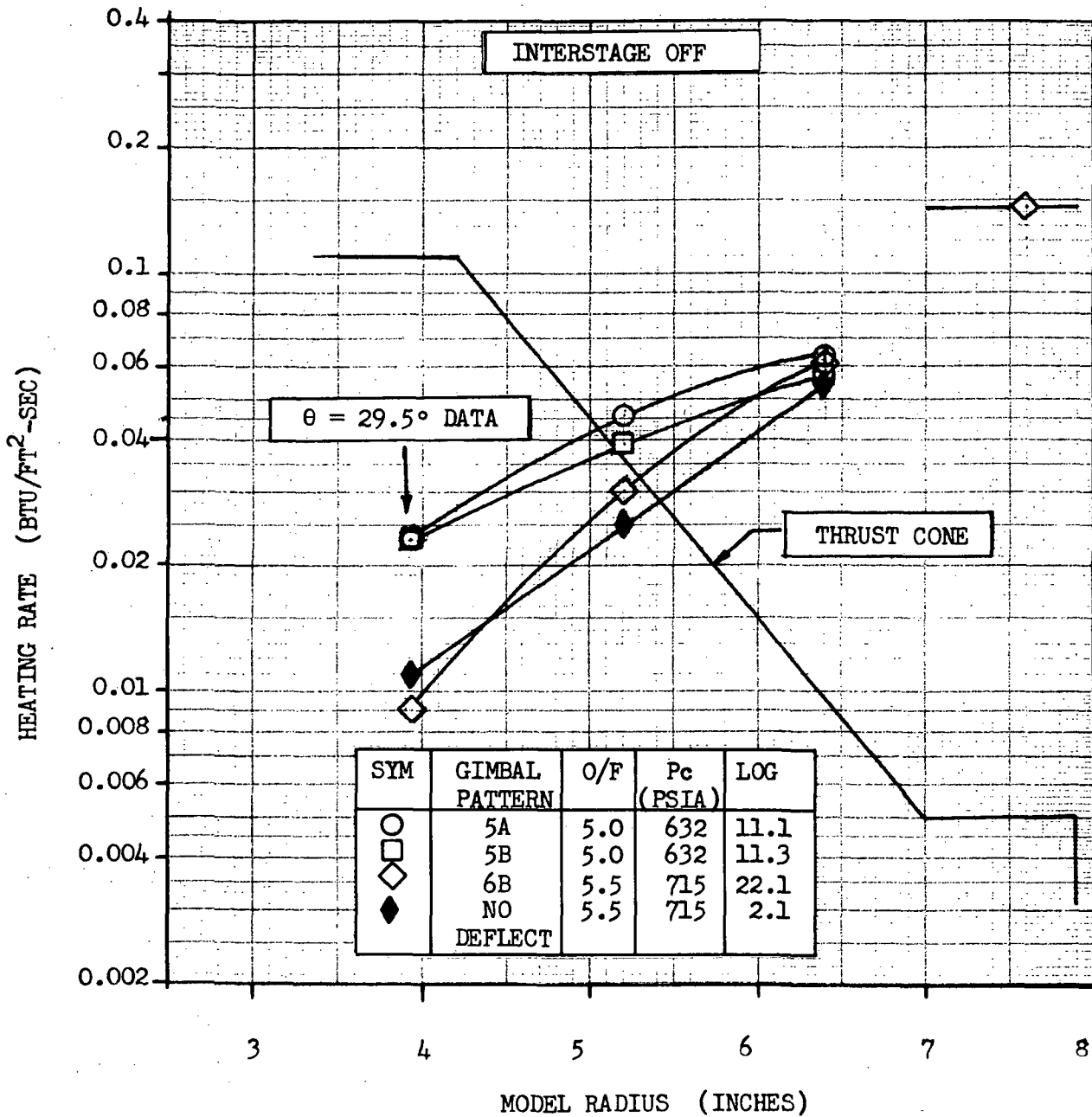
Figure 5.9.2-2 Thrust Cone Heating Rates at θ = 37° With
Single Actuator Failure Outboard

SD73-SA-0061
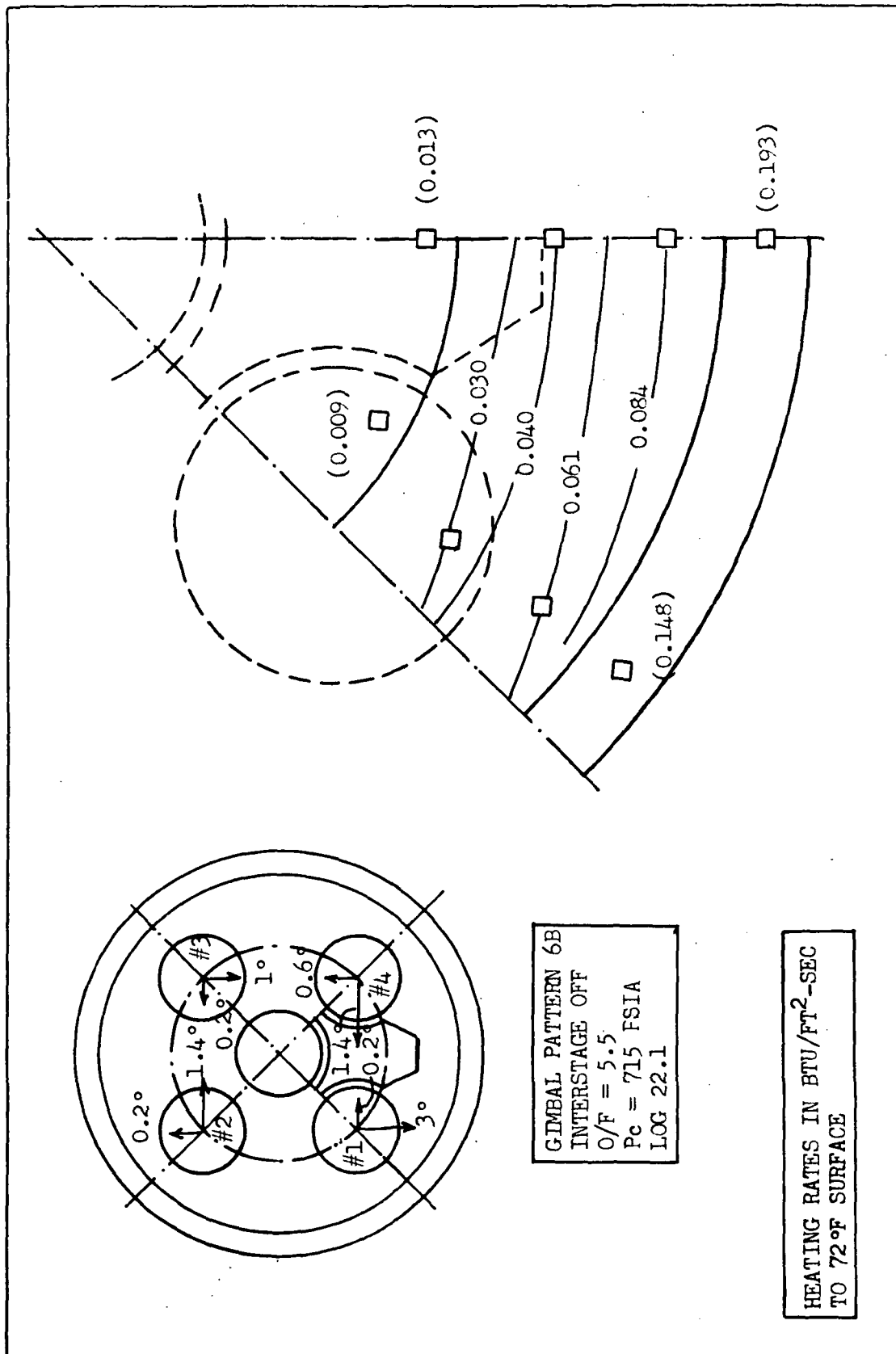
Figure 5.9.2-3 Thrust Cone Heating Rates With Single Actuator Failure Outboard
Case 6B, Interstage Off, O/F = 5.5

GIMBAL PATTERN 6B
INTERSTAGE ON
O/F = 5.5
Pc = 715 PSIA
LOG 22.2

HEATING RATES IN BTU/FT²-SEC
TO 72°F SURFACE
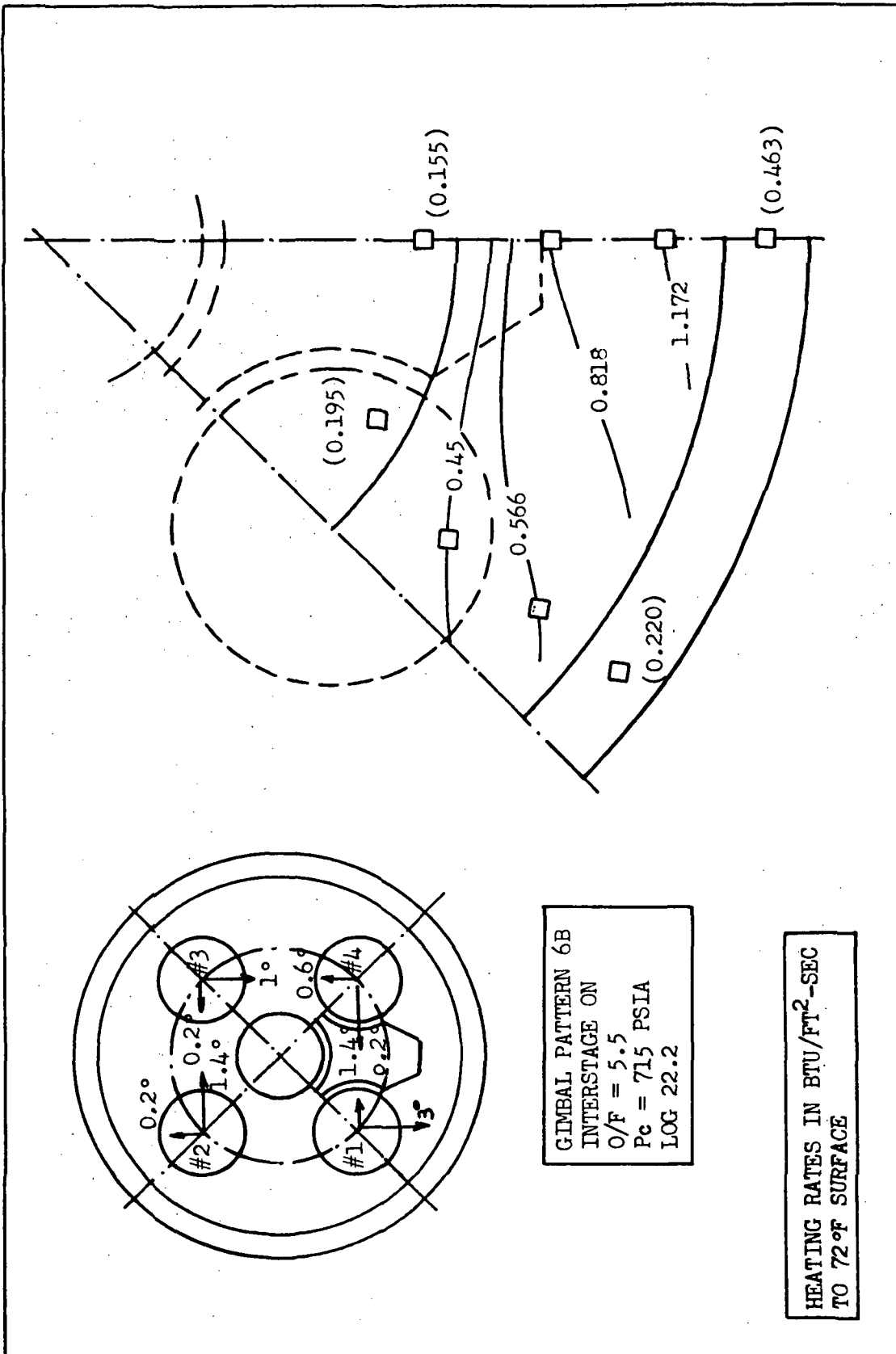
Figure 5.9.2-4   Thrust Cone Heating Rates With Single Actuator Failure Outboard
Case 6B, Interstage On, O/F = 5.5

SD73-SA-0061

The highest thrust cone heating rates were measured with gimbal pattern 3B and interstage-on, Figure 5.9.2-5. The peak heating rate of 1.94 Btu/ft^2-sec is 25 percent higher than the corresponding nominal value. The thrust cone region heating rates between the heat shield and the thrust cone region were measured with the ring gages shown in Figure 3.4-4 with the single actuator failure outboard Case 3B deflection pattern. The results are shown in Figure 5.9.2-6. Comparison with the corresponding no-deflection heating rates presented in Figure 5.6.2-3 shows that the 3B case peak heating rates are more than double the nominal values.

Heating rates in the vicinity of Engine Number 4 with the single actuator failure gimbal pattern 6B deflections are shown in Figure 5.9.2-7 for one row of gages, with and without the interstage.

5.9.3 Interstage Heating Rates

Interstage heating rates were measured for the single-actuator-failure-outboard gimbal patterns 3B and 6B, Figures 5.9.3-1 and 5.9.3-2 respectively. Only one row of gages was used in each case. It was found that, at the locations measured, the interstage heating rates were lower than the nominal values for both gimbal patterns.

SD73-SA-0061
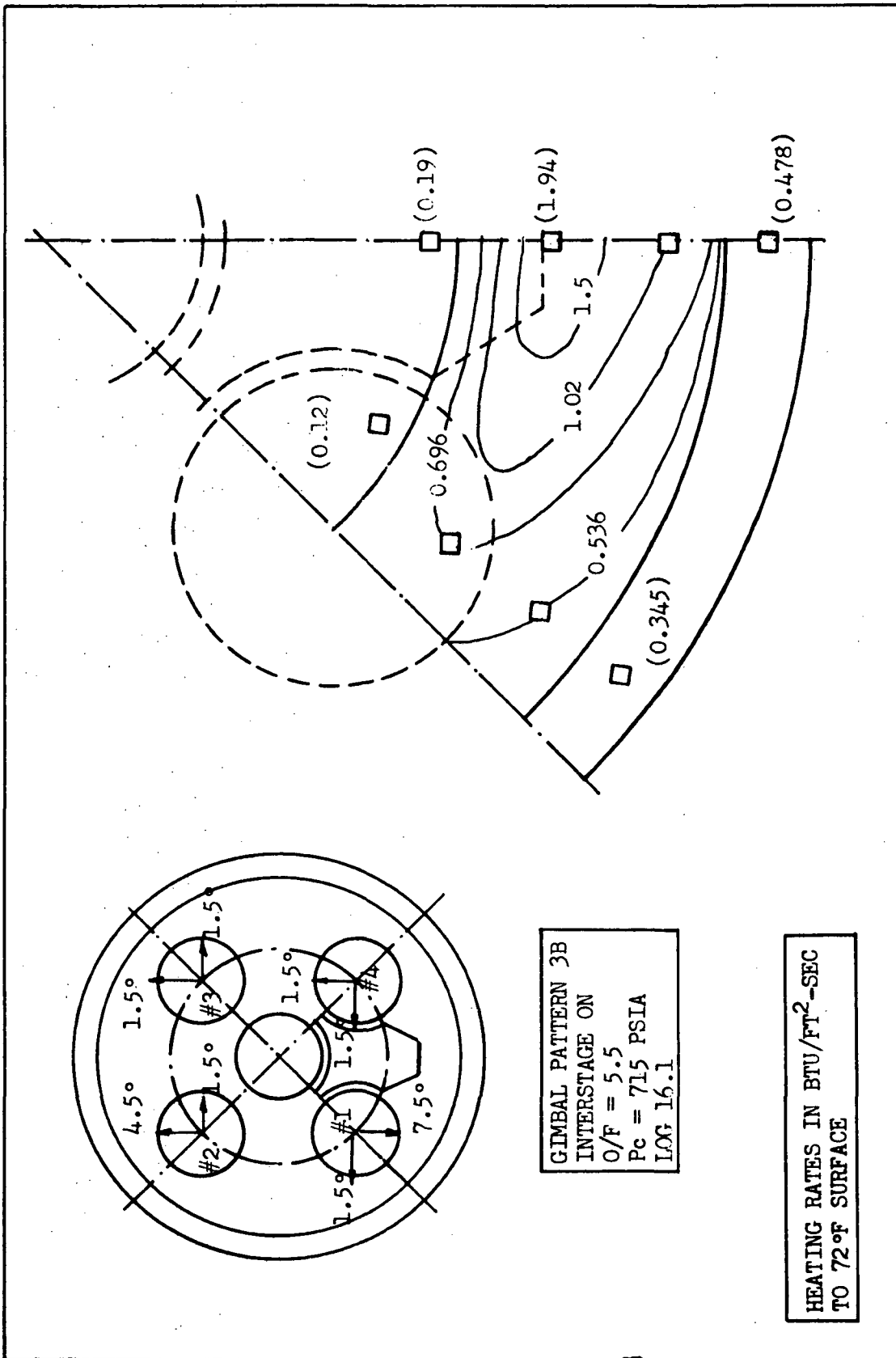
Figure 5.9.2-5   Thrust Cone Heating Rates With Single Actuator Failure Outboard
Case 3B, Interstage On, O/F = 5.5

GIMBAL PATTERN 3B
INTERSTAGE ON
O/F = 5.5
Pc = 715 PSIA
LOG 16.1

HEATING RATES IN BTU/FT²-SEC
TO 72°F SURFACE

GIMBAL PATTERN 3B
INTERSTAGE OFF
O/F = 5.0
Pc = 632 PSIA
LOG 14.3

SYM	GAGE
○	Q_{70}
□	Q_{80}
◇	Q_{90}
△	Q_{100}
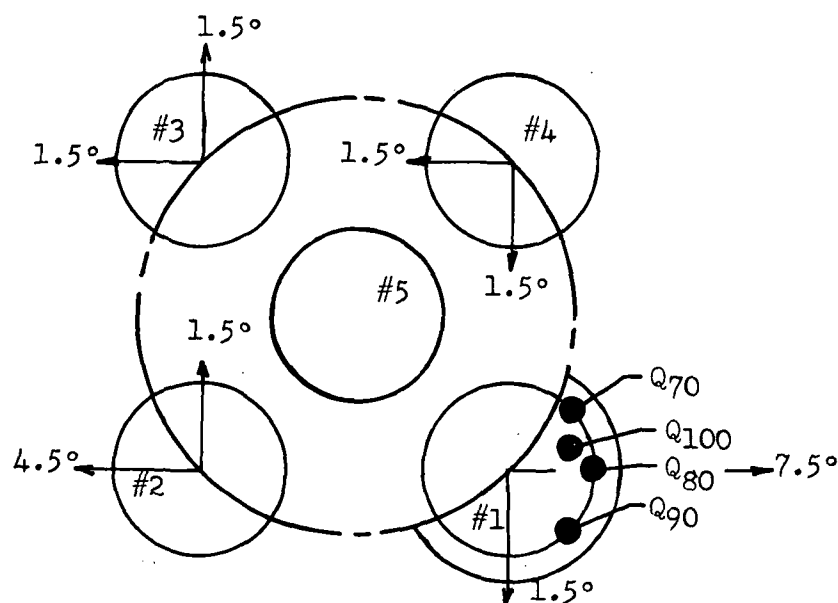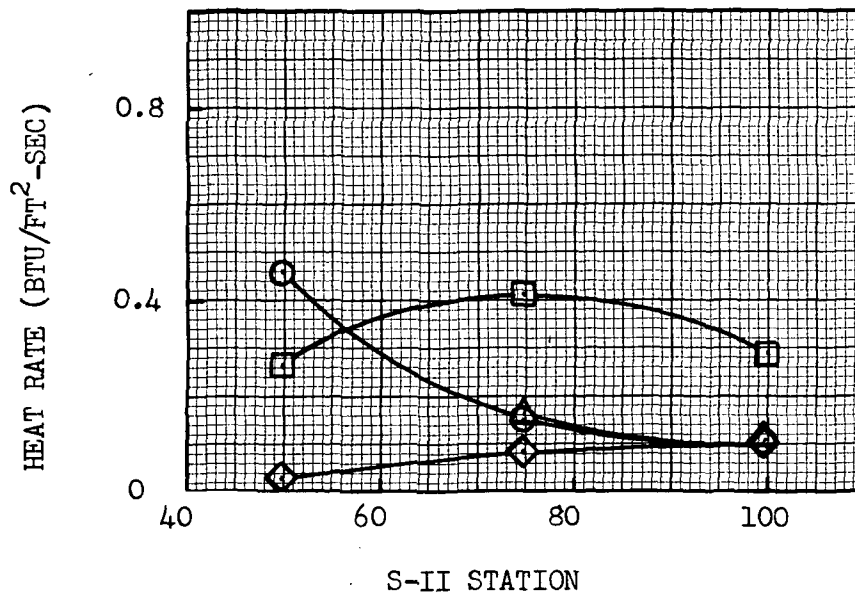
Figure 5.9.2-6 Thrust Cone Region Heating at Engine #1
with Gimbal Pattern 3B

SD73-SA-0061

GAGE Q110
GIMBAL PATTERN 6B
GAGE ON #4 SIDE OF ENGINE #1
O/F = 5.5
Pc = 715 PSIA
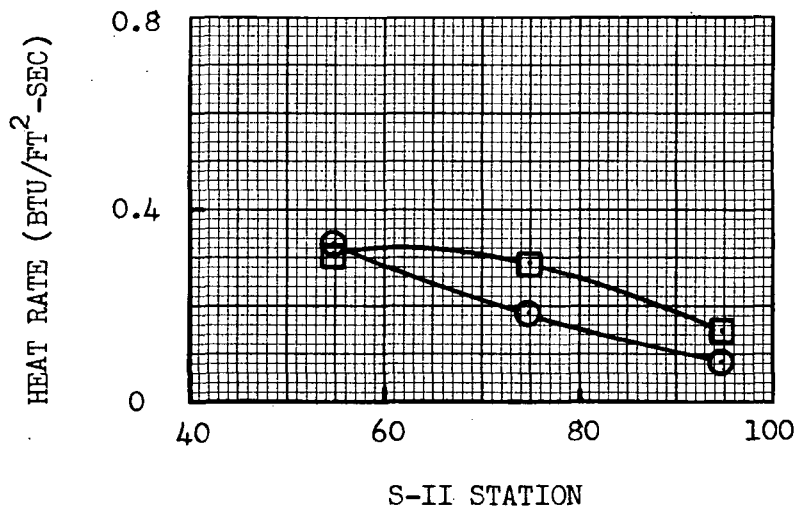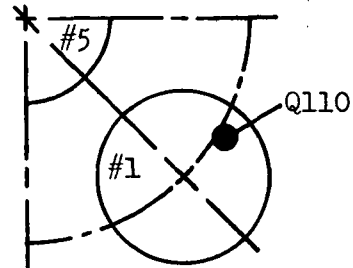
SYM	INTERST	LOG
○	OFF	22.1
□	ON	22.2

Figure 5.9.2-7 Thrust Cone Region Heating at Engine #4
with Gimbal Pattern 6B

SYM	GIMBAL PATTERN	LOG
○	3B	16.1
□	NO DEFLECT	15.3.1

O/F = 5.5
Pc = 715 PSIA
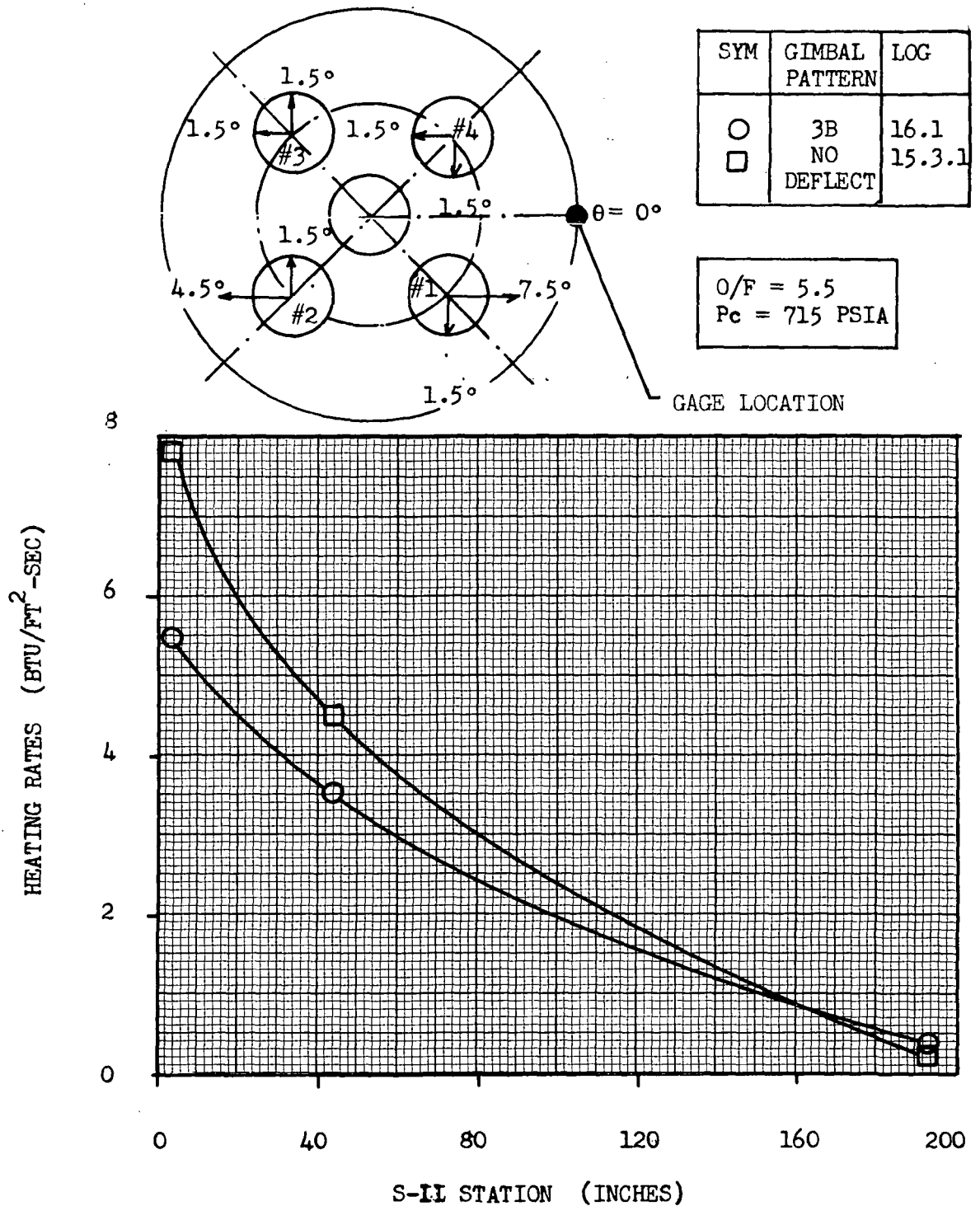
Figure 5.9.3-1 Interstage Heating Rates With Single Actuator
Failure Outboard Case 3B

SYM	GIMBAL PATTERN	LOG
O	6B	22.2
–·–	NO	15.3.1
	DEFLECT	15.3.2

θ = 0°

θ = 29.2°

O/F = 5.5
Pc = 715 PSIA

GAGE LOCATION
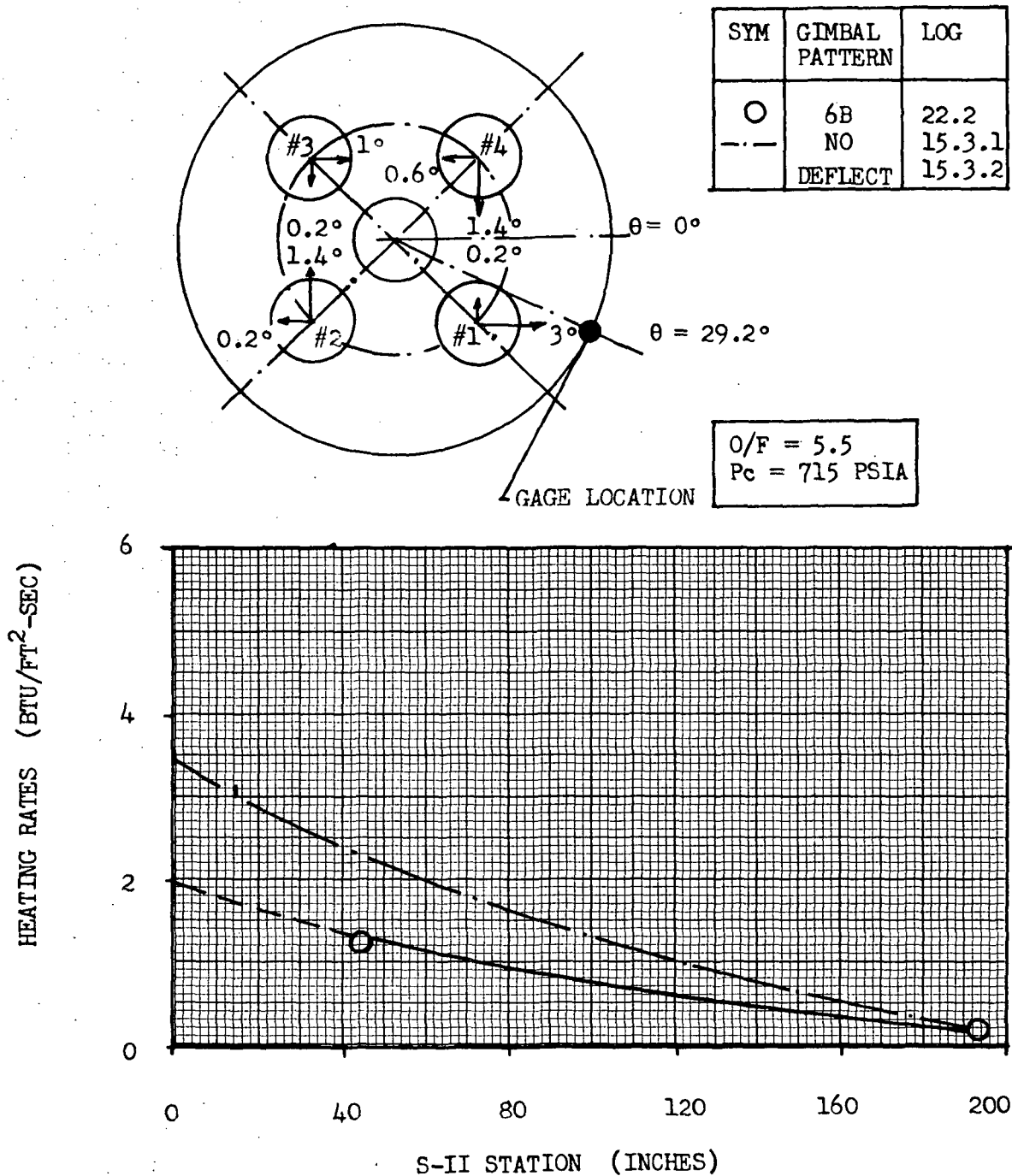
Figure 5.9.3-2   Interstage Heating Rates With Single Actuator
Failure Inboard Case 6B

- 142 -

5.10 BASE REGION ENVIRONMENT WITH DUAL ACTUATOR FAILURE INBOARD

Heat shield, thrust cone and engine nozzle heating rates were measured with dual-actuator-failure-inboard gimbal patterns shown in Figure 5.10-1. The test runs were carried out at O/F = 5.0 and 5.5 with the interstage-off condition. It was found that the dual-actuator-failure condition produces a very severe base region thermal environment. For example, gimbal pattern 7 produced the highest heating rates to the heat shield of all the failure conditions investigated in this test program; the test average value being 21.0 Btu/ft^2-sec at gage Q15 location. Also, gimbal pattern 4A-a produced heating rates to the Number 1 Engine flexible curtain attachment flange almost equal to the peak value of 29.8 Btu/ft^2-sec measured with the single-actuator-failure-inboard gimbal pattern 3C. As expected, the dual actuator failure inboard condition produces very high heating rates to the center engine nozzle; the peak test average heating rate measured to the center engine nozzle was 359 Btu/ft^2-sec with gimbal pattern 4A-a.

No interstage heating rates were obtained for the dual-actuator-failure-inboard condition and very limited pressure data was obtained for the thrust cone region only.

5.10.1 Heat Shield Heating Rates

Heat shield heating rates were measured for the dual actuator failure gimbal patterns shown in Figure 5.10-1. Typical heat shield heating rate distributions are presented in Figure 5.10.1-1, 5.10.1-2 and 5.10.1-3 for gimbal pattern cases 7, 11 and 4A-a respectively. Comparison of these distributions with the heat shield nominal heating rate distribution of Figure 5.6.1-3 shows that with the 5° actuator failure condition the peak heat shield heating rate increases by a factor of 3 and shifts from the heat shield centerline toward Engine Number 1.

The effect of failed actuator deflection angle on the various heat shield and flexible curtain attachment flange heating rates is shown in Figure 5.10.1-4. It is seen that the peak heat shield heating rate occurs at the heat transfer gage Q15 location with 5° engine deflections while the flexible curtain attachment flange peak heating rate occurs at gage Q10 location with 7.5° engine deflections.

Gimbal patterns 4A-a and 4A-b are mirror images of each other; consequently, combining the results of each provides the heating rate distribution for all of the heat shield quadrant. The results are shown in Figure 5.10.1-5. The heating rates on the centerline of the heat shield are the average values of deflection Case 4A-a and 4A-b data. Q8 and Q52 gage data were also averaged to account for the mirror image gimbal patterns. Comparison of the O/F = 5.0 heating rates, presented in Figure 5.10.1-5, with the corresponding heating rate distribution for O/F = 5.5, presented in Figure 5.10.1-3, shows that although the distributions are very similar, the O/F = 5.5 heating rates are 50% higher than the corresponding O/F = 5.0 values. This is considerably higher than the 13% increase expected due to mixture ratio and chamber pressure increase.
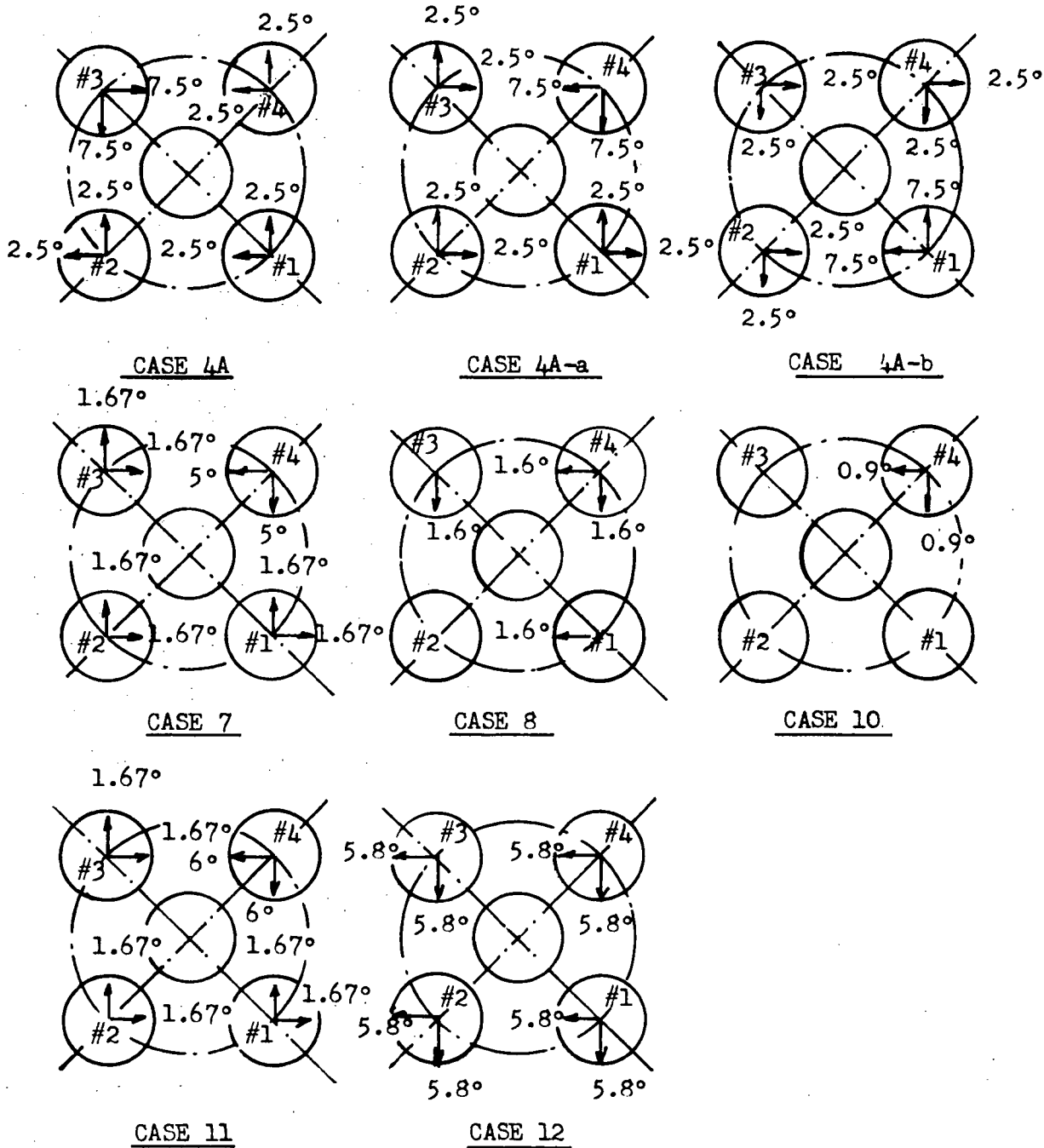
Figure 5.10-1 Dual Actuator Failure Inboard Gimbal Patterns
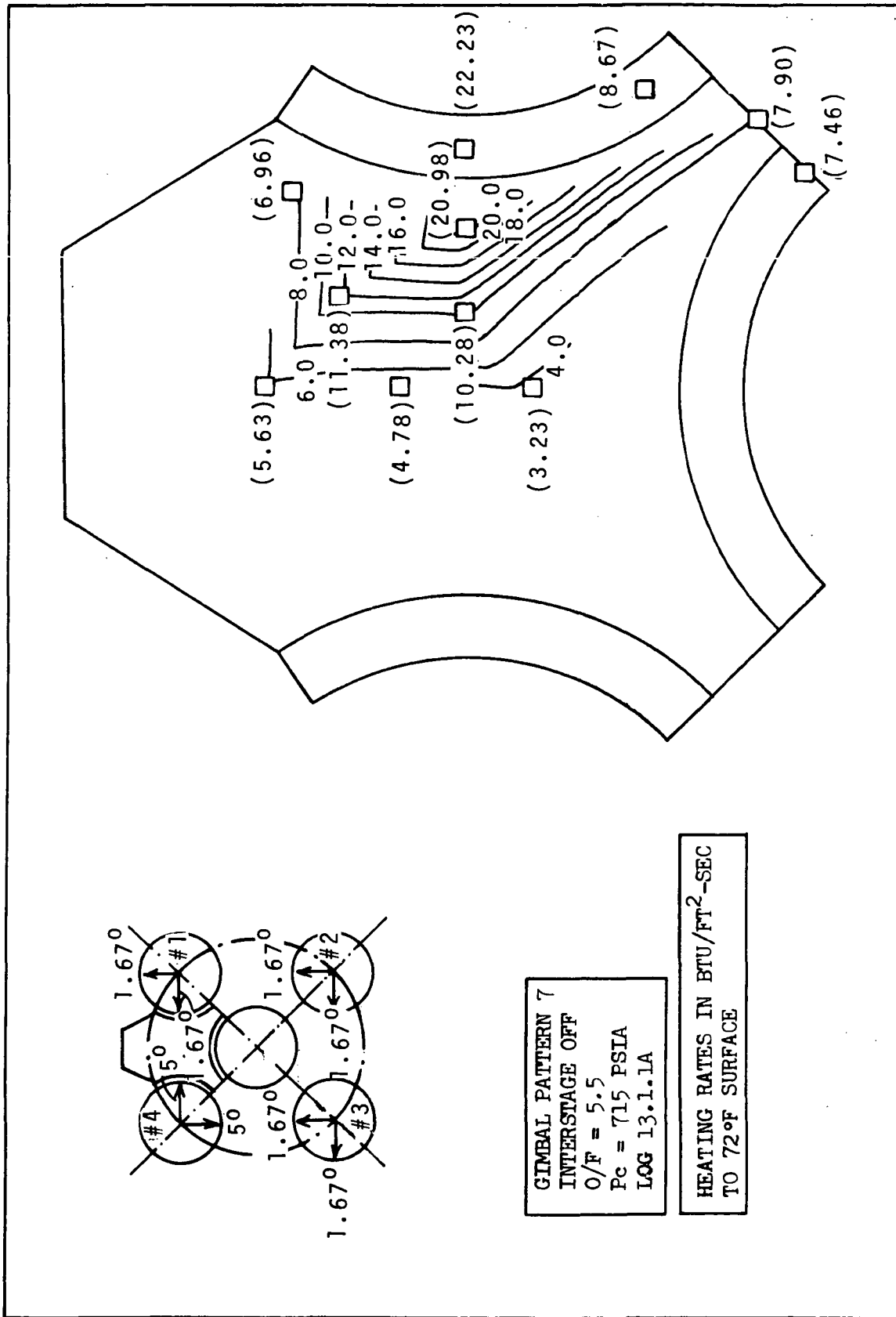
Figure 5.10.1-1 Heat Shield Heating Rates with Dual Actuator Failure Inboard, Gimbal Pattern 7, Interstage Off, O/F = 5.5

GIMBAL PATTERN 7
INTERSTAGE OFF
O/F = 5.5
Pc = 715 PSIA
LOG 13.1.1A

HEATING RATES IN BTU/FT²-SEC
TO 72°F SURFACE

SD73-SA-0061
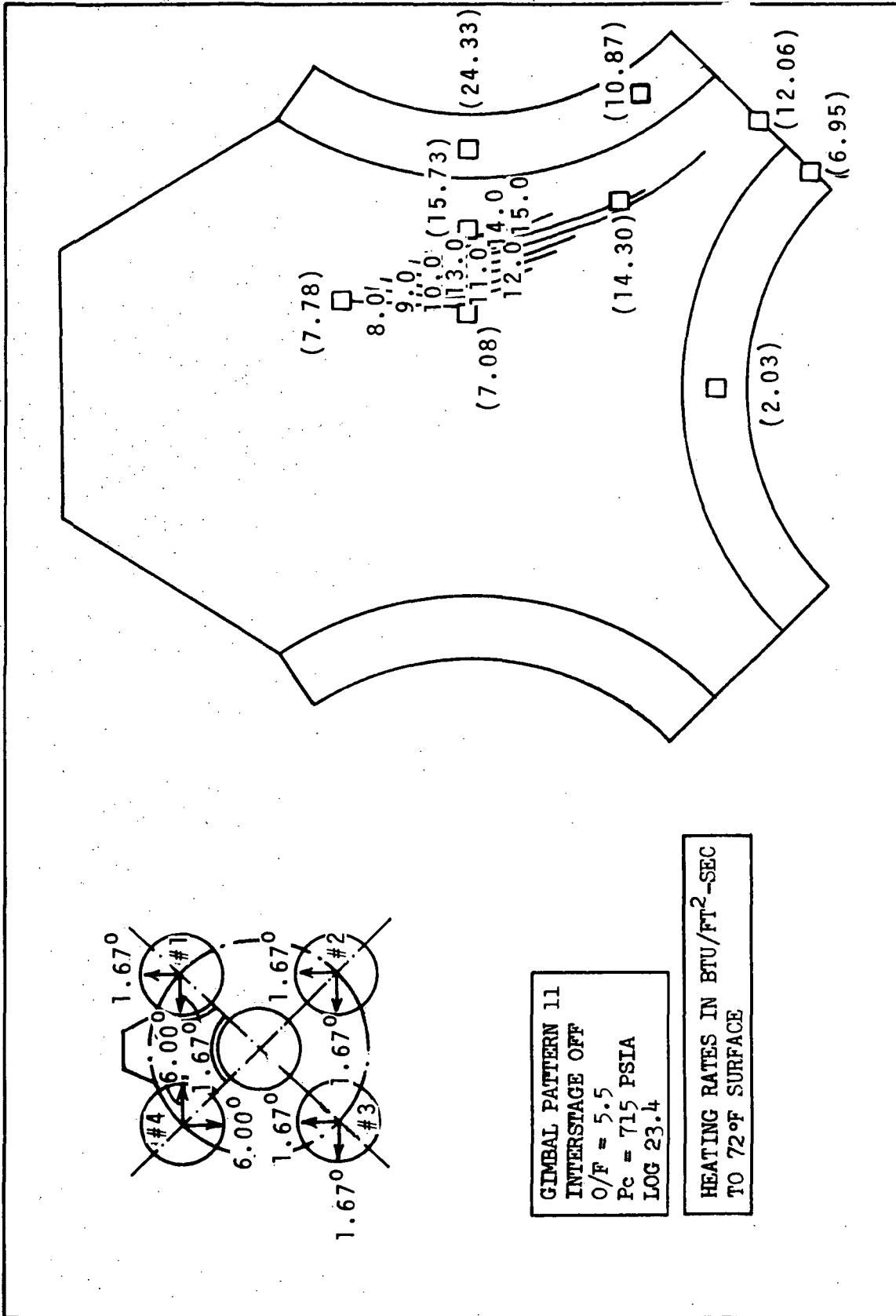
Figure 5.10.1-2 Heat Shield Heating Rates with Dual Actuator Failure
Inboard, Gimbal Pattern 11, Interstage Off, O/F = 5.5

GIMBAL PATTERN 11
INTERSTAGE OFF
O/F = 5.5
Pc = 715 PSIA
LOG 23.4

HEATING RATES IN BTU/FT^2-SEC
TO 72°F SURFACE

SD73-SA-0061
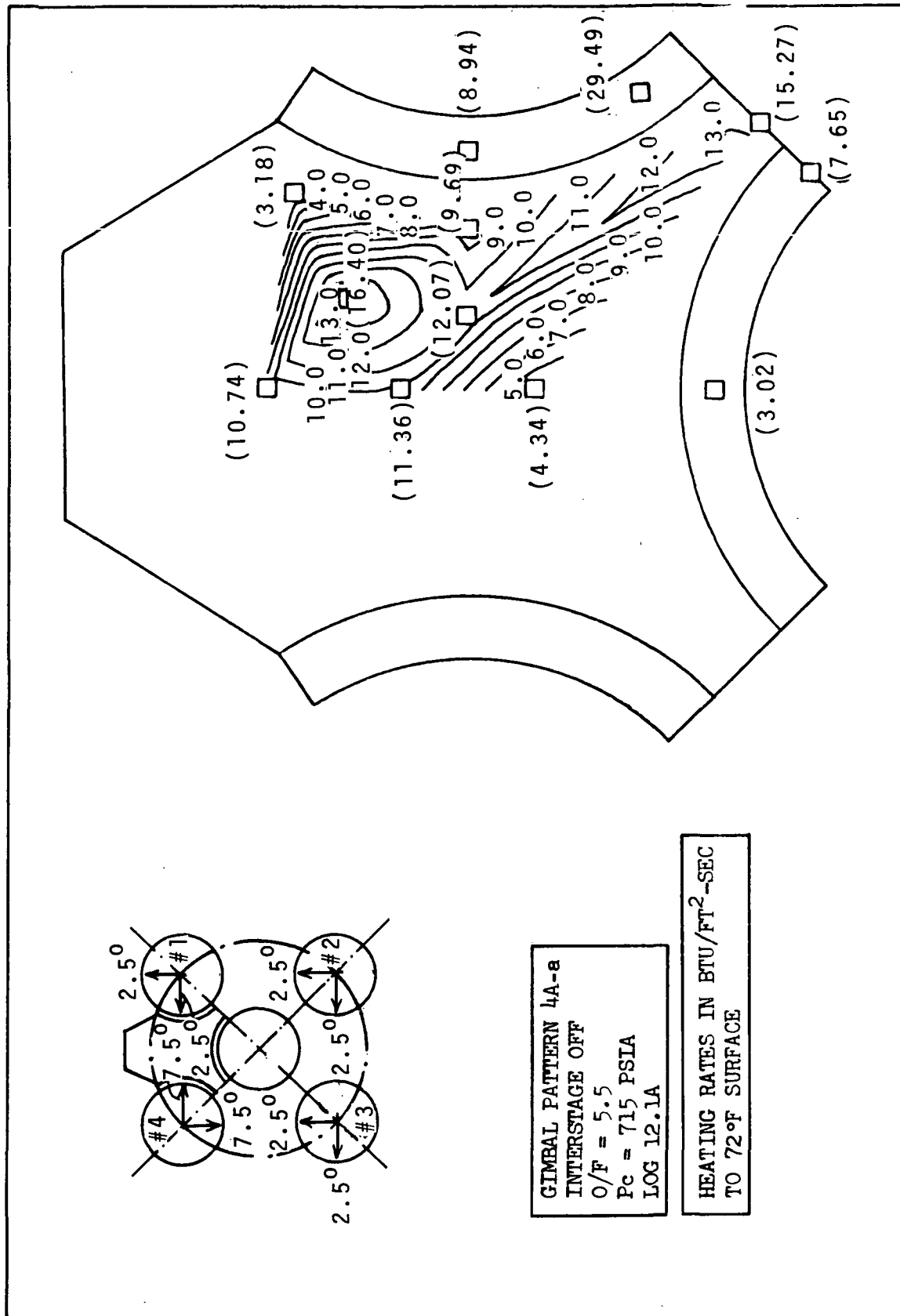
Figure 5.10.1-3   Heat Shield Heating Rates with Dual Actuator Failure
Inboard, Gimbal Pattern 4A-a, Interstage Off, O/F = 5.5

GIMBAL PATTERN 4A-a
INTERSTAGE OFF
O/F = 5.5
Pc = 715 PSIA
LOG 12.1A

HEATING RATES IN BTU/FT²-SEC
TO 72°F SURFACE
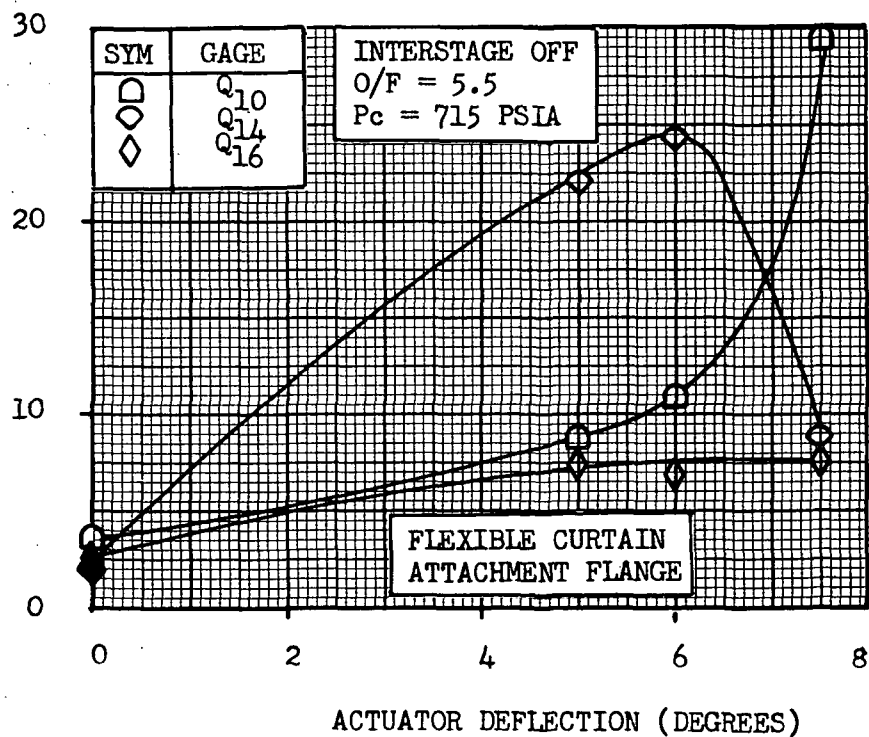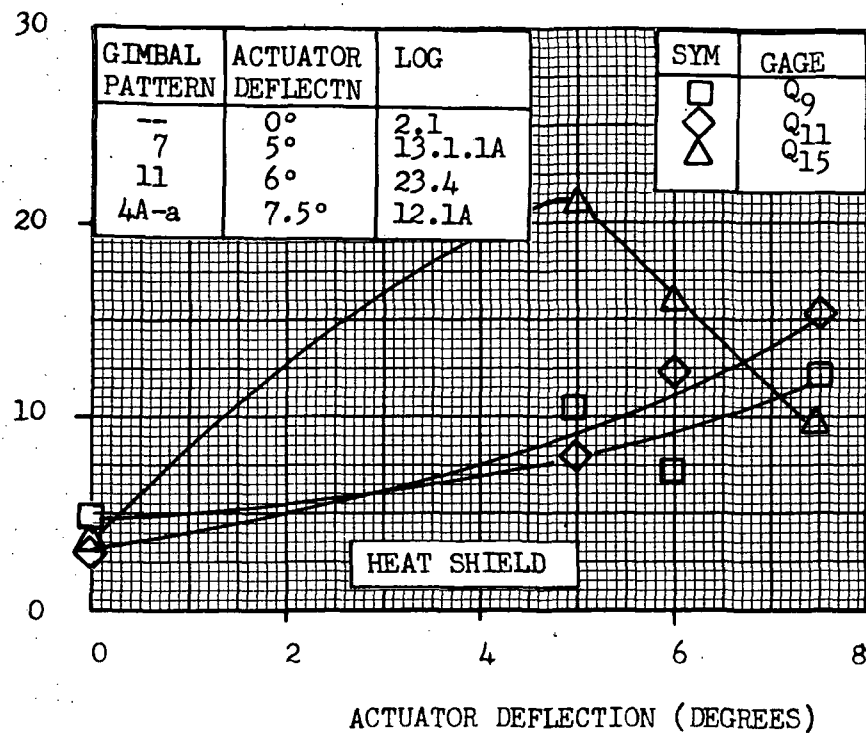
Figure 5.10.1-4 Heat Shield Heating Rate Variation With
Dual Actuator Deflection Inboard Angle
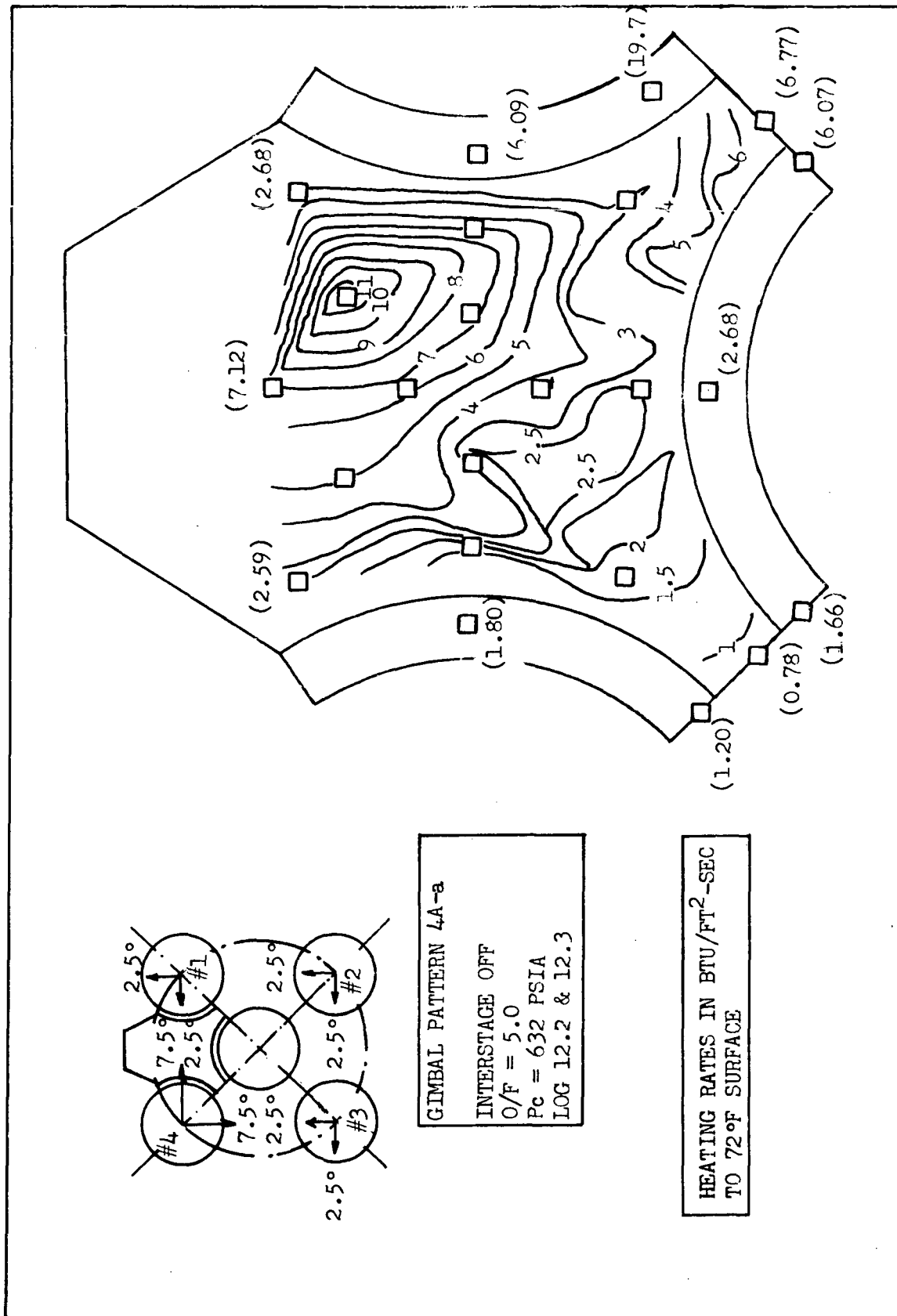
Figure 5.10.1-5 Heat Shield Heating Rates With Dual Actuator Failure Inboard, Gimbal Patterns 4A-a And 4A-b

GIMBAL PATTERN 4A-a

INTERSTAGE OFF
O/F = 5.0
Pc = 632 PSIA
LOG 12.2 & 12.3

HEATING RATES IN BTU/FT^2-SEC
TO 72°F SURFACE

Heating rate distribution in the vicinity of Engine Number 1 with dual-actuator-failure of 7.5° on Engine Number 3 (gimbal pattern 4A) is presented in Figure 5.10.1-6. Comparison with the corresponding nominal heating rate distribution of Figure 5.6.1-2 shows that the gimbal pattern 4A peak heating rate is 18 percent below the nominal peak value and that it shifts towards the center engine.

5.10.2 Thrust Cone Heating Rates

Very limited thrust cone heating rate data were obtained for the dual-actuator-failure-inboard conditions. The thrust cone heating rates at $\theta = 0°$ for several gimbal patterns are shown in Figure 5.10.2-1 together with the nominal heating rates for the same location.

It is seen that gimbal patterns 4A-a and 4A-b produce heating rates 12% above the nominal value at the gage Q_{24} location; otherwise the dual-actuator-failure-inboard heating rates are equal to or less than the nominal values.

5.10.3 Engine Nozzle Heating Rates

Considerable amount of center engine nozzle heating rate data were obtained for the various dual-actuator-failure gimbal cases shown in Figure 5.10-1.

Two heating rates on the center engine nozzle lip were recorded in Log 6.1 for the gimbal pattern 4A. The average heating rate opposite the deflected engine (gage N2) was 58.9 Btu/ft^2-sec, while 45 degrees away peripherally (gage N1) the average heating rate measured was 4.1 Btu/ft^2-sec.

Most of the test cases were run with an O/F mixture of 5.5. Some heating rate data for gimbal patterns 4A-a and 4A-b were obtained with mixture ratio of 5.0 and are recorded in data Logs 12.1 and 12.3. However, these data were from 2 to 3 times lower than the corresponding O/F = 5.5 heating rates for distances greater than 7 inches (full scale) from the nozzle exit plane. These results appear to be erroneous and therefore are not included in the discussion.

Center engine nozzle heating rates for 0.9°& 1.6°, 5°, 6° and 7.5° dual actuator failure conditions are presented in Figures 5.10.3-1, 5.10.3-2, 5.10.3-3, and 5.10.3-4 respectively.

It is seen that for small actuator deflections, Figure 5.10.3-1, the center engine heating rate distributions are very similar to the nominal distribution (Figure 5.6.4-1) where the peak heating rate occurs at 7 to 11 inches (full scale) from the nozzle exit plane. With increasing engine deflection, the peak shifts toward the nozzle exit plane and with deflections equal to or greater than 5°, the peak heating rate occurs at the exit plane. With these large actuator deflections the heating rates decrease exponentially with distance from the exit plane as shown in Figures 5.10.3-2 through 5.10.3-4.

SD73-SA-0061

Space Division
North American Rockwell
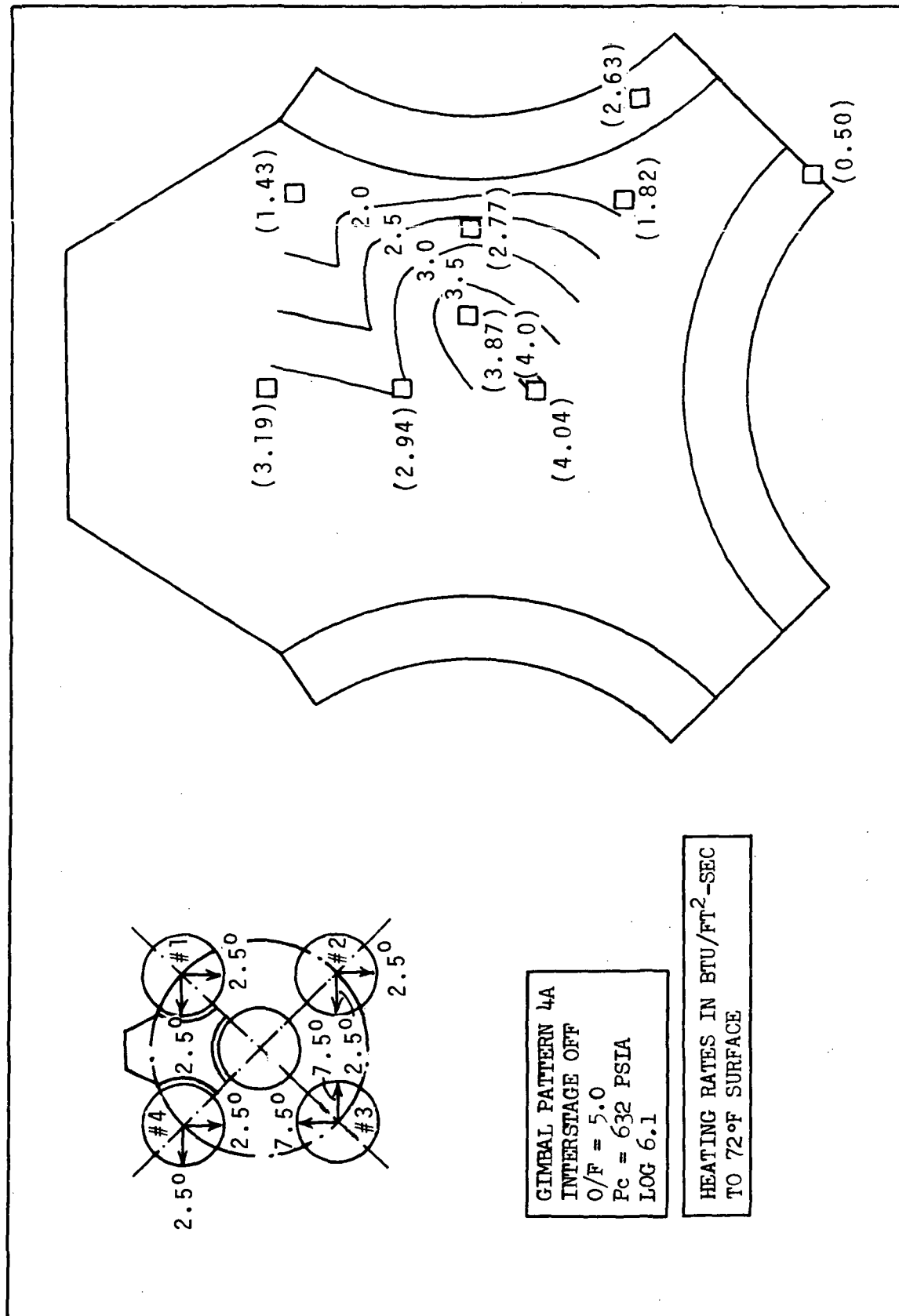
Figure 5.10.1-6 Heat Shield Heating Rates with Dual Actuator Failure
Inboard, Gimbal Pattern 4A, Interstage Off, O/F = 5.0

GIMBAL PATTERN 4A
INTERSTAGE OFF
O/F = 5.0
Pc = 632 PSIA
LOG 6.1

HEATING RATES IN BTU/FT²-SEC
TO 72°F SURFACE
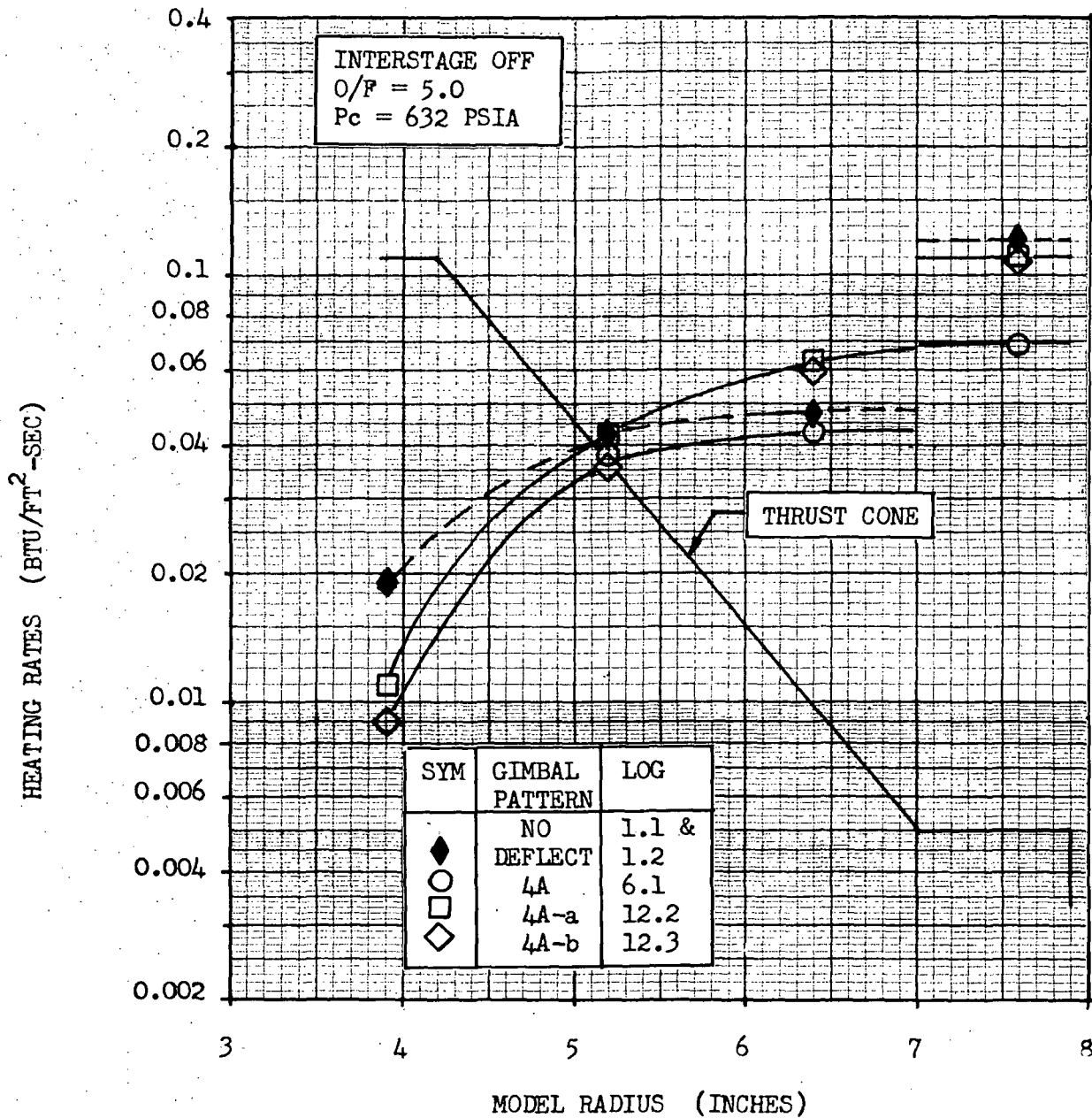
Figure 5.10.2-1   Thrust Cone Heating Rates At θ = 0° With
Dual Actuator Failure Inboard Deflections

SD73-SA-0061
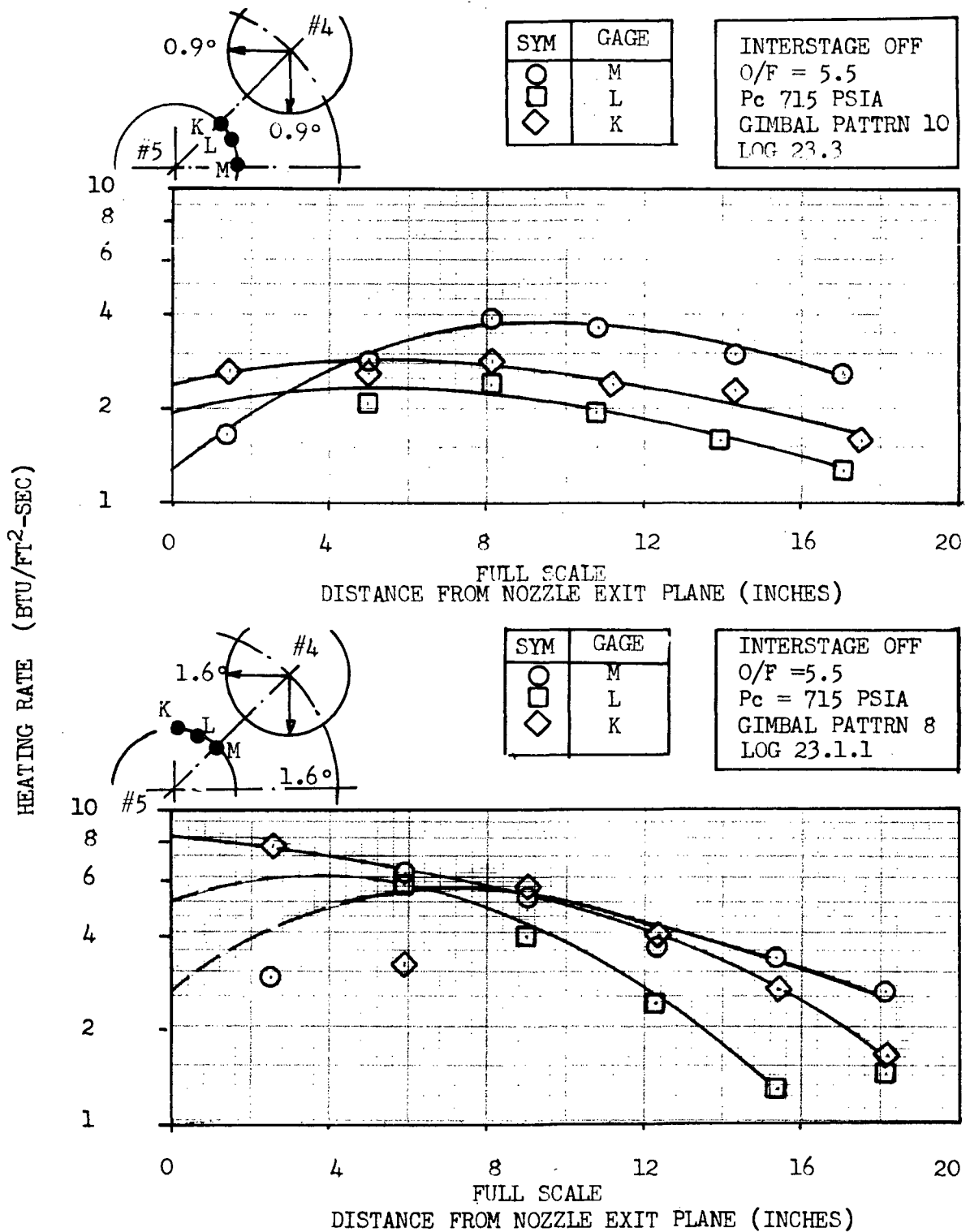
Figure 5.10.3-1   Center Engine Nozzle Heating Rates With
Dual Actuator Deflection Case 8 And 10

Θ = 315°

Θ = 0°

#4

5°   5°

#5   #1

SYM	GAGE	Θ°	GIMBAL PATTERN	LOG
◯	K	315	⎫	
☐	L	337.5	⎬ #12	23.5
◇	M	0	⎭	
◐	L	311	⎫ #7	13.1.1A
⊡	K	292.5	⎭	

INTERSTAGE OFF
O/F = 5.5
Pc = 715 PSIA
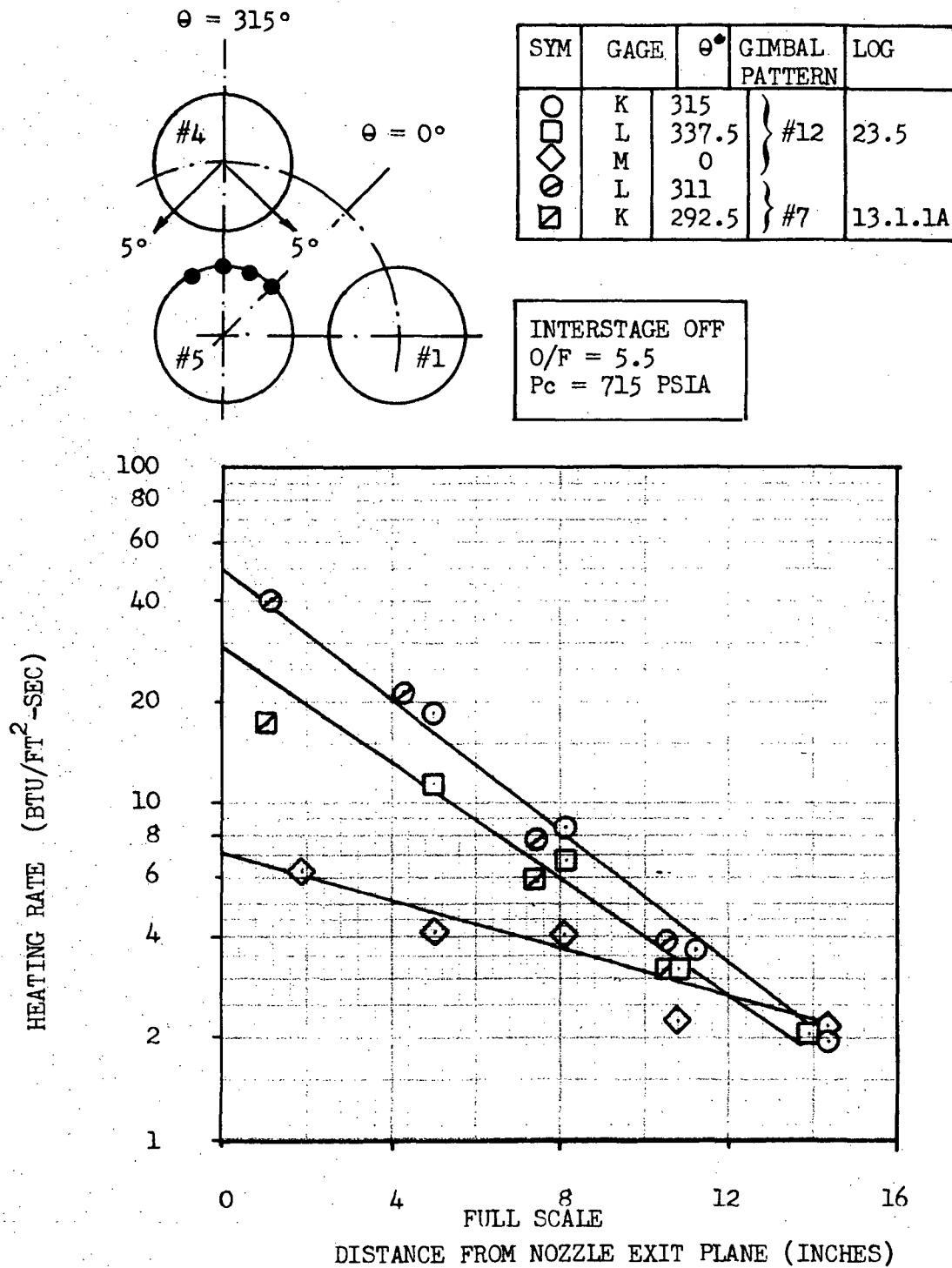
Figure 5.10.3-2   Center Engine Nozzle Heating Rates With
Dual Actuator Failure Inboard At 5°

SD73-SA-0061

Θ = 315°

Θ = 0°

SYM	GAGE	Θ°
○	K	315
□	L	337.5
◇	M	0

INTERSTAGE OFF
GIMBAL PATTERN 11
O/F = 5.5
Pc = 715 PSIA
LOG 23.4

#4

6°   6°

#5   #1

HEATING RATE (BTU/FT^2-SEC)

FULL SCALE

DISTANCE FROM NOZZLE EXIT PLANE (INCHES)
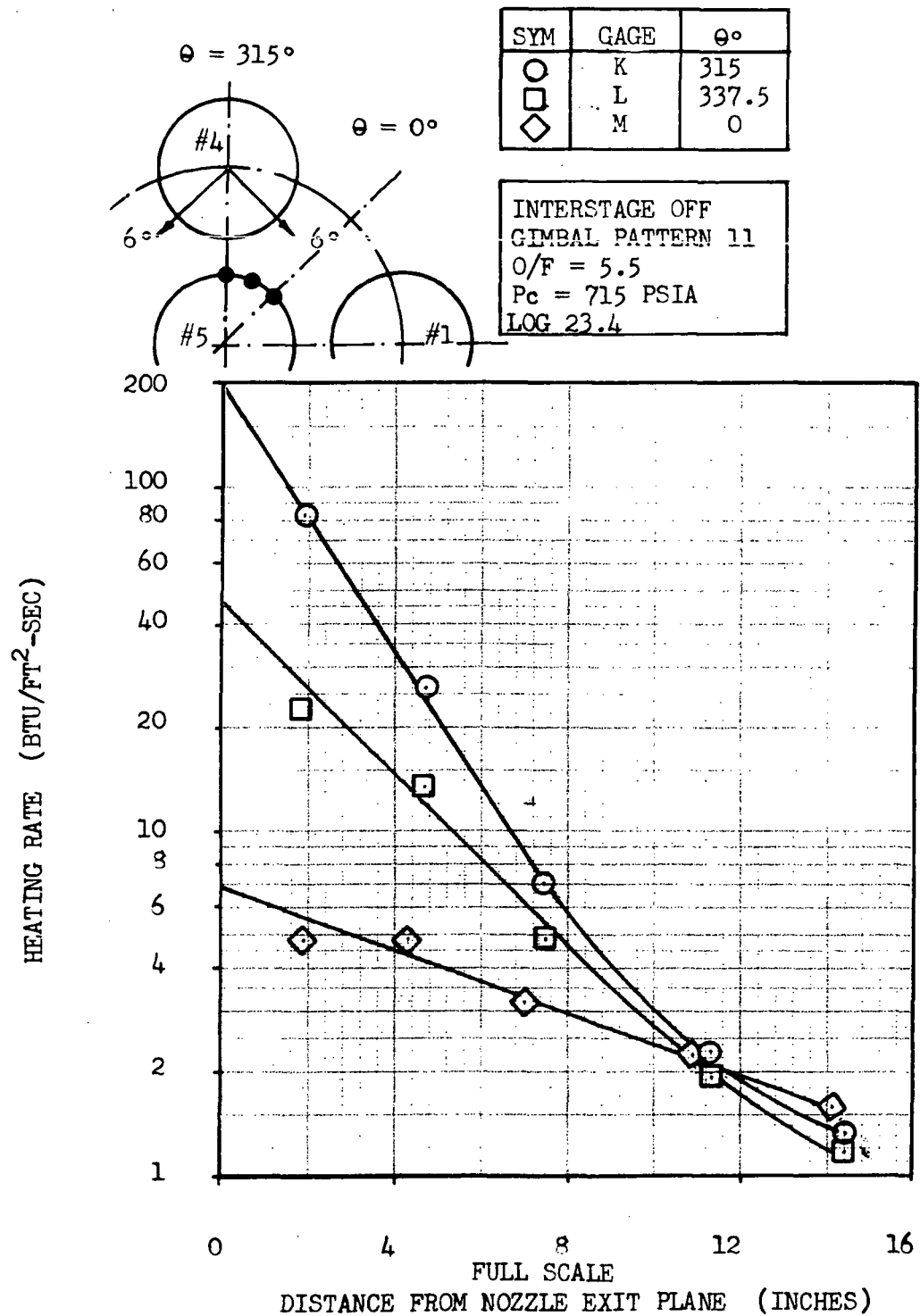
Figure 5.10.3-3   Center Engine Nozzle Heating Rates With
Dual Actuator Failure Inboard At 6°

     SD73-SA-0061

SYM	GAGE	Θ°
□	K	292.5°
○	L	315°
◇	M	337.5°

INTERSTAGE OFF
GIMBAL PATTERN 4A-a
O/F = 5.5
Pc = 715°
LOG 12.1A
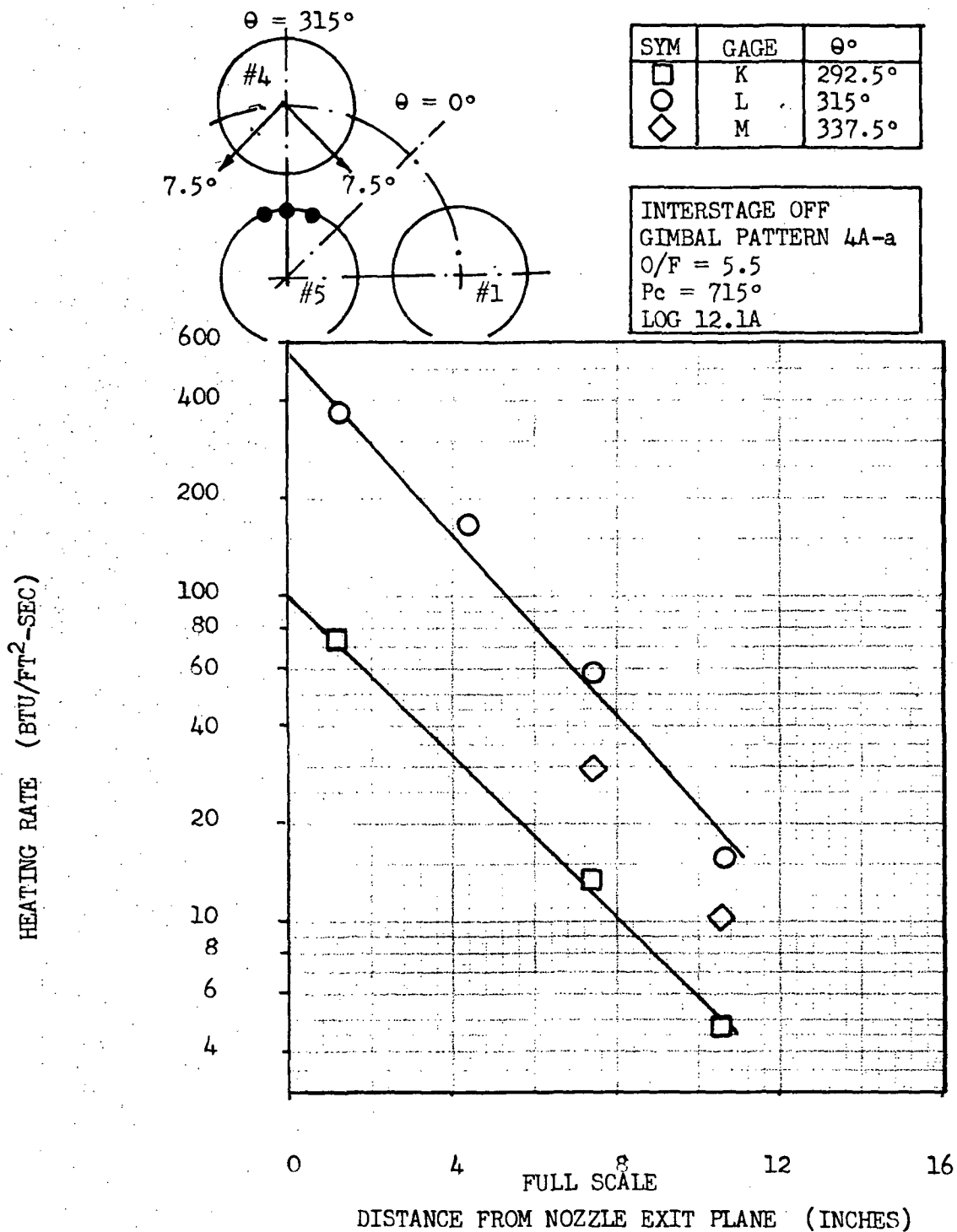
Figure 5.10.3 -4 Center Engine Nozzle Heating Rates With
Dual Actuator Failure Inboard At 7.5°

The variation of nozzle external heating rates with engine actuator deflection angle inboard is shown in Figure 5.10.3-5 for three peripheral locations on the nozzle. It is seen that the nozzle heating rates are most sensitive to outboard engine deflection at the point closest to the outboard engine, i.e., $\theta = 315°$ and the least sensitive at $\theta = 0°$ with the actuators failed on the Number 4 Engine.

Outboard engine heating rates were measured for small actuator deflection angles, e.g., Cases 10 and 8. These nozzle heating rates are plotted in Figure 5.10.3-6. Comparison with the nominal outboard engine heating rate distribution of Figure 5.6.4-1 shows that the dual actuator failure Case 10 and Case 8 heating rates are practically identical to the nominal case in magnitude and distribution.

The effect of thrust build up, or chamber pressure variation, on the center engine nozzle heating rates was investigated and the results are recorded in data Logs 23.5, 23.6 and 23.7 with $O/F = 5.5$ and $P_c = 715$, 465 and 215 psia respectively. Typical results for one of the three rows of gages used in these tests are presented in Figure 5.10.3-7. It is seen that the nozzle heating rates are proportional to the chamber pressure, which agrees well with the results of Section 5.3 where chamber pressure effects on heat shield and thrust cone heating rates were investigated.
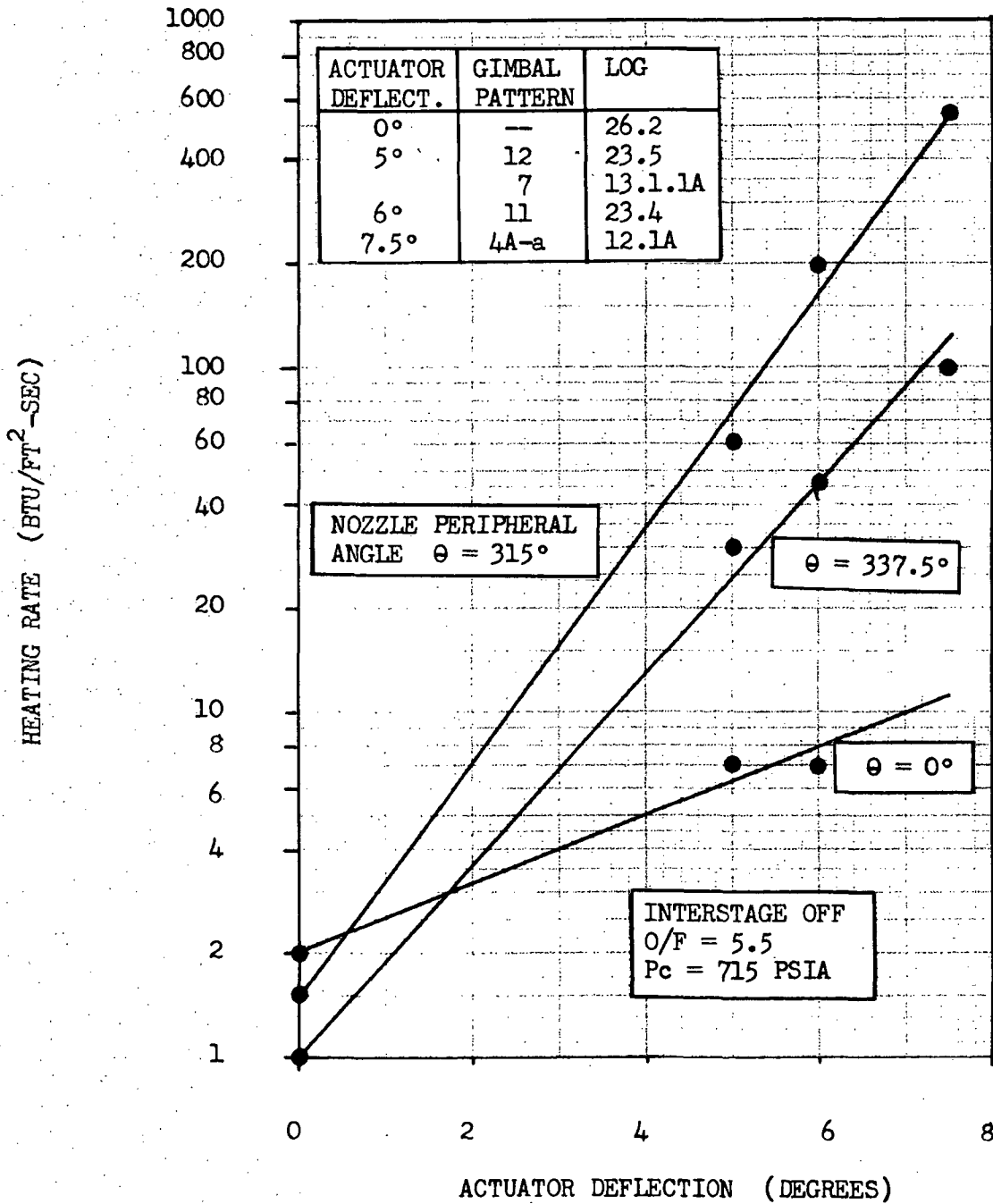
Figure 5.10.3-5 Nozzle External Heating Rates At x = 0 With
Dual Actuator Failure Inboard Deflections
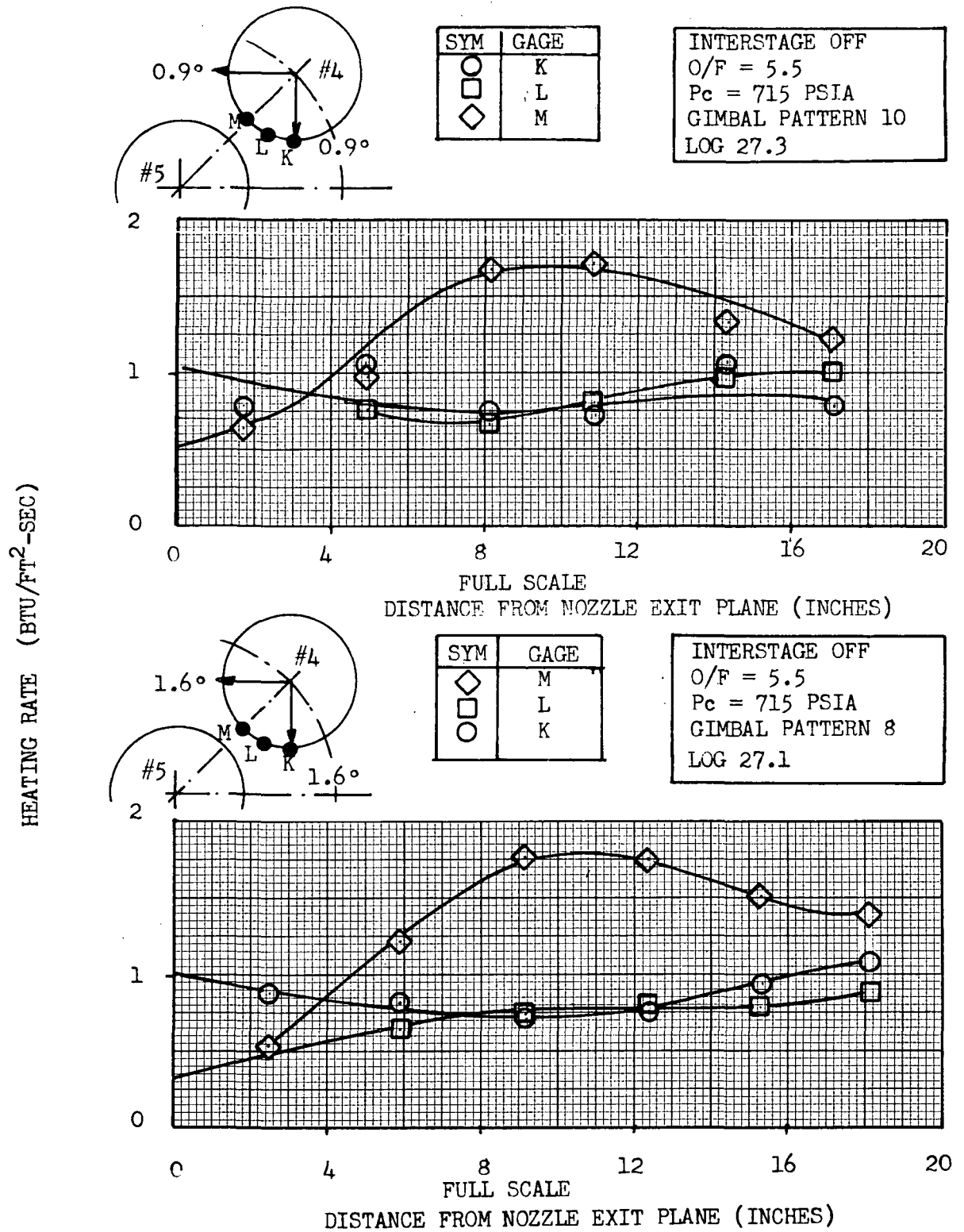
Figure 5.10.3-6   Outboard Engine Nozzle Heating Rates With Dual
Actuator Inboard Case 8 And 10
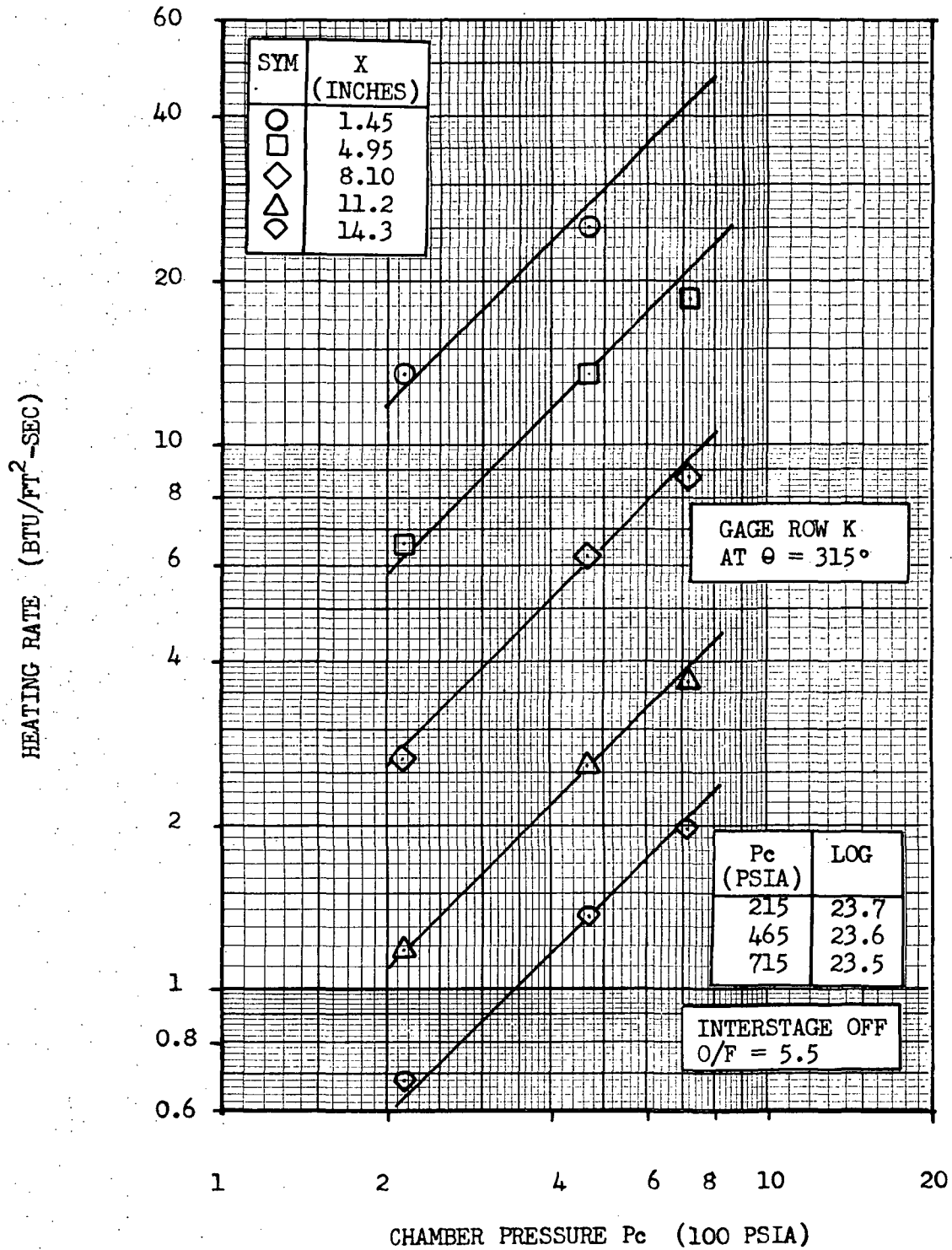
Figure 5.10.3-7 Variation Of Center Engine Nozzle External Heat Rates With Pc For Dual Actuator Failure Case 12

SD73-SA-0061

5.11 BASE REGION ENVIRONMENT WITH NOMINAL TRIM AND STRUCTURAL COMPLIANCE
      DEFLECTIONS

Heat shield, thrust cone and interstage heating rates were measured with the nominal trim and structural compliance gimbal patterns shown in Figure 5.11-1. No pressure data were obtained. Most of the runs were made for gimbal pattern Case 9B at an O/F mixture ratio of 5.5.

It was found that the relatively small engine deflections caused some of the local heat shield heating rates to increase by a factor of 3. Thrust cone heating rates increased by 60 percent above the nominal values. This illustrates the sensitivity of the base region thermal environment to engine deflections.

5.11.1 Heat Shield Heating Rates

Heat shield heating rate distributions are presented in Figures 5.11.1-1, 5.11.1-2 and 5.11.1-3 for gimbal patterns 9, 9A and 9B respectively. Comparison with the heat shield nominal heating rate distribution of Figure 5.6.1-2 shows that the relatively small engine deflections increase local heating rates by 40 to 200 percent above the nominal values. Gimbal Case 9 produces the most severe heating rates; the peak value increasing 60 percent above the nominal value.

A comparison of the nominal heating rate distribution with the heating rates corresponding to gimbal patterns 9, 9A and 9B is presented in Figure 5.11.1-4. It is seen that the heat shield centerline heating rates, within the engine pitch circle, are affected the most by the engine deflections, while the heating rates around the outboard engine are affected the least.

Figure 5.11.1-5 shows the heat shield heating rate distribution for the gimbal pattern 9B case with a mixture ratio of 5.5. It was found that on the average, the O/F = 5.5 heating rates were 20% higher than the corresponding O/F = 5.0 heating rates.

The effect of interstage on the gimbal pattern 9B heating rates is obtained by comparing the heating rates of Figures 5.11.1-5 and 5.11.1-6 for the interstage-off and interstage-on conditions respectively. It is seen that except for three heat shield gage locations Q1, Q2, and Q9, the effect of the interstage is to cause a slight reduction of the heat shield heating rates; the average reduction being about 5 percent.

5.11.2 Thrust Cone Heating Rates

A comparison of the nominal trim and structural compliance thrust cone heating rates with the nominal no-deflection heating rates is shown in Figure 5.11.2-1. It is seen that at $\theta = 0°$, the interstage-off heating rates are increased by 50 to 60 percent by the gimbal pattern 9 and 9B deflections and from 0 to 20 percent by gimbal pattern 9A. Referring to gimbal pattern 9A engine deflections, Figure 5.11-1, it is seen that the heating rates near Engine Number 1 could very likely increase more than the observed increase at $\theta = 0°$.
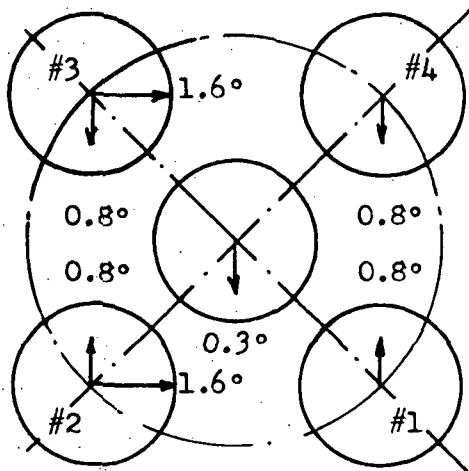
CASE 9
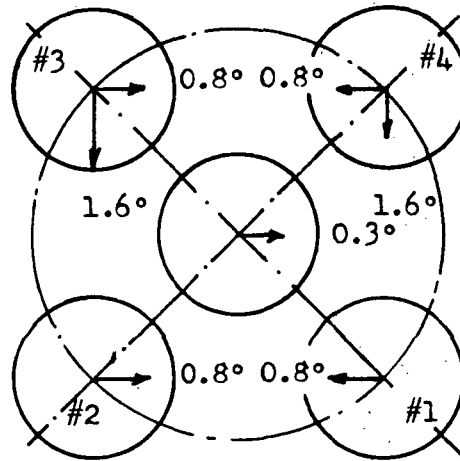
CASE 9A
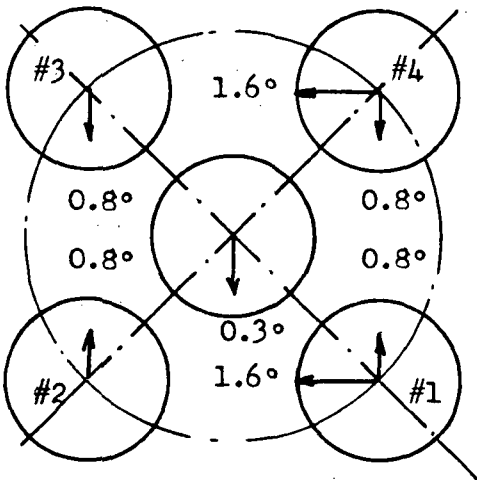
CASE 9B

Figure 5.11-1 Nominal Trim And Structural Compliance
Gimbal Patterns

SD73-SA-0061
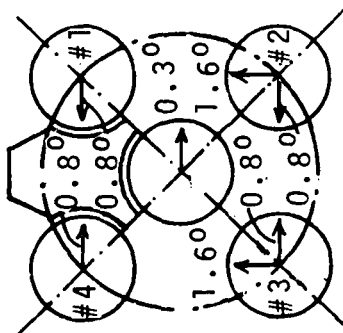
Figure 5.11.1-1 Heat Shield Heating Rates with Nominal Trim and Structural Compliance, Gimbal Pattern 9, Interstage Off, O/F = 5.0
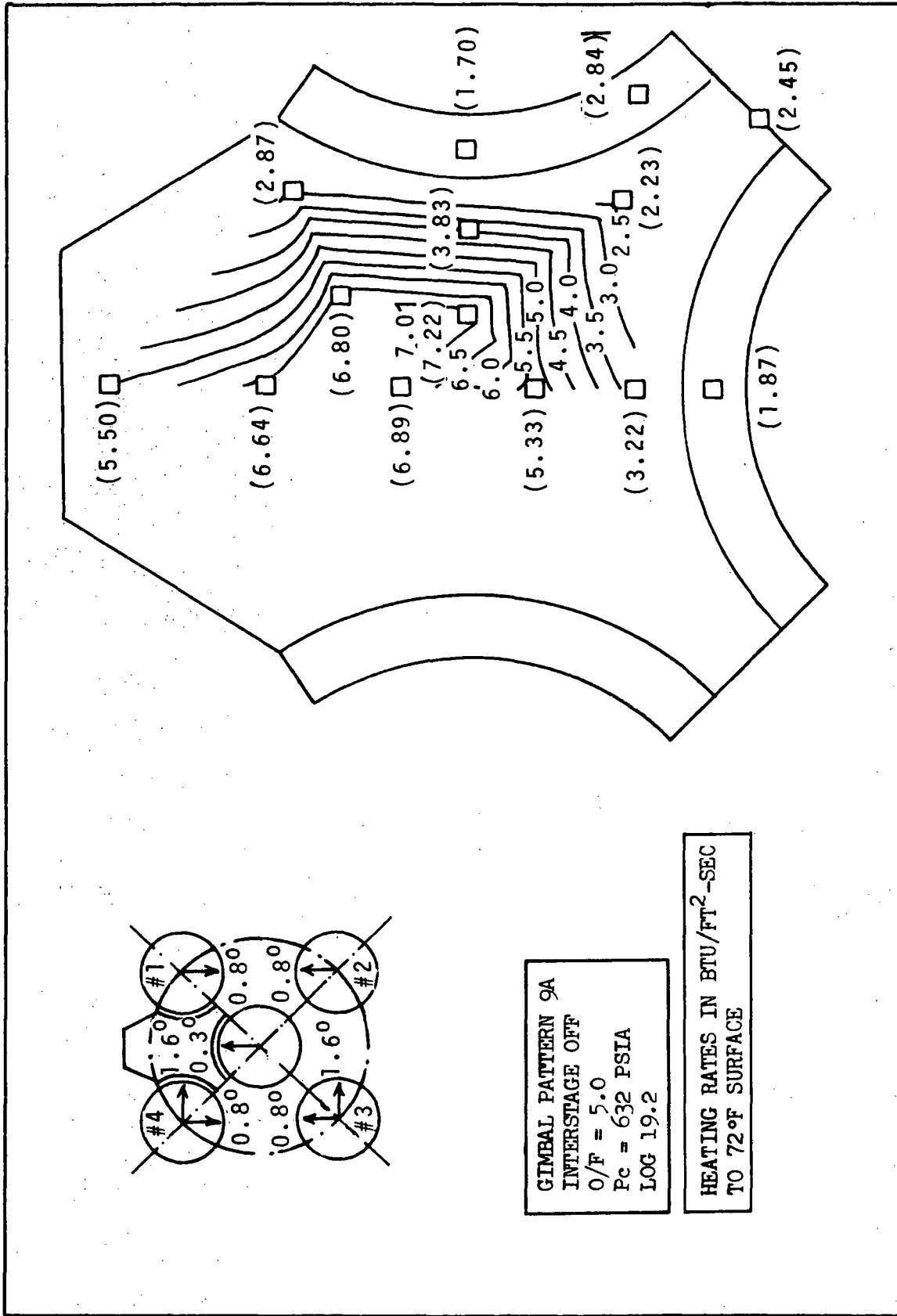
Figure 5.11.1-2 Heat Shield Heating Rates with Nominal Trim and Structural Compliance, Gimbal Pattern 9A, Interstage Off, O/F = 5.0

GIMBAL PATTERN 9A
INTERSTAGE OFF
O/F = 5.0
Pc = 632 PSIA
LOG 19.2

HEATING RATES IN BTU/FT^2-SEC
TO 72°F SURFACE
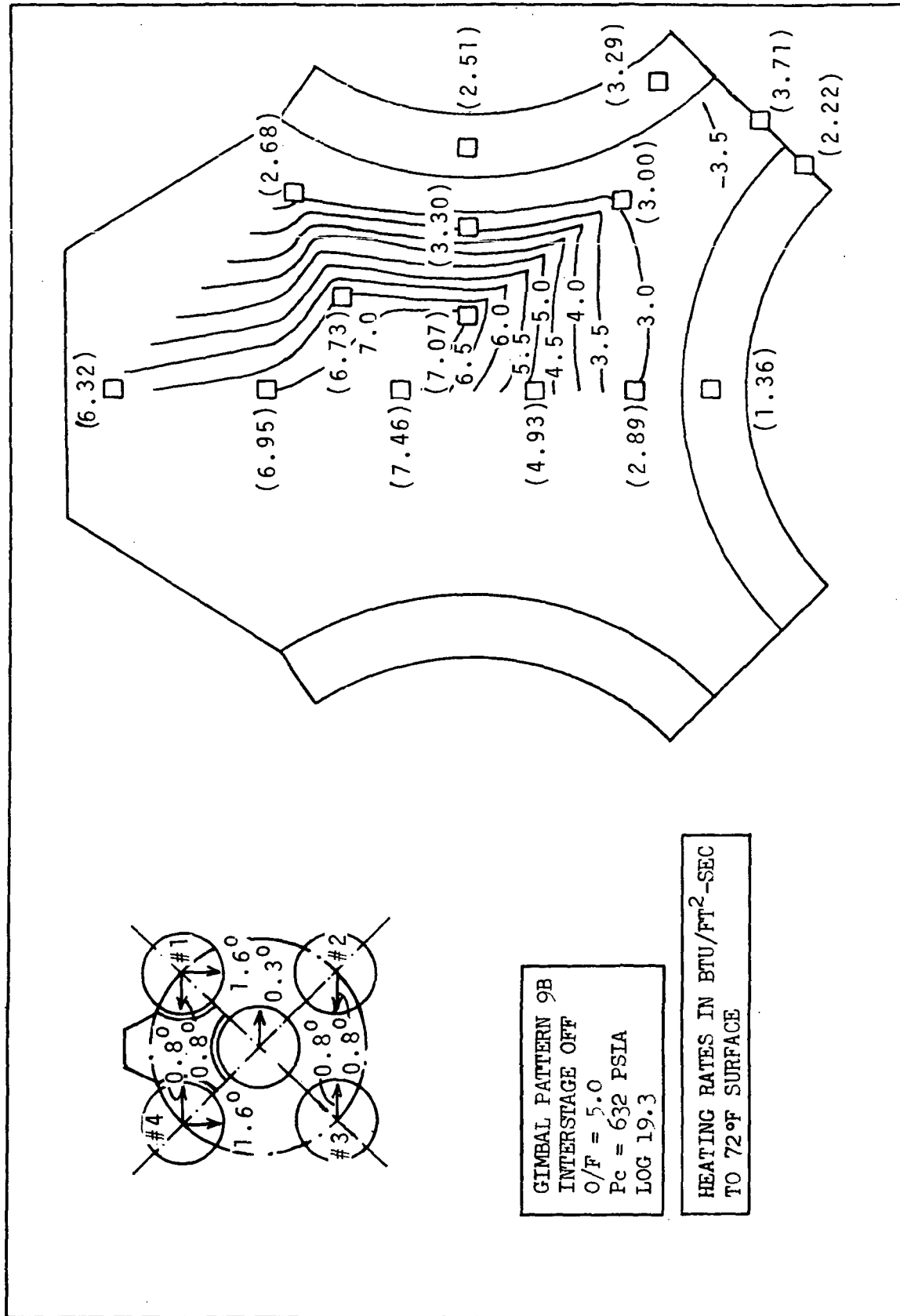
Figure 5.11.1-3 Heat Shield Heating Rates with Nominal Trim and Structural Compliance, Gimbal Pattern 9B, Interstage Off, O/F = 5.0
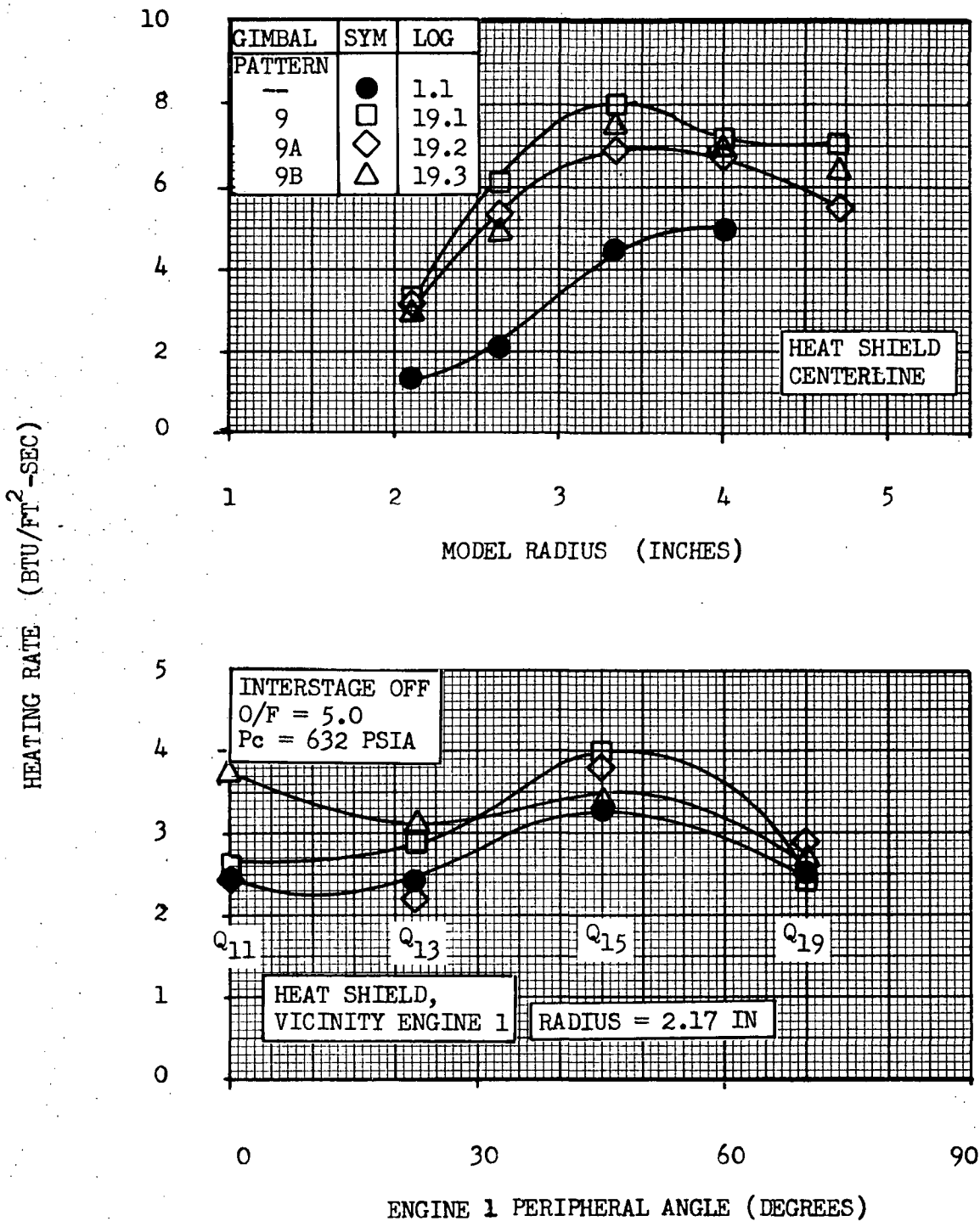
Figure 5.11.1-4   Heat Shield Heating Rates With Nominal
Trim And Structural Compliance Deflections
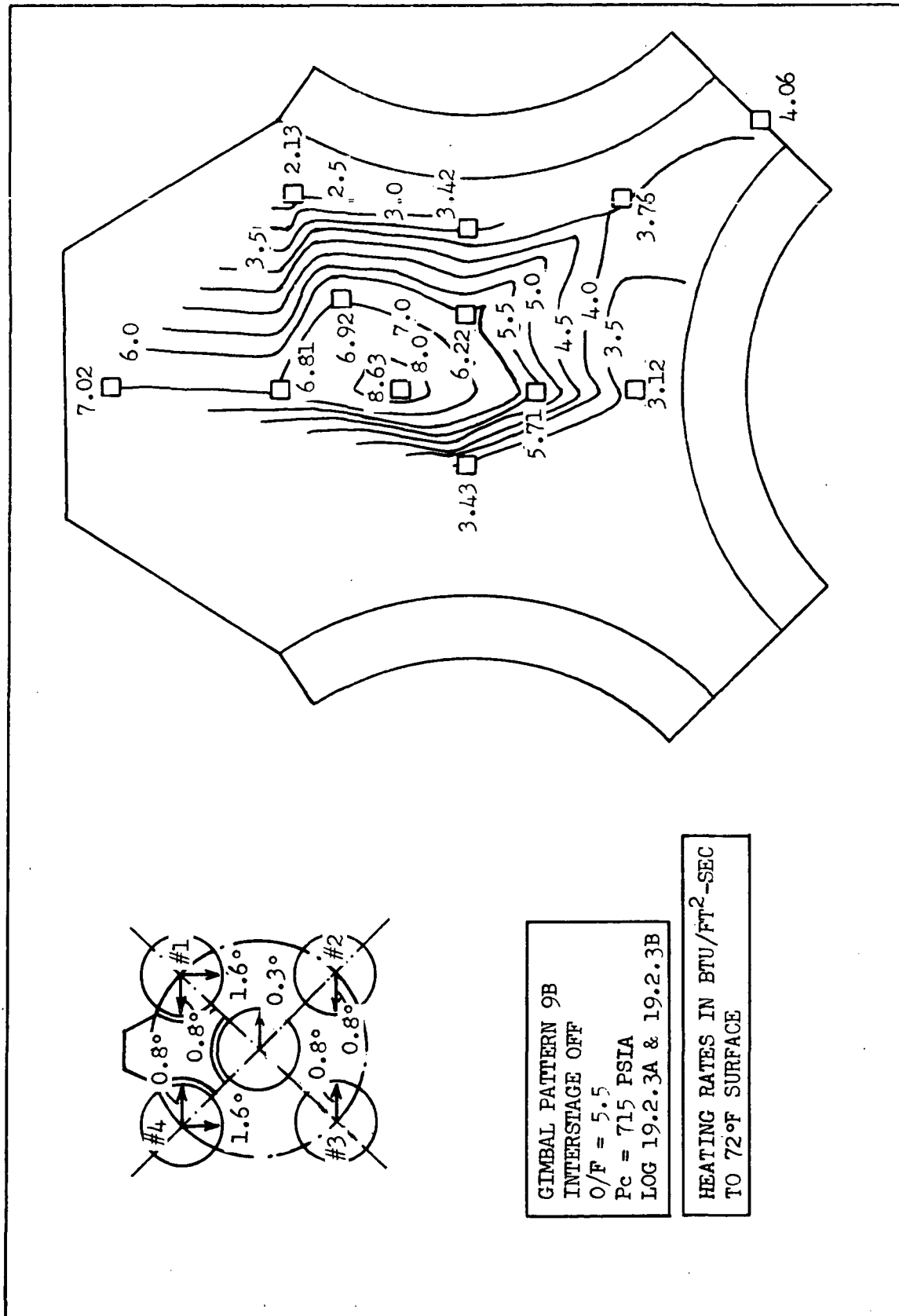
Figure 5.11.1-5 Heat Shield Heating Rates with Nominal Trim and Structural Compliance Gimbal Pattern 9B, Interstage Off, O/F = 5.5

GIMBAL PATTERN 9B
INTERSTAGE OFF
O/F = 5.5
Pc = 715 PSIA
LOG 19.2.3A & 19.2.3B

HEATING RATES IN BTU/FT^2-SEC
TO 72°F SURFACE

SD73-SA-0061
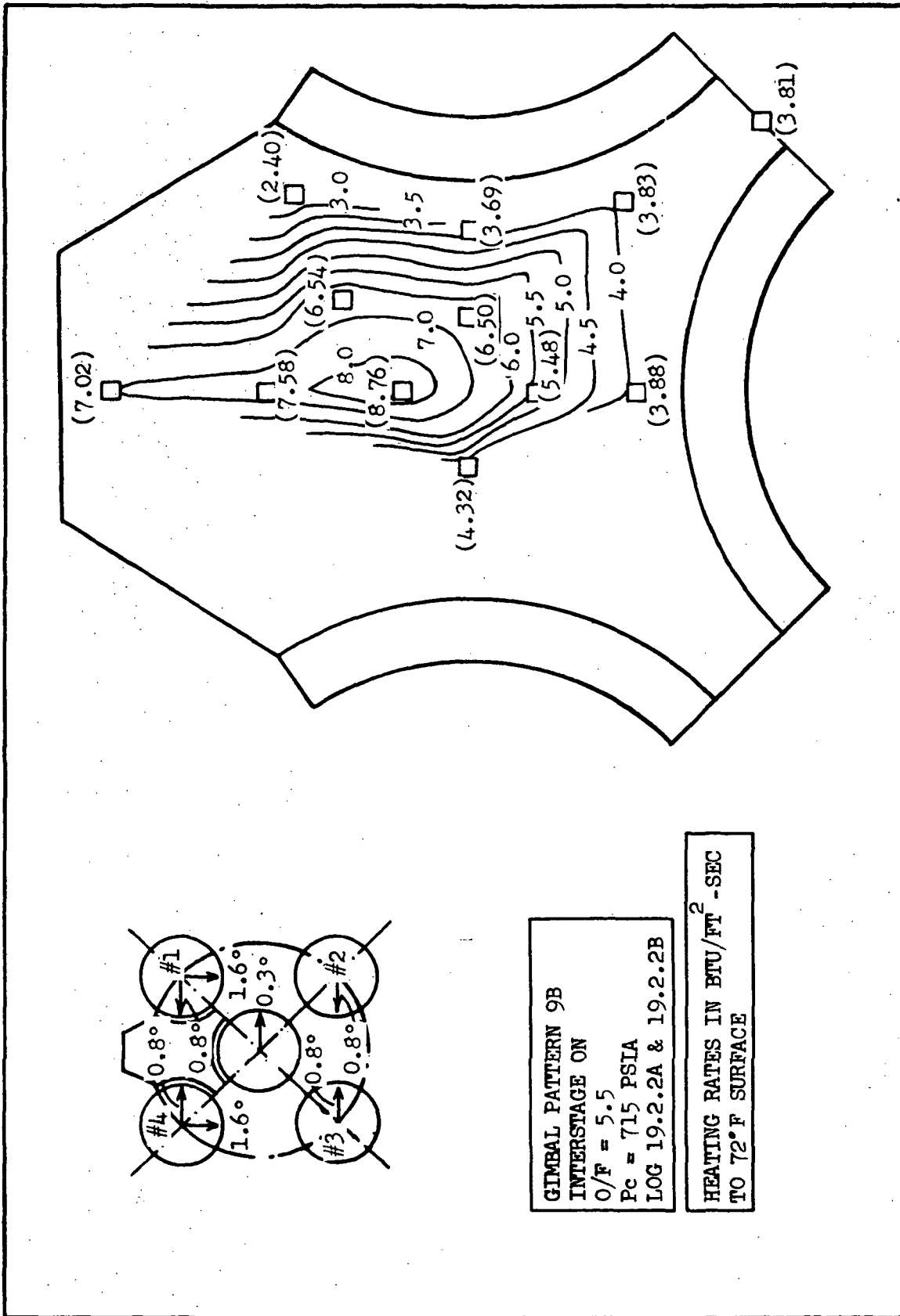
Figure 5.11.1-6 Heat Shield Heating Rates with Nominal Trim and Structural Compliance
Gimbal Pattern 9B, Interstage On, O/F = 5.5

GIMBAL PATTERN 9B
INTERSTAGE ON
O/F = 5.5
Pc = 715 PSIA
LOG 19.2.2A & 19.2.2B

HEATING RATES IN BTU/FT^2-SEC
TO 72°F SURFACE
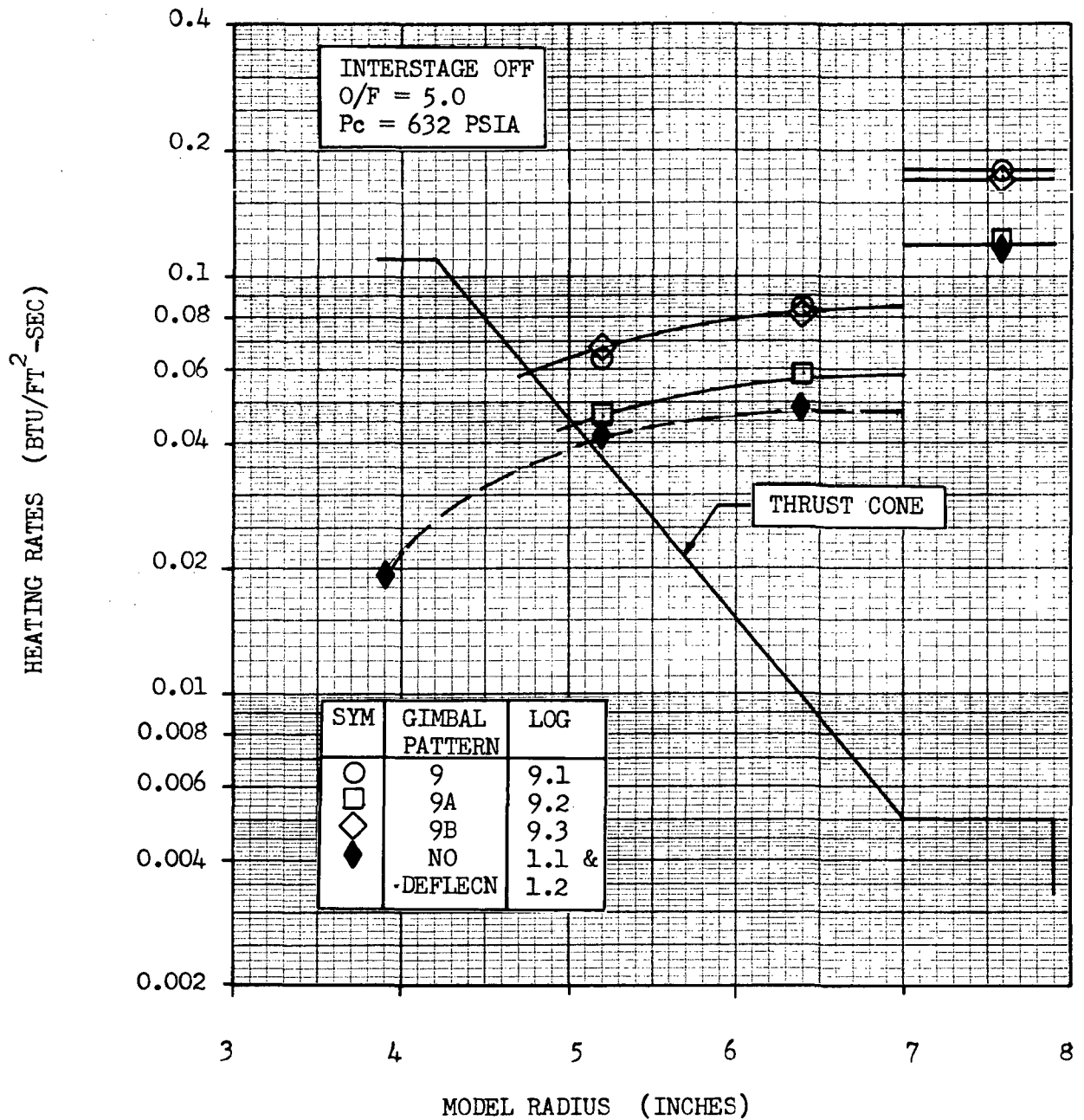
Figure 5.11.2-1 Thrust Cone Heating Rates At $\theta = 0°$ With Nominal
Trim And Structural Compliance Gimbal Patterns

The thrust cone interstage-on heating rate distribution with gimbal pattern 9B deflections is shown in Figure 5.11.2-2 for an O/F mixture ratio of 5.5. Comparison with the corresponding nominal heating rate distribution of Figure 5.6.2-2 shows that the heating rates at $\theta = 0°$ are slightly lower than the nominal values, while the heating rates near Engine Number 1 are increased by 38 percent.

Base region heating rates for the region between the heat shield and the thrust cone surface measured by means of the ring gages shown in Figure 3.4-5 are presented in Figure 5.11.2-3 for the interstage-on and interstage-off conditions with nominal trim gimbal pattern 9B deflections. Comparison with the nominal heating rates (Figure 5.6.2-3) for this region shows that the case 9B heating rates are practically unchanged from the nominal values. Several additional heating rates for this region are recorded in data Logs 19.1 and 19.2 for deflection cases 9 and 9A respectively.

5.11.3 Interstage Heating Rates

Interstage heating rates were measured for one nominal trim-structural compliance gimbal pattern only, namely, Case 9B. The results are shown in Figure 5.11.3-1 together with the corresponding nominal interstage heating rates. It is seen that at Station 0, the gimbal pattern 9B heating rate is only 40 percent of the nominal value while at Station 193, the heating rates are practically identical with the nominal value.

SD73-SA-0061
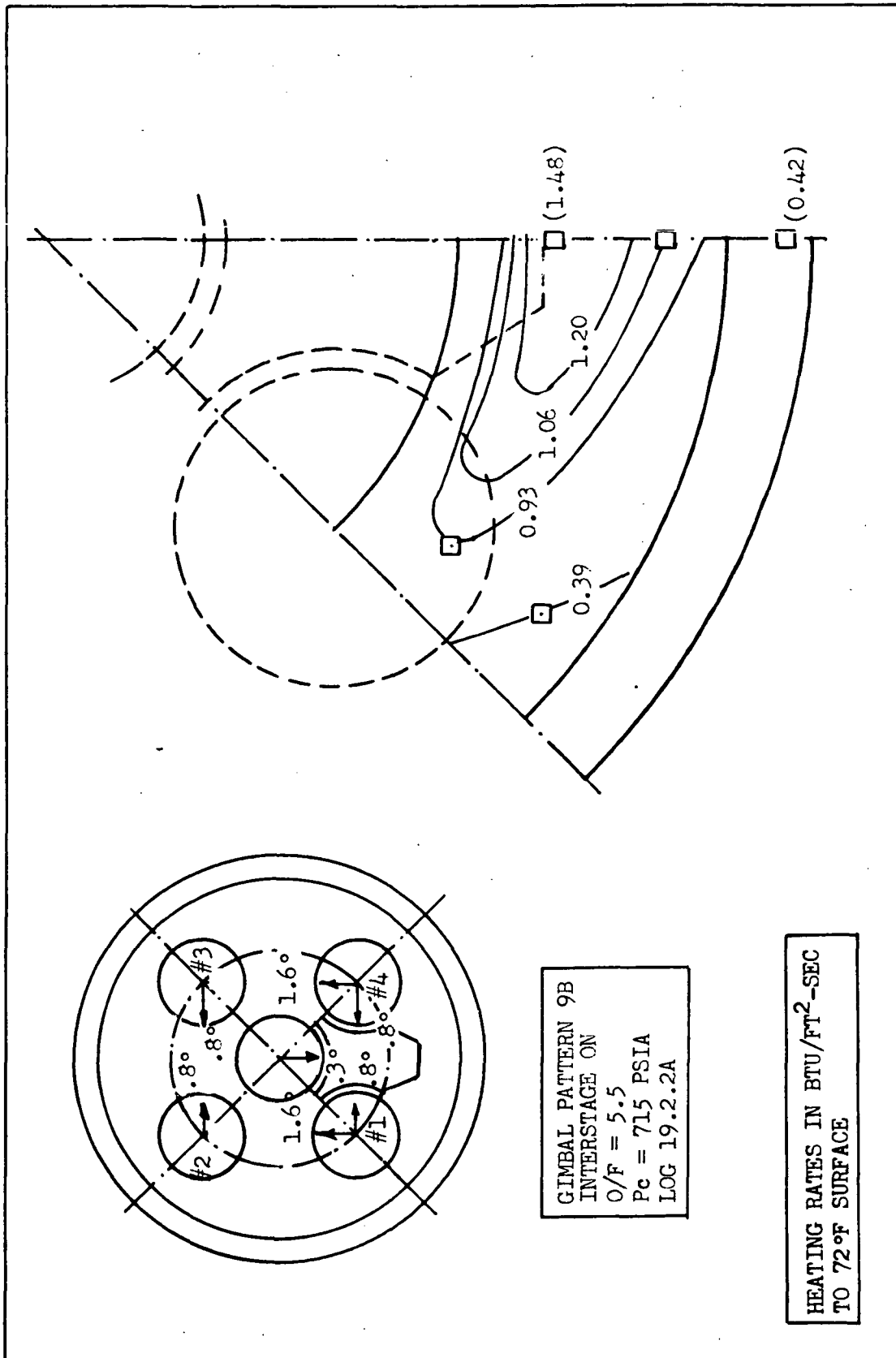
Figure 5.11.2-2 Thrust Cone Heating Rates With Nominal Trim And Structural Compliance

GIMBAL PATTERN 9B
INTERSTAGE ON
O/F = 5.5
Pc = 715 PSIA
LOG 19.2.2A

HEATING RATES IN BTU/FT^2-SEC
TO 72°F SURFACE

SD73-SA-0061

GIMBAL PATTERN 9B
GAGES ON #1 SIDE OF ENGINE #2

SYM	GAGE	O/F	Pc	LOG
○	Q110B	5.5	715	19.2.2A & 19.2.2B
□	Q120B	5.5	715	19.2.3A
△	Q110B	5.0	632	19.3

INTERSTAGE ON

S-II STATION

INTERSTAGE OFF

S-II STATION
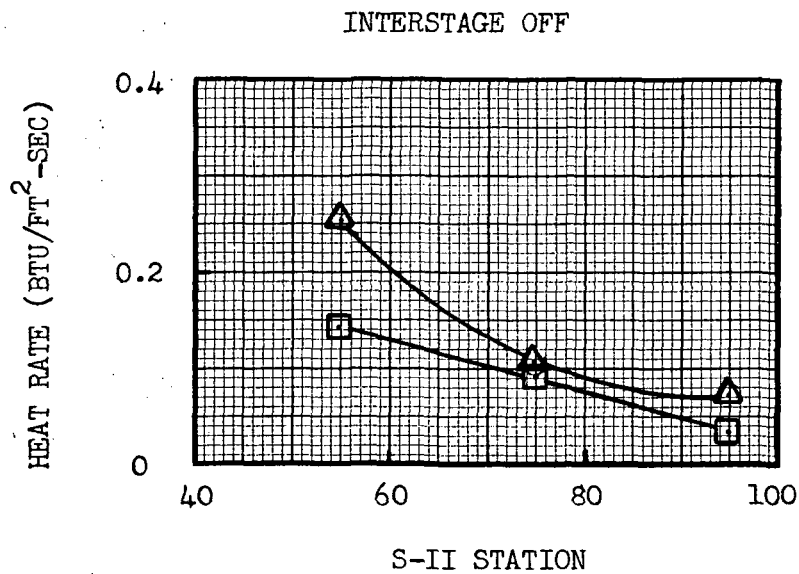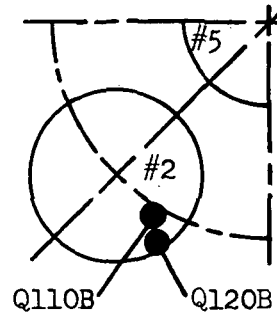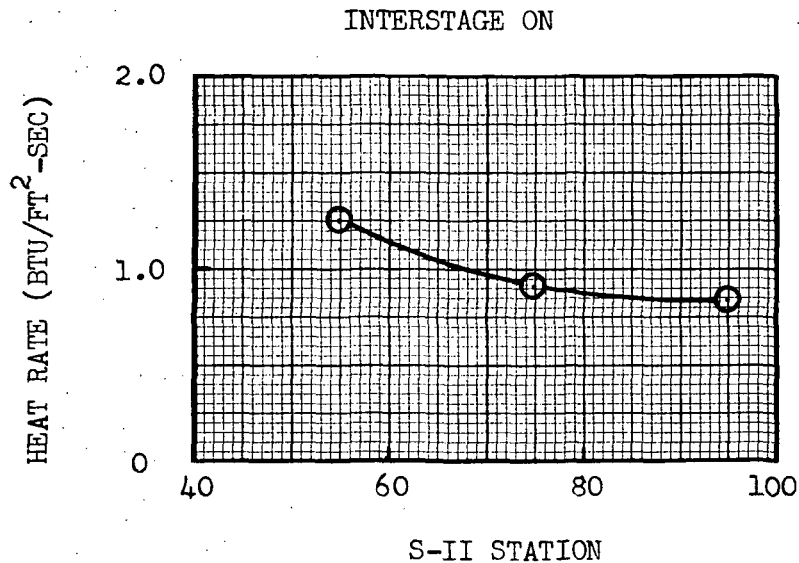
Figure 5.11.2-3 Thrust Cone Region Heating Rates with Gimbal Pattern 9B

SD73-SA-0061

SYM	GIMBAL PATTERN	LOG
O	9B	19.2.2A
---	NO DEFLECN	15.3.1 & 15.3.2

θ = 0°

θ = 29.2°

GAGE LOCATION

O/F = 5.5
Pc = 715 PSIA

HEATING RATE (BTU/FT^2-SEC)

S-II STATION (INCHES)
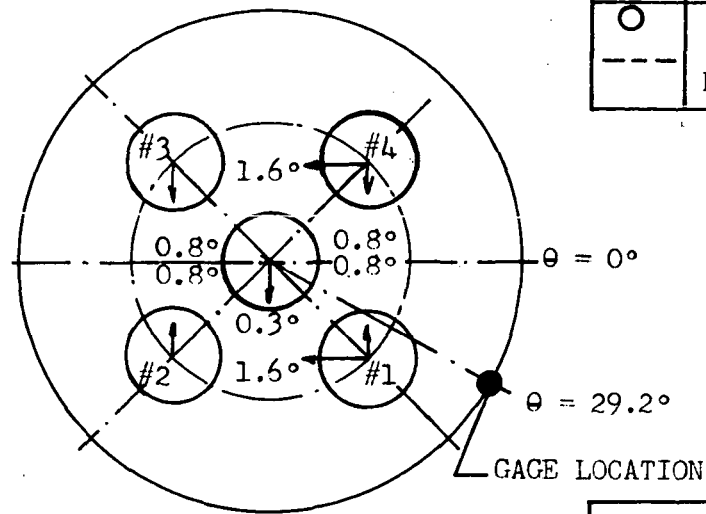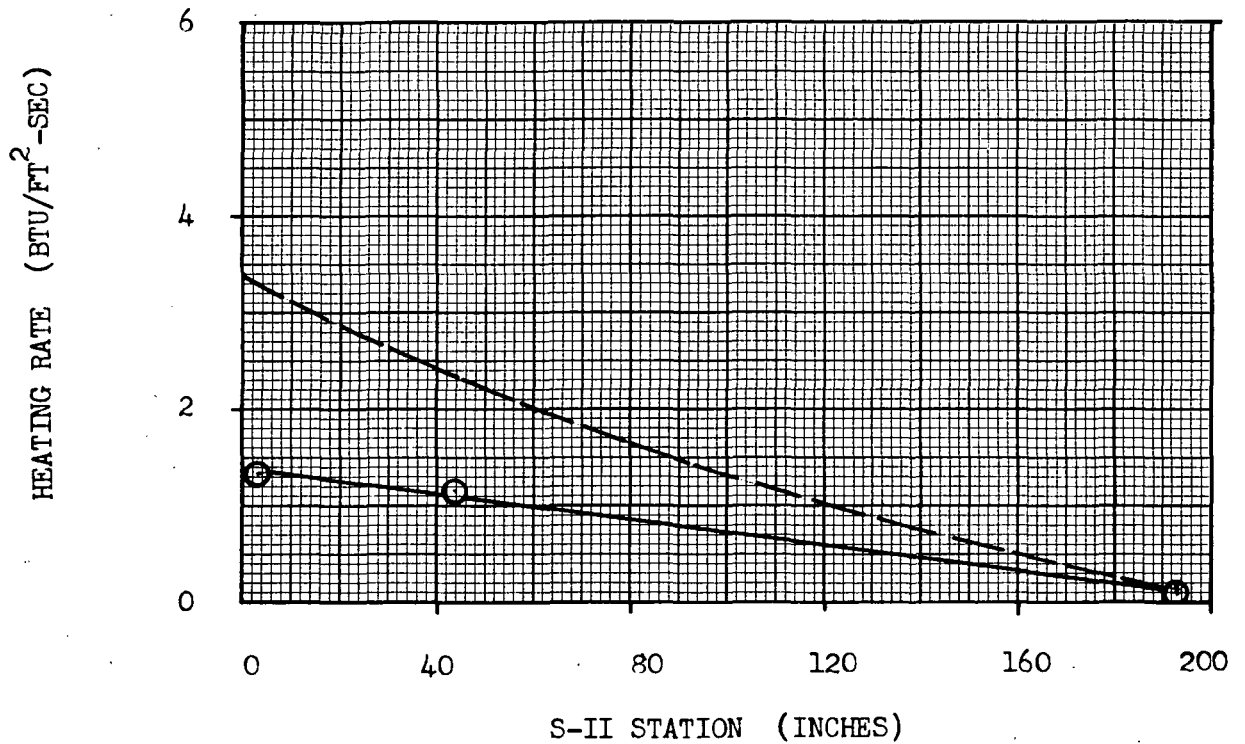
Figure 5.11.3-1 Interstage Heating Rates At θ = 29.2° With
Nominal Trim And Compliance Gimbal Pattern 9B

SD73-SA-0061

5.12   MISCELLANEOUS TESTS

Tests were run during this test program in order to study the effect of heat shield geometry and nozzle boundary layer on base region heating rates. Additional tests were run in order to determine flow symmetry in the nozzles, measure base region static and stagnation pressures in the plane of the nozzle exits, measure the incident radiative heat flux to the heat shield and thrust cone and determine the heating rates to the inoperative center engine nozzle. The results obtained from these tests are presented and discussed in the following sections.

5.12.1   Effect of Disk on Thrust Cone Heating Rates

In an attempt to evaluate the causes of thrust cone heating, a 19 inch disk was installed at Station 5 as shown in Figures 5.12.1-1 and 5.12.1-2. Heating rates to the thrust cone and heat shield were measured. The resulting thrust cone heating rates are shown in Figure 5.12.1-3. It is seen that, except for gage Q22, at model radius 3.92 inches, the disk causes a considerable reduction of the thrust cone heating rates, the heating rates being from 1/2 to 1/3 the nominal values. Considering the reverse flow pattern in the base region it is difficult to see why the heating rates would increase at Q22 in the presence of the disk; consequently, the validity of the Q22 measurement is questionable.

These thrust cone heating rate data indicate that the flow impinging on the thrust cone arrives by two different paths. One path consists of the flow expansion from the plume interaction regions and impinging directly onto the thrust cone. The second and longer path consists of the reverse flow portion which is deflected by the heat shield and turned by the expansion process at the edge of the heat shield to impinge on the thrust cone. Therefore, with the disk, the direct impingement flow path is eliminated and the thrust cone heating rates are considerably reduced.

Some heat shield heating rates were also measured with the disk installed. The results are shown in Figures 5.12.1-4, the constant heating rate contours, and Figure 5.12.1-5 where the corresponding nominal values are also shown for comparison. It is seen that the heat shield heating rates are practically unchanged by the presence of the disk, except for gage Q3 on the heat shield centerline and 3.3 inch radius where the heating rate increased from 4.0 to 5.5 BTU/ft^2-sec. Since the heat shield heating rates are practically unaffected by the presence of the disk, it appears that the flow reversed to the base heat shield originates from the portion of the plume interaction regions which lie within the engine pitch circle.
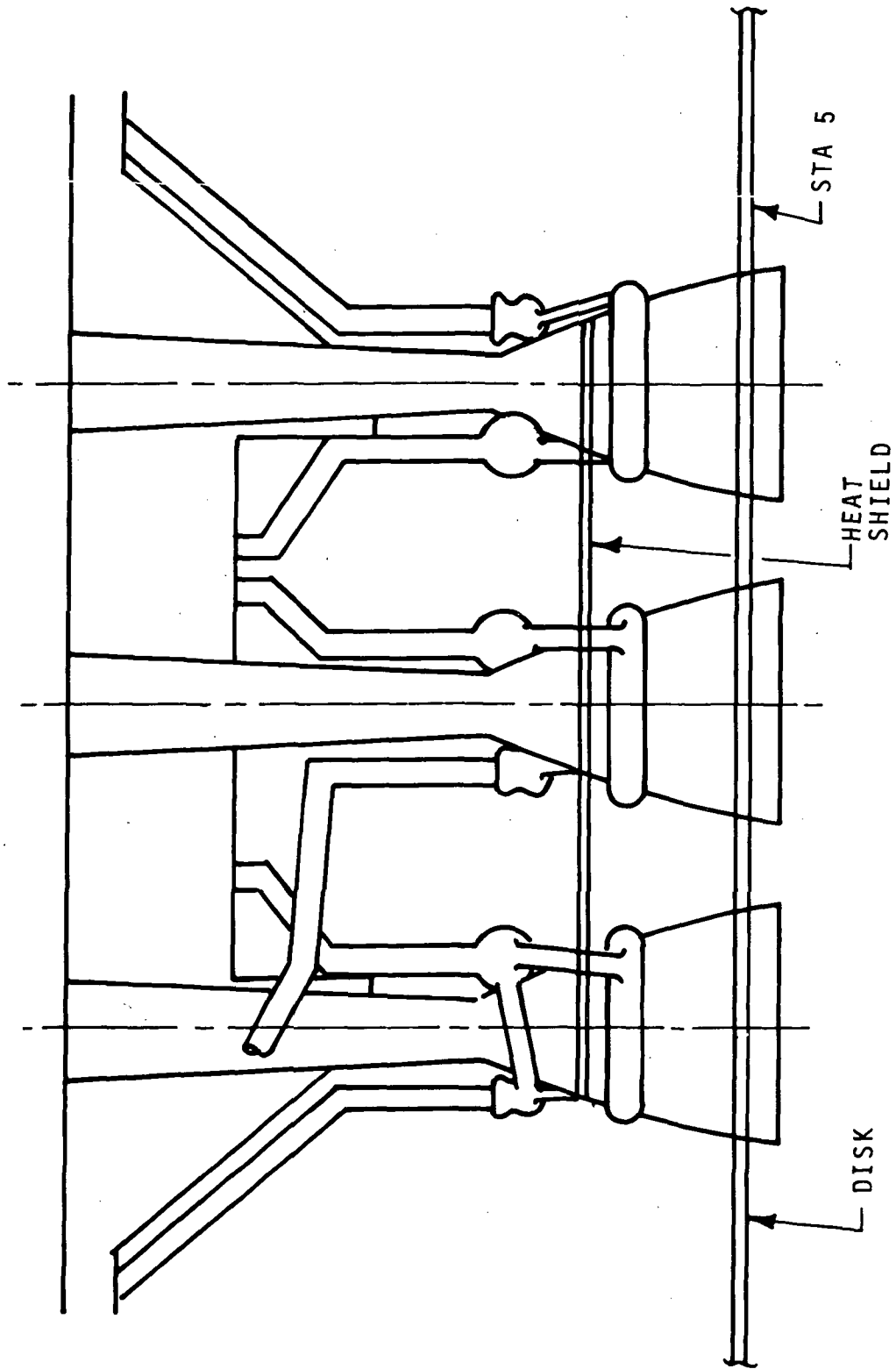
Figure 5.12.1-1 Side View Showing Disk in Position

SD73-SA-0061
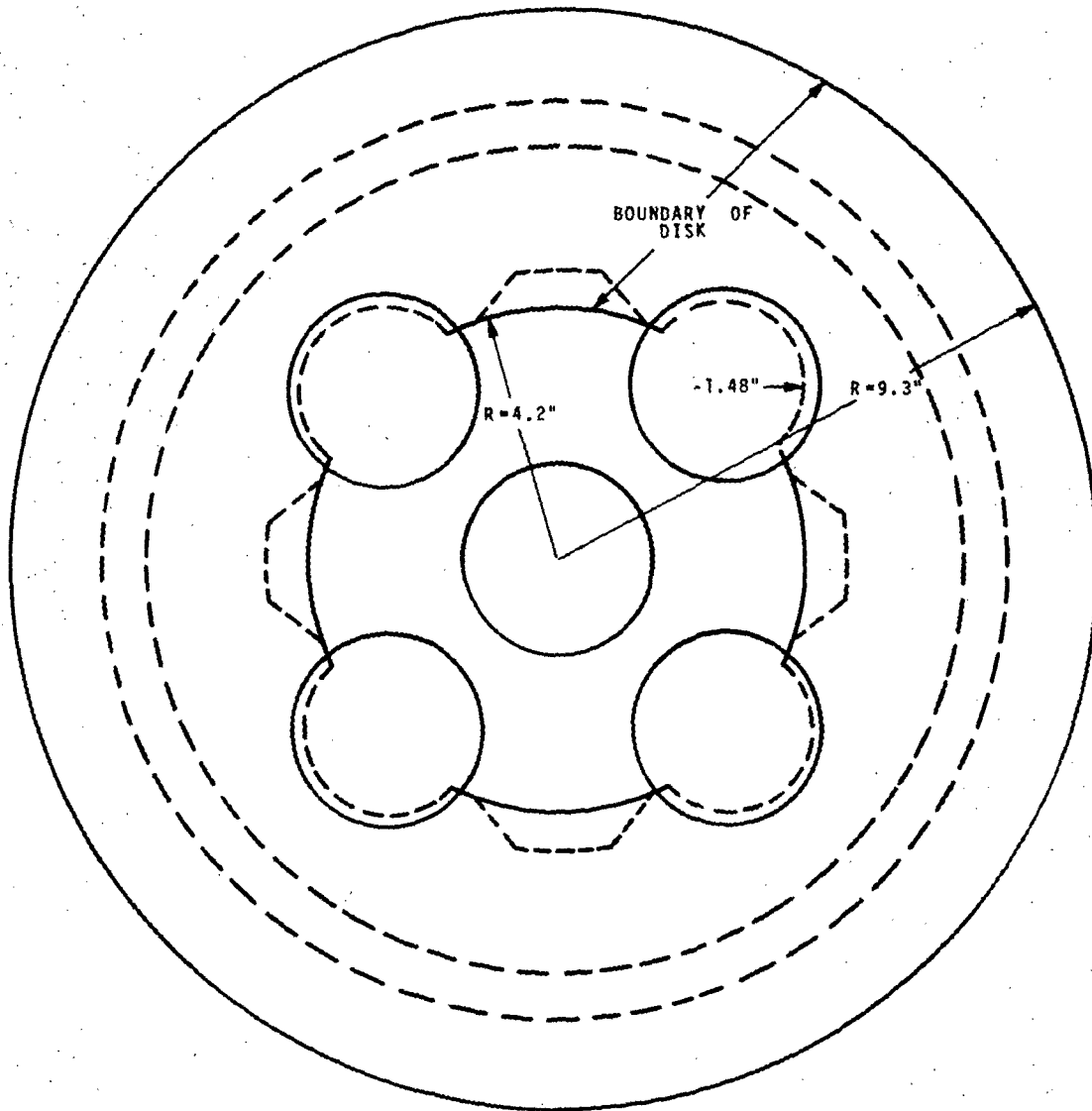
Figure 5.12.1-2   End View Showing Disk in Position

SD73-SA-0061

NO DEFLECTION
INTERSTAGE OFF
O/F = 5.0
Pc = 632 PSIA

SYM	LOG
◊	1.1 & 1.2
	NOMINAL
O	C05
	WITH DISK
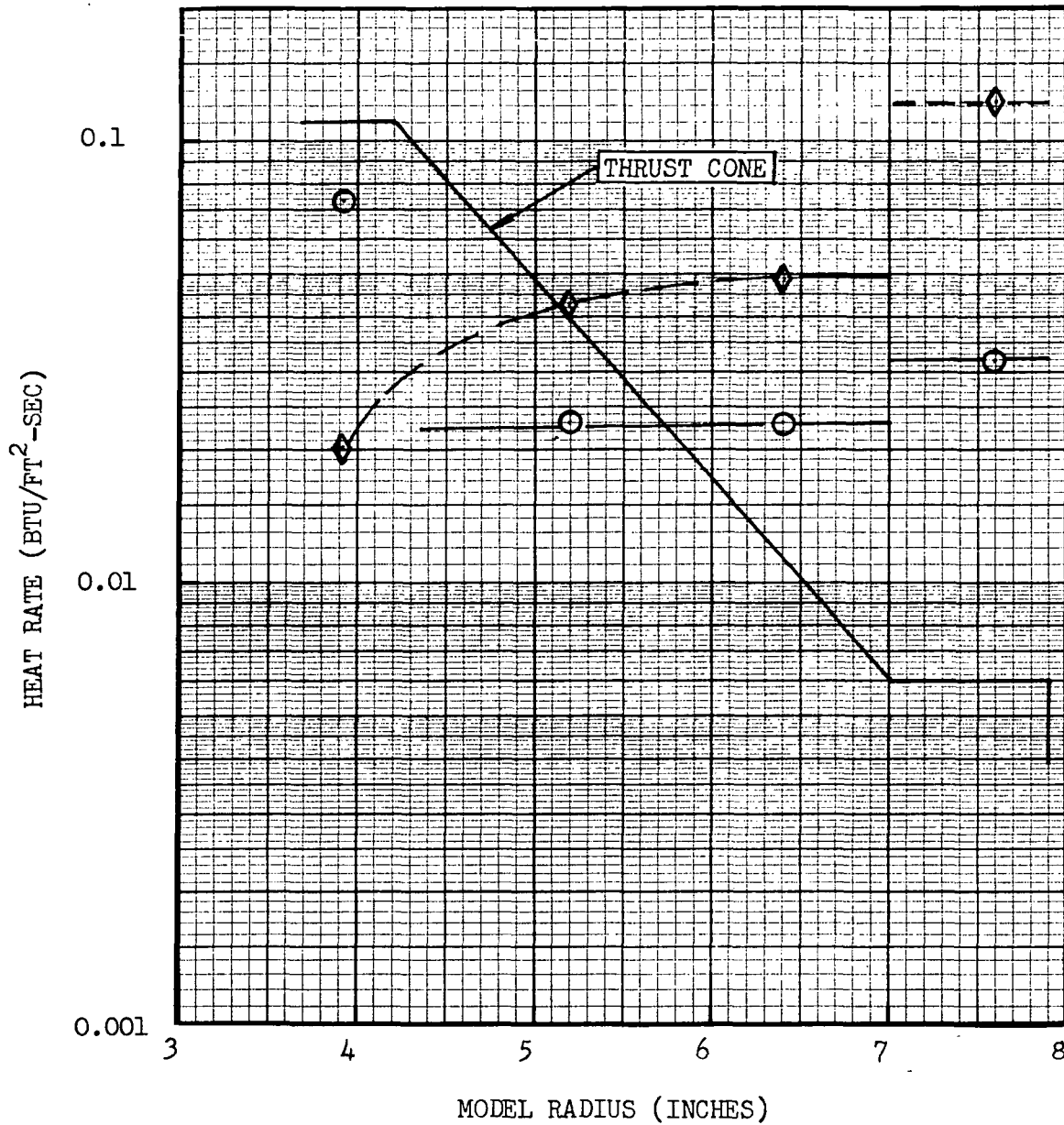
Figure 5.12.1-3 Effect of 19" Disk on Thrust Cone Heating Rates
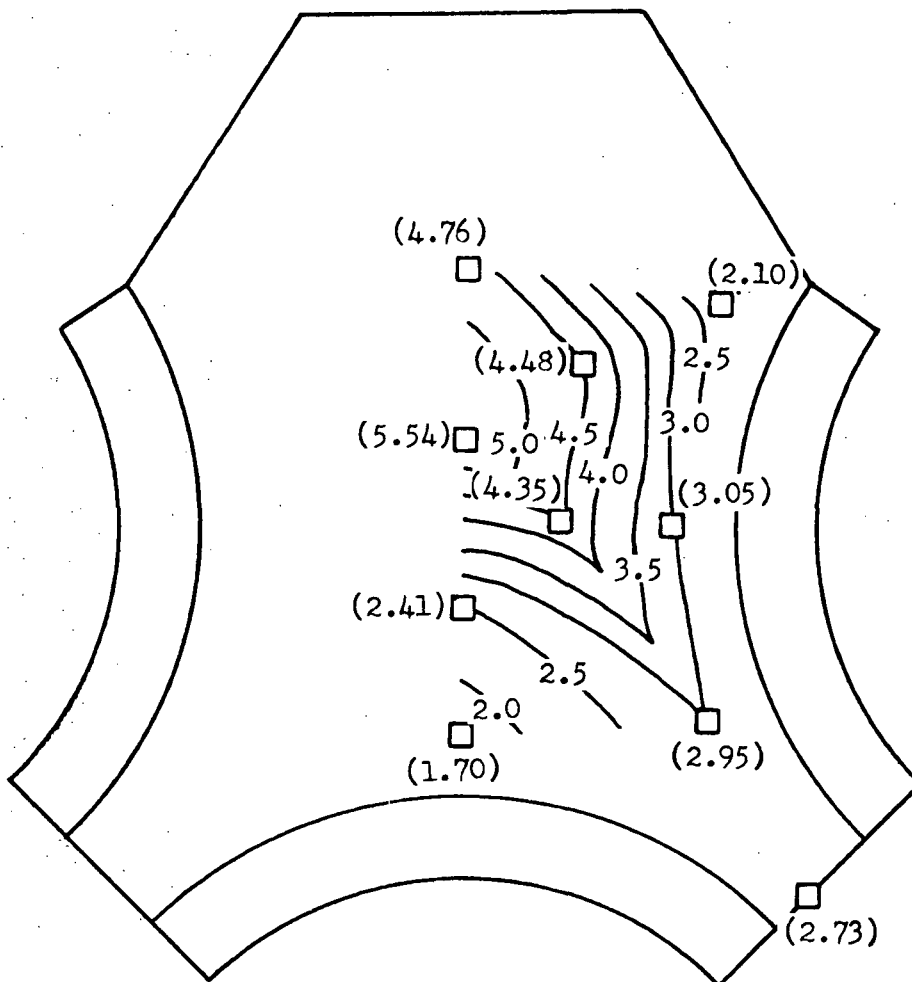
SD73-SA-0061

Figure 5.12.1-4 Heat Shield Heating Rates With 19 Inch Disk,
                 No Deflections, Interstage Off, O/F = 5.0

VARIATION ALONG HEAT SHIELD CENTERLINE

NO DEFLECTION
INTERSTAGE OFF
O/F = 5.0
Pc = 632 PSIA

SYM	LOG
O	CO5 (19" DISK)
□	1.1 & 1.2 (NOM.)

PERIPHERAL VARIATION AROUND ENGINE #1 AT R = 2.1 MODEL INCHES
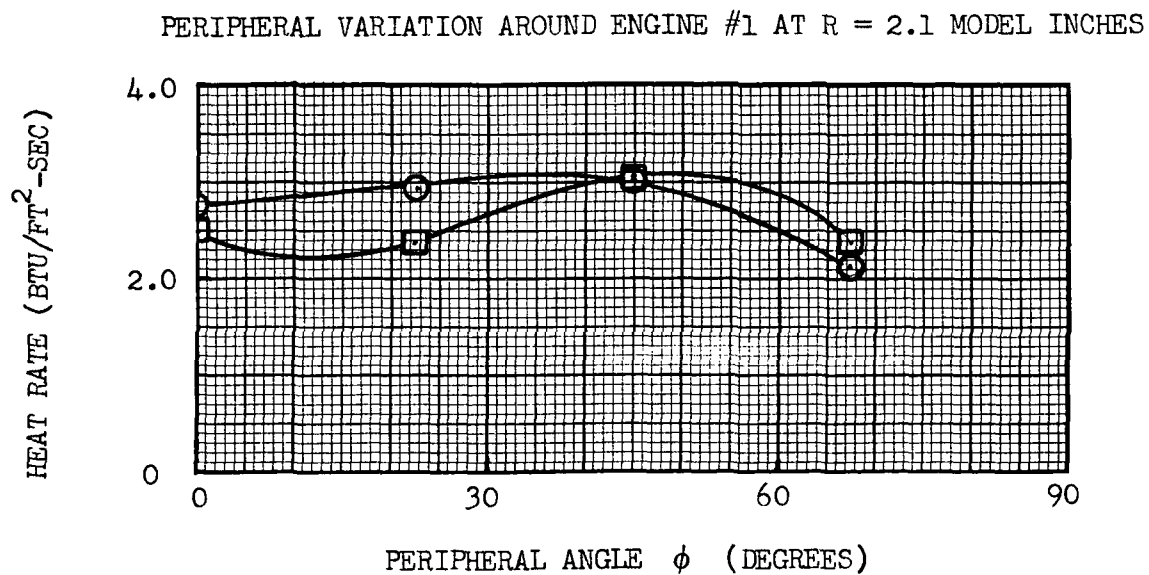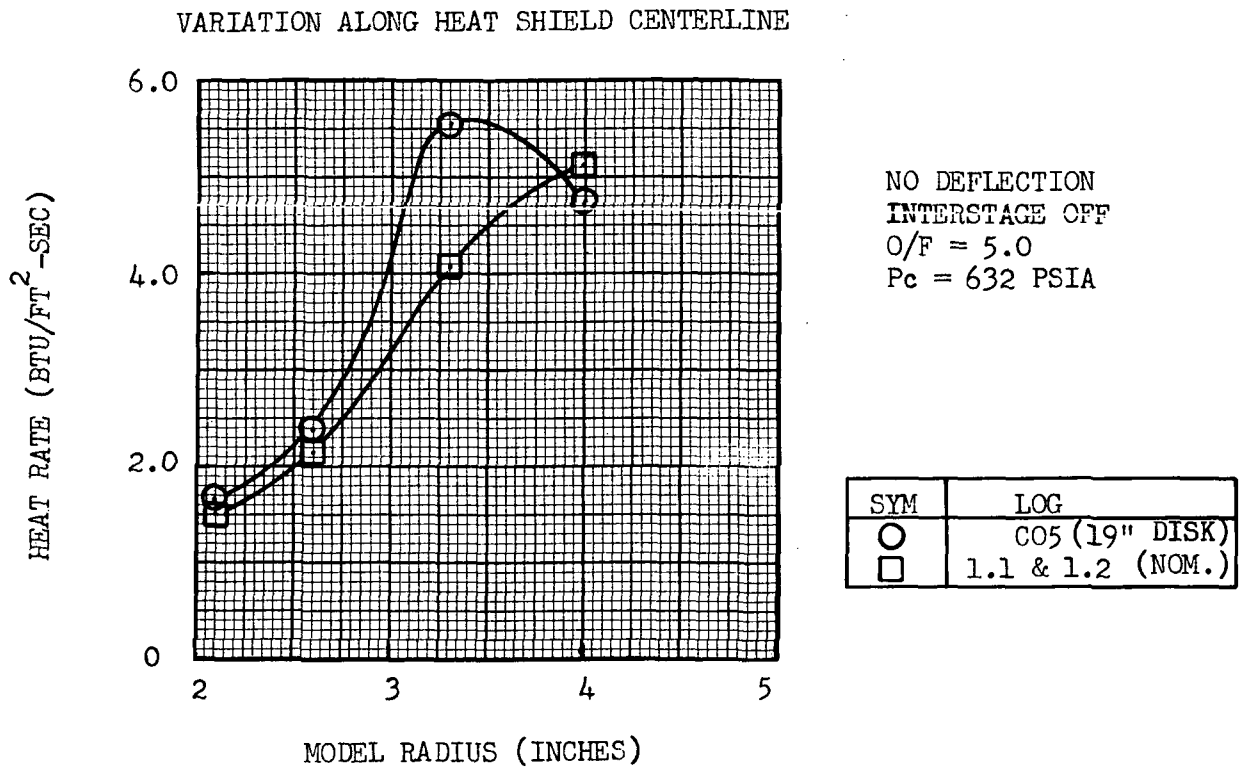
Figure 5.12.1-5 Effect of 19 Inch Disk on Heat Shield Heating Rates

SD73-SA-0061

5.12.2 Comparison of the Base Region Environments with the 210" and the 256" Configuration Heat Shields

The purpose of this test was to determine the effect of the 210" heat shield configuration on the thrust cone thermal environment. Both thrust cone and heat shield heating rates were measured.

Leakage of the nozzle adapters occurred during the test runs which rendered the thrust cone data to be of doubtful validity; the results indicating lower thrust cone heating rates with the 210 inch heat shield than with the 256 inch heat shield, which is opposite to the results obtained in Reference 8.

The 210 inch heat shield heating rate distribution is shown in Figure 5.12.2-1. A comparison of the 210 inch and the nominal configuration 256 inch heat shield heating rates is presented in Figure 5.12.2-2. Also shown for comparison are the corresponding heat shield heating rates obtained in the CAL test program, Reference 8. The present test results indicate that the heating rates along the centerline of the 210 inch heat shield are significantly higher than the corresponding nominal configuration values. These results are opposite to those obtained in the CAL test program as shown in Figure 5.12.2-2, where the 210 inch heat shield heating rates were lower than the 256 inch heat shield values. Also, note the appreciable discrepancy shown in Figure 5.12.2-2 between the present test and the CAL test heating rates along the heat shield centerline of the 210 inch heat shield.

One would expect that the shape and dimensions of the heat shield would not affect the heat shield heating rates except near the edge of the heat shield. In view of this and the large discrepancy between the heating rate results of the CAL test program and the present program for the 210 inch heat shield, the 210 inch heating rates along the heat shield centerline appear to be of questionable validity.

5.12.3 Base Region Environment with S-IV Type Heat Shield

Heat shield and thrust cone heating rates were measured with the S-IV type heat shield shown in Figure 5.12.3-1. The primary purpose of this test was to determine the thrust cone environment for this configuration.

The S-IV type heat shield heating rates are shown in Figure 5.12.3-2 and Figure 5.12.3-3 where the nominal configuration heating rates are also shown for comparison. From Figure 5.12.3-3 it is seen that the S-IV type heat shield heating rates are comparable to the nominal configuration values with some reduction at large radial values from the center engine.

A comparison of the thrust cone heating rates with the S-IV type heat shield and the 256 inch heat shield nominal configuration is shown in Figure 5.12.3-4. It is seen that there is an appreciable reduction of the heating rates with the larger diameter S-IV type heat shield; the peak heating rate is reduced 35% from the nominal value.

SD73-SA-0061
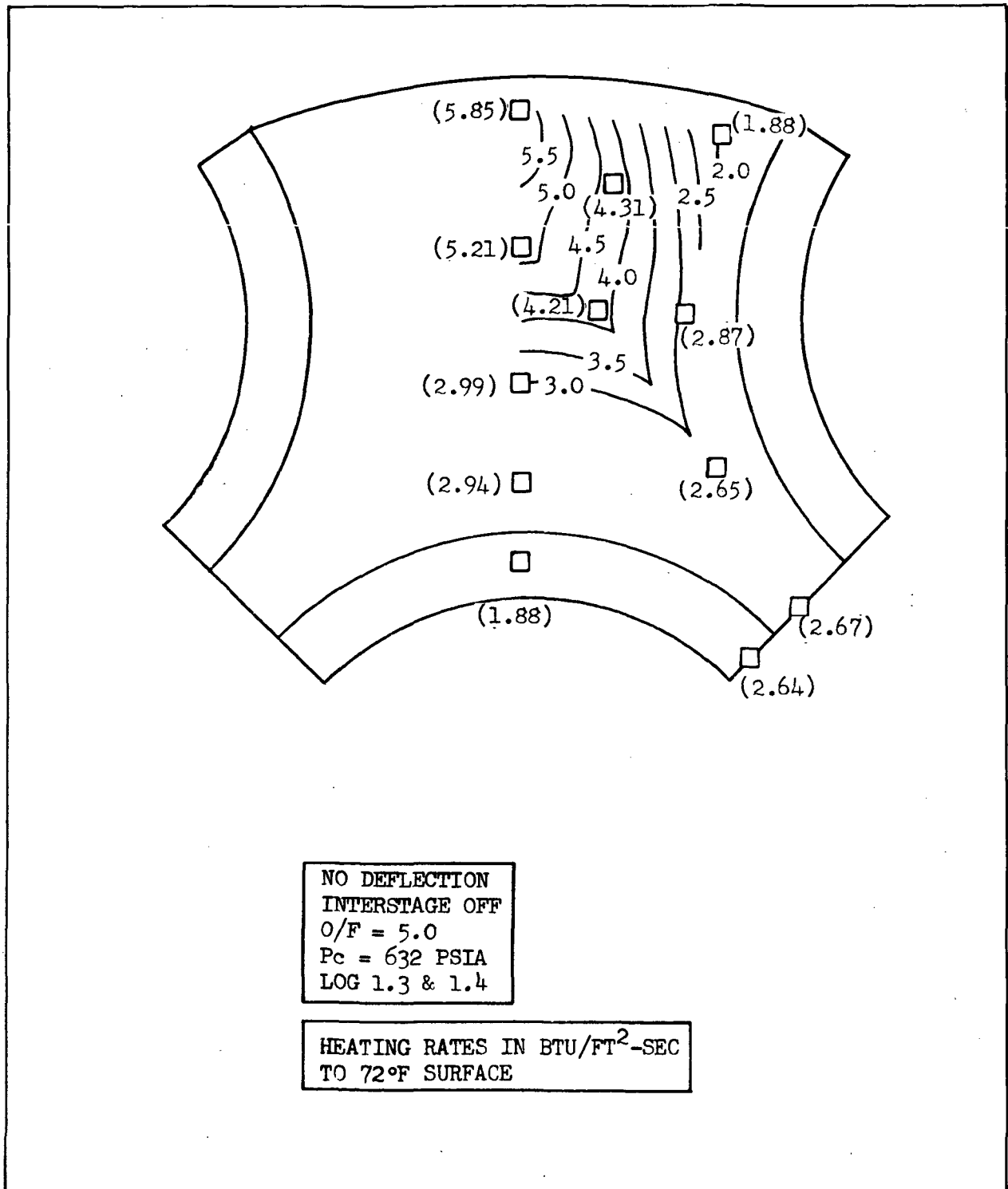
Figure 5.12.2-1 Heat Shield Heating Rates (210 Inch Heat Shield)
No Deflections, Interstage Off, O/F = 5.0

VARIATION ALONG HEAT SHIELD CENTERLINE

O/F = 5.0
Pc = 632 PSIA
INTERSTAGE OFF

SYM	LOG	HEAT SHIELD
O	1.1 & 1.2	256"
●	REF 8	256"
□	1.1 & 1.2	210"
■	REF 8	210"

HEAT RATE (BTU/FT²-SEC)

MODEL RADIUS (INCHES)

PERIPHERAL VARIATION AROUND ENGINE #1 AT R = 2.1 MODEL INCHES

HEAT RATE (BTU/FT²-SEC)

PERIPHERAL ANGLE ϕ (DEGREES)
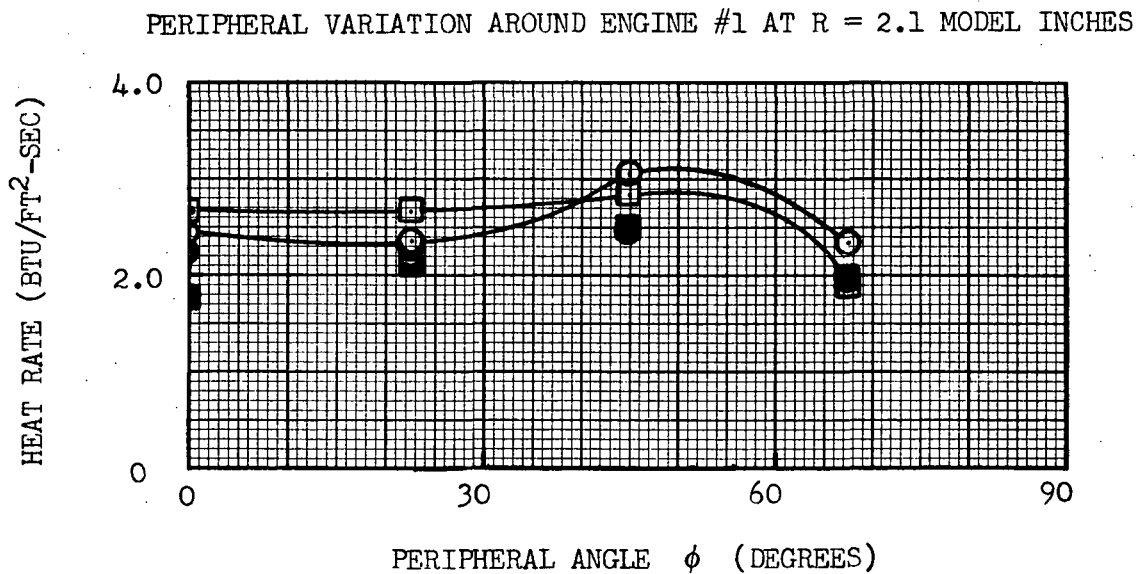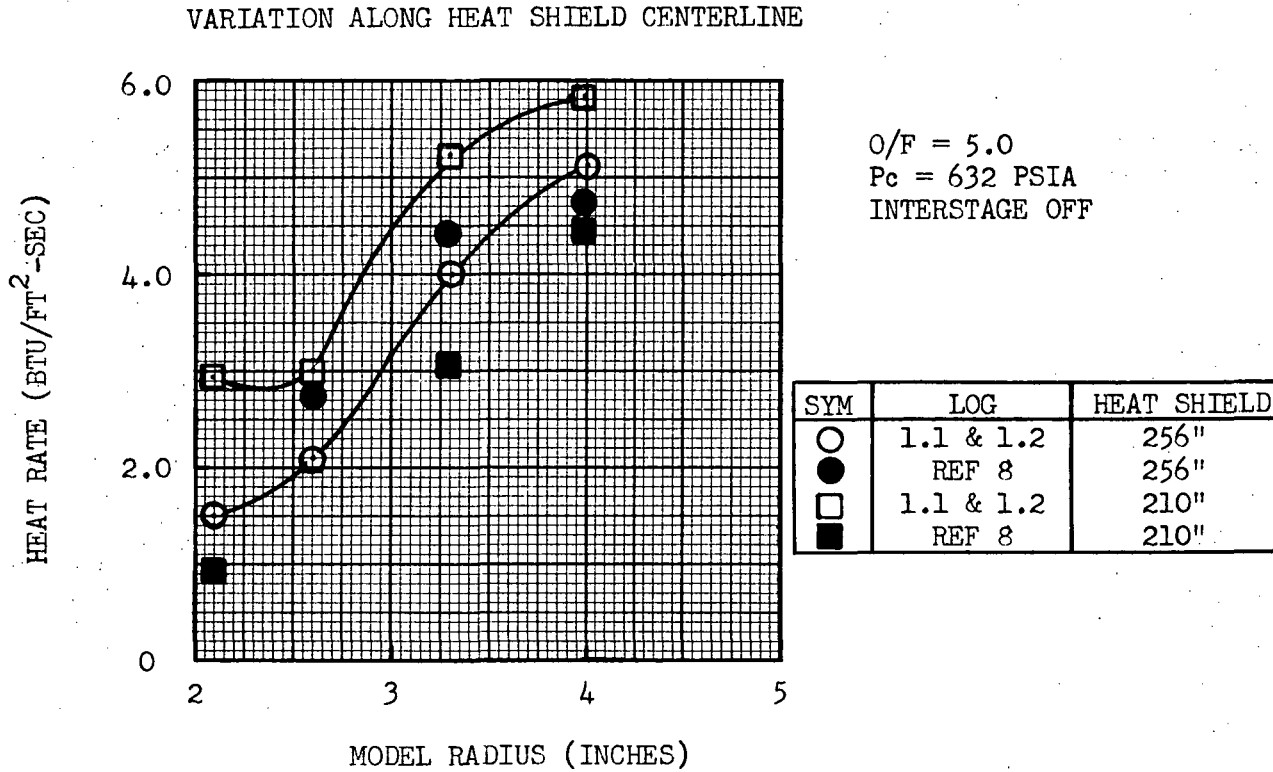
Figure 5.12.2-2 Comparison of 210 Inch and Nominal Heat Shield
Heating Rates

SD73-SA-0061
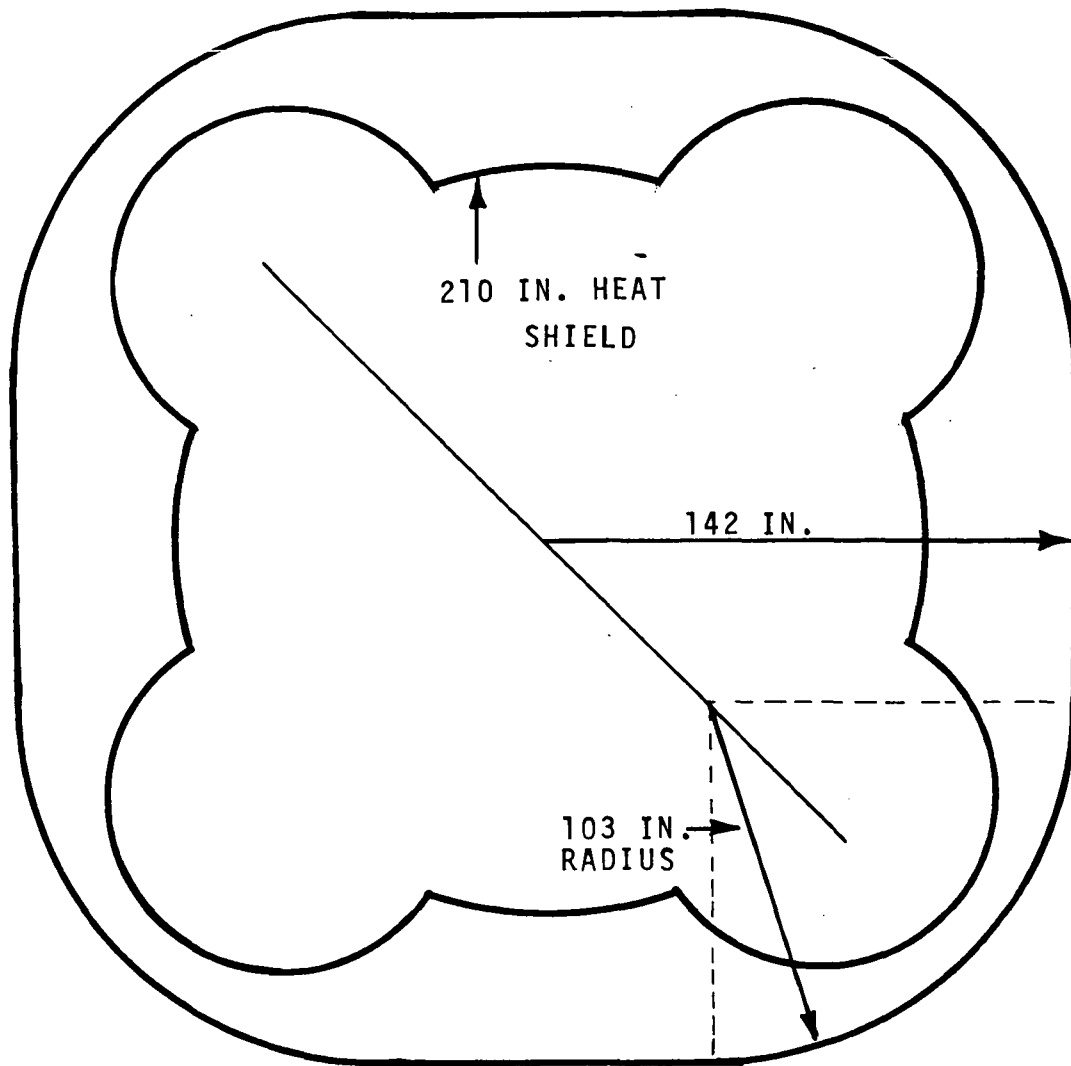
Figure 5.12.3-1   End View of Simulated S-IV Heat Shield
at Station 44

210 IN. HEAT
SHIELD

142 IN.

103 IN.
RADIUS

SD73-SA-0061
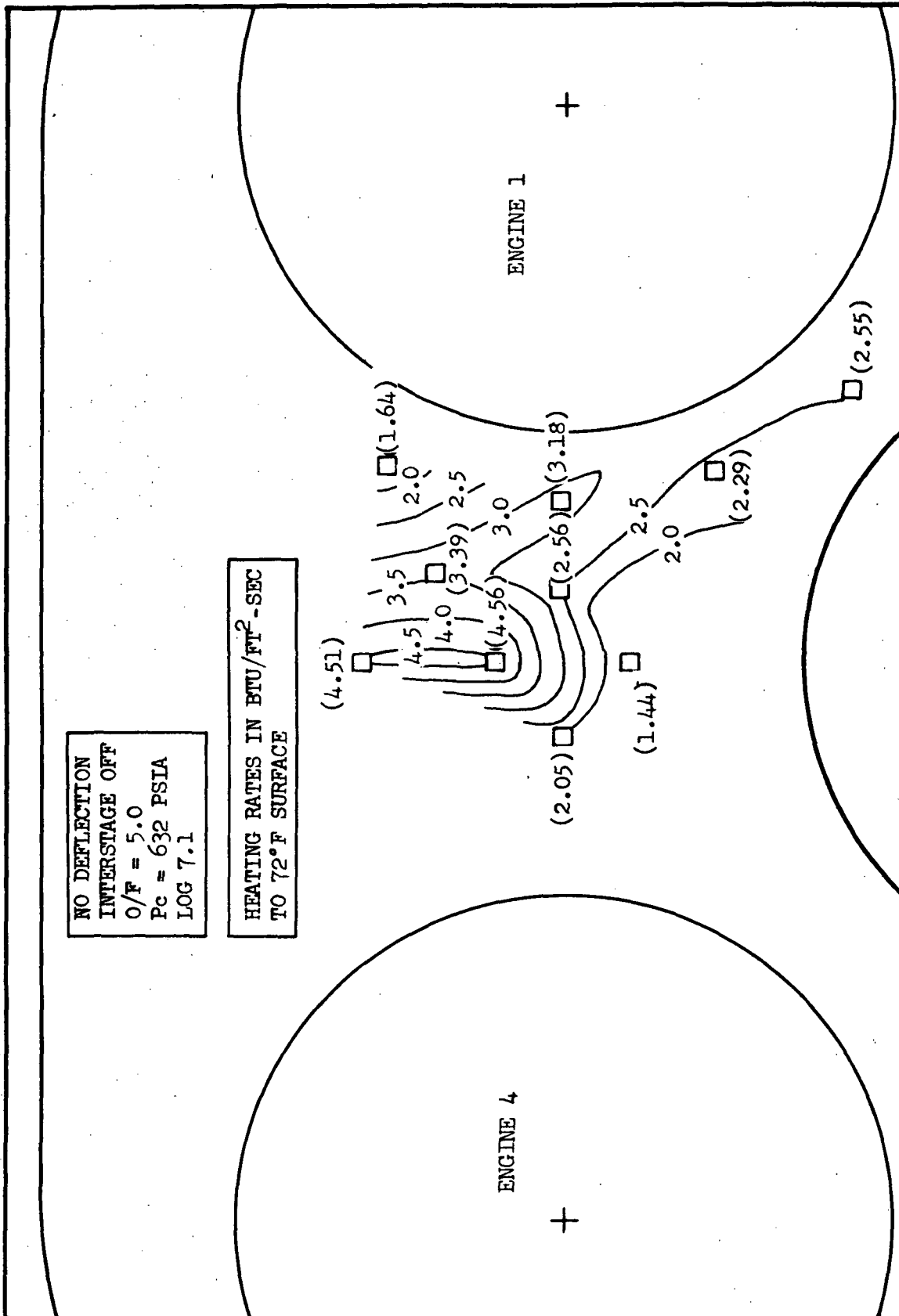
Figure 5.12.3-2 Heat Shield Heating Rates (S-IV Type Heat Shield)
No Deflections, Interstage Off, O/F = 5.0

VARIATION ALONG HEAT SHIELD CENTERLINE

NO DEFLECTION
INTERSTAGE OFF
O/F = 5.0
Pc = 632 PSIA

SYM	LOG
O	1.1 & 1.2 (NOM.)
□	7.1 (S-IV TYPE)

PERIPHERAL VARIATION AROUND ENGINE #1 AT R = 2.1 MODEL INCHES
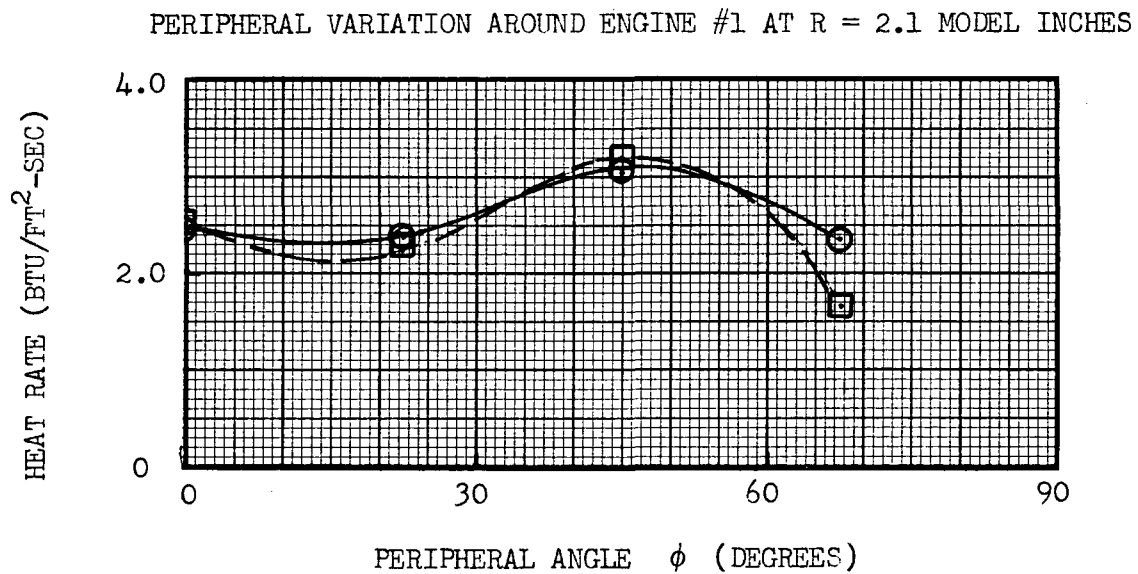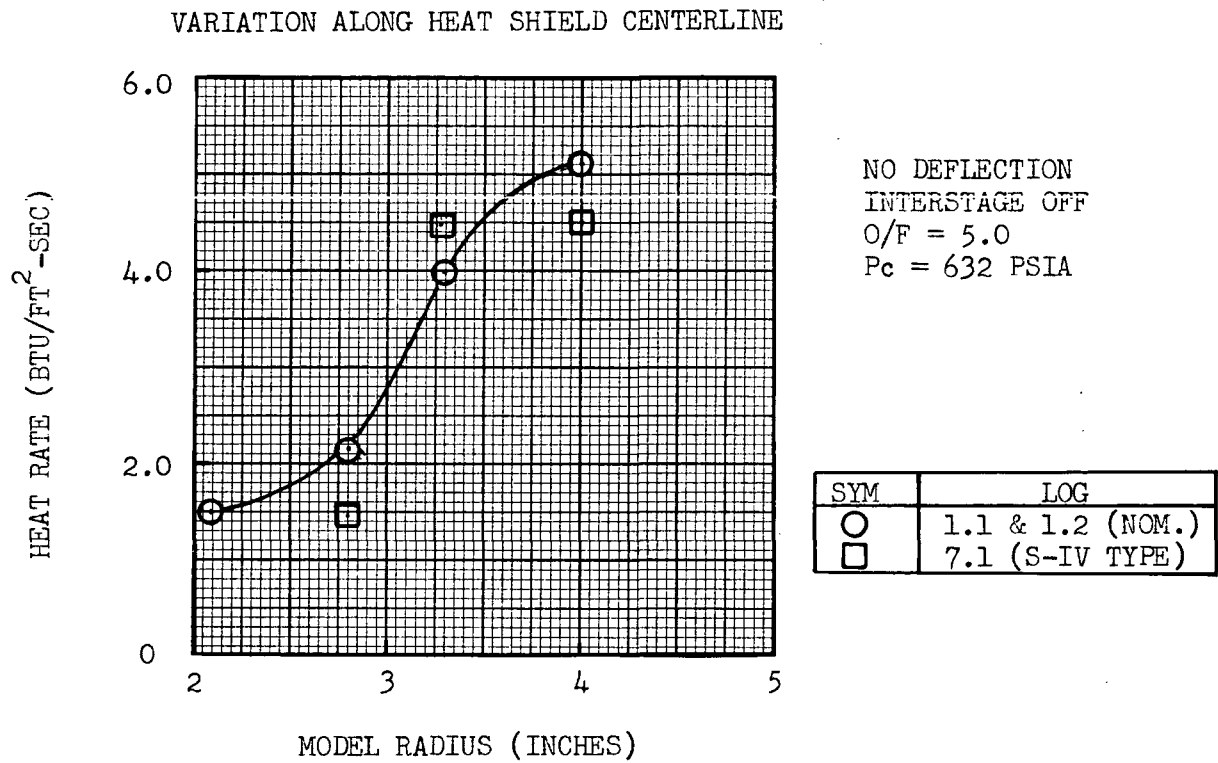
Figure 5.12.3-3 Comparison of S-IV Type and Nominal Heat Shield
Heating Rates

SD73-SA-0061

NO DEFLECTION
INTERSTAGE OFF
O/F = 5.0
Pc = 632 PSIA

SYM	LOG
◇	1.1 & 1.2 NOMINAL
◯	7.1 S-IV TYPE

HEAT RATE (BTU/FT²-SEC)

MODEL RADIUS (INCHES)
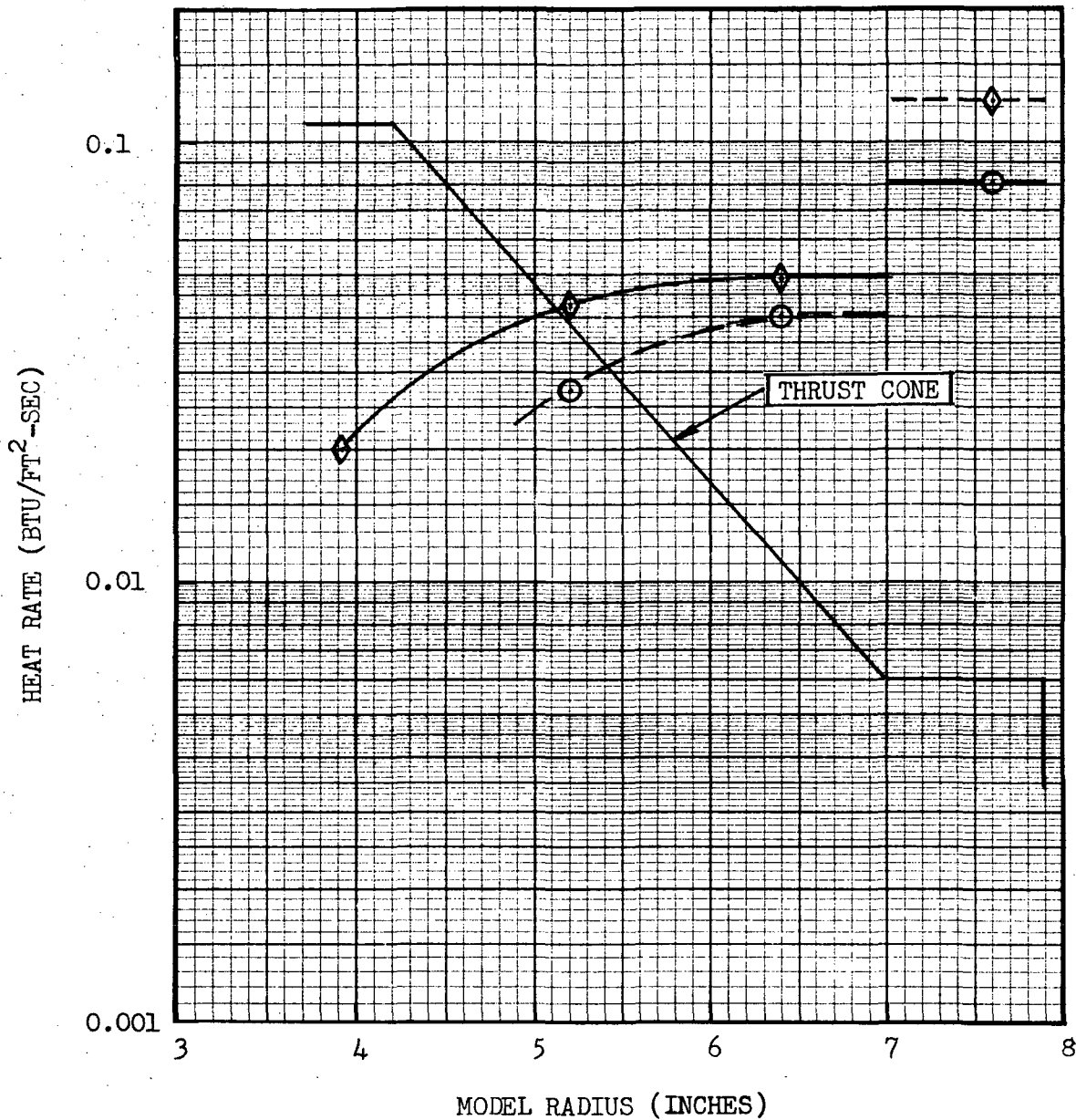
THRUST CONE

Figure 5.12.3-4 Thrust Cone Heating Rates with S-IV Type Heat Shield

SD73-SA-0061

5.12.4 Determination of Pressures Within the Pitch Circle

Pressures were measured in the plane of the nozzle exits between engines 2, 3, and 5 by means of the static and stagnation pressure probe arrangement shown in Figure 5.12.4-1. The results are recorded in data Logs 8.1 and 8.2. The average stagnation probe pressure recorded was 0.099 psia and the average static-probe pressure was 0.061 psia. The three engine test results of Reference 6 show that the flow in this region is supersonic. Consequently, both the static and stagnation pressure probes in this case measured pressures downstream of the bow shock formed ahead of the probe.

5.12.5 Effect of Boundary Layer Bleed on the Base Region Environment

The effect of nozzle boundary layer on the base region thermal environment was studied by using the evacuated TPE gas injection manifold and injection slots (see Figure 3.3-3) to bleed off the nozzle boundary layer during the model test firing.

The heat shield heating rate distribution corresponding to the test runs with nozzle boundary layer bleed is presented in Figure 5.12.5-1.

A comparison with the nominal heat shield heating rates is shown in Figure 5.12.5-2. It is seen that the heating rates with boundary layer bleed are lower than the nominal values; the peak heating rate being reduced by approximately 14%. These results are contrary to those expected from the analytical considerations of the reverse flow phenomena, i.e., one would expect that reducing the nozzle boundary layer thickness would increase the reversed gas average stagnation temperature and hence increase the base region heating rates.

Heat shield pressures along the heat shield centerline are shown in Figure 5.12.5-3 for the test conditions with and without nozzle boundary layer bleed. It is seen that boundary layer bleed has no effect on the heat shield pressures.

Finally, thrust cone heating rates at $\theta = 0°$ with boundary layer bleed are shown in Figure 5.12.5-4 together with the corresponding nominal values for comparison. It is seen that boundary layer bleed causes an increase of the thrust cone heating rates for model radii greater than 5.2 inches. The peak heating rate is increased 18% above the nominal value.

5.12.6 Nozzle Flow Symmetry Test

In order to test for flow symmetry within the nozzles, the nozzles were instrumented with pressure and heat transfer gages as shown in Figure 5.12.6-1. The test results are recorded in data Logs C04.1 and C04.3 and summarized in Table 5.12.6-1. It is seen that the nozzle pressures are very uniform with peripheral location within a nozzle and from nozzle to nozzle. The standard deviation of the mean is 3.6% for the pressure measurements.

Rev July 6, 1973

STAGNATION PRESSURE PROBE

STATIC PITOT PROBE

SPOOLIE

TRANSDUCER

SPRING MOUNT

PLASTIC TUBE

INSERT ADAPTABLE TO INCREASE HEIGHT

BASE INSERT

LEADS
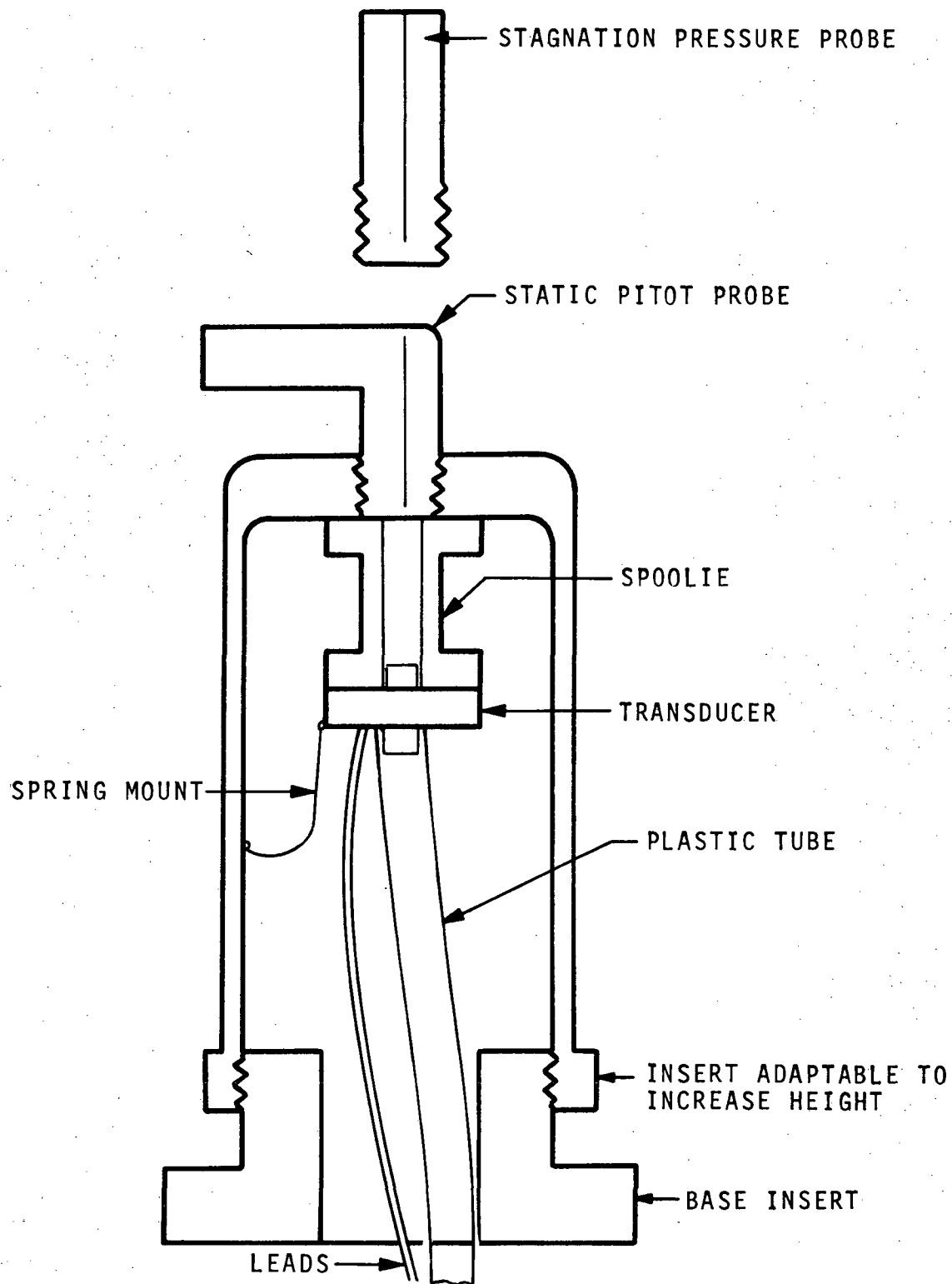
Figure 5.12.4-1   Schematic of Pressure Probe

NO DEFLECTION
INTERSTAGE OFF
O/F = 5.0
Pc = 632 PSIA
LOG 9.1.1

HEATING RATES IN BTU/FT^2-SEC
TO 72°F SURFACE
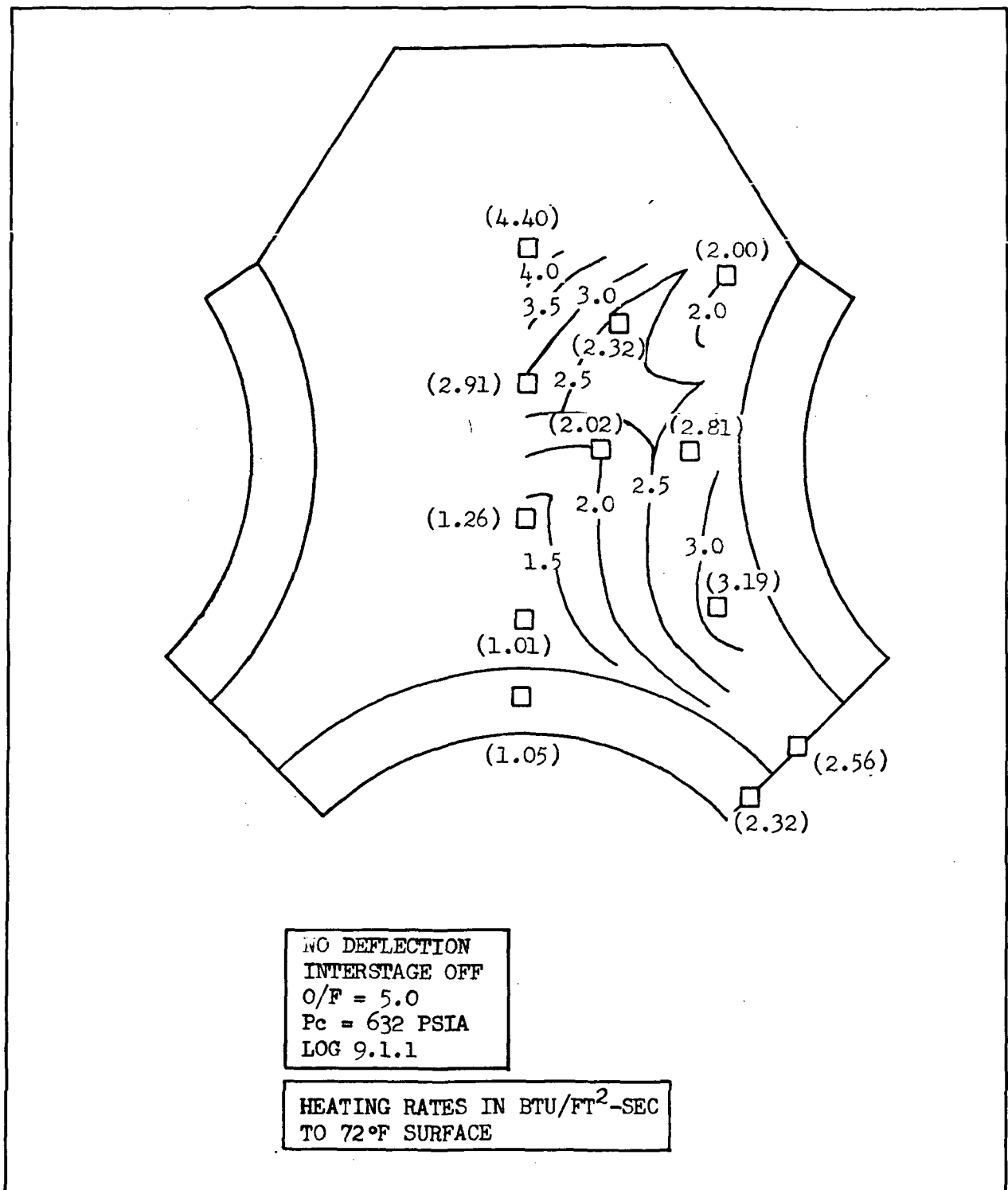
Figure 5.12.5-1   Heat Shield Heating Rates With Boundary Layer Bleed,
No Deflections, Interstage Off, O/F = 5.0

VARIATION ALONG HEAT SHIELD CENTERLINE

NO DEFLECTION
INTERSTAGE OFF
O/F = 5.0
Pc = 632 PSIA

SYM	LOG
O	1.1 & 1.2 NOMINAL
□	9.1.1 & 9.1.2 WITH BLEED

PERIPHERAL VARIATION AROUND ENGINE #1 AT R = 2.1 MODEL INCHES
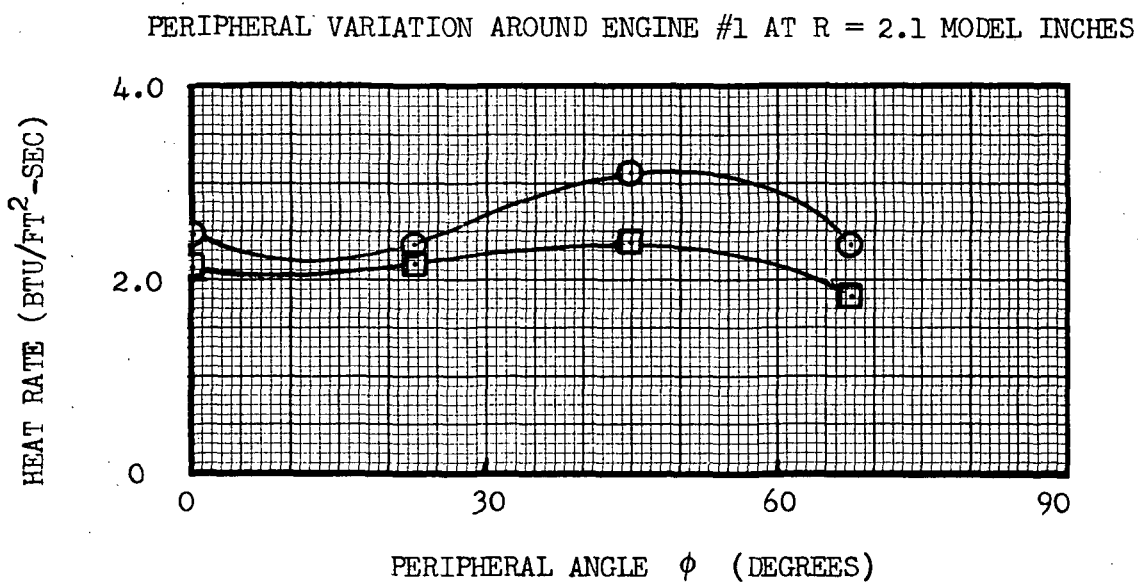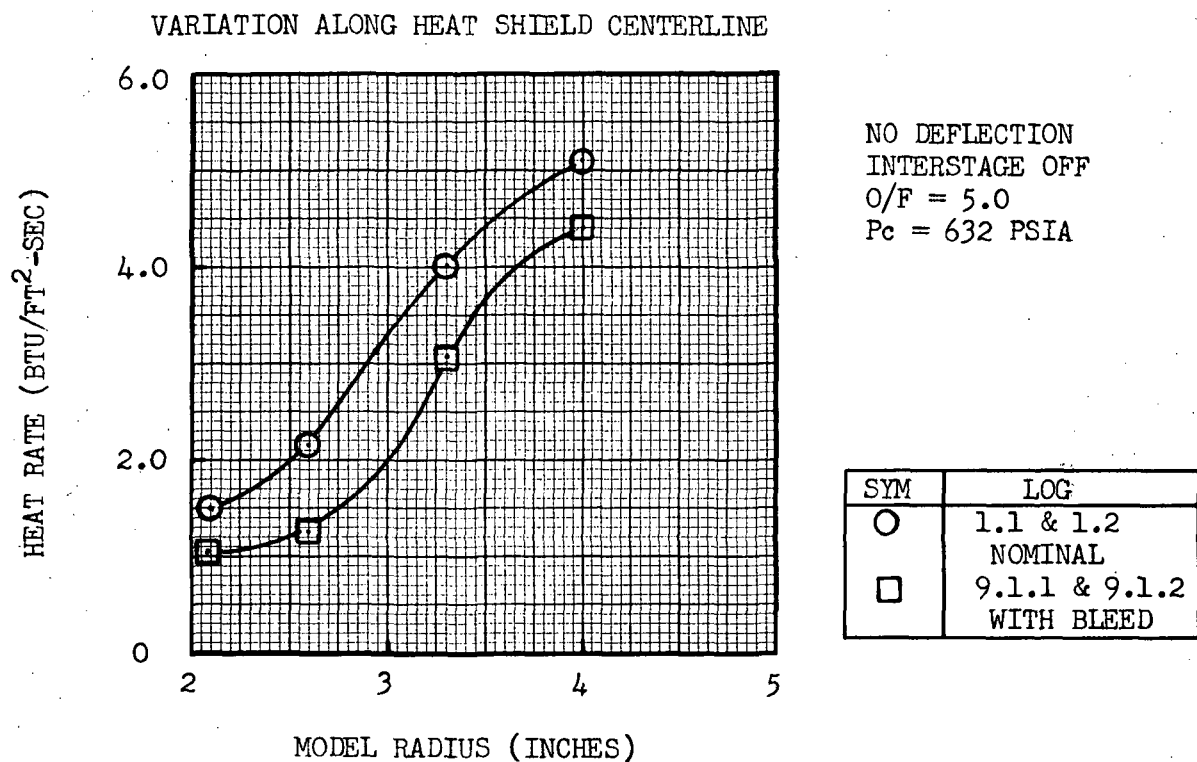
Figure 5.12.5-2 Effect of Nozzle Boundary Layer Bleed on Heat Shield
Heating Rates

SYM	LOG
◯	2.1 REDUCED TO 632 PSIA
☐	9.1.1 & 9.1.2
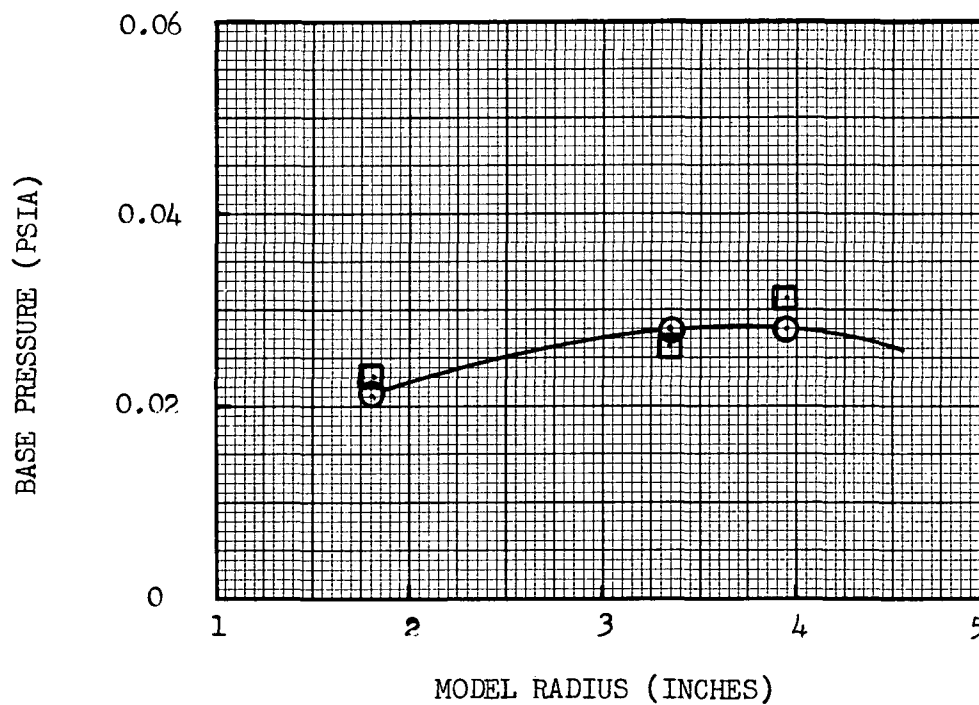
Figure 5.12.5-3 Effect of Nozzle Boundary Layer Bleed on
Heat Shield Pressures

SD73-SA-0061
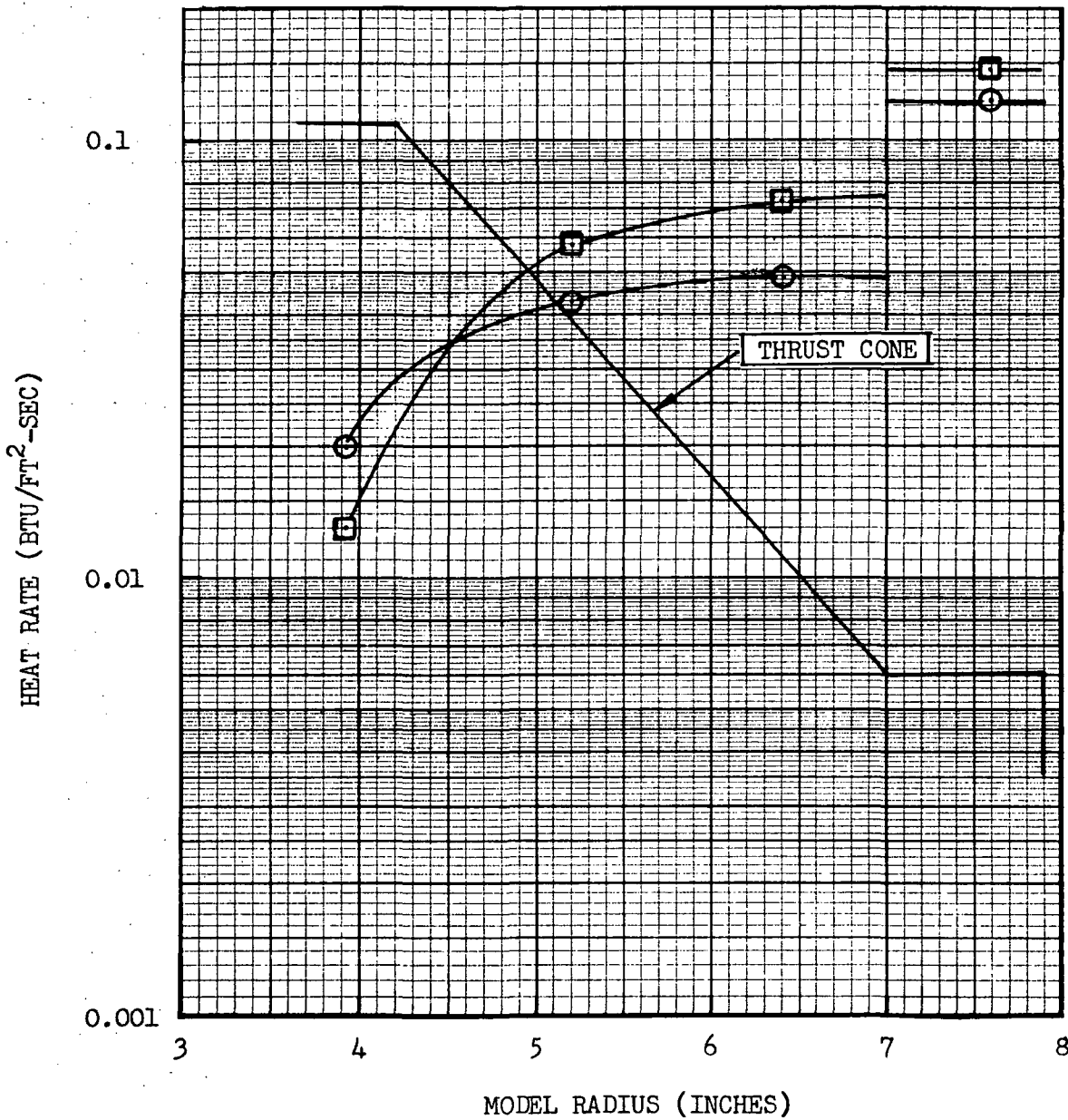
Figure 5.12.5-4 Effect of Nozzle Boundary Layer Bleed on Thrust Cone Heating Rates

SD73-SA-0061
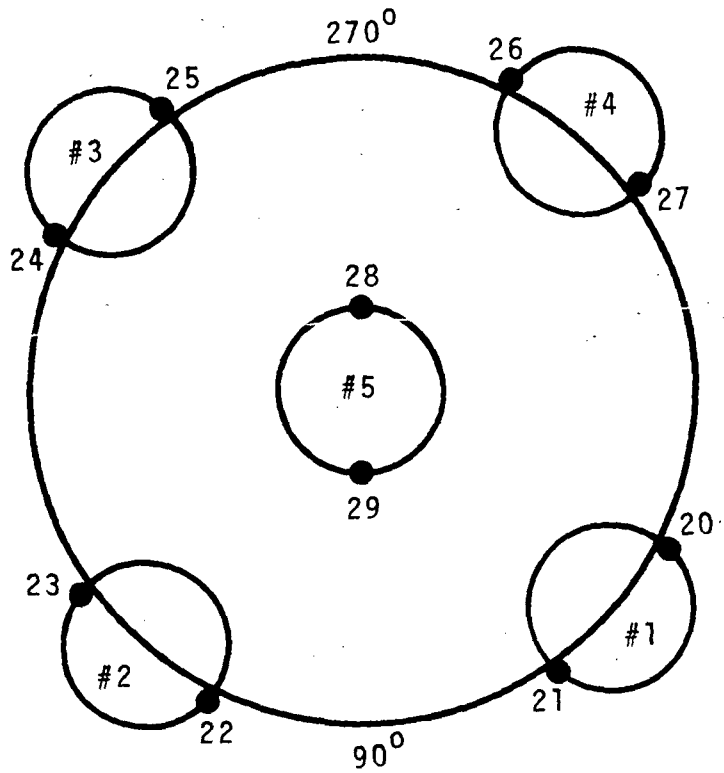
PRESSURE

HEAT TRANSFER
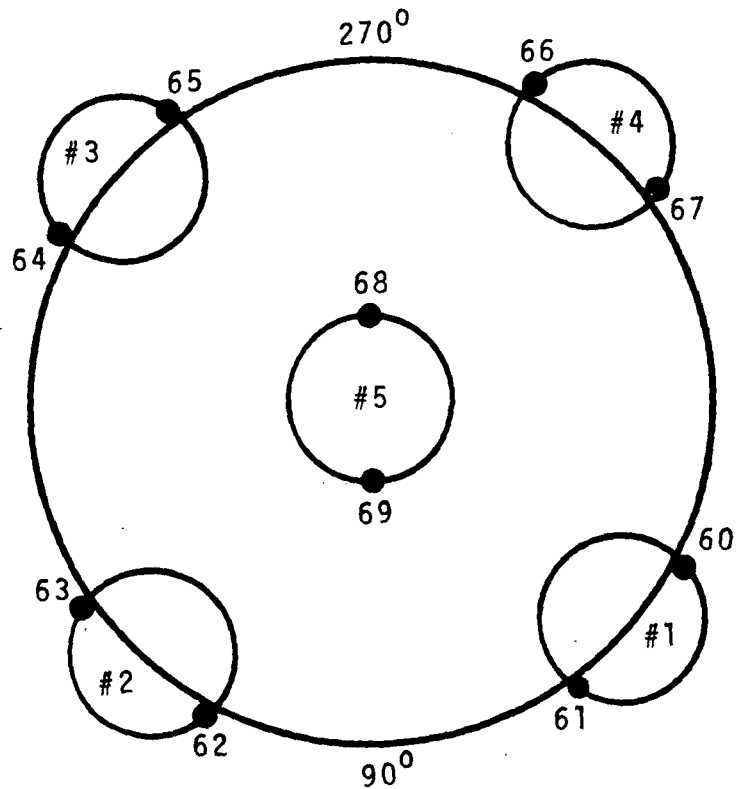
Figure 5.12.6-1 Nozzle Flow Symmetry Test Pressure and Heat Transfer Gage Locations

SD73-SA-0061

Table 5.12.6-1

Nozzle Flow Symmetry Results

ENGINE NUMBER	LOG	GAGE ID			
		P		Q	
		(Psia)		Btu/Ft^2 – Sec	
		P_{20}	P_{21}	Q_{60}	Q_{61}
1	C04.1	3.43	3.38	230	176
	C04.3	3.55	3.56	209	198
		P_{22}	P_{23}	Q_{62}	Q_{63}
2	C04.1	3.31	3.35	146	196
	C04.3	3.52	3.49	–	–
		P_{24}	P_{25}	Q_{64}	Q_{65}
3	C04.1	3.30	3.28	180	182
	C04.3	3.35	3.56	211	169
		P_{26}	P_{27}	Q_{66}	Q_{67}
4	C04.1	3.36	3.55	336	280
	C04.3	3.40	3.73	–	–
		P_{28}	P_{29}	Q_{68}	Q_{69}
5	C04.1	3.60	3.52	186	232
	C04.3	3.59	3.89	220	229

The heat transfer data, on the other hand, shows appreciable
variation with peripheral location and from run to run. The standard
deviation of the mean is 10% for the heat transfer measurements. This
illustrates the difficulty of obtaining consistent heat transfer
measurements.

Based on the nozzle pressure and heat transfer results, it appears
that the flow within the nozzles was symmetrical.

5.12.7 Environment of the Inoperative Center Engine Nozzles

Heating rates to the inoperative center engine nozzle are presented
in Figures 5.12.7-1 and 5.12.7-2. Comparison of these nozzle external
heating rates with the corresponding nominal values of Figure 5.6.4-1
shows that while the inoperative engine heating rate distribution is
changed from that for the nominal case, the peak external heating rate to
the center engine nozzle is comparable to the nominal value.

Inoperative center engine nozzle internal and lip heating rates are
shown in Figure 5.12.7-2. It is seen that the maximum nozzle internal
heating rate occurs near the lip and decreases rapidly with nozzle
station. The test average heating rate to the nozzle lip was 7.35
Btu/ft^2-sec at the peripheral location shown in Figure 5.12.7-2. Taking
into consideration the source of the reverse flow, i.e., the plume
interaction regions and the nominal heating rate distribution of the
center engine (Figure 5.6.4-1), the heating rates to the inoperative
center engine nozzle could be considerably higher than the measured value
at locations 45° peripherally from the gage N_5 location shown in
Figure 5.12.7-2.

5.12.8 Incident Radiative Heat Flux to the Base Region

Incident radiative heat flux from the model exhaust plumes to the
base region was measured during some of the test runs of this test program
by means of dual element thin film platinum strip gages. This type of
gage was first used in the CAL test program, Reference 8. The gage
consists of two strips of platinum fused to the upper and lower surfaces
of a quartz substrate in such a way that the strips are mutually
perpendicular. The upper strip senses both radiative and convective
heating, while the lower strip receives only radiative heating.

The total and radiative values recorded during various test runs are
presented in Table 5.12.8-1. It is seen that the measured values of
incident radiative heat to the heat shield for the various nominal trim
gimbal patterns is practically constant, while the two interstage-off
thrust cone measurements show a factor of 3 variation.
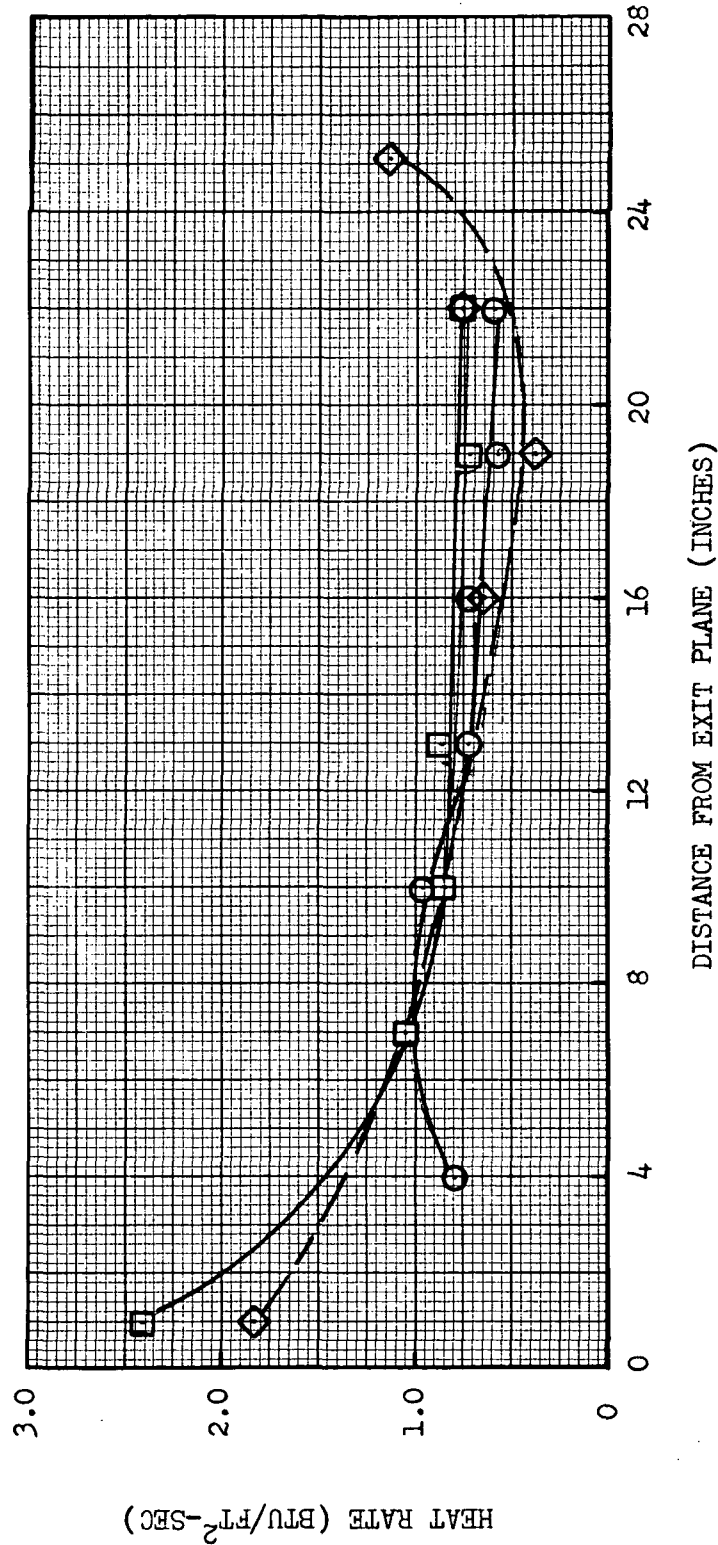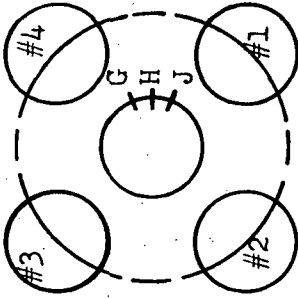
Figure 5.12.7-1 External Heating Rates to the Inoperative Center Engine Nozzle

SD73-SA-0061

N$_5$ (7.35)
NOZZLE LIP GAGE

#1

HEATING RATES IN
BTU/FT^2-SEC TO 72°F
SURFACE

6"

N$_3$ (5.90)

43"

N$_1$ (0.57)

N$_2$
(0.78)

NO DEFLECTIONS
O/F = 5.0
P$_c$ = 632 PSIA
LOG 4.1

SECTION AA
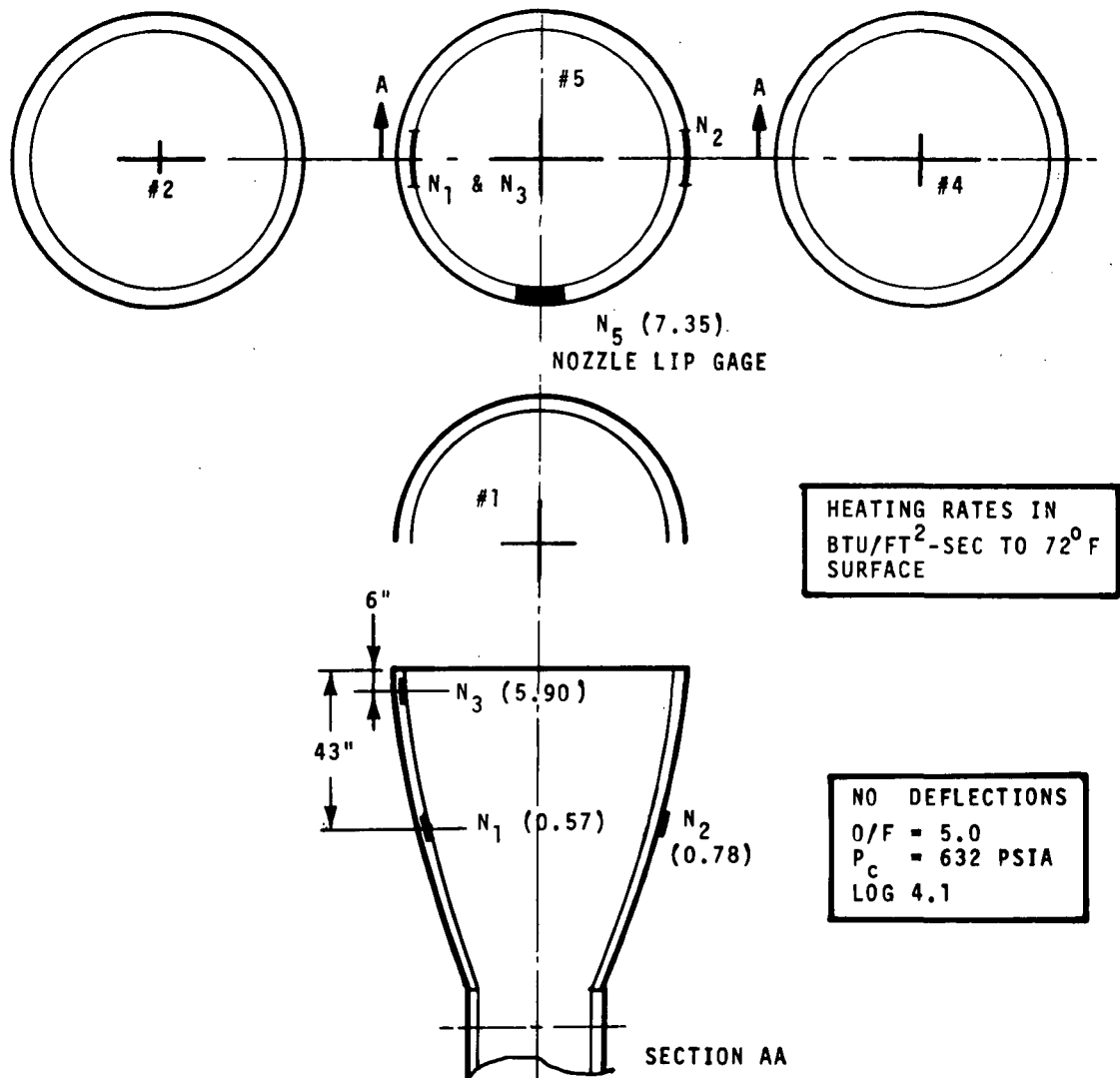
Figure 5.12.7-2   Heating Rates to the Inoperative
Center Engine

Table 5.12.8-1

Summary of Scale Model Base Region

Incident Radiative Heat Flux Measurements

LOG	O/F	Pc (psia)	Inter-Stage	Gimbal Pattern	Q24 (Thrust Cone) Btu/ft^2 - Sec		Q4 (Heat Shield) Btu/ft^2 - Sec	
					Total	Radiative	Total	Radiative
14.1.1A	5.0	632	OFF	-	0.075	0.020	-	-
16.3.1	5.5	715	ON	3C	0.676	0.017	-	-
19.1	5.0	632	OFF	9	-	-	7.11	0.042
19.2	5.0	632	OFF	9A	-	-	6.64	0.041
19.3	5.0	632	OFF	9B	-	-	6.95	0.040
24.1.1	5.5	715	OFF	-	0.113	0.006	-	-

NOTE: Radiative values are not corrected for transmissivity of the quartz or the absorptivity of the platinum strip gages.

Rev July 6, 1973

SD73-SA-0061

It should be noted that the radiative heating rates listed in Table 5.12.8-1 are not corrected for the transmissivity of the quartz or the absorptivity of the platinum strip gages. Since the quartz is opaque to radiation above 4.0 microns, approximately 23% (for effective plume interaction region temperature of 3500 R) of the incident radiation from the water vapor is cut-off by the quartz. Assuming the absorptivity of the platinum strips to be 0.3, then the model test gage indicated radiative heat rate of 0.04 Btu/ft^2-sec to the heat shield corresponds to an incident radiative heat flux of 0.17 Btu/ft^2-sec.

Analytical estimates of gaseous plume radiation scaling effects are reported in Reference 9. In Reference 9 it was analytically determined that, for a line of sight passing through the S-II stage engine exhaust plume interaction zones, the radiative intensity for a 1/25 scale model was 10% of the corresponding full scale value. Assuming this is true for all lines of sight, then one would expect the incident radiative heat flux to the 1/25 scale model heat shield to be approximately 0.1 Btu/ft-sec, compared with the 0.17 Btu/ft^2-sec model test indicated value.

6.0 COMPARISON WITH ANALYTICAL PREDICTIONS

6.1 METHODOLOGY OF BASE FLOW ANALYSIS

The objective of the analytical portion of this study is to predict, as completely as possible, the quantitative effects of the various factors influencing multiple-engine base flow. This involves the systematic evaluation of the history of the plume gases during their travel from nozzle to base heat shield.

The analysis breaks down into five parts:

1. Definition of the main (inviscid) nozzle flow field.

2. Definition of the properties of the nozzle boundary layer including the effects of film cooling by the injection of a gas whose composition differs from that of the primary flow.

3. Analysis of plume expansion including the non-uniform boundary flow at the nozzle lip.

4. Definition of the impingement flow fields resulting from plume interactions.

5. Description of the recirculating flow field, including pressure and heat transfer distributions on the base heat shield.

The analytical methods employed are believed to give realistic numerical solutions for the first three steps. Even for those, however, certain idealizations have been made: Full chemical and thermodynamic equilibruim is assumed throughout the nozzle and plume flow fields; tangential momentum of the injected coolant is not taken into account; flow in the expanding plume is considered to be inviscid even in the boundary; lastly, the pressure acting on the boundary is assumed to be uniform circumferentially. Nevertheless, the methods take into account the principal known influences on nozzle and plume flow.

The plume interaction zones dealt with in step 4 are complex, three-dimensional flow fields involving shocks, mixed supersonic and subsonic flow, and turbulent mixing. A complete evaluation is well beyond present analytical capabilties. Useful semi-quantitative information, however, has been obtained from a simplified analysis based on Newtonian flow applied in the plane containing the axes of interacting plumes.

The recirculating flow field to which the engine cluster and heat shield are exposed is also far too complex for exact analysis. Here no comparable simplified analysis has been devised but a qualitative picture of the magnitude and distribution of heat transfer rates has been obtained from the impingement analyses.

Analytical predictions have been made for six different combinations of chamber pressure and mixture ratio. Five of these correspond to the model tests and one to the full scale flight conditions. In addition, the effect of external pressure was considered in one of the model cases and both the presence and absence of turbopump exhaust (TPE) injection was evaluated for the full scale case. The cases are summarized in Table 6-1.

Table 6-1 Summary of Analytical Flow Field Predictions

Case No.	Scale	P_c (psia)	O/F	P_{amb} (psfa)	TPE Injection
I	1/25	300	5.0	0.075	No
II	1/25	450	5.0	0.075	No
III	1/25	546	4.5	0.075	No
IV	1/25	632	5.0	0.075	No
Va	1/25	715	5.5	0.075	No
Vb	1/25	715	5.5	0.250	No
Vc	1/25	715	5.5	0.750	No
VIa	Full	727.5	5.8	0.075	No
VIb	Full	727.5	5.8	0.075	Yes

6.1.1 Definition of the Inviscid Flow Field in the J-2 Nozzle

The inviscid flow field within the J-2 nozzle is required both to evaluate the edge conditions used in the computation of the internal boundary layer, and to provide a start line for the analysis of the plume flow field. The program chosen to evaluate the inviscid nozzle flow is a method-of-characteristics (MOC) program developed by Lockheed (Reference 14). This particular program takes into account non-isentropic effects due to the presence of internal shock waves. The nozzle solution is started from a transonic line located just downstream of the throat, along which flow properties are specified as the result of a transonic flow solution for the J-2 throat region.

The Lockheed program is limited to handling only one shock of the right-running family. However, the J-2 nozzle produces two shocks, as shown in Figure 6.1.1-1. One forms within the nozzle and reflects from the axis before reaching the exit plane. The other forms beyond the lip. At a point downstream of the exit plane, both the reflected internal shock and the lip shock will appear together and intersect. This region is excluded from solution by the limitations of the Lockheed program. Therefore, a complete plume startline running from the nozzle lip to the axis cannot be obtained without some approximations.
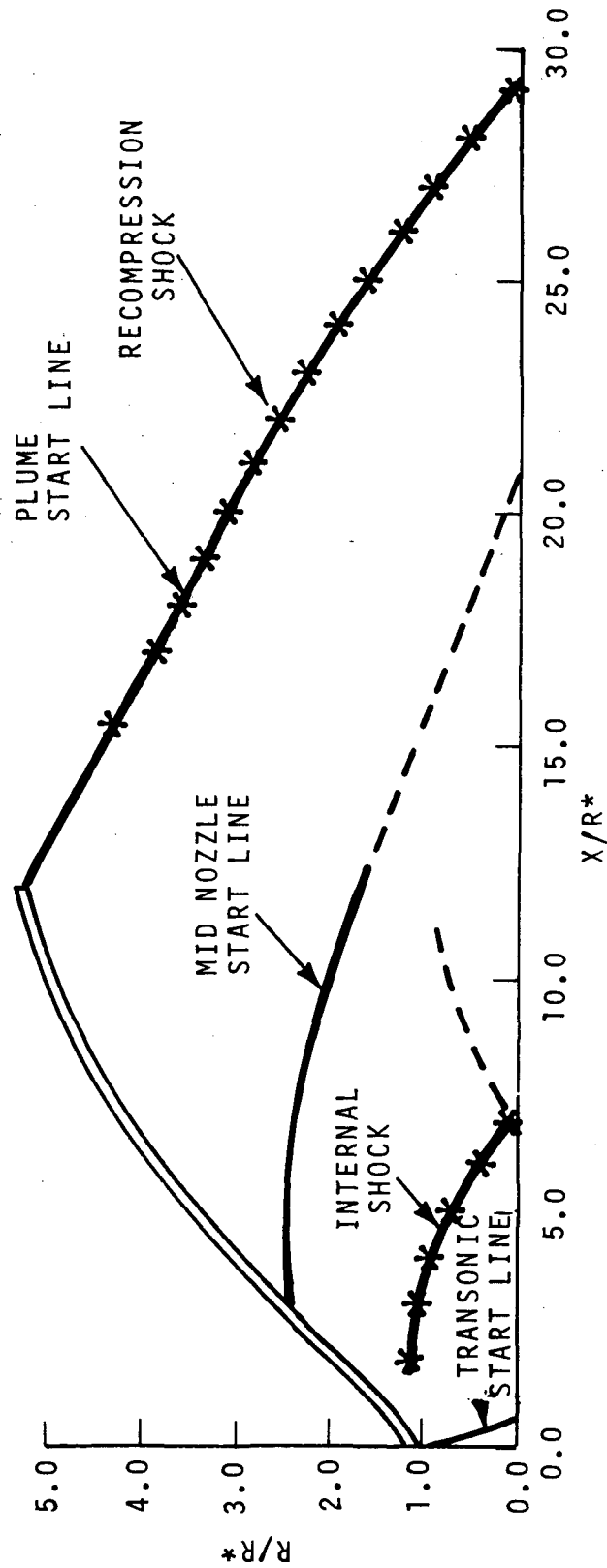
Figure 6.1.1-1 J-2 Nozzle Flow Field (Inviscid)

SD73-SA-0061

In the present work, nozzle flow was calculated by two successive applications of the MOC program. The first application stopped automatically when the internal shock intersected the axis. The solution was restarted from a new right-running line established in the following way: The last left-running characteristic (LRC) obtained prior to the intersection of the internal shock with the axis was followed outward until the local flow angle variation was reasonably uniform. This rather ill-defined point occurred at about 1.6 throat radii and bounded the inner 8% of the nozzle flow. The upstream portion of the new start line was established by tracing a right-running characteristic (RRC) from the point in question back to the nozzle wall. The downstream portion was obtained by an analytical extrapolation of the RRC from the same point. In this procedure, it is assumed that the extrapolated characteristic was isentropic and that the local flow angle varied as in source flow. Thus the properties specified in the inner core of the nozzle do not reflect the rather strong shock effects there. This approximation however, should not significantly influence the portion of the plume involved in impingement.

6.1.2 Nozzle Boundary Layer Calculations

At the nozzle exit, flow properties near the nozzle wall will differ significantly from those obtained by an inviscid calculation, due to heat transfer, mass transfer, and friction in the boundary layer. Since the outermost portion of the plume is involved in the interaction leading to flow reversal, this boundary layer effect cannot be ignored.

Because the nozzle boundary layer is exposed to widely varying edge conditions during its growth along the nozzle surface, simple approximate solutions are inappropriate. Therefore, the numerical method of Reference 15 was chosen which solves the boundary equations by an implicit finite difference technique. This boundary layer program was developed for use with real air flow and for the present study required two modifications. First, thermodynamic and transport properties subroutines for $O_2 - H_2$ mixtures were substituted for the subroutines used for air. Secondly the effect of injecting mass with a composition different from the primary flow was evaluated by an integral method of determining the local concentration.

6.1.2.1 Thermodynamic Properties

Thermodynamic properties were evaluated for equilibrium mixtures of oxygen and hydrogen by means of a subroutine which solves the equations of chemical equilibrium. A system of seven species (H_2O, H_2, O_2, OH, H, O and HO_2) were found to be the only ones of significance over the range of conditions reached in rocket combustion chambers and nozzles. The procedure followed was equivalent to that followed by the standard NASA/ Lewis thermochemical program of Reference 16. The gas is assumed to be a mixture of ideal gases. Each of five chemical reactions involving the seven species is characterized by an equilibrium expression. These equilibrium equations and two atom balance equations (for O and H) are solved simultaneously to give equilibrium composition.

The individual thermodynamic properties of the constituents are evaluated from coefficients presently in use in the NASA/Lewis program. They are based on curve fits of the data over the ranges 300 to 1000K and 1000 to 5000K. At temperatures below room temperature, condensation of the water vapor can take place. Thus, true equilibrium requires that the mixture be treated as two phases in this regime, which would be a considerable complication. However, the condensation process takes more time than is probably available during rapid plume expansions. Therefore, in the present work the mixture is considered to be supercooled and the individual gases are treated as ideal down to absolute zero.

6.1.2.2 Transport Properties

The transport properties viscosity, thermal conductivity and Prandtl number are computed by a subroutine based on the approach described in Reference 17. It is primarily a subroutine for computing transport properties of non-reacting mixtures. Nevertheless, the subprogram output gives a good engineering estimate of the equilibrium conductivity in the following way. A survey of the tabulated properties in Reference 18 shows that while equilibrium conductivity can be many times as great as frozen conductivity, the corresponding Prandtl numbers differ by at most ten or twenty percent. Thus,

$$\frac{C_{p,Froz.} \mu}{k_{Froz.}} \sim \frac{C_{p,Eq.} \mu}{k_{Eq.}} \qquad (6\text{-}1)$$

In other words, since viscosity is the same in both frozen and equilibrium mixtures, the change in conductivity is approximately proportional to specific heat, a thermodynamic property. Therefore

$$k_{Eq.} \sim \frac{C_{p,Eq.} \mu}{Pr_{,Froz.}} \qquad (6\text{-}2)$$

Equation 6-2 is used as the basis for evaluating conductivity for O_2-H_2 mixtures.

6.1.2.3 TPE Injection Effects

In the standard version of the boundary layer program of Reference 15, the fluid is treated as a uniform single component gas (air) and diffusion of species is not considered. In the present case, when calculating the effect of TPE injection this is no longer a realistic assumption. In fact, the turbopump exhaust gas is quite different (mixture ratio 1.0 compared with 5.8 for the primary gas) and this difference can be expected to have a substantial effect on both the heat transfer to the nozzle and the average properties of the boundary layer gas itself.

It was not practical to modify the boundary layer program to include the effect of diffusion explicitly. As an alternative, a simpler modification was undertaken. In this approach, momentum and energy transport are evaluated by finite-difference quations, exactly as before. The local thermodynamic and transport properties are evaluated for the local mixture ratio. The local mixture itself, however, is not evaluated exactly but computed from an analytical concentration profile which matches the wall mixture and the total amount of excess hydrogen injected. In effect the concentration is determined by an integral method.

The gas mixture resulting from the injection of a concentration at the wall different from that in the primary stream is regarded as a primary gas (mixture ratio m_0) mixed with a certain mass fraction (ω) of pure hydrogen. It is convenient to express local concentration in terms of ω which goes from a maximum value at the wall to zero at the edge of the concentration boundary layer.

The analytical profile chosen is one used by Schlichting (Reference 19) to describe the mixing of two streams having unequal velocities. As applied here to the mixing of streams having different values of ω it becomes

$$\omega = \omega_{max}\left[1 - 3(y/b)^2 + 2(y/b)^3\right] \tag{6-3}$$

where y is the distance normal to the wall and b is the width of the concentration boundary layer.

Equation 6-3 contains two arbitrary parameters which can be matched to the injection conditions. In the region where injection is taking place ω_{max} is simply the excess hydrogen fraction at the wall ω_w. The value of b at a given station S is such that the amount of excess hydrogen contained in the concentration boundary layer is equal to the total amount injected up to that station. Thus

$$2\pi\omega_{max} \int_{S_1}^{S} \rho_w V_w R \, ds = 2\pi\int_0^b \rho U\omega R \, dy \tag{6-4}$$

where S_1 is the station where injection commences. In the right hand integral, ω is given by Equation 6-3 and b is solved for by successive approximations.

The procedure is similar for stations beyond the region of injection. The concentration boundary is assumed to grow in proportion to the growth of the velocity boundary layer.

$$b = b_2(\delta/\delta_2) \tag{6-5}$$

where δ_2 is the velocity boundary layer thickness of the end of the injection region. The maximum excess hydrogen fraction ω_{max} is then found from Equations 6-3 and 6-4 by successive approximations.

6.1.2.4 Boundary Layer Calculation Results

The modified boundary layer program was applied to the 1/25 scale model and full scale cases listed in Table 6-1. For the cases corresponding to the model test runs, the nozzle wall temperature, a program input, was set at 532R along the entire nozzle length. This reflects the fact that model tests are of very short duration i.e., a few milliseconds, so that little wall heating is encountered. On the other hand, in the full scale runs, nozzle wall temperatures were assumed to be those occurring at steady state and varied from about 1500R near the nozzle throat to 430R at the lip. Both the large differences in scale and the differences in wall temperature history have significant affects on the property variations within the boundary layer.

Figure 6.1.2-1 presents non-dimensional temperature and velocity profiles for all non-TPE cases, both model and full scale. Velocity profiles are quite similar for all cases but there are differences between model and full scale temperature profiles. The similarity of all the model profiles makes it possible to estimate the characteristics of a new case, provided edge properties (Ve and Te) and boundary layer thickness (δ) are known.

The boundary layer thickness can be expected to vary primarily with the Reynolds number. Figure 6.1.2-2 illustrates this. There is scatter, due to the complex effect of property variations, but the general trend is as expected. For comparison, the full scale boundary layer with TPE is also plotted. The thickening of the boundary layer with TPE is clearly evident. This is also shown in Figure 6.1.2-3 which shows the development of the various boundary layer thicknesses (velocity, momentum, concentration, and displacement) along the nozzle wall. All except the displacement thickness show substantial increases beginning at the point of TPE injection. The displacement thickness goes slightly negative due to strong wall cooling.

Figure 6.1.2-4 gives the velocity, temperature and mixture ratio profiles for the full scale TPE injection case. The presence of hydrogen-rich gas near the wall tends to lower the temperature there. As will be seen later, this results in much lower recovery temperatures in the plume gases reversed by exhaust plume interaction.

6.1.3 Definition of Plume Flow Field

In the present study the most significant portion of the plume is the boundary region, which is strongly influenced by the property gradients present in the nozzle boundary layer. Plume flow fields with strong boundary gradients have been evaluated by the rotational method of characteristics (Reference 20) and by a Lagrangian method (Reference 21).
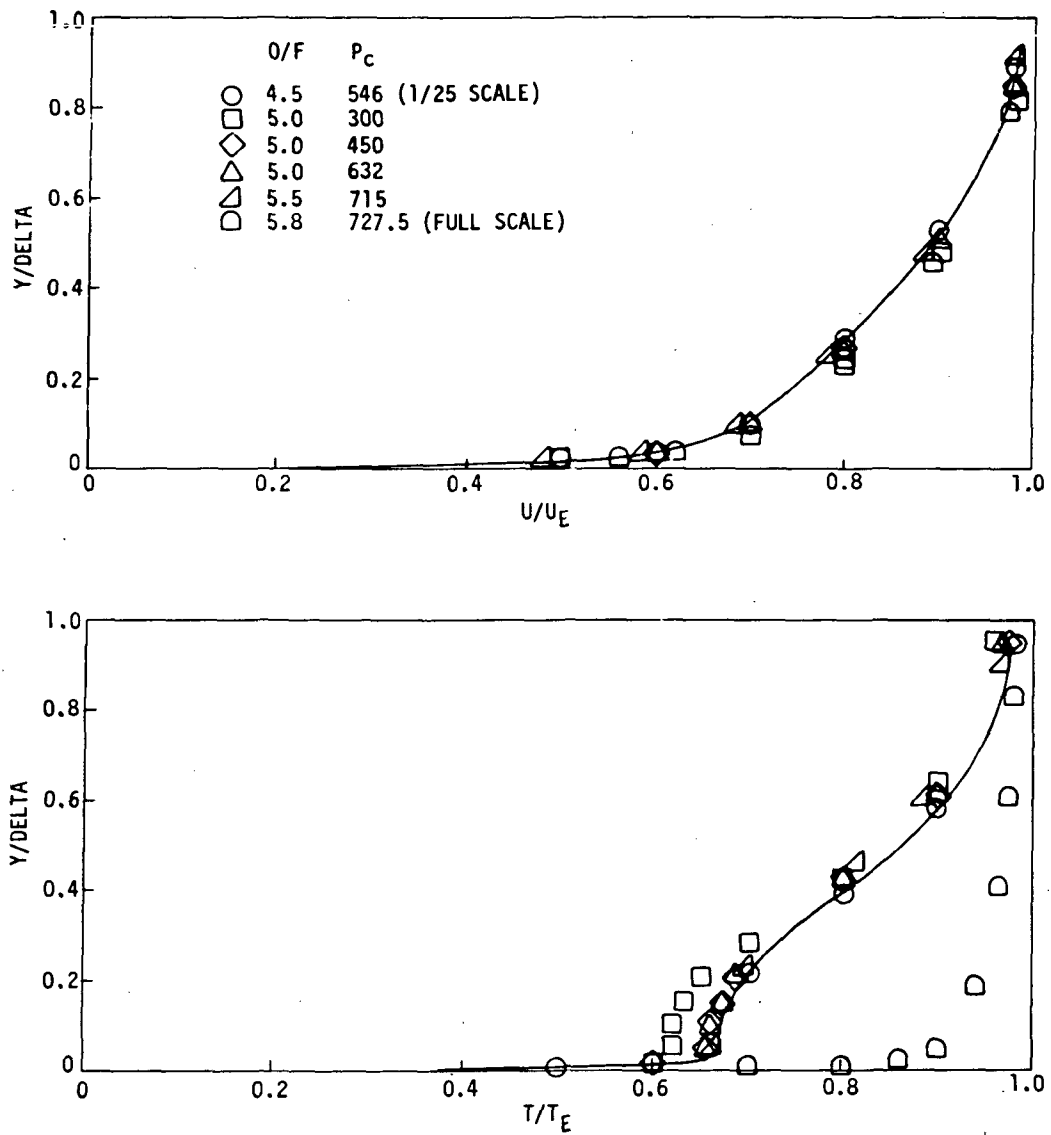
Figure 6.1.2-1   Non Dimensional Velocity and Temperature Profiles in the
                 J-2 Boundary Layer
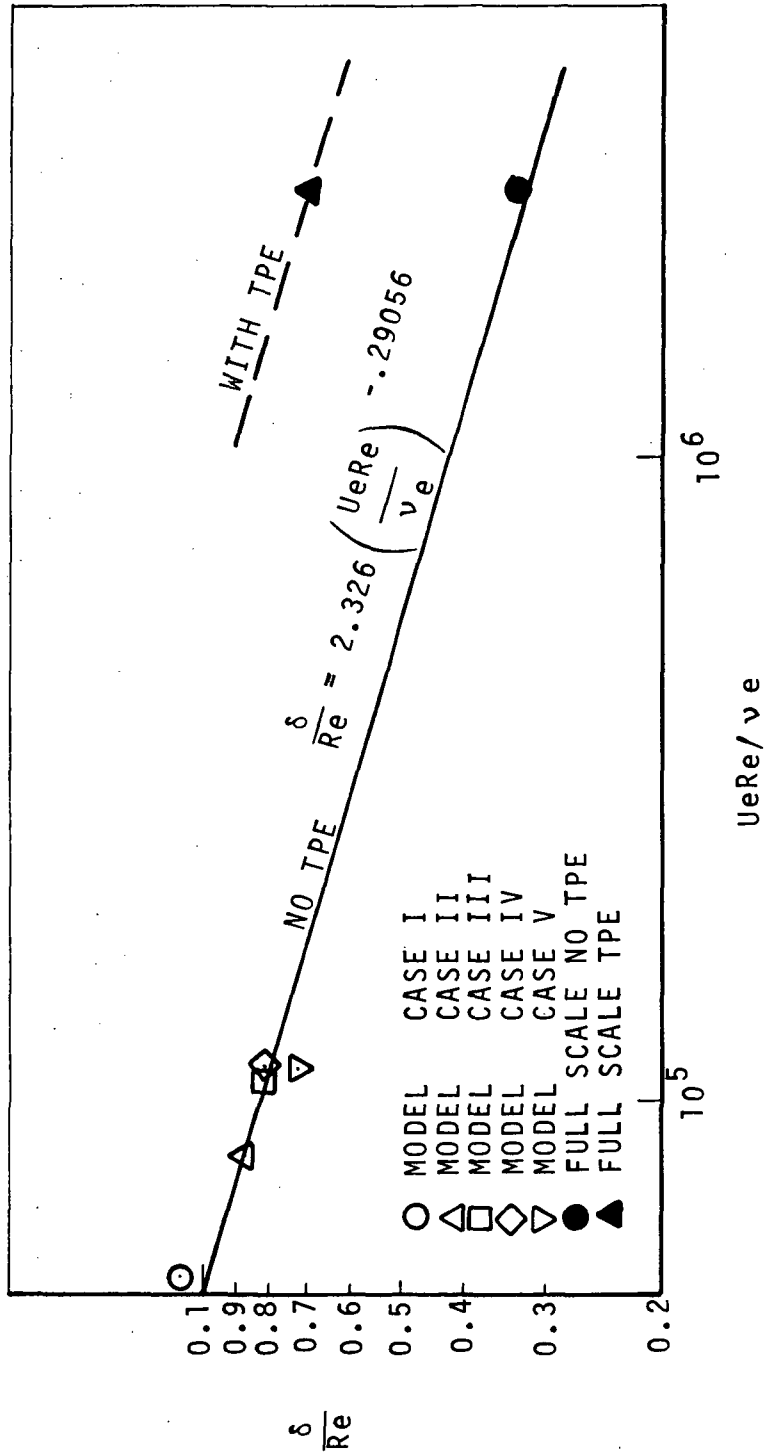
Figure 6.1.2-2 Relative Boundary Layer Thickness for the
J-2 Nozzle
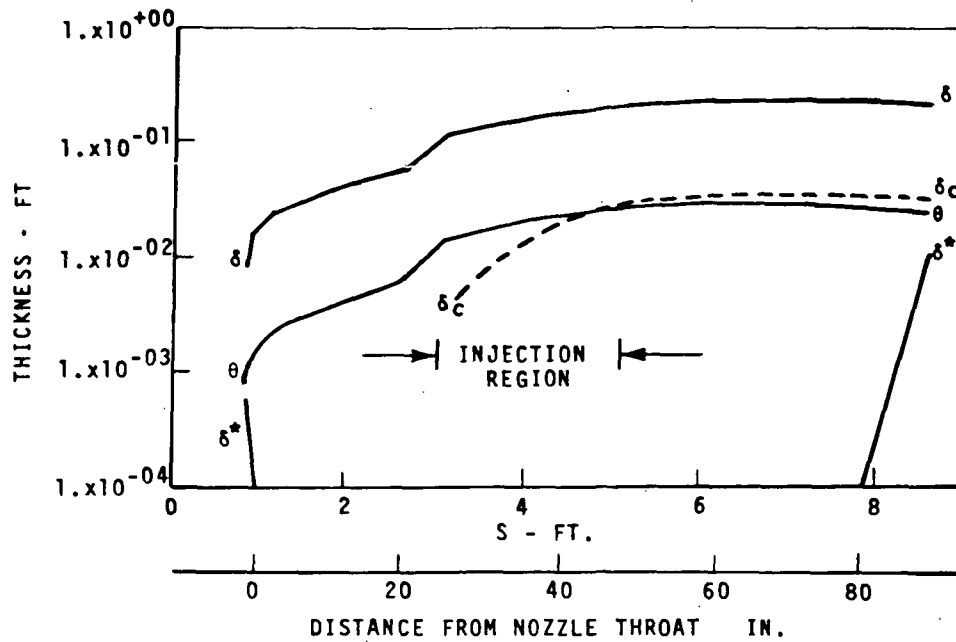
Figure 6.1.2-3 Typical Variation of Nozzle Boundary Layer
Thicknesses
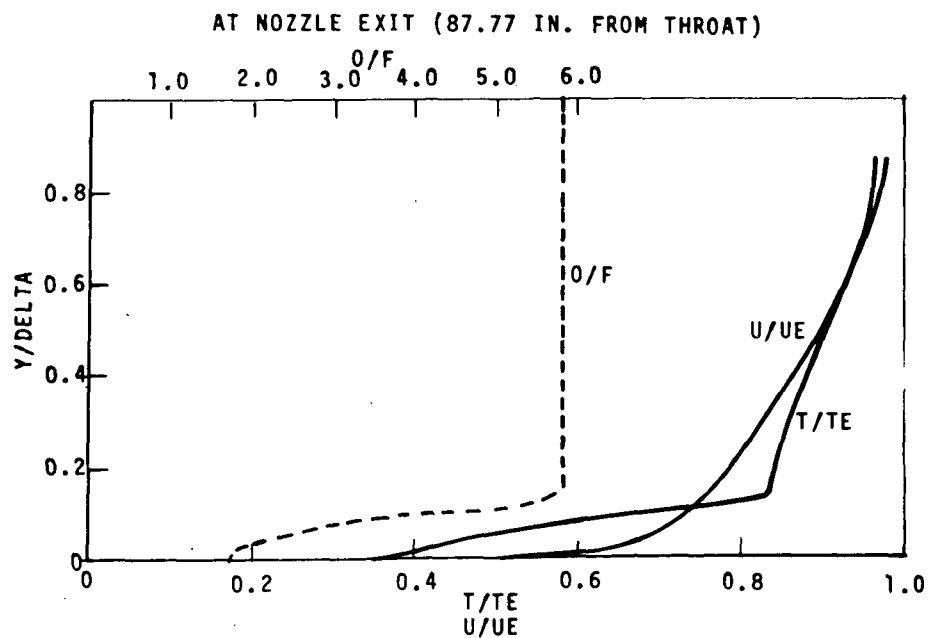
Figure 6.1.2-4 Velocity, Temperature, & Concentration Profiles
with TPE Injection

SD73-SA-0061

In this work a third method, shock capturing, has been employed.
Shock capturing is a marching technique in which the inviscid flow
equations are expressed in conservation-law form and are integrated
numerically by a two-step predictor-corrector process. The method has
several features which recommend it for the present problem. Grid
spacing may be fixed and uniform along coordinates perpendicular to the
marching direction. This feature greatly simplifies control of the
coverage and resolution of a given solution. Moreover, the coordinate
system may be chosen so that high resolution is achieved in the region
where strongest property gradients appear i.e., the nozzle lip. No
special provision is required for internal shock waves which may be
present in the flow field; they appear automatically as part of the
solution.

6.1.3.1 Application of Shock Capturing to the Plume Problem

The flow field equations for the plume problem have been formulated
from the generalized equations presented by Kutler and Lomax (Reference 22).
The geometry chosen is shown in Figure 6.1.3-1. It is an axisymmetric
system described by a coordinate ζ which measures distance from the nozzle
lip, and a coordinate η which measures the angle from the downward
vertical. For convenience the constant ζ surfaces are termed "shells"
and the constant η lines (surfaces) are termed "rays". The finite-
difference solution proceeds in the ζ direction.

The generalized conservation law-equations specialize in the present
case to

$$\frac{\partial E_i}{\partial \zeta} + \frac{\partial F_i}{\partial \eta} + H_i = 0, \qquad i = 1,2,3 \qquad (6-6)$$

where the E's, F's, and H's are as follows:

i	E	F	H
1	$\zeta R \rho U$	$R \rho V$	0
2	$\zeta R \left(P + \rho U^2 \right)$	$R \rho U V$	$P(1-R) - R\left(P + \rho V^2\right)$
3	$\zeta R \rho U V$	$R\left(P + \rho V^2\right)$	$R \rho U V - P X$

The above procedure has been programmed for the IBM 370 computer.
Numerical integration of Equation 6-6 proceeds from one shell to the
next and from the upper boundary to the lower, using a predictor-corrector
procedure. The solution starts from an initial shell at which properties
are computed from a Prandtl-Meyer expansion centered on the nozzle lip.
The expansion may be taken from a low supersonic Mach number within the
nozzle boundary layer. The solution then proceeds outward between an
upper free boundary and a lower data line determined by merging a
rotational RRC through the boundary layer flow with the start line
obtained from the inviscid nozzle flow field (Section 6.1.1). Static
pressure at the free boundary is evaluated from the pressure and Mach
number of the external flow by Newtonian theory. Boundary coordinates
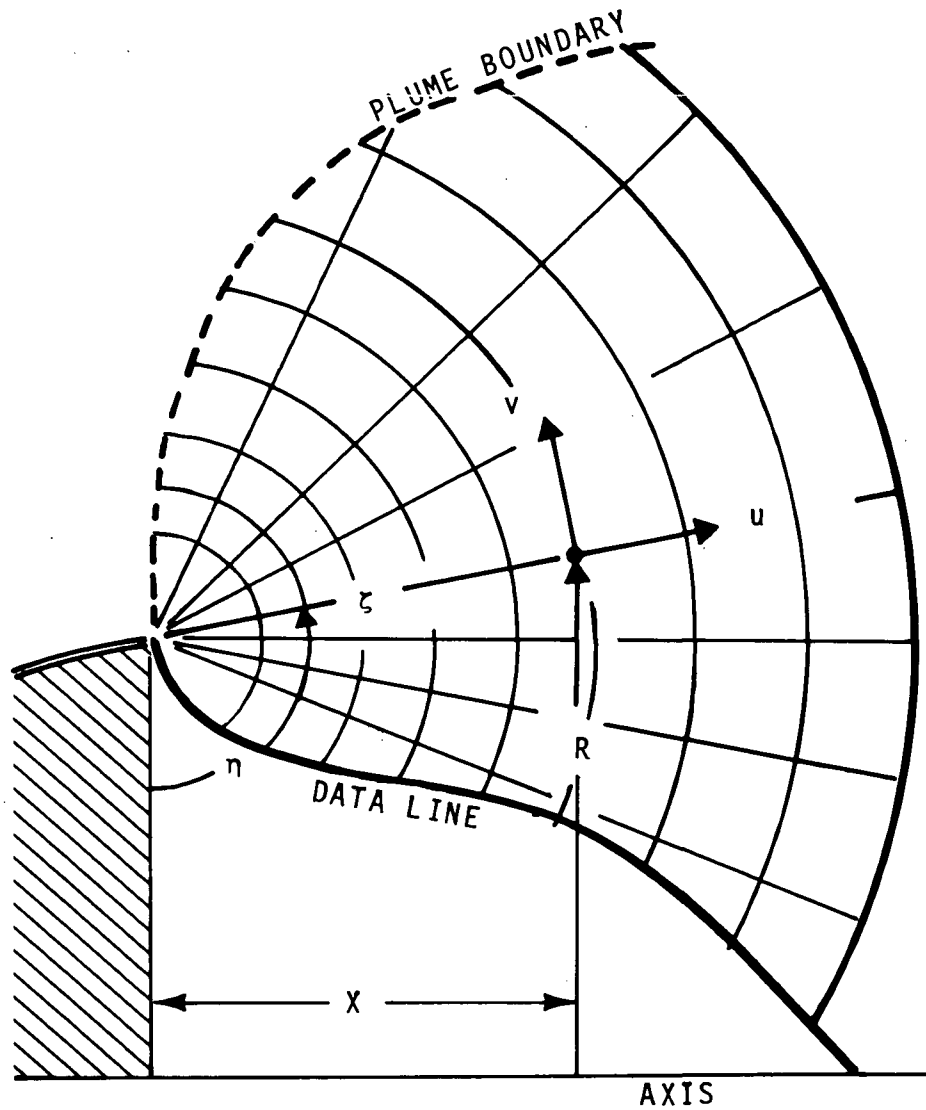
Figure 6.1.3-1 Lip-Centered Coordinate System used in
Shock Capturing Analysis

SD73-SA-0061

for each new shell are found from the intersection of the boundary streamline with a left-running characteristic from the previous shell.

The variables F_i and H_i are functions of E_i and must be evaluated at each step of the integration. This involves the prior solution of the physical variables v, u, ρ and P. For an ideal gas with constant specific heat this can be done exactly in closed form. For a real gas mixture an iterative solution is required. In the present work, it has been found possible to combine this property iteration with the predictor-corrector cycle in such a way that both ideal gas and real gas problems are handled with the same logic. This procedure has resulted in important savings of computer time for real gas problems.

6.1.3.2 Typical Plume Property Distributions for the 1/25 Scale Model

The shock capturing program was applied to all six cases listed in Table 6-1. For all cases the ambient pressure surrounding the plume was taken to be 0.075 psfa, the nominal value for the model test cell. For Case V (Pc = 715 psia, 1/25 scale model at O/F = 5.5) additional runs were made at higher ambient pressures. The effect of nozzle boundary layer was included for all cases. For the full scale Case VI runs were also made for the boundary layer with TPE injection. Figures 6.1.3-2,3,4 illustrate typical plume flow fields for the 1/25 scale J-2 with boundary layer.

The velocity distribution of Figure 6.1.3-2 shows clearly the strong influence of the thick plume boundary layers in model runs. The velocity in an isoenergetic plume, one having constant stagnation enthalpy throughout, increases monotonically away from the axis. In the present case, however, the stagnation enthalpy decreases toward the boundary due to the effect of nozzle wall cooling. Thus, as one moves away from the axis the velocity first increased due to expansion but finally decreases because the limiting velocity, which is proportional to the square root of the stagnation enthalpy decreases.

Figure 6.1.3-2 also shows the variation of stagnation enthalpy flux, defined as $\rho U(h + 1/2 \ U^2)$, which is the upper limit on heat transfer due to impingement. Unlike velocity, the stagnation enthalpy flux decreases continuously away from the axis.

Static and dynamic pressure (Figure 6.1.3-3) show the expected decrease away from the plume axis. Although not shown clearly in the figures, the static pressure reaches a minimum just inside the plume boundary and then rises to match the boundary pressure.

Isotherms are shown in Figure 6.1.3-4. Generally, temperature falls off away from the axis, due both to the decrease in stagnation enthalpy and to the expansion itself. At distances greater than about four exit radii there are anomalous variations in static temperature near the plume boundary. These appear to be purely numerical problems connected with the finite difference procedure. They do not affect that part of the flow field used in the present work.
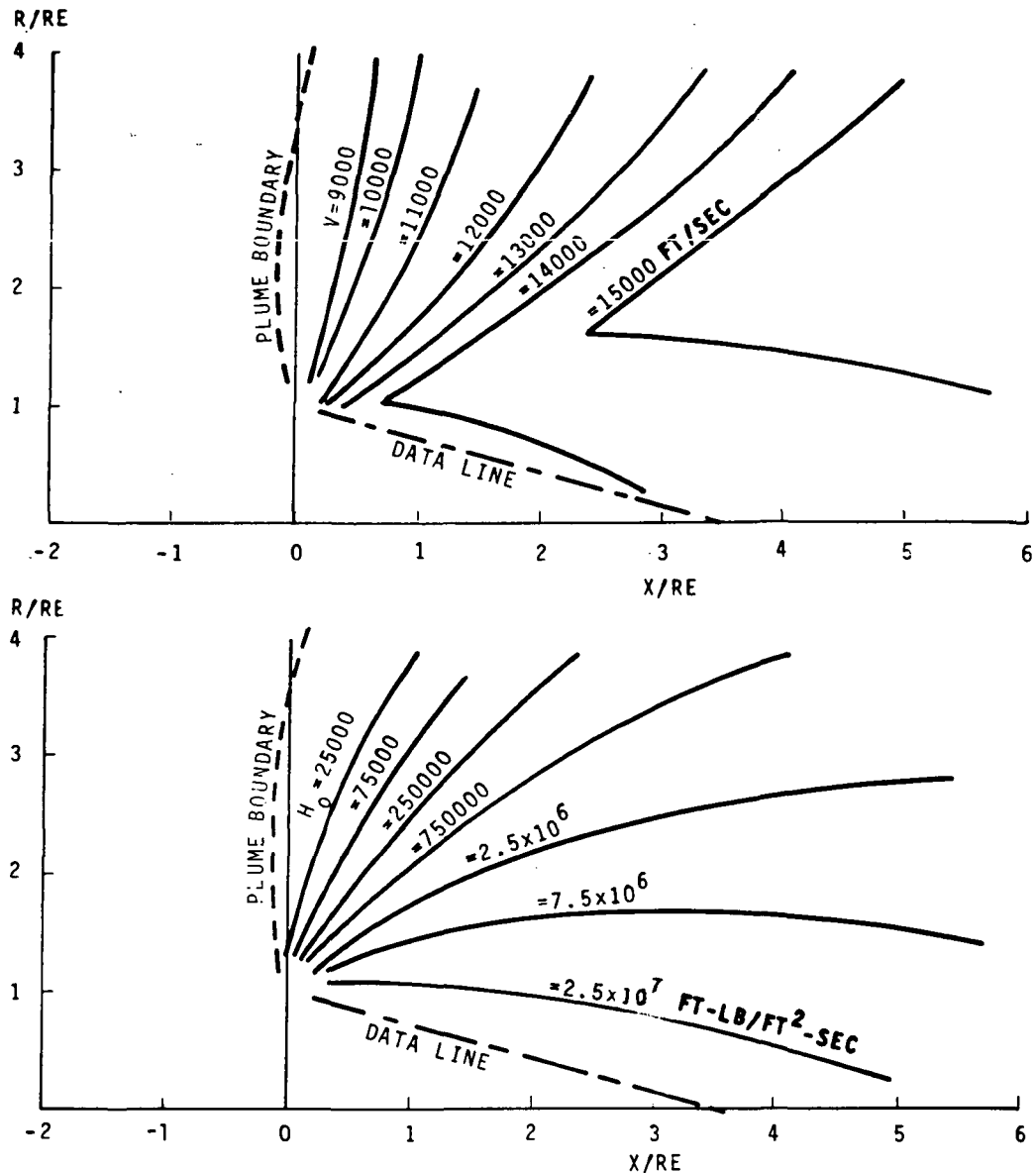
Figure 6.1.3-2   Typical Distribution of Velocity and Stagnation
Enthalpy Flux in J-2 Model Plume
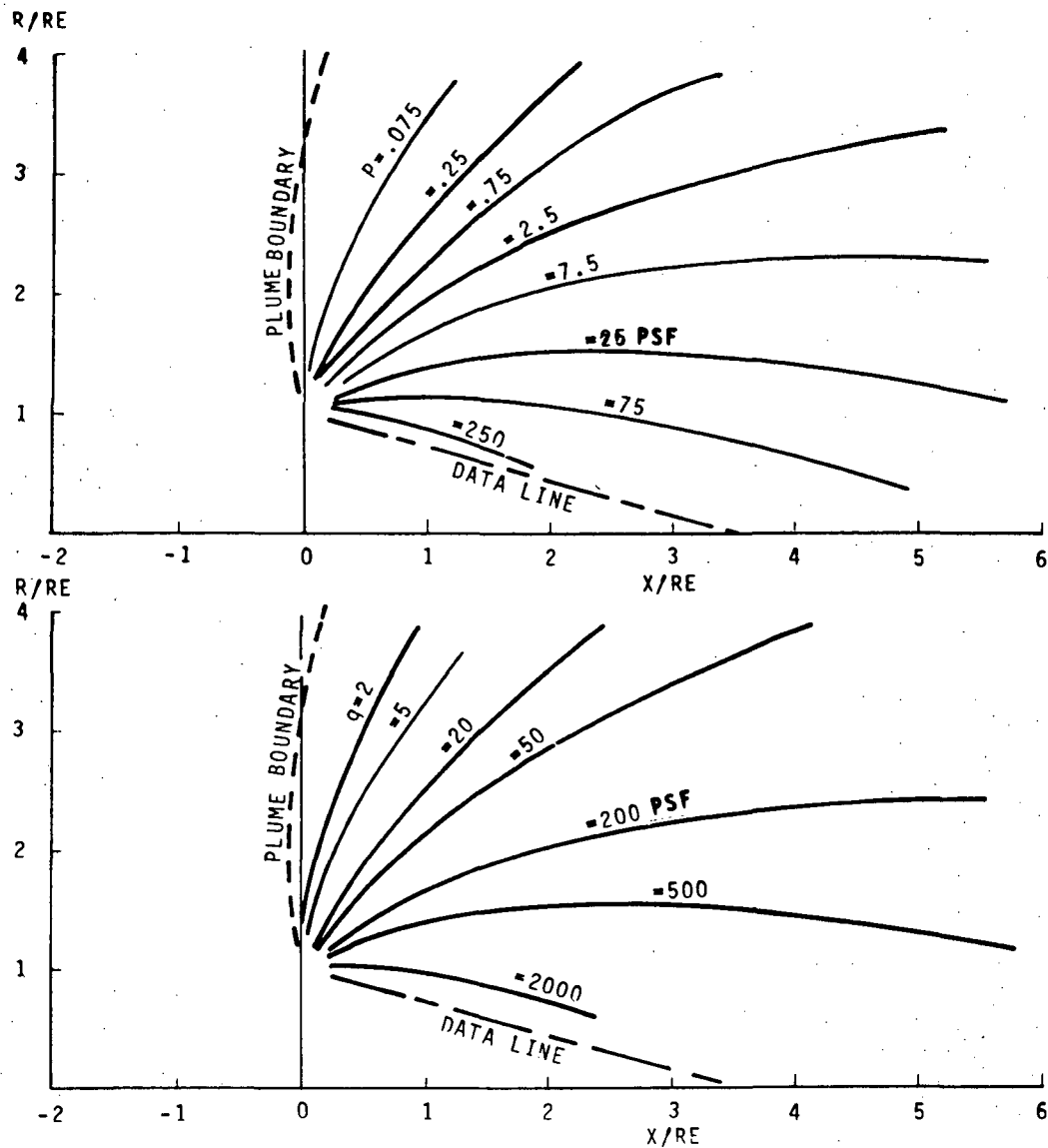
Figure 6.1.3-3   Typical Distribution of Static Pressure and
Dynamic Pressure in J-2 Model Plume

Rev July 6, 1973

SD73-SA-0061
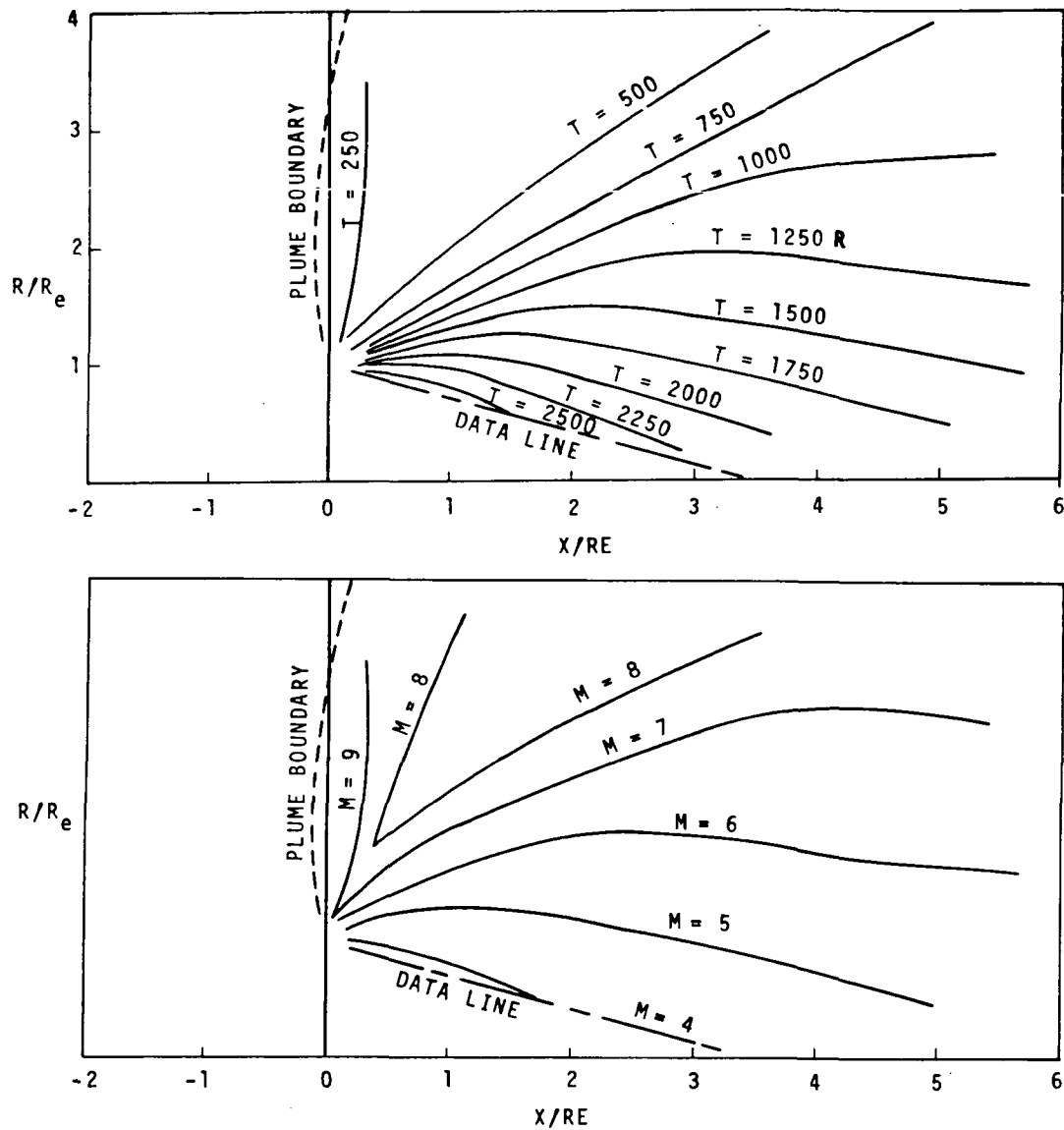
Figure 6.1.3-4   Typical Isotherm and Isomach Profiles
in J-2 Model Plumes

Rev July 6, 1973

SD73-SA-0061
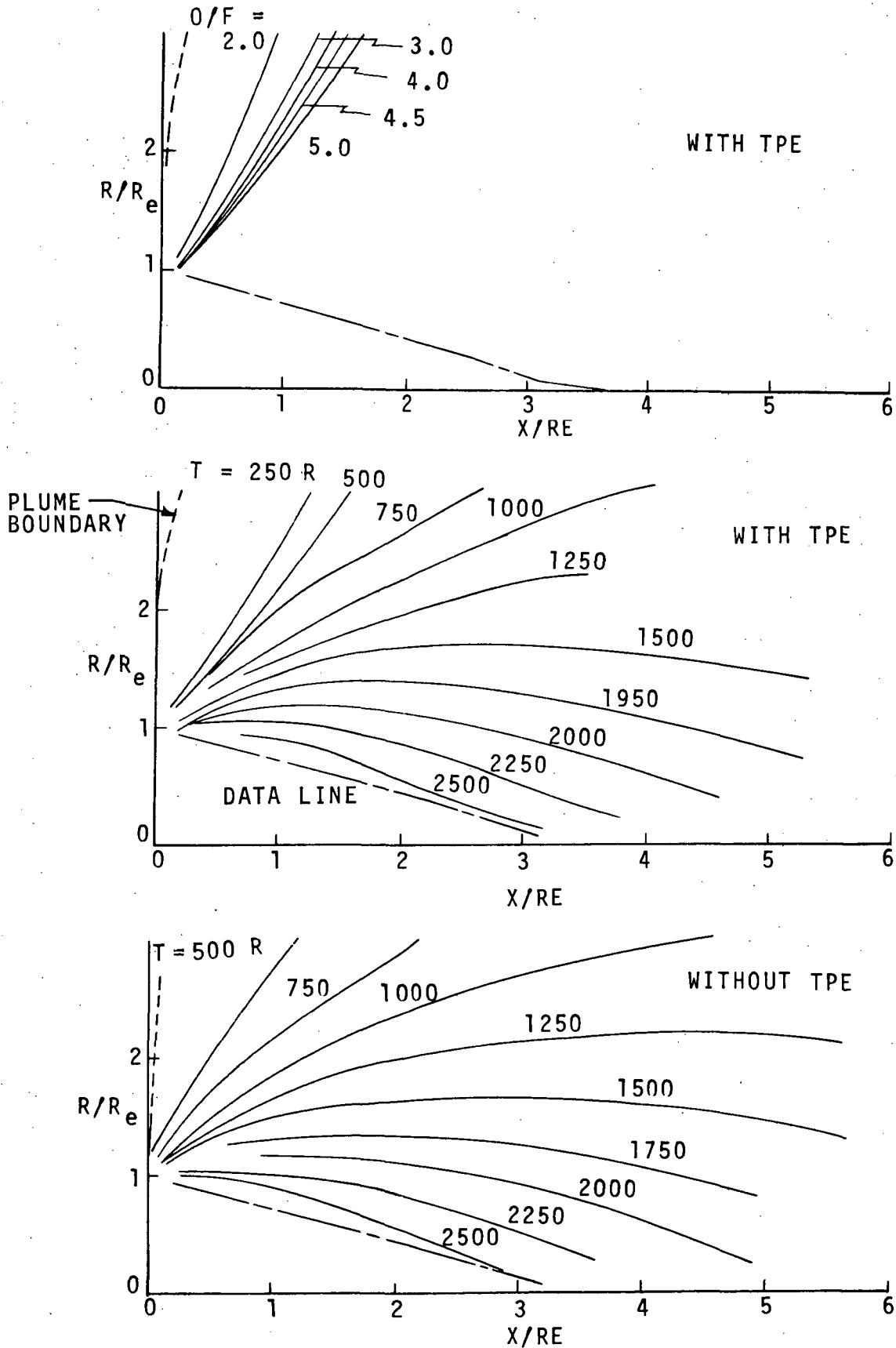
Figure 6.1.3-5 Concentration Profiles and Isotherms for Full Scale J-2 Plume

SD73-SA-0061

The Mach number distribution presented in Figure 6.1.3-4 displays the combined effects of the velocity and the sound speed variations. The end result is two maxima, one near the boundary and one corresponding to the velocity plateau.

6.1.3.3 Property Distributions for Full Scale Plumes

Property distributuons both for TPE and non-TPE injection are identical within the plume core, but vary markedly at the boundaries. Figure 6.1.3-5 shows the mixture ratio profiles (for TPE) and isotherms both for TPE and non-TPE. Strong differences are noticeable, which are later reflected in differences in the recovery temperature of the reversed gases.

6.1.4 Definition of the Impingement Flow Field

The flow field which results from the mutual interactions of the individual plumes is extremely complex and no attempt has been made at a complete description. However, trends and approximate levels can be established for the significant impingement parameters based on a greatly simplified approach. Attention has been restricted to the case of two plumes undergoing symmetrical, co-planar gimballing; that is, their axes rotate an equal amount toward or away from each other, in the same plane. Moreover, only flow within that plane is considered.

6.1.4.1 Impingement Properties Based on Newtonian Theory

The geometry of the two-plume impingement process is illustrated in Figure 6.1.4-1. Newtonian impact results in a flow velocity which is the tangential component of the initial velocity

$$V_2 = V_1 \cos(\theta + \beta) \tag{6-7}$$
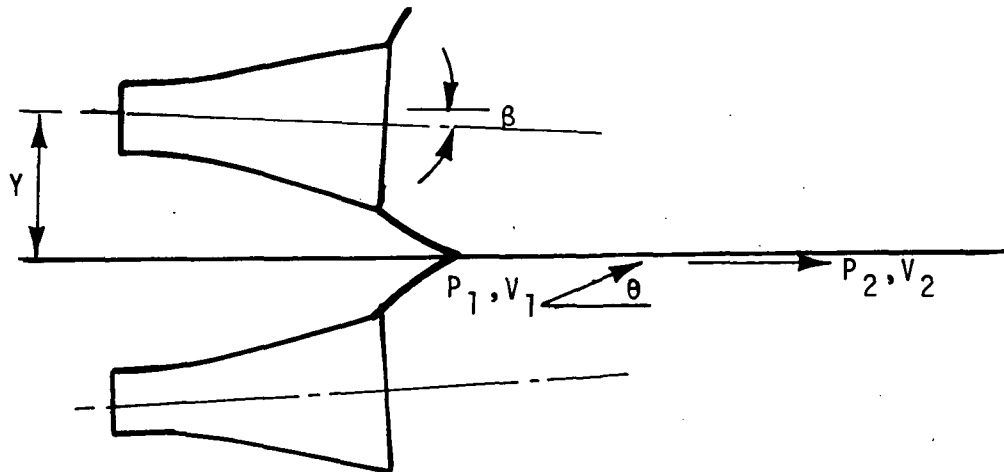
Figure 6.1.4-1 Two-Plume Impingement Geometry (Symmetrical Co-Planar Gimballing)

Rev July 6, 1973

SD73-SA-0061

and an impact pressure based on the normal velocity component

$$P_2 = P_1 + \rho_1 \left[V_1 \sin(\theta + \beta) \right]^2 \qquad (6\text{-}8)$$

Other post-impingement properties can be derived as required. The enthalpy is obtained from the stagnation enthalpy of the streamline in question

$$h_2 = h_0 - 1/2 \left(V_2 \right)^2 \qquad (6\text{-}9)$$

The pressure and enthalpy determine the entropy. The entropy in turn, together with the stagnation enthalpy, defines the isentropic stagnation pressure after impingement.

Symbolically

$$S_2 = S(o/F, P_2, h_2) \qquad (6\text{-}10)$$

$$P_{02} = P(o/F, S_2, h_0) \qquad (6\text{-}11)$$

where the functional notation corresponds to the real gas property relationships computed by the $O_2 - H_2$ thermodynamic subroutine.

6.1.4.2 Flow Reversal After Impingement

The above relationships have been incorporated into a computer program which carries out a step-by-step evaluation of impingement properties along the plane of impingement using as input the plume properties calculated by shock capturing. The geometry is shown in Figure 6.1.4-2.
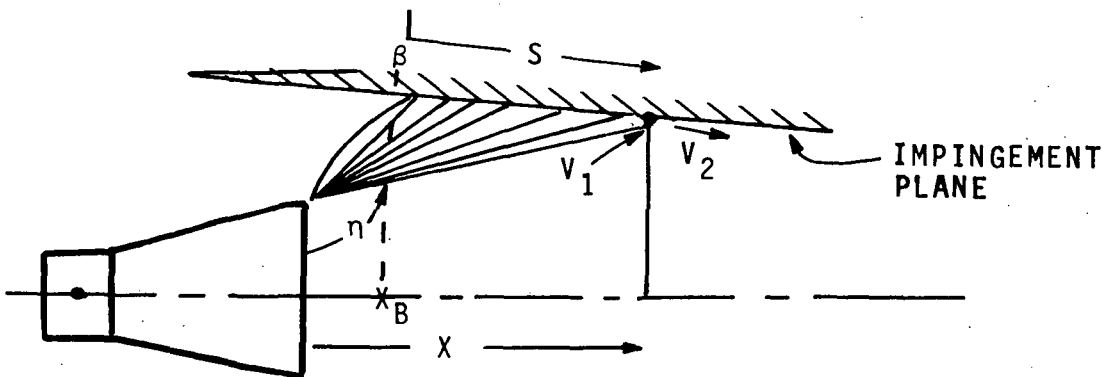
Figure 6.1.4-2 Evaluation of Impingement Parameters

Beginning with the plume boundary, the pre-impingement properties along each ray at the impingement plane are found by interpolation. Equations 6-7 through 6-11 are then applied to compute the corresponding static and stagnation pressures after impingement.

A typical variation is shown in Figure 6.1.4-3. Both pressures remain together near the outer boundary, indicating low velocity after impingement. The initial dip is a result of over-expansion near the boundary. The small inflection coincides with the plume streamline coming from the boundary layer point nearest the wall. The reversal there is a consequence of the finite difference approximation and does not reflect a physically real trend.

As distance from the exit plane increases, the static pressure approaches a maximum value, reflecting the increasing importance of the impingement angle $(\theta+\beta)$. The stagnation pressure continues to rise. The Chapman-Korst criterion (References 23,24) establishes the discriminating streamline which separates the reversed flow from that which continues downstream: That flow which has a stagnation pressure after impingement less than the peak static pressure in the impinge region will be reversed.

It can be assumed that the reversed flow will be well-mixed by the time it reaches the base region. Thus, it is the mass-average properties of the reversed flow which are of interest, in particular the stagnation temperature. This should correspond to the recovery temperature measured at the base heat shield. For the $O_2 - H_2$ mixtures this was done by first evaluating average enthalpy and mixture ratio, integrated from the plume boundary inward.

Thus, the total mass flow is given by

$$\dot{m} = 2\pi \int_0^S \rho U R \sin(\theta + \beta) ds \qquad (6\text{-}12)$$

the hydrogen mass flow

$$\dot{m}_H = 2\pi \int_0^S \rho U R \sin(\theta + \beta)\left(\frac{1}{\overline{O/F}+1}\right) ds \qquad (6\text{-}13)$$

the total enthalpy

$$H_0 = 2\pi \int_0^S \rho U R\, h_0 \sin(\theta + \beta) ds \qquad (6\text{-}14)$$

the mass mean mixture ratio

$$\overline{O/F} = \left(\dot{m} - \dot{m}_H\right)/\dot{m}_H \qquad (6\text{-}15)$$

and the mean stagnation enthalpy

$$\overline{h}_{02} = H_0/\dot{m} \qquad (6\text{-}16)$$

Rev July 6, 1973
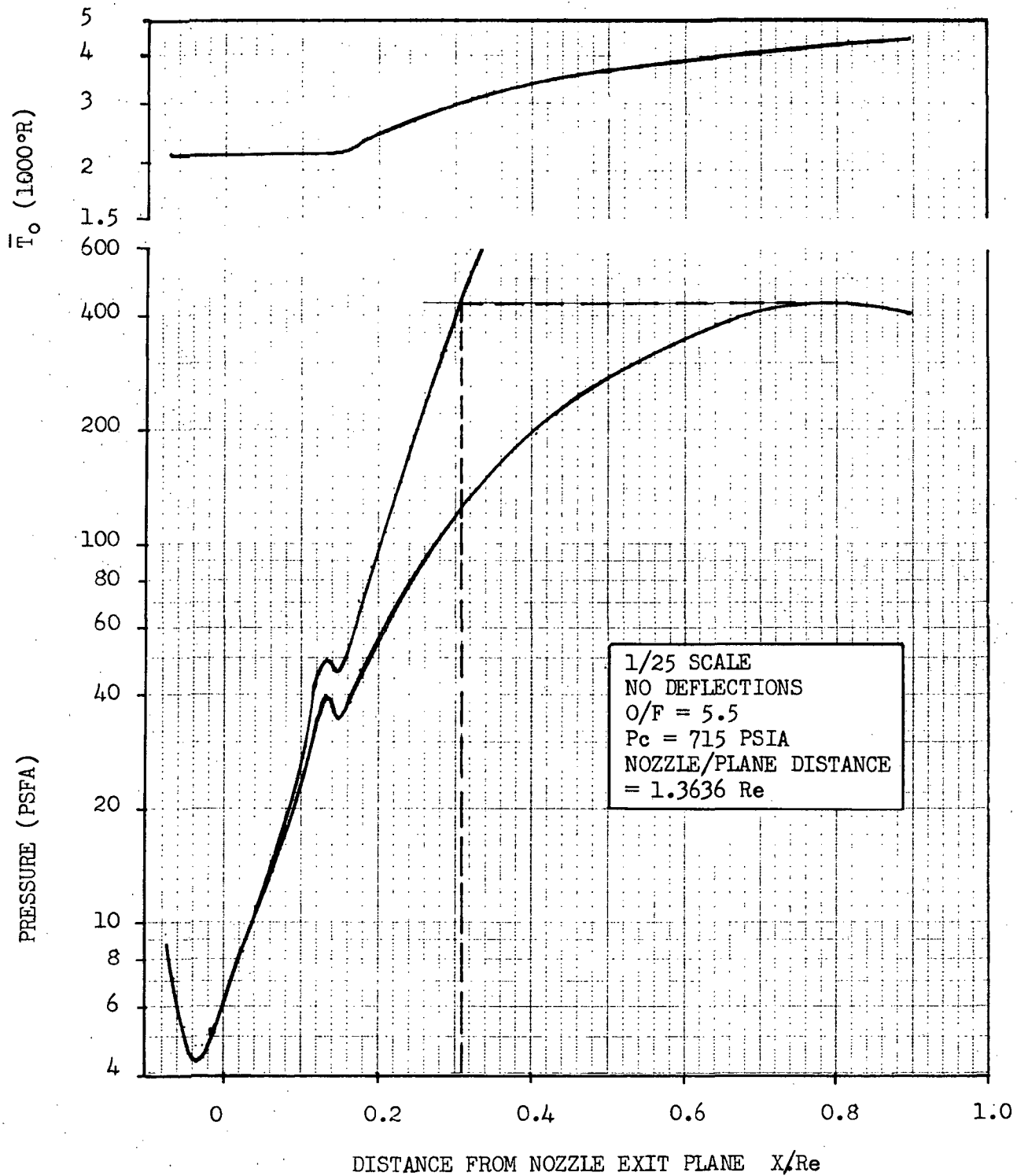
Figure 6.1.4-3 Typical Variation Of Impingement Parameters
After Impingement

The average stagnation temperature $(\bar{T}_{o}2)$ is obtained from the stagnation pressure using the thermodynamic properties subroutine. Symbolically

$$\bar{T}_{o2} = T \ (\ \overline{O/F},\ P_{o2},\ \bar{h}_{o2}\ ) \tag{6-17}$$

Average stagnation temperature is also plotted in Figure 6.1.4-3 as a function of impingement location. The value of $\bar{T}_{o2}$ corresponding to the discriminating streamline is the analytical value corresponding to the recovery temperature.

6.1.5 Description of the Base Flow Field

Ideally, the final step in the analyses would be a synthesis of the impingement results of the preceding section, leading to a complete description of the base flow field and the distribution of surface pressures and heat transfer rates on and around the heat shield. One approach much used in the past (Reference 25) has been to sum the individual elements of mass being reversed from each section of the impingement zone. This total mass is balanced against the outflow of mass from the base region. Predictions based on this approach usually yield reasonable base pressures, but give no detail about heat transfer distributions.

An alternative approach is to treat the flow as the result of the interactions of more or less independent, sheet-like jets of reversed flow, each one having a temperature, a stagnation pressure and initial direction determined by the plume impingement process. In principle, evaluation of the impingement of these reversed jets on the base structure could give both pressure and heat transfer distributions. Neither the first nor second approach has been completely implemented in the present work. However, the second approach is used in a qualitative way to discuss the analytical-experimental comparisons.

6.1.5.1 Off-Axis Impingement Effects

The amount, direction, and properties of the flow reversed from individual regions of plume intersection will determine the detailed distribution of pressure and heat transfer in the base region. The impingement analysis described in the preceding section is highly specialized. It applies strictly only to the regions A and B in Figure 6.1.5-1 where impingement occurs in the planes containing two plume axes. In fact, most of the reversed flow comes from off-axis impingement. The reversing flow is approximately two-dimensional in the plane of symmetry between plumes and the streamlines have a substantial lateral velocity

A preliminary analysis of this two dimensional impingement flow was carried out at Space Division previous to the present study. Individual streamlines were computed by integrating the two dimensional equations of fluid motion in a pressure field established by Newtonian impingment.

Rev July 6, 1973

SD73-SA-0061

STREAMLINE
PATHS IN THE
IMPINGEMENT PLANE

LOCUS OF POINTS DEFINING
PLUME INTERSECTION

VIEW R-R
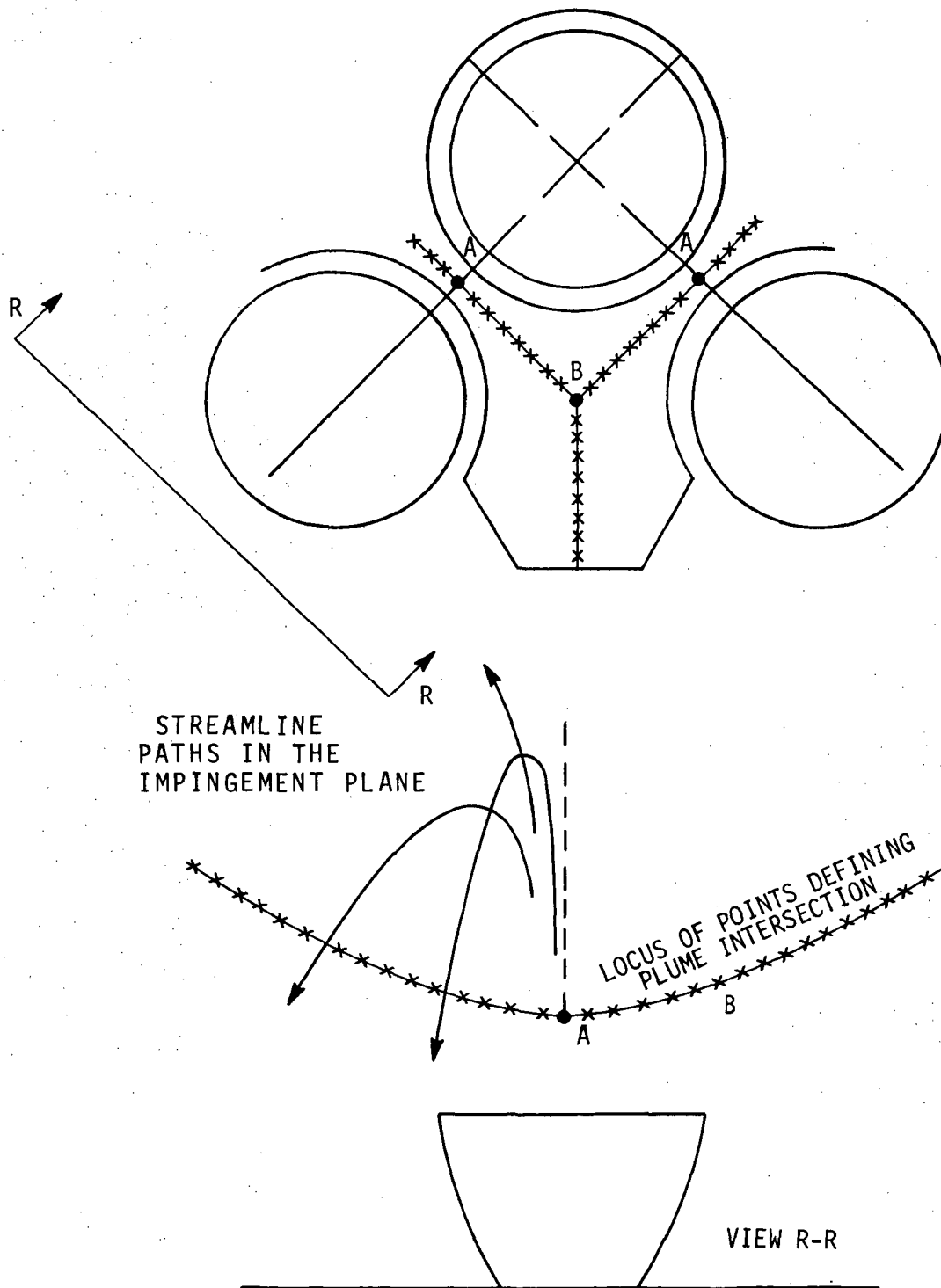
Figure 6.1.5-1 Plume Interaction Geometry for Quadrant
of S-II Cluster

Although many approximations were made in the plume flow fields, the qualitative results are of interest here. They showed that much of the reversed flow left the impingement zone with angles of $45°$ or more from the vertical. Figure 6.1.5-2 is a graphical representation for the RL-10 engine.

6.1.5.2 An Analytical Heat Transfer Parameter

Even though quantitative predictions of base heat shield heat transfer have not been attempted, it is useful to establish a parameter, based on local plume impingement parameters which should indicate the general trends. Basically the local heat transfer due to impingement of a jet of reversed gases on the heat shield, should be proportional to the temperature difference and a film coefficient.

The temperature difference can be evaluated with some confidence since both the average stagnation temperature of the gas and the surface temperature are known. In all that follows, the recovery temperature is equated to $\overline{T}_{o2}$. The film coefficient is less certain. Presumably it depends primarily on local mass velocity, and secondly on scale and temperature through the variation in temperature-dependent transport properties. In Reference 4, some experimental and analytical justification is given for a variation with the 0.8 power of the local stagnation pressure and that assumption is used here. The temperature effect on the film coefficient is ignored and scale effect is not involved since only trends within either model or full scale tests are being compared.

The final heat transfer parameter is simply

$$Q \equiv P_{o2}^{0.8} \, (\overline{T}_{o2} - T_W) \qquad\qquad (6\text{-}18)$$

For all model comparisons and normalized full scale calculations the surface temperature Tw was taken as 532R.

6.2 ANALYTICAL RESULTS

All of the plumes listed in Table 6-1, both model and full scale, have been analyzed using the impingement program. The analysis considers impingement at the two engine spacings which occur in the S-II cluster, namely, the "close" distance between center and outer engines, and the "far" distance between the outer engines. The spacings (Y/Re) from engine gimbal point to impingement plane (see Figure 6.1.4-1) are 1.3636 and 1.9284 respectively. For each spacing a range of positive gimbal angles were considered. The results of these impingement calculations for recovery temperature $\overline{T}_{o2}$, stagnation pressure P_{o2}, and heat transfer parameter Q are summarized in Table 6-2 for the model and Table 6-3 for the full scale conditions.
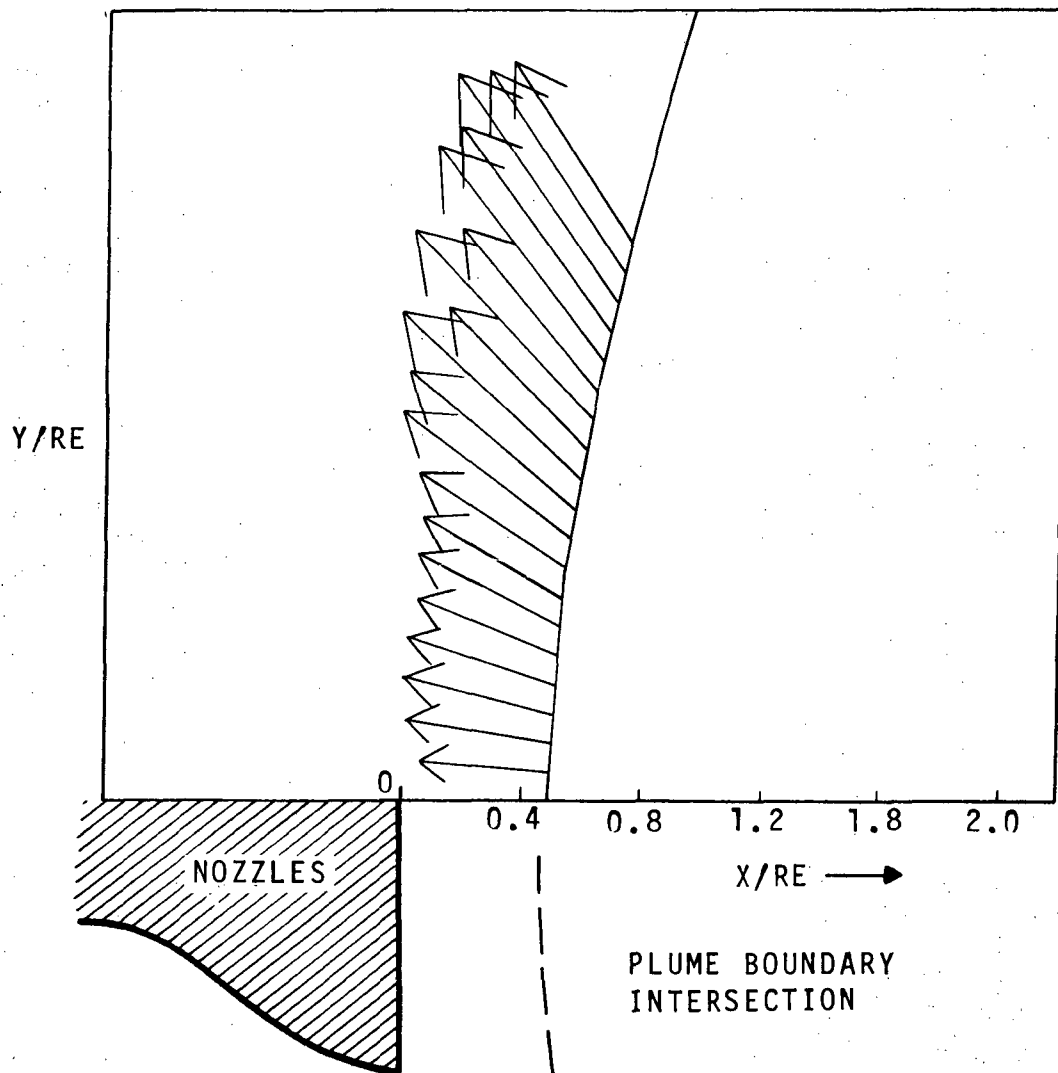
Figure 6.1.5-2   Reverse Mass Flow Distribution
in Impingement Plane

Table 6-2   Impingement Results (1/25 Scale Model)

CASE	P_c (PSIA)	O/F	P_{amb} (PSFA)	y/R_e	GIMBAL ANGLE (β)	m_{rev}/m_{tot}	P_{02} (PSFA)	T_{02} (°R)	$Q \times 10^{-5}$
I	300	5.0	0.075	1.3636	0°	.0102	217.	2504.	1.46
					1°	.0104	258.	2516.	1.68
					2°	.0100	296.	2491.	1.86
					4°	.0086	407.	2430.	2.32
					6°	.0047	546.	2378.	2.86
				1.9284	0°	.0141	102.	2701.	0.87
					1°	.0149	116.	2730.	0.99
					2°	.0156	132.	2759.	1.11
					4°	.0173	173.	2814.	1.41
					8°	.0200	296.	2898.	2.24
II	450	5.0	0.075	1.3636	0°	.0096	297.	2685.	2.04
					1°	.0096	343.	2681.	2.29
					2°	.0096	413.	2685.	2.67
					4°	.0086	615.	2650.	3.60
					6°	.0040	795.	2578.	4.28
				1.9284	0°	.0124	125.	2832.	1.10
					1°	.0131	143.	2860.	1.23
					2°	.0139	164.	2894.	1.40
					4°	.0154	214.	2943.	1.77
					8°	.0183	378.	3036.	2.89
III	546	4.5	0.075	1.3636	0°	.0091	337.	2585.	2.16
					1°	.0092	401.	2590.	2.49
					2°	.0093	490.	2596.	2.93
					4°	.0084	722.	2562.	3.93
					6°	.0039	946.	2488.	4.70
				1.9284	0°	.0119	142.	2725.	1.16
					1°	.0126	162.	2750.	1.30
					2°	.0134	186.	2783.	1.47
					4°	.0149	246.	2834.	1.88
					8°	.0178	432.	2915.	3.06
IV	632	5.0	0.075	1.3636	0°	.0090	408.	2753.	2.72
					1°	.0092	486.	2760.	3.14
					2°	.0091	581.	2759.	3.62
					4°	.0081	846.	2718.	4.80
				1.9284	0°	.0120	174.	2902.	1.47
					1°	.0127	199.	2927.	1.65
					2°	.0135	228.	2958.	1.87
					4°	.0150	298.	3005.	2.36
					8°	.0178	521.	3086.	3.81

Table 6-2 (Continued)

CASE	P_c (PSIA)	O/F	P_{amb} (PSFA)	Y/R_e	GIMBAL ANGLE (β)	m_{rev}/m_{tot}	P_{02} (PSFA)	T_{02} ($^{\circ}$R)	Q x 10^{-5}
Va	715	5.5	0.075	1.3636	0°	.0089	432.	3012.	3.18
					1°	.0090	509.	3015.	3.64
					2°	.0089	612.	3011.	4.21
					4°	.0078	875.	2963.	5.49
				1.9284	0°	.0118	182.	3165.	1.69
					1°	.0125	208.	3199.	1.90
					2°	.0132	238.	3226.	2.15
					4°	.0146	311.	3276.	2.71
					8°	.0174	548.	3375.	4.41
Vb	715	5.5	0.250	1.3636	0°	.0089	432.	3014.	3.19
					1°	.0090	509.	3016.	3.64
					2°	.0090	612.	3012.	4.21
					4°	.0078	875.	2966.	5.49
					6°	.0038	1231.	2941.	7.14
				1.9284	1°	.0126	208.	3204.	1.91
					2°	.0133	238.	3231.	2.15
					4°	.0147	311.	3280.	2.71
					8°	.0174	548.	3376.	4.41
Vc	715	5.5	0.750	1.3636	1°	.0090	509.	3017.	3.64
					2°	.0090	612.	3013.	4.21
					4°	.0077	875.	2971.	5.51
					6°	.0038	1231.	2950.	7.17

SD73-SA-0061

Table 6-3 Impingement Results (Full Scale)
(P_c = 727.5 psia, O/F = 5.8, P_{amb} = 0.075 psfa)

CASE	M_c	Y/R_e	GIMBAL ANGLE (β)	O/F (RE- VERSED)	m_{rev}/m_{tot}	P_{02} (PSFA)	$\overline{T0}_2$ (°R)	Q x 10^{-5}
VIa (NO TPE)	1.59	1.3636	4°	5.8	.0052	647.	4226	6.55
			6°	5.8	.0029	1107.	4288	10.24
	1.82	1.3636	0°	5.8	.0061	323.	4216	3.75
			1°	5.8	.0061	381.	4228	4.29
			2°	5.8	.0061	458.	4235	4.98
			4°	5.8	.0052	646.	4234	6.56
			6°	5.8	.0030	1107.	4291	10.24
		1.9284	0°	5.8	.0094	159.	4261	2.16
			1°	5.8	.0099	182.	4285	2.42
			2°	5.8	.0106	210.	4313	2.73
			4°	5.8	.0118	275.	4360	3.42
			8°	5.8	.0138	474.	4449	5.42
VIb (WITH TPE)	1.82	1.3636	0°	1.90	.0078	386.	2289.	2.06
			1°	1.91	.0079	461.	2296.	2.39
			2°	1.90	.0079	551.	2294.	2.75
			4°	1.87	.0070	801.	2256.	3.63
			6°	1.67	.0037	1191.	2116.	4.57
		1.9284	0°	2.02	.0104	160.	2422.	1.10
			1°	2.05	.0110	183.	2455.	1.24
			2°	2.08	.0116	208.	2485.	1.40
			4°	2.13	.0126	262.	2534.	1.72
			8°	2.28	.0152	471.	2678.	2.95

An additional parameter included is the relative mass flow reversed, m_{rev}/m_{tot}. This is the amount of boundary flow reversed per engine per 2π radians of circumference. For the full scale engine with TPE (Case VI b) the mass-averaged mixture ratio (O/F) is also included.

For most runs the ambient pressure (P_{amb}) was set at 0.075 psfa, corresponding to a nominal altitude of 240,000 ft. This value was varied parametrically in Cases Vb and Vc to reflect the effect of increased local pressure on the plume boundary. For model plume calculations the nozzle boundary layer point nearest the wall was selected to have a Mach number of about 1.6. This cut-off Mach number (M_c) was apparently too low to get complete plume solutions for the full scale cases. It required an increase to $M_c = 1.82$ to obtain a full plume. However, impingement calculations for the partial plume with $M_c = 1.59$ were included to assess the effect on the overall results. It turned out that these variations of M_c and ambient pressure produced very small changes in plume properties beyond half a radius from the lip and negligible changes in impingement parameters. However, the insensitivity to external pressure does not extend to indefinitely lower altitudes. When the plume boundary angle is decreased sufficiently by external pressure flow reversal does not occur at all.

In the following sections, the effects of different independent variables on the impingement parameters are discussed. The analytical results are compared, where possible, with the experimental data.

6.2.1 Effect of Mixture Ratio

During normal operation of the J-2 there is a relationship between mixture ratio (O/F) and chamber pressure (P_c). Figure 6.2.1-1 illustrates the combined effect of O/F and P_c variation on the impingement parameters. As expected, the recovery temperature, the stagnation pressure and the heat transfer parameter all increase with mixture ratio. The stagnation pressure increases at a rate slightly less than $P_c^{1.0}$ while the heat transfer parameter increases at a rate slightly greater than $P_c^{1.0}$. As shown in Figure 5.2.1-1, results from the present test show a linear relation between heat transfer and chamber pressure.

6.2.2 Effect of Chamber Pressure

In Figure 6.2.2-1 the influence of P_c alone (at O/F = 5.0) is shown. Recovery temperature, stagnation pressure, and the heat transfer parameter all increase with chamber pressure. Stagnation pressure increases at almost a linear rate whereas heat transfer increases somewhat more slowly. Both the present test data (see Figure 5.3.1-1) and that from Reference 1 confirm an approximately linear variation of heat transfer rates with chamber pressure.

Reference 1 also presents experimental measurements of recovery temperature using the heated-surface method. In this method heat transfer to the base is measured for a series of base surface

O/F	P_c (PSIA)
4.5	546
5.0	632
5.5	715
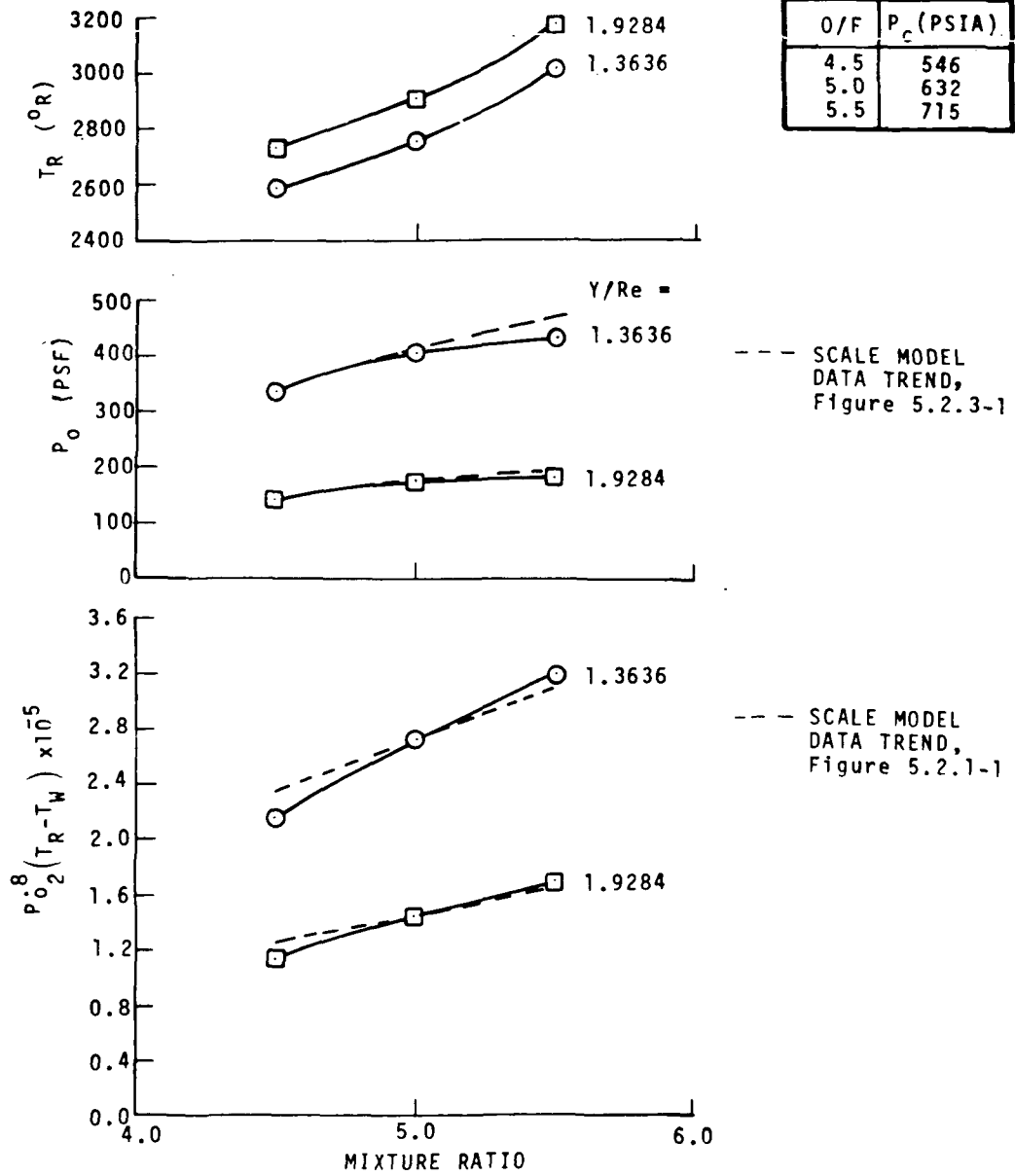
Figure 6.2.1-1 Combined Mixture Ratio, Chamber Pressure Effects
(Model Scale)

SD73-SA-0061
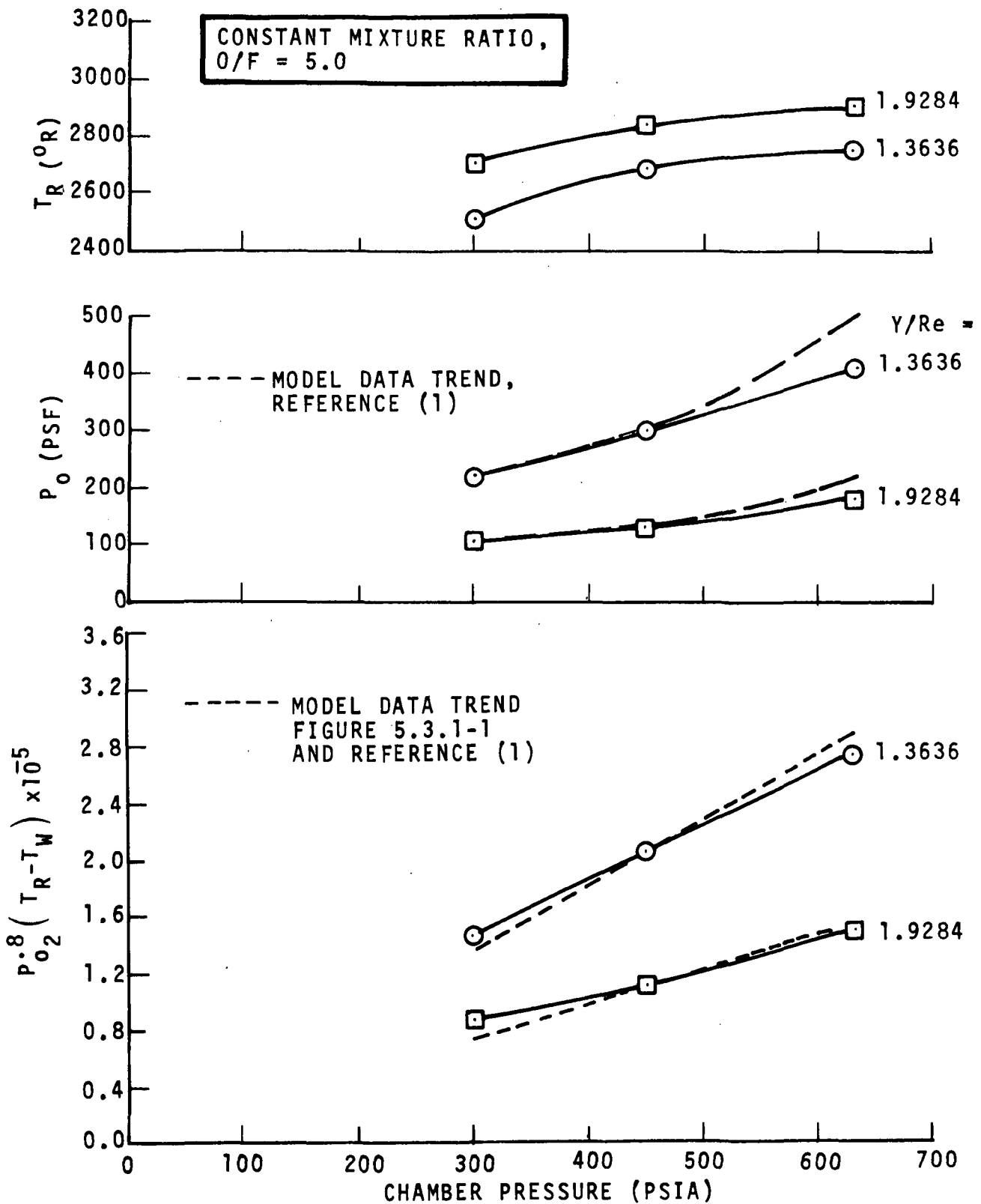
Figure 6.2.2-1 Effect of Chamber Pressure at Constant Mixture
Ratio (Model Scale)

SD73-SA-0061

temperatures and the resulting curve is extrapolated to zero heat
transfer. Figure 6.2.2-2 shows such plots for the conditions of Cases
I, II, and IV. The analytical predictions are superimposed covering
the range for close and far engine spacings. The agreement is quite good
considering the scatter in data and the simplifications in the analysis.

6.2.3 Effect of Plume Boundary Pressure

For Case V conditions, plume and impingement parameters were
computed for three ambient pressures covering a factor of ten. These
runs were chosen to investigate the sensitivity of the impingement
parameters to external pressure. The ambient pressure, either in an
altitude cell or in flight, may not correspond to the actual environment
of the plume in a multi-engine cluster. Table 6-4 summarizes the results.

TABLE 6-4 Effect of Ambient Pressure on Plume
Impingement Parameters

(1/25 Scale Model, P_c = 715 psia, O/F = 5.5, Y/Re = 1.3636, β = 1°)

Pamb(psfa)	M_B	θ_B^o	$\overline{T}_{o2}(R)$	P_{o2}(psfa)	Q x 10^{-5}
0.075	9.252	101.29	4016	509	3.64
0.25	7.787	95.36	3016	509	3.64
0.75	6.632	88.98	3017	509	3.64

As may be seen, in spite of substantial differences in the boundary Mach
number (M_B) and flow angle (θ_B) after expansion at the nozzle lip, the
impingement parameters are essentially constant. Thus below a certain
minimum value, the external pressure is not a critical factor in
determining the impingement parameters.

6.2.4 Effect of Symmetrical Engine Deflections

Impingement parameters have been computed for symmetrical gimballing
of engines for angles up to 6° (close engine spacing) and 8° (far engine
spacing). Figures 6.2.4-1, 2, 3 illustrate the effects for low, medium,
and high mixture ratios.

In general, recovery temperature is rather insensitive to gimballing.
For the far spacing, it increase only slightly with gimbal angle and for
close spacing the temperature actually decreases slightly. The pressure,
however, increases fairly rapidly and the heat transfer parameter almost
as rapidly.

It is difficult to compare the analytical results with experimental
data because in the latter, gimbal patterns are much more complex than
the symmetrical, co-planar pattern. In general at least three engines
influence the flow in any quadrant of the base region and each of the
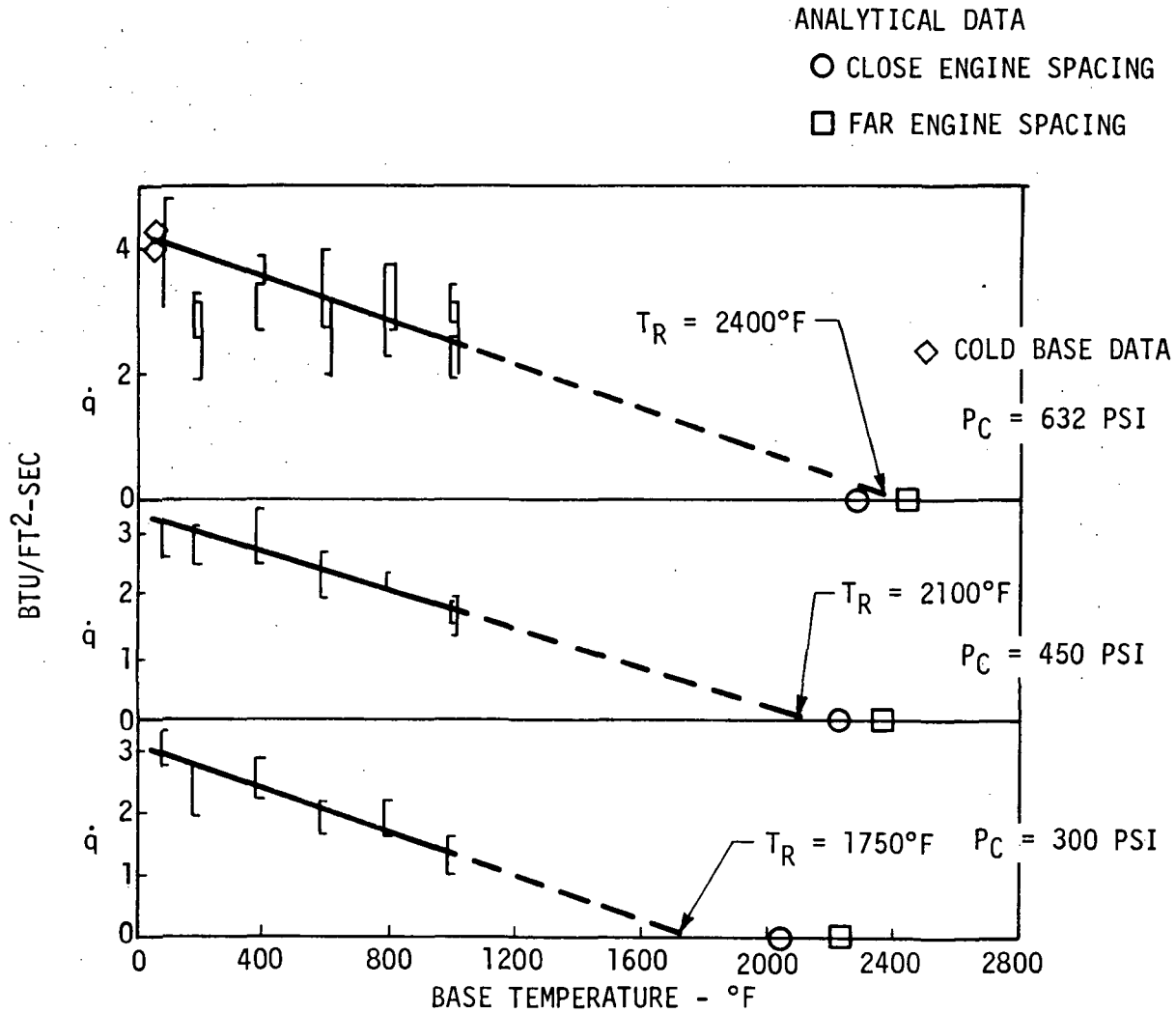
Figure 6.2.2-2   Analytical-Experimental Comparison of Recovery
Temperature for Model J-2 Tests
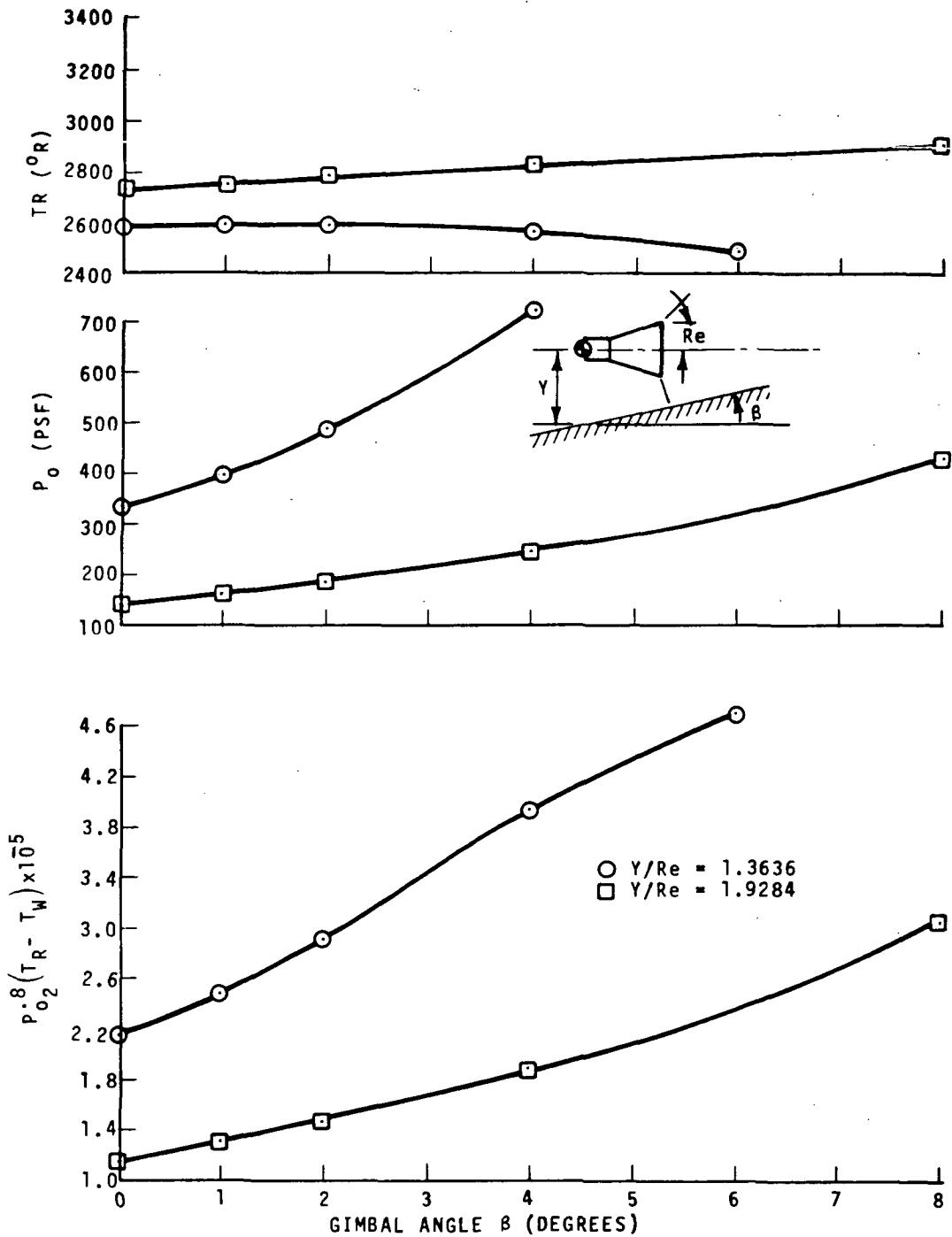
Figure 6.2.4-1 Effect of Co-Planar Gimballing on
Impingement Parameters (O/F = 4.5, P_c = 546 PSIA)
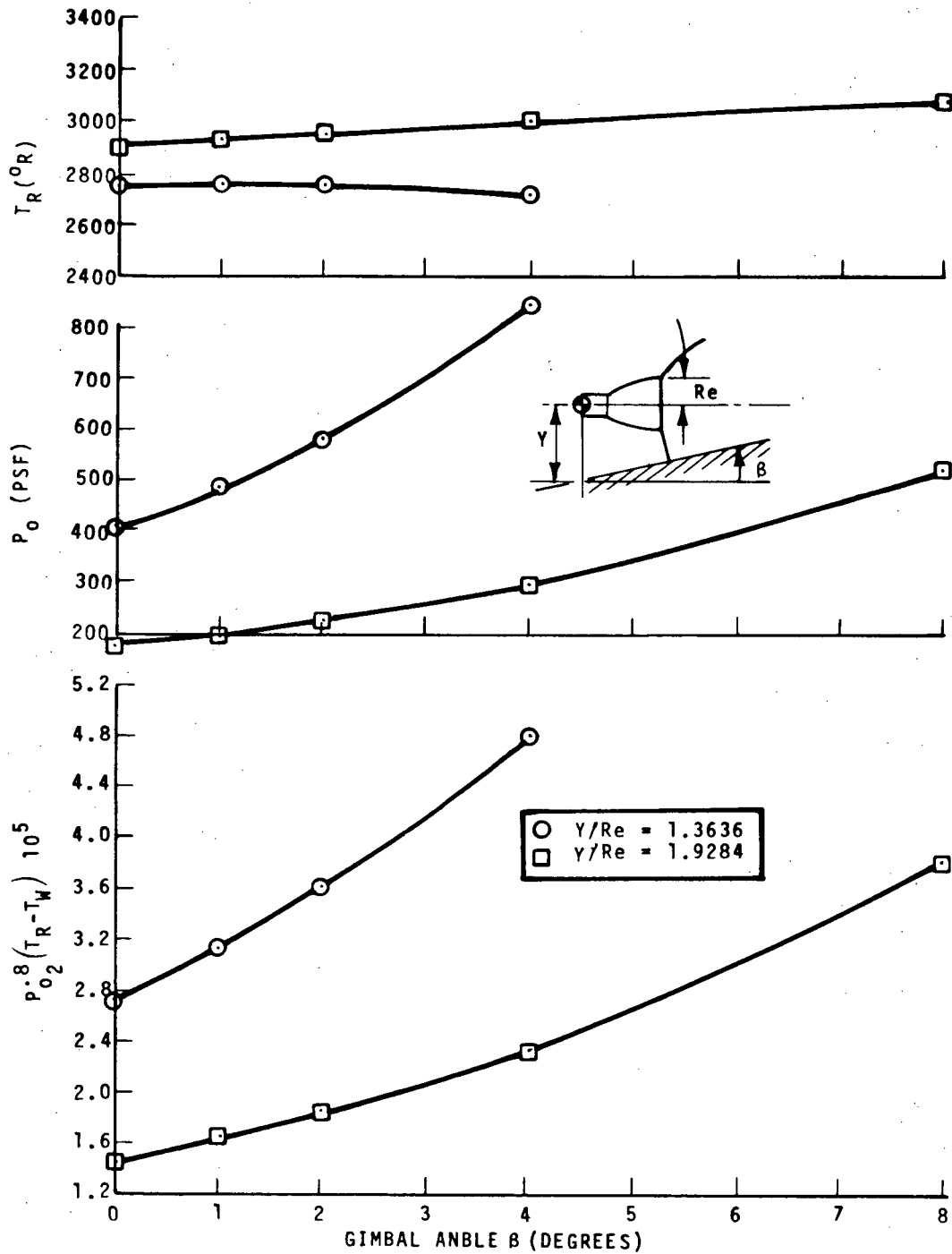
Figure 6.2.4-2   Effect of Co-Planar Gimballing on Impingement
Parameters (O/F = 5.0, P_c = 632 PSIA)
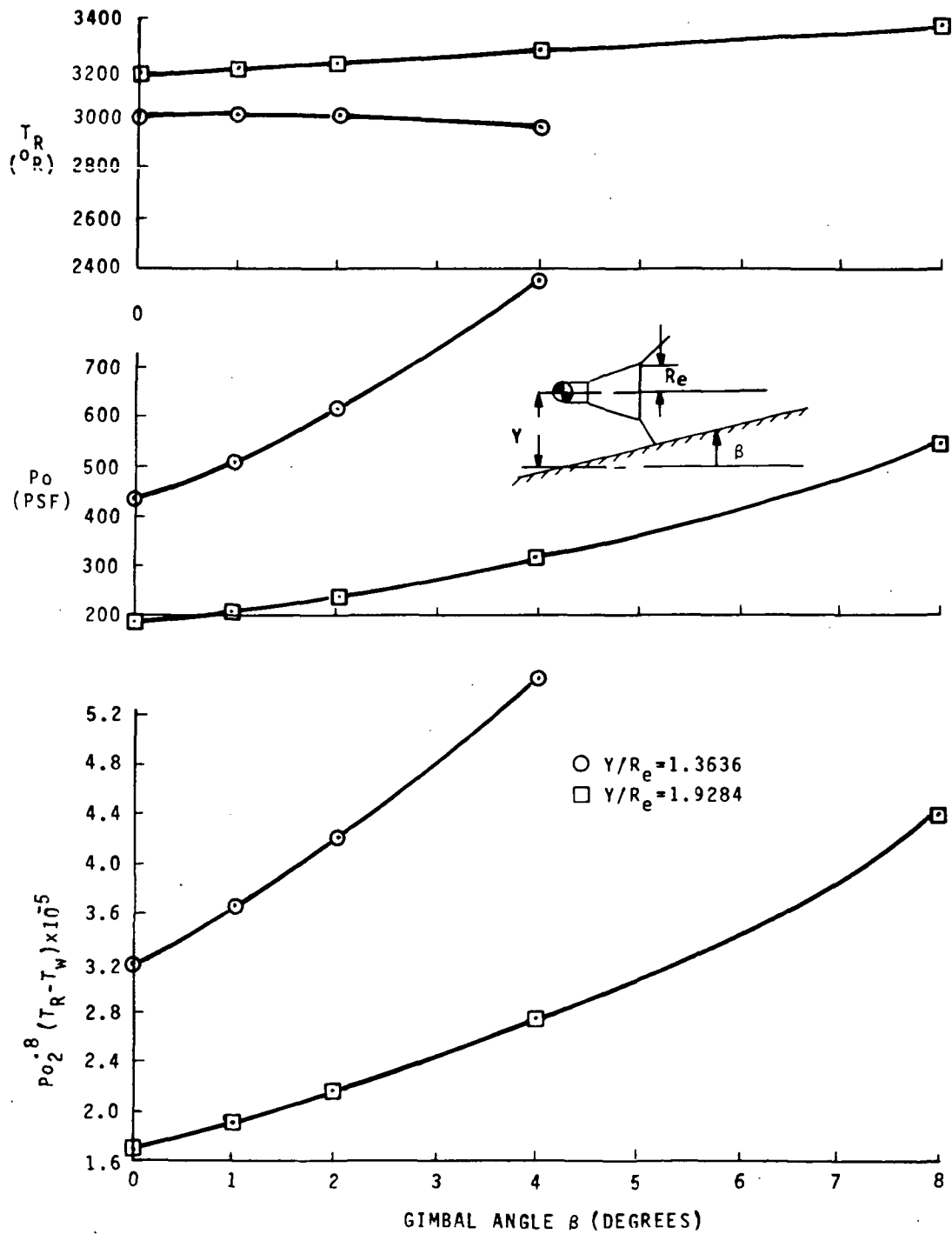
Figure 6.2.4-3   Effect of Co-Planar Engine Gimballing on
Impingement Parameters (O/F=5.5, P_c=715 psia)

outer engines gimbal in two directions. The resulting heat transfer distributions on the base heat shield shift and change level in a complicated fashion. A rough correspondence has been established between experimental and analytical results in the following way. An average gimbal angle between outer engine pairs is defined as $\bar{\beta} = (\beta_1 + \beta_2)/2$ where β_1 and β_2 are the algebraic values of the gimbal angle components in the plane containing axes of the outer engines. Gimbal components at right angles are ignored. The maximum heat transfer rate anywhere within the quadrant bounded by the engines is chosen as the correlating variable. Figure 6.2.4-4 shows the results for various gimbal patterns at one mixture ratio. For comparison the analytical heat transfer parameter, evaluated for the outer engine spacing, is included. Although there is considerable scatter, the experimental trend matches the slope of the analytical prediction indicating a rough proportionality between maximum heat transfer and the heat transfer parameter Q.

Even more extreme gimbal patterns occur during double actuator failure and heat transfer rates are correspondingly high. In this case an outboard engine gimbals as much as 10.6^o inward toward the center engine (see pattern 4A-a, Figure 5.10-1). The outboard plume impinges on the nozzle of the center engine and peak heating occurs on the heat shield and flex curtain of the adjacent outboard engine, i.e., engine #1 for gimbal case 4A-a. Here too, the impingement analysis gives a reasonable prediction. If the impingement plane is considered to be the actual surface of the center nozzle, the total inclination between surface and outboard plume axis is 15.1^o. The parameter Q in this case is 6.0 times the value for no gimballing. This compares well with the observed factor of 5.3 for the ratio of peak heating rates to the heat shield with gimbal patterns 4A-a and the no deflection case.

6.2.5 Full Scale Results

Impingement parameters for the full scale J-2 are shown in Figure 6.2.5-1. Results are shown both with and without TPE for comparison. The most noticeable difference is in the level of the recovery temperature, which is about 2000R lower for the TPE case. This effect results from the injection of hydrogen-rich gas into the boundary layer. The stagnation pressure of the reversed gas is changed relatively little, so that the difference in heat transfer parameter is due primarily to the difference in recovery temperature.

An approximate evaluation of the effect of scale can be obtained by comparing the full scale results without TPE to the model case Va. Chamber conditions are nearly the same (P_c = 715 versus 727.5 and O/F = 5.5 versus 5.8). Figure 6.2.5-2 shows the impingement parameters plotted against exit Reynolds number (essentially proportional to the geometrical scale). Pressures are relatively insensitive but the full scale case shows a considerable increase in recovery temperature. This reflects the relatively thinner boundary layer and the fact that more of the reversed flow comes from the outer portion of the layer where stagnation enthalpy is higher.

$$P_C = 715 \text{ PSIA}, \text{ O/F} = 5.5$$

O   NO DEFLECTION
△   OUTBD ENGINE OUT
□   SINGLE ACTUATOR FAILURE
▽   NOMINAL TRIM & COMPLIANCE
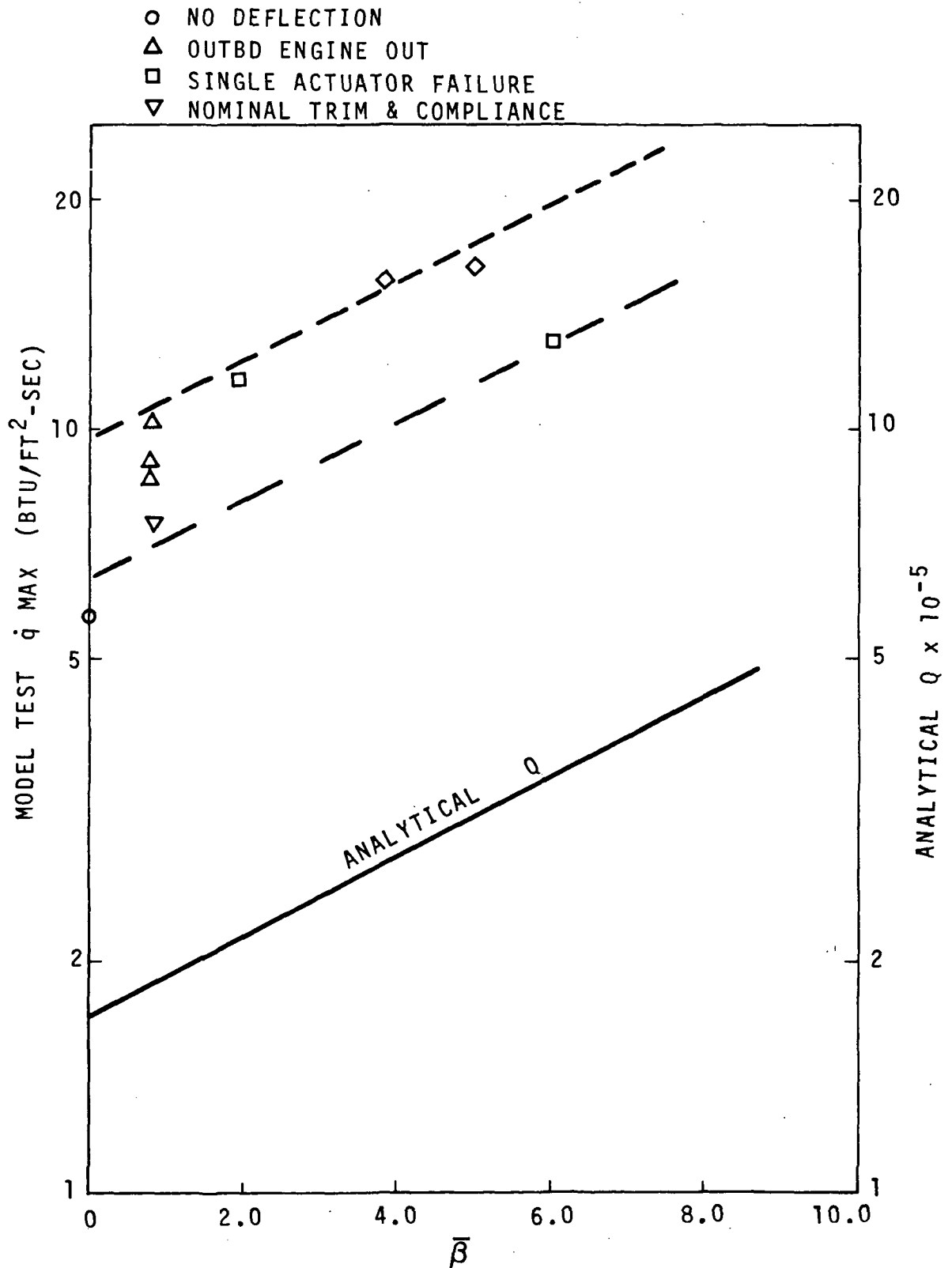
Figure 6.2.4-4   Analytical-Experimental Comparison of Base Heat Transfer during Gimballing
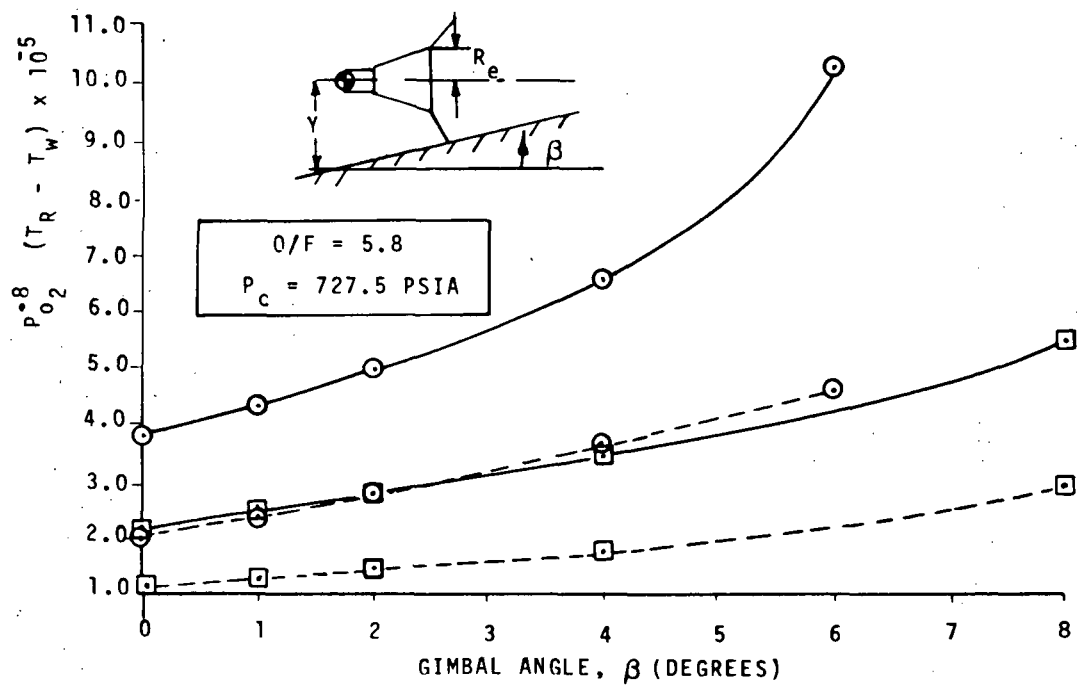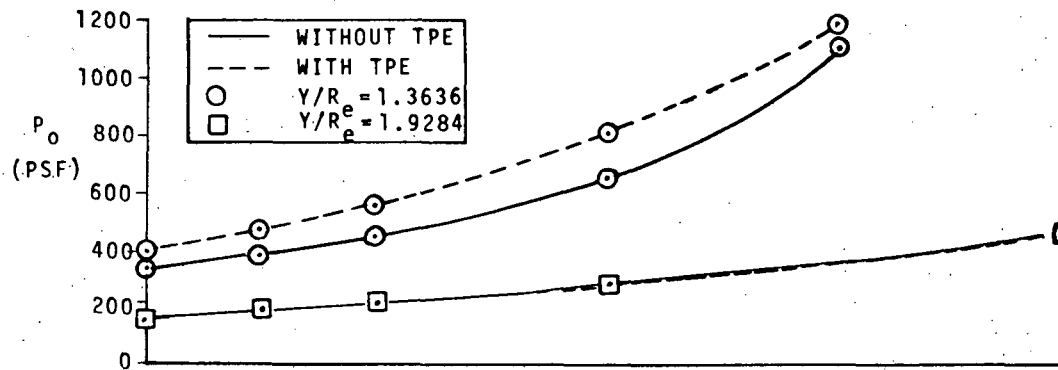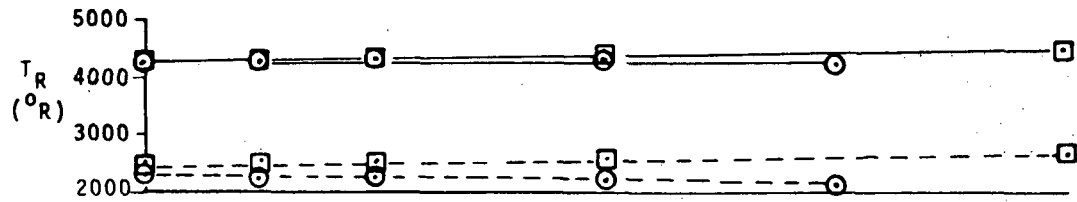
Figure 6.2.5-1   Effect of Co-Planar Gimballing
for Full Scale Plumes
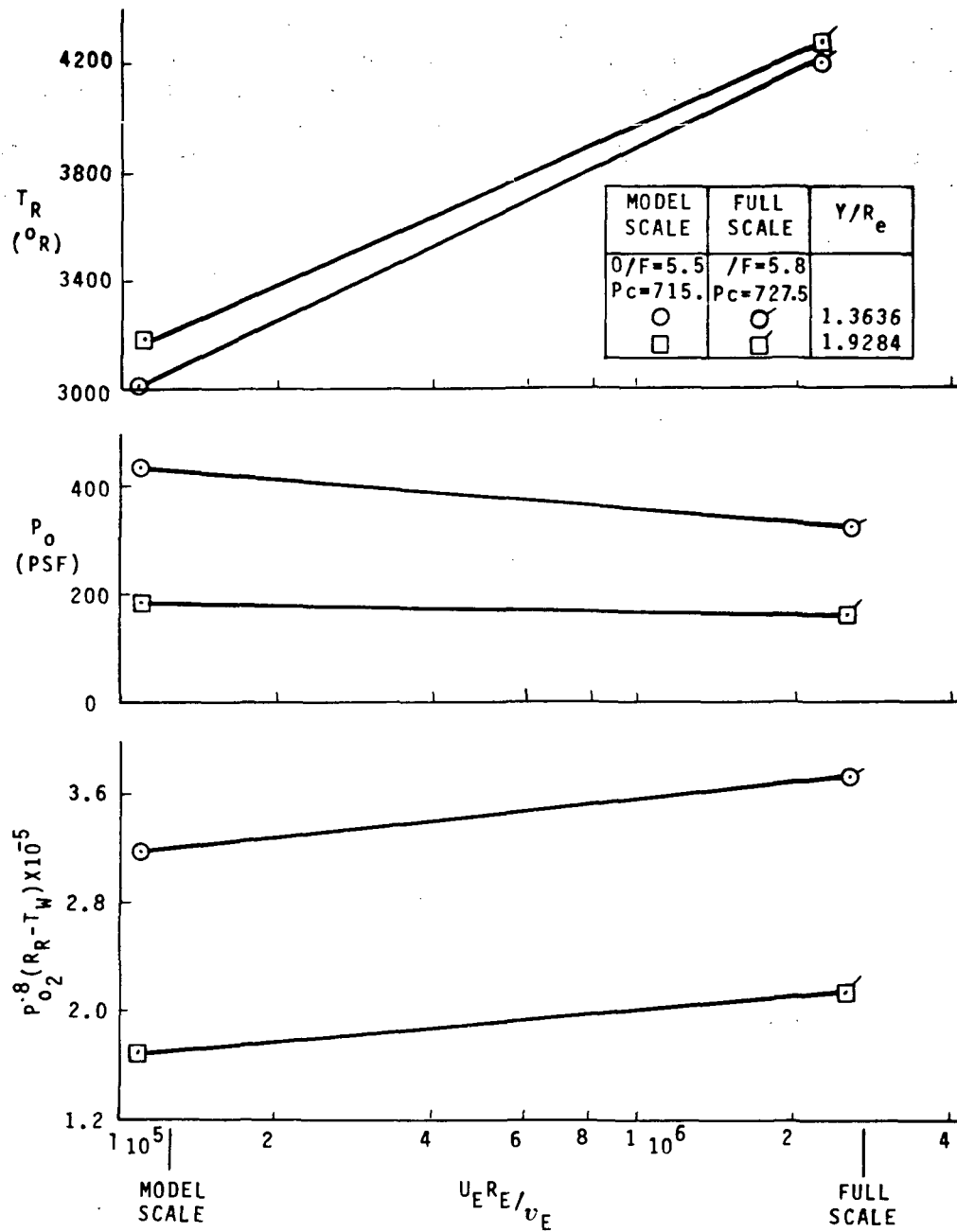
Figure 6.2.5-2 Variation of Impingement Parameters
with Reynolds Number

SD73-SA-0061

Both Figures 6.2.5-1 and 6.2.5-2 show clearly the necessity for TPE injection to reduce recovery temperatures in the full scale case. Without TPE the level would be above 4000R whereas with TPE, the level drops to about 2200R, not far above the experimental value of 1400-1600R.

There is an additional observation tending to confirm the correctness of the recovery temperature predictions. The predicted recovery temperature for the far spacing is about 130R higher than that for close spacing (see Table 6-3). This compares favorably with the recovery temperature rise observed on CECO during flight when only the far spacing occurs between active engines.

7.0 COMPARISON WITH FLIGHT DATA

The 1/25 scale model S-II base region thermal environment test results
are compared in this section with flight data and analytical predictions
wherever possible. In order to compare flight and model heating rate data,
it is necessary to normalize the flight data to the scale model conditions.
Flight data normalization includes radiometer correction, gas recovery
temperature probe correction, total heat flux calorimeter temperature
mismatch correction, film coefficient wall temperature correction, chamber
mixture ratio-chamber pressure correction and steady state engine deflections
correction.

7.1 FLIGHT DATA NORMALIZATION

The various procedures used to normalize S-II base region flight
heating rate data are described in the folowing sections.

7.1.1 Radiometer Correction

Analysis has shown that the output of the radiometer used on the
S-II base heat shield does not give a correct indication of plume
radiation. In part this is due to the low-frequency-radiation being
cut-off by the quartz window which shields the sensing element of the
gage from convective heating. About one-third of the incoming plume
radiation is blocked in this way. However, the window itself radiates
as it gradually becomes heated by convection from the recirculating
plume gases. This window radiation over-corrects for the blocked plume
radiation and results in a large over-estimate, particularly in the
latter portion of a flight.

The radiometer is idealized as two parallel, edge-supported discs,
thermally coupled by radiation and conduction across a narrow air gap as
shown in Figure 7.1.1-1. Analysis of the transient output of the
radiometer is limited to regions where special knowledge exists, namely,
near ignition and near engine shut-off.

Since readings are available from an adjacent total heat transfer gage,
the steady-state heat balances for the radiometer can be solved to give a
value of the corrected radiation. This procedure is based on the assumption
that both the radiometer and the total gage receive the same total heat
input.

The low-frequency component of the plume radiation is not sensed
directly by the radiometer and its effect on the quartz window cannot
be distinguished from convective heating. Its magnitude can be inferred,
however, by considering the ratio of intensities above and below the
cut-off frequency of quartz.

7.1.1.1 Interpretation of Radiometer Transients

The radiometer is idealized as two parallel, edge-supported disks,
thermally coupled by radiation and conduction across a narrow
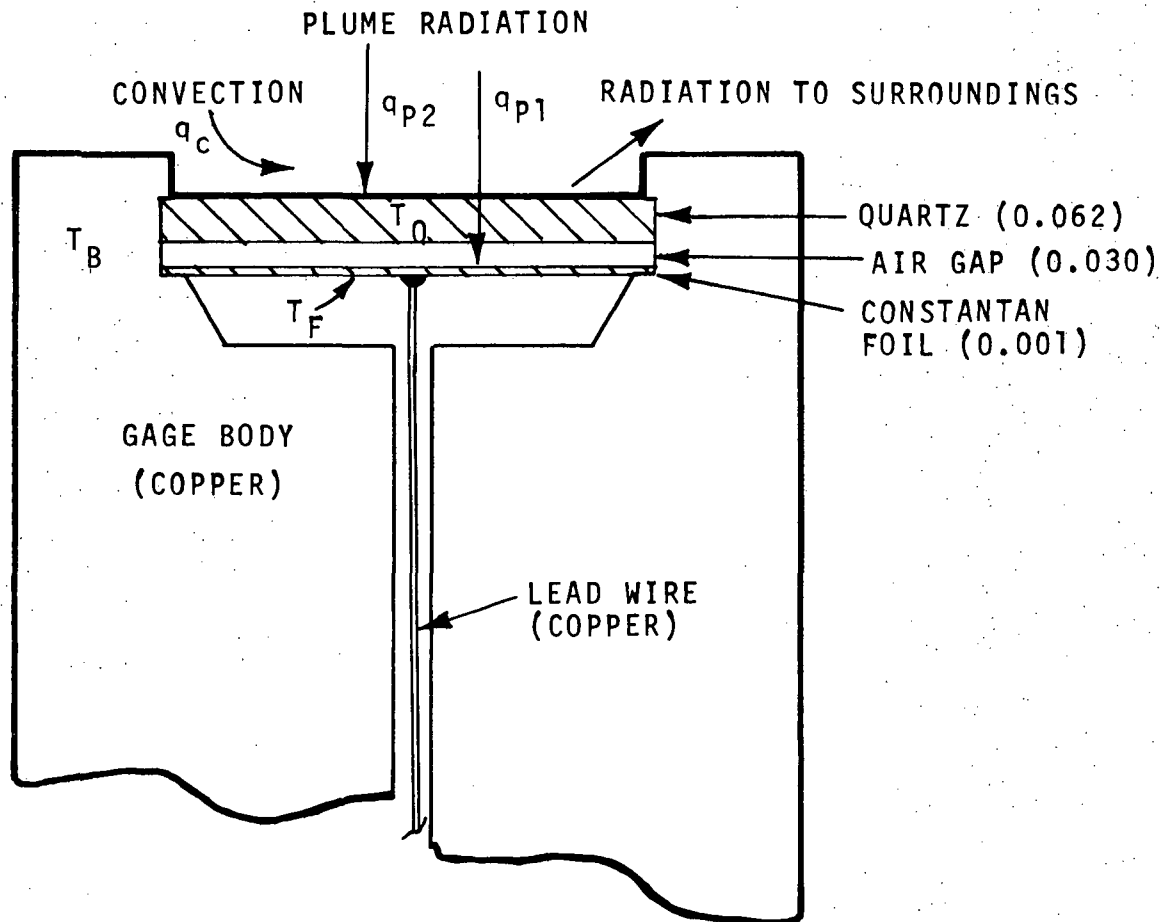
Figure 7.1.1-1 Radiometer Configuration

SD73-SA-0061

air gap (see Figure 7.1.1-1). For the outer disk (the quartz window) the heat balance equation is

$$h_c\left(T_G - T_Q\right) + q_{p2} + \left(k_A / \delta A + h_{r1}\right)\left(T_F - T_Q\right)$$

$$- h_{r2}\left(T_Q - T_S\right) + 2\delta_Q k_Q \frac{1}{r} \frac{\partial T_Q}{\partial r} = \delta_Q \rho_Q C_{p_Q} \frac{\partial T_Q}{\partial t} \qquad (7\text{-}1)$$

The temperature gradient term (representing radial conduction) was approximated by the expression for the center of a disk with parabolic temperature distribution

$$2\delta_Q k_Q \frac{1}{r} \frac{\partial T_Q}{\partial r} = -4 \frac{\delta_Q k_Q}{r_B^2} \left(T_Q - T_B\right) \qquad (7\text{-}2)$$

The heat balance equation for the sensing foil (the inner disk) is simpler since, by assumption, it is always in a quasi-steady state because of its very small thermal capacity.

$$q_{p1} + \left(k_A / \delta_A + h_{r1}\right)\left(T_Q - T_F\right) = 4\delta_F k_F \left(T_F - T_B\right) / r_B^2 \qquad (7\text{-}3)$$

The same approximation (equation 7-2) was used for the radial conduction term in the foil.

Under the assumption that coefficients and source and sink temperatures remain constant with time, the heat balances yield equations of the form

$$D + GT_Q(t) = T_F(t) \qquad (7\text{-}4)$$

and

$$T_F(t) = T_F(\infty) + \left[T_F(o) - T_F(\infty)\right] e^{-\beta t} \qquad (7\text{-}5)$$

The foil temperature, T_F, is obtained directly from the indicated gas output through a knowledge of the body temperature, the gage slope during calibration and the thermoelectric power of the copper-constantan couple.

$$T_F = T_B + q_{ind}(S/E) \qquad (7\text{-}6)$$

The experimental gage output may thus be converted to a foil temperature history and fitted to the theoretical expression (Equation 7-5). The quantities $T_F(\infty)$, $T_F(0)$ and β are related theoretically to to the terms in Equations 7-1, 7-2 and 7-3.

In order to avoid the difficulties associated with the radial conduction term, it was necessary to restrict transient analysis of the gage to the initial transient where the conduction term is negligible and to after shut -off when the plume radiation is zero.

Since independently measure total heat transfer rates are available, they can be combined with the radiometer readings to solve the steady-state heat balance equations and obtain corrected plume radiation at any time in flight where both total and radiometer gage outputs are reasonably constant.

7.1.1.2 Plume Radiation and Total Heat Transfer from
          Post-Ignition Transient

At about 10 seconds from S-II engine start, the radiometer output settles into a regular rising curve which is well-approximated by Equation 7-5. The time at the beginning of this regular region is designated by t_o.

At the onset of convective heating (t_i) the quartz window temperature has its initial value, that of the gage body T_B. During the interval (t_o - t_i) the window temperature rises somewhat. This increase can be approximated from the slope of the radiometer output, evaluated at t_o. This is accomplished by first converting radiometer output to foil temperature by means of Equation 7-6 followed by a least-squares fit to Equation 7-5. In Equation 7-6, the initial condition is evaluated at t_o and time is measured from that point on.

The slope of the foil temperature at the initial point (t_o) is given by

$$\left(\frac{dT_F}{dt}\right)_o = \left[T_F(\infty) - T_F(0)\right]\beta \qquad (7\text{-}7)$$

The foil temperature slope is related to the quartz temperature slope by differentiating Equation 7-3 under the assumption that the coefficients remain constant.

$$\frac{dT_Q}{dt} = \frac{\left(k_A/\delta_A + h_{r1} + 4\delta_F k_F/r_B^2\right)}{\left(k_A/\delta_A + h_{r1}\right)}\frac{dT_F}{dt} \qquad (7\text{-}8)$$

Finally, the quartz temperature at t_o is related to the initial value (T_B) by

$$T_Q = T_B + (t_o - t_i)\left(\frac{dT_Q}{dt}\right)_{t_o} \qquad (7\text{-}9)$$

Once the quartz temperature at t_o is known, the true high frequency plume radiation can be computed from Equation 7-3. The body temperature of the gage is not taken strictly as a constant but is assumed to increase at the rate of 0.18 degrees per second, based on an analysis of the

overall gage heat transfer. The radial conduction term is not evaluated from the geometry and properties of the foil which are not known very accurately. Instead, its value is computed from the gage calibration curve from

$$\frac{4\delta_F k_F}{r_B^2} = \frac{E}{S} - \frac{k_A}{\delta_A} - h_{r1}$$ (7-10)

where the conductances on the righthand side are evaluated at room temperature.

The low-frequency component of the plume radiation is not sensed directly by the radiometer and its effect on the quartz window cannot be distinguished from convective heating. Its magnitude can be inferred, however, by considering the ratio of intensities above and below the cut-off frequency of quartz.

$$q_{p2} = f_{rad} \, q_{p1}$$ (7-11)

It is reasonable to assume that plume radiation falling on the radiometer is equal to that which would fall on an adjacent total heat transfer gage. If the surface temperatures of the radiometer window and the total gage are not too different, than the convective heat transfer and the total heat transfer will also be the same. This assumption is made here in order to compare total heat transfer as deduced by the two gages.

The quartz heat balance (Equation 7-1) can be written

$$q_{tot} = q_{p1} + (k_A/\delta_A + h_{r1})(T_Q - T_F) + h_{r2}(T_Q - T_S)$$
$$+ q_{cond} + (\rho\delta C_p)_Q \frac{dT_Q}{dt}$$ (7-12)

where q_{cond} is the radial conduction term for the quartz window. During the post-ignition transient its value is zero. All quantities on the right hand side are thus known or calculable from the radiometer transient, and Equation 7-12 provides an estimate of the intital value of the total heat transfer from the radiometer alone.

7.1.1.3 Plume Radiation from Steady-State Gage Outputs

At flight times when the radiometer and an adjacent total gage have both reached steady state, Equation 7-3 and 7-12 can be solved for the quartz temperature, which then yields plume radiation from Equation 7-3 and 7-11.

During steady state, the time derivative in the quartz heat balance (Equations 7-12) is zero and the radial conduction term is given by Equation 7-2. Moreover, the as yet unknown plume radiation q_{p1} can be

eliminated by substitution from the foil heat balance (Equation 7-3).
The resulting expression is

$$q_{tot} = 4\delta_F k_F (T_F - T_B)/r_B^2 + h_{r2}(T_Q - T_S)$$

$$+ 4\delta_Q k_Q (T_Q - T_B)/r_B^2 \qquad (7-13)$$

q_{tot} is available from the total heat gage output. T_F is computed from
the radiometer output by Equation 7-6. T_B is estimated from an initial
temperature and the 0.18 F/sec rise previously mentioned. Thus Equation
7-13 can be solved directly for the quartz temperature. The quartz
temperature in turn is used in Equation 7-3 to give the high frequency
plume radiation, while Equation 7-11 gives the low-frequency component.

7.1.1.4 Analysis of the Post Shut-off Transient

The typical outputs of an adjacent pair of gages during the shut-off
phase are shown in Figure 7.1.1-2. As in the case of the ignition
transient, two times are identified, one corresponding to the end of
convective heating (t_i) and the other to the beginning of the regular
portion of the final radiometer transient curve (t_o). The foil temperature
and foil temperature slope at t_o are obtained by a least-squares fit as
before. The foil temperature immediately after shutoff (T_F+) is found by
extrapolating back to the t_i using the foil temperature slope. The quartz
temperature at t_i can now be evaluated from Equation 7-3, noting that the
plume radiation is zero.
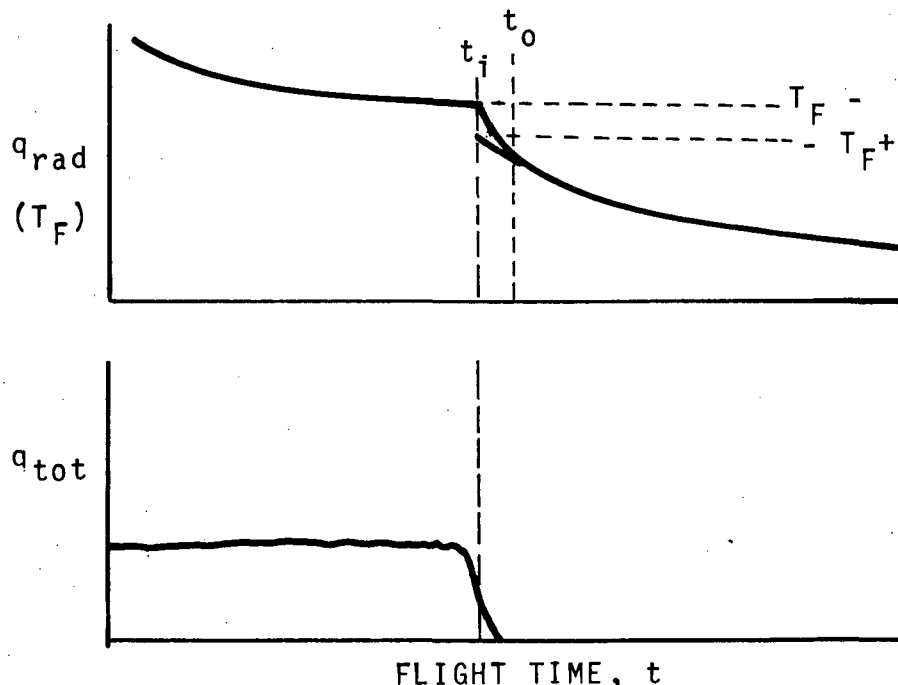
Figure 7.1.1-2 Typical Gage Output during Shut-Off Transient

The foil temperature slope at t_i is also used with Equation 7-8 to obtain the quartz temperature slope.[1] This slope in turn may be subsituted into the quartz heat balance, Equation 7-12. The value of q_{tot} obtained in this way can be compared with its ideal value of zero to obtain an estimate of the overall consistency of the analysis.

The quartz temperature immediately before shutoff will be the same as that immediately after. Its value can be substituted into Equation 7-3 to give a value of the high-frequency plume radiation. Here, the foil temperature T_F is obtained from the indicated radiometer signal just before shutoff. The low-frequency component is obtained from Equation 7-11 as before. The quartz temperature T_Q and the foil temperature T_F can also be substituted into the steady-state form of the quartz heat balance (Equation 7-13) to give an estimate of the total heating independent of any total heat transfer gage.

7.1.1.5 Typical Flight Radiometer Analysis Results

The foregoing equations have been incorportated into a radiometer correction computer program. Typical results obtained from this program for two Apollo-Saturn flights (AS-504 and AS-505) for which complete base heating information was available are presented next. The radiometer chosen was C692-206. An adjacent gage (C720-206) was used for total heat transfer readings.

The results of the radiometer correction program are shown in Table 7.1.1-1. As may be seen, the corrected radiation is always less than the indicated radiation except at the very beginning. There are two consistency tests which tend to support the overall correctness of the method. First, the total heating values derived solely from analysis of the radiometer transients agree quite well with the values measured by an independent total gage. Secondly, the corrected radiation values based on transient analysis agree fairly well with the values obtained from a steady-state analysis in the same time segment (where plume conditions presumably have not changed greatly).

A further test of the method was made using a thermal analyzer program. The indicated output of the radiometer was predicted, using as inputs the measured total heating and the corrected radiant heating obtained from the radiometer correction program. Figure 7.1.1-3 shows the computer radiometer output for the AS-504 flight, superimposed on the flight data history. The corresponding total heat transfer history is shown below. For comparison, the corrected radiation and predicted total heating values are superimposed. The radiometer output predictions follow the observed records very well as to shape and the differences in level are no larger than the tolerance band indicated for the corrected radiation.

The radiometer analysis results of Table 7.1.1-1 were used as a basis to adjust the analytically predicted incident radiative heat flux values for each total heat flux gage location during flight data normalization, as shown in Table 7.2-4.

SD73-SA-0061

Table 7.1.1-1 Results of Radiometer Correction Program

Flight Time (Sec)	Time Segment	BTU/FT²-Sec			
		Radiation		Total Heating	
		Indicated	Corrected	Indicated	Computed
	Flight AS-504				
172.5	Post Ignition	0.65	0.68 ± .03	2.40	2.62 ± .18
400.0	Ignition- PMR Step	1.25	0.65 ± .11*	3.00	---*
535.0	PMR Step-Shutdown	0.76	0.22 ± .06*	2.05	---*
537.0	Pre Shutdown	0.76	0.18 ± .01	2.05	2.11 ± .12
537.0	Post Shutdown	0.63	0.00	0.00	-.07
	Flight AS-505				
170.0	Post Ignition	0.64	0.74 ± .03	2.20	2.45 ± .18
460.0	Ignition - CECO	1.28	0.87 ± .11*	2.80	---*
488.5	CECO-PRM Step	1.16	0.63 ± .11*	2.80	---*
550.0	PMR Step-Shutdown	0.61	0.26 ± .06*	1.50	---*
551.0	Pre Shutdown	0.61	0.07 ± .01	1.50	1.87 ± .12
551.0	Post Shutdown	0.57	0.00	0.00	+ .15

* Radiation computed from steady-state data; no estimate of total heating possible for steady state.

Space Division
North American Rockwell
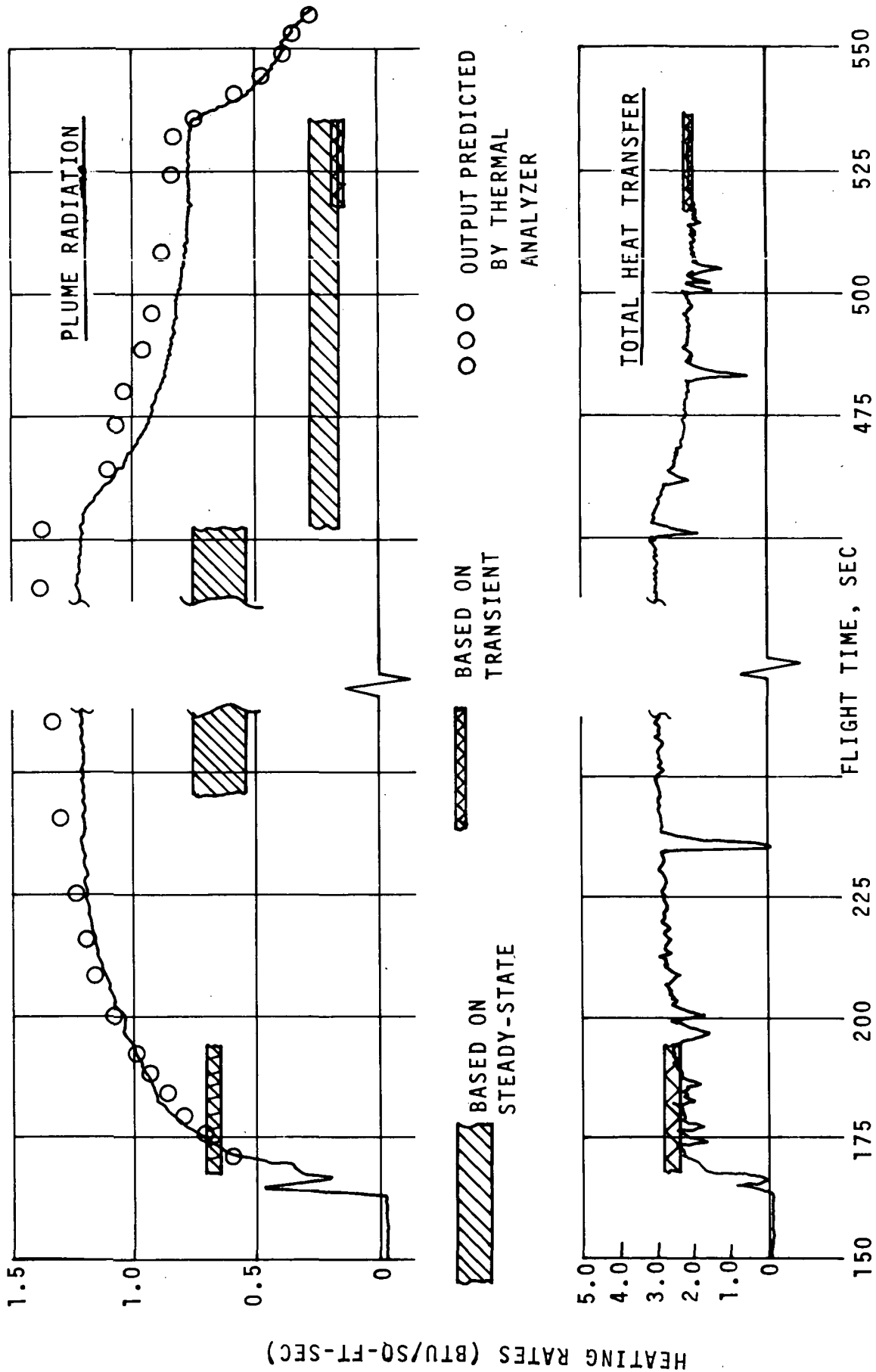
Figure 7.1.1-3 Indicated and Corrected Heating Rates for Flight AS-504

SD73-SA-0061

7.1.2   Total Heat Transfer Calorimeter Correction

The S-II stage base region is instrumented with Gardon or thin-foil-sensor type total heat flux gages. These gages are calibrated by means of a radiative source while during flight a combination of convective and radiative heating is measured. In addition, temperature discontinuities exist between the heat shield, the calorimeter body and the calorimeter's sensor foil. These temperature discontinuities affect the boundary layer and hence, the heat transfer to the gage.

Therefore, in order to obtain an accurate evaluation of the heat transfer during flight, it is necessary to correct for all of these effects. The procedures used for flight data evaluation are discussed in the following sections.

7.1.2.1   Heat Transfer Coefficient at the Sensor Surface

The total heat flux calorimeter is shown schematically in Figure 7.1.2-1.
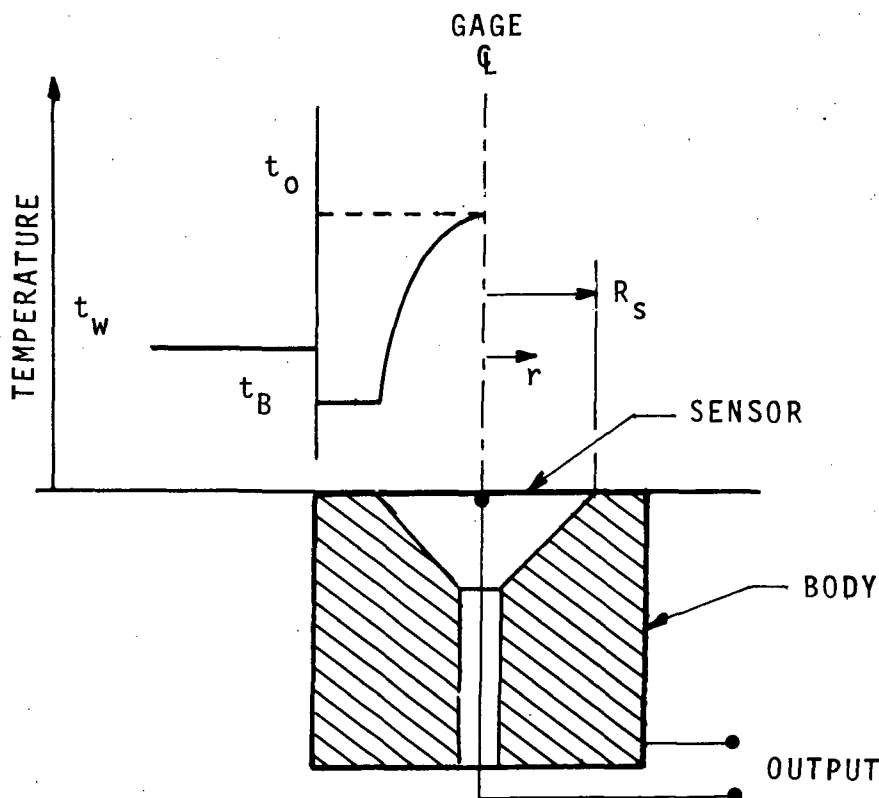
Figure 7.1.2-1   Total Heat Flux Gage Schematic

The calorimeter consists of a thin metal constantan disk, suspended over a cavity, which is thermally and electrically attached to a copper body or heat sink thus forming a thermocouple junction at the interface. A thin copper wire is attached to the center of the sensor disk forming a second thermocouple junction. The gage e.m.f. output is therefore proportional to the temperature difference between the two junctions, i.e., the gage body temperature and the sensor centroidal temperature.

In this analysis, the external environment is assumed to be changing slowly in comparison with the calorimeter's time constant (0.5 seconds) so that at any time in flight, the calorimeter temperatures can be represented by steady state distributions corresponding to the external environment at that instant.

Under these conditions, the steady state heat balance equation for the colorimeter sensor is given by

$$\frac{d^2 T}{dR^2} + \frac{1}{R}\frac{dT}{dR} + \frac{1}{\delta k}\left\{ q_r - hT - \sigma \alpha (T + t_{aw})^4 \right\} = 0 \quad (7\text{-}14)$$

where

$$T = t(r) - t_{aw}$$

$$R = r/R_s$$

or solving for T, we have

$$T = \frac{R_s^2}{\delta k} \int_0^r \frac{1}{R} \int_0^r R\left[hT - q_r + \sigma \alpha (T + t_{aw})^4 \right] dR dR$$

$$+ \int_0^r C_1 dR + C_2 \quad (7\text{-}15)$$

The boundary conditions are

$$\frac{dT}{dR}(0) = 0$$

$$T(1) = T_B$$

hence $\quad C_1 = 0 \quad$ and

$$C_2 = T_b - \frac{R_s^2}{\delta k} \int_0^1 \frac{1}{R} \int_0^1 R\left[hT - q_r + \sigma \alpha (T + t_{aw})^4 \right] dR dR$$

$$T(o) = C_2 \quad (7\text{-}16)$$

From the gage calibration conditions

$$T_o - T_b = Q\left(\frac{R_s^2}{4\delta k}\right) = K\ Q$$

where Q is the gage indicated output; hence

$$C_2 = T_b + K\ Q \tag{7-17}$$

K is either computed from the calorimeter properties or obtained directly from the calibration data. The gage body temperature is either measured during flight or an approximate value is computed analytically. If the incident radiative heat flux and the recovery temperature are known from independent measurements, then equations 7-15 and 7-16 can be solved iteratively by means of numerical integration for the film coefficient (h), at the sensor surface and the corresponding sensor temperature (T) distribution.

7.1.2.2 Calorimeter Body Temperature History

Since the S-II base region total heat flux calorimeter body temperature was not measured during flight, the following approximate procedure was used to calculate the calorimeter body temperature history which is require to accurately evaluate the film coefficient at the calorimeter sensor surface.

Neglecting the reradiation heat loss from the sensor, the sensor temperature distribution is given by

$$t - t_b = \left(q_r/h + t_{aw} - t_b\right)\left\{1 - \frac{I_0(Nr)}{I_0(NR_s)}\right\} \tag{7-18}$$

where
$$N^2 = h/\delta k$$

The heat conducted from the sensor foil to the calorimeter body is

$$q_1 = -\ 2\pi R_s\ k\delta\left(\frac{dT}{dr}\right)_{r=R_s}$$

The heat received by convection and radiation from the surroundings is

$$q_2 = A_t \left\{ h\left(t_{aw} - t_b\right) + \alpha\, q_r \right\}$$

Therefore, the rate of temperature change with time is given by

$$\frac{dt_b}{d\theta} = \left(t_{aw} - t_b\right)\left\{ A\,h + B\,\frac{I_1(NR_s)}{I_0(NR_s)} \right\} + q_r\left\{ A + \frac{B}{h}\,\frac{I_1(NR_s)}{I_0(NR_s)} \right\} \qquad (7\text{-}19)$$

where
$$A = A_t/\rho\,Cp\,V$$

$$B = 2\pi R_s\,k\delta N/\rho\,Cp\,V$$

Hence, knowing the initial calorimeter body temperature t_{b_0} prior to ignition of S-II engines from the base region temperature measurements, the body temperature history is obtained from

$$t_{b_\theta} = t_{b_0} + \int_0^\theta \frac{dt_b}{d\theta}\,d\theta \qquad (7\text{-}20)$$

7.1.2.3 Temperature Mismatch Correction

The effect of step-wise temperature discontinuities on heat transfer coefficients has been extensively studied both analytically and experimentally. During the four-engine scale model base heating test of Reference 4, temperature discontinunity effects between the heated heat shield and the cooled slug-type calorimeter were investigated experimentally. Measured values of the film coefficient at the cooled calorimeter surface were as much as 80 percent above the corresponding value for an isothermal surface. This illustrates the importance of correcting the calorimeter flight data for temperature mismatch effects before comparisons can be made with the isothermal scale model heat transfer results.

The ratio of the heat transfer coefficients h_w at an isothermal surface to that at the asymptotic thin-foil-type calorimeter sensor is derived in Reference 11 as

$$\frac{h_s}{h_2} = 1 + H_1\,\frac{\left(t_w - t_b\right)}{\left(t_{aw} - t_b\right)} + H_2\,\frac{\left(t_0 - t_b\right)}{\left(t_{aw} - t_0\right)} \qquad (7\text{-}21)$$

SD73-SA-0061

where

$$H_1 = 2\left(\frac{\gamma R_s}{x_o}\right)^{\beta} \frac{2^{\beta+1}-1}{\beta_2} - 1$$

$$H_2 = 1 - 4\left(\frac{\gamma R_s}{x_o}\right)^{\beta} \left[\frac{2^{\beta+1}-1}{\beta_3} - \frac{2^{\beta+3}-1}{\beta_4}\right] \qquad (7\text{-}22)$$

where

$$\beta_i = (\beta+1)(\beta+2) \ldots (\beta+i) \qquad (7\text{-}23)$$

and

$$\left.\begin{array}{l} \gamma = 3/4 \\[6pt] \beta = -1/3 \end{array}\right\} \text{ for laminar flow}$$

$$\left.\begin{array}{l} \gamma = 9/10 \\[6pt] \beta = -1/9 \end{array}\right\} \text{ for turbulent flow}$$

Equation 7-21 is used to evaluate the heat transfer coefficient h_w to the heat shield during S-II flight from the value h_s at the calorimeter surface previously evaluated using the procedure of Section 7.1.2-1.

Due to the uncertainty of the flow pattern on the heat shield, during flight data analysis the value of x_o in equations 7-22, i.e., the boundary layer starting length, was arbitrarily assigned the value of one foot. Since the flow is assumed to the turbulent and the film coefficient ratio varies as x_o to the -1/9 power, it is expected that the error introduced by this assumption is small.

7.1.2.4 Wall Temperature Correction

Having determined the film coefficient to the heat shield during flight, it is required to obtain the value corresponding to the cold wall model test conditions. Therefore, it is necessary to account for the wall temperature effect on the film coefficient.

For turbulent flat plate heat heat transfer assuming that

$$h \sim \frac{k^*}{x} \left(\frac{\rho^* u x}{\mu^*}\right)^{4/5} Pr^{*1/3}$$

where * denotes that the property is evaluated at the reference temperature t* which is defined as

$$t^* = 0.22\ t_\infty + 0.28 t_{aw} + 0.50 t_w$$

then the wall temperature effect on the film coefficient reduces to

$$\frac{h_2}{h_1} = \left(\frac{k_2^*}{k_1^*}\right)\left(\frac{T_1^*\ \mu_1^*}{T_2^*\ \mu_2^*}\right)^{4/5}\left(\frac{Pr_2^*}{Pr_1^*}\right)^{1/3} \tag{7-24}$$

Similarly, for laminar flat plate heating let

$$h \sim \frac{k^*}{x}\left(\frac{\rho^*\ u\ x}{\mu^*}\right)^{1/2} Pr^{*1/3}$$

then

$$\frac{h_2}{h_1} = \left(\frac{k_2^*}{k_1^*}\right)\left(\frac{T_1^*\ \mu_1^*}{T_2^*\ \mu_2^*}\right)^{1/2}\left(\frac{Pr_2^*}{Pr_1^*}\right)^{1/3} \tag{7-25}$$

for laminar flow.

7.1.2.5 Typical Results

The preceding total heat flux calorimeter correction procedures have been incorporated into a computer program. Typical results for a total heat flux calorimeter are presented in Figure 7.1.2-2 for a particular flight. Note that the temperature mismatch effect is small during the initial portion of the flight, when the heat shield and gage temperature are not too different, and increases with flight time.

7.1.3 Gas Recovery Temperature Probe Data Reduction

The S-II stage base heat shield is instrumented with probes to measure the gas recovery temperature. The probes, (Figure 7.1.3-1) have a high heat capacity and emissivity with the result that a large discrepancy may exist between the probe indicated temperature and the actual gas recovery temperature.

Therefore, it is necessary to perform a thermal analysis of the probe in order to correlate the indicated or probe thermocouple junction temperature and the gas recovery temperature.

The discrepancy between the indicated and actual recovery temperature varies with probe location since it is dependent on the local heating rates.
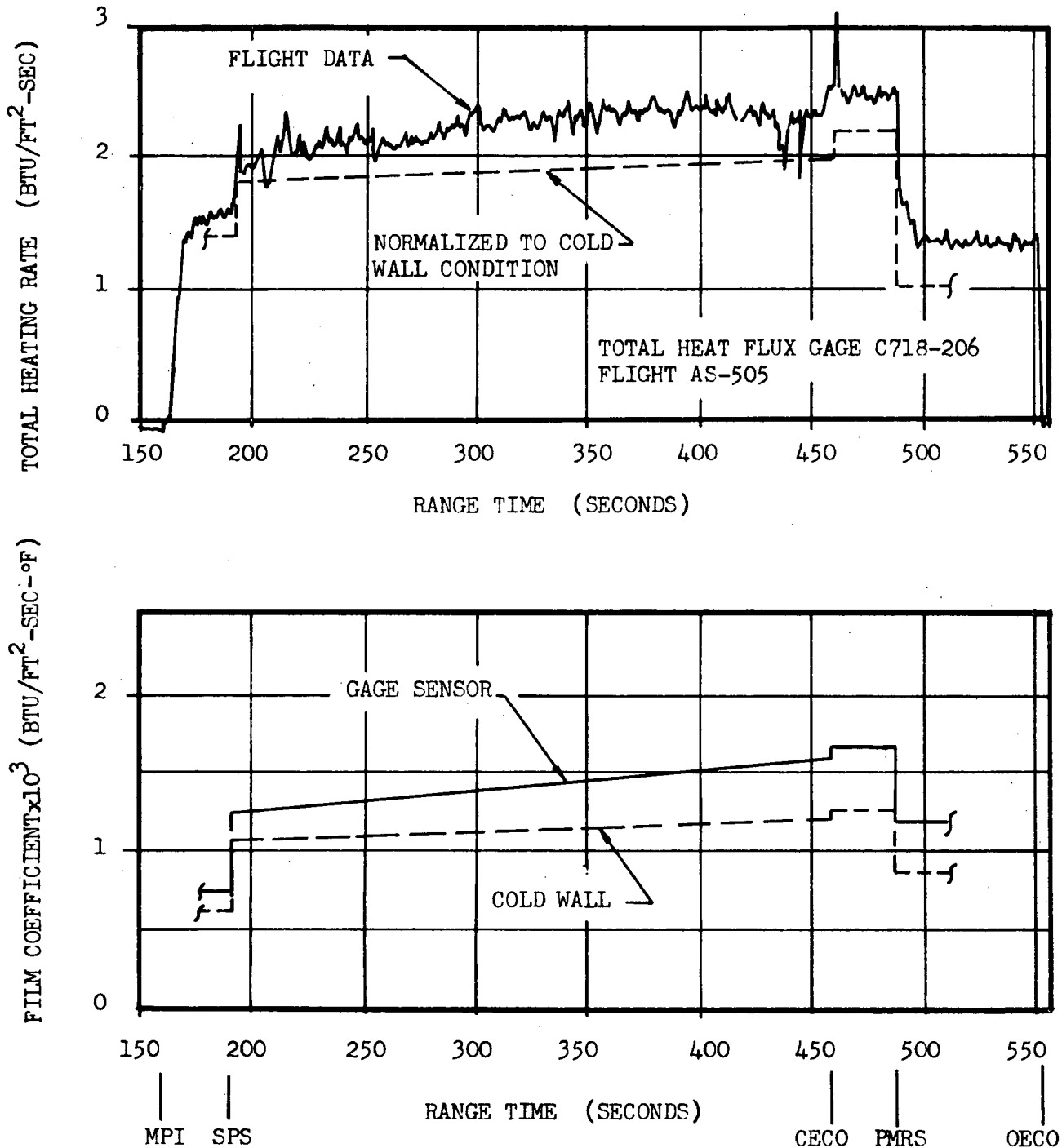
Figure 7.1.2-2 Typical Results For Total Heat Flux Gage
Flight Data Normalization

0.295

0.15 INCHES DIAMETER

THERMOCOUPLE JUNCTION

ALUMINA

1.5

0.30 INCHES DIAMETER

STEEL HOUSING

3.25
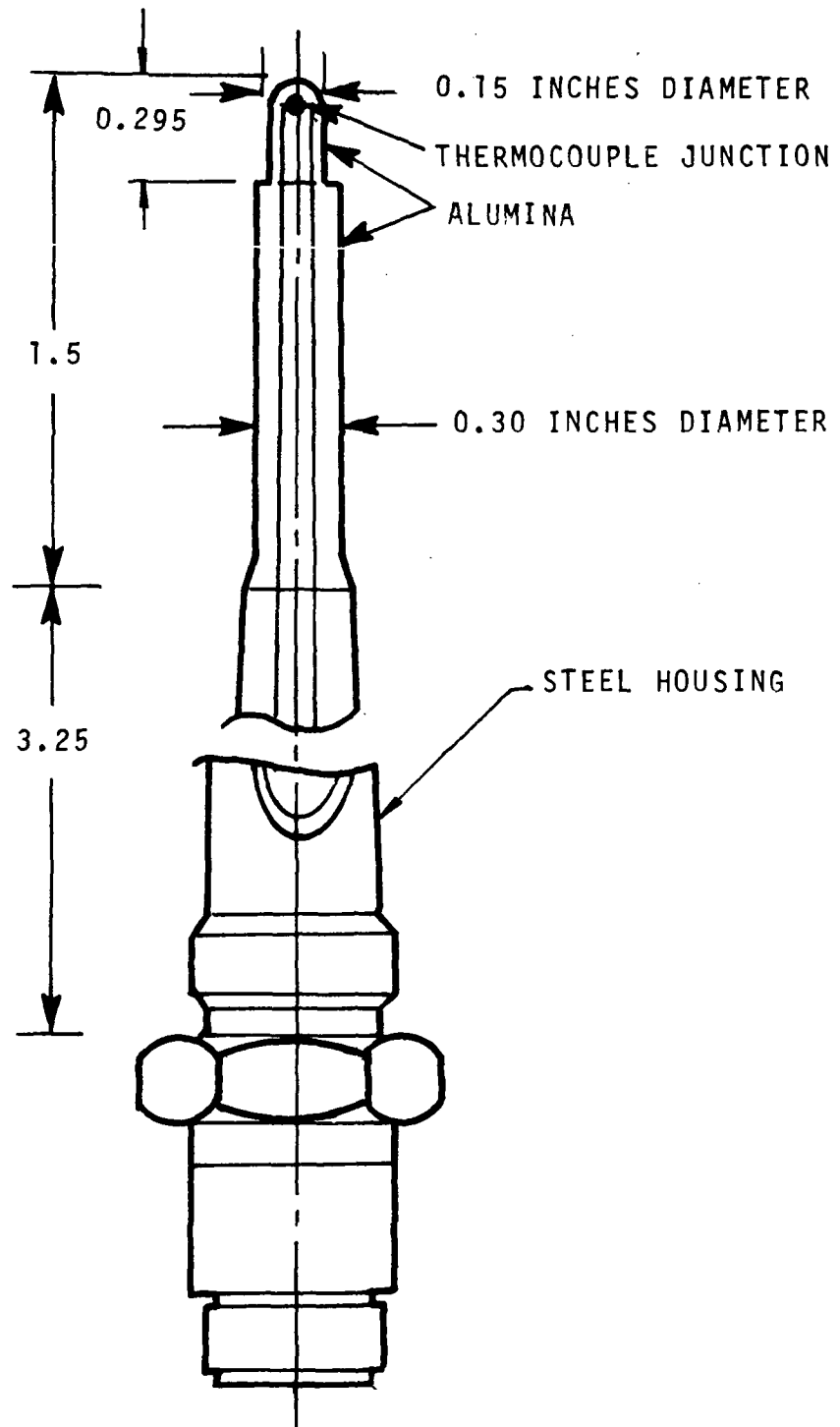
Figure 7.1.3-1 Gas Recovery Temperature Probe

By assuming a value of the gas recovery temperature it is possible to evaluate the heat shield flat plat film coefficient in the vicinity of the probe. The corresponding value of the probe film coefficient is obtained from semiempirical flat-plate-to-cylinder heating rate corelations of the film coefficient. Using this value of the film coefficient and the corresponding assumed value of recovery temperature, thermal analysis of the probe gives the corresponding probe thermocouple junction temperature. Therefore, by assuming several values of the gas recovery temperature, corresponding analytical values of probe indicated temperature are obtained. Comparison of these temperatures with the probe indicated flight temperature yields the value of the gas recovery temperature in the vicinity of the probe.

7.1.3.1 Cylinder Convective Heat Transfer Coefficient

The average heat transfer coefficient h_c to a cylindrical surface in cross flow is given in Reference 13 as

$$Nu_D = C_1 \ Re_D^{m_1} \ Pr^{n_1} + C_2 \ Re_D^{m_2} \ Pr^{n_2} \qquad (7\text{-}26)$$

where

$$Nu_D = \frac{h_c \ D}{k}$$

In Equation 7-26 the first term on the right hand side represents the laminar region on the windward side of the cylinder and the second term represents the turbulent seperated flow on the leeward side.

Comparisons were made between the cylinder heating rates given by Equation 7-26 with various constants and exponents taken from References 13, 26, 27 and the results obtained from the analysis of the AS-503 S-II stage base region environment. It was found that the best agreement was obtained with

$$C_1 = 0 \qquad\qquad C_2 = 0.342$$

$$m_2 = 0.466 \qquad\qquad n_2 = 0.333$$

For an assumed value of the gas recovery temperature, the heat transfer coefficient at the heat shield surface is evaluated from the total heat flux calorimeter measurement, heat shield surface temperature measurement and the measured or computed value of the incident radiative heat flux using the procedure outlined in Section 7.1.2.

Then, assuming that the heat shield film coefficient can be represented by Colburn's equation for turbulent flat plate heating

$$h = 0.0296 \left(\frac{k}{x}\right) \left(\frac{\rho \ u \ x}{\mu}\right)^{4/5} Pr^{1/3}$$

Then the local Reynolds number based on the probe cylinder diameter is

$$Re_D = \left[\frac{h_x^{1/5} Pr^{-1/3}}{0.0296k} \right]^{5/4} D \qquad (7\text{-}27)$$

and the average film coefficient to the cylindrical gas recovery temperature probe h_c is obtained from Equations 7-26.

7.1.3.2 Recovery Temperature Probe Thermal Model

The recovery temperature probe construction is shown in Figure 7.1.3-1 and the equivalent thermal model in Figure 7.1.3-2 where the temperature of node (5) represents the probe indicated temperature.

The transient heat transfer problem is solved by replacing the physical model by a number of nodes interconnected by conductors. Each node has a heat capacitance, which can be equal to or greater than zero, and a time dependent temperature. Therefore, the thermal model reduces to a space-dimensionless system with time as the only independent variable.

The heat transfer equation for the nodal system is

$$c_i \frac{dT_i}{d\theta} = \sum_j K_{ij} T_j - T_i \sum K_{ij} \qquad (7\text{-}28)$$

where

C_i is the capacitance of node i

T_i is the temperature of node i

K_{ij} is the conductance between node i

and node j

θ is time

In order to solve this equation for $T_{i,\theta+\Delta\theta}$, the assumption is made that Tj remains constant over the interval $\Delta\theta$ i.e., dT_j is zero.

The heat balance equation is solved by finite difference techniques using the forward difference alternating direction method of solution.

The temperature $T_{i,n}$ of node i at time $\theta_o + n\Delta\theta$ is computed from

$$T_{i,n} = \left(T_{i,n-1} - T_{i,s} \right) e^{-p} + T_{i,s} \qquad (7\text{-}29)$$

where

$$T_{i,s} = \frac{\sum_{j=1}^{i-1} K_{i,j} T_{j,n} + \sum_{j=1+n}^{m} K_{i,j} T_{j,n-1}}{\sum_{j=1}^{m} K_{i,j}} \qquad (7\text{-}30)$$

SD73-SA-0061
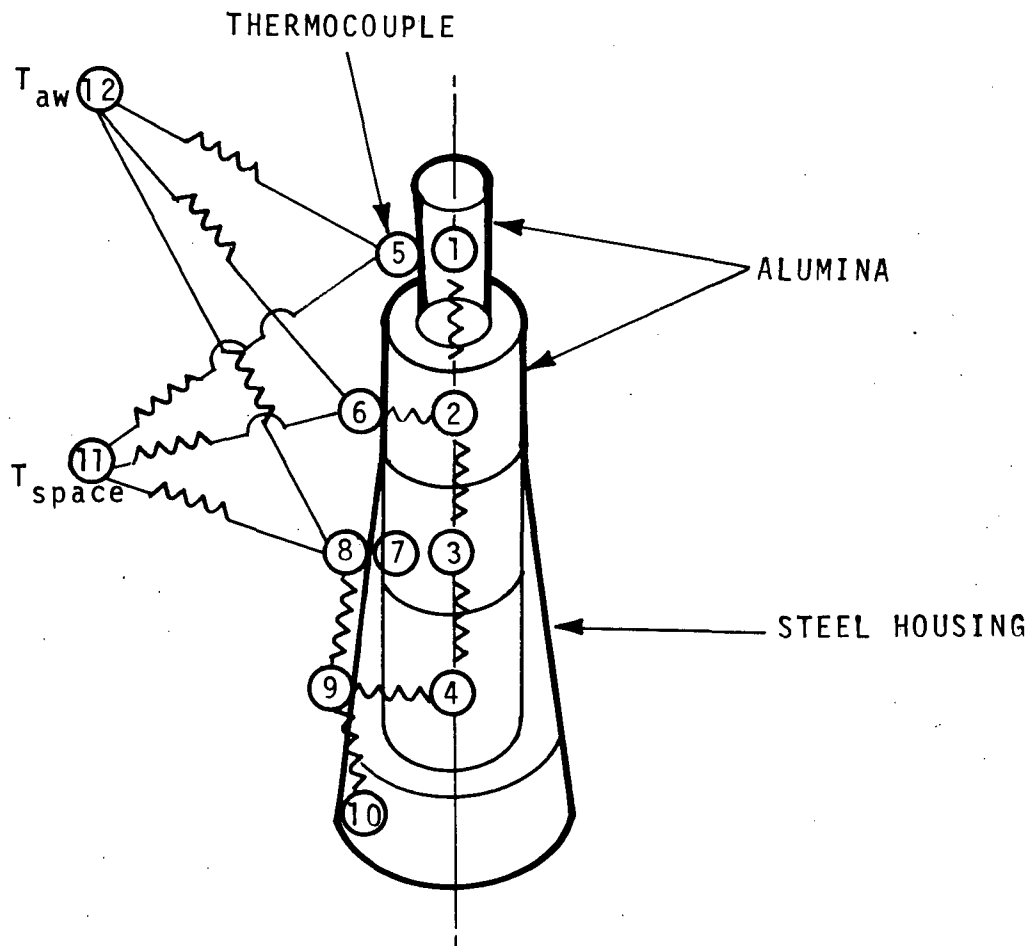
Figure 7.1.3-2   Gas Recovery Temperature Probe Thermal Model

for
$$i = 1, 2, \ldots m \quad \text{if} \quad n \quad \text{is odd}$$

$$T_{i,s} = \frac{\displaystyle\sum_{j=1}^{i-1} K_{i,j} T_{j,n-1} + \sum_{j=i+1}^{m} K_{i,j} T_{j,n}}{\displaystyle\sum_{j=1}^{m} K_{i,j}} \qquad (7\text{-}31)$$

for

$$i = m, m-1, \ldots 1 \quad \text{if} \quad n \quad \text{is even}$$

and

Also,
$$P = \frac{\Delta\theta}{C_i} \sum_{j=1}^{m} K_{i,j}$$

$T_{i,n}$ is the temperature of the ith node at time $\theta_o + n\Delta\theta$ in the transient calculation

or

$T_{i,n}$ is the temperature of the ith node at the nth iteration in the steady state calculation

and

m is the number of nodes.

Thus the sequence in which the node temperatures are computed is reversed at each time increment.

7.1.3.3 Gas Recovery Temperature Probe Analysis Results

The foregoing gas recovery temperature analysis procedure has been incorporated into the recovery temperature probe flight data reduction program. A typical flight indicated and computed probe temperature histories are shown in Figure 7.1.3-3 together with the corresponding gas recovery temperature. The flight probe data and the various other parameters associated with this sample case are presented in Table 7.1.3-1.
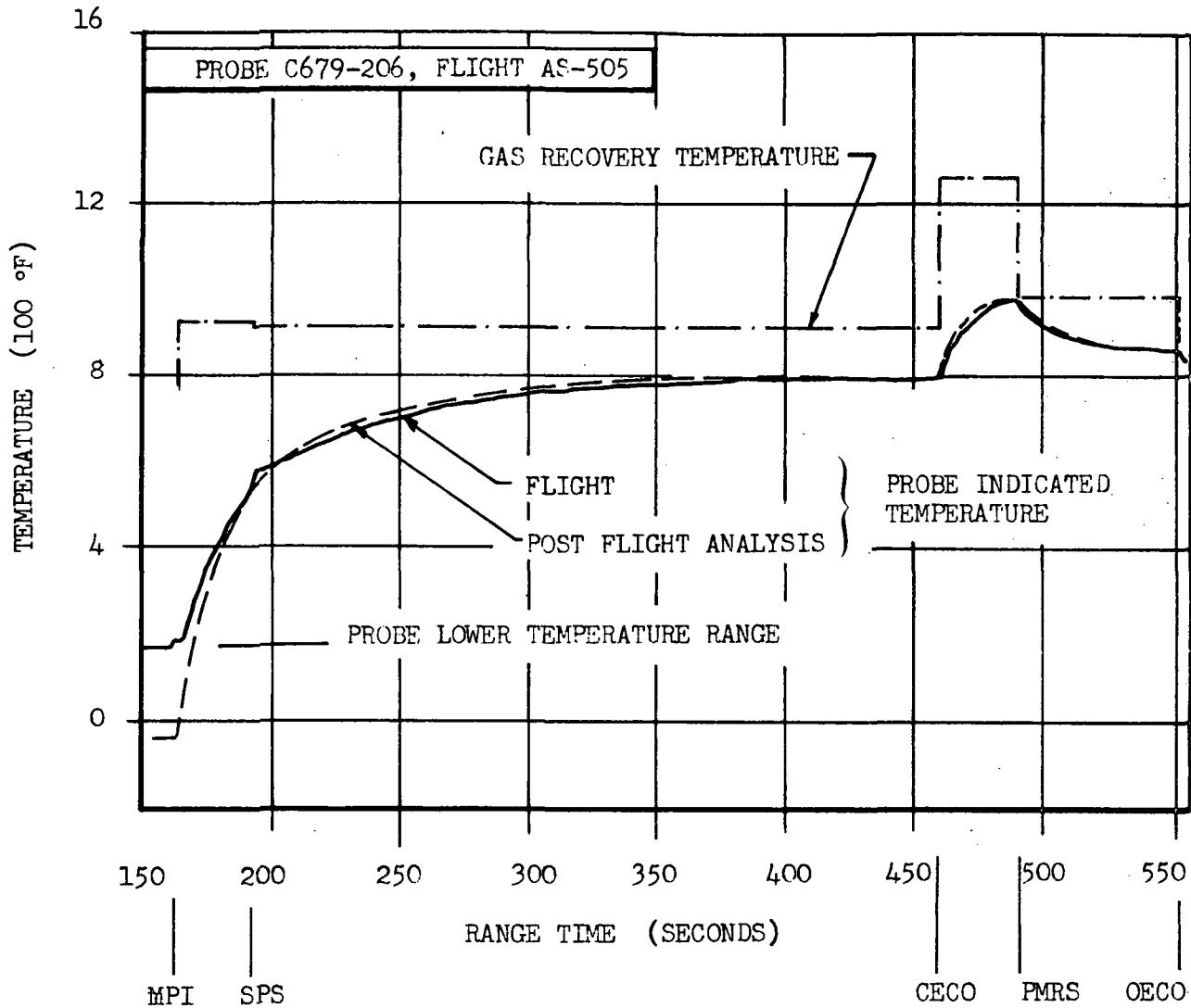
Figure 7.1.3-3   Typical Results Of Gas Recovery Temperature
Probe Flight Data Analysis Results

TABLE 7.1.3-1

Gas Recovery Temperature Probe
Post Flight Analysis Sample Case

Flight AS-505, Gas Recovery Temperature Probe C679-206

Range Time (Sec)	Event	Recovery Temp. Probe (°F)	Total Q (C722-206) Btu/Ft2-Sec	Incident Radiative Q* Btu/Ft2-Sec	Heat Shield T (C711-206) (°F)	Gas Recovery Temperature (°F)
163.1	MPI	-50.0	1.90	0.89	-50.0	915.0
	SPS-	540.0	1.90	0.89	300.0	915.0
192.3						
	SPS+	540.0	1.975	0.89	300.0	912.0
	CECO-	800.0	2.20	0.89	735.0	912.0
460.6						
	CECO+	800.0	2.40	0.65	735.0	1275.0
	PMRS-	1000.0	2.40	0.65	775.0	1275.0
488.5						
	PMRS+	1000.0	1.375	0.23	775.0	987.0
	OECO-	860.0	1.375	0.23	625.0	987.0
552.6						
	OECO+					

* Post Flight Corrected Value (Section 7.1.1)

Rev July 6, 1973

SD73-SA-0061

7.1.4 Mixture Ratio and Chamber Pressure Correction

In order to normalize the flight data heating rates to the scale model test conditions, the experimentally derived results of section 5.2 were used to correct for chamber pressure and mixture ratio differences i.e., heating rates were assumed to be proportional to chamber pressure.

7.1.5 Nominal Steady State Gimbal Angle Correction

The flight data previously reduced to the scale model test cold wall conditions were corrected to the null engine position using the results of the analytically derived engine deflection effects for the full scale engine with TPE injection presented in Figure 6.2.5-1. From Figure 6.2.5-1 it is seen that the effects of engine deflection on base pressure (P_b) and heating rates are given by

$$P_B = P_{B_o} e^{0.158 \bar{\beta}} \qquad\qquad q = q_o e^{0.137 \bar{\beta}}$$

In each case the exponent was taken as the average value for the two engine spacings shown which correspond to the center-outboard and outboard-outboard engine spacings for the S-II stage.

7.2 COMPARISON OF FLIGHT, MODEL, AND ANALYTICAL RESULTS

Flight data for flights AS-503 through AS-505 were normalized to the model test conditions using the methodology outlined in Section 7.1. AS-501 and AS-502 flight data were not included in the comparisons because the gas recovery temperature was not recorded during these flights.

Starting with flight AS-506, the base region instrumentation was reduced to 6 gages. These included: One heat shield radiometer, one gas recovery temperature probe and one total heat flux gage. Since these gages were located in different heat shield quadrants, and no heat shield surface temperature measurements were available, the base region thermal environment of these flights could not be evaluated with the same degree of accuracy. Consequently, AS-506 and subsequent flights data are omitted from these comparisons.

The locations of the S-II stage base region flight instrumentation are shown in Figure 7.2-1, and the gage coordinates are listed in Table 7.2-1.

A summary of the AS-503 through AS-505 flight nominal steady state flight engine deflections and operating conditions is given in Table 7.2-2.

Heat shield gas recovery temperature and total heat flux gage flight data together with the normalized values are presented in Tables 7.2-3 and 7.2-4 respectively.

Thrust cone heating rates and pressures recorded during flights AS-503 through AS-505 are given in Tables 7.2-5 and 7.2-6 respectively.
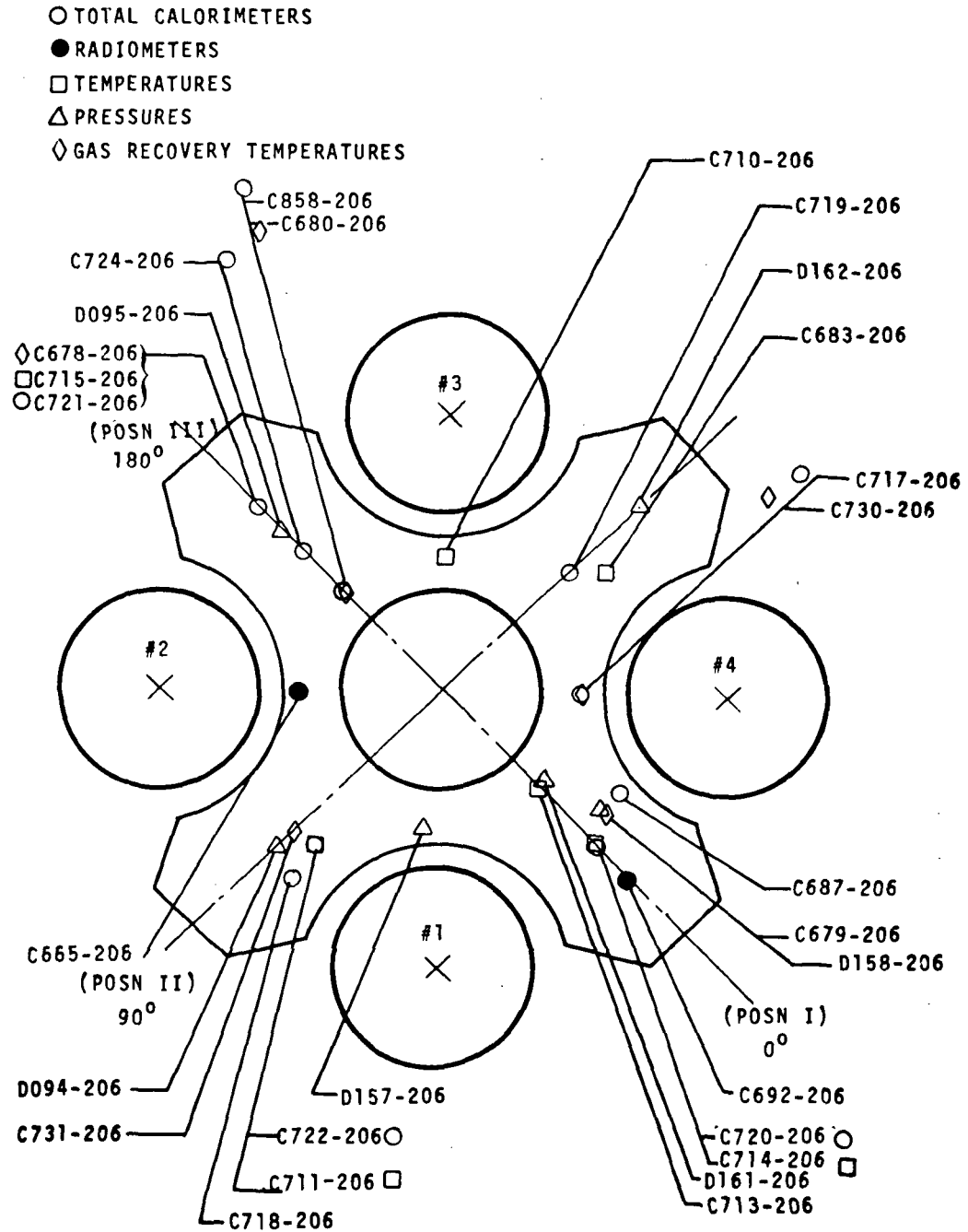
Figure 7.2-1   S-II Base Heat Shield Aft Face Flight
Instrumentation Locations

SD73-SA-0061

Table 7.2-1
S-II Base Region Flight Instrumentation Coordinates

HEAT SHIELD AFT SURFACE TOTAL HEATING RATE GAGES

GAGE ID	ST (IN)	θ°	R (IN)
C665-206*	44.0	135.0	53.5
C687-206	44.0	344.0	77.0
C692-206*	44.0	0.0	100.0
C717-206	44.0	315.0	53.0
C718-206	44.0	82.0	91.0
C719-206	44.0	270.0	65.0
C720-206	44.0	0.0	83.0
C721-206	44.0	180.0	100.0
C722-206	44.0	83.0	75.0
C724-206	44.0	180.0	75.0
C858-206	44.0	180.0	52.5

THRUST CONE TOTAL HEATING RATE GAGES

GAGE ID	ST (IN)	θ°	R (IN)
C666-208	133.0	272.0	144.0
C688-208	115.0	272.0	124.0
C701-206	196.0	270.0	180.0
C821-208	156.0	272.0	163.0

HEAT SHIELD AFT SURFACE PRESSURE GAGES

GAGE ID	ST (IN)	θ°	R (IN)
D094-206	44.0	90.0	85.0
D095-206	44.0	180.0	85.0
D157-206	44.0	50.0	53.0
D158-206	44.0	351.0	75.0
D161-206	44.0	354.0	53.0
D162-206	44.0	270.0	100.0
D187-206**	140.0	2.0	130.0

* RADIOMETER
**THRUST CONE PRESSURE

Table 7.2-2 Flight Data Summary of Engine Deflections, PMR and P_c

ENGINE	FLIGHT REGIME	AS-503 PMR	AS-503 P_c (PSIA)	AS-503 $\theta_p°$	AS-503 $\theta_y°$	AS-504 PMR	AS-504 P_c (PSIA)	AS-504 $\theta_p°$	AS-504 $\theta_y°$	AS-505 PMR	AS-505 P_c (PSIA)	AS-505 $\theta_p°$	AS-505 $\theta_y°$
1	MPI-CECO	5.77	719	+0.09	-0.07	5.77	720	-0.50	-0.10	5.82	723	-0.93	-0.66
	CECO-PMRS			-0.23	-0.25			-0.60	-0.22	5.82	723	-1.15	-0.81
	PMRS-OECO	4.56	557			4.80	591	-0.85	-0.66	4.48	560	-1.29	-0.93
2	MPI-CECO			-0.09	-0.10			-0.85	-0.66			-0.86	-0.66
	CECO-PMRS			-0.32	-0.27			-1.10	-0.74			-1.15	-0.85
	PMRS-OECO											-1.28	-0.97
3	MPI-CECO			+0.05	-0.12			-0.11	-0.61			-0.81	-0.69
	OECO-PMRS			-0.21	-0.47			-0.35	-0.85			-1.08	-1.08
	PMRS-OECO											-1.21	-1.23
4	MPI-CECO			-0.15	+0.01			-0.15	-0.30			-1.04	-0.81
	CECO-PMRS			-0.46	-0.04			-0.30	-0.55			-1.31	-1.18
	PMRS-OECO											-1.44	-1.33

ENGINE DEFLECTION SIGN CONVENTION:
PITCH AND YAW DEFLECTIONS OF EACH OUTBOARD ENGINE TOWARD
THE CENTER ENGINE ARE POSITIVE

NOTE:
1) PMR AND P_c ARE AVERAGE VALUES FOR THE FIVE ENGINES
2) NO EARLY CECO PRIOR TO AS-505 FLIGHT

Table 7.2-3 Summary of Flight Gas Recovery Temperature Analysis

GAGE ID.	EVENT	AS-503 GAGE INDIC	AS-503 T_{aw} °F	AS-504 GAGE INDIC	AS-504 T_{aw} °F	AS-504 GAGE INDIC	AS-504 T_{aw} °F
C678 -206	MPI	-50*	931	-50*	990	-50*	895
		625	931	675	990	650	895
	SPS		1055		1057		1078
						950	1078
	CECO	**	**	**	**	1100	1337
		950	1055	935	1057		
	PMRS	825	888	870	962	950	987
C679 -206	MPI	-50*	804	-50*	718	-50*	915
		500	804	475	718	540	915
	SPS		876		855		912
						800	912
PMRS	CECO	**	**	**	**	1000	1272
		800	876	775	855		
	PMRS	705	753	725	782	860	987
C680 -206	MPI	-50*	966	-50*	887	-50*	1212
		440	966	550	887	550	1212
	SPS		955		962		904
						800	904
	CECO	**	**	**	**	925	1142
		825	955	850	962		
	PMRS	700	754	750	802	800	909

*ESTIMATED PROBE TEMPERATURE

**NO EARLY CECO PRIOR TO AS-505 FLIGHT

Table 7.2-3 (Concluded) Summary of Flight Gas Recovery Temperature Analysis

GAGE ID	EVENT	AS-503 GAGE INDIC.	AS-503 T_{aw} °F	AS-504 GAGE INDIC	AS-504 T_{aw} °F	AS-505 GAGE INDIC.	AS-505 T_{aw} °F
C730 -206	MPI	-50*	1128	-50*		-50*	1065
		525	1128			500	1065
	SPS		1041				941
	CECO	**	**	FAILED		800	941
		860	1041			950	1205
	PMRS	750	846			830	951
C731 -206	MPI	-50*	967	-50*	887	-50*	1285
		660	967	550	887	575	1285
	SPS						989
			1167		962	860	989
	CECO	**	**	**	**		
		1010	1167	850	962	985	1185
	PMRS						
		860	979	750	802	840	975

* ESTIMATED PROBE TEMPERATURE
**NO EARLY CECO PRIOR TO AS-505 FLIGHT

SD73-SA-0061

TABLE 7.2-4

Total Heat Flux Flight Data Summary

FLIGHT EVENT	GAGE ID	FLIGHT AS-503			POST FLIGHT ANALYSIS						NORMALIZED HEATING RATES			
							FILM COEFFICIENT x10³			FLIGHT O/F ENGINE POSITION		MODEL O/F	
		O/F	Pc PSIA	GAGE READING	Q RAD	Taw °F	GAGE	HEAT SHIELD	COLD WALL	FLIGHT	NULL	5.5 Pc=715	5.0 Pc=632
SPS-	C687	5.77	719	1.40	0.846	988	0.687	0.562	0.589	0.540	0.548	0.484	0.428
SPS+		5.77	719	1.40	0.846	988	0.687	0.562	0.589	0.540	0.548	0.484	0.428
PMRS-		5.77	719	1.70	0.846	988	1.058	0.678	0.771	0.706	0.717	0.713	0.630
PMRS+		4.56	557	1.20	0.302	844	1.200	0.724	0.830	0.641	0.673		
SPS-	C717			1.50	0.750	988	0.878	0.730	0.761	0.697	0.700	0.696	0.615
SPS+				1.40	0.750	988	0.774	0.642	0.670	0.614	0.617	0.614	0.542
PMRS-				1.75	0.750	988	1.205	0.812	0.908	0.832	0.836	0.831	0.735
PMRS+				1.00	0.267	844	0.985	0.628	0.708	0.546	0.564		
SPS-	C720			2.50	0.909	988	1.819	1.438	1.527	1.399	1.412	1.404	1.241
SPS+				3.40	0.909	988	2.858	2.269	2.411	2.210	2.230	2.218	1.960
PMRS-				3.50	0.909	988	3.374	1.998	2.322	2.128	2.147	2.135	1.887
PMRS+				2.00	0.324	844	2.451	1.358	1.592	1.229	1.253		
SPS-	C721			2.40	0.870	988	1.744	1.398	1.478	1.355	1.371	1.363	1.205
SPS+				3.50	0.870	988	2.992	2.354	2.509	2.299	2.335	2.320	2.052
PMRS-				3.75	0.870	988	3.789	2.327	2.676	2.453	2.491	2.477	2.189
PMRS+				2.75	0.310	844	3.657	2.090	2.424	1.871	1.968		
SPS-	C722			2.50	0.894	988	1.833	1.517	1.589	1.456	1.456	1.447	1.279
SPS+				2.75	0.894	988	2.115	1.754	1.837	1.684	1.684	1.675	1.480
PMRS-				3.00	0.894	988	2.653	1.701	1.933	1.772	1.772	1.762	1.557
PMRS+				1.75	0.318	844	2.028	1.222	1.400	1.081	1.123		

HEATING RATES IN BTU/FT²-SEC
FILM COEFFICIENT IN BTU/FT²-SEC-°F

Table 7.2-4 (Continued)

Total Heat Flux Flight Data Summary

FLIGHT EVENT	GAGE ID	O/F	Pc PSIA	GAGE READING	Q RAD	Taw °F	GAGE	HEAT SHIELD	COLD WALL	FLIGHT	NULL	5.5 Pc=715	5.0 Pc=632
		FLIGHT AS-503			POST FLIGHT ANALYSIS — FILM COEFFICIENT x10³					NORMALIZED HEATING RATES — FLIGHT O/F ENGINE POSITION		MODEL O/F	
SPS-	C858	5.77	719	1.40	0.807	988	0.722	0.600	0.625	0.573	0.582	0.579	0.512
SPS+		5.77	719	1.55	0.807	988	0.879	0.731	0.762	0.698	0.709	0.705	0.623
PMRS-		5.77	719	2.15	0.807	988	1.618	1.091	1.220	1.119	1.136	1.129	0.999
PMRS+		4.56	557	1.20	0.310	844	1.206	0.769	0.866	0.669	0.703		
		FLIGHT AS-504											
SPS-	C687	5.77	720	1.50	0.846	916	0.853	0.689	0.723	0.610	0.662	0.657	0.581
SPS+		5.77	720	1.50	0.846	916	0.853	0.689	0.723	0.610	0.662	0.657	0.581
PMRS-		5.77	720	1.70	0.846	916	1.147	0.742	0.837	0.707	0.768	0.763	0.674
PMRS+		4.80	591	1.25	0.428	810	1.179	0.728	0.825	0.609	0.679		
SPS-	C717			1.25	0.750	916	0.666	0.545	0.569	0.480	0.491	0.488	0.431
SPS+				1.25	0.750	916	0.666	0.545	0.569	0.480	0.491	0.488	0.431
PMRS-				1.50	0.750	916	0.997	0.655	0.735	0.621	0.635	0.631	0.557
PMRS+				1.00	0.380	810	0.559	0.631	0.465	0.488			
SPS-	C718			2.00	0.901	916	1.376	1.135	1.185	1.000	1.064	1.057	0.934
SPS+				2.00	0.901	916	1.376	1.135	1.185	1.000	1.064	1.057	0.934
PMRS-				2.50	0.901	916	2.137	1.505	1.578	1.333	1.417	1.407	1.244
PMRS+				2.10	0.459	810	2.401	1.539	1.698	1.253	1.407		
SPS-	C719			1.50	0.854	916	0.845	0.623	0.673	0.568	0.579	0.575	0.508
SPS+				1.75	0.854	916	1.131	0.834	0.901	0.761	0.775	0.769	0.680
PMRS-				2.00	0.854	916	1.520	0.897	0.104	0.878	0.894	0.888	0.785
PMRS+				1.50	0.432	810	1.532	0.858	0.100	0.739	0.773		

HEATING RATES IN BTU/FT²-SEC
FILM COEFFICIENT IN BTU/FT²-SEC-°F

Table 7.2-4 (Continued)

Total Heat Flux Flight Data Summary

FLIGHT EVENT	GAGE ID	FLIGHT AS-504			POST FLIGHT ANALYSIS		FILM COEFFICIENT x 10³			NORMALIZED HEATING RATES			
		O/F	Pc PSIA	GAGE READING	Q RAD	Taw °F	GAGE	HEAT SHIELD	COLD WALL	FLIGHT O/F ENGINE POSITION FLIGHT	NULL	MODEL O/F 5.5 Pc=715	MODEL O/F 5.0 Pc=632
SPS−	C720	5.77	720	2.50	0.909	916	1.967	1.457	1.573	1.328	1.365	1.355	1.198
SPS+		5.77	720	2.50	0.909	916	1.967	1.457	1.573	1.328	1.365	1.355	1.198
PMRS−		5.77	720	3.00	0.909	916	2.860	1.676	1.944	1.641	1.687	1.675	1.481
PMRS+		4.80	591	2.00	0.460	810	2.309	1.284	1.499	1.106	1.166		
SPS−	C721			2.60	0.870	916	2.130	1.579	1.704	1.439	1.570	1.559	1.378
SPS+				2.60	0.870	916	2.130	1.579	1.704	1.439	1.570	1.559	1.378
PMRS−				3.30	0.870	916	3.365	1.967	2.281	1.926	2.101	2.086	1.844
PMRS+				2.50	0.440	810	3.142	1.736	2.026	1.495	1.667		
SPS−	C722			2.00	0.894	916	1.383	1.140	1.190	1.005	1.069	1.062	0.938
SPS+				2.00	0.894	916	1.383	1.140	1.190	1.005	1.069	1.062	0.938
PMRS−				2.50	0.894	916	2.144	1.412	1.584	1.337	1.422	1.412	1.412
PMRS+				2.00	0.452	810	2.260	1.417	1.599	1.180	1.326		
SPS−	C724			2.25	0.901	916	1.674	1.239	1.337	1.129	1.232	1.223	1.081
SPS+				2.50	0.901	916	1.973	1.461	1.577	1.332	1.454	1.444	1.276
PMRS−				2.75	0.901	916	2.512	1.475	1.710	1.444	1.576	1.565	1.383
PMRS+				2.00	0.456	810	2.299	1.278	1.492	1.101	1.227		
SPS−	C858			2.25	0.807	916	1.768	1.462	1.526	1.289	1.407	1.397	1.235
SPS+				2.50	0.807	916	2.069	1.715	1.790	1.512	1.650	1.639	1.448
PMRS−				2.75	0.807	916	2.616	1.725	1.935	1.634	1.784	1.772	1.565
PMRS+				2.00	0.408	810	2.360	1.482	1.672	1.234	1.377		

HEATING RATES IN BTU/FT^2-SEC
FILM COEFFICIENT IN BTU/FT^2-SEC-°F

Table 7.2-4 (Continued)

Total Heat Flux Flight Data Summary

FLIGHT EVENT	GAGE ID	FLIGHT AS-505			POST FLIGHT ANALYSIS					NORMALIZED HEATING RATES			
							FILM COEFFICIENT × 10³			FLIGHT O/F ENGINE POSITION		MODEL O/F	
		O/F	Pc PSIA	GAGE READING	Q RAD	Taw °F	GAGE	HEAT SHIELD	COLD WALL	FLIGHT	NULL	5.5 Pc=715	5.0 Pc=632
SPS-	C687	5.82	723	1.30	0.846	1020	0.566	0.466	0.488	0.462	0.507	0.501	0.443
SPS+		5.82	723	1.20	0.846	1020	0.466	0.383	0.401	0.380	0.417	0.412	0.365
CECO-		5.82	723	1.40	0.846	1020	0.699	0.462	0.522	0.494	0.542	0.536	0.474
CECO+		5.82	723	2.00	0.613	1228	1.278	0.899	1.004	1.160	1.324	1.309	1.157
PMRS+		4.48	560	1.25	0.219	987	1.153	0.739	0.841	0.769	0.893		
SPS-	C717			1.50	0.750	1020	0.851	0.701	0.734	0.695	0.779	0.770	0.681
SPS+				1.50	0.750	1020	0.851	0.701	0.733	0.695	0.779	0.770	0.681
CECO-				1.75	0.750	1020	1.171	0.780	0.878	0.832	0.933	0.923	0.816
CECO+				2.00	0.540	1228	1.344	0.953	1.062	1.228	1.427	1.411	1.247
PMRS+				1.25	0.194	987	1.192	0.775	0.877	0.804	0.951		
SPS-	C718			1.50	0.901	1020	0.719	0.592	0.619	0.588	0.665	0.658	0.581
SPS+				2.00	0.901	1020	1.232	1.019	1.066	1.011	1.144	1.131	1.000
CECO-				2.25	0.901	1020	1.582	1.062	1.193	1.139	1.288	1.274	1.126
CECO+				2.50	0.653	1228	1.609	1.065	1.201	1.590	1.862	1.841	1.627
PMRS+				1.25	0.233	987	1.180	0.759	0.863	0.789	0.941		
SPS-	C719			1.75	0.854	1020	1.017	0.796	0.848	0.803	0.915	0.905	0.800
SPS+				1.75	0.854	1020	1.017	0.796	0.848	0.803	0.915	0.905	0.800
CECO-				2.25	0.854	1020	1.600	1.057	1.193	1.155	1.315	1.300	1.149
CECO+				2.25	0.619	1228	1.648	1.075	1.218	1.386	1.633	1.615	1.427
PMRS+				1.00	0.221	987	0.907	0.580	0.661	0.605	0.725		

HEATING RATES IN BTU/FT²-SEC

FILM COEFFICIENT IN BTU/FT²-SEC-°F

Table 7.2-4 (Continued)
Total Heat Flux Flight Data Summary

FLIGHT EVENT	GAGE ID	FLIGHT AS-505			POST FLIGHT ANALYSIS					NORMALIZED HEATING RATES			
		O/F	Pc PSIA	GAGE READING	Q RAD	Taw °F	FILM COEFFICIENT x 10³			FLIGHT O/F ENGINE POSITION		MODEL O/F	
							GAGE	HEAT SHIELD	COLD WALL	FLIGHT	NULL	5.5 Pc=715	5.0 Pc=632
SPS-	C720	5.82	723	2.50	0.909	1020	1.762	1.306	1.417	1.344	1.486	1.469	1.299
SPS+		5.82	723	2.75	0.909	1020	2.033	1.480	1.616	1.532	1.694	1.675	1.481
CECO-		5.82	723	3.00	0.909	1020	2.555	1.568	1.809	1.715	1.897	1.876	1.658
CECO+		5.82	723	2.90	0.659	1228	2.178	1.445	1.649	1.907	2.110	2.087	1.844
PMRS+		4.48	560	1.50	0.235	987	1.520	0.919	1.065	1.021	1.191		
SPS-	C722			1.50	0.894	1020	0.725	0.938	0.981	0.593	0.671	0.664	0.587
SPS+				1.90	0.894	1020	1.135	0.951	1.003	0.930	1.052	1.040	0.919
CECO-				2.25	0.894	1020	1.612	1.075	1.210	1.147	1.298	1.275	1.127
CECO+				2.32	0.647	1228	1.583	1.125	1.254	1.449	1.697	1.678	1.483
PMRS+				1.10	0.231	987	1.012	0.659	0.746	0.682	0.813		
SPS-	C724			2.25	0.901	1020	1.499	1.148	1.232	1.168	1.282	1.268	1.121
SPS+				3.00	0.901	1020	2.318	1.780	1.912	1.812	1.989	1.967	1.739
CECO-				3.25	0.901	1020	2.898	1.858	2.117	2.007	2.023	2.001	1.768
CECO+				3.30	0.653	1228	2.601	1.795	2.024	2.340	2.672	2.642	2.336
PMRS+				1.80	0.233	987	1.900	1.193	1.367	1.251	1.454		
SPS-	C858			1.50	0.807		0.801	0.660	0.691	0.655	0.718	0.710	0.628
SPS+				1.90	0.807		1.211	1.001	1.048	0.993	1.089	1.077	0.952
CECO-				2.10	0.807		1.521	1.015	1.142	1.082	1.187	1.174	1.038
CECO+				2.10	0.584		1.420	1.009	1.124	1.300	1.586	1.568	1.386
PMRS+				1.10	0.208		1.030	0.670	0.759	0.694	0.807		

HEATING RATES IN BTU/FT²-SEC
FILM COEFFICIENT IN BTU/FT²-SEC-°F

TABLE 7.2-5

Thrust Cone Flight Heating Rates

GAGE	EVENT	HEATING RATES (Btu/ft^2-sec)						
		Measured Total			Radiative*	Convective		
		AS-503	AS-504	AS-505		AS-503	AS-504	AS-505
C666	MPI							
	SPS-	1.10	0.44	0.97	0.027	1.080	0.416	0.946
	SPS+	0.11	0.11	0.14	0.013	0.098	0.098	0.128
	CECO-	---	---	0.10	0.013	---	---	0.088
	CECO+	---	---	0.14	0.010	---	---	0.131
	PMRS-	0.08	0.12	0.14	0.010	0.068	0.108	0.131
	PMRS+	0.04	0.09	0.09	0.006	0.033	0.083	0.085
C688	MPI							
	SPS-	0.57	0.37	0.49	0.017	0.554	0.355	0.475
	SPS+	0.08	0.08	0.06	0.001	0.079	0.079	0.059
	CECO-	---	---	0.06	0.001	---	---	0.059
	CECO+	---	---	0.10	0.0007	---	---	0.099
	PMRS-	0.09	0.11	0.10		0.089	0.109	0.099
	PMRS+	0.06	0.09	0.07	0.0004	0.059	0.089	0.069
C701	MPI							
	SPS-	0.42	0.42	0.54	0.106	0.326	0.326	0.446
	SPS+	0.16	0.15	0.15	0.101	0.070	0.060	0.060
	CECO-	---	---	0.120	0.101	---	---	0.030
	CECO+	---	---	0.115	0.070	---	---	0.052
	PMRS-	0.15	0.11	0.115	0.070	0.060	0.020	0.052
	PMRS+	0.06	0.07	0.04	0.040	0.007	0.017	0.004
C821	MPI							
	SPS-	0.80	1.05	1.10	0.033	0.770	1.021	1.071
	SPS+	0.12	0.11	0.09	0.022	0.100	0.090	0.070
	CECO-	---	---	0.07	0.022	---	---	0.050
	CECO+	---	---	0.07	0.016	---	---	0.055
	PMRS-	0.11	0.09	0.07	0.016	0.090	0.070	0.055
	PMRS+	0.05	0.06	0.03	0.010	0.038	0.048	0.018

* Analytical
Note: No early CECO prior to AS-505 flight.

TABLE 7.2-6

Heat Shield Flight Pressures

GAGE	EVENT	Pressure (PSIA)					
		Flight			With Gimbal Correction		
		AS-503	AS-504	AS-505	AS-503	AS-504	AS-505
D094 -206	MPI						
	SPS-	0.071	0.065	0.061	0.071	0.069	0.080
	SPS+	0.061	0.058	0.068	0.061	0.062	0.078
	CECO-	---	---	0.052	---	---	0.060
	CECO+	---	---	0.038	---	---	0.045
	PMRS-	0.055	0.048	0.036	0.055	0.052	0.043
	PMRS+	0.030	0.029	0.022	0.031	0.033	0.027
D095 -206	MPI						
	SPS-	0.074	0.078	0.071	0.075	0.086	0.079
	SPS+	0.071	0.058	0.077	0.072	0.064	0.086
	CECO-	---	---	0.060	---	---	0.069
	CECO+	---	---	0.048	---	---	0.055
	PMRS-	0.059	0.053	0.047	0.060	0.058	0.054
	PMRS+	0.032	0.035	0.030	0.034	0.039	0.035
D157 -206	MPI						
	SPS-	0.050	0.050	0.045	0.050	0.053	0.051
	SPS+	0.030	0.032	0.031	0.030	0.034	0.035
	CECO-	---	---	0.023	---	---	0.026
	CECO+	---	---	0.020	---	---	0.023
	PMRS-	0.025	0.025	0.020	0.025	0.026	0.023
	PMRS+	0.015	0.021	0.012	0.016	0.023	0.014
D158 -206	MPI						
	SPS-	Not Recorded	0.065	0.031	Not Recorded	0.067	0.035
	SPS+		0.043	0.025		0.044	0.028
	CECO-		---	0.025		---	0.028
	CECO+		---	0.018		---	0.021
	PMRS-		0.034	0.019		0.035	0.022
	PMRS+		0.028	0.002		0.029	0.002
D161 -206	MPI						
	SPS-	0.055	0.047	0.037	0.056	0.048	0.042
	SPS+	0.041	0.032	0.024	0.041	0.033	0.027
	CECO-	---	---	0.018	---	---	0.020
	CECO+	---	---	0.015	---	---	0.018
	PMRS-	0.034	0.026	0.014	0.034	0.027	0.016
	PMRS+	0.022	0.021	0.005	0.023	0.022	0.006

Note: No early CECO prior to AS-505 flight

TABLE 7.2-6 (Concluded)

Heat Shield Flight Pressures

GAGE	EVENT	Pressures (PSIA)					
		Flight			With Gimbal Correction		
		AS-503	AS-504	AS-505	AS-503	AS-504	AS-505
D162 -206	MPI						
	SPS-	0.043	0.061	0.058	0.043	0.062	0.067
	SPS+	0.040	0.060	0.052	0.040	0.061	0.060
	CECO-	---	---	0.042	---	---	0.048
	CECO+	---	---	0.032	---	---	0.039
	PMRS-	0.038	0.049	0.032	0.038	0.050	0.039
	PMRS+	0.016	0.034	0.019	0.017	0.036	0.023
D187* -206	MPI						
	SPS-	0.034	0.033	0.036			
	SPS+	0.004	0.003	0.004			
	CECO-	---	---	0.002			
	CECO+	---	---	0.002			
	PMRS-	0.003	0.002	0.002			
	PMRS+	0.003	0.002	0.002			

Note: No early CECO prior to AS-505 flight.

7.2.1 Nominal Flight Region Environment

A comparison of nominal flight and scale model base region environments is made in the following sections. The nominal flight conditions are interstage off, no engine deflections, chamber mixture ratio of 5.5, and chamber pressure of 715 psia.

7.2.1.1 Gas Recovery Temperature

A summary of the flight gas recovery temperature is shown in Table 7.2.1-1 for the various flight regimes. These data, unlike the heating rates and pressures, are unconnected for engine deflection effects because model data is not available to determine the effect of gimballing on the base region gas recovery temperature and because the analytical results of Figure 6.2.5-1 indicate that the gas recovery temperature for the full scale engine with TPE injection is insensitive to symmetrical co-planar engine deflections within the range experienced during nominal flight.

The gas recovery temperature during a particular flight will generally have three different values. These correspond to: flight prior to CECO, CECO to PMR shift, and after PMR shift.

In the gas recovery temperature probe analysis, the probe data were analyzed for one additional flight regime, i.e., interstage-on, although the gas recovery temperature is unaffected by the interstage. This was done in order to reflect the recorded changes of the total heat flux gage readings which occurred after interstage separation. The total heat flux data are used as input to the gas recovery temperature probe flight data reduction program described in Section 7.1.3. Ideally, the analysis should show identical gas recovery temperature prior to and after interstage separation; consequently, the two values are average for each gage.

From Table 7.2.1-1 it is seen that the base region gas recovery temperature during nominal flight is 988 F. This is considerably lower than the 2300 F and 2500 F model test values determined in References 8 and 1, or the analytically predicted value of 1900 F in Section 6.0.

Note that in Section 6.0 plume interaction region properties analysis indicates that the full scale J-2 engine reverse flow bulk stagnation temperature with TPE injection is approximately 750 F lower than the corresponding temperature for the 1/25 scale model and 1500 F lower than the full scale engine value without TPE injection. The predominant reason for the difference is TPE injection into the full scale engine nozzle.

7.2.1.2 Heat Shield Heating Rates

The convective heating rate distribution on the heat shield during nominal flight with interstage-off is presented in Figure 7.2.1-1. The heating rates are the average values for the three flights shown normalized to the scale model test conditions.

Space Division
North American Rockwell

Space Division
North American Rockwell

TABLE 7.2.1-1

Summary of Nominal Flight Gas Recovery Temperatures

| GAGE ID | Gas Recovery Temperature (°F) | | | | | | |
| | AS-503 | | AS-504 | | AS-505 | | |
	ON/OFF	PMRS	ON/OFF	PMRS	ON/OFF	CECO	PMRS
C678-206	993	888	1024	962	987	1337	1113
C679-206	840	753	787	782	914	1272	987
C680-206	961	754	958	697	1058	1142	909
C730-206	1085	846	*	*	1003	1205	951
C731-206	1067	979	925	802	1137	1185	975
AVERAGE OF ALL GAGES	989	844	924	811	1020	1228	987

* Failed during flight

Flight Average Recovery Temperatures

FLIGHT	T_{aw} (°F)	REMARKS
MPI - PMRS PMRS - OECO	988 828	with 5 engines on
CECO - PMRS PMRS - OECO	1228 987	with center engine out

- 279 -   SD73-SA-0061

TABLE 7.2.1-1

Summary of Nominal Flight Gas Recovery Temperatures

GAGE ID	Gas Recovery Temperature (°F)						
	AS-503		AS-504		AS-505		
	ON/OFF	PMRS	ON/OFF	PMRS	ON/OFF	CECO	PMRS
C678-206	993	888	1024	962	987	1337	1113
C679-206	840	753	787	782	914	1272	987
C680-206	961	754	958	697	1058	1142	909
C730-206	1085	846	*	*	1003	1205	951
C731-206	1067	979	925	802	1137	1185	975
AVERAGE OF ALL GAGES	989	844	924	811	1020	1228	987

* Failed during flight

Flight Average Recovery Temperatures

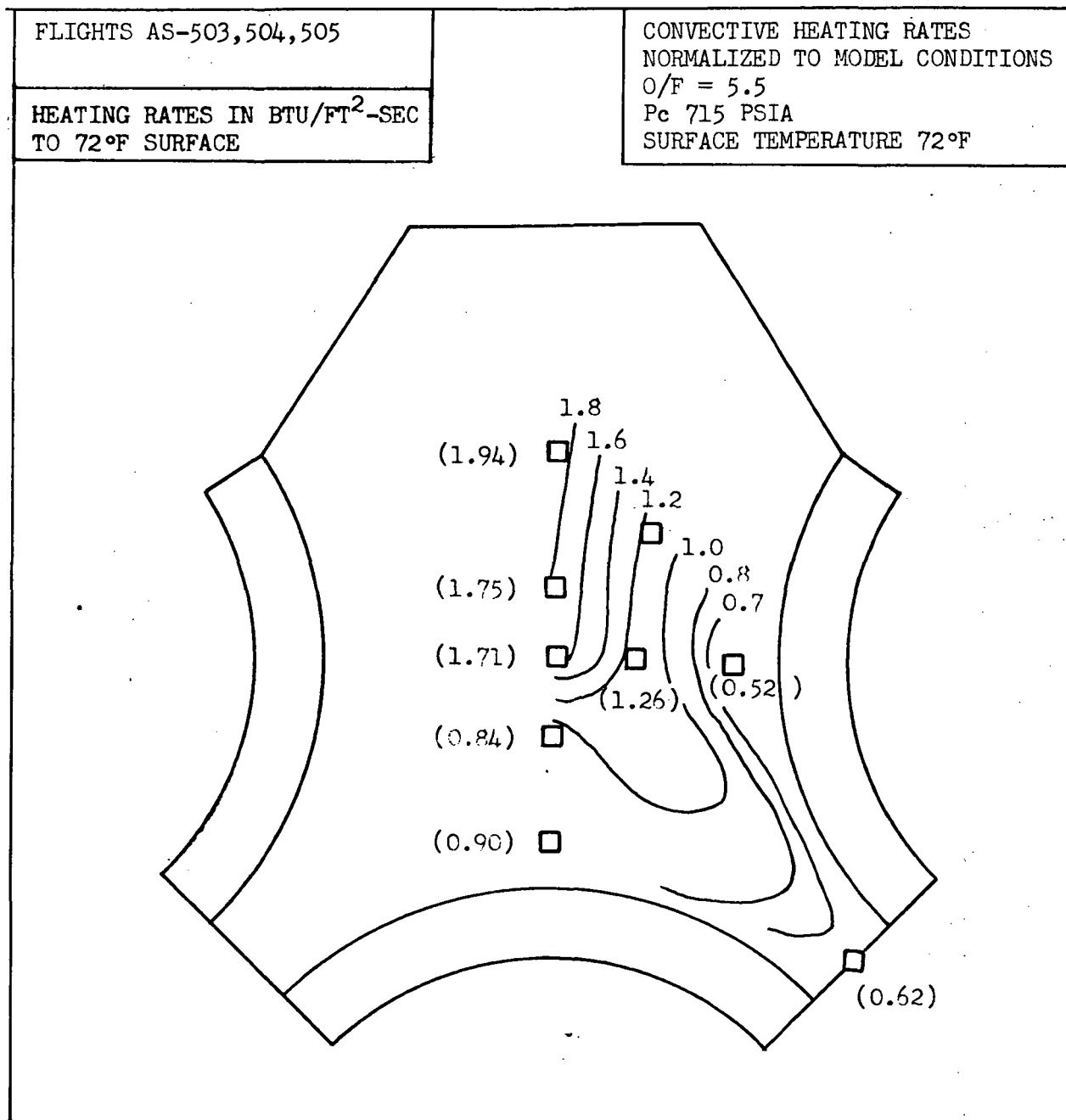| FLIGHT	T_{aw} (°F)	REMARKS
MPI - PMRS PMRS - OECO	988 828	with 5 engines on
CECO - PMRS PMRS - OECO	1228 987	with center engine out

Figure 7.2.1-1 Heat Shield Nominal Flight Convective
Heating Rates With Interstage Off

Comparison with the corresponding scale model heating rate distribution of Figure 5.6.1-3 shows that, although the flight heating rates are considerably lower, the distributions are quite similar with the highest heating rates occurring on the heat shield centerline and full scale radius 80 to 100 inches. The heating rates in both cases are lowest near the center engine. A comparison of model and flight heating rates along the heat shield centerline is presented in Figure 7.2.1-2. It is seen that the model heating rates follow the flight data trend very well and that the model heating rates are approximately 2.4 times the corresponding flight values.

Comparison of the analytical results presented in Figures 6.2.5-1 and 6.2.4-3 for the full scale and model reversed flow properties respectively, indicates that the model heating rates are 1.6 times the flight values; however, this does not take into account the different scale of the base region onto which the reversed flows impinge.

It is interesting to note that if the base heat shield heating rates follow the turbulent flat plate heating law, as indicated by chamber pressure effect results, then the heating rate scaling factor for the 1/25 scale model and the full scale vehicle becomes 1.9. Combining this with the analytically predicted reversed flow property heating rate ratio of 1.6 results in the model-to-full-scale heating rate ratio of about 3.0, which compares reasonably well with the value of 2.4 obtained from comparison of flight and scale model heating rates.

7.2.1.3 Thrust Cone Heating Rates

A comparison of the flight and scale model thrust cone heating rates is shown in Figure 7.2.1-3 for the $\theta = 0°$ location. Unlike the heat shield heating rate data, the thrust cone heating rates have not been corrected for temperature mismatch effects. This is because of the low heating rates and low structural temperatures experienced in this region during flight with the result that no large temperature differences exist between the structure, total heat flux gage body and the thin foil sensor of the gage. However, the flight measured total heating rates were corrected for the incident radiative heat flux by subtracting the analytically predicted radiative heating rates for each gage as shown in Table 7.2-5.

From Figure 7.2.1-3, it is seen that the flight thrust cone convective heating rates are higher than the model values, which is opposite to the results obtained for the heat shield. No explanation for this difference can be offered at the present time.

7.2.1.4 Base Region Pressures

The heat shield flight pressure distribution is shown in Figure 7.2.1-4. Comparison with the corresponding model pressure distribution shown in Figure 5.6.5-1 shows that the flight peak heat shield pressure is approximately 2.2 times the corresponding model value. Also, it is seen that the flight pressures show a larger spatial variation than the model values.

	DATA	O/F	Pc(PSIA)	SOURCE
O	FLIGHT*	5.5	715	AS-503,504,505
□	MODEL	5.5	715	LOG 2.1

* NORMALIZED TO MODEL CONDITIONS
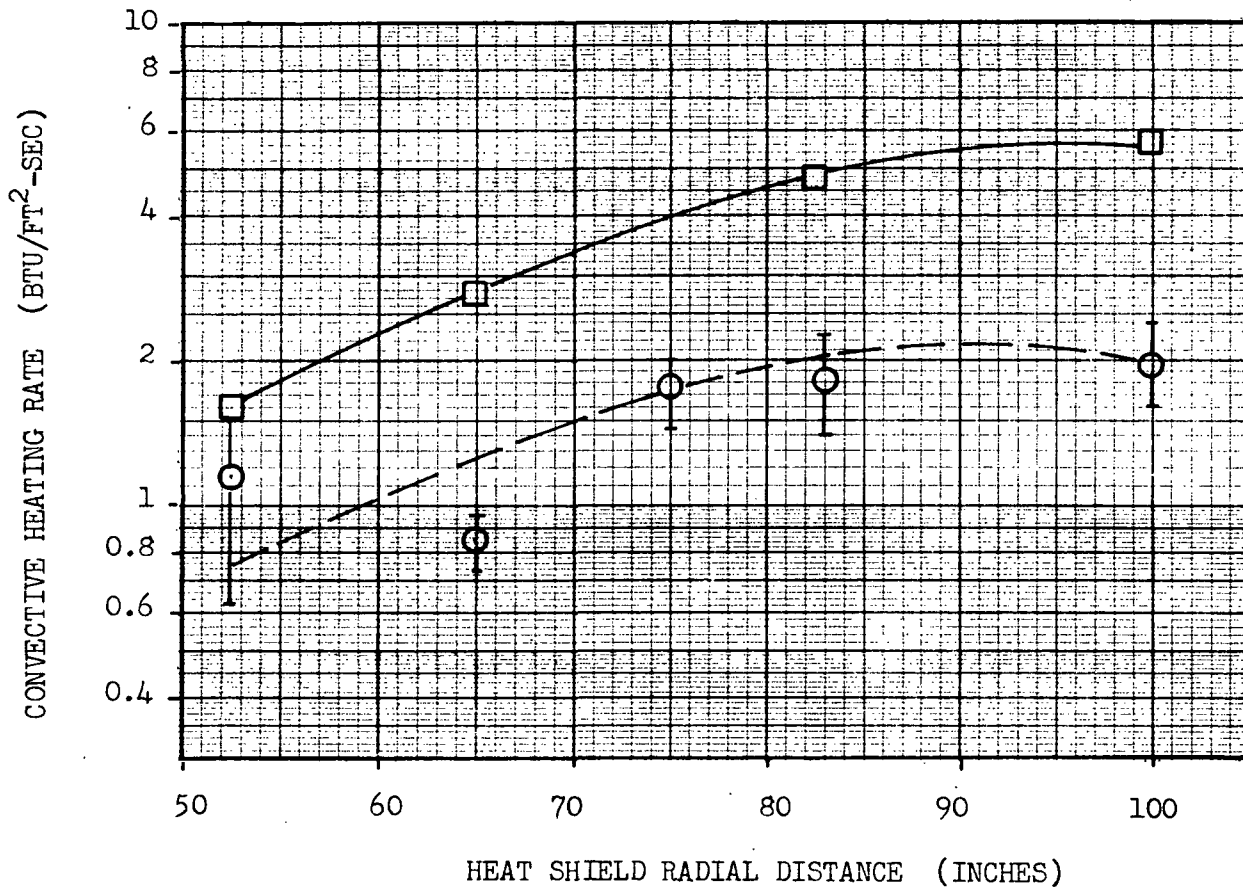
Figure 7.2.1-2 Comparison of Flight and Model Heat Shield Centerline
Heating Rates, Interstage Off, No Deflections

DATA		O/F	Pc(PSIA)	SOURCE
○	FLIGHT	5.8	720	AS-503,504,505
◊	MODEL	5.5	715	LOG 2.1
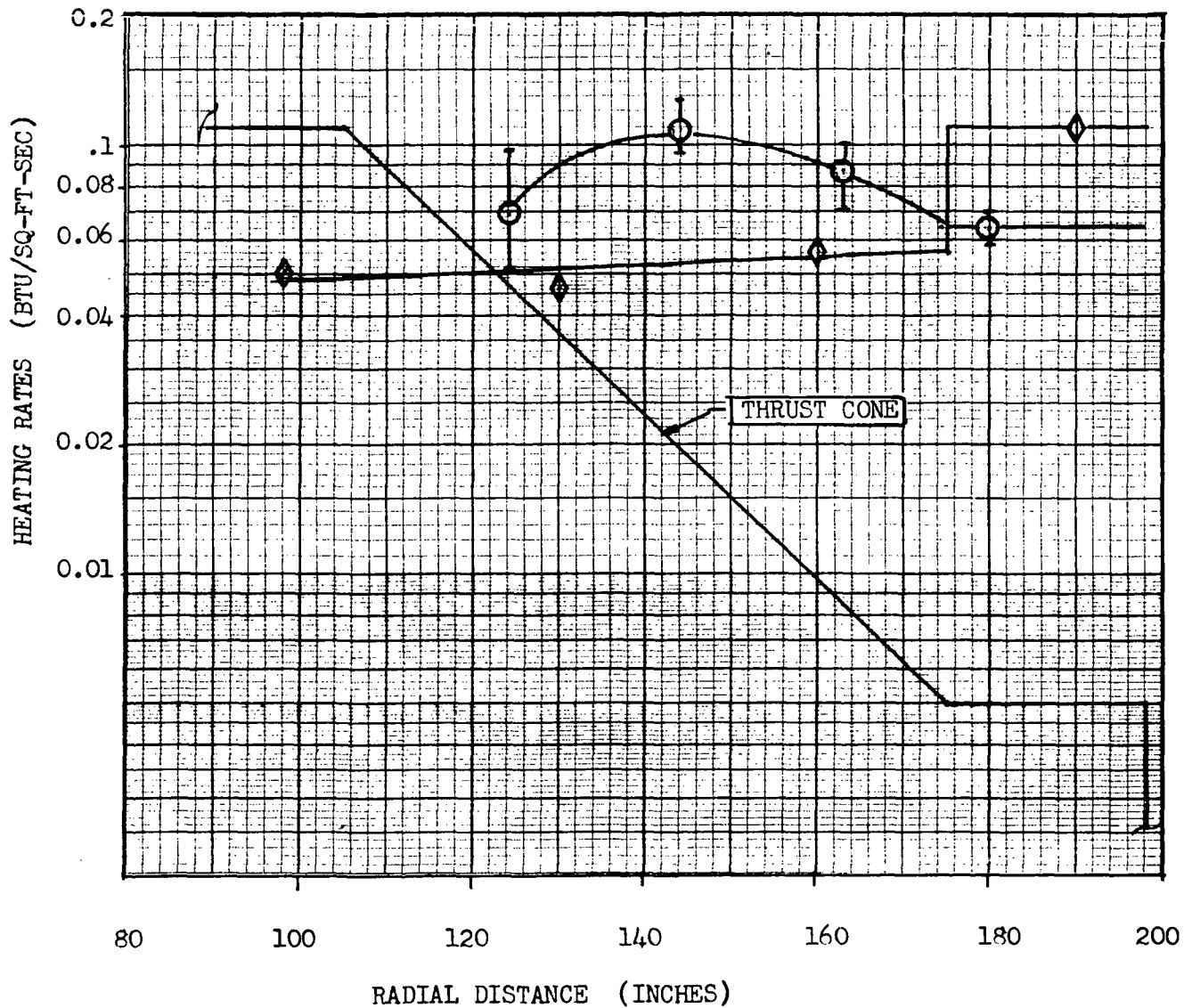
Figure 7.2.1-3 Comparison Of Flight And Model Thrust Cone Convective
Heating Rates At θ = 0°, Interstage Off

SD73-SA-0061

FLIGHT PRESSURES CORRECTED TO
NULL ENGINE POSITION IN PSIA

O/F = 5.8, Pc = 720 PSIA

(0.054) □   0.050

0.04

(0.071) ▫

0.06
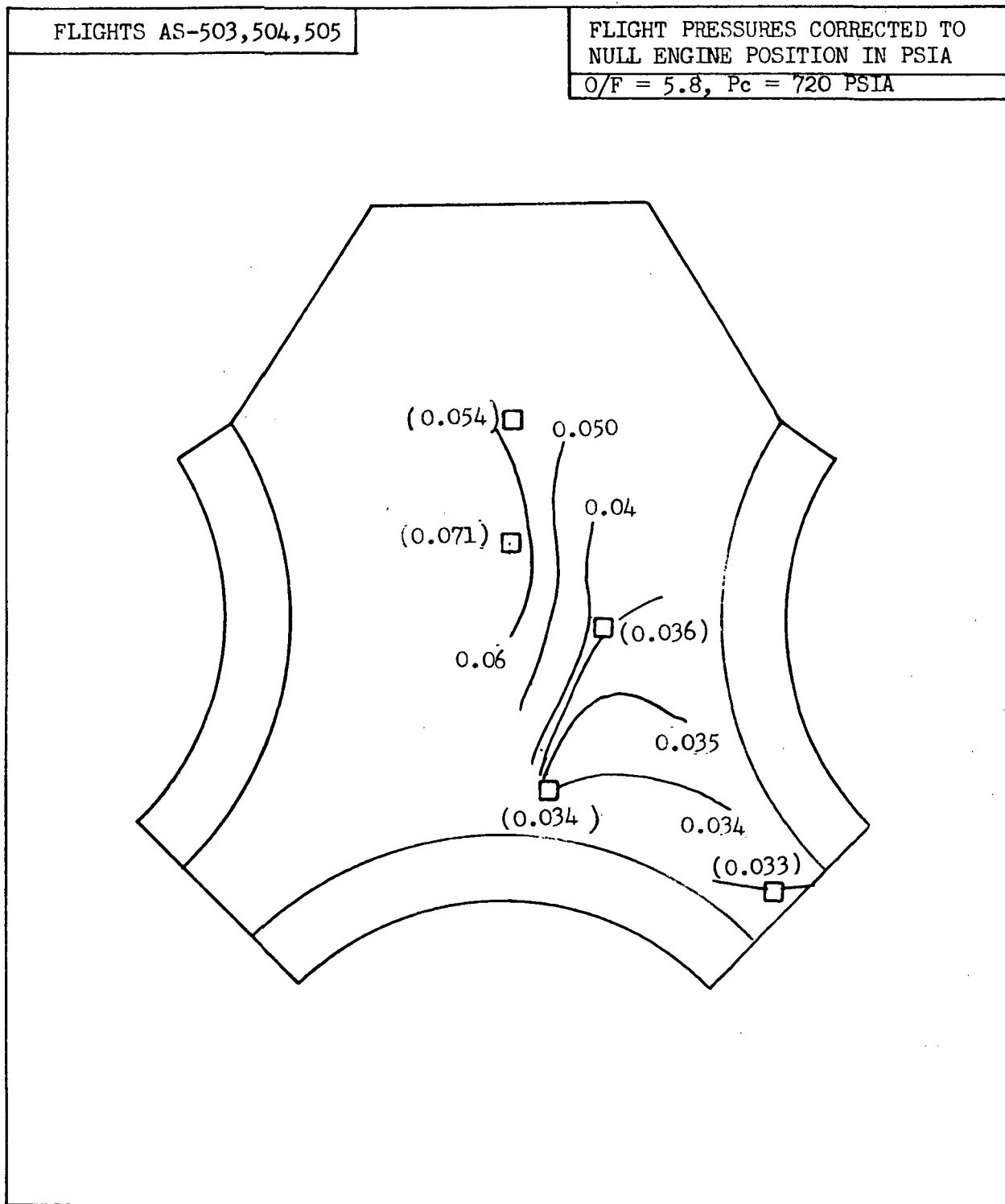
□ (0.036)

0.035

□

(0.034)   0.034

(0.033)
□

Figure 7.2.1-4   Heat Shield Nominal Flight Pressures With Interstage Off

Note that the flight and model pressures near the center engine are nearly equal and that the difference between them increases with radial distance along the heat shield.

These observed differences between the flight and model pressures could be due to the fact that during flight, the pressure outside the engine cluster is a function of the dynamic pressure of the external flow. Consequently, in the case of the flight data, the ambient pressure to which the reversed flow expands is higher than that in the case of the model test at the same altitude. The result is that at the edge of the heat shield, the flight impact pressures will be higher than the corresponding scale model values.

This reverse flow expansion model is substantiated to some degree by flight data which shows slightly decaying base pressures throughout the flight at most pressure transducer locations.

7.2.2 Effect of Interstage

The results of the model test program indicate that the interstage has a very strong effect on the thrust cone environment and an insignificant effect on the heat shield environment. Therefore, it is of interest to determine the corresponding effect from the flight data and compare with the test model results.

7.2.2.1 Heat Shield Heating Rates

A comparison of the flight heat shield convective heating rates, normalized to the model test conditions, is shown in Figure 7.2.2-1. It is seen that there is a noticeable increase of the heating rates after interstage separation at larger radial distances along the heat shield centerline. The increase, based on flight average values, is as much as 30 percent. However, it should be noted that there is a considerable scatter of the interstage-off heating rates as indicated in Figure 7.2.2-1, which means that this increase was not observed during all of the flights. Note that unlike the interstage-off values, the interstage-on heating rate gages show very little variation from flight to flight.

The model test data, while indicating a weak interstage effect, showed an opposite trend with the interstage-on heating rates being generally slightly higher than the interstage-off values as shown in Figure 5.5.1-1.

7.2.2.2 Thrust Cone Heating Rates

The effect of interstage on the flight thrust cone convective heating rates is shown in Figure 7.2.2-2. It is seen that the effect of interstage is to increase the thrust cone heating rates by as much as a factor of 10. The corresponding model results, presented in Figure 5.4.2-1, show that the interstage increases the thrust cone heating rates by a factor of 30 at some locations.

○ INTERSTAGE OFF
◇ INTERSTAGE ON

FLIGHTS AS-503,504,505
FLIGHT DATA NORMALIZED TO
O/F = 5.5
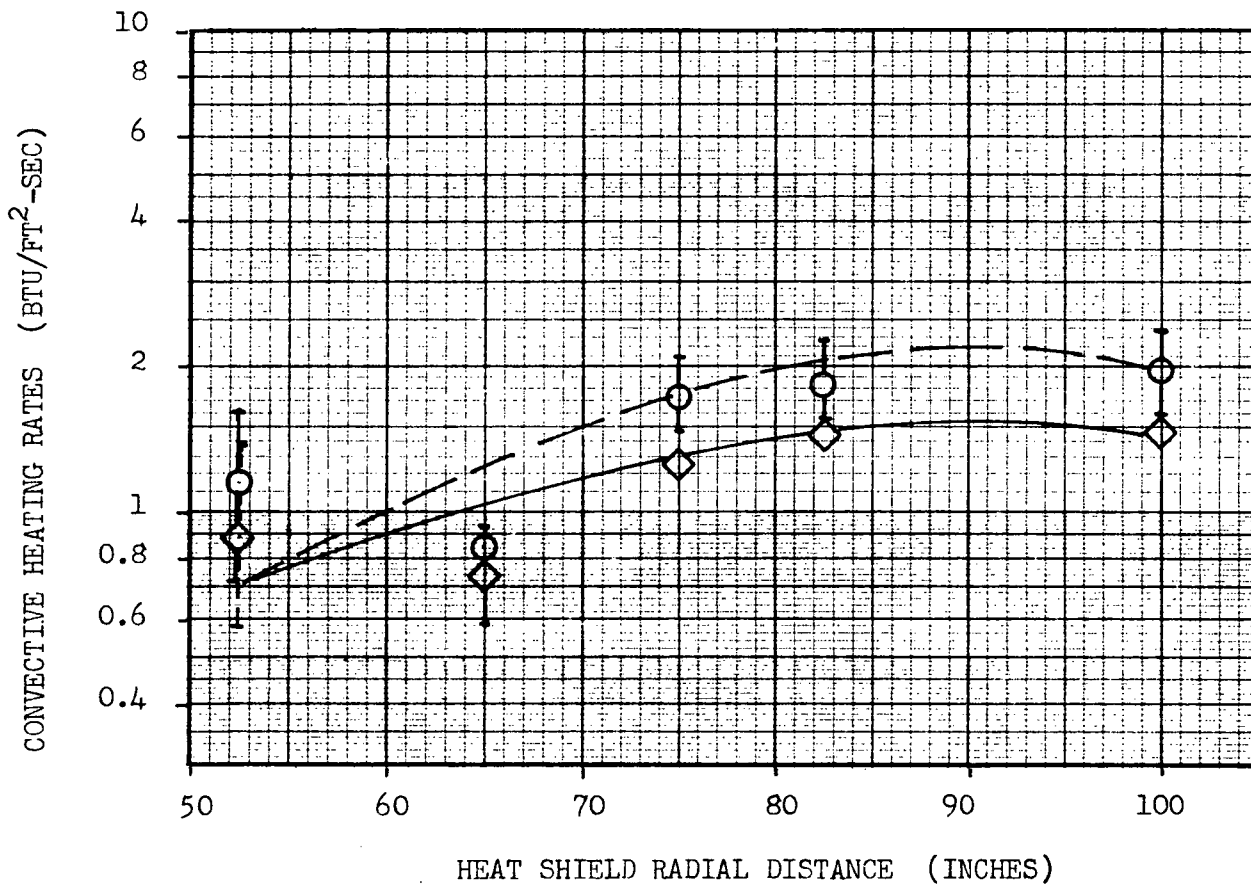Pc = 715 PSIA
SURFACE TEMPERATURE 72°F

Figure 7.2.2-1 Effect Of Interstage On Flight Heat Shield
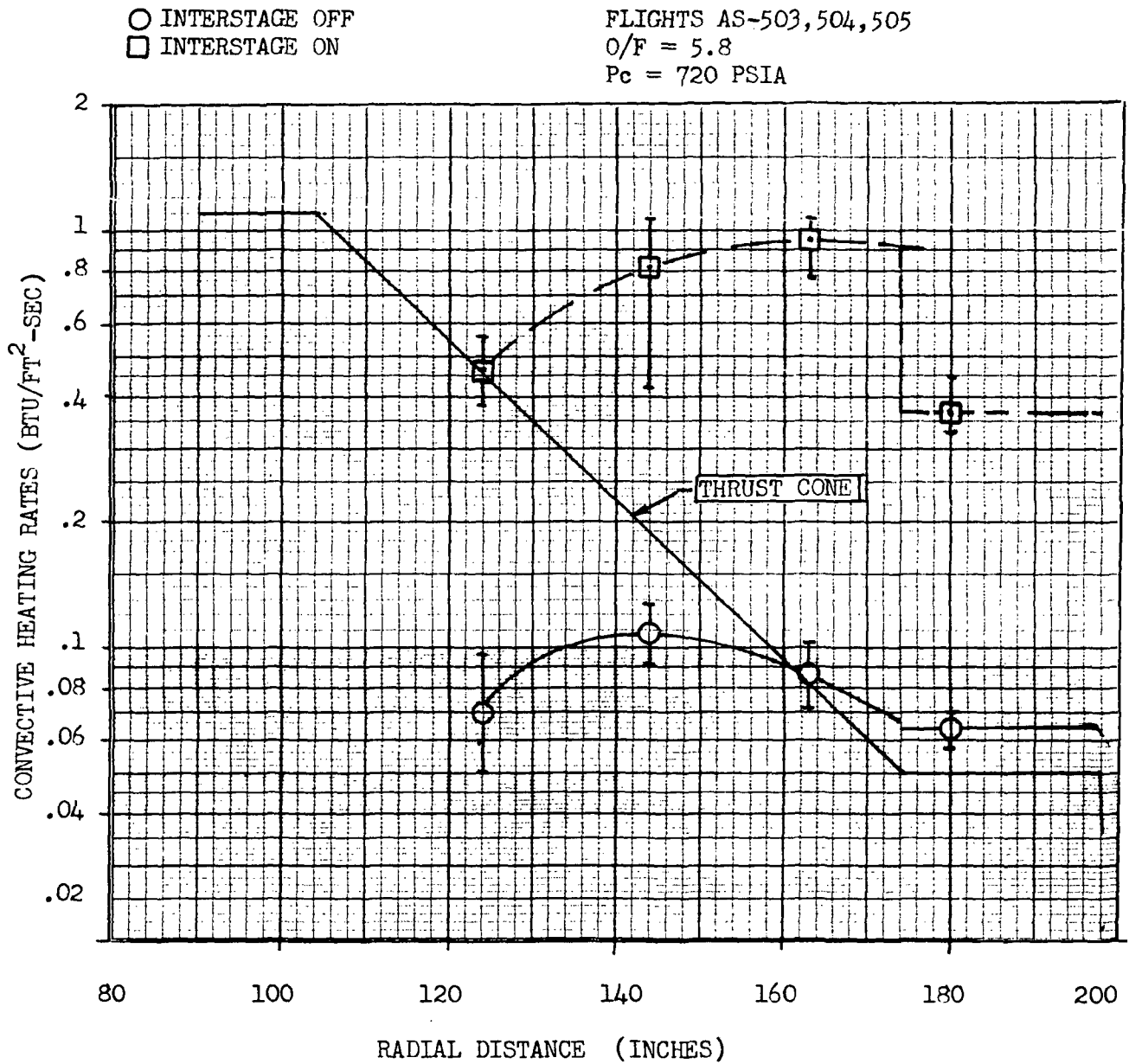Centerline Heating Rates

Figure 7.2.2-2 Effect Of Interstage On Thrust Cone Flight
Heating Rates

SD73-SA-0061

It should be noted that the interstage-off flight thrust cone heating rates are higher than the corresponding model values, while the interstage-on thrust cone flight heating rates are approximately the same as the model values.

7.2.2.3 Base Region Pressures

A comparison of the heat shield flight pressures with and without the interstage is shown in Table 7.2.2-1. It is seen that most of the interstage-off pressures are slightly lower than the corresponding interstage-on values, the average reduction being 20 percent. No heat shield pressures were recorded for the interstage-on case in the present test series; however, the CAL test data of Reference 8 indicates a 10 percent reduction of heat shield pressures after interstage separation.

One thrust cone pressure is recorded during flight and is listed in Table 7.2.2-1, where it is seen that with interstage on, the thrust cone pressure is approximately 60 percent of the average heat shield value. After interstage separation, the thrust cone pressure is extremely low, and most probably is equal to the pressure downstream of the oblique shock which turns the external flow ahead of the exhaust plumes.

7.2.3 Effect of Center Engine Cut-Off

At approximately 460 seconds flight time, the center engine is shut down and the flight is completed with the four outboard engines. This results in a change of the base region thermal environment. This flight procedure was introduced starting with flight AS-505, which was the last flight with full base region instrumentation. The data obtained on the AS-505 flight was analyzed to determine the effect of CECO on the base region thermal environment, and the results are discussed in the following sections.

7.2.3.1 Gas Recovery Temperature

A summary of the flight gas recovery temperature results is presented in Table 7.2.1-1, where it is seen that the recovery temperature after CECO increases by approximately 200 F. This is in good agreement with the analytical results of section 6.0, where it was determined that the stagnation temperature of the reversed flow for the far-engine-spacing case (corresponding to CECO) is about 130 F higher than for the close-engine-spacing case (Table 6-3, Case VI b). No model test data are available for comparison with these results.

7.2.3.2 Heat Shield Heating Rates

A comparison of the heat shield centerline heating rates prior to and after CECO for flight AS-505 is shown in Figure 7.2.3-1. There is an increase in convective heating rates at most gage locations; the average increase for all the heat shield gages being 45%. Taking into account the gas recovery temperature increase, this corresponds to a 19 percent increase of the average convective heat transfer coefficient.

Rev July 6, 1973

TABLE 7.2.2-1

Effect of Interstage on Base Region Pressures

TRANSDUCER	PRESSURE (PSIA)		P_{off}/P_{on}
	P_{on}	P_{off}	
D 094-206	0.074	0.067	0.905
D 095-206	0.080	0.074	0.925
D 157-206	0.051	0.033	0.647
D 158-206	0.051	0.036	0.706
D 161-206	0.049	0.034	0.694
D 162-206	0.057	0.054	0.947
D 187-206*	0.034	0.004	0.117

* Thrust Cone Pressure

O PRIOR TO CECO
□ AFTER CECO

AS-505 FLIGHT DATA NORMALIZED TO MODEL CONDITIONS
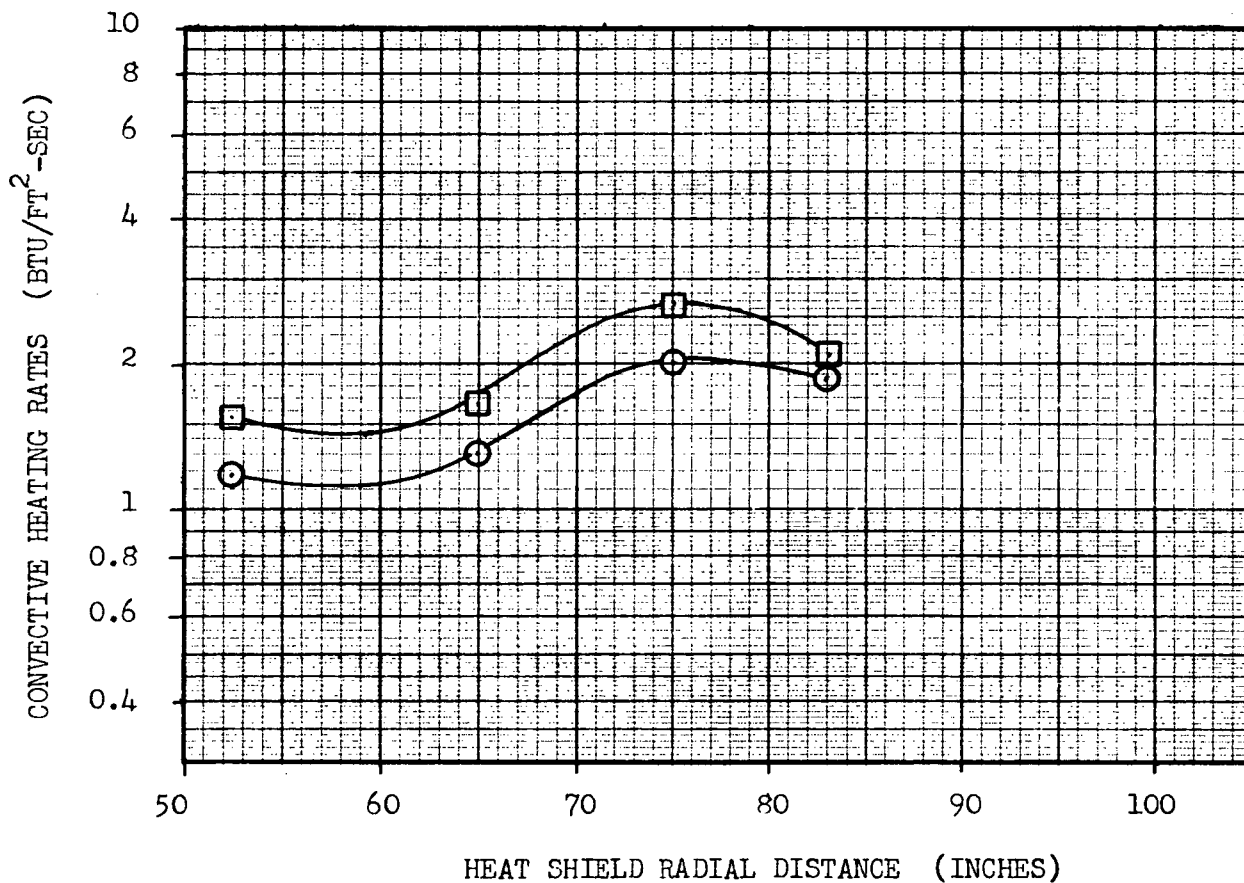O/F = 5.5   SURFACE TEMPERATURE 72°F
Pc = 715 PSIA

Figure 7.2.3-1   Effect Of CECO On Heat Shield Centerline
Heating Rates During Flight

These flight data CECO heating rate results are not substantiated by the analytical results of Section 6.0, which show that the effect of CECO increases the gas recovery temperature and decreases the heating rate parameter based on the reversed flow stagnation pressure and temperature. However, it should be pointed out that, while the analytical results show a decrease in reverse flow stagnation pressure, an increase in the reverse flow mass results; therefore, an alternate definition of the heating rate parameter based on mass flow velocity (ρu) would indicate that the heating rates after CECO increase by 35 percent which is in good agreement with the flight results.

7.2.3.3 Thrust Cone Heating Rates

A comparison of the thrust cone heating rates just after and just prior to CECO is shown in Table 7.2.3-1. It is seen that there is a very wide variation of the CECO effect for the different heat transfer gages, which may be in part due to the difficulty of accurately measuring the very low heating rates experienced in this region. However, on the average, the thrust cone heating rates show a 45 percent increase of the convective heating rates after CECO, which is in agreement with the heat shield results.

Table 7.2.3-1

Effect of CECO on Thrust Cone Heating Rates (Flight AS-505)

GAGE ID	Convective Heating Rates (BTU/Ft^2-sec)		q_{+CECO}/q_{-CECO}
	q_{-CECO}	q_{+CECO}	
C666-206	0.088	0.131	1.45
C688-206	0.059	0.099	1.54
C701-206	0.030	0.052	1.75
C821-206	0.050	0.050	1.10
			Average = 1.45

SD73-SA-0061

7.2.3.4 Base Region Pressures

A comparison of the heat shield pressures just prior to and just after CECO is shown in Table 7.2.3-2 where it is seen that the effect of center engine cut-off is to reduce the heat shield pressures by 8 to 25 percent; the average reduction for all the transducers being 18 percent. There is no noticeable effect on the thrust cone pressures.

The analytical results of Section 6.0 also indicate a pressure drop after center engine cut-off; however, the indicated reduction is larger than experienced in flight. For example, from Table 6-3, Case VI b, (the full scale engine with TPE injection) the ratio of the stagnation pressures of the reversed flow after CECO (high engine spacing) to that prior to CECO (average of the low and high engine spacing) is 0.60; somewhat lower than the flight average value of 0.82

TABLE 7.2.3-2

Effect of CECO on Base Region Pressures (Flight AS-505)

GAGE	PRESSURE (PSIA)		$\dfrac{P_{+CECO}}{P_{-CECO}}$
	P_{-CECO}	P_{+CECO}	
D094-206	0.060	0.045	0.75
D095-206	0.070	0.056	0.80
D157-206	0.026	0.024	0.92
D158-206	0.028	0.021	0.75
D161-206	0.020	0.018	0.90
D162-206	0.048	0.039	0.82
D187-206*	0.002	0.002	
			Average = 0.82

* Thrust Cone Pressure

7.2.4   Effect of PMR Shift

At about 60 seconds prior to S-II engine shut down, the J-2 engine operating conditions are changed from O/F = 5.8, P_c = 720 psia to O/F = 4.5 and P_c = 550 psia due to trajectory optimization requirements. The resulting changes of the base region environment observed during flight are compared with scale model test results and analytical predictions in the following sections.

7.2.4.1 Gas Recovery Temperature

The effect of PMR shift on base region gas recovery temperature is shown in Figure 7.2.4-1 together with the analytical results, corresponding to the scale model test conditions and the S-II model test results of Reference 1 for comparison. It is seen that the AS-503 and AS-504 flight data is in good agreement with the model test data of Reference 1 but shows a much stronger chamber pressure dependence than that indicated by the analytical results.

The AS-505 flight recovery temperature data, with the center-engine-out configuration, shows a much stronger variation with mixture ratio, chamber pressure change than the five engine data of flights AS-503 and AS-504. No full scale engine analytical results are available to substantiate this difference between the four and five engine flight data.

7.2.4.2 Heat Shield Heating Rates

Inspection of the normalized flight heating rates presented in Table 7.2-4 prior to and after PMR shift shows that there is considerable variation of the PMR shift effect in the flight results. This is especially true for the gages indicating low heating rates. Part of this data scatter may be due to some of the simplifying assumptions used in normalizing flight data. Examples of this are the use of the co-planar gimbal results for engine deflection correction and the constant value of the boundary layer starting length for all gages in the temperature mismatch correction.

Consequently, in order to obtain an estimate of the PMR shift effect, it was necessary to average the heating rates of all gages for each flight. The results are presented in Figure 7.2.4-2 together with scale model and analytical data trends for comparison.

It is seen that an appreciable variation of the PMR effect exists between the heating rates of the three flights, flight AS-505 (with center engine out) showing the stronger variation which is at least consistent with the gas recovery temperature results with Figure 7.2.4-1.

7.2.4.3 Thrust Cone Heating Rates

The effect of PMR shift on thrust cone heating rates is shown on Figure 7.2.4-3 together with the experimental trend established from the
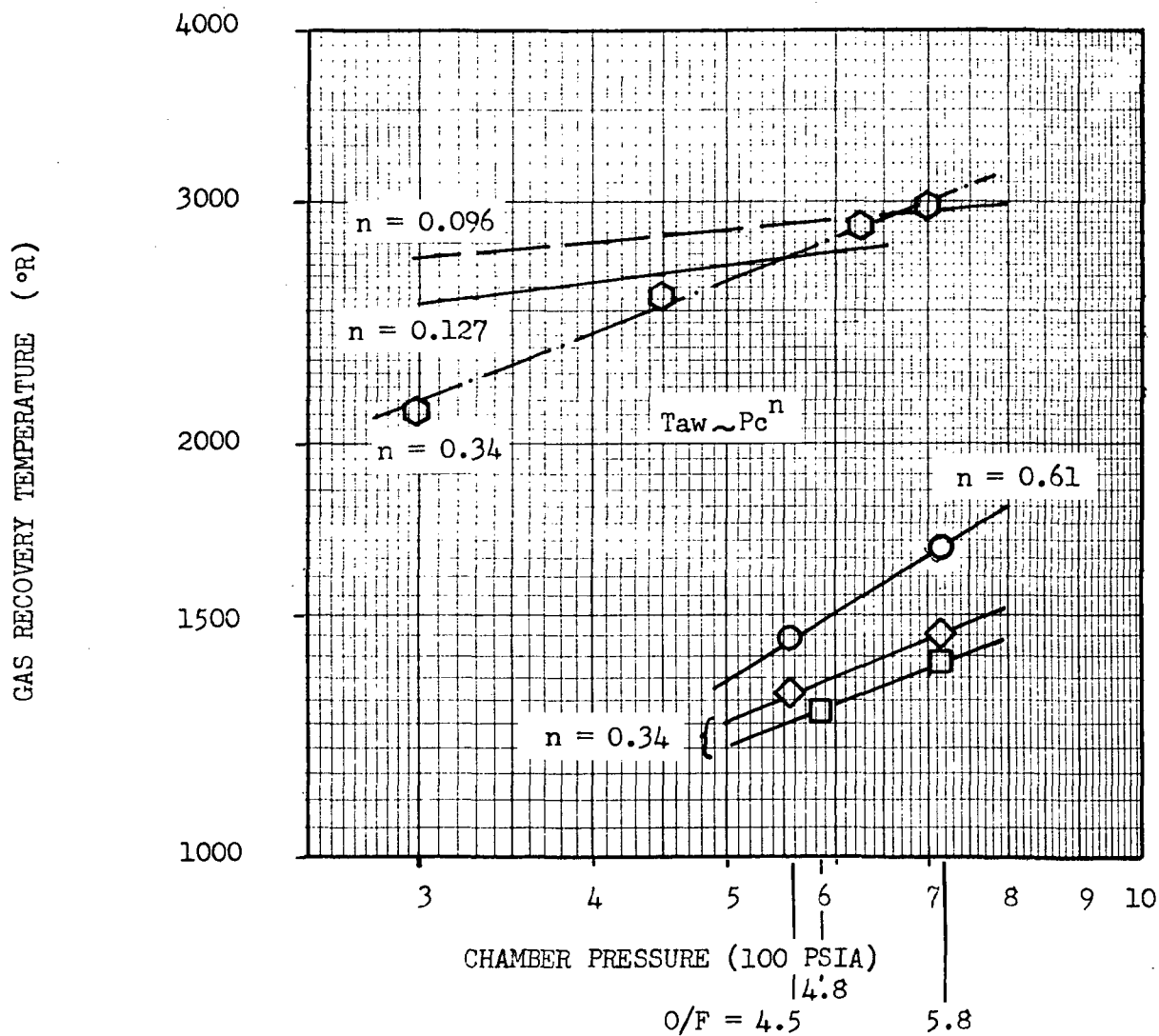
Figure 7.2.4-1 Effect Of PMR Shift On Base Region
Gas Recovery Temperature
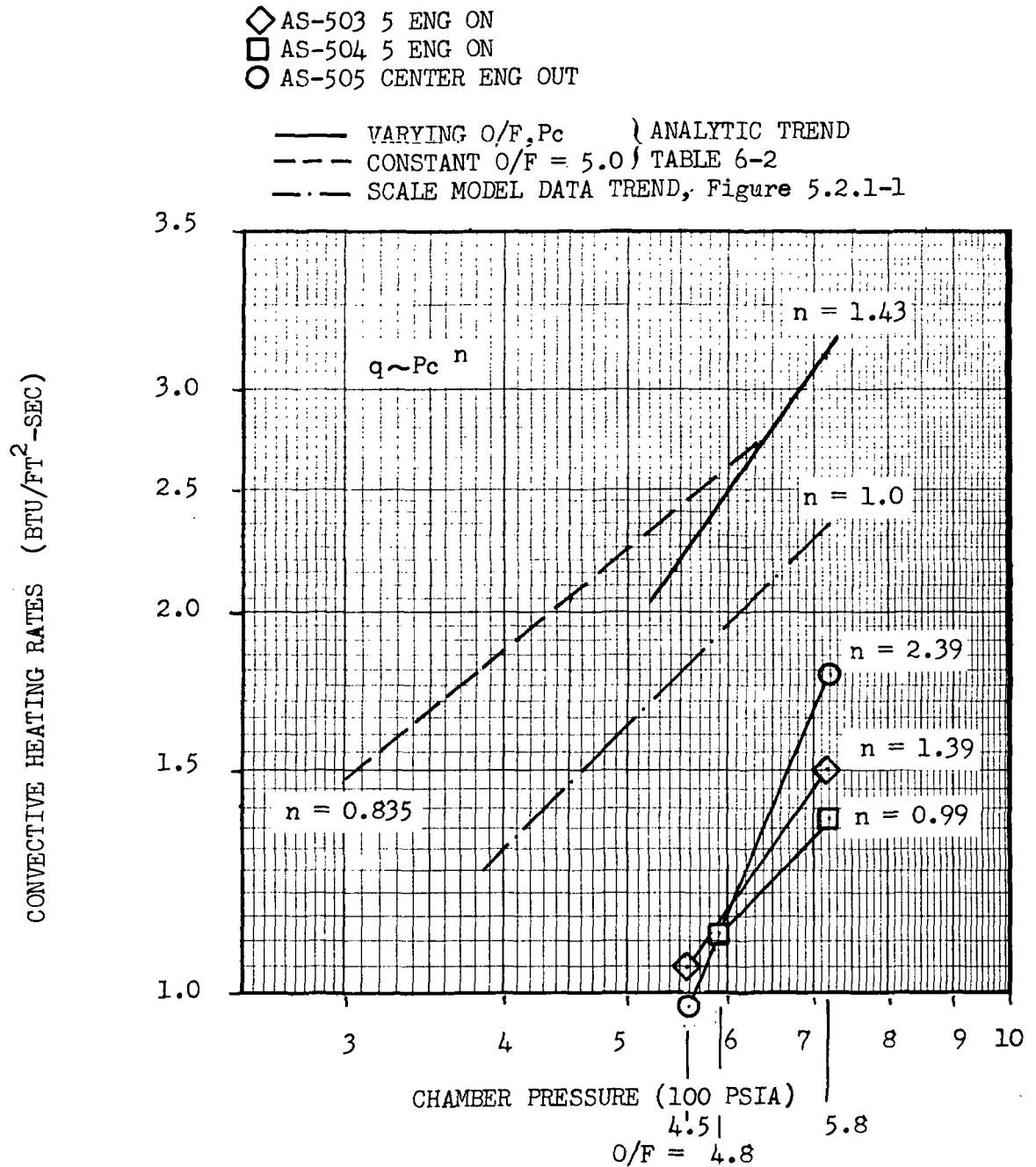
Figure 7.2.4-2 Effect Of PMR Shift On Heat Shield
Heating Rates

Space Division
North American Rockwell

◇ AS-503 5 ENG ON
□ AS-504 5 ENG ON
○ AS-505 CENTER ENG OUT

— · — MODEL DATA TREND
COSTANT O/F = 5.0, Figure 5.3.2-1
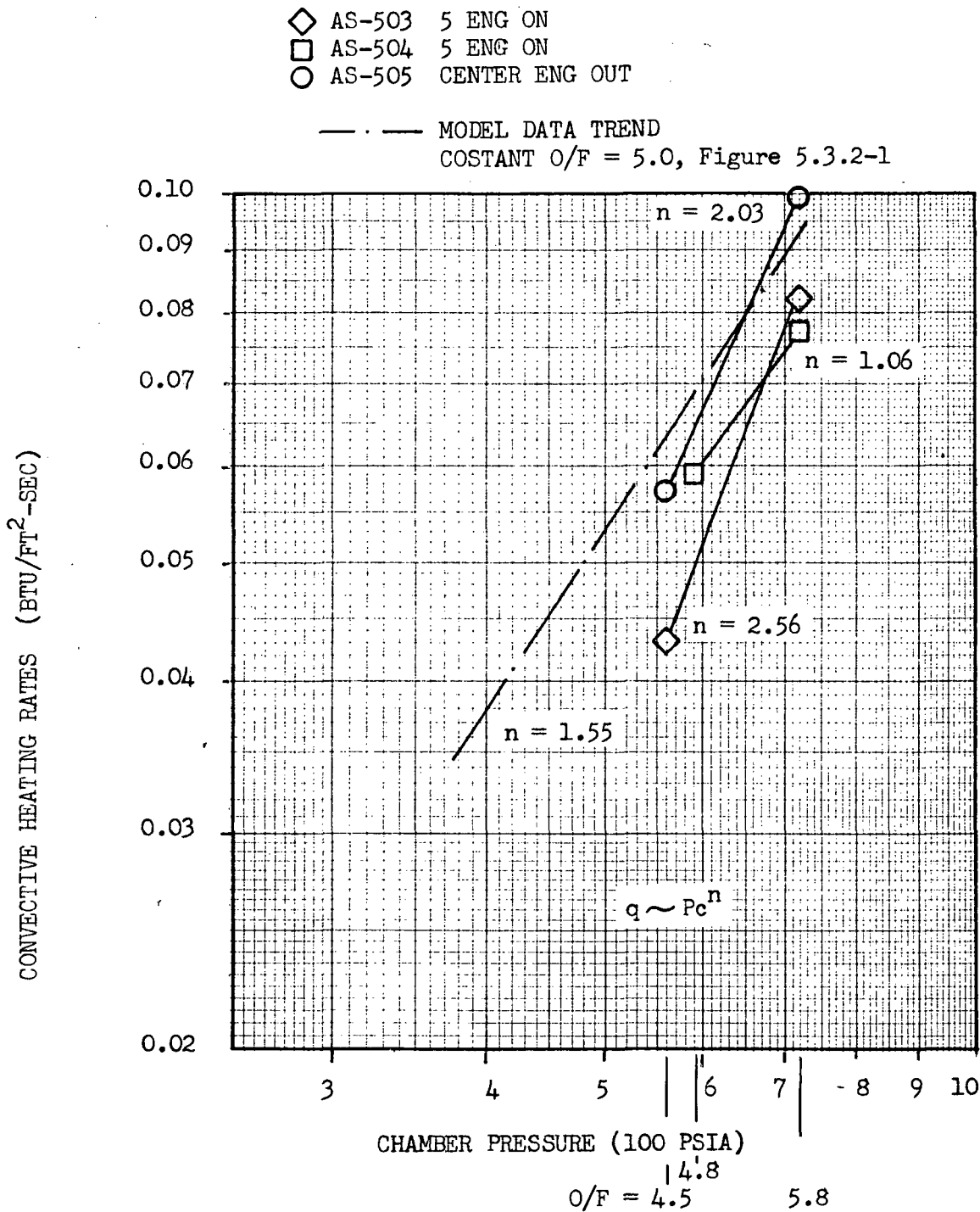
Figure 7.2.4-3 Effect Of PMR Shift On Thrust Cone
Heating Rates

model test data. It is seen that the flight data trend is in reasonably good agreement with the model results, although appreciable variation exists between the data of the three flights shown.

7.2.4.4 Heat Shield Pressures

The effect of PMR shift on heat shield flight pressures is presented in Figure 7.2.4-4 together with analytically predicted trends as well as the empirical trend based on scale model test results.

It is seen that the flight data shows a stronger dependence on PMR, chamber pressure change than indicated by both analytical and scale model test results.

SD73-SA-0061

◇ AS-503   5 ENG ON
□ AS-504   5 ENG ON
○ AS-505   CENTER ENG OUT

— — — VARYING O/F,Pc   } ANALYTIC TREND
———— CONSTANT O/F = 5.0 } Table 6-2
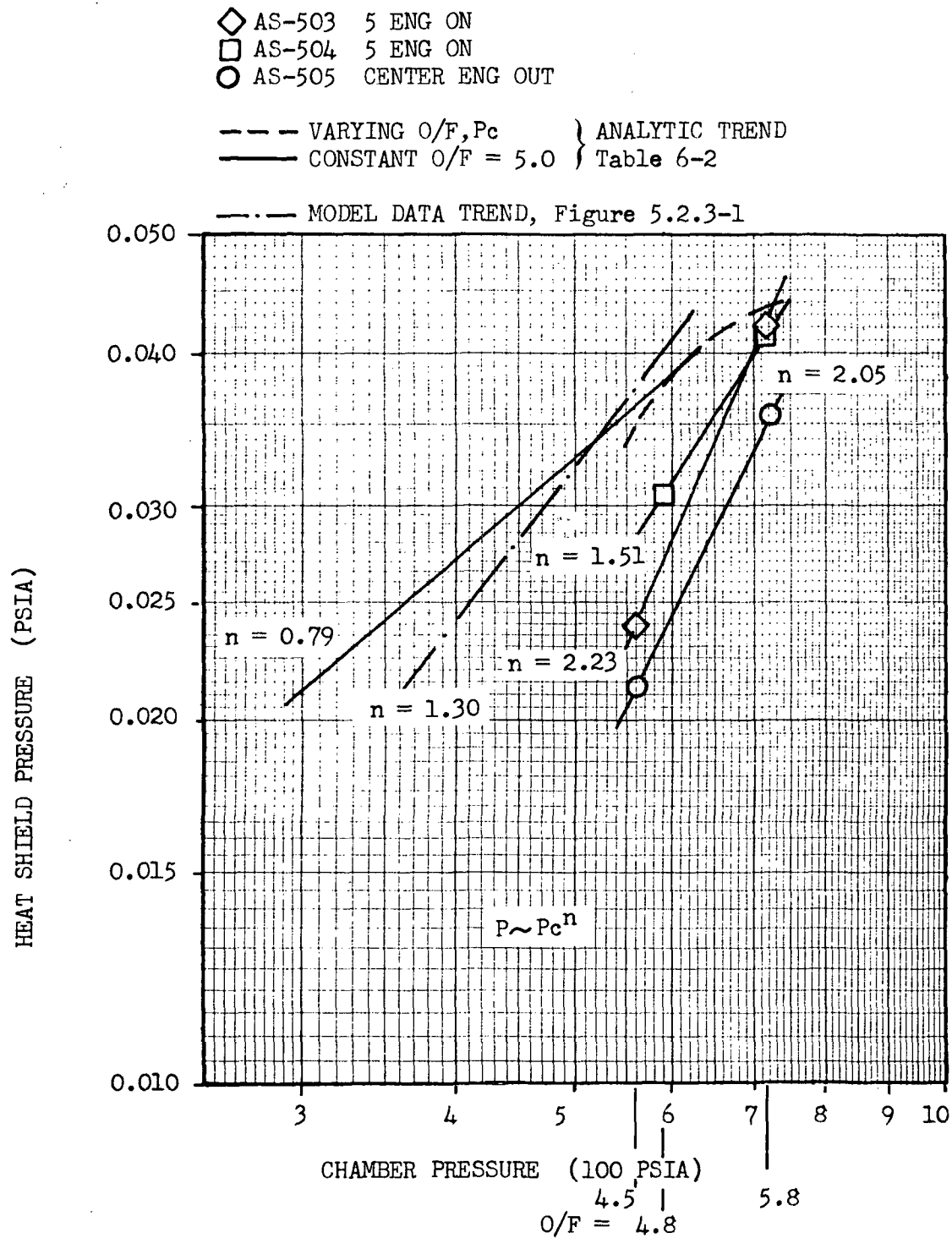
—·— MODEL DATA TREND, Figure 5.2.3-1

Figure 7.2.4-4   Effect Of PMR Shift On Heat Shield
Pressures

8.0 CONCLUSIONS AND RECOMMENDATIONS

The results of these tests demonstrated again the feasibility of using the short-duration test technique for determining the base region environment of multi-engine vehicle configurations. The scale model test program was successful in providing S-II Stage base region thermal environment design data.

The results of the present test program and the CAL program were in agreement. The effect of extending the test time to 6-7 milliseconds (from 3-4 milliseconds available during the CAL program) was determined to be minimal. The one notable difference was the higher interstage-on thrust cone pressures measured during the present test program.

Flight and scale model heating rate distributions were in agreement. However, the model heat shield heating rate level was 2.4 times the flight value. TPE injection was determined to be the primary reason for the reduction of full scale vehicle heating rates. Flight heat shield pressures were determined to be double the model values; the difference was most probably due to the dynamic pressure of the external flow present during full scale flight only. The flight data was found to exhibit a larger degree of scatter which could not be accounted for by engine operating effects, engine misalignments, precant, or the steady state engine deflection effects.

The analytical procedures formulated in this report successfully predict the effects of engine operating conditions, and to a lesser degree, engine gimballing and engine spacing. TPE injection, scaling, and nozzle spacing were found to have a very pronounced effect on the reversed flow properties. The same methodology could be applied to the analysis of configurations other than that of the S-II stage. Whereas the one dimensional reverse flow model predicts the overall thermal environment of the base region, spatial distributions could be obtained by extension of the present methodology to include the two dimensional reverse flow field as indicated in Section 6.1.5.1.

In conjunction with further development of the anlytical model, it is desirable that future model tests provide heating rate and gas recovery temperature data for large range of co-planar engine deflections. Such data, not available at the present time, would be very useful in the development and verification of the analytical model.

SD73-SA-0061

REFERENCES

1. Rickard, W. D.: <u>High Altitude Investigations on the Saturn S-II Stage Using Short-Duration Techniques Part I - Parameter Studies</u>, CAL Report No. HM-1510-Y-17 (I), (April 1965).

2. Bird K. D., Matthis, C. L. and Reece, J. W.: <u>The Application of Short-Duration Techniques to the Experimental Study of Base Heating Part I - High Altitude Testing Technique and Experimental Results for a 4-Engine Rocket Configuration</u>, CAL Report HM-1510-Y-1 (I), (April 1962).

3. Rickard W. D., and Dennis, R. J.: <u>High Altitude Base Heating and Pressure Distribution Investigations on the Saturn S-IV 6-Engine Rocket Using Short-Duration Techniques</u>, CAL Report No. HM-1510-Y-3, (June 1963).

4. Sergeant, R. J.: <u>The Application of Short-Duration Techniques to the Experimental Study of Base Heating Part II: A Study of Reynolds Number and Temperature Effects on Base Heating for a Four-Engine Hot Rocket Configuration Operating at High-Altitude</u>, CAL Report No. HM-1510-Y-1 (II) (April 1965).

5. Gwin, Hal S.: <u>Impulse Base Flow Facility Technical Handbook</u>, MSFC Technical Memorandum X-53716, (March 13, 1968).

6. Reardon, J. E., Hand, A. E., McKay, G. B. and Fuller, C. E.: <u>Short Duration Base Pressure and Heat Transfer Test of 1/25 Scale, 3-Engine, J-2 Nozzle Model</u>, Hayes International Corp. Engineering Report No. 1551, (November 1968).

7. Hendershot, K. C.: <u>Flow Metering Venturis for S-II and S-IV Base Heating Models</u>, CAL Internal Memo No. AHRD-PS-64-3, (June 1964).

8. Rickard, W. D.: <u>High Altitude Investigations on the Saturn S-II Stage Using Short-Duration Techniques Part II-Prototype Base Environment</u>, CAL Report No. HM-1510-Y-17 (II), (April 1965).

9. Reardon, J. E.: <u>Prediction of Radiation from Rocket Exhaust Gases</u>, AIAA Paper No. 70-841, 5th Thermophysics Conference, Los Angeles (June 29, 1970)

10. Vida, R. L.: <u>Transient Surface Temperature Measurements</u>, CAL Report No. 114, (March 1962)

Rev July 6, 1973

REFERENCES

11. Woodruff, L. W., Hearne, L. F., and Keliher, T. J.:
    Interpretation of Asymptotic Calorimeter Measurements
    AIAA Journal Vol. 5, (1967) pp 795-797.

12. Skinner, G. T.: Analog Heat Transfer Network to Convert
    Surface Temperature to Heat Flux, CAL Report No. CAL-100,
    (February 1960).

13. Richardson, P. D.: Heat and Mass Transfer in Separated
    Flows Chemical Engineering Science, Pergaman Press, Vol. 18,
    (1963) pp 149-155.

14. Rocket Exhaust Plume Computer Program Improvement, Volume
    IV-Final Report. LMSC/HREC D16220-IV-A, Rev. A (January 1972).

15. Waiter, S. A. and LeBlanc, L. P.: Solution of the Equations
    of the Compressible Boundary Layer (Laminar Transition
    Turbulent) by an Implicit Finite Difference Technique,
    North American Rockwell, Space Division Report SD 69-484
    (September 1969)

16. Zeleznik, Frank J. and Gordon, Sanford: A General IBM 704
    or 7090 Computer Program for Computation of Chemical
    Equilibrium Compositions, Rocket Performance and Chapman-
    Jouget Detonations, NASA TN D-1454, (October 1962).

17. Adler, B. K. and Anderson, R. B.: Transport Properties of
    Polar and Polyatomic Gas Mixtures (1J 956) North American
    Aviation, Space Division Report SID 67-490 (June 1967).

18. Svehla, Roger A.: Thermodynamic and Transport Properties
    for the Hydrogen Oxygen System, NASA Report SP-3011 (1964).

19. Schlichting, Dr. Hermann: Boundary Layer Theory, 6th Ed.
    McGraw-Hill, New York (1968), pp. 687-8.

20. Weinbaum, Sheldon: Rapid Expansion of a Supersonic Boundary
    Layer and its Application to the Near Wake. AIAA J.V.4,
    (February 1966) pp 217-226.

21. Boynton, Frederick P.: Exhaust Plumes from Nozzles with
    Wall Boundary Layers, J. Spacecraft V.5, (October 1968)
    pp 1143-47.

REFERENCES

22. Kutler, Paul and Lomax, Harvard: A Systematic Development of the Hypersonic Flow Fields Over and Behind Wings and Wing-Body Configurations Using a Shock-Capturing Finite-Difference Approach. AIAA Paper No. 71-99, 9th Aerospace Sciences Meeting, New York, (January 27, 1971).

23. Korst, H. H.: A Theory for Base Pressures in Transonic and Supersonic Flow. J. Applied Math., (December 1956) pp 593-600.

24. Chapman, D. R., et. al.: Investigation of Separated Flows in Supersonic and Subsonic Streams with Emphasis on the Effect of Transition, NACA Report 1356 (1958).

25. French, E. P. and Korkan, K. D.: Quantitative Models of Base Flow for Multiple Engine Vehicles. North American Rockwell, Space Division Report SD 68-759 (December 1968).

26. Kreith, Frank: Principles of Heat Transfer, Scranton: International Text Book Company, (1961) pp 370.

27. Eckert, E. R. G.: Heat and Mass Transfer, New York: McGraw-Hill, (1959) pp 242.

SD73-SA-0061